Dissertation

Von der Universität Bayreuth
zur Erlangung des Grades eines
Doktors der Naturwissenschaften (Dr. rer. nat.)
genehmigte Abhandlung

Understanding the impact of processing and nanostructure on lead halide perovskite optoelectronic devices

---

von
Simon Biberger
aus Ingolstadt, Deutschland

Gutachter:

Prof. Dr. Anna Köhler **(1. Gutachter)**	Experimentalphysik II Universität Bayreuth 95440 Bayreuth, Deutschland
Prof. Dr. Georg Herink **(2. Gutachter)**	Experimentalphysik VIII Universität Bayreuth 95440 Bayreuth, Deutschland

Tag der Einreichung: 30.04.2024

Tag des Kolloquiums: 11.10.2024

1 Deutsche Zusammenfassung

Das Hauptziel der Arbeit ist es, die Auswirkungen der Verarbeitung und der daraus resultierenden Nanostruktur auf die optoelektronischen Eigenschaften von Bleihalogenid-Perowskit-Schichten und Ladungsextraktionsschichten zu verstehen, die üblicherweise in optoelektronischen Bauelementen auf der Basis von Bleihalogenid-Perowskiten verwendet werden. Die Dissertation behandelt dieses Thema in sechs Kapiteln, die in drei Blöcke unterteilt sind. Diese drei Themenblöcke und die entsprechenden Artikel sind auch in der Abbildung 1.1 dargestellt.

Figure 1.1: Überblick über die verschiedenen Forschungsprojekte und die entsprechenden Publikationen.

Der erste Block (blau, Publikation 1 + 2, siehe Kapitel 9 + 10) befasst sich mit der Verarbeitung von Metallhalogenid-Perowskiten in Lösung mittels Spin-Coating, der aktuell am häufigsten eingesetzten Verarbeitungstechnik zur Herstellung von Perowskit-Schichten im Labormaßstab. Im ersten Artikel *'How*

the ionic liquid BMIMBF$_4$ influences the formation and optoelectronic properties of MAPbI$_3$ films' wurde der Einfluss einer ionischen Flüssigkeit auf die Filmbildung und die endgültigen optoelektronischen Eigenschaften von $MAPbI_3$ während des einstufigen Spin-Coatings und des Solvent-Engineering-Ansatzes mittels optischer multi-modaler In-situ-Spektroskopie untersucht. Die aus dieser Studie gewonnenen Einsichten und Erkenntnisse haben die im zweiten Artikel *'Improved control of perovskite thin film fabrication via reactive spin coating and real time In-Situ feedback'* vorgestellten Untersuchungen direkt inspiriert und initiiert. In dieser Arbeit wurde der experimentelle In-Situ-Aufbau, der in Publikation 1 verwendet wurde, modifiziert, um ein Feedback aus den optischen Spektren während der Verarbeitung eines $MAPbI_3$ -Dünnfilms zu erhalten. Auf der Grundlage dieses Echtzeit-Feedbacks wurde erstmals die Perowskit-Kristallisation in Abhängigkeit von systeminternen Parametern und nicht von systemexternen Parametern induziert. Dieser reaktive Spin-Coating-Ansatz ermöglicht die Herstellung von Perowskit-Dünnschichten mit gleichbleibender Qualität und gleichbleibenden optoelektronischen Eigenschaften ohne Optimierungsschritte bei Variation der externen Parameter.

Der zweite Themenblock (grün, Publikation 3, 4, 5, siehe Kapitel 11, 12, 13) meiner Dissertation befasst sich mit der lösungsmittelfreien alternativen Verarbeitung von Bleihalogenidperowskit zur Entkopplung von Synthese und Filmbildung. Dabei werden bereits synthetisierte Perowskit-Pulver verwendet, um (dünne/dicke) Perowskit-Schichten zu herzustellen. In Publikation 3 *'First of Their Kind: Solar Cells with a Dry-Processed Perovskite Absorber Layer via Powder Aerosol Deposition and Hot-Pressing'* wurden $MAPbI_3$-Absorberschichten mittels Pulver-Aerosol-Abscheidung (PAD) und einem optionalen Heißpressschritt verarbeitet. In dieser Arbeit konnten erstmals voll funktionsfähige trocken prozessierte Perowskit-Solarzellen mit Wirkungsgraden bis zu 6% realisiert werden. Der gesamte Solarzellenstapel wurde Schicht für Schicht untersucht, um Potenziale zur Verbesserung der optoelektronischen Funktionalität jeder einzelnen Schicht und des Stapels als Ganzes zu identifizieren. Eine weitere detaillierte Studie mit besonderem Schwerpunkt auf den Auswirkungen des (Heiß-)Pressens auf die optoelektronischen Eigenschaften von PAD $MAPbI_3$-Filmen wurde in Artikel 4 *'Orientation and Grain Size in MAPbI$_3$ Thin Films: Influence on Phase Transition, Disorder, and Defects'* durchgeführt. In dieser Veröffentlichung wurde dargestellt, wie kleine Unterschiede in der Morphologie (d.h. kristallographische Orientierung oder Korngröße) optoelektronische und strukturelle Eigenschaften, insbesondere Phasenübergang, Defekte und energetische Unordnung, beeinflussen. Ähnliche Untersuchungen zum Zusammenhang zwischen kristallographischen Veränderungen und den daraus resultierenden optoelektronischen Eigenschaften wurden in der letzten Studie - Publikation 5, *'Structural Diversity in Layered Hybrid Perovskites, A_2PbBr_4 or $AA'PbBr_4$, 'Templated by Small Disc-Shaped Amines'* - dieses Blocks durchgeführt. Hier wurden die Spacermoleküle systematisch variiert, um 2D-Perowskit-Schichten mit unterschiedlichen Korrugationslängen und Kristallstrukturen zu erzeugen, und die entsprechenden optoelektronischen Eigenschaften wurden für eine mögliche Anwendung in einer Weißlicht-LED charakterisiert.

Der dritte Block (gelb, Publikation 6, siehe Kapitel 14) und die letzte Studie *'Intricacies and Mechanism of p-Doping Spiro-MeOTAD Using Cu$(TFSI)_2$'* innerhalb dieser Arbeit knüpft an die lösungsmittelfreie Prozessierung an, nur jetzt nicht mehr einer Perowskitschicht, sondern einer Ladungsextraktionsschicht

für Bleihalogenid-Perowskit-basierte Solarzellen. Der Schwerpunkt dieses Projekts lag auf dem Verständnis des genauen Dotierungsmechanismus eines aufgedampften Lochtransportmaterials mit einem mitverdampften Dotierstoff und der Auswirkung der Dotierstoffkonzentration auf die optoelektronischen Eigenschaften der entsprechenden Filme. Mit Hilfe dieses Co-Verdampfungsansatzes könnte man den Bedarf an Lösungsmitteln bei der Herstellung von Perowskit-Solarzellen weiter reduzieren.

2 English Abstract

The main aim of the thesis is to understand the impact of the processing and the resulting nanostructure on the optoelectronic properties of lead halide perovskite layers and charge extraction layers, which are commonly used in lead halide perovskite-based optoelectronic devices. The thesis addresses this issue in six chapters, which shall be grouped into three blocks. These three research areas and the corresponding articles are also shown in Figure 2.1.

Figure 2.1: Overview of the different research projects and the corresponding research articles. The projects can be divided into three research areas.

The first block (blue, Publication 1 + 2, see chapters 9 + 10) deals with the solution processing of metal halide perovskites via spin coating, which is the state-of-the-art processing technique to fabricate perovskite layers on a lab scale. In the first article, *'How the ionic liquid $BMIMBF_4$ influences the formation and optoelectronic properties of $MAPbI_3$ films'*, the impact of an ionic liquid on the film formation

and the final optoelectronic properties of $MAPbI_3$ during the one-step spin coating and the solvent engineering approach was investigated via optical multi-modal in-situ spectroscopy. The insights and findings gained from this study directly inspired and initiated the investigations presented in the second article 'Improved control of perovskite thin film fabrication via reactive spin coating and real time in-situ feedback'. In this work, the experimental in-situ setup, which was used in Publication 1, was modified to obtain feedback from the optical spectra during the processing of a $MAPbI_3$ thin film. Based on this real-time feedback, the perovskite crystallite was induced depending on system-internal parameters rather than system-external ones. This reactive spin coating approach allows to fabricate perovskite thin films with consistent quality and optoelectronic properties without any optimization steps while varying external parameters.

The second topic block (green, Publication 3, 4, 5, see chapters 11, 12, 13) of my thesis will be about solvent-free alternative processing of lead halide perovskite to decouple the synthesis and the film formation. Here, already synthesized perovskite powders are used to process (thin/thick) perovskite layers. In Publication 3, *'First of Their Kind: Solar Cells with a Dry-Processed Perovskite Absorber Layer via Powder Aerosol Deposition and Hot-Pressing'*, $MAPbI_3$ absorber layers were processed via powder aerosol deposition (PAD) and an optional hot-pressing step. For the first time, fully functioning dry-processed perovskite solar cells with efficiencies up to 6% could be realized in this work. Further, the whole solar cell stack was investigated layer-by-layer to identify potentials for improvement of the optoelectronic performance of each layer and the stack as a whole. An additional in-depth study with a particular focus on the impact of the (hot-)pressing step on the optoelectronic properties of PAD $MAPbI_3$ film was published in article 4, *'Orientation and Grain Size in $MAPbI_3$ Thin Films: Influence on Phase Transition, Disorder, and Defects'*. This publication presented how small differences in morphology (i.e. crystallographic orientation or grain size) impacts optoelectronic as well as structural properties, in particular phase transition, defects, and energetic disorder. Similar investigations on the relationship between crystallographic changes and the resulting optoelectronic properties were conducted on pressed perovskite pellets in the last study – Publication 5, *'Structural Diversity in Layered Hybrid Perovskites, A_2PbBr_4 or $AA'PbBr_4$, 'Templated by Small Disc-Shaped Amines'* – of this block. Here, the spacer molecules were systematically varied to induce 2D perovskite sheets with different corrugation lengths and crystal structures, and the corresponding optoelectronic properties were characterized for potential application in a white light LED.

The third block (yellow, Publication 6, see chapter 14) and the last study within this thesis, *'Intricacies and Mechanism of p-Doping Spiro-MeOTAD Using $Cu(TFSI)_2$'*, ties in with the solvent-free processing, only now no longer of a perovskite layer, but of a charge extraction layer for lead halide perovskite based solar cells. The focus of this project was to understand the exact doping mechanism of an evaporated hole transport material with a co-evaporated dopant and the effect of dopant concentration on the optoelectronic properties of the respective films. Using this co-evaporation approach, one could further reduce the need for solvents when fabricating perovskite solar cells.

Contents

3 Motivation and Research Question

Hybrid perovskites, in particular lead-halide perovskites, have attracted a lot of attention in recent years due to their outstanding properties suitable for optoelectronic devices, such as solar cells,[1–7] light emitting diodes (LED)[8–14] or photo- and X-ray detectors.[15–18] A big advantage of this material class is the chemical tunability: Different materials or a combination thereof can be introduced into the ABX_3 crystal structure in order to flexibly tailor and optimize the optoelectronic properties, such as band gap, of the perovskite.[19–25] Thus, in the case of perovskite solar cells, the power conversion efficiency could be increased from 3.8%, as reported in the first study in 2009,[1] to currently over 26%, making perovskite solar cells (PSC) even more efficient on lab scale than silicon-based cells.[6] Similar improvements could also be observed for perovskite LEDs since their introduction in 2014 and an external quantum efficiency of up to 28% is achieved.[9, 11, 26–28] These advances make perovskite based optoelectronic devices one of the most promising candidates for the next generation of photovoltaic and LED technologies. However, despite great progress in research, there are still some challenges that need to be solved before perovskite devices are ready for the commercial market. These challenges include the following aspects:

There are gaps in fundamental understanding of the relation between the physical/chemical properties and processes to the resulting optoelectronic properties and device applications. For example, it is observed that minimal changes in processing conditions, such as environmental atmosphere (e.g. humidity) or composition of the starting solution, can have a major influence on the resulting perovskite layer, or that oxygen and light can induce negative effects within the perovskite layer during operation of the perovskite solar cell, negatively impacting the efficiency of the solar cells.[29–35] Much of the research is currently based on trying out different perovskite compositions, additives and additional intermediate layers and testing what effect each change has on the final devices. However, this trial-and-error approach always requires the fabrication of complete devices. As the crystallization of the perovskite film is very sensitive to the ambient conditions, a complete understanding of the film formation and the resulting film properties is crucial in order to narrow down the parameter space to be tested, to make the development of the solar cells more efficient and to ensure a high level of reproducibility. In this context, in-situ methods, i.e. measurement methods for characterizing the material properties during perovskite film formation via spin coating, have become increasingly important.[36–46] These in-situ methods, such as X-ray scattering or optical spectroscopy, can be used to investigate and identify the individual process phases of film formation. In addition, the influences of processing changes, such as the addition of an additive or an additional layer below the perovskite layer, can be understood and correlated with the resulting final film properties. The knowledge gained from the in-situ studies can be used to develop

manufacturing protocols to obtain reproducible, high-quality absorber layers independently of laboratory and environment conditions. Analogously, in the field of LED application, where low dimensional perovskites are especially promising due to the tunability of their optoelectronic properties, it is still not fully understood which spacer molecule and the corresponding crystal structure leads to optimal optoelectronic properties.[20, 47–50]

Secondly, the described sensitive dependence between film formation and final film properties in standard spin coating and all other solution-based processes is still an ongoing research focus of many projects. However, it can be overcome with the help of powder-based/dry film processing methods such as pressing[51–55], evaporation[56–58] or powder aerosol deposition (PAD).[59–62] The perovskite powders can be produced stoichiometrically pure and independently before film fabrication, and show outstanding chemical stability over years.[63] Thus, the powder-based approach enables material synthesis and film formation to be completely decoupled from each other. This makes films directly processed from powder a promising alternative to solution-processing. Here, the challenge that needs to be addressed is the understanding of the relationship between the powder properties and the final film properties and how these properties can be influenced by the processing. Currently, thick films with a thickness of around 1 mm are primarily produced from perovskite powders by pressing and are employed as X-ray detectors. In addition, as the dry processing does not require large quantities of toxic solvents such as dimethylformamide (DMF),[64, 65] the dry processing consequently represents a technically very interesting approach to producing perovskite films for absorber layers in solar cells. However, this requires layer thicknesses in the range of approx. 1 µm, which was not possible before this work. But, after resolving this issue, the dry processing could be a potential method for producing perovskite solar cells with consistent efficiency on a larger surface area (10.000 cm^2) than the standard method via spin coating used on laboratory scale (solar cell size: $< 1\,cm^2$), which is not viable for upscaling.[66–68]

Besides the perovskite layer itself, the charge transport layers also play a decisive role in the overall performance of the final optoelectronic devices.[69–71] In the context of PSCs, organic semiconductors are often used as charge extraction layers. For that, however, the electronic properties of the organic semiconductor need to be improved via doping, as the intrinsic conductivity of this class of semiconductors is typically too low.[72–76] Here, the most common approach for charge transport layers in PSCs is doping via air-oxidation enhanced by additives.[74, 77] Unfortunately, this doping method is not yet fully controllable and the doping process can induce device degradation and efficiency losses. Thus, there is a need for new, controlled and reliable doping approaches.[69, 78–82]

Based on these considerations, **the central question of my work therefore is, how the processing and the resulting nanostructure affect the optoelectronic properties of lead halide perovskite layers and charge extraction layers, which are commonly used in lead halide perovskite-based optoelectronic devices.** For this purpose, I investigated both wet solution-based and dry powder-based processes for perovskite film fabrication, as well as a new processing approach for doped hole extraction layers via co-evaporation. These projects may be grouped into three central subtopics:

1. Relationship between film formation and final film properties of perovskite films processed from solution

One focus of my research is the understanding of perovskite film formation and what effects the observed processes have on the final properties. I use multimodal in-situ optical spectroscopy to investigate the individual steps of the perovskite film formation process during spin coating. With these measurements we can then understand whether there are correlations between observable intermediate phases and the resulting final nanostructure and the optoelectronic properties of the film and how these correlations can be influenced by additives. The findings of these studies are presented in chapters 9 and 10.

2. Powder-based and dry-processed perovskite thick and thin films and the influence of nanostructured perovskite powders on their optoelectronic properties

The second focus of my work is on powder-based and dry-processed perovskite layers. Here, the layers are processed from powder into thick films (1 mm thick pellets) by pressing or into thin films by powder aerosol deposition (PAD) (and pressing). I am interested in how the nanostructure of the starting powders or changes in the nanostructure induced by pressing influence the optical and optoelectronic properties. The corresponding studies can be found in chapters 11 - 13 of this work.

3. Alternative doping mechanism for organic hole transport materials.

The last research focus of this thesis (see chapter 14) is the understanding of an alternative doping approach for organic hole transport materials via co-evaporation of the organic component and the respective dopant in order to obtain a more controlled and efficient doping and a more homogeneously doped charge transport layer.

4 Lead Halide Perovskites

4.1 Structure, Composition and Optoelectronic Properties

The term *perovskite* generally refers to a specific crystal structure that was first found in the mineral $CaTiO_3$ and named after the Russian mineralogist Lev Perovski.[83] All materials classified as perovskites show an ABX_3 structure, which is depicted in figure 4.1a). The A position is occupied by a cation while the B and X positions correspond to a metal and an anion, respectively.[84, 85] The structure consists of an BX_6 network in an octahedral arrangement, where the A cations occupy the interstitial spaces in between the octahedras. Thus, there is a limitation to the size of the ions in order to form a stable crystal structure. Goldschmidt described the condition for stable perovskite crystals by a geometrical tolerance factor t

$$t = \frac{r_A + r_X}{\sqrt{2} \cdot (r_B + r_X)}, \tag{4.1}$$

where r_i is the corresponding effective ionic radius of the A, B, and X ions.[86] The value for t has to be in the range between 0.8 and 1 for stable structures. As a consequence many different material combinations fulfill this requirement and adapt the ABX_3 structure.[87, 88] Halide perovskites, where a monovalent organic molecule, such as methylammonium (MA) or formadinium (FA), take the A position, a (semi-)metal (Pb, Bi, Sn,...) occupies the B position and a halide, e.g. iodine, chlorine or bromide, fills the X position, were first reported in 1893 by Wells [89] and characterized by Weber in 1978.[90]

The archetypical and most studied halide perovskite composition is methylammonium lead iodine ($MAPbI_3$), as this composition showed promising optoelectronic properties when employed in a solar cell.[1] One of these properties is the high absorption coefficient, which stems from direct band gap with an E_{Gap} of 1.6 eV.[84, 91] The valence band maximum (VBM) is obtained from the hybridization of the 5p iodine and 6s lead orbital, while the conduction band minimum (CBM) is due to the empty 6p lead orbital.[92–94] While the lead and iodine orbitals define the overall band structure and are important for the good ambipolar intrinsic conductivity and photovoltaic properties, the organic molecule also influences the crystal structure and optical properties.[84, 85] Hence, the optoelectronic properties can be adapted and tailored to a certain band gap by simply changing the A cation or the halide or even by mixing different halides (see figure 4.1b)).[21, 93–95] Similar band gap tuning can be obtained by substituting the MA with Cs or FA for an E_{Gap} of 1.7 eV or 1.5 eV, respectively.[95, 96] The metal in the B position can also be varied: By replacing Pb with Sn, E_{Gap} is reduced from 1.6 eV to 1.2 eV.[97, 98] This chemical flexibility and adaptability is another property that makes this class so interesting for

optoelectronic application.

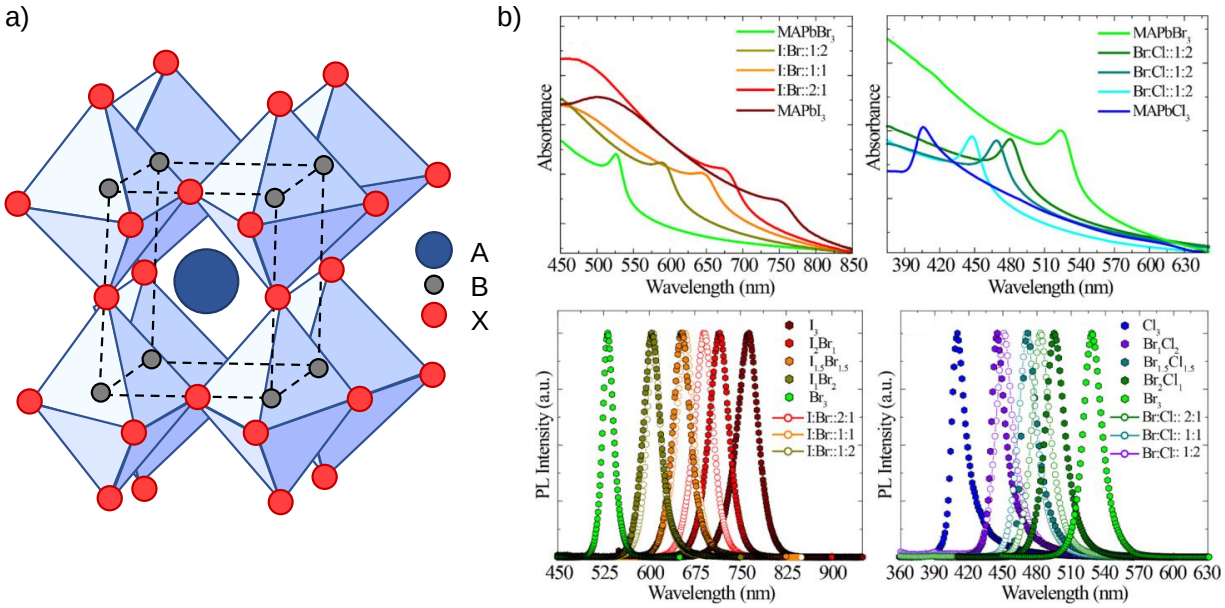

Figure 4.1: a) ABX_3 perovskite crystal structure. For metal halide perovskite compositions, the A position is occupied by a cation like methyl ammonium, the B position by metal, e.g. lead, and a halide (iodine, chloride, etc.) occupies the X position. b) UV-vis and PL spectra of $MAPbI_3$ and $MAPbBr_3$ (left panels) and of $MAPbCl_3$ and $MAPbBr_3$ (right panels) with the different stoichiometrically mixed compositions. Adapted with permission from Roy et. al.[21] Copyright 2021 American Chemical Society.

In addition, the hybrid perovskites also exhibit a high dielectric constant and a low exciton binding energy, resulting in an effective electron-hole separation and generation of free charges at room temperature once light is absorbed.[99–104] These generated free charges usually have a long lifetime and the electrons and holes can relax to the VBM and the CBM, respectively, before recombining radiatively.[102, 105, 106] So for an ideal perovskite, only a narrow emission is expected at the band edge and thus changes as the band gap is tuned as shown in the lower panels of in figure 4.1b).[21]

As always, real perovskite films do not form perfect crystals and defects are usually present within the crystal structure. However, unlike other inorganic semiconducting materials, such as silicon, perovskites have a rather high defect tolerance. Due to the lead and iodine orbitals involved in the band structure, only shallow traps can form close to the CBM or VBM instead of deep traps within the band gap.[85, 104] Additionally, the temperature at which the perovskite is investigated influences not only the exciton separation and de-trapping of charges, but also the fundamental crystal structure itself and thus again the optoelectronic properties. In the case of $MAPbI_3$ perovskite, the unit cell changes below 160 K from the tetragonal phase to an orthorhombic phase, which results in a band gap increase and thus in a shift of the absorption edge and the position of the emission peak.[107, 108] Similarly above 330 K, the crystal system exhibits a cubic structure instead of the tetragonal one, where the absorption is shifted to higher energies.[109–111]

4.2 Low Dimensional Perovskites

In addition to the described chemical tunability of 3D perovskites, it is also possible to obtain perovskite structures with lower dimensionality. The term dimensionality refers to the spatial direction in which the perovskite crystal forms. This is either called 2D if the crystal extends in one plane or 1D if the crystal only forms in one spatial direction.[20, 49, 112, 113] Even 0D structures are possible, in which only individual, spatially separated octahedra form.[114–116]

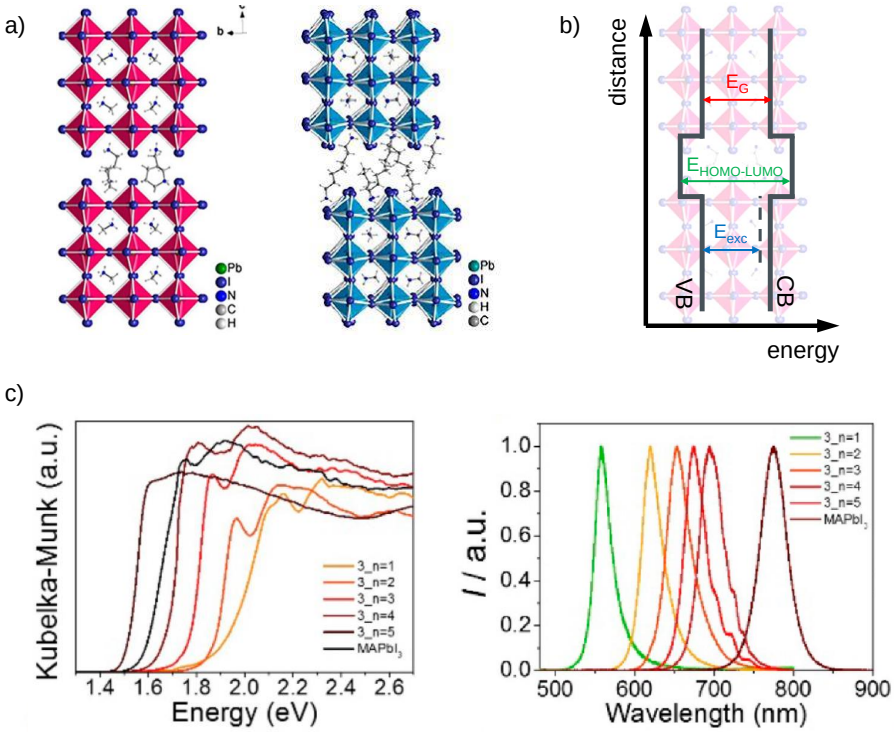

Figure 4.2: a) structural phases for low dimensional halide perovskites: Dion-Jacobson phase (left) and Ruddlesden-Popper (right) phase. Adapted with permission from Mao et. al.[117] Copyright 2018 American Chemical Society. b) Schematic energy diagram for the 2D perovskite phases in a). Adapted from Straus and Kagan.[118] Copyright 2018 American Chemical Society. c) Absorption and photoluminescence as a function of perovskite sheet thickness. Adapted with permission from Mao et. al.[117] Copyright 2018 American Chemical Society.

By introducing spacer molecules that are too bulky to fulfill the Goldtschmidt rule (eq. 4.1) into the perovskite crystal, the 3D structure is interrupted in one direction, as shown in figure 4.2a), and 2D perovskite sheets are obtained. Depending on the choice of spacer (monovalent or divalent), the perovskite layers can be aligned with each other (Dion-Jacobson type) or shifted against each other (Ruddlesden-Popper type).[49, 113]

As a consequence of the structural variation, the optoelectronic properties of the resulting low dimensional perovskite materials are also affected. As discussed above, the 3D perovskite exhibits a band-like electronic transport and a high dielectric constant ϵ_r. By incorporating organic molecules with a typically much lower ϵ_r, this band structure is also affected.[113] Thus, as the spacer molecules confine the

electronic structure of the perovskite to 2D, the resulting structure can be compared to a 2D quantum well structure (see fig. 4.2b)). In addition, the variation of the dielectric constant results e.g. in an increase of the exciton binding energy and E_{Gap}.[119–121] As depicted in figure 4.2c), by adding additional perovskite sheets (marked by number n), the optical properties of the 2D structures can be further fine-tuned.[117, 122]

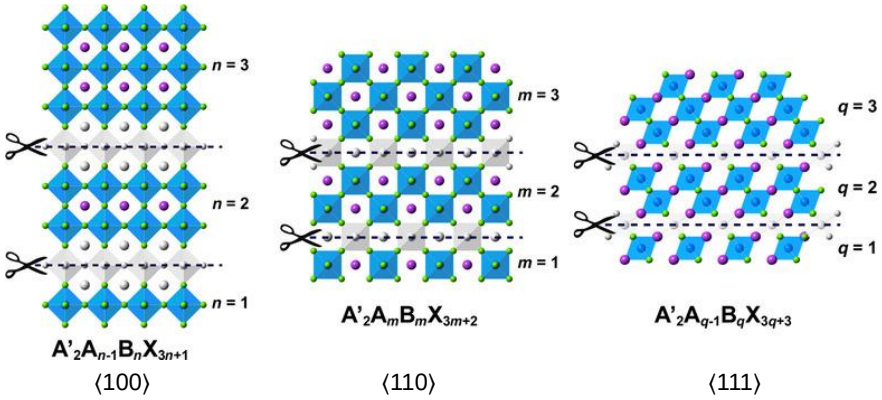

Figure 4.3: Schematic cuts along ⟨100⟩, ⟨110⟩ and ⟨111⟩ of a 3D perovskite structure and the resulting two-dimensional perovskites from these cuts. Reprinted with permission from Ortiz-Cervantes et al.[113] Copyright 2019 Wiley-VCH Verlag GmbH & Co. KGaA.

In previous discussions, the plane along which bulk perovskite is cut has not yet been taken into account. However, the perovskite can be cleaved along different planes by the appropriate choice of spacer molecule. The resulting subclasses and their structural formulas are illustrated in Figure 4.3. The cut along the ⟨100⟩ plane is the most common, and mainly employed in perovskite solar cells as a capping layer for the 3D absorber layer since the 2D materials are less prone to degradation and less sensitive to humidity.[2, 123–126] However, additional interesting optoelectronic properties can be observed in the other two classes of 2D perovskites with cuts along ⟨110⟩ and ⟨111⟩ due to an increased degree of corrugation in the perovskite sheet.[112] These materials often show, besides the narrow emission as shown in figure 4.2c), a broad strongly Stokes-shifted (additional) emission. Thus, these materials could be used for direct white-light generation. The origin of broad white-light emission is typically ascribed to the formation of self trapped excitons (STE) due to strong electron-phonon coupling.[127–132] However, the STE being the sole origin of this white light emission is not fully agreed upon. As Kahmann et al. showed, the broad emission could also simply stem from defect state emission.[127] Nevertheless, the 2D perovskite materials are promising candidates to further improve perovskite solar cells as well as an emissive layer for easily tunable and color-pure or broad-emissive white-light LEDs.

5 Perovskite Processing Methods

To process high-quality perovskite films suitable for optoelectronic devices, several processing methods were explored and optimized.[3, 29, 32, 41, 53, 63, 70, 133–135]. The most common and relevant methods for processing high-quality thin films are solution-based techniques such as spin coating[134, 136] or slot-die coating.[41, 137] Solvent-free alternatives for thin film fabrication include thermal evaporation[3, 135] or powder-aerosol deposition.[59, 60, 138] For an application as an X-ray detector, thick perovskite films are required. Here, the processing of pre-synthesized powders into thick films via pressing is a promising approach.[17, 18, 139]

In this chapter, the perovskite processing methods investigated within this thesis are briefly introduced and discussed: First, the wet solution-based spincoating used in chapters 9 and 10 and subsequently, the dry powder-processing via powder-aerosol deposition or pressing relevant for chapters 11-13 are described.

5.1 Solution-based Thin Film Processing

The most commonly used processing method of perovskite thin films on lab scale is spincoating. For this approach, the precursor constituents for the perovskite (e.g. for $MAPbI_3$ MAI and PbI_2) are firstly dissolved in the desired stoichiometry in organic solvents like dimethylformamide (DMF) and then spin-coated onto a substrate, where the perovskite is formed. To complete the crystallization process, the films are thermally annealed after the spincoating. Figure 5.1 depicts the two different approaches of spin coating investigated in this thesis.

The simplest way to obtain a perovskite thin film is the one-step processing (see fig. 5.1 top). As the name suggests, the perovskite thin film is deposited using a single spin coating step. After the precursor solution is distributed on the substrate, the spinning is initiated and the substrate is spun until the perovskite starts to crystallize upon evaporation of the solvent. The advantage of this method is the simplicity of the process. A disadvantage of this method is that – without any precursor chemistry optimization like additives [140–142] – it results in perovskite films with incomplete coverage and insufficient film quality due to formation of precursor-solvent complexes in a needle-like manner prior to perovskite formation.[41, 136]

To suppress the detrimental complex formation, the one step process was modified and the so-called solvent engineering method (see fig. 5.1 bottom) was developed.[143] Similar to the one-step approach,

the precursor solution is dispensed onto a substrate and the spincoating process is started. The difference to the one-step process is that the perovskite crystallization is induced prior to solvent complex formation by dripping an antisolvent onto the rotating precursor solution film. The antisolvent has to be miscible with the solvent used to prepare the precursor solution, but should not be a solvent for the precursor materials. The solubility strength of the precursor solvent is immediately strongly reduced and the perovskite starts to crystallize. The choice of the antisolvent and the timing and speed of the antisolvent dripping is critical for the resulting perovskite film quality and consequently the device performance.[32, 34]

At the end of the spin coating, independent of the method, the films are placed on a hot plate for thermal annealing to complete the film crystallization.

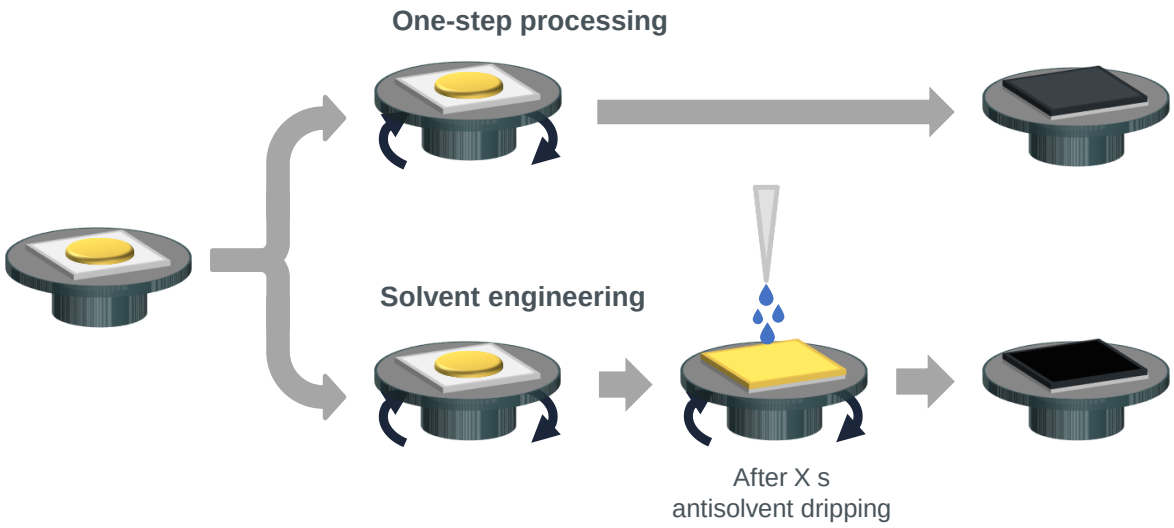

Figure 5.1: Sketch of the different solution-based thin film processing methods used in this thesis. top: One-step spincoating approach. Substrate with precursor solution is spun until perovskite is formed. bottom: Solvent engineering approach. The perovskite crystallization is induced by dripping an antisolvent onto the rotating substrate.

Despite the drawbacks of the solution processing due to the delicate interconnection between material synthesis and film formation, this method of processing in general, and solvent engineering in particular, still represents the state-of-the-art method to produce high quality perovskite films.

5.2 Powder-based Thin and Thick Film Processing

As an alternative method that decouples the material synthesis from the film formation, the processing of readily synthesized perovskite powders emerged in the recent years.[144, 145] Different methods, such as mechanochemical synthesis,[63, 146, 147] precipitation reactions[148–150] or thermal annealing,[151, 152] have been developed to synthesize phase pure perovskite powders.

In the following section, the mechanochemical synthesis via ball milling will be explained in more detail,

as this method is relevant for chapters 11 and 12. An illustration of the ball milling process is shown in Figure 5.2. The corresponding precursor materials are weighed out in powder form in the desired stoichiometry and filled into the milling jar (white (MAI) and yellow (PbI_2) powder). Zirconium balls and a small amount of cyclohexane as a milling agent are added. The milling jar is then tightly sealed and placed in the planetary ball mill. The milling jar undergoes two different rotational movements. On the one hand, it rotates around its own axis, and on the other hand, it rotates around the main axis of the planetary ball mill. This causes the zirconium balls to be repeatedly tossed back and forth in the milling jar. The kinetic energy released when the balls hit the precursor powder is sufficient to achieve the complete synthesis of perovskite powder. After the milling process, the cyclohexane evaporates and the dry-powder is sieved through a fine mesh to break up agglomerates and to obtain homogeneous powders.

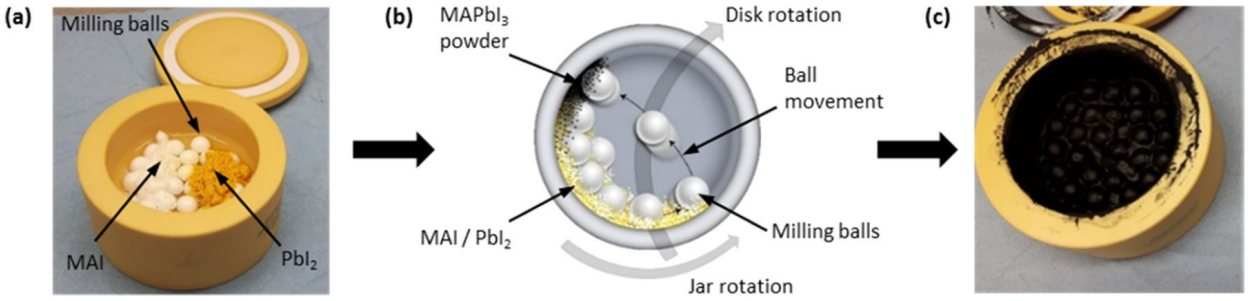

Figure 5.2: a) Photograph of a milling jar loaded with milling balls, MAI, and PbI_2 precursor powders. b) Schematic of the ball milling procedure for the mechanochemical synthesis of perovskite powders. c) Photograph of the milling jar from a) after the milling process with the synthesized black $MAPbI_3$ powder. Reprinted with permission from Leupold et al.[63] Copyright 2019 American Chemical Society.

With this synthesis method, large quantities in the range up to kilograms of perovskite powder can be synthesized in a short amount of time. These amounts of powders are required for processing perovskite layers via powder-aerosol deposition or the pressing of powders to pellets (see figure 5.3)

The perovskite thin films investigated in chapters 11 and 12 were processed via powder-aerosol deposition (PAD) method (see figure 5.3 top). In brief, a perovskite aerosol is generated by passing a carrier gas (N_2, O_2, He) through the fine powder. This aerosol stream is subsequently accelerated to speeds up to 600 $m\,s^{-1}$ and impacts onto the substrate. Upon impact, the powder particles deform, break up and form an adherent layer on the substrate.[59, 60, 138] Subsequently impacting particles densify and increase the layer thickness further. This film formation mechanism is called room-temperature consolidation (RTIC).[153] The PAD processing can be fine tuned by optimizing the amount of carrier gas flow, the perovskite powder particle size and the number of overpasses of the aerosol jet over the substrate.[138] The obtained films are dense and without voids throughout the cross-section of the film. Yet, the grain size is relatively small and the surface roughness is increased compared to perovskite films processed via spin coating.

To improve these issues, the PAD perovskite film can be optionally hot-pressed. By pressing the PAD perovskite film with pressures up to 25 MPa at temperatures up to 120 °C, a compaction and even a

sintering of the perovskite layer is achieved. This results in a perovskite layer with improved morphology (reduced surface roughness, increased grain size) and optoelectronic properties.[138, 154]
The same pressing setup and pressing procedure (see figure 5.3 bottom) are used to produce thick layers from perovskite powder.[53, 55] One obtains a free-standing thick perovskite film from this approach and similar beneficial effects of pressing on the perovskite film properties can be observed. The films exhibit a density comparable to that of a single crystal.[53]

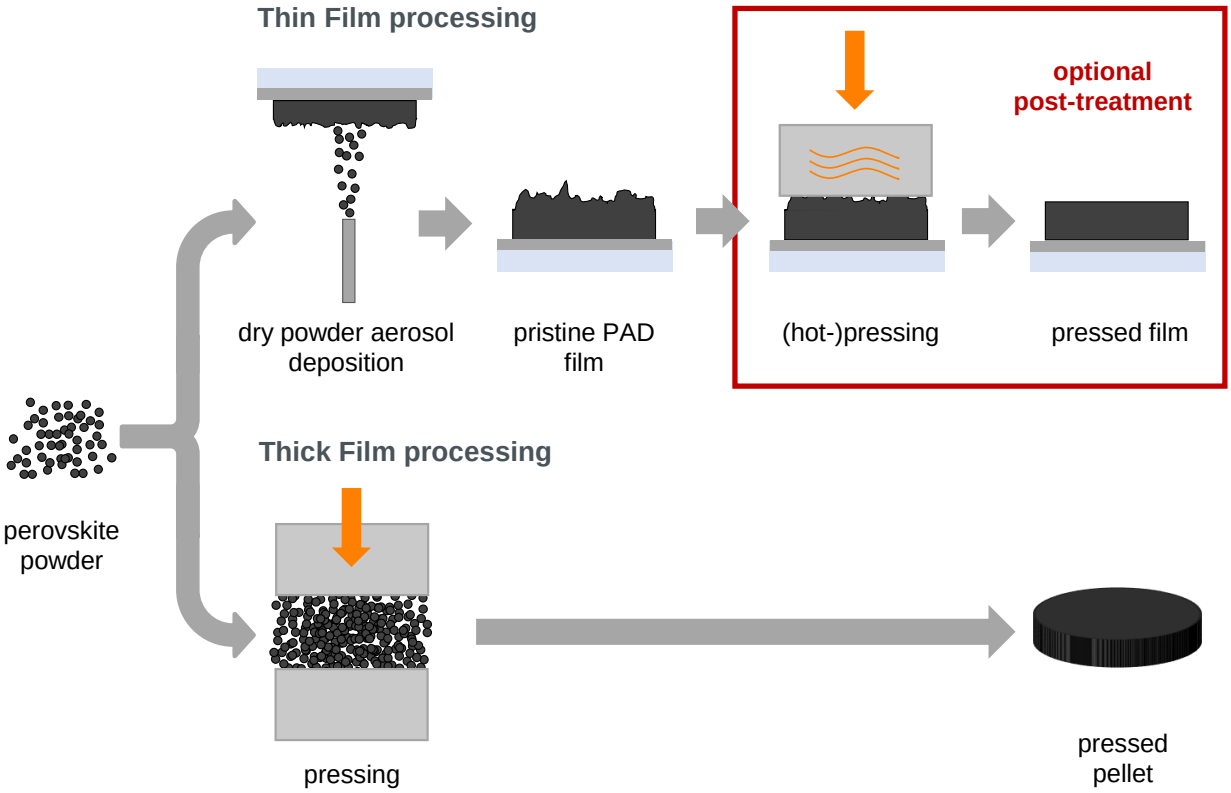

Figure 5.3: Schematic Illustration of the dry powder-based processing methods used within this thesis. top: Thin films are processed via powder aerosol deposition of pre-synthesized powders (see figure 5.3) onto a substrate. The resulting perovskite films can be (hot-)pressed to improve the structural and optoelectronic properties of the films. Reprinted with permission according to the CC BY 4.0 license from Biberger et al.[138] Copyright 2023 the authors. bottom: Thick perovskite films/pellets are processed by pressing pre-synthesized perovskite powder into dense layers with a thickness of $\approx 1\,\mathrm{mm}$.

6 Fundamentals of perovskite solar cells

This chapter provides a brief introduction to the general architecture of state-of-the-art planar perovskite solar cells as well as to the methods used in this work to characterize the solar cells. For more detailed discussions on perovskite optoelectronics in general the reader is referred to textbooks by e.g. Tsutomu Miyasaka.[85, 155]

6.1 Solar cell stack

The first working perovskite solar cells ever built were developed as dye-sensitized solar cells (DSSC).[1] In the case of DSSC, the perovskite material was employed as the sensitizer for a mesoporous TiO_2 scaffold, which in turn served as the electron transport layer on top of a FTO electrode. The device structure was completed by a second FTO electrode coated with platinum, which was positioned upside down on top of the sensitized TiO_2 scaffold, and the gaps between the two substrate were filled with an electrolyte to facilitate hole extraction. With stack architecture, DSSCs with efficiencies of around 3.8 % could be realized. The liquid electrolyte was replaced by a solid hole transport material and the device efficiencies were increased to around 10 %.[156] Since then the advancement of perovskite photovoltaics and the improvement of device performance was the focus of many research groups around the world. As a consequence the device efficiency was increased stepwise up to a current record efficiency of 26.1 %.[6] During this development process the architecture of the solar cells changed as well. First the perovskite thickness was increased[157] and then compact electron transport layer materials were introduced,[5, 158–160] resulting in a planar architecture for the state-of-the-art solar cells stack (see fig. 6.1). This planar solar cell configuration works similarly to a p-n junction solar cell, where the perovskite is sandwiched as an intrinsic (i) semiconductor between the electron (n) transport layer (ETL) and the hole (p) transport layer (HTL). Depending on which transport layer is applied to the transparent conductive electrode below the perovskite layer, the configuration is referred to as n-i-p (regular structure) if the ETL is applied first, or p-i-n (inverted) if the HTL is applied first. For both, regular and inverted, the stack is commonly completed by a metal contact. The overlap of the metal contact and the transparent electrode below defines the active area of the final device (see green area in fig. 6.1f))

As I fabricated solar cells in n-i-p configuration within project 3 (see chapter 11) of this thesis, I will briefly discuss the most commonly used materials and their processing for this stack configuration.[161]

Two different transparent conductive oxides are usually used as electrode materials: fluorine-doped tin oxide (FTO) or indium tin oxide (ITO). As the ETL, compact SnO_2 or a combination of compact and mesoporous TiO_2 is coated on top of the electrode via spin coating or chemical bath deposition, or via spray pyrolysis and spincoating, respectively. To improve the wetting of the perovskite precursor solution, the substrates are treated with UV-ozone or O_2-plasma prior to perovskite deposition.

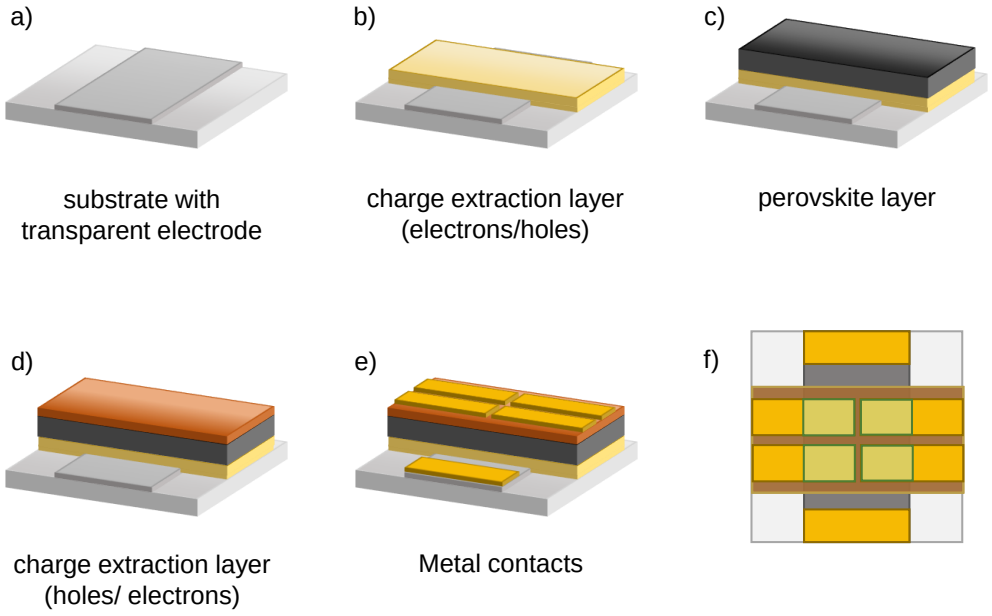

Figure 6.1: a) - e) Sketch of fabrication steps to obtain a complete planar perovskite solar cell stack. f) top view of the solar cell stack. The green rectangles indicate the active areas of the resulting four solar cells on each substrate.

The perovskite as the absorber layer is commonly processed from solution. As already described, a variety of different perovskite compositions are available to tune the optical properties to the requirements of different applications. The established processing approach for high-quality perovskite layers is the described solvent engineering method, where the crystallization is induced by dispensing an anti-solvent during spin coating. As the HTL, Spiro-MeOTAD doped with Li-TFSI and FK209 is commonly spin-coated on top of the perovskite layer. Yet, Spiro-MeOTAD can cause degradation processes. Therefore new HTL materials are currently investigated.[75, 162–170] The n-i-p stack is usually completed by evaporating gold as the counter-electrode onto the HTL layer.

6.2 J-V characteristics and hysteresis

The most important figure of merit of any solar cell is the power conversion efficiency (PCE) η. In a nutshell, the PCE is the ratio between the electrical power density P_{out} one can obtain from the device compared to the power input to the device P_{in}:

$$\eta = \frac{\textit{electrical power delivered}}{\textit{incident light power}} = \frac{P_{out}}{P_{in}}. \tag{6.1}$$

In the case of solar cells, P_{in} is provided by the sun or in a laboratory by a solar simulator. Considering the solar spectrum and the absorption of the atmosphere, the supplied P_{in} integrated over the whole solar spectrum equals 100 $\frac{mW}{cm^2}$.[85, 171, 172]
Since the inner photoelectric effect constitutes the fundamental basis for the absorption and thus the operation of the solar cell, the PCE can never reach unity. This relation means that the absorption of an photon takes only place if the energy of the photon is sufficient to elevate an electron from the valence band to the conduction band. Consequently, if the energy of the photon E_{photon} is smaller than the band gap energy E_{gap}, this photon can not be absorbed and converted into electrical power by the photoactive material. Unfortunately, if E_{photon} exceeds E_{gap}, there are additional energy loss mechanisms to take into account. One loss path to consider is the thermalization of the excess energy as the electron relaxes to the lowest possible energy in the conduction band. The second major loss contribution is the recombination of electron-hole pairs, either radiatively or non-radiatively (Auger, Shockley-Read-Hall, surface recombination).[85]
Thus, for an ideal device with a given E_{gap}, where only thermalization and radiative losses are present, a theoretical maximum PCE can be determined. Additionally, as the maximum extractable current density (also named short-circuit current density J_{SC}) decreases and the maximum obtainable voltage (open-circuit voltage V_{OC}) in contrast increases with increasing band gap, one can find a band gap energy range (1.1 - 1.4 eV) where P_{out} and thus PCE reaches a maximum. The theoretical radiative limit for the PCE of an ideal device (Shockley-Queisser limit) is $\approx 33\%$.[85, 172]

The PCE is commonly determined experimentally by measuring the current response of a device while sweeping the applied voltage. The measured current values are divided by the active area of the device (see figure 6.1f)) in order to obtain current density. An exemplary current density-voltage (J-V) curve, together with all parameters necessary to calculate the efficiency, is depicted in figure 6.2a). In the dark, solar cells behave like a regular diode, but once the devices are illuminated, additional charges are generated as described and the J-V curve is shifted. As the electrical power density output is calculated by

$$P_{out} = J \cdot V, \tag{6.2}$$

neither the operation point with the highest current density (0 V, J_{SC}) nor with the highest voltage (V_{OC}, 0 mA/cm^2) results in extractable power. Therefore, one needs to find the point of maximum power output (V_{MPP}, J_{MPP}) where the area of the resulting rectangle is maximized. This is marked with the orange rectangle in figure 6.2a). One can additionally introduce the fill factor (FF) as another figure

of merit for solar cells. The *FF* is a geometrical factor and compares the areas of the two rectangles drawn in figure 6.2. It is a measure of the recombination of electron-hole pairs happening inside the device when a finite internal electric field is present. Thus, equation 6.3 can be written as

$$\eta = \frac{J_{MPP} \cdot V_{MPP}}{100\ \frac{mW}{cm^2}} = \frac{FF \cdot J_{SC} \cdot V_{OC}}{100\ \frac{mW}{cm^2}}, \tag{6.3}$$

to calculate the PCE of a solar cell.

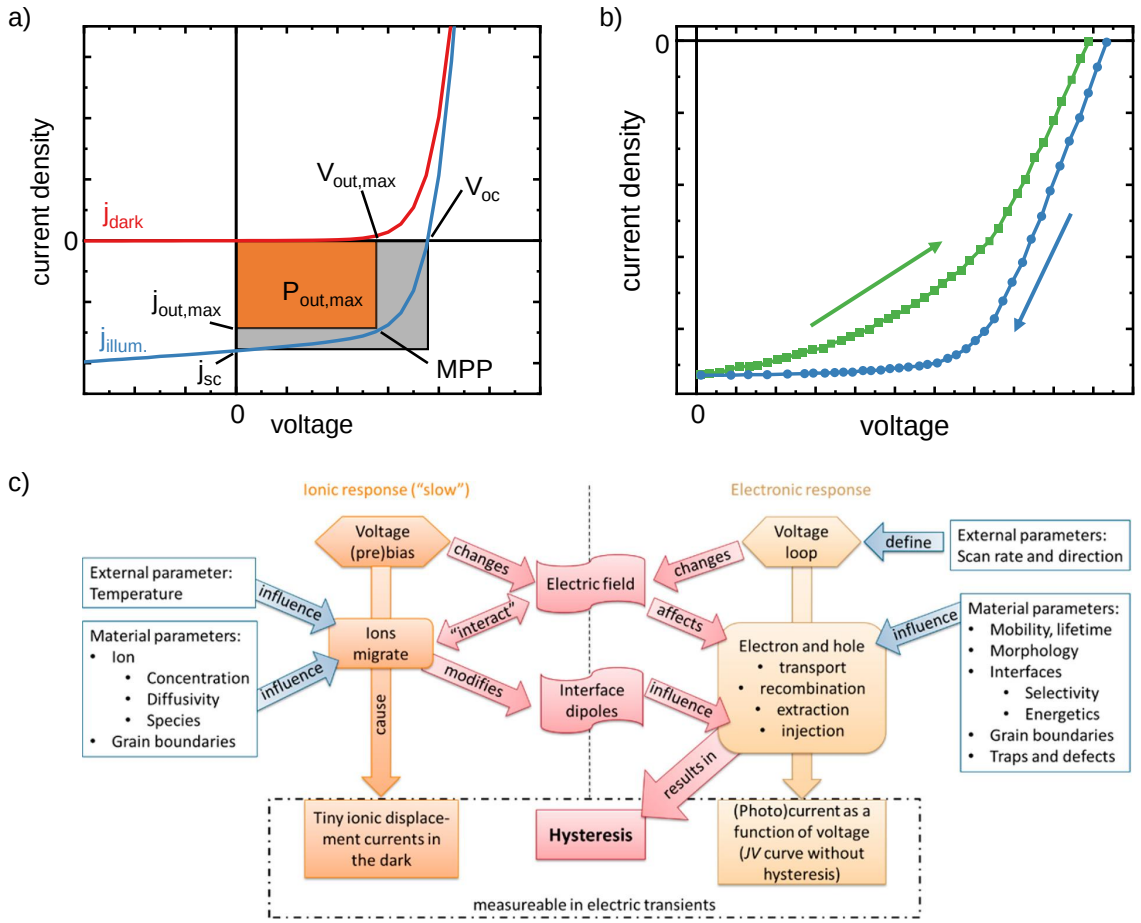

Figure 6.2: a) Typical J-V curve of a solar cell in the dark and under illumination. The relevant parameters to evaluate the solar cell performance are marked.[172] b) Illustration of the scan-direction-dependent hysteresis effect in J-V-curves of n-i-p perovskite solar cells. Adapted with permission from Chen et al.[173] Copyright 2016 American Chemical Society. c) Overview over the interplay between ionic (left) and electronic (right) response upon applying a voltage. Reprinted with permission from Tress.[174] Copyright 2017 American Chemical Society.

The J-V characteristics discussed so far represent the behavior of an inorganic solar cell such as silicon devices, where the J-V curve is identical independent of the the scan direction.[175] In the case of perovskite solar cells, a mismatch between the scanning directions can be observed in the J-V curves as shown in figure 6.2b).[176, 177] This mismatch of the measured current density between the reverse ($V_{oc} \rightarrow 0\,V$,

blue) and the forward direction ($0\,V \rightarrow V_{oc}$, green) is called hysteresis.[176] The origin was and is the focus of many investigations.[85, 173, 178] Potential causes discussed in literature for the hysteresis are (1) the intrinsic defects within the perovskite,[179, 180] (2) the accumulation of charges at the interfaces to the charge extraction layers,[181, 182] (3) ferroelectric behavior,[183–185] and (4) ion migration.[186–188]
The severity of the hysteresis can be quantified by hysteresis indices *HI*, e.g. based on the difference in efficiency:[178, 189]

$$HI_{PCE} = \frac{PCE_{reverse} - PCE_{forward}}{PCE_{reverse}} \tag{6.4}$$

How large the HI is, meaning how pronounced the hysteresis is, depends not only on the discussed material inherent, but also on many variables of the measurement, such as scan speed of the sweep or pre-treatment before the sweep (light-soaking, poling, ...).[174, 178, 190] Depending on the choice of measurement parameter, the hysteresis can be increased or suppressed, e.g. when sweeping too fast, the slow ionic contribution to the hysteresis is eliminated. An overview over the interconnection between ionic and electronic contributions to the hysteresis is displayed in figure 6.2c). The in literature currently prevailing origin of hysteresis is ion migration in combination with trapping and de-trapping processes at defect sites within the perovskite layer and an energy misalignment at the interfaces.[85, 174, 191]
In order to mitigate this hysteric effect, several approaches were developed: e.g grain boundary engineering where the HI was reduced by enlarging the grains and thus reducing the grain boundaries and potential trap sites.[192] Additionally, the overall reduction of defects is the key for further mitigation of the hysteresis effect. On the one hand, this is implemented by e. g. adding volatile [193] and non-volatile additives [4, 23, 25, 194–197] to the precursor solution in order to passivate the defect sites within the perovskite layer (defect engineering). On the other hand, as previously discussed, the interfaces to the charge extraction layers also play a decisive role. Here, it has been shown that the inverted structure exhibits significantly reduced to almost non-existent hysteresis compared to the regular structure. Therefore, the interface engineering, i.e. the choice of the extraction layers [78, 81, 198–201] and the successful passivation of the perovskite interfaces [123, 202–206], is of great importance.

6.3 Light-intensity dependence of J-V curves

In order to analyse the devices further and to identify and differentiate between loss mechanisms as described above as well as parasitic losses from series/shunt resistance,[207–209] light-intensity dependent measurement can be of great help.[85, 210] Here, J-V curves are recorded at different light-intensities. The attenuation of the light-intensity is usually facilitated by neutral-density filters to obtain uniform reduction over the whole solar spectrum. By plotting and analyzing the obtained values for *FF* and V_{OC} as a function of incident light-intensity and comparing these results with those of theoretical modeling via drift-diffusion simulations, one can gain valuable insights about the dominating loss mechanism. In theory, the value of *FF* should be unchanged when the light-intensity is reduced. Concomitantly, the V_{OC} should have an exponential dependence of the light-intensity and the lower the slope on a logarithmic scale the better.[210]

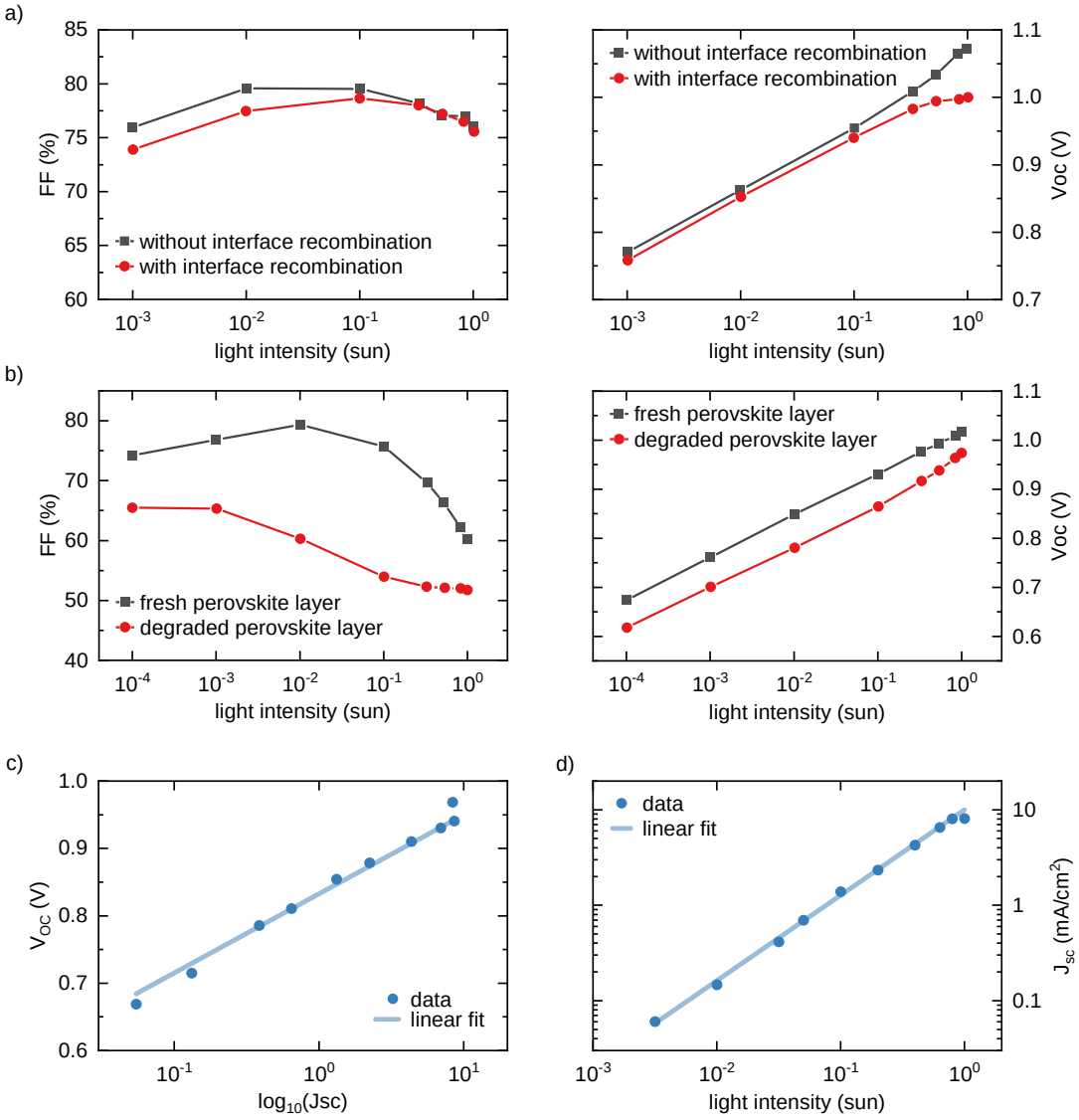

Figure 6.3: Experimental examples for FF and V_{oc} as a function of light intensity for a) interface recombination and b) trap recombination in the bulk as the dominating loss mechanisms. Adapted with permission according to the CC BY 4.0 license from Glowienka et al.[210], c) V_{oc} as a function of the J_{sc}, obtained from the light intensity-dependent J-V-curves. From the slope of the linear fitting the values of the ideality factors n are extracted. d) Light intensity-dependence of the J_{sc}. α values are extracted from the slope of the linear fitting.c) and d) adapted with permission according to the CC BY 4.0 license from Biberger et al.[138]. Copyright 2023 the authors.

In figure 6.3, two experimental examples for different dominating loss origins are presented. In the first example (figure 6.3a)), the recombination at the perovskite interfaces can be identified as the predominant origin for losses as the V_{OC} saturates for high intensities when interface recombination is present. The difference in FF is insignificant.[211] The second example, shown in figure 6.3b), illustrates what effect a degraded perovskite layer as the main origin for losses has on FF and V_{OC}. Here, the FF is strongly influenced by increased bulk recombination due to degradation while the slope and the absolute

values of the V_{OC} are only marginally affected by this loss mechanism. Similar to the two presented examples, the effects of extraction barriers, series and shunt resistance are discussed in great detail by Glowienka and Galagan.[210]
However, as one can conclude from the examples, more than one loss mechanism is usually present in a real devices, but the careful analysis of light-dependent measurements helps to narrow down the most dominant loss factors.

A second method to analyze light-intensity dependent J-V curves is the determination of the ideality factor n_{id} and inverse Langevin factor α. Based on the value of these figures of merit, one can theoretically conclude whether monomolecular (trap-assisted, nonradiative) or bimolecular (band to band, radiative) recombination predominantly takes place. n_{id} can be determined from a linear fit to the V_{OC} vs. J_{SC} on a logarithmic scale as shown in figure 6.3c) using the relation

$$n_{id} = \frac{e \cdot m}{k_B \cdot T}, \tag{6.5}$$

where m is the slope of the linear fit, e is the elementary charge, k_B is the Boltzmann constant and T is the temperature. α is directly obtained by fitting J_{SC} vs. light-intensity (see figure 6.3d)) and extracting the slope. In theory, n_{id} can take values between 1 and 2, with a value of 1 for ideal solar cells in which only radiative recombination in the bulk occurs, and when n_{id} approaches 2, trap-assisted non-radiative recombination can be inferred.[85, 212, 213] The extracted values for α can be interpreted in a similar way: α reaches a value of 1 if the monomolecular recombination is dominant and is close to 0.5 for bimolecular recombination.[213–215]
However, this simple interpretation is not always valid in the case of perovskite photovoltaics, as fundamental assumptions for derivation of the ideality factor are sometimes not fulfilled. As a result, there are devices where the obtained n_{id} is close to 1, while the overall performance of the device is poor.[212, 213] In contrast, there are highly efficient devices with an ideality factor of 1.5.[216] Caprioglio et al. showed that one has to take more into account when interpreting n_{id} for perovskite solar cells. The 'classical' interpretation is limited to cases when only Shockley-Read-Hall recombination in the bulk is presented and effects like energy level offsets at the interfaces and interface recombination can be fully excluded.[213] Nevertheless, as long as these limitations are considered, important insight can be obtained from these light intensity-dependent measurements.

6.4 Organic Semiconductors as Charge extraction layers

Organic semiconductor materials are often used as charge extraction layers, especially as HTL, in both (n-i-p and p-i-n) solar cell configurations. Since the charge transport properties of organic semiconductors (OSC) differ significantly from the inorganic/hybrid crystalline semiconductors, a brief introduction to organic semiconductors, and in particular the doping of this material class, is provided in this section. Organic compounds consist of hydrocarbons with a few heteroatoms such as sulfur or nitrogen. Their semiconducting property is based on a conjugated π-electron system, in which charge carriers can delocalize over several carbon atoms.[172] In contrast to well-ordered inorganic/hybrid crystalline semiconductor materials, OSC commonly do not form a long-range well-ordered crystalline structure, but a more or less amorphous or semi-crystalline film. As a consequence, charges are more localized on polymer chains or molecules. Hence, the transport of charge carriers is not band-like as it is the case for inorganics, but a hopping motion from one site to the next (see 6.4a).[217–219]
Additionally, the intrinsic charge carrier densities and the mobilities in an OSC are rather low, so that the conductivity needs to be extrinsically generated by injection, dissociation of photo-generated electron-hole pairs, or intentional or unintentional doping.[172]

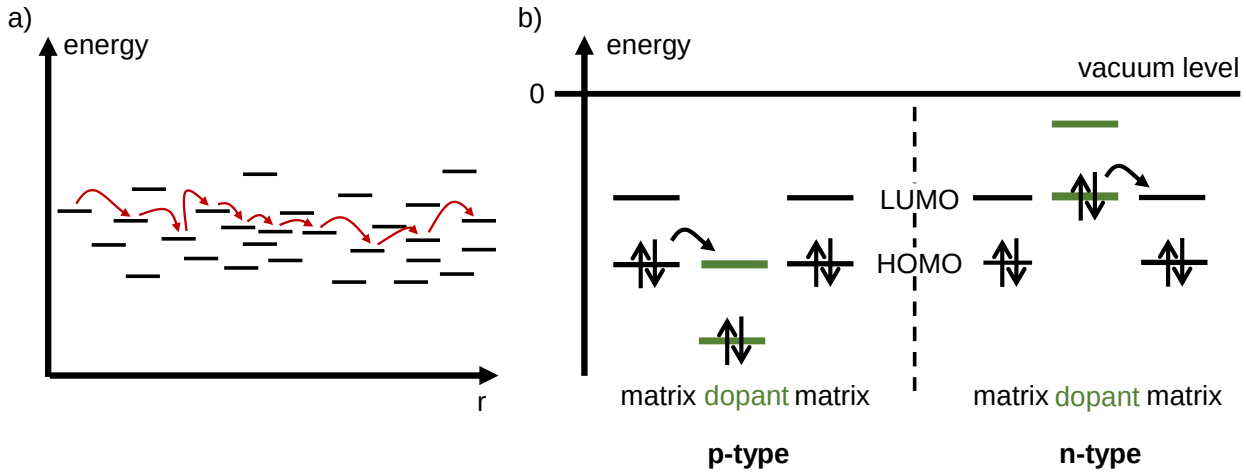

Figure 6.4: a) Illustration of charge transport via hopping between localized states in organic semiconductors, in contrast to band-like transport in classical semiconductors. b) Simplified illustration of the molecular levels for p-type and for n-type doping. Adapted with permission from Walzer et. al [220]. Copyright 2007 American Chemical Society.

Especially if one wants to use an OSC as a charge extraction layer in a perovskite solar cell, the conductivity for the respective charge carrier type has to be intentionally increased. A first approach of doping organic semiconductors was exposing polyacetylene to a vapor of halogens (e.g. chlorine, bromine, or iodine) resulting in an enhancement of the conductivity by up to seven orders of magnitude.[221] But using halogens or alkali metals is an unstable type of doping since those materials have the tendency to diffuse over time.[222]
A much more stable and over the past years well-established doping technique is molecular doping. This

method depends on the electron transfer from the dopant (n-type) or to the dopant (p-type) within the polymer matrix. The energy levels of the dopant have to match the HOMO/LUMO of the polymer as illustrated in figure 6.4b). The first controllable and stable molecular doping process was reported by Blochwitz et al. In this work, phtalocyanine was p-doped by co-sublimation of F_4TCNQ.[223] By molecular doping, the conductivity can be tuned over several orders of magnitude (e.g. P3HT with F_4TCNQ: $10^{-5} - 1 \frac{S}{cm}$).[224, 225]

There are two different fundamental interaction mechanisms for molecular doping that are discussed in literature.[224, 226–229] These two mechanism are exemplarily explained for the case of p-type doping.
The first mechanism is ion pair formation (IPA). This mechanism is based on an integer charge transfer from the HOMO of the polymer (OSC) to the LUMO of the dopant. A detailed description of the electron transfer is given by Tietze et al.[229] Figure 6.5a) shows the interaction between the two molecules (left) and the resulting shift of the energy levels of the ions within the polymer matrix (right).The energy levels of the affected polymer chain and dopant shift due to reorganization after the transfer of the charge.
In the case of a charge transfer complex formation (CPX), the transfer of the charge does not occur from the polymer onto the dopant, but the polymer and the dopant form a complex with hybridized orbitals as depicted in figure 6.5b).[230] The parent molecules of the complex determine the amount of transferred charges that can also be non-integer values.[227]
It is important to note that successful n-type doping is more difficult to obtain since a high lying HOMO is required as depicted in figure 6.4b). However, materials with these energetic properties are prone to reduction by oxygen.[172]

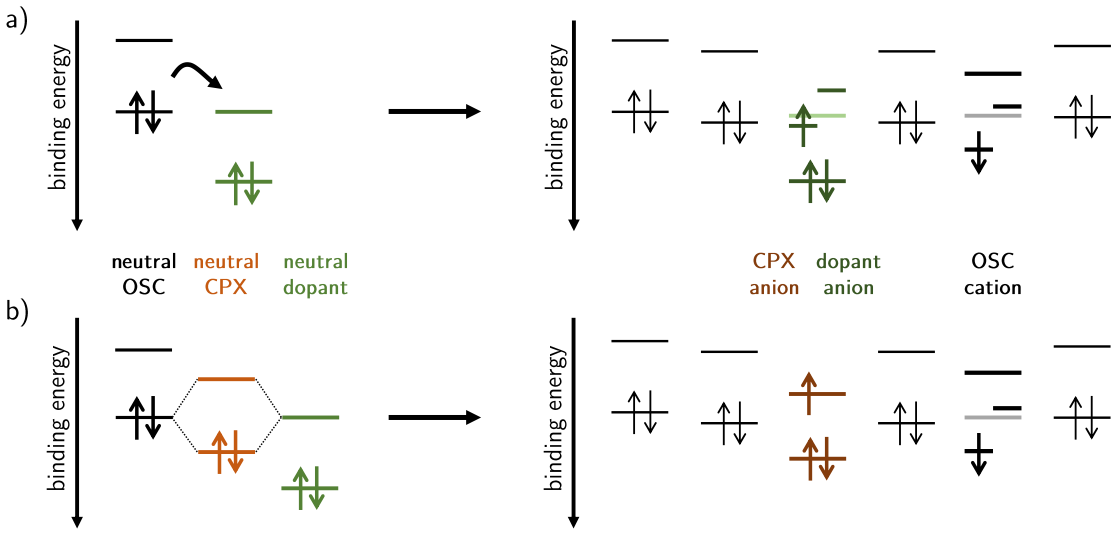

Figure 6.5: Illustration of the energy levels for p-type doping for a) IPA and b) CPX in a disordered matrix. The light colored lines show the energy levels before the energy level splitting of the cation/anion upon doping. Adapted with permission according to the CC BY 4.0 license from Salzmann et al.[224]. Copyright 2016 American Chemical Society.

The resulting complex is then the effective dopant of another neutral molecule/polymer chain. This doping mechanism is mostly reported for small conjugated molecules rather than for polymers.
The doping efficiency of CPX decreases again after a certain amount of dopant is added, since the complex is the effective dopant and at some point there are more complexes than neutral chains that can transfer charges.
Although both mechanisms result in a doped molecule/polymer chain, only IPA seems to contribute to an increase in conductivity.

The doping of hole-transport materials (HTM) for perovskite devices is typically facilitated by mixing additives such as LiTFSI (lithium bis(trifluoromethylsulfonyl) amine) and tBP (4-tertbutylpyridine) into the HTM solution and exposing the films to air.[72, 73, 77] Here, the LiTFSI acts as the effective dopant in the presence of oxygen. The organic semiconductor, such as Spiro-MeOTAD, forms a complex with oxygen and an electron transfer from the Spiro-MeOTAD can occur after photo or thermal excitation (see equation 6.6). The Li salt is required as the $TFSI^-$ stabilizes the doped Spiro-MeOTAD and changes the equilibrium towards the doped Spiro-MeOTAD by forming Li oxide complexes (see equation 6.7). Consequently, conductivity is increased by two orders of magnitude.[74]

$$\text{Spiro}-\text{MeOTAD} + O_2 \longleftrightarrow \text{Spiro}-\text{MeOTAD}^{\bullet\oplus}\, {O_2}^{\bullet\ominus} \tag{6.6}$$

$$\text{Spiro}-\text{MeOTAD}^{\bullet\oplus}\, {O_2}^{\bullet\ominus} + \text{LiTFSI} \longrightarrow \text{Spiro}-\text{MeOTAD}^{\oplus}\, \text{TFSI}^{\ominus} + \text{Li}_x\text{O}_y \tag{6.7}$$

The tBP is not necessary for doping Spiro-MeOTAD, but by adding it into HTM solution, the resulting layer becomes more homogeneous and the interfacial contact to the perovskite layer improves.[231] In order to further increase the performance of Spiro-MeOTAD , the cobalt complex FK209 is often mixed as second dopant into the HTM stock solution.[232, 233]
As already mentioned, it is important to note that the described doping procedure and the HTM on its own can cause long-term stability issues of the perovskite layer and as a consequence of the whole device due to possible chemical reactions with the radical Spiro-MeOTAD or the tBP.[234] Hence, the development of new (ideally doping free) HTMs and new doping approaches are the focus of many research efforts.

7 Content of the Individual Publications

In this chapter, I want to give a more detailed summary of each individual article and how each article contributes to the overall research questions of my thesis.

In Publication 1, I investigated the influence of the ionic liquid (IL) $BMIMBF_4$ on the film formation of $MAPbI_3$ when a film is processed from solution via one-step spin coating as well as via the solvent engineering method. For the latter, perovskite crystallization is induced by dispensing an antisolvent (AS) onto the rotating solvent film instead of by evaporation of the solvent. To be able to dispense an AS during the measurement, I had to first modify our multimodal in-situ optical spectroscopy setup. Via a capillary, a syringe and a custom-designed contraption for the capillary, I was able to dispense the AS reproducibly onto the substrate without interfering with the measurement. With this setup I was able to record absorption and photoluminescence spectra and track the intensity of the light of a green LED, scattered by my sample, simultaneously during the spin coating process. I particularly chose $BMIMBF_4$ as an additive because the class of ionic liquids in general is a popular class of materials to add to the precursor solution because of its beneficial effects on the performance of perovskite solar cells due to the passivation of defects.[235]
With this study, I wanted to understand if this additive impacts the timings of the film formation and resulting nanostructure of $MAPbI_3$ films. By analyzing the absorption spectra in combination with the evolution of intensity of the scattered green LED, I could extract the timing of the perovskite-solvent complex formation, and by fitting the photoluminescence and considering quantum confinement effects, I could calculate the size of the growing crystallites and thus determine growth rates. The morphology of the final films was characterized by SEM and XRD measurements.
With the one-step spin coating experiments, I revealed that the IL has no influence on the perovskite-solvent-complex formation, but the more IL content is in the precursor solution the later and slower the perovskite crystallization takes place. From the solvent engineering experiments, I could conclude that the IL influences the crystallite growth similarly: The more IL in the precursor solution the slower the growth. Further, I could identify that the IL already interacts with precursor materials when still in solution and consequently affects the evolution of the PbI_4^{2-} properties in the solvent film before any crystallization is triggered by the AS. I found that the slower crystallization rates when the IL is added into the precursor solution correspond to smaller grains in the final perovskite film, which is known to decrease the device efficiency. Thus, one has to be aware of the potential impact of processing timing and has to balance the positive effect of passivation and the detrimental effect of more grain boundaries

when using ILs as additives.

The effect of the IL on the evolution of the precursor solution properties of e.g. the PbI_4^{2-} species found in Publication 1, was the starting point for Publication 2. It is known that small variations in e.g. processing atmosphere, temperature, speed of AS dispensing, additives etc. can influence the ideal point in time to dispense the AS in order to obtain the best perovskite film and device quality. Therefore, I investigated if I can improve the reproducibility of processing films independent of these external factors by relying on optical signatures of the materials as a trigger for the AS dispensing. In order to do that, we first had to develope the optical in-situ spin coater setup and its software, used in Publication 1, further to enable a real-time feedback loop from the optical spectra, and a syringe pump was added to dispense the AS automatically. The idea of this approach was that the small variations, such as processing atmosphere, can be compensated by the feedback loop approach. To demonstrate this new approach for processing perovskite films, I chose to vary the spin speed of the spin coater to simulate different formation kinetics like solvent evaporation rates. As a parameter of interest that triggered the AS dispensing, the precursor solvent film thickness was selected as this value can be determined from the interference pattern in the absorption spectra. For comparison, a second series of perovskite films was also fabricated where the AS was dispensed at a preset time like it is usually done. First, I processed $MAPbI_3$ in DMF as a simple model halide perovskite. Here, I found that the final films processed via the new reactive approach showed a consistent quality in cross-section and top-view SEM images independent of the spin speed. This was the result of a similar crystallite growth during the film formation which I could extract from the evolution of the PL peak position. In contrast, I identified a strong variation in the growth of the films processed via the standard time-based approach which in turn resulted in inconsistent film quality with large voids in the layer. In order to check if the findings of the reactive processing of $MAPbI_3$ can be generalized and applied to more complex perovskite compositions, I repeated the experiments for $(MA_{0.17}FA_{0.83})Pb(I_{0.83}Br_{0.17})_3$, which is used in high efficiency devices. The cross-section SEM images revealed that the films processed via the reactive approach are consistent in quality independent of the spin speed, as it was the case for the $MAPbI_3$ experiments. In the case of the complex composition, the time-based approach also yields larger voids with decreasing spin speeds. Thus, I could present a new processing approach to reliably and reproducibly fabricate perovskite thin films with consistent layer properties without the need for extensive optimization steps when process parameters intentionally or unintentionally change.

Considering the complex nature of solution-based processing techniques, an alternative solvent-less processing approach to fabricate perovskite thin films and their application as absorber layers in solar cells was investigated in Publication 3. The films were deposited via dry-powder aerosol deposition (PAD) and optionally hot-pressed. Therefore, the material synthesis and film formation were decoupled from each other. The generation of perovskite aerosol, and thus the film fabrication via PAD was optimized by a coworker to obtain perovskite absorber layers with a thickness suitable for solar cells. Additionally, the parameters of the hot-pressing step were developed to further improve the perovskite layer quality. I successfully manufactured fully working solar cells using these dry-processed perovskite films. However, when I measured and analyzed the solar cell data, the overall device performance lagged behind the

solution-based counterparts. GIWAXS (grazing incidence wide angle x-ray scattering) revealed how the hot-pressing step is influencing the perovskite octahedra orientation on a unit cell level. Here, the octahedra orientation changes from a random orientation to a preferred orientation along (110) & (020) upon hot-pressing. From the SEM images and Urbach analysis, we could determine that the PAD perovskite layer itself however is on par with solution-processed layers. To further understand the observed performance losses and to pinpoint the origin for these losses within our processing steps, I conducted absorption measurements of the electron-transport layer (ETL) from which could be concluded that the defect density in the ETL is increased after PAD processing. This was also suggested by conductive AFM (atomic force microscopy) measurements, where we could observe a shift in the onset potential once the ETL was exposed to the PAD process. From my light-intensity dependent solar cells measurements and their analysis, I could determine the ideality factor and the inverse recombination factor for the solar cells. With this analysis, I could further corroborate that monomolecular (trap-assisted) recombination at the interfaces between the perovskite layer and the charge extraction layers is the main origin of the performance losses. Nevertheless, we are confident that by optimization of the processing, efficient perovskite solar cells can be obtained in the future using our novel dry thin film fabrication process.
In the context of this thesis, this project shows that the perovskite layers obtained from PAD show similar properties to solution-processed ones. Further, the perovskite layer can be influenced by post-treatment steps such as hot-pressing. However, our findings show that it is important to consider that perovskite processing steps can influence underlying layers of the solar cell stack.

To develop a more detailed understanding of the pressing process of PAD perovskite films in general and to investigate what impact the temperature during pressing has on the resulting optoelectronic properties, the study presented in Publication 4 was conducted. Here, the relationship between morphology (e.g. grain size) and optoelectronic properties (e.g. phase transition) in particular was investigated. I measured SEM images which showed an increased grain size with increased pressing temperature. This morphological difference was also reflected in the XRD. Here, an increased preferred crystallographic orientation along (110) & (020) could be observed for the films pressed at elevated temperatures. Additionally, the phase transition temperature shifted to higher temperatures due to less strain in the hot-pressed samples and we found a decrease in defect density in these films as well. Thus, we could conclude that pressing especially at elevated temperature further improves the optoelectronic properties of the PAD perovskite films, which in turn is beneficial for the complete device.

In Publication 5 the focus was also on powder-based samples. We studied a set of different 2D lead-based perovskite materials, pressed into thick pellets. This material class is highly relevant for LED application. By incorporating disc-shaped monoprotonated amines as spacer molecules into the composition, the 3D perovskite can be sliced along different crystal planes, as discussed in section 4.2. By a careful selection of spacer molecules our chemistry collaborators obtained three 2D perovskite systems with a different degree of corrugation (DoC). In this context the DoC describes how many neighboring perovskite octahedra are connected via a trans conformation until a cis connection appears and the smaller the number of trans connected octahedra the higher the DoC. The first of the three materials belongs to $\langle 001 \rangle$ class of 2D perovskites, meaning the perovskite sheet consists only of trans connections

between the octahedra. The remaining two investigated systems are members of the ⟨110⟩ class with a zig-zag structured perovskite sheet with either three or two trans connections (see fig. 4.3). Thus, this set of 2D perovskites enabled us to study the effect of their nanostructure (DoC) on their resulting optoelectronic properties.
After a thorough crystallographic analysis of the perovskite materials, I investigated the photophysical properties in dependence on the DoC via steady-state absorption and temperature-dependent photoluminescence spectroscopy. From the absorption spectra, I found that with an increasing DoC, the optical band gap and the energetic spacing between the excitonic and band-to-band absorption increases, which is consistent with the idea of a greater electronic confinement upon increasing DoC. From temperature-dependent PL measurements, I could identify two different emissive species – a high-energy and a low-energy one. The ratio between the two species changes as a function of DoC. The higher the DoC the more dominant the broad white light emission was. I associated the high-energy emission with the emission of the exciton state and the broad emission with the emission from the so-called self-trapped exciton. Alternatively, the broad emission can also stem from an increase in defect density as the perovskite sheets become more corrugated. Hence, this study shows the effect of small variations on the crystallographic level on the macroscopic optoelectronic properties of this lead-based low-dimensional class of perovskites.

To extend the solvent-less processing from the perovskite layer to a charge extraction layer on the way to possible future fully dry processed solar cells, the hole transport material (HTM) Spiro-MeOTAD was investigated in Publication 6. The layer was fabricated via thermal co-evaporation of the HTM with the copper complex $Cu(TFSI)_3$. The focus of this study was to understand the details of the doping mechanism of Spiro-MeOTAD with $Cu(TFSI)_3$ on the molecular level and the resulting macroscopic transport properties. By employing different spectroscopic and electronic characterization techniques a conclusive understanding of the doping process could be gained. In particular, I performed and analyzed CELIV-measurements (**c**harge **e**xtraction by **l**inear **i**ncreasing **v**oltage) to extract the hole mobility as a function of $Cu(TFSI)_3$ concentration and temperature-dependent absorption measurements to confirm the temperature-independent CT state formation. The doping process can be divided into three different steps: 1. Formation of a coulombically bound CT state of the HTM with the copper complex, 2. Temperature-activated, reversible dissociation of the CT state where a free charge is generated, 3. Transport of generated free charges. Additionally, it was found that this doping approach has a remarkable doping efficiency of 50% at 10mol% of $Cu(TFSI)_3$ in the film. Combining this HTM processing with the PAD perovskite layer shows a lot of promise for a reduction of toxic solvents in the fabrication of perovskite solar cells.

In summary, with these 6 publications, I considerably contributed to the development of a fundamental understanding of how either the typical solution-based or the novel dry-powder-based processing of perovskite materials and the evaporation of HTM impact the nanostructure and the corresponding optoelectronic properties of the respective films. These findings will help to improve lead halide perovskite-based devices in the future.

8 Authors' Contributions

1. How the ionic liquid $BMIMBF_4$ influences the formation and optoelectronic properties of $MAPbI_3$ thin films

Simon Biberger, Konstantin Schötz, Philipp Ramming, Nico Leupold, Ralf Moos, Anna Köhler, Helen Grüninger, Fabian Panzer

in *Journal of Materials Chemistry A*, **2022**, 10, 35, 18038-18049

FP initiated the project. FP, KS and SB planned the experiments. SB prepared all samples, conducted all In-Situ experiments and analyzed the data with support of KS. PR conducted the time-resolved PL measurements and SB analyzed the data. NL measured XRD data and conducted the Rietveld refinement under the supervision of RM. HG measured and analyzed the solution NMR spectra. SB, together with KS and FP, outlined and wrote the manuscript. AK edited the manuscript. All authors critically read the manuscript and commented on the manuscript. FP supervised the project.

2. Reactive spin coating based on real-time in-situ feedback for improved control of perovskite thin film fabrication

Simon Biberger, Maximilian Spies, Konstantin Schötz, Frank-Julian Kahle, Nico Leupold, Ralf Moos, Helen Grüninger, Anna Köhler, Fabian Panzer

in *Journal of Materials Chemistry C*, **2024**, 12, 6415-6422

FP and SB initiated the project. FP, SB, MS, and KS planned the experiments. MS modified the software and syringe pump setup with help from KS and SB. SB and MS conducted the In-Situ experiments. SB conducted the optical measurements after annealing (steady state PL/absorption), and TRPL with support by Philipp Ramming. NL under supervision of RM and HG (with support by Christopher Greve) obtained the XRD data. SB conducted the SEM measurements. SB and MS analyzed the In-Situ data. SB analyzed the SEM, XRD and TRPL data. FP, SB, MS, KS and FJK discussed all results and outlined the manuscript. SB wrote the first draft of the manuscript. AK edited the manuscript. All authors critically read the manuscript and commented on the manuscript. FP supervised the project.

3. First of their kind: Solar cells with a dry-processed perovskite absorber layer via powder aerosol deposition and hot-pressing

Simon Biberger*, Nico Leupold*, Christina Witt*, Christopher Greve, Paul Markus, Philipp Ramming, Daniel Lukas, Konstantin Schötz, Frank-Julian Kahle, Chenhui Zhu, Georg Papastavrou, Eva M. Herzig, Anna Köhler, Ralf Moos, Fabian Panzer (*Contributed equally)

In *Solar RRL*, **2023**, 2300261

FP initiated and planned the project. Thin film samples were deposited by NL and DL vie PAD method under supervision of RM by using powders prepared by Irene Bauer and Monika Daubinger. Information about PAD processing including developments were provided by NL. CW established hot-pressing of thin films deposited by PAD method and performed the hot-pressing of all pressed films for the paper. SB manufactured, measured and analyzed the solar cells (J-V curves, solar cell metrics including light-intensity-dependent measurements) under supervision of FP and AK. CW determined surface roughness and film thickness of films using a profilometer and NL measured film thickness with an LSM. NL conducted XRD measurements, FJK did XPS measurements and SB and Angelika Mergner recorded SEM images. PR measured TRPL curves and SB measured absorption spectra under supervision of FP and AK. CW and KS did the Urbach energy analyses under supervision of FP. CG, under supervision of EMH, analyzed the GIWAXS data, which he measured together with CZ. PM performed and interpreted conductive AFM measurements under supervision of GP. FP, SB, NL and CW developed the concept of the paper and together with KS and FJK results were discussed and related to literature reports. FP, SB, NL, CW and regarding the GIWAXS data CG wrote the manuscript, which was revised by all authors.

4. Orientation and Grain Size in $MAPbI_3$ Thin Films: Influence on Phase Transition, Disorder and Defects

Christina Witt, Konstantin Schötz, Meike Kuhn, Nico Leupold, **Simon Biberger**, Philipp Ramming, Frank-Julian Kahle, Anna Köhler, Ralf Moos, Eva M. Herzig, Fabian Panzer

In *The Journal of Physical Chemistry C*, **2023** 127, 22, 10563-10573

FP supervised the project. CW pressed the thin film samples, which were deposited by NL and DL vie PAD method under supervision of RM by using powder prepared by Irene Bauer and Monika Daubinger. CW determined surface roughness and film thickness of films. SB, under supervision of FP and AK, recorded SEM images, where CW analyzed corresponding grain sizes. NL, under supervision of RM, conducted XRD measurements and analyzed them via Rietveld Refinement Method. MK, under supervision of EMH, contributed to the XRD analyses in terms of crystallographic orientation. FJK

recorded and evaluated XPS spectra. KS and CW measured temperature- and fluence-dependent PL and absorption spectra under supervision of FP and AK. PR, under supervision of FP and AK, measured TRPL curves, assisted by KS and CW. MK took microscope images of a film during cooling in a LINKAM stage, where temperature control was performed by FJK and CW. All analyses in the paper (i.e., morphological and optical analyses) were performed by CW, except for the evaluation of the XRD measurements via Rietveld Refinement Method. Regarding the optical analyses, CW was advised by KS and FP. FP, KS and CW developed the concept of the paper and discussed and interpreted the results. CW created the design of all figures and tables. FP, KS and CW wrote the manuscript, which was revised by all authors.

5. Structural Diversity in Layered Hybrid Perovskites, A_2PbBr_4 or $AA'PbBr_4$, Templated by Small Disc-Shaped Amines

Yuan-Yuan Guo, Lin-Jie Yang, **Simon Biberger**, Jason A McNulty, Teng Li, Konstantin Schötz, Fabian Panzer, Philip Lightfoot

in *Inorganic Chemistry*, **2020**, 59, 17, 12858–12866

PL initiated the project. YYG, LJY, JAM and TL synthesized the perovskite structures, measured, analyzed and discussed the crystallite structure, all under the supervision of PL. SB conducted all photophysical measurements and their analysis under the supervision of Fabian Panzer. SB discussed the results with FP and KS. YYG wrote the first draft of the manuscript except the photophysical properties chapter. SB wrote the first draft of the photophysical properties chapter and edited this section of the paper together with KS and FP. All authors critically read the manuscript and commented on the manuscript. PL supervised the project.

6. Intricacies and Mechanism of p-Doping Spiro-MeOTAD Using $Cu(TFSI)_2$

Adrian Hochgesang, **Simon Biberger**, Jeannine Grüne, John Mohanraj, Frank-Julian Kahle, Vladimir Dyakonov, Anna Köhler, Mukundan Thelakkat

in *Advanced Electronic Materials*, **2022**, 8, 10, 2200113

MT initiated the project. AH prepared the co-evaporated samples, measured room temperature optical spectroscopy, prepared and measured temperature dependent Mott-Schottky devices, temperature dependent electrical conductivity, mobility and activation energies for hopping transport and charge transfer state dissociation. He also, performed the Negative Differential Susceptance Mobility Measure-

ments. SB conducted and analyzed the temperature-dependent UV/Vis/NIR absorption experiments, as well as the MIS-CELIV measurements. JG measured and analyzed all EPR data. JM measured and evaluated the UPS data, and FJK assisted with the MIS-CELIV experiment. AH and MT wrote the first draft of the manuscript. All authors critically read the manuscript and commented on the manuscript. MT, AK, and VD supervised the project.

9 How the Ionic Liquid $BMIMBF_4$ Influences the Formation and Optoelectronic Properties of $MAPbI_3$ Films

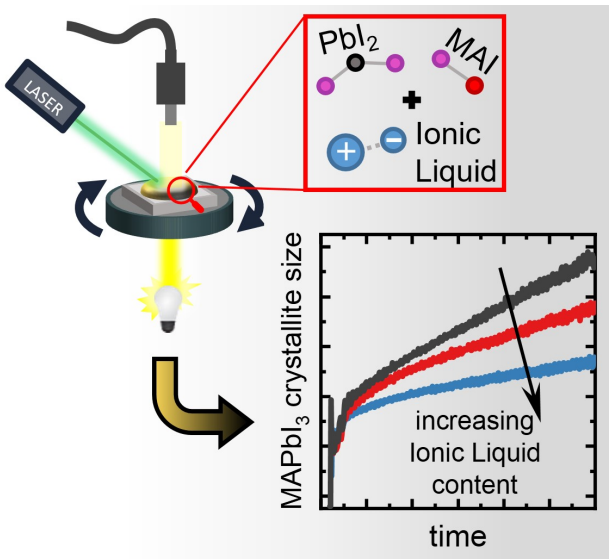

Simon Biberger, Konstantin Schötz, Philipp Ramming, Nico Leupold, Ralf Moos, Anna Köhler, Helen Grüninger, Fabian Panzer

Published in
Journal of Material Chemistry A, **2022**, 10, 35, 18038-18049

Volume 10
Number 35
21 September 2022
Pages 17841–18434

Journal of Materials Chemistry A

Materials for energy and sustainability

rsc.li/materials-a

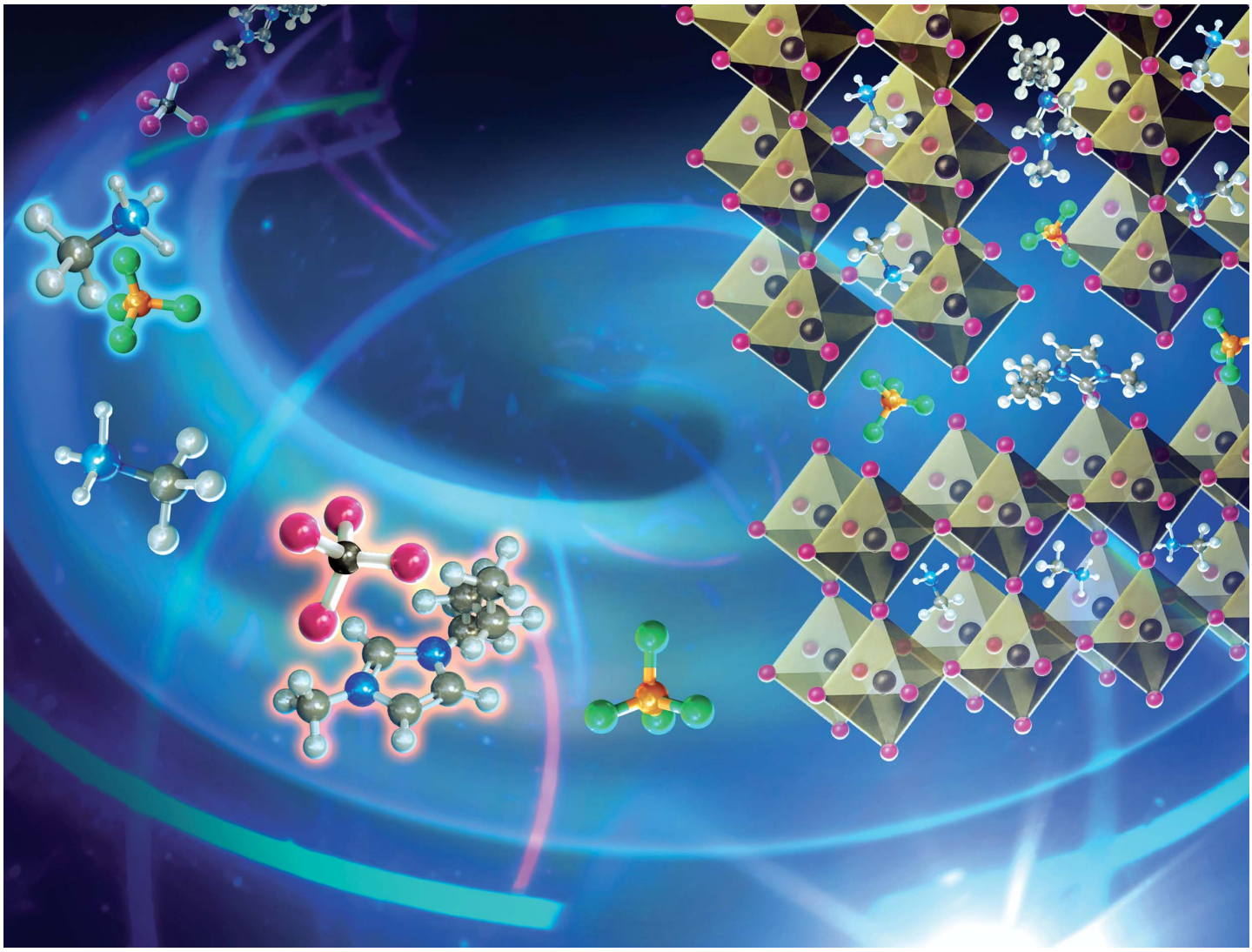

ISSN 2050-7488

ROYAL SOCIETY OF CHEMISTRY

PAPER
Fabian Panzer *et al.*
How the ionic liquid $BMIMBF_4$ influences the formation and optoelectronic properties of $MAPbI_3$ thin films

Journal of Materials Chemistry A

ROYAL SOCIETY OF CHEMISTRY

PAPER

View Article Online
View Journal | View Issue

Cite this: J. Mater. Chem. A, 2022, 10, 18038

How the ionic liquid BMIMBF$_4$ influences the formation and optoelectronic properties of MAPbI$_3$ thin films†

Simon Biberger,[a] Konstantin Schötz,[a] Philipp Ramming,[a] Nico Leupold,[b] Ralf Moos,[b] Anna Köhler,[a] Helen Grüninger[c] and Fabian Panzer*[a]

While using additives such as ionic liquids (IL) is known to boost the efficiency and stability of perovskite solar cells, it is still unclear how ILs impact the difficile perovskite film formation process. Here we investigate the impact of the IL BMIMBF$_4$ on the film formation of the model halide perovskite MAPbI$_3$ by multimodal optical *in situ* spectroscopy during solution processing *via* one-step spin coating and a solvent engineering approach. One-step processing experiments reveal that IL in the precursor solutions does not affect the formation of perovskite–solvent complexes, but higher IL contents delay the perovskite transformation with decreased growth rates. For solvent engineering, the perovskite growth rate decreases with later anti-solvent (AS) dripping as the properties of PbI_4^{2-} species in the precursor solutions change during drying. Here the IL also affects the evolution of the PbI_4^{2-} properties, as the IL cation interacts with the PbI_4^{2-}. This interaction appears to reduce the perovskite growth rates after initiating perovskite formation by AS dripping. Still, in the as-coated films the IL efficiently passivates defect states. Thus, our work provides important insights into how decisive ILs impact the sensitive interconnection between precursor properties, film formation process and final optoelectronic functionality of perovskite thin films.

Received 3rd June 2022
Accepted 22nd July 2022

DOI: 10.1039/d2ta04448j

rsc.li/materials-a

1. Introduction

Within the last decade the rise of metal halide perovskites (MHPs) as light absorbers in solar cells is unprecedented, so that today they are considered as one of the most promising candidates for next-generation photovoltaics.[1,2] The rapid increase of perovskite solar cell efficiencies was initially achieved by optimizing the MHP composition, developing new solution processing approaches and tailored charge extraction layers.[3–8] A more recent key development to improve the efficiency and the stability of perovskite solar cells is the usage of passivating additives to reduce the number of defect states in the perovskite grain boundaries or at its interface to the charge extraction layers. This is either achieved by introducing passivating layers below and on top of the perovskite layer,[9–14] or by mixing different types of additives into the precursor solution.[15–21] The advantage of the latter approach is that the passivating effect is not limited to the interface, but also improves the perovskite grain boundary properties. For this bifunctional passivation approach of MHPs, ionic liquids (IL) have turned out to be especially suitable.[10,22–25] For example, Snaith *et al.* mixed 1-butyl-3-methylimidazoliumtetrafluoroborate (BMIMBF$_4$) into the precursor solutions of different halide perovskites, which lead to an extraordinary high stability of resulting solar cells and improved optoelectronic film properties.[26]

Another important aspect affecting the optoelectronic properties of perovskites is their morphology, which in turn is decisively determined by the exact crystallization processes that occur during the solution based thin film preparation. While developing a general understanding of the perovskite film formation has been an important research focus for several years, in particular investigated by *in situ* characterization methods,[27–35] the exact role of ionic liquids during solution processing is still not well understood. In particular, it is not yet clear how adding an IL to the precursor solutions leads to the beneficial optoelectronic final film properties, and whether the IL interacts with the precursors, intermediate states and the perovskite during the film formation process, possibly influencing the latter.[36–40]

In this work, we study the influence of the ionic liquid BMIMBF$_4$ on the film formation of the model halide perovskite methylammonium lead iodide (MAPbI$_3$) by multimodal *in situ* optical spectroscopy. We simultaneously measured absorption, photoluminescence (PL) and scattered light during solution

[a]Experimental Physics II, University of Bayreuth, Bayreuth, Germany. E-mail: fabian.panzer@uni-bayreuth.de
[b]Department of Functional Materials, University of Bayreuth, Bayreuth, Germany
[c]Northern Bavarian NMR Centre (NBNC) and Inorganic Chemistry, University of Bayreuth, Bayreuth, Germany

† Electronic supplementary information (ESI) available. See https://doi.org/10.1039/d2ta04448j

View Article Online
Paper Journal of Materials Chemistry A

based thin film processing by spin coating. The sub-second time resolution of our *in situ* measurement setup allows to access all relevant formation kinetics, so that a detailed understanding of the role of the IL in the film formation process can be developed.

We focus on the film formation during one-step spin coating as well as during the solvent engineering approach. In the one-step spin coating experiments, where the substrate is spun until the solvent is completely evaporated, we investigate the influence of the IL on the formation of solvent complex structures. Furthermore, we address how the IL affects the transition of these solvent complexes into perovskite, as well as the subsequent perovskite growth.

In the solvent engineering approach, the perovskite crystallization is triggered by dripping an anti-solvent (AS) onto the spinning precursor solution after a well-defined time. By systematic variation of the AS dripping time point, we investigate the influence of the IL on the evolution of iodoplumbate states in the precursor solution and the subsequent perovskite crystallization kinetics. Here, the presence of the IL appears to facilitate the formation of PbI_4^{2-} in the precursor solution, resulting in a reduced perovskite growth rate after AS dripping. By X-ray diffraction (XRD), scanning electron microscopy (SEM) and PL characterizations, we also evaluate how the changes in the formation process impact on the final film properties. This finally allows us to understand the differences of the grain size, film stability and non-radiative recombination rates that occur in films with different IL content.

2. Experimental

2.1 Precursor solutions

All materials were used as received. Lead(II) iodide (PbI_2, 98%) and methylammonium iodide (MAI, 99%) were purchased from TCI. PbI_2 and MAI were weighed in a stoichiometry of 1 : 1 and dissolved in DMF (Acros). The ionic liquid (IL) $BMIMBF_4$ (Sigma-Aldrich) was diluted with DMF and the appropriate amount added to the solutions containing IL so that the overall concentration of all solutions was 1.2 M. Before spin-coating, all solutions were filtered with a 0.2 μm syringe filter.

2.2 Thin-film fabrication

ITO substrates were cleaned in an ultrasonic bath with soap water (Hellmanex), deionized water, acetone, and isopropanol and treated with oxygen plasma prior to use. The substrates were transferred into a nitrogen-filled glove box. As additional extraction layers, poly[bis(4-phenyl)(2,4,6-trimethylphenyl) amine] (PTAA, Sigma-Aldrich; 1.5 mg ml^{-1} in toluene, 6000 rpm for 30 s, 10 min at 100 °C) and poly(9,9-bis(3′-(*N*,*N*-dimethyl)-*N*-ethylammonium-propyl-2,7-fluorene)-*alt*-2,7-(9,9-dioctyl-fluorene))dibromide (PFN-Br, Sigma-Aldrich; 0.5 mg ml^{-1} in methanol, 5000 rpm for 20 s) were spin-coated onto the ITO substrate. The spin coating of the perovskite layer was then carried out on a custom-built spin coater at a spin speed of 2000 rpm for all samples, using 80 μl of precursor solution per sample. For the samples fabricated *via* the solvent engineering approach 500 μl of diethyl ether (Honeywell) was dripped onto the substrates as AS at the respective timings. The obtained perovskite films were annealed at 100 °C for 1 h.

2.3 *In Situ* optical spectroscopy

All optical *in situ* data were recorded with a home-built setup, detailed in Section S1 in the ESI.† In brief, three different optical channels (photoluminescence (PL), scattered light, and absorption) were recorded at a frame rate of 11.7 Hz/15 Hz for the one-step processing/solvent engineering measurements. PL and the scattered light were recorded simultaneously in one spectrum. PL/scattered light and absorption were then recorded alternating frame by frame. To ensure reproducibility we recorded at least two coatings for each sample, which turned out to be quasi-identical. In addition, to avoid any impact of a built-up of solvent atmosphere, a fan was placed above the spin coater (see Fig. S1†).

2.4 Liquid-state NMR spectroscopy

MAI, PbI_2 and MAI + PbI_2 precursor were dissolved in DMF-d7 (each 1.2 M) with and without 5 mol% IL. In case of PbI_2 and PbI_2 + 5 mol% IL additionally a drop of DMSO-d6 was added to dissolve the PbI_2 entirely. Liquid-state NMR spectra of the precursor solutions were recorded on a Bruker Avance III and Avance III HD systems operating at a magnetic field strength of 9.4 T (400 MHz, ^{19}F and ^{207}Pb experiments) and 14.1 T (600 MHz; ^{1}H and ^{13}C experiments), respectively. Probe heads used were a Bruker 5 mm diffusion HFX probe (400 MHz) and a standard liquid-state Bruker 5 mm HCN probe (600 MHz). The chemical shift was referenced using 1 M lead nitrate solution in D_2O for ^{207}Pb (−2990 ppm) and 0.05% trifluoro-toluene solution in $CDCl_3$ for ^{19}F (−63.72 ppm) as secondary references. The ^{13}C and ^{1}H NMR spectra are referenced to tetramethylsilane (TMS). All experiments were performed at room temperature.

The ^{1}H NMR spectra (ν_0 (^{1}H) = 600.1 MHz) were obtained with a single pulse (SP) excitation with a pulse length of 3.0 μs corresponding to 30° tip angle and a recycle delay of 1 s. The ^{13}C NMR spectra (ν_0 (^{13}C) = 150.9 MHz) were acquired with an SP sequence, a 6 μs pulse length corresponding to a 45° tip angle and a recycle delay of 3 s. During ^{13}C acquisition, proton broadband decoupling was applied using a waltz-16 sequence with ν_{nut} = 3.6 kHz. ^{19}F NMR spectra (ν_0 (^{19}F) = 376.5 MHz) were obtained with a SP excitation with a pulse length of 4.1 μs corresponding to 30° tip angle and a recycle delay of 5 s. ^{207}Pb NMR spectra (ν_0 (^{207}Pb) = 83.71 MHz) obtained with a SP excitation with a pulse length of 12.0 μs corresponding to 90° tip angle and a recycle delay of 0.5 s. A chemical shift range from −1500 to 2000 ppm was "scanned" in ~500 ppm steps.

2.5 XRD

The XRD patterns were collected in reflection mode using a Bruker D8 Discover A25 with Cu $K_{\alpha I}$ radiation (λ = 0.15406 nm), whereby the $K_{\alpha II}$-rays are removed by a Ge-$K_{\alpha I}$-monochromator. The diffractometer was operated at 40 kV and 40 mA. The 2θ range was set from 10° to 45° with a step size of 0.016°.

View Article Online
Journal of Materials Chemistry A Paper

2.6 SEM

The film morphology was characterized by SEM using a Zeiss Leo 1530 instrument FE-SEM with Schottky-field-emission cathode, In-lens detector, and SE2 detector. The accelerating voltage was 3 kV. Prior to measurement, the samples were sputtered with 2 nm platinum.

2.7 TR-PL

For time-resolved photoluminescence curves, time-correlated single-photon counting (TCSPC) measurements were performed with a PicoQuant MT200 confocal fluorescence microscope in combination with a PMA Hybrid PMT 40 photomultiplier tube (PicoQuant) and a TimeHarp 260 Pico TCSPC board (PicoQuant). The samples were excited with a 560 nm diode Laser (PicoQuant LDH-D-TA-560) with a frequency of 2.0 MHz and a pulse width of 68 ps. The laser beam was focused on the sample with an Olympus Objective with 4× magnification and the emission was filtered with a 561 nm long-pass filter before detection. The excitation fluence was set to 300 nJ cm^{-2}.

2.8 Microscopy

Images of the films obtained by one-step processing were taken with a Leica DM 2700M using a Leica N Plan EPI objective (100×/0.85 BD).

3. Results and discussion

We monitored the optical properties of the $MAPbI_3$ precursor solution during the film processing using an extended version of the setup described by Buchhorn *et al.*[41] In brief, a drop of precursor solution is deposited onto a rotating substrate, and while the film forms from the wet solvent layer, its absorption, photoluminescence (PL), and scattered light are recorded simultaneously. To determine the optical density, the transmitted light of a white light LED placed below the substrate is collected by an optical fiber and led to a detection unit. From these spectra and a reference transmission spectrum of a blank substrate measured before the processing, the optical density is determined.[27] To differentiate between effects of absorption and scattering in the optical density (OD) spectra, we also measured the light intensity $I_{scatter}$ of a green LED (peak wavelength of 500 nm or 2.48 eV respectively; in the following referred to as scatter-LED) that is scattered in the sample plane. More scattering centers lead to an increase, and more absorption results in a decrease of $I_{scatter}$. Additionally, the PL is excited with a laser and both, the scattered LED light and the PL are collected by the same optical fiber. More details of the setup and the optical detection setup are given in Section S1 in the ESI.†

We use this system to investigate the one-step and the solvent engineering solution processing of $MAPbI_3$ thin films. One-step processing of $MAPbI_3$ using a dimethylformamide (DMF) based precursor solution typically results in films with incomplete coverage, as solvent-complexes crystallize in a needle-like manner, as depicted in Fig. 1b and S2,† predefining also the morphology of the perovskite phase.[28] For the processing condition that we use in our work (DMF as solvent, processing at room temperature, precursor solution concentration of 1.2M and a MAI : PbI_2 ratio of 1 : 1) the predominant structure of these complexes was found to be $(MA)_2(DMF)_2$-Pb_2I_6.[29,42–44] Their formation can be avoided by the so-called solvent engineering method, where an anti-solvent is dripped onto the rotating wet precursor film prior to the formation of the complex phase.[44] For good film quality, the point in time when the anti-solvent is dripped prior to solvent complex formation is crucial. Thus, we first investigate how the presence of the IL impacts on solvent complex phase formation for the one-step processing before focusing on the solvent engineering method.

3.1 One-step processing

We spin-coated equimolar solutions of PbI_2 and MAI dissolved in DMF (1.2M with different contents of IL). Fig. 1a illustrates the typical evolution of the PL, the scattered light and the optical density in the first 130 s of spin coating for the solution without IL, which serves as reference solution. The time t = 0 corresponds to the start of the spin coating.

In the first 15 s, no changes in the PL and the scattered light are observable. In contrast, a sine-like modulation in the OD between 1.5 eV and 2.0 eV is present. This modulation is indicative of a white light interference effect and from it, the evolution of the solvent layer thickness during spin coating can be extracted. While after 15 s there is still no signal detectable in the PL, the intensity of the scattered light and the OD begin to increase, with the latter exhibiting a flat spectral shape. This rise of OD, together with a strong increase of scattered light intensity, is evidence that scattering centers form within the solution film. Since there is no perovskite signature in the PL channel observable, we can exclude the formation of $MAPbI_3$ crystallites at this point of spin coating time, and we associate these scattering centers with the formation of solvent-complex structures. Hence, we call the point in time, at which the intensity of the scattered light and the OD exhibits the strongest rise, $t_{complex}$.

After the initial rise, the scattering intensity stays roughly constant for 6 s and then drops to values below the initial value (also see Fig. S3†). This drop is a sign for the transformation from the solvent-complex phase to a perovskite phase, where the latter absorbs the light of the scatter-LED.[28] The formation of perovskite crystallites is underpinned by the concomitant appearance of perovskite emission signatures in the PL spectrum after 21 s. The moment of the strongest PL increase we refer to as t_{pero}. A broad and asymmetric PL signal appears at 1.9 eV, and its peak monotonously shifts to lower energies and gains intensity during the further spin coating (see Fig. S4† for PL spectra at different times). Similarly, also the OD signal changes from t_{pero} onwards, where the OD spectrum becomes slightly more pronounced at higher energies (see Fig. S5†). From the spectral shape of the OD and from the observed presence of perovskite PL, we conclude that the OD increase is not only due to scattering, but also due to additional absorption of perovskite crystallites that form from t_{pero} onwards. For the

View Article Online
Paper Journal of Materials Chemistry A

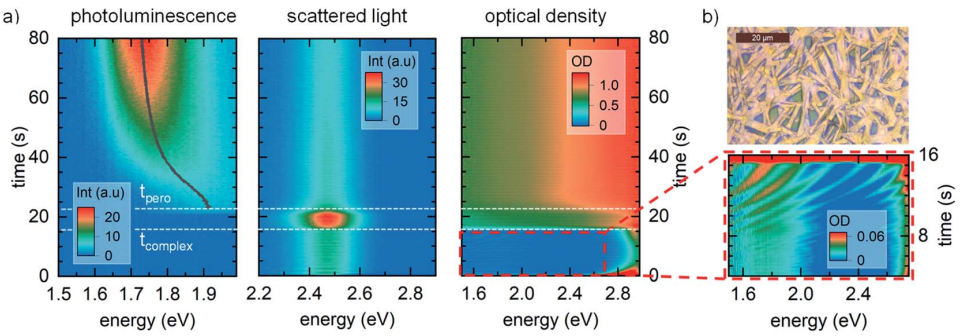

Fig. 1 (a) Heat maps of photoluminescence (PL), scattered light, and optical density (OD) measurements during the one-step processing at 2000 rpm of the reference solution without IL. In the PL map the peak position of each spectrum is indicated as black line. The time points of the highest formation rate of solvent-complex phase $t_{complex}$ and of perovskite phase t_{pero} are indicated as white dashed lines. The magnification of the OD heat map in the first 15 s of spin coating shows the temporal evolution of the interference pattern due to thin-film interference. (b) Optical microscopy image of the resulting film obtained by one-step processing the reference solution at 2000 rpm.

one-step processing of solutions containing IL, we observe the same qualitative evolution of the different optical properties (Fig. S6†).

Next, we analyzed the time evolution of the different optical properties quantitatively. We first focused on the white light interference effect in the OD spectra and extract the evolution of the solvent layer thickness during spin coating by optical modelling of the interference fringes as described in the ESI (Section S2†). We find the thickness for the reference sample to drop to 2 µm within the first 15 s of spin coating (Fig. S7†). The evolution of the film thickness is identical also for the solutions containing the IL, indicating that the IL has no influence on the evaporation rate of the solvent before complex phase formation (see Fig. S7† for detailed analysis and differentiation between solution throw-off and evaporation).

For all precursor solutions considered in our study, the interference pattern vanishes and the OD rises when $t_{complex}$ is reached (after approx. 16 s). Fig. 2a shows the OD at 1.6 eV for the reference sample and the samples containing 1 mol% and 5 mol% of IL as a function of spin coating time. Since this energy is below the absorption edge of bulk $MAPbI_3$ (~1.65 eV),[45,46] only scattering effects due to the formation of solvent complexes cause the OD increase in Fig. 2a.[28,42] As the OD increases similarly for all IL contents, we conclude the formation of solvent complexes to be largely independent of the IL content in our case.

As mentioned above, the formation process of the solvent complex structures is also reflected in an increase of $I_{scatter}$. Furthermore, the time evolution of $I_{scatter}$ also contains the information about the subsequent perovskite formation process, corresponding to a drop of $I_{scatter}$. To evaluate the point in time and duration of both formation processes in more detail, we analyze the time derivative $dI_{scatter}/dt$ (see Fig. 2b). In the time evolution of $dI_{scatter}/dt$, the positive peak corresponds to the highest formation rate of solvent-complex phase and from its position we extract $t_{complex}$, whereas the negative peak is associated with the highest transformation rate of the solvent complexes to perovskite, determining t_{pero}.[28] By fitting the peaks with a log–normal function, $t_{complex}$ and t_{pero} were quantified (Fig. 2d top). Additionally, the full width at half maximum (FWHM) of the peak fits corresponds to the duration of the formation processes, indicated by the width of the shaded areas in the top panel of Fig. 2d.

We find the duration of the solvent-complex formation to be ~1.8 s, and $t_{complex}$ = 16 s, both values being largely independent of the IL content. When it comes to the transformation of the solvent complex to perovskite, t_{pero} increases from 21.4 s (0 mol%) to 21.8 s (1 mol%) to 23.8 s for 5 mol% of IL, suggesting a more delayed perovskite formation for higher IL concentration. Especially for 5 mol%, the duration of the transformation is 3.1 s, clearly larger compared to the FWHM of 1.9 s for the reference sample.

As a next step we analyzed the evolution of the PL properties during spin coating. The peak position of the first perovskite PL spectrum that appears during the spin-coating process is located at ~1.9 eV. This energy is considerably higher than typical bulk PL peak energies of 1.6 eV,[27] suggesting the presence of a quantum confinement effect. The subsequent shift of the PL peak position for $t > t_{pero}$ reflects a reduction of the quantum confinement as the initial perovskite crystallites grow.[47,48] Based on the quantum mechanical particle in a box model,[49] the energetic position of the PL peak E_{PL} can be related to the crystallite size d by

$$E_{PL} = E_g + \frac{b}{d^2} \quad (1)$$

where we set the $MAPbI_3$ bulk band gap value E_g = 1.59 eV,[27,45,46,50] and the constant b = 3 eV nm^2,[51,52] based on literature values. We extract the PL peak position by fitting an asymmetric hyperbolic secant to the measured PL spectra, and quantified the evolution of the perovskite crystallite size using eqn (1) (Fig. 2c; also see Fig. S8† for details).

We observe two distinct time periods at which the crystallite size appears to increase with different rates: a fast initial growth and a reduced growth at later times. This observation is in accordance with the results from Schötz and Greve *et al.*,[28] who

View Article Online
Journal of Materials Chemistry A Paper

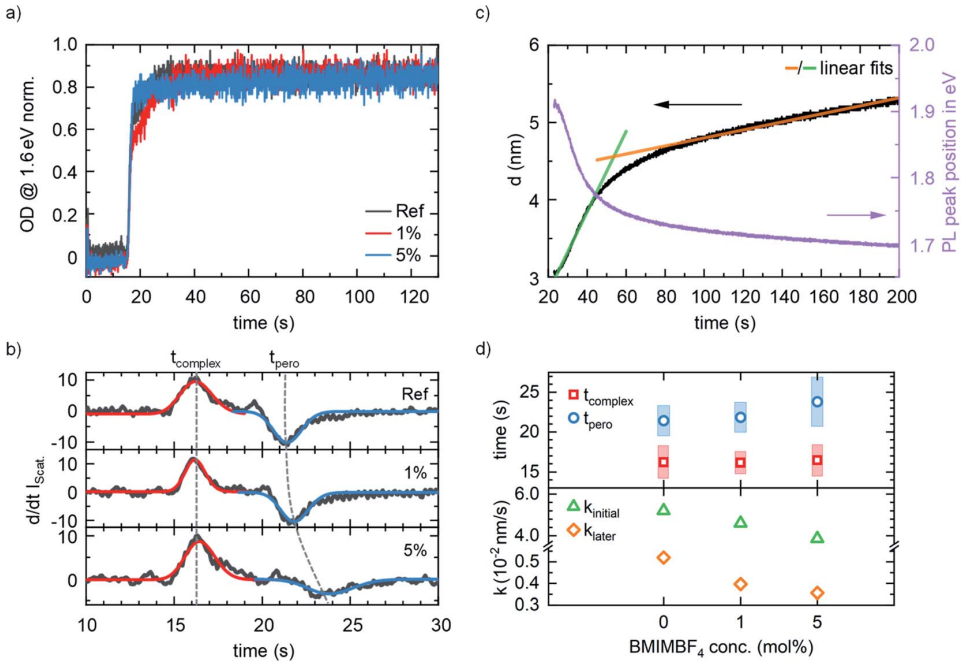

Fig. 2 (a) Time evolution of the optical density at 1.6 eV for reference sample and samples containing 1 mol% and 5 mol% of IL. (b) Time derivative d$I_{scatter}$/dt of the intensity at 2.48 eV of the scatter-LED for the three solutions. The positive (red) and negative (blue) peaks are fitted with a log–normal function. (c) Time evolution of the PL peak position (purple) and the calculated crystallite size (black) according to eqn (1) for the reference solution. The green and orange lines are linear fits, from which the perovskite crystallite growth rates are extracted. (d) $t_{complex}$ and t_{pero} as extracted from the d$I_{scatter}$/dt analysis in (b), for all IL contents. The shaded area represents the FWHM of the fitted log–normal functions (top). The initial crystallite growth rates (orange) and the growth rates later on (green) as a function of IL content (bottom).

associated the fast initial growth with free growth of the small crystallites within the grain boundaries of the solvent complex phase. Once the perovskite crystallization proceeds towards the grain boundaries of the solvent complex phase, its growth becomes limited, resulting in the slower perovskite growth at later times.[28]

From linear fits to the evolution of the crystallite size, we extract the growth rates for both periods. This analysis was performed for all coatings, and the obtained growth rates are shown in Fig. 2d as a function of IL content. With increasing IL content, the initial growth rate decreases from 5.2×10^{-2} nm s^{-1} for the reference solution, to 4.6×10^{-2} nm s^{-1} (1 mol%), to 3.9×10^{-2} nm s^{-1} for the solution containing 5 mol%. Similarly, the rates for the later growth decrease from 5.2×10^{-3} nm s^{-1} (reference), to 4.0×10^{-3} nm s^{-1} (1 mol%) and to 3.6×10^{-3} nm s^{-1} (5 mol%). Thus, the presence of IL seems to hamper both perovskite growth processes.

From the one-step processing experiments, we conclude that the IL has no impact on the evolution of the solvent layer thickness prior to $t_{complex}$. Further, the IL neither affects the point in time when the solvent-complex formation take place, nor its rate. However, the IL delays and slows down the initial transformation of the complex phase to the perovskite phase and also hampers perovskite growth rates at later times. An explanation for this behavior could be that the IL interacts with the solvent complexes and thus hinders the solvent from evaporating from the complex structures, leading to a delayed perovskite formation. Recently, it was suggested that the BMIM$^+$-ion of the IL coordinates to PbI$_3$,[53] which might also be the case in our samples. In this case, the presence of such coordinated structures might interrupt the perovskite crystallization from the $(MA)_2(DMF)_2Pb_2I_6$ solvent complex structures, leading to reduced overall perovskite growth rate.

3.2 Solvent engineering

After investigating the influence of IL on the formation of solvent complex structures, where we found no influence on the solvent complex formation but on the perovskite growth, the question arises whether IL impacts the perovskite formation and possibly the precursor properties also in the case of solvent engineering.

In analogy to the one-step processing experiments, for our solvent-engineering experiments we used the same precursor solutions (1.2M PbI$_2$ and MAI dissolved in DMF), *i.e.* without IL and with 1 mol% and 5 mol% of IL content, and tracked the film formation during spin coating by the multimodal spectroscopy approach. From our investigations in Section 2.1, we know that the solvent-complex phase begins to form after 15 s, independent of the IL content. For the solvent engineering experiments, we thus varied the AS dripping time point t_{ASD} after the start of the spin coating between 6 s, 12 s, and 15 s. Here t_{ASD} = 6 s

View Article Online
Paper Journal of Materials Chemistry A

allows to investigate the effect of a relatively early AS dripping on the film formation, $t_{ASD} = 12$ s represents an AS dripping time point that is often used to prepare high efficient perovskite solar cells,[54] and $t_{ASD} = 15$ s is close to the latest possible addition of the AS prior to solvent complex formation.

Fig. 3a shows the time evolution of the PL, the scattered light, and the optical density during the film processing, using a precursor solution without IL and an AS dripping time point of $t_{ASD} = 15$ s. Within the first 15 s of spin coating, the optical spectra evolve identically to the case of one-step processing, *i.e.*, no PL intensity is present, the scatter LED intensity stays constant, and the OD spectra exhibit a sine-like modulation around zero, due to a thin-film interference effect. The constant scatter intensity and the negligible OD intensity below 2.5 eV are evidence that no solvent complexes are formed up to this point in time.

At ~15 s, when the AS is dripped onto the rotating precursor solution film on the substrate, all optical properties change drastically. Perovskite PL with a peak at 1.65 eV appears immediately and its intensity substantially increases and decreases again, all within ~2 s. While the appearance of the PL signal suggests the initial formation of perovskite crystallites, we attribute the drastic change of PL intensity to an improved light in- and out-coupling as long as the AS is present and not yet fully spun away from the probed sample area. In the moment of adding the AS, the intensity of the scattered light vanishes and remains absent for the rest of the spin coating, suggesting that no scattering centers form throughout the entire spin coating process. Simultaneously, the OD above 1.8 eV rises promptly. We associate the OD increase above 1.8 eV to stem from absorption of nanoconfined perovskite crystallites,[47,48,55] in line with the PL properties in the moment of AS dripping (*see above*).

After the initial perovskite formation period, *i.e.* from ~17 s onwards, the PL intensity rises again, accompanied by a shift of the PL peak to lower energies. Similarly, the absorption onset shifts to ~1.6 eV (Fig. 3b). These changes indicate a growth of the perovskite crystallites.[47,55] Qualitatively, the evolution of optical properties for the other AS dripping times and IL contents exhibit a similar behavior (Fig. S9–S11†).

To investigate the impact of AS dripping time on the initial perovskite formation kinetic in more detail, we consider the time evolution of the OD at 1.8 eV (Fig. 3c). From Fig. 3c, it becomes clear that regardless of t_{ASD}, the OD at 1.8 eV increases rapidly at the moment of AS dripping and then quickly approaches a maximum value. We attribute the kink in the

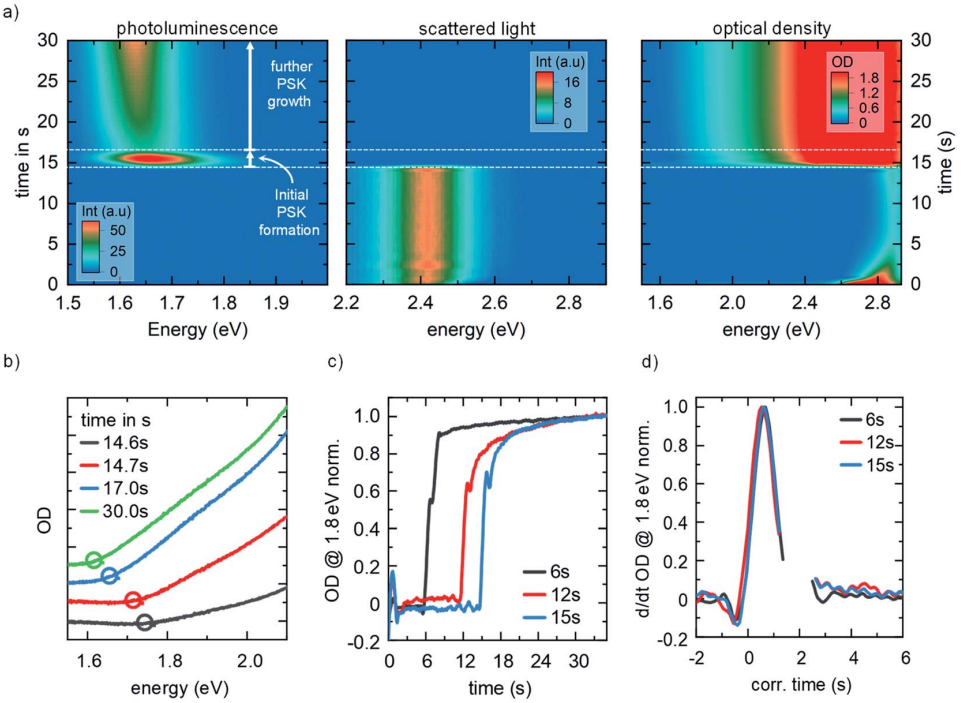

Fig. 3 (a) Heat maps of photoluminescence (PL), scattered light, and optical density (OD) measurements during spin coating using the solvent engineering approach at 2000 rpm of a reference solution. Here, the AS was dripped after 15 s. The white arrows indicate the time ranges of initial perovskite (PSK) formation and further PSK growth, with the dashed white horizontal lines indicating their starting time. (b) OD spectra at different times during the processing of reference solution during solvent engineering (solid lines). Circles indicate the absorption onset at each time step, and for clarity the spectra were shifted vertically. (c) Time evolution of the OD at 1.8 eV during processing of the reference solution with different AS dripping time points. (d) Normalized time derivative of the OD at 1.8 eV (smoothed, see Section S3 for details) during processing of the reference solution with different AS dripping time points. The time axis is shifted so that $t = 0$ corresponds to the moment of AS dripping.

View Article Online
Journal of Materials Chemistry A Paper

steep OD increase to the changes in light outcoupling during the presence of AS in the probed sample area. Fig. 3d shows the time derivative of the OD at 1.8 eV, where we shifted the time axis, so that $t = 0$ corresponds to the moment of AS dripping. Similar to the approach from the $dI_{scatter}/dt$ analysis in Fig. 2b, the FWHM of the resulting dOD/dt peak is a measure for the duration of the initial perovskite crystallization process. Here the identical shape and width of the dOD/dt peaks for the different AS dripping time points in Fig. 3d suggests that the rate of initial perovskite formation is independent from the AS dripping time points.

After having analyzed the kinetics of the initial perovskite formation upon dripping the AS, and how it depends on the AS dripping time point, we analyzed the kinetics of the perovskite growth during further spin coating. To this end, we extracted the crystallite size from the time evolution of the perovskite PL peak position using eqn (1), analogous to the analysis in Fig. 2c. Fig. 4a–c show how the crystallite size for the different AS dripping time points (black lines) evolves, and Fig. 4d summarizes corresponding perovskite growth rates k_{growth}, obtained by linear fits to the data in Fig. 4a–c. For the precursor solution without IL, increasing the AS dripping time point from 6 s, to 12 s to 15 s results in k_{growth} values of 15.4×10^{-2} nm s^{-1}, 6.6×10^{-2} nm s^{-1} and 9.0×10^{-2} nm s^{-1} respectively. Thus, t_{ASD} does not correlate directly with the resulting perovskite crystallite growth rates, where the increase of k_{growth} for increasing t_{ASD} from 12 s to 15 s is particularly notable.

To understand this behavior, we reconsider the OD spectra in the one-step processing experiments from Section 2.1 (*i.e.* Fig. 1), with a focus on the evolution of their high energy spectral range prior to the formation of solvent-complex structures, *i.e.* within the first 16 s of spin coating (Fig. 5a). These spectra show an increase in the range above ~2.7 eV, which we associate with the absorption onset of the iodoplumbate species PbI_4^{2-} that is known to be present in MAPbI$_3$-DMF precursor solution.[56,57] After the initial throw-off of precursor solution, it becomes clear from Fig. 5a, that between ~7–9 s of spin coating, the absolute intensity of the PbI_4^{2-} absorption remains mainly constant, and increases afterwards. Due to the limited spectral range that we can detect reliably with our measurement system, it is not possible to resolve whether the observed gain in intensity is due to an increasing amount of PbI_4^{2-}, or if the PbI_4^{2-} absorption peak broadens. The latter would indicate a polynucleation of the PbI_4^{2-} complex, as suggested by Valencia *et al.*[57]

Nevertheless, from the rise in absorption in Fig. 5a, it becomes clear that the properties of the iodoplumbate species in the precursor solution change between 10 s and 15 s of spin

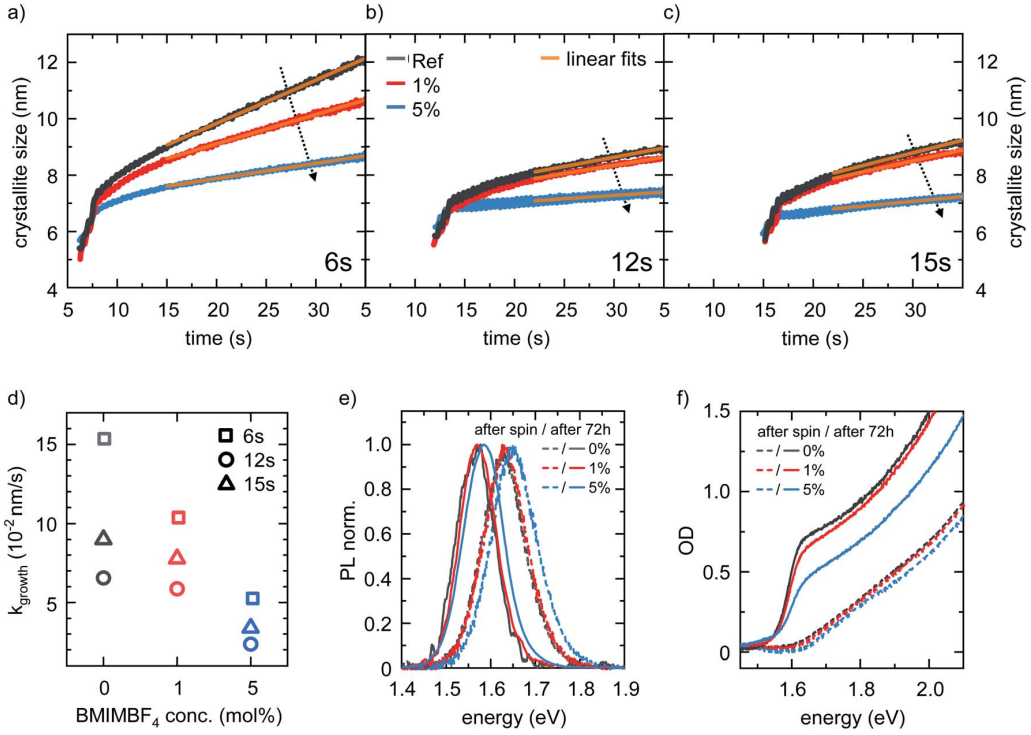

Fig. 4 Time evolution of the crystallite size, calculated from eqn (1), for the different IL contents and AS dripping time points (a) 6 s, (b) 12 s, (c) 15 s, together with linear fits, from which the crystallite growth rates were extracted. (d) Extracted crystallite growth rates as a function of the IL concentration and different AS dripping time points. (e) Normalized PL spectra for the different IL contents directly after spin coating and after 72 h without thermal annealing after spin coating (smoothed, see Section S3). (f) Comparison of the absorption spectra directly after spin coating (dashed lines) and after 72 h (solid lines).

View Article Online
Paper Journal of Materials Chemistry A

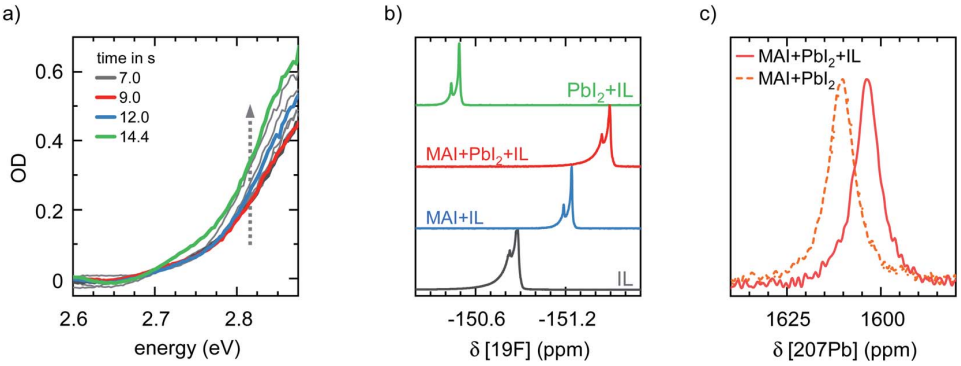

Fig. 5 (a) Temporal evolution of the absorption spectra of the reference solution in the UV-range. (b) ^{19}F NMR spectra probing the BF_4^- anion of the IL solution, the single precursor solutions with 5 mol% of IL, and the $MAPbI_3$ solution with 5 mol% of IL. Due to the boron isotopes $^{10}BF_4^-$/$^{11}BF_4^-$ two ^{19}F signals are present. (c) ^{207}Pb NMR spectra of $MAPbI_3$ solutions without and with 5 mol% of IL. The solvent for all precursor solutions is DMF-d7. In case of PbI_2 a drop of DMSO-d6 was added to dissolve PbI_2 entirely.

coating. Manser *et al.* demonstrated that an increased amount of PbI_4^{2-} complexes in $MAPbI_3$ precursor solutions lead to decreased perovskite formation after solution processing and during annealing.[58] We thus associate the changes of the PbI_4^{2-} properties or of its relative amount in the precursor solution with the changes of the perovskite growth rate for different AS dripping time points.

Based on these insights, we investigated the influence of the IL on the initial perovskite formation upon AS dripping. Here we find the kinetics of the decrease of the scattered light intensity and the increase of the OD at 1.8 eV to be independent of the presence of IL in the precursor solution, for all three AS dripping time points considered (Fig. S12 and S13†). Thus, we conclude that the presence of IL in the precursor solution does not impact the initial perovskite formation kinetics.

Regarding the perovskite growth during further spin coating (corresponding to the time ranges considered for extracting the perovskite growth rates in Fig. 4a–c), it becomes clear that the growth rates for $t_{ASD} = 6$ s (squares in Fig. 4d) exhibits the highest value, decreases for 12 s (circles), and increases again for $t_{ASD} =$ 15 s (triangles). Thus, the qualitative behavior for the solution with 0% IL prevails also for both IL containing solutions. From Fig. 4d it also becomes clear that, in general, the perovskite growth rate decreases with increasing IL concentration. This behavior is similar to the correlation between IL content and k_{growth} found in the one-step processing experiments (Fig. 2d).

For 5 mol% IL containing precursor solutions and AS dripping time points of 12 s and 15 s, k_{growth} exhibits values below 0.05 nm s^{-1} (Fig. 4d). These low k_{growth} values during further spin coating are also reflected in the optical properties of the films on longer time scales, *e.g.,* 72 h after the spin coating process. Here, we find the PL peak position of the samples processed from the reference solution and the 1 mol% IL containing solution to be at 1.57 eV, *i.e.* at the typical bulk $MAPbI_3$ value. This suggests that in these samples the perovskite crystallites have grown to sizes exceeding the typical confinement limit of ~20 nm.[52] In contrast, the PL peak of the sample processed from the 5 mol% IL containing precursor solution appears at a higher energy at 1.59 eV (Fig. 4e), which we assign to PL contribution of perovskites crystallites that still exhibit a confinement effect. In the corresponding absorption spectra, the effect of IL hampering the perovskite crystallization is reflected as well, where 72 h after spin coating the extent of the formation of a typical $MAPbI_3$ absorption spectrum is diminished for increasing IL content (Fig. 4f).

We next address the underlying mechanism that causes the hampered perovskite growth when IL is present in the precursor solution. Here, we find the intensity of the PbI_4^{2-}-associated absorption edge prior to AS dripping to be higher for increasing IL contents (Fig. S14†). This increase suggests that the IL impacts the precursor properties, *i.e.*, it either leads to an increased amount of PbI_4^{2-}, or to a more pronounced polynucleation of the precursor states.

To verify a possible interaction of the IL with the constituents of the precursor solution, we conducted liquid state NMR spectroscopic measurements of solutions containing only MAI or PbI_2, and precursor solutions (*i.e.* MAI + PbI_2) with and without IL. The obtained ^{19}F and ^{207}Pb NMR spectra are depicted in Fig. 5b and c (see Fig. S15 and S16† for ^{13}C and ^{1}H spectra). ^{19}F NMR spectroscopy probes the anion BF_4^- of the IL in the precursor solutions. While all ^{19}F NMR spectra (Fig. 5b) exhibit the typical double peak for BF_4^- due to the coexistence of the boron isotopes $^{10}BF_4^-$ and $^{11}BF_4^-$,[59] the ^{19}F chemical shift changes depending on the ions present in the solutions. As such, the chemical shift of $^{11}BF_4^-$ of pure IL in DMF is −150.88 ppm (150.82 ppm $^{10}BF_4^-$), and a shift of the resonances to higher ppm values (−150.49 ppm $^{11}BF_4^-$; −150.44 ppm $^{10}BF_4^-$) is observed for the PbI_2 precursor solution and lower ppm values for the MAI (−151.24 ppm $^{11}BF_4^-$; −151.18 ppm $^{10}BF_4^-$) and the MAI + PbI_2 (−151.50 ppm $^{11}BF_4^-$; −151.44 ppm $^{10}BF_4^-$) precursor solutions. An upfield-shift (shift to lower ppm values) of the BF_4^- signal in both, the pure MAI and the $MAPbI_3$ precursor solutions is observed, while in the case of the pure PbI_2 solution a downfield-shift occurs, indicating that the BF_4^- anion predominantly interacts with the MA^+ cations. This is further reflected in the ^{1}H NMR spectra (Fig. S16†) of the precursor solutions, where the

View Article Online
Journal of Materials Chemistry A Paper

BMIM$^+$ cation of the IL is probed. The ^{1}H signals of the alkyl region of the BMIM$^+$ also exhibit a characteristic shift, reversed to the observations in the ^{19}F spectra: while no shift is observed for pure MAI + IL solutions compared to pure IL, the signals are upfield-shifted in pure PbI_2 and $MAPbI_3$ precursor solutions (Fig. S16b†). This in turn suggests that the BMIM$^+$ cation of the IL interacts with the PbI_x complexes in the solutions. This finding is further corroborated, by probing the PbI_4^{2-} complexes in $MAPbI_3$ precursor solutions with and without IL. Here, the ^{207}Pb signal shifts from 1610 ppm for MAI + PbI_2 to 1604 ppm upon addition of IL (Fig. 5c). This upfield shift of the ^{207}Pb resonance indicates a slight increase of electron density at the Pb atoms, probably due to an interaction of the PbI_4^{2-} with the IL cation, which is in line with recent literature reports.[53] In summary, the change of chemical shifts for BF_4^-, BMIM$^+$ and PbI_4^{2-} prove that the ions of the ionic liquid impact on the electronic environment of the precursors, confirming an interaction of the IL with the precursors already in solution, predominantly between BF_4^- and MA$^+$, as well as BMIM$^+$ and PbI_4^{2-}.

3.3 Final film properties

Having examined the influence of the IL on crystallite growth and film formation, we finally address how the differences in the film formation during the solvent engineering approach transfer to the final $MAPbI_3$ film properties.

Fig. 6a shows SEM images of the final $MAPbI_3$ thin films prepared using t_{ASD} = 12 s, for different amounts of IL. After spin coating, the films were stored in an inert atmosphere for eight weeks before the SEM characterization. From Fig. 6a it becomes clear, that the reduced perovskite growth rate for higher IL contents found in Section 2.2 results in a decrease of the grain size in the final thin film. Interestingly, frayed areas are present in the reference film, indicating a partial degradation of the perovskite. In contrast, the film morphologies of the two IL-containing films do not show such areas, indicating a beneficial effect of the IL on the chemical stability of the perovskite thin film, which is in line with the findings from literature.[26]

The decrease of grain size for increasing IL content is accompanied by a decrease of perovskite crystallite size and microstrain, as concluded from Rietveld refinement analysis of the XRD patterns of the final films (Fig. 6b). We speculate that the decrease in microstrain also relates to the improved stability of the film with higher IL content, similar to the behavior found for $MAPbI_3$ in powder form, which exhibited negligible microstrain and remarkable chemical stability for more than 2.5 years.[60]

Fig. 6c shows the integrated PL intensity of films processed with t_{ASD} = 12 s, directly after spin coating, after 72 h, and after thermal annealing at 100 °C for 60 minutes, normalized to the intensity directly after spin coating. In this sequence, the reference film shows the most drastic relative decrease in PL intensity, while the corresponding decrease of PL intensity for the sample containing 1 mol% IL is less pronounced. 72 h after spin coating, the sample containing 5 mol% IL even shows an increase in PL intensity. Moreover, from the corresponding evolution of the absolute PL intensities (Fig. S17†) we find that

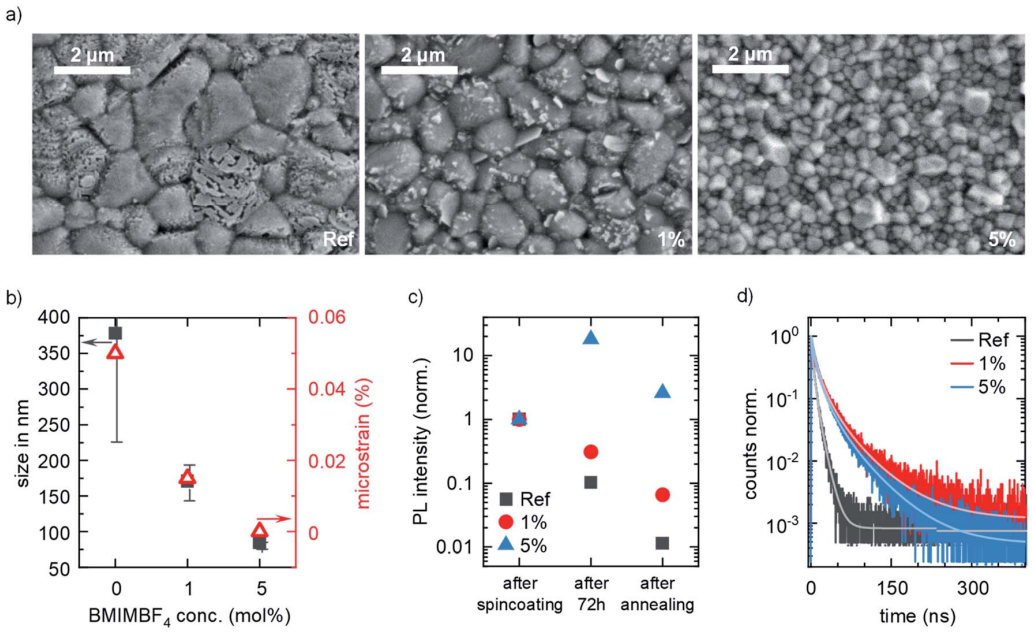

Fig. 6 (a) Top view SEM images of $MAPbI_3$ films containing different amounts of IL. (b) $MAPbI_3$ crystal size and microstrain extracted from XRD patterns of $MAPbI_3$ thin films containing different amounts of the IL BMIMBF$_4$. (c) PL intensity of films processed with t_{ASD} = 12 s, directly after spin coating, after 72 h, and after thermal annealing, normalized to the intensity directly after spin coating. (d) Time-resolved PL decay curves of annealed films, together with fits using eqn (2).

View Article Online
Paper Journal of Materials Chemistry A

in all cases, *i.e.* directly after spin coating, 72 h after spin coating and after annealing, the PL intensity is higher, the higher the IL content. These observations suggest that even before annealing, where we expect solvent molecules to still be present in the thin films, more non-radiative decay channels are passivated with increasing IL content.[60–64]

To evaluate this behavior in more detail, we performed time-resolved photoluminescence (TRPL) measurements of the annealed films with different IL content (Fig. 6d), and analyzed the PL decays using a rate equation of the form

$$\frac{dn}{dt} = -k_1 n - k_2 n^2 - k_3 n^3. \quad (2)$$

Here, n is the photoinduced charge carrier density within the perovskite, and k_1, k_2 and k_3 are associated with trap-mediated recombination due to defects, bimolecular (radiative) and Auger recombination, respectively. k_2 and k_3 can be considered material constants, whereas k_1 depends on the defect density in the sample. To fit the TRPL curves, k_2 and k_3 were set to 6.8×10^{-10} cm^3 s^{-1} and 10^{-28} cm^6 s^{-1}, respectively,[65] and we estimated the initial value of the charge carrier density n based on the experimental conditions (see experimental section) to be on the order of 5×10^{16} cm^{-3}. From our fits we obtain k_1 values of 4.3×10^7 s^{-1}, 7.2×10^6 s^{-1} and 8.2×10^6 s^{-1} for the reference film and the films containing 1 mol% and 5 mol% IL, respectively (for more details see Section S4†). Thus for an increasing IL content in the precursor solution the non-radiative, defect assisted recombination rate reduces, which is in line with literature reports.[66] At the same time, it is also known from literature, that k_1 increases for smaller grain sizes in MAPbI$_3$ thin films.[67] Thus we conclude that in our case, the passivation of defect states by the IL in the final thin films appears to be the dominant effect causing the observed changes of k_1, whereas the decrease of grain size of the films with higher IL content (Fig. 6a) appears to play only a minor role in determining k_1.

4. Conclusion

We investigated the impact of the ionic liquid BMIMBF$_4$ on the film formation processes of MAPbI$_3$, monitored by multimodal optical *in situ* spectroscopy during spin coating, employing one-step processing, as well as a solvent engineering approach. The one-step processing experiments revealed that the IL had no effect on the formation of the perovskite–solvent complexes. However, higher IL contents in the precursor solutions lead to delayed perovskite transformation with decreased growth rates, presumably due to the IL interaction with the complex structures hampering solvent evaporation.

In the solvent engineering experiments, we find that the perovskite growth rate decreases with later AS dripping time points, which was associated with changing properties of the PbI_4^{2-} species in the precursor solutions during drying. Furthermore, the IL also affects the properties and temporal evolution of the PbI_4^{2-} species in the precursor solution, where the BF_4^- anion and the cation of the IL preferably interact with the MA^+ cations and the PbI_4^{2-}, respectively. These interactions appear to be directly related to the observed reduction in perovskite growth rates with increasing IL content after initiating the perovskite formation by AS dripping.

Furthermore, the identified selectivity of interaction between IL anion with MA^+ and IL cation with the PbI_4^{2-}-species opens up the potential for versatile control and tailoring precursor properties and thus perovskite formation by targeted selection of IL constituents.

The crystallization-inhibiting effect of the IL resulted in smaller grain sizes of the final films with higher IL content. Here, we found that films containing IL exhibit less microstrain, which in turn can explain their increased stability. Regarding the optoelectronic film properties, we deduced from our PL analyses that the IL reduces non-radiative decay of excited states already in the as-coated thin films. This effect persists after annealing, suggesting an efficient passivation of defects in the perovskite films containing IL, which outcompetes a possible decrease of non-radiative decay rate due to the decreasing perovskite grain size with increasing IL content.

Our work thus reveals the important role the IL plays in the entire process of solution-based perovskite film manufacturing, influencing the precursor chemistry, the subsequent crystallization properties during solution processing, and the optoelectronic properties of the final thin-films.

Especially, the clear impact of the IL on the evolution of the precursor states emphasizes the importance of taking into account the dynamic changes of the precursor properties, in order to develop improved solution processing protocols in the future. Here, adaptive processing approaches, where *e.g.* the anti-solvent is dripped not after a fixed pre-defined point in time during processing, but is dripped whenever a specific precursor property has evolved, appears to be an attractive future direction.

Thus, our work represents an important building block in developing a better understanding about the sensitive relationship between the presence of additives in perovskite precursor solutions and the entire film formation processes, facilitating more tailored solution processing strategies in the future.

Conflicts of interest

There are no conflicts to declare.

Acknowledgements

S. B., K. S., and F. P. acknowledge financial support from the German National Science Foundation *via* the Projects 423895689 (SPP 2196), KO 3973/2-1, MO 1060/32-1 and PA 3373/3-1 and further acknowledge support by the Bavarian State Ministry of Science, Research, and the Arts for the Collaborative Research Network "Solar Technologies go Hybrid". We also thank Meike Kuhn for help with optical microscopy, the Department of Metal and Alloys (Prof. Uwe Glatzel) for the possibility to conduct XRD measurements, and Martina Heider and the KeyLab "Electron and Optical Microscopy" of the Bavarian Polymer Institute (BPI) for assistance with SEM images

View Article Online
Journal of Materials Chemistry A Paper

and access to the MT200 system. H. G. thanks the German National Science Foundation for financial support within Grant GR 5505/2-1, and Dr Kristian Schweimer for standard ^{1}H and ^{13}C liquid-state NMR measurements within the Northern Bavarian NMR Centre.

References

1 NREL, *Best Research-Cell Efficiency Chart*, **https://www.nrel.gov/pv/cell-efficiency.html**, accessed March 7, 2022.
2 H. Min, D. Y. Lee, J. Kim, G. Kim, K. S. Lee, J. Kim, M. J. Paik, Y. K. Kim, K. S. Kim, M. G. Kim, T. J. Shin and S. Il Seok, *Nature*, 2021, **598**, 444–450.
3 A. K. Jena, A. Kulkarni and T. Miyasaka, *Chem. Rev.*, 2019, **119**, 3036–3103.
4 N. J. Jeon, J. H. Noh, Y. C. Kim, W. S. Yang, S. Ryu and S. I. Seok, *Nat. Mater.*, 2014, **13**, 897–903.
5 D. Liu, L. Wu, C. Li, S. Ren, J. Zhang, W. Li and L. Feng, *ACS Appl. Mater. Interfaces*, 2015, **7**, 16330–16337.
6 Y. Li, L. Ji, R. Liu, C. Zhang, C. H. Mak, X. Zou, H.-H. Shen, S.-Y. Leu and H.-Y. Hsu, *J. Mater. Chem. A*, 2018, **6**, 12842–12875.
7 Z. Zhou, S. Pang, Z. Liu, H. Xu and G. Cui, *J. Mater. Chem. A*, 2015, **3**, 19205–19217.
8 A.-N. Cho and N.-G. Park, *ChemSusChem*, 2017, **10**, 3687–3704.
9 G. Wu, R. Liang, M. Ge, G. Sun, Y. Zhang and G. Xing, *Adv. Mater.*, 2022, **34**, 2105635.
10 R. Yin, K.-X. Wang, S. Cui, B.-B. Fan, J.-W. Liu, Y.-K. Gao, T.-T. You and P.-G. Yin, *ACS Appl. Energy Mater.*, 2021, **4**, 9294–9303.
11 Z. Cheng, C. Gao, J. Song, D. Ding, Y. Chen, J. Wang, D. Zhang, L. Chen, X. Wang, Z. Yang, F. Liu, H. Liu and W. Shen, *ACS Appl. Mater. Interfaces*, 2021, **13**, 40778–40787.
12 T. Bu, J. Li, F. Zheng, W. Chen, X. Wen, Z. Ku, Y. Peng, J. Zhong, Y.-B. Cheng and F. Huang, *Nat. Commun.*, 2018, **9**, 4609.
13 P. Xu, H. He, J. Ding, P. Wang, H. Piao, J. Bao, W. Zhang, X. Wu, L. Xu, P. Lin, X. Yu and C. Cui, *ACS Appl. Energy Mater.*, 2021, **4**, 10921–10930.
14 M. Degani, Q. An, M. Albaladejo-Siguan, Y. J. Hofstetter, C. Cho, F. Paulus, G. Grancini and Y. Vaynzof, *Sci. Adv.*, 2021, **7**, eabj7930.
15 Y.-M. Xie, Q. Yao, Z. Zeng, Q. Xue, T. Niu, R. Xia, Y. Cheng, F. Lin, S.-W. Tsang, A. K.-Y. Jen, H.-L. Yip and Y. Cao, *Adv. Funct. Mater.*, 2022, **32**, 2112126.
16 M. Wang, Y. Yin, W. Cai, J. Liu, Y. Han, Y. Feng, Q. Dong, Y. Wang, J. Bian and Y. Shi, *Adv. Funct. Mater.*, 2022, **32**, 2108567.
17 J. Han, K. Kim, J.-S. Nam, S. J. Hong, E. J. Choi, D. Kim, I. Chung, H.-S. Lin, T.-D. Kim, M. S. Strano, B. Han, J.-W. Oh, H. D. Kim and I. Jeon, *Adv. Energy Mater.*, 2021, **11**, 2101221.
18 F. Zhang, D. Bi, N. Pellet, C. Xiao, Z. Li, J. J. Berry, S. M. Zakeeruddin, K. Zhu and M. Grätzel, *Energy Environ. Sci.*, 2018, **11**, 3480–3490.
19 N. De Marco, H. Zhou, Q. Chen, P. Sun, Z. Liu, L. Meng, E.-P. Yao, Y. Liu, A. Schiffer and Y. Yang, *Nano Lett.*, 2016, **16**, 1009–1016.
20 D.-H. Kang, C. Ma and N.-G. Park, *ACS Appl. Mater. Interfaces*, 2022, **14**, 8984–8991.
21 W. Zhao, H. Lin, Y. Li, D. Wang, J. Wang, Z. Liu, N. Yuan, J. Ding, Q. Wang and S. (Frank) Liu, *Adv. Funct. Mater.*, 2022, **32**, 2112032.
22 M. Salado, M. A. Fernández, J. P. Holgado, S. Kazim, M. K. Nazeeruddin, P. J. Dyson and S. Ahmad, *ChemSusChem*, 2017, **10**, 3846–3853.
23 S. Wang, Z. Li, Y. Zhang, X. Liu, J. Han, X. Li, Z. Liu, S. (Frank) Liu and W. C. H. Choy, *Adv. Funct. Mater.*, 2019, **29**, 1900417.
24 R. Han, Q. Zhao, A. Hazarika, J. Li, H. Cai, J. Ni and J. Zhang, *ACS Appl. Mater. Interfaces*, 2022, **14**, 4061–4070.
25 A. Wang, X. Deng, J. Wang, S. Wang, X. Niu, F. Hao and L. Ding, *Nano Energy*, 2021, **81**, 105631.
26 S. Bai, P. Da, C. Li, Z. Wang, Z. Yuan, F. Fu, M. Kawecki, X. Liu, N. Sakai, J. T.-W. Wang, S. Huettner, S. Buecheler, M. Fahlman, F. Gao and H. J. Snaith, *Nature*, 2019, **571**, 245–250.
27 M. Chauhan, Y. Zhong, K. Schötz, B. Tripathi, A. Köhler, S. Huettner and F. Panzer, *J. Mater. Chem. A*, 2020, **8**, 5086–5094.
28 K. Schötz, C. Greve, A. Langen, H. Gorter, I. Dogan, Y. Galagan, A. J. J. M. van Breemen, G. H. Gelinck, E. M. Herzig and F. Panzer, *Adv. Opt. Mater.*, 2021, **9**, 2101161.
29 R. Munir, A. D. Sheikh, M. Abdelsamie, H. Hu, L. Yu, K. Zhao, T. Kim, O. E. Tall, R. Li, D.-M. Smilgies and A. Amassian, *Adv. Mater.*, 2017, **29**, 1604113.
30 M. Qin, P. F. Chan and X. Lu, *Adv. Mater.*, 2021, **33**, 2105290.
31 K. Schötz and F. Panzer, *J. Phys. Chem. A*, 2021, **125**, 2209–2225.
32 S. Pratap, F. Babbe, N. S. Barchi, Z. Yuan, T. Luong, Z. Haber, T.-B. Song, J. L. Slack, C. V. Stan, N. Tamura, C. M. Sutter-Fella and P. Müller-Buschbaum, *Nat. Commun.*, 2021, **12**, 5624.
33 M.-C. Tang, H. X. Dang, S. Lee, D. Barrit, R. Munir, K. Wang, R. Li, D.-M. Smilgies, S. De Wolf, D.-Y. Kim, T. D. Anthopoulos and A. Amassian, *Sol. RRL*, 2021, **5**, 2000718.
34 K. Suchan, J. Just, P. Becker, E. L. Unger and T. Unold, *J. Mater. Chem. A*, 2020, **8**, 10439–10449.
35 O. Shargaieva, H. Näsström, J. Li, D. M. Többens and E. L. Unger, *Front. Energy Res.*, 2021, **9**, 749604.
36 M. R. Ahmadian-Yazdi, F. Zabihi, M. Habibi and M. Eslamian, *Nanoscale Res. Lett.*, 2016, **11**, 408.
37 J.-H. Lee, K. Jung and M.-J. Lee, *J. Alloys Compd.*, 2021, **879**, 160373.
38 Y. Yan, Y. Yang, M. Liang, M. Abdellah, T. Pullerits, K. Zheng and Z. Liang, *Nat. Commun.*, 2021, **12**, 6603.
39 J. A. Aguiar, S. Wozny, N. R. Alkurd, M. Yang, L. Kovarik, T. G. Holesinger, M. Al-Jassim, K. Zhu, W. Zhou and J. J. Berry, *ACS Energy Lett.*, 2016, **1**, 155–161.

40 A. Alberti, I. Deretzis, G. Mannino, E. Smecca, F. Giannazzo, A. Listorti, S. Colella, S. Masi and A. La Magna, *Adv. Energy Mater.*, 2019, **9**, 1803450.
41 M. Buchhorn, S. Wedler and F. Panzer, *J. Phys. Chem. A*, 2018, **122**, 9115–9122.
42 Y. Zhong, R. Munir, J. Li, M.-C. Tang, M. R. Niazi, D.-M. Smilgies, K. Zhao and A. Amassian, *ACS Energy Lett.*, 2018, **3**, 1078–1085.
43 A. A. Petrov, I. P. Sokolova, N. A. Belich, G. S. Peters, P. V. Dorovatovskii, Y. V. Zubavichus, V. N. Khrustalev, A. V. Petrov, M. Grätzel, E. A. Goodilin and A. B. Tarasov, *J. Phys. Chem. C*, 2017, **121**, 20739–20743.
44 A. A. Petrov, A. A. Ordinartsev, K. A. Lyssenko, E. A. Goodilin and A. B. Tarasov, *J. Phys. Chem. C*, 2022, **126**, 169–173.
45 S. D. Stranks, P. K. Nayak, W. Zhang, T. Stergiopoulos and H. J. Snaith, *Angew. Chem., Int. Ed.*, 2015, **54**, 3240–3248.
46 T. Meier, T. P. Gujar, A. Schönleber, S. Olthof, K. Meerholz, S. van Smaalen, F. Panzer, M. Thelakkat and A. Köhler, *J. Mater. Chem. C*, 2018, **6**, 7512–7519.
47 F. Panzer, C. Li, T. Meier, A. Köhler and S. Huettner, *Adv. Energy Mater.*, 2017, **7**, 1700286.
48 L. Polavarapu, B. Nickel, J. Feldmann and A. S. Urban, *Adv. Energy Mater.*, 2017, **7**, 1700267.
49 J. A. Sichert, Y. Tong, N. Mutz, M. Vollmer, S. Fischer, K. Z. Milowska, R. García Cortadella, B. Nickel, C. Cardenas-Daw, J. K. Stolarczyk, A. S. Urban and J. Feldmann, *Nano Lett.*, 2015, **15**, 6521–6527.
50 Y. Kayanuma, *Phys. Rev. B: Condens. Matter Mater. Phys.*, 1988, **38**, 9797–9805.
51 K. P. Goetz, A. D. Taylor, F. Paulus and Y. Vaynzof, *Adv. Funct. Mater.*, 2020, **30**, 1910004.
52 A. Buin, R. Comin, A. H. Ip and E. H. Sargent, *J. Phys. Chem. C*, 2015, **119**, 13965–13971.
53 E. S. Parrott, J. B. Patel, A.-A. Haghighirad, H. J. Snaith, M. B. Johnston and L. M. Herz, *Nanoscale*, 2019, **11**, 14276–14284.
54 S. Zhang, T. Xiao, F. Fadaei Tirani, R. Scopelliti, M. K. Nazeeruddin, D. Zhu, P. J. Dyson and Z. Fei, *Inorg. Chem.*, 2022, **61**, 5010–5016.
55 M. Saliba, J.-P. Correa-Baena, C. M. Wolff, M. Stolterfoht, N. Phung, S. Albrecht, D. Neher and A. Abate, *Chem. Mater.*, 2018, **30**, 4193–4201.
56 L. N. Quan, M. Yuan, R. Comin, O. Voznyy, E. M. Beauregard, S. Hoogland, A. Buin, A. R. Kirmani, K. Zhao, A. Amassian, D. H. Kim and E. H. Sargent, *J. Am. Chem. Soc.*, 2016, **138**, 2649–2655.
57 B. Li, Q. Dai, S. Yun and J. Tian, *J. Mater. Chem. A*, 2021, **9**, 6732–6748.
58 A. M. Valencia, O. Shargaieva, R. Schier, E. Unger and C. Cocchi, *J. Phys. Chem. Lett.*, 2021, **12**, 2299–2305.
59 J. S. Manser, B. Reid and P. V. Kamat, *J. Phys. Chem. C*, 2015, **119**, 17065–17073.
60 B.-M. Su, S. Zhang and Z. C. Zhang, *J. Phys. Chem. B*, 2004, **108**, 19510–19517.
61 N. Leupold, K. Schötz, S. Cacovich, I. Bauer, M. Schultz, M. Daubinger, L. Kaiser, A. Rebai, J. Rousset, A. Köhler, P. Schulz, R. Moos and F. Panzer, *ACS Appl. Mater. Interfaces*, 2019, **11**, 30259–30268.
62 N. Myung, Y. Bae and A. J. Bard, *Nano Lett.*, 2003, **3**, 747–749.
63 B. Dänekamp, N. Droseros, F. Palazon, M. Sessolo, N. Banerji and H. J. Bolink, *ACS Appl. Mater. Interfaces*, 2018, **10**, 36187–36193.
64 L. K. van Vugt, S. J. Veen, E. P. A. M. Bakkers, A. L. Roest and D. Vanmaekelbergh, *J. Am. Chem. Soc.*, 2005, **127**, 12357–12362.
65 T. W. Crothers, R. L. Milot, J. B. Patel, E. S. Parrott, J. Schlipf, P. Müller-Buschbaum, M. B. Johnston and L. M. Herz, *Nano Lett.*, 2017, **17**, 5782–5789.
66 L. M. Herz, *Annu. Rev. Phys. Chem.*, 2016, **67**, 65–89.
67 V. D'Innocenzo, A. R. Srimath Kandada, M. De Bastiani, M. Gandini and A. Petrozza, *J. Am. Chem. Soc.*, 2014, **136**, 17730–17733.

Electronic Supplementary Material (ESI) for Journal of Materials Chemistry A.

Supplementary Information

How the Ionic Liquid $BMIMBF_4$ influences the formation and optoelectronic properties of $MAPbI_3$ thin films

Simon Biberger[1], Konstantin Schötz[1], Philipp Ramming[1], Nico Leupold[2], Ralf Moos[2], Anna Köhler[1], Helen Grüninger,[3] Fabian Panzer[1*]

[1]Experimental Physics II, University of Bayreuth, Bayreuth, Germany;

[2]Department of Functional Materials, University of Bayreuth, Bayreuth 95440, Germany;

[3]Northern Bavarian NMR Centre (NBNC) and Inorganic Chemistry, University of Bayreuth, Bayreuth, Germany.

Corresponding Author:

[*]E-Mail: fabian.panzer@uni-bayreuth.de

S1: Detailed description of the measurement setup

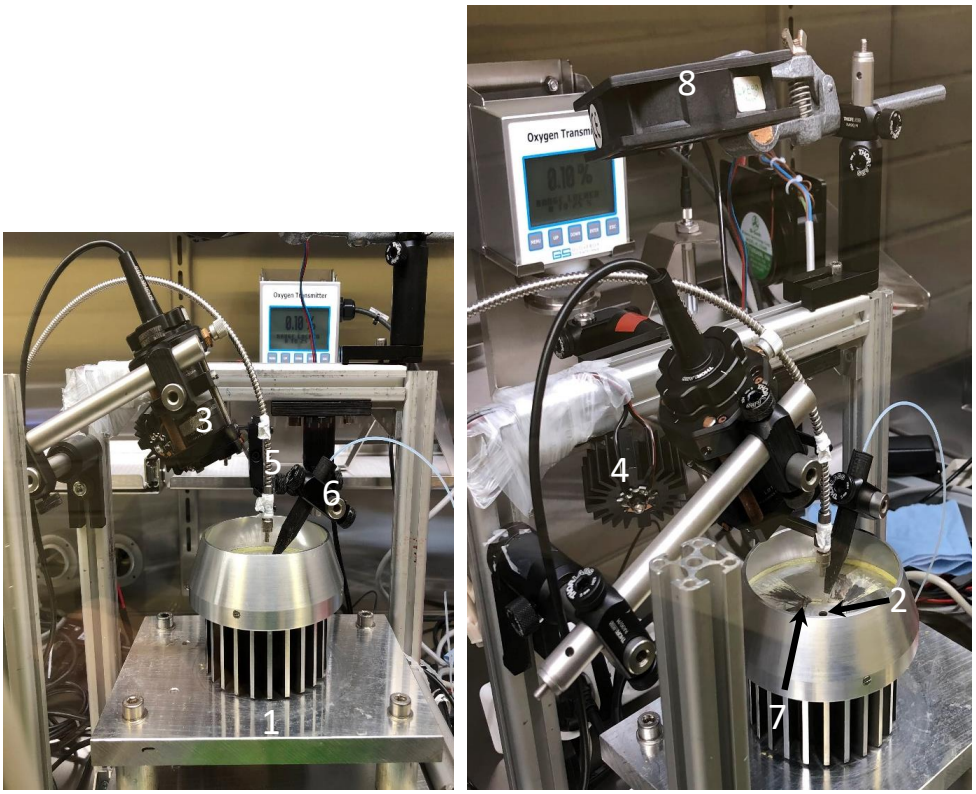

Fig. S1: Photographs of the setup used for measuring the in situ optical data during spin coating.

The setup for measuring the in situ optical data during spin-coating. It consists of a custom-built spin-coater (1) with a hole in the middle (2). Underneath the spin-coater a white-light LED is placed. Its light shines through the hole in the middle of the spin-coater and serves as a white light for transmission measurements. A laser diode (405 nm) in combination with focusing optics and a diaphragm (3) are mounted above the spin-coater for exciting the sample for PL measurements. An LED emitting at 490 nm (4) is placed next to the laser, whose scattered light can be detected (referred to as scatter-LED). The circular area probed by our optical measurements during the spin-coating has a diameter of 5 mm in the center of the substrate. White-light and excitation laser are turned on and off alternatingly, so that either transmission or PL is probed. Transmitted light, PL and scattered LED light are collected with one optical fiber (5),

which is coupled to the detection system. The detection system consists of a CCD camera, coupled to a spectrograph, and a home-built detection setup, which is described in detail in Supporting Reference 1. In brief, the detection setup switches the optical path between transmission and PL measurements, so that for PL measurements, the laser wavelength is blocked by a suitable filter. In contrast, for transmission measurements, the transmitted light is coupled into the spectrograph without additional filtering. The detection setup further synchronizes the CCD camera with the white-light LED, the laser and the optical path switching. Using this setup, we can record PL and transmission during spin-coating quasi-simultaneously (i.e., alternating frame by frame) with a rate of more than 10 Hz. From the transmission measurements, the optical density (OD) is calculated based on a reference measurement prior to spin-coating. Scattered LED light is recorded during the PL measurements. For experiments using the solvent engineering, the antisolvent can be applied via a syringe connected to a capillary (6). The substrate is physically held into place by barriers (7) to ensure the measurements during the processing are taken from the same sample area. To avoid a built-up of solvent atmosphere which can impact the film formation properties, a fan (8) is placed above the spin coater chuck.

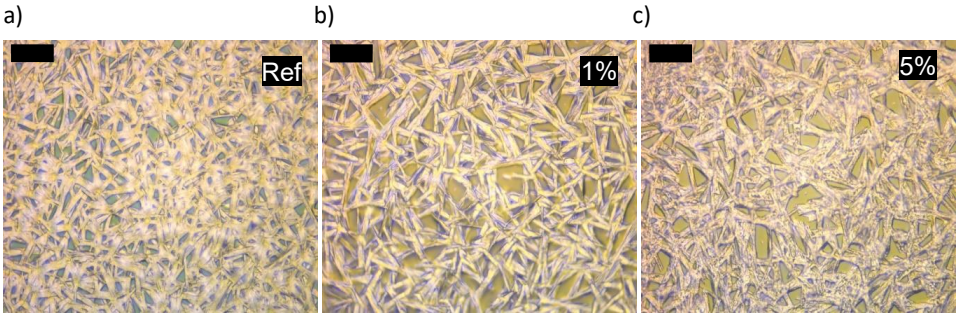

Fig. S2: Microscopy image of a) the reference film, b) the film with 1 mol% $BMIMBF_4$ and c) the film with 5 mol% $BMIMBF_4$ processed via one-step spin coating of $MAPbI_3$ in DMF at 2000 RPM. The scale bar is 20 µm.

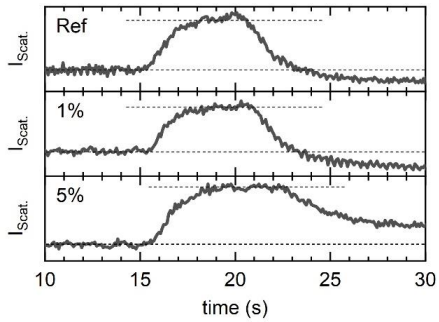

Fig. S3: Time evolution of the intensity of the scattered light during one-step spin coating at 2000 RPM of $MAPbI_3$ in DMF with different IL contents as indicated. The dashed lines indicate the initial intensity level and the high intensity level after solvent-complex formation.

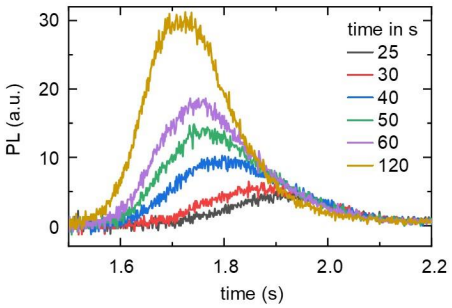

Fig S4: PL spectra at different times of the reference sample processed without IL via one-step spin coating at 2000 RPM of $MAPbI_3$ in DMF.

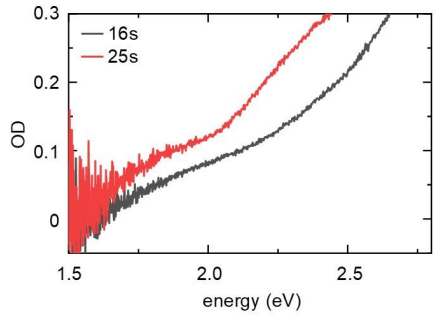

Fig. S5: Absorption spectra after 16 s (black) and 25 s (red) of the reference sample processed without IL via one-step spin coating at 2000 RPM.

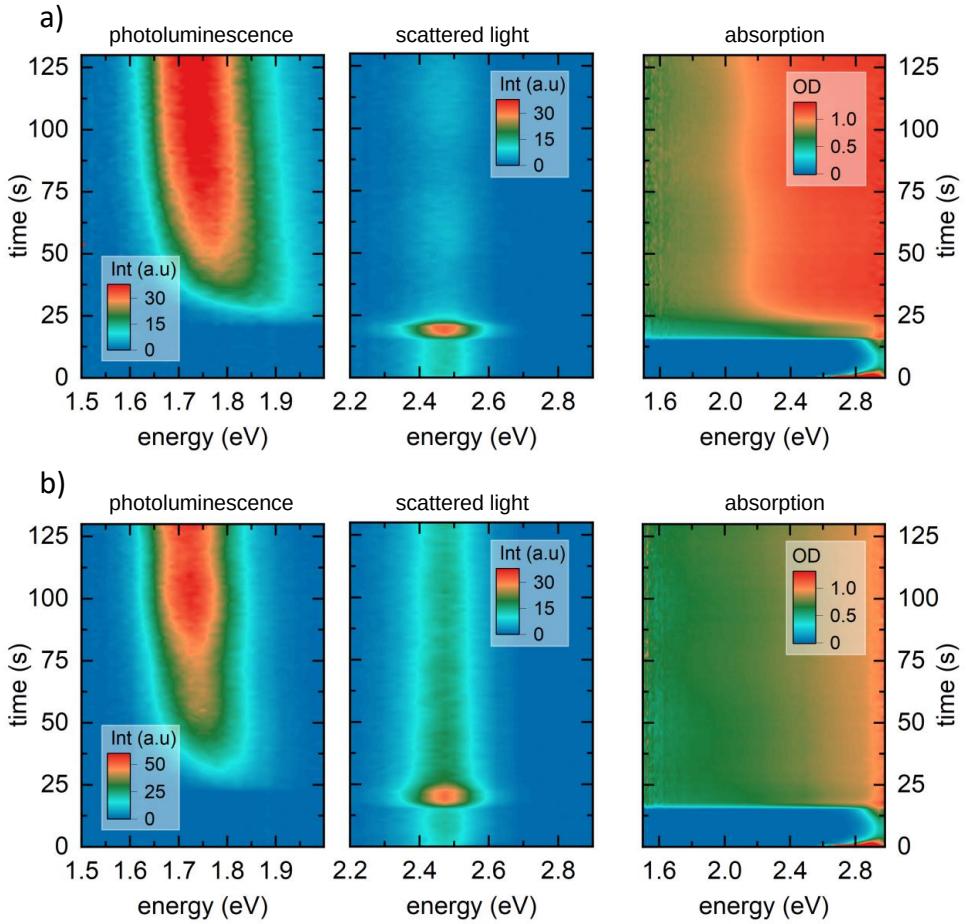

Fig. S6: Heat maps of photoluminescence (PL), scattered light, and optical density (OD) measurement during one-step spin coating at 2000 RPM of the solutions with a) 1 mol% $BMIMBF_4$ and b) 5 mol% $BMIMBF_4$.

S2: Estimation of layer thickness based on white light interference:

As described in our previous work[1], prior to the formation of the intermediate phase, we observe a sinusoidal modulation of the OD spectrum upon spin-coating (see Figure S7a). Such a modulation is indicative of positive and negative interference of white light caused by a thin layer and reflection at its interfaces. If the refractive index of the

layer causing the interference is known, the thickness of the layer can be calculated from the distance of adjacent extrema in the OD using[2,3]

$$d = \frac{\lambda_1 \lambda_2}{2(n_2\lambda_1 - n_1\lambda_2)}, \quad \text{(S1)}$$

where λ_i is the wavelength of the extremum *i* and n_i is the refractive index at wavelength λ_i. Assuming that *n* is roughly constant in the investigated spectral range, i.e. $n_1 \approx n_2$, and converting the wavelength to energy, Equation S1 can be re-written to

$$d = \frac{hc}{2n\Delta E}, \quad \text{(S2)}$$

where ΔE is the energetic difference of two adjacent extrema in the OD. ΔE was extracted from the frequency of a sine function of the form

$$OD = \sin\big(\Delta E * (x + x0)\big) + y0 + m * x \quad \text{(S3)}$$

fitted to the OD (see black dashed line in Figure S7a. The thickness of the layer was then calculated using the refractive index of DMF, that is n = 1.43. The calculated layer thickness using Equation S2 is shown in Figure S7b. Note that if the refractive index of the solution layer is higher than of pure DMF due to the presence of solute PbI_2, the resulting layer thickness would be smaller. Thus, the layer thickness calculated with the refractive index of DMF can be seen as an upper limit to the actual layer thickness of the solution layer.

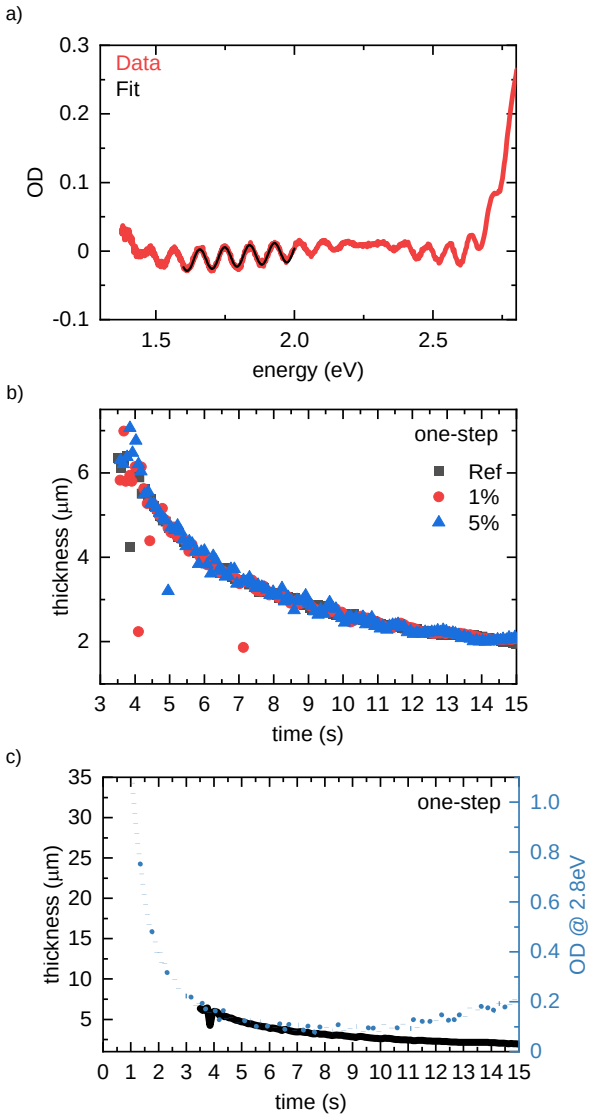

Fig. S7: a) Sinusoidal modulation of the measured OD spectrum caused by white light interference (red) together with a sine function following Equation S3, fitted to the measured OD (black) b) Time evolution of the solution layer thickness as extracted from the white light interference during one-step spin coating at 2000 rpm for precursor solutions containing different contents of $BMIMBF_4$. c) Evolution of the solution layer thickness of the reference precursor solution (black solid), together with the evolution of the OD at 2.8eV (blue dotted) within the first 15s of spin coating. Between 3.5s and 7s, both the solution layer thickness and the OD at 2.8eV follow the same qualitative decrease. While the solution layer thickness

continuously keeps decreasing after 7s, the OD at 2.8 eV stays constant until 9s, and increases afterwards. The fast decrease of OD and solution layer thickness in the first 7s indicates a throw-off of precursor solution, while between 7s and 9s the constant OD and continuous decrease of solution layer thickness suggest a mere evaporation of the solvent. The increase of OD from 9s onwards, while the solution layer thickness further decreases, can be associated to the change of the iodoplumbate precursor properties.

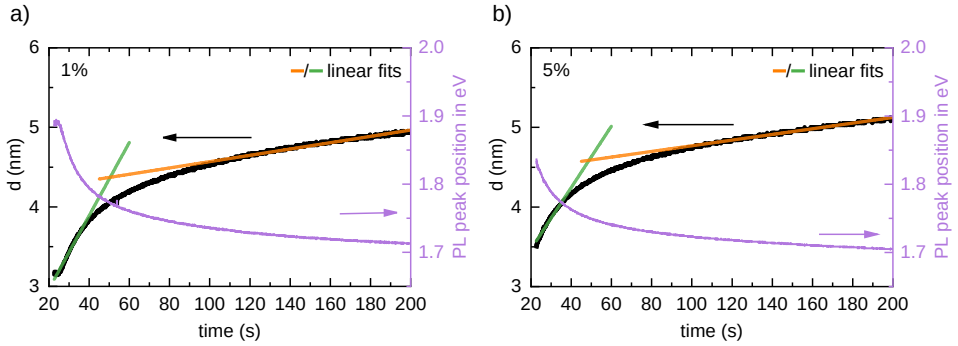

Fig. S8: Time evolution of the PL peak position (pink) and the resulting crystallite size (black), calculated via quantum confinement, for a) the solution with 1 mol% of IL and b) the solution with 5 mol% of IL. The green and orange lines show linear fits, from which the crystallite growth rates are extracted.

For fitting the PL spectra, we use an empirical line shape in the form of an asymmetric hyperbolic secant, that is

$$I(E) = I_0 \frac{2}{e^{\frac{E-E_0}{\sigma_1}} + e^{\frac{E-E_0}{\sigma_2}}} \qquad \text{(S4)}$$

S3: Aliasing effect and smoothing of the data

All signal intensities (transmitted white light, scattered LED light, PL) depend slightly on the angular position of the spin coater, i.e. the detectable intensities change with the frequency of the spin coater due to the rotation of the spin coater. Combined with the finite frequency of detection, this leads to aliasing when the Nyquist criterion cannot be met. As a result, the recorded signal is modulated with the aliasing frequency. Since the modulation is always much faster than the observed processes during film formation, the data can be corrected against this modulation. As reported in our earlier work,[1] this frequency can be filtered out by applying a notch filter in this frequency range or by using a Savitzky-Golay filter with a window size of 25 points and a polynomial order of 2. Both methods resulted in a similarly smooth curve. Therefore, we treated the data with a Savitzky-Golay filter when smoothing was indicated.

Additionally, the same smoothing method was applied to the PL spectra after 72 hours in Figure 4e due to a poor signal to noise ratio.

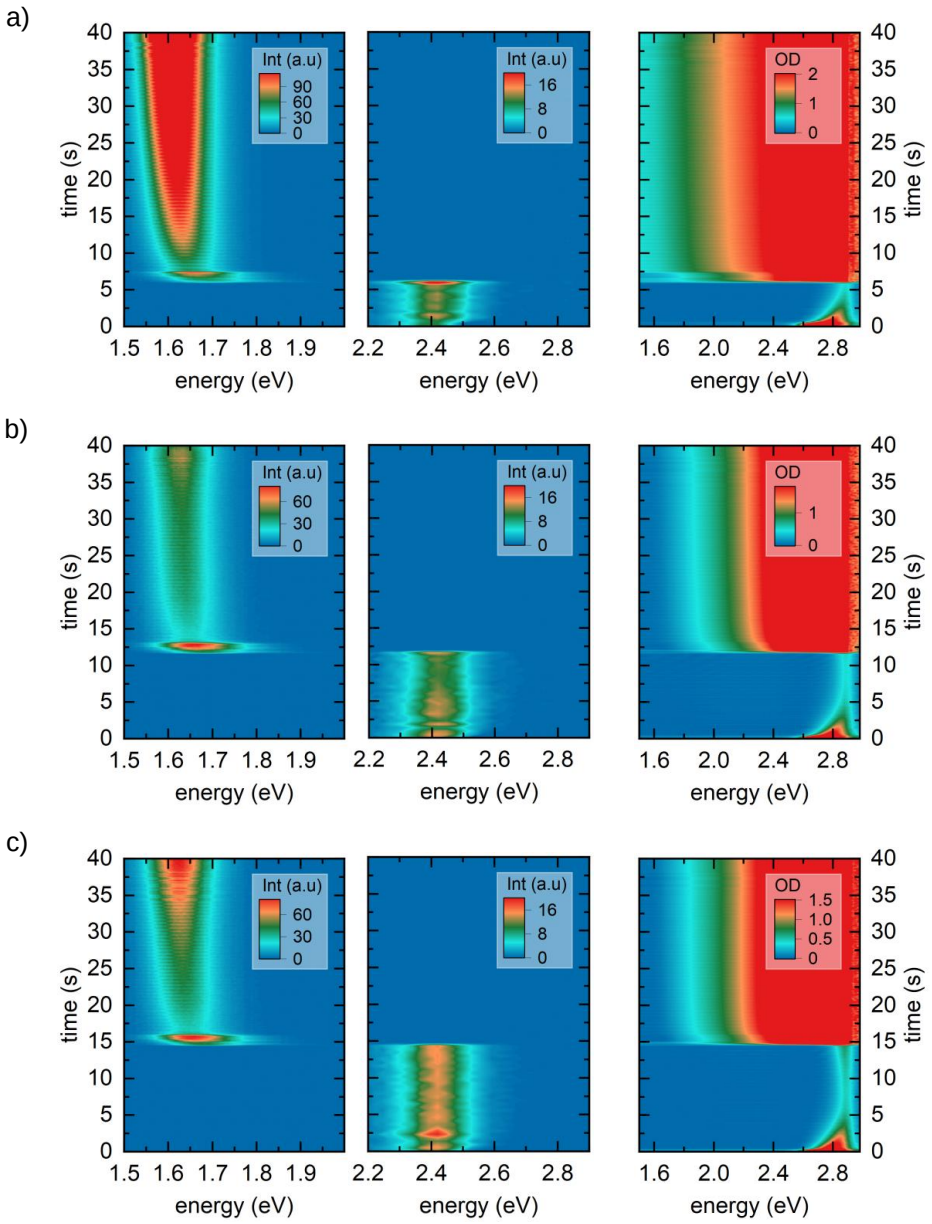

Fig. S9: Heat maps of photoluminescence (PL), scattered light, and optical density (OD) measurement at 2000 RPM of the reference solution without IL, processed via the solvent engineering approach. The antisolvent was dripped after a) 6 s, b) 12 s, and c) 15 s.

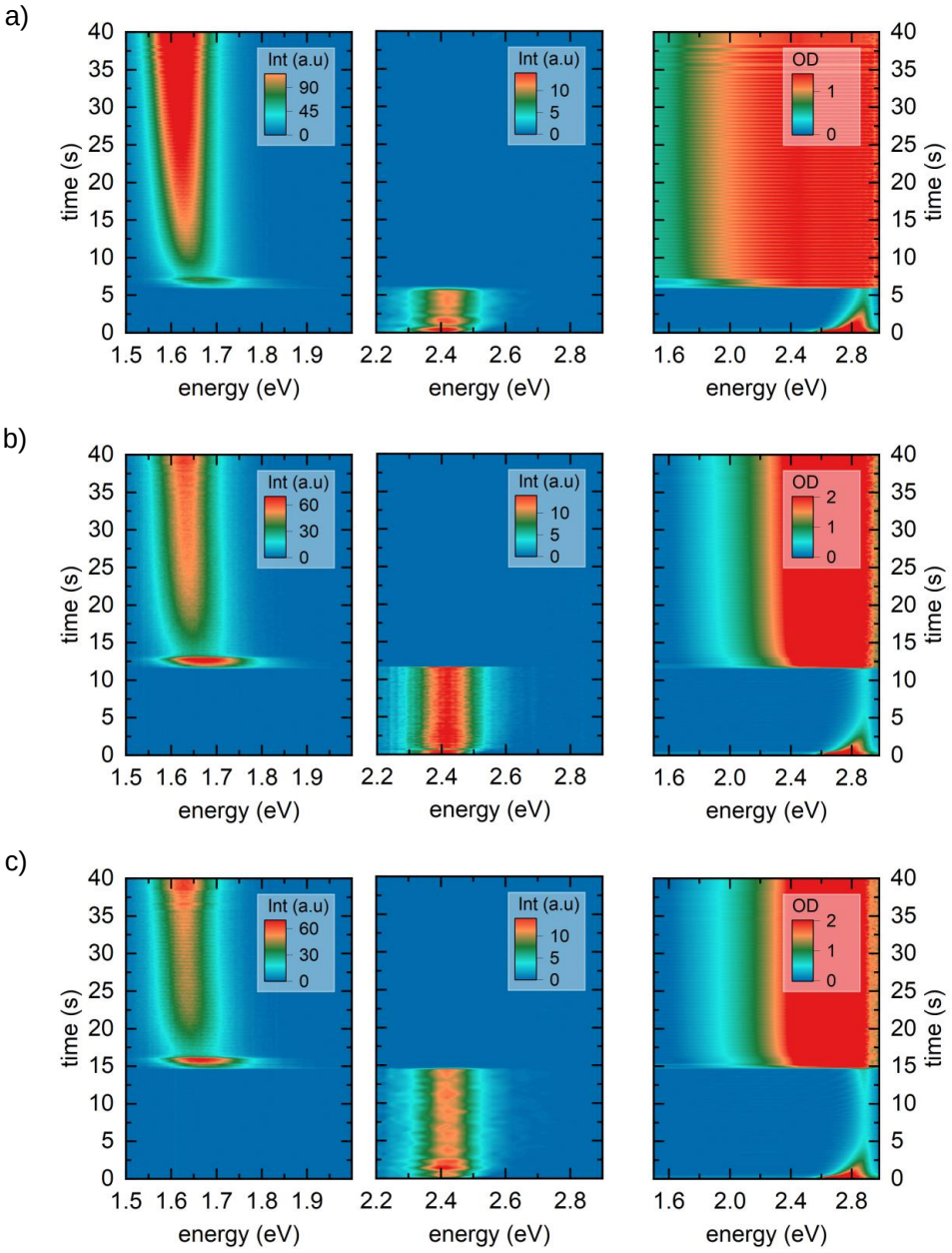

Fig. S10: Heat maps of photoluminescence (PL), scattered light, and optical density (OD) measurement at 2000 RPM of the solution with 1mol% $BMIMBF_4$, processed via the solvent engineering approach. The antisolvent was dripped after a) 6 s, b) 12 s, and c) 15 s.

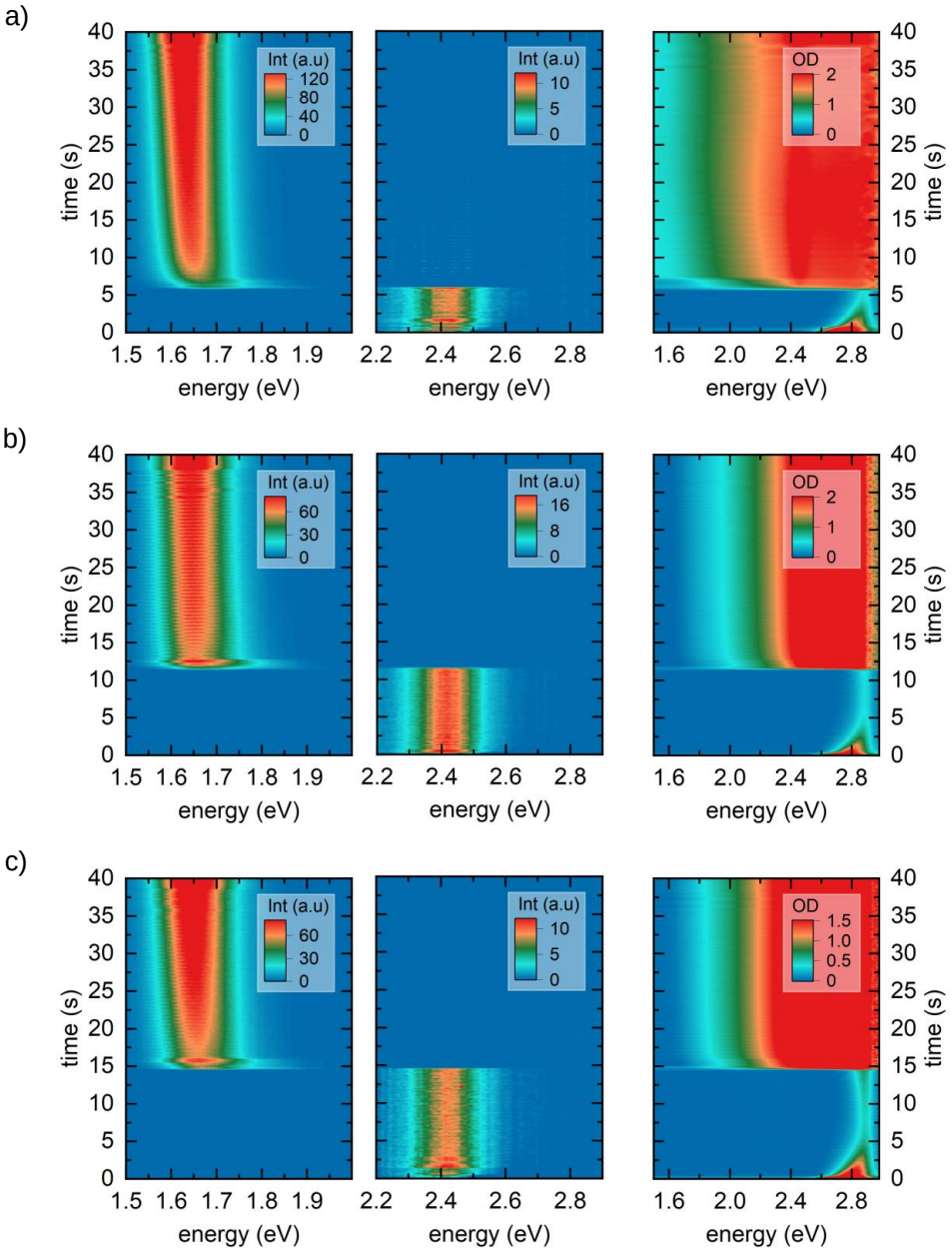

Fig. S11: Heat maps of photoluminescence (PL), scattered light, and optical density (OD) measurement at 2000 RPM of the solution with 5mol% $BMIMBF_4$, processed via the solvent engineering approach. The antisolvent was dripped after a) 6 s, b) 12 s, and c) 15 s.

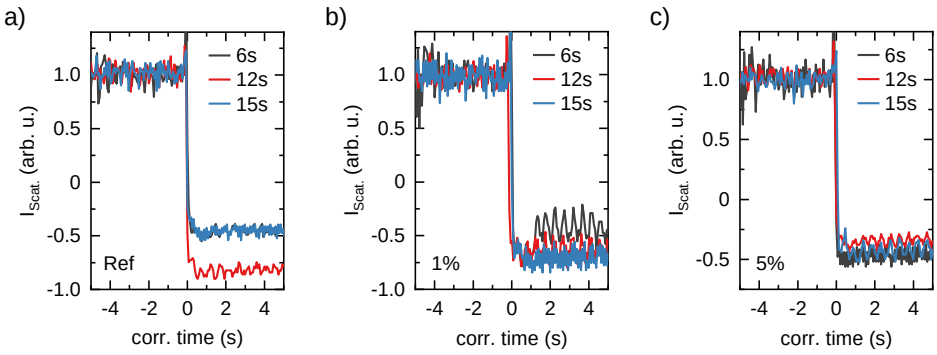

Fig. S12: Normalized temporal evolution of the intensity of the scattered light for different anti-solvent dripping time points for a) the samples without IL, b) the samples with 1 mol% of IL and c) the samples with 5 mol% of IL. t = 0 of the time axis is shifted to match the time of the AS dripping.

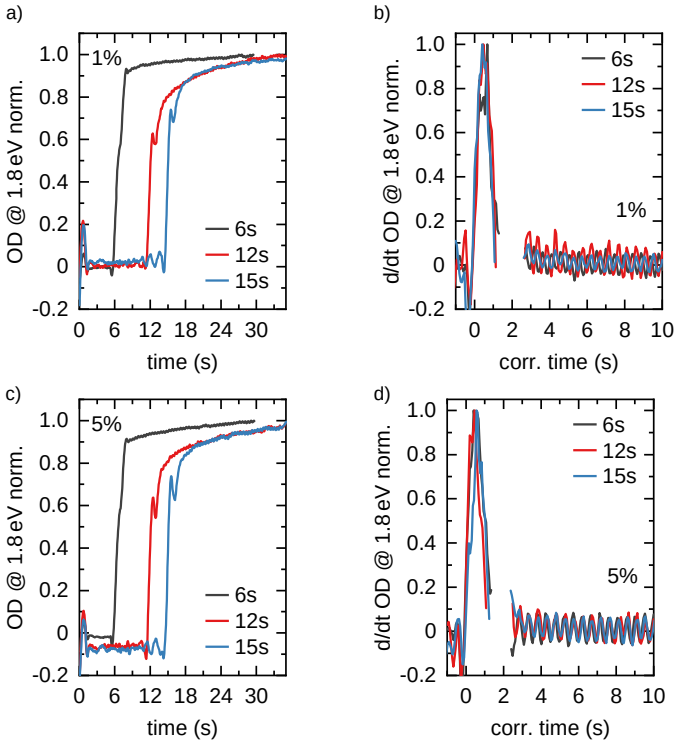

Fig S13: a) Time evolution of the OD at 1.8 eV for the 1mol% IL sample and for different anti-solvent dripping time points. b) normalized time derivative of the OD at 1.8 eV for the 1mol%

IL sample and for different AS dripping time points. t = 0 of the time axis is shifted to match the time of the AS dripping. c) Time evolution of the OD at 1.8 eV for the 5mol% IL sample and for different AS dripping time points. d) Normalized time derivative of the OD at 1.8 eV for the 5mol% IL sample and for different AS dripping time points. t = 0 of the time axis is shifted to match the time of the AS dripping

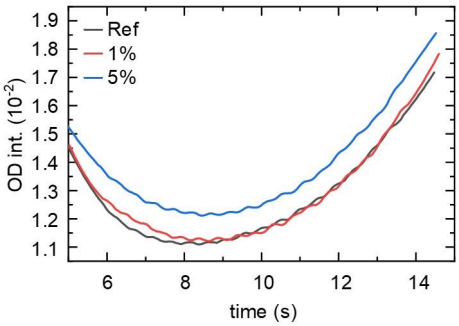

Fig S14: Time evolution of the OD, integrated between 2.84eV and 2.87eV, for precursor solutions, containing different amounts of IL as indicated.

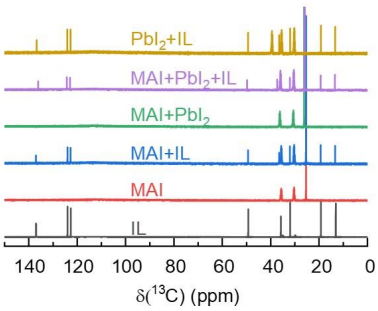

Fig S15: ^{13}C NMR spectra of the IL solution, the single precursors solutions with and without 5 mol% IL, and the MAPbI$_3$ solution with 5 mol% IL. The solvent for all precursor-solutions is DMF-d7. In case of PbI$_2$ a drop of DMSO-d6 was further added to solve PbI$_2$ entirely.

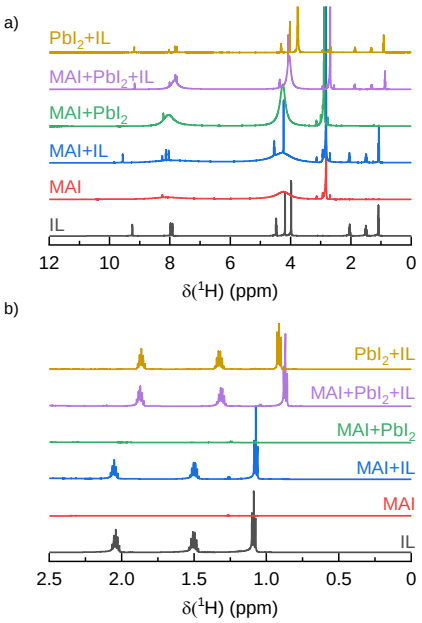

Fig S16: a) ^{1}H NMR spectra of the IL solution, the single precursor solutions with and without 5 mol% IL, and the MAPbI$_3$ solution with and without 5 mol% IL. The solvent for all precursor-solutions is DMF-d7. In case of PbI$_2$ a drop of DMSO-d6 was further added to solve PbI$_2$ entirely. b) Enlarged view of a) in the alkyl region between 0 and 3 ppm.

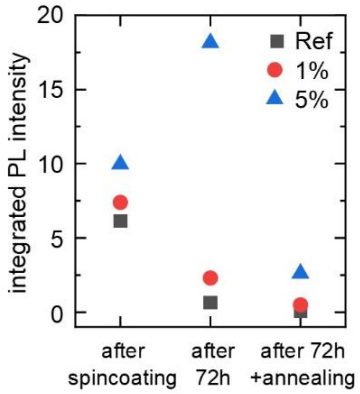

Fig S17: Alternative representation of Fig. 6c in the main text with absolute (integrated) values of the PL intensities.

S4: Details on the TRPL fittings

For fitting the TRPL data, we used the rate equation of the form[4]

$$\frac{dn}{dt} = -k_1 n - k_2 n^2 - k_3 n^3, \quad \text{(S5)}$$

where n is the (excess) charge carrier density after photoexcitation, and k_1, k_2, k_3 are the (defect related) monomolecular, (radiative) bimolecular and Auger recombination, respectively. k_2 = 6.8x10-10 cm^3s^{-1} and $k_3 = 10^{-28}$ cm^6s^{-1} were fixed as material parameters based on literature reports, and n(t=0) was estimated as a starting value to be on the order of $5x10^{16}$ cm^{-3} based on the experimental conditions. Equation S5 was then solved numerically using the forward Euler algorithm with time steps of Δt = 200 ps. From the decay of the charge carrier density, the (normalized) PL decay was calculated according to

$$I_{PL,fit}(t) \propto n(t)^2. \quad \text{(S6)}$$

Equation S6 was then fitted to the experimental data using a least squares approach, where Equation S5 was solved in every iteration of the fitting procedure. k_1 and n(t=0) were considered free parameters, resulting in k_1 values of $4.3x10^7$ s^{-1}, $7.2x10^6$ s^{-1}, $8.2x10^6$ s^{-1} for the reference film and the films containing 1 mol% and 5 mol% IL, respectively. For n(t=0), we obtain values of $2.1x10^{17}$ cm^{-3}, $1.2x10^{17}$ cm^{-3}, $1.4x10^{17}$ cm^{-3} for the reference film and the films containing 1 mol% and 5 mol% IL, agreeing well with the estimated initial value.

Supporting References

1K. Schötz, C. Greve, A. Langen, H. Gorter, I. Dogan, Y. Galagan, A. J. J. M. van Breemen, G. H. Gelinck, E. M. Herzig and F. Panzer, *Advanced Optical Materials*, 2021, **9**, 2101161.
2R. Munir, A. D. Sheikh, M. Abdelsamie, H. Hu, L. Yu, K. Zhao, T. Kim, O. E. Tall, R. Li, D.-M. Smilgies and A. Amassian, *Advanced Materials*, 2017, **29**, 1604113.
3J. C. Manifacier, J. Gasiot and J. P. Fillard, *J. Phys. E: Sci. Instrum.*, 1976, **9**, 1002–1004.
4L. M. Herz, *Annual Review of Physical Chemistry*, 2016, **67**, 65–89.

10 Reactive Spin Coating based on Real-Time In-Situ Feedback for Improved Control of Perovskite Thin Film Fabrication

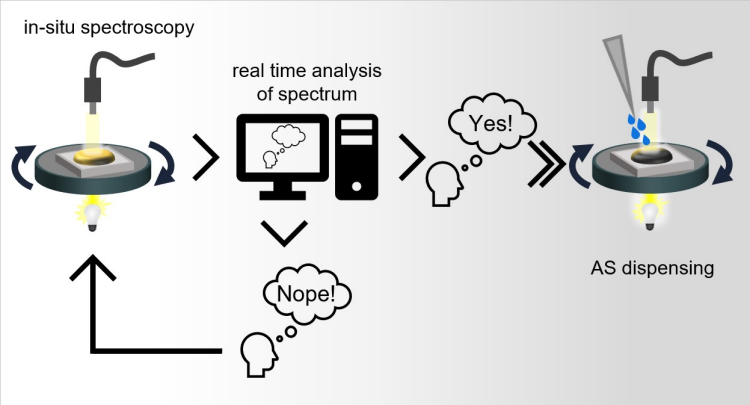

Simon Biberger, Maximilian Spies, Konstantin Schötz, Frank-Julian Kahle, Nico Leupold, Ralf Moos, Helen Grüninger, Anna Köhler, Fabian Panzer

Published in
Journal of Material Chemistry C, **2024**, 12, 6415-6422

Volume 12
Number 18
14 May 2024
Pages 6361–6704

Journal of Materials Chemistry C

Materials for optical, magnetic and electronic devices

rsc.li/materials-c

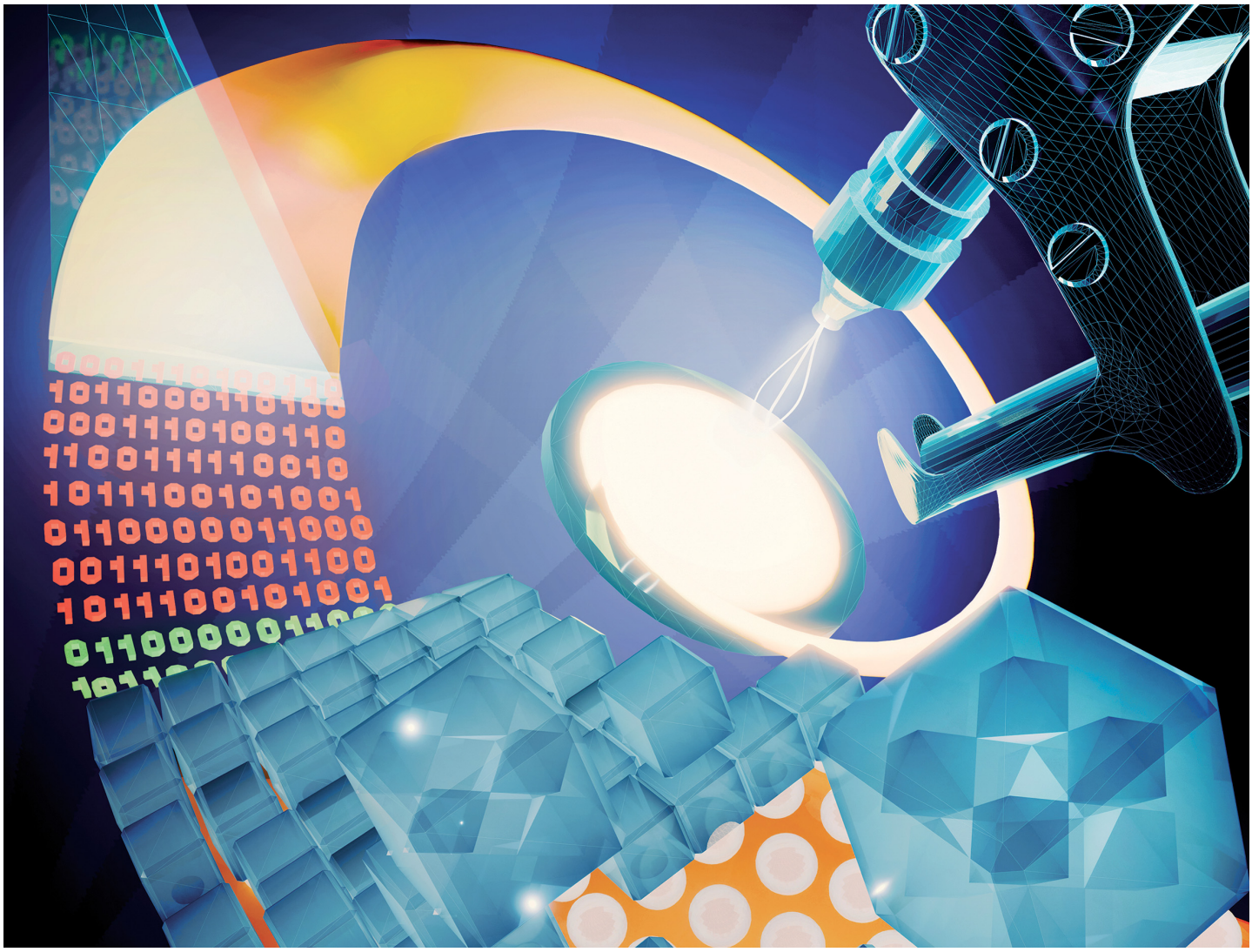

ISSN 2050-7526

ROYAL SOCIETY OF CHEMISTRY

PAPER
Fabian Panzer *et al.*
Reactive spin coating based on real-time *in situ* feedback for improved control of perovskite thin film fabrication

Journal of Materials Chemistry C

ROYAL SOCIETY OF CHEMISTRY

PAPER

View Article Online
View Journal | View Issue

Cite this: J. Mater. Chem. C, 2024, 12, 6415

Reactive spin coating based on real-time *in situ* feedback for improved control of perovskite thin film fabrication†

Simon Biberger,[a] Maximilian Spies,[a] Konstantin Schötz,[a] Frank-Julian Kahle,[a] Nico Leupold,[b] Ralf Moos,[b] Helen Grüninger,[c] Anna Köhler[a] and Fabian Panzer *[a]

Received 26th November 2023,
Accepted 3rd April 2024

DOI: 10.1039/d3tc04361d

rsc.li/materials-c

Efficient perovskite solar cells require metal halide perovskite (MHP) films of consistent and reproducible high quality. MHP films are frequently prepared through a solution-based solvent-engineering spin coating approach. This processing involves considering various controllable parameters (*e.g.* spin speed) and ones that are more difficult to control (*e.g.* changes in atmosphere) to fabricate MHP films reliably. To address this issue, we developed a closed-loop feedback system based on a multimodal optical *in situ* spectroscopy spin coater system. We combine this system with real-time monitoring and analysis of the optical spectra during the spin coating process. As soon as a parameter of interest reaches a predefined target level, perovskite crystallization is automatically induced by dispensing the antisolvent *via* a syringe pump. To demonstrate our approach, we optically monitor the precursor solution film thickness as the parameter of interest during the spin coating. We intentionally vary the evaporation kinetics by spin coating at different spin speeds between 2000 and 1250 rpm and compare our reactive method to the common time-based approach. We find that our method reliably counteracts effects like variation in solvent evaporation rate due to atmospheric changes and reduces the human impact on the processing, thus leading to reproducible film quality for all spin speeds without any optimization steps.

1. Introduction

With PCEs up to 26.1%[1] and operational stabilities of several thousand hours,[2,3] metal halide perovskites (MHP) based solar cells have improved tremendously in the last 10 years. These highly efficient solar cells require a high quality of the MHP film itself. The state-of-the-art processing method for the majority of such high-quality MHP films is the solution-based solvent engineering spin coating approach.[4] In this approach, the MHP crystallization is commonly induced by dispensing an antisolvent (AS) onto the precursor solution film on the spinning substrate after a certain time of spinning. This time-based approach has several processing parameters that have to be considered.[5] Some of these, such as the spin speed, are easy to control while others are more subtle and hence more difficult to control. Consequently, the recipes (containing *e.g.* spin speed, timing of AS dispensing, composition of the precursor solution) used to fabricate MHP films with this approach are usually developed empirically, differ from lab to lab around the world, and are often transferable only with limited success from one lab to the other.[4] A significant factor responsible for the commonly observed discrepancies in PCE differences between batches and even within a batch of solar cells[6,7] are processing parameters that cannot easily be controlled, such as changes in atmospheric conditions or the quality of precursor material.[6,8] An additional influence can be the researcher who fabricates the perovskite layer, as his or her skill and comportment may, despite all control efforts, subconsciously control exactly when, how fast, and how much AS is dispensed.[6,9–12]

In this work, we present our recent development of a reactive spin coating approach that aims to eliminate the impact of changing process parameters like atmosphere on the processing. By implementing a syringe pump for autonomous AS dispensing, we further aim to exclude possible variations in AS dispensing. We compensate for possible changes in processing parameters by real-time tracking. For this, we evaluate the optical properties of the precursor solution *via* multimodal optical *in situ* spectroscopy and dispense the AS based on the

[a] Soft Matter Optoelectronics (EP II), University of Bayreuth, Bayreuth 95440, Germany. E-mail: fabian.panzer@uni-bayreuth.de
[b] Department of Functional Materials, University of Bayreuth, Bayreuth 95440, Germany
[c] Northern Bavarian NMR Centre (NBNC) and Inorganic Chemistry, University of Bayreuth, Bayreuth 95440, Germany

† Electronic supplementary information (ESI) available. See DOI: https://doi.org/10.1039/d3tc04361d

View Article Online
Paper Journal of Materials Chemistry C

evolving film properties. In this way, we progress from the commonly used time-based spin coating approach where the AS is dispensed after an empirically determined fixed time after the start of the spin coater, to a more fundamental reactive processing approach where the AS is dispensed when a certain parameter of interest that reflects the progress of the film formation (*e.g.* precursor solution film thickness, precursor state composition,[13] *etc.*) reaches a target value. The capability of this approach is demonstrated by simulating a change in formation kinetics, originating for example from varying evaporation rates of the solvent, by employing different spin speeds of the spin coater between 2000 and 1250 rpm.[14,15] For reference, we also processed perovskite films by the time-based spin coating approach for all spin speeds. After the measurements, we analyze the *in situ* data further to extract the perovskite growth rates and investigate the morphology of the resulting film.

The results of the reactive spin coating approach show a consistent quality of the perovskite layer independent of the rotation speed and concomitantly the solvent evaporation rate. This implies a successful and automated compensation of the change in formation kinetics. Notably, for all spin speeds a similar crystallite growth rate and morphology can be observed. In contrast, the films made with the time-based method exhibit significant differences in film morphology for the different spin speeds, and crystallite growth rates also vary widely. Thus, our findings prove the potential of the reactive spin coating method to compensate for varying processing parameters that are difficult to control otherwise, *e.g.* environmental changes and the variation of human reaction time, in order to reproducibly fabricate MHP films with consistent quality, independent of processing conditions.

2. The reactive spin coating concept

For our novel spin coating approach, we extended a home-built multimodal optical *in situ* measurements setup (see Fig. S1, ESI†) as described in detail by Buchhorn *et al.*[16] with a syringe pump. An in-house Python program controls all components and, moreover, records and analyzes the optical spectra in real time. The general concept of the reactive spin coating is shown schematically in Fig. 1. We initiate the spin-coating after deposing the solution with the precursors onto the substrate. With the start of rotation, absorption and PL are recorded and continuously analyzed on the fly. In our program routine, the determination of the precursor solution film thickness (the "parameter of interest" (POI)) occurs continuously. Once the previously specified target value is obtained, the program allows for the antisolvent to be dispensed onto the sample in a fully automated fashion. In this way, the crystallization of the perovskite gets initiated automatically at the intended precursor solution film thickness, independent of uncontrollable fluctuations in the solvent evaporation rate, *e.g.* due to changes in the room temperature or ventilation. Once the spin-coating is finished, we manually take the sample and anneal it. Obviously, this procedure (initiate process, examine, determine POI, trigger an action when POI reaches target value) can be adapted to suit any POI that is directly or indirectly measurable during the film processing, such as the concentration of certain iodoplumbate species,[17–19] and any desired action.

As mentioned, for demonstration purposes we chose the precursor solution film thickness as the parameter of interest.[5,20] For the investigated material system and other commonly used MHP compositions, the parameter thickness d of the precursor solution film can be extracted from an interference pattern that emerges in the absorption spectra between 1.6 eV and 2.4 eV after $\approx$ 5 s.[17,20] This pattern is caused by white light thin-film interference between the upper and lower interface of the precursor solution layer (Fig. 2a)[18] and it is spectrally manifested in a sine-like modulation of the otherwise flat absorption spectrum of the precursor solution layer in this energy range. According to Manifacier *et al.*[21] the thickness d of such a film can be calculated by taking advantage of this sinusoidal pattern, using eqn (1):

$$d = \frac{\lambda_1 \lambda_2}{2(\lambda_1 n_2 - \lambda_2 n_1)} \quad (1)$$

where λ_1 and λ_2 are the wavelengths of two consecutive extrema in the optical density (OD). n_1 and n_2 are the refractive indices of the sample at the respective wavelengths. Assuming n is constant in the investigated spectral range and is given by the refractive index of dimethylformamide (DMF, n_{DMF} = 1.43), the layer thickness can be written in terms of the frequency of the observed sine wave (ω) since the extrema are uniformly spaced in units of energy (see ESI† for details):

$$d = \frac{hc\omega}{4\pi n_{DMF}} \quad (2)$$

where h is the Planck constant and c is the speed of light in vacuum. To illustrate and explain the reactive processing for our chosen parameter of interest in more detail, the evolution of the OD of the precursor solution layer is plotted against energy and time after starting the spin coating in Fig. 2b. For every time frame, a sinusoidal pattern emerges, therefore leading to a stripe pattern in the 2D map that broadens with

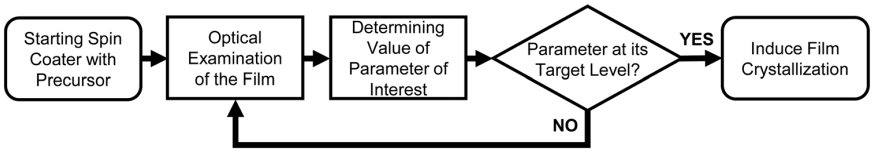

Fig. 1 Flowchart of the general scheme of the reactive spin coating procedure.

View Article Online
Journal of Materials Chemistry C Paper

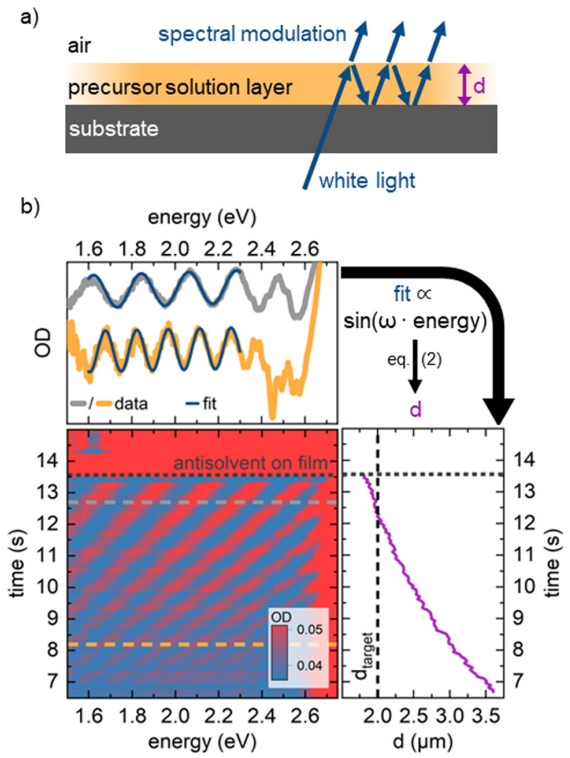

Fig. 2 (a) Schematics of the origin of thin film interference pattern used to calculate the film thickness. (b) Depiction of the real-time measurement of solvent layer thickness using *in situ* absorption spectroscopy (lower left panel). For every time frame (*e.g.*, at the grey/orange dashed lines) a sine-like function is fitted to the absorption data (upper panel) to calculate the solvent layer thickness from the frequency ω of the sine wave using eqn (2). Once this thickness (right panel) decreases below a critical target thickness, the antisolvent is dispensed by an automated syringe pump.

increasing time. The upper left plot in Fig. 2b shows two exemplary slices of the 2D OD map at different time frames. In this representation, one can easily observe a decrease in frequency ω with increasing time. The parameter ω is obtained by fitting a sine-like function and the precursor solution layer thickness is then calculated using eqn (2). These calculations are performed between two consecutive absorption spectrum measurements and therefore yield a real-time plot of the precursor solution layer thickness, that is depicted on the right in Fig. 2b. Once this extracted thickness decreases below a certain target thickness d_{target}, in this work 2 μm, the dispensing of antisolvent is initiated. As soon as the antisolvent reaches the precursor film, the OD rises due to perovskite crystallization and the white light interference originating from the precursor solution film vanishes (black dotted line in Fig. 2b). Further, we set an additional condition: a series of data points (in our case 9) must be smaller than the target thickness before the initiation of the antisolvent dispensing. This makes our method more robust against noise induced fluctuations in the extracted precursor solution layer thickness.

3. Comparing reactive *vs.* time-based spin coating

To show the capabilities of our approach, we compare the processing of (1) methylammonium lead iodide ($MAPbI_3$, 1.2 M of equimolar lead iodide and methylammonium iodide in DMF) and (2) a mixed cation and halide composition ($(MA_{0.17}FA_{0.83})Pb(I_{0.83}Br_{0.17})_3$, 1.2 M in DMF) thin films on glass substrates either *via* the new reactive or the established time-based spin coating method. We simultaneously record the absorption and PL during the film formation with the optical *in situ* spin coater setup as described. As the target value for the precursor solution layer thickness, we selected 2 μm since we obtained good $MAPbI_3$ thin films in our previous work when the film was spun at 2000 rpm and the AS was dispensed at this solution layer thickness.[5] For the time-based approach, the AS dispensing was initiated 12 s after the start of the spin coating for all spin speeds which corresponds to the time necessary to reach a precursor solution layer thickness of 2 μm for 2000 rpm. To simulate a change in formation kinetics, such as a change in evaporation rate, we varied the spin speed of the spin coater between 2000 and 1250 rpm in 250 rpm steps. This results in a reduction of the solvent evaporation rate constant from 0.21 s^{-1} for 2000 rpm to 0.15 s^{-1} for 1250 rpm (for details on the calculation of the evaporation rate constant see Fig. S2, ESI†). First, the recorded *in situ* data (absorption and PL) are analyzed in more detail to characterize possible differences between the two processing methods that can already be observed during film formation. Then, the optoelectronic properties and morphology of the final films after annealing are investigated and possible differences are identified. Finally, we discuss how the findings obtained from the model system $MAPbI_3$ are translated to the more complex $(MA_{0.17}FA_{0.83})Pb(I_{0.83}Br_{0.17})_3$ composition, which is used in high-efficiency perovskite solar cells.[4]

3.1 Analyzing the film formation

The 2D heat maps for all $MAPbI_3$ thin films processed *via* the two spin coating approaches at 2000 and 1250 rpm are shown in Fig. 3 (see Fig. S3 for heat maps of all spin speeds, ESI†). We obtain the familiar optical signatures of perovskite formation as discussed in detail previously.[5] In brief, once the AS is dispensed onto the substrate, the expected absorption edge and the perovskite PL signature appear in the absorption channel and the PL channel, respectively. For each spin speed and processing approach we track the peak position of the emerging perovskite PL signal. From this, we calculate the crystallite size for each point in time. This is possible because quantum confinement effects shift the PL peak energy of small crystallites to higher energies compared to values for bulk $MAPbI_3$ (for details on the peak fitting and crystallite size calculation see, eqn (S6) and (S7), ESI†).[19,22,23] The obtained crystallite sizes as a function of time are shown in the left panel in Fig. 4a and b. The time $t = 0$ on the time axes marks the point in time of the AS dispensing. We extract the growth rates for all measurements from linear fits of the crystallite growth after 10 s, with resulting growth rates being shown in Fig. 4c. It is

View Article Online
Paper Journal of Materials Chemistry C

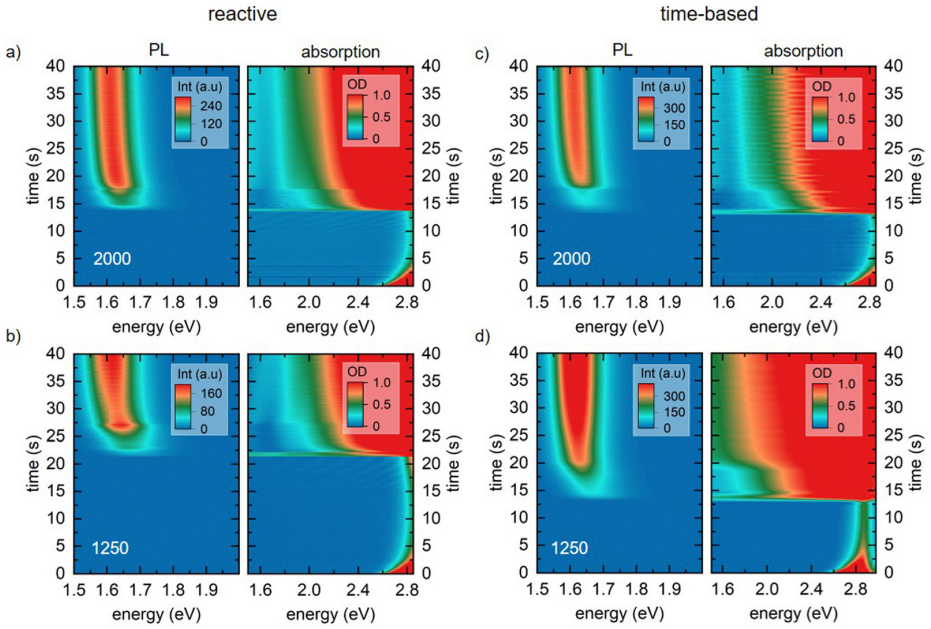

Fig. 3 Heat maps of photoluminescence (left) and absorption (right) measurements of $MAPbI_3$ solutions during spin coating *via* the reactive spin coating approach (a) and (b) and for the time-based approach (c) and (d) for spin speeds of 2000 and 1250 rpm.

obvious from the plot and the extracted growth rates that for the reactive spin coating, we observe a similar growth rate of perovskite crystallites regardless of the spin speed. In contrast, the obtained growth rates of the samples processed by the time-based method differ significantly between the different spin speeds. For the time-based spin coating, we chose to dispense the AS after spinning for 12 s at 2000 rpm when a precursor solution layer thickness of 2 μm is reached. It is therefore straightforward that the growth rate of the 2000 rpm time-based sample is similar to the 2000 rpm reactive sample. However, when reducing the spin speed in the time-based approach, the growth rate first increases to 0.46 nm s^{-1} for a spin speed of 1750 rpm and then decreases to 0.325 nm s^{-1} for 1500 rpm and further to 0.086 nm s^{-1} for 1250 rpm. Thus, the evolution of the crystallite size already indicates that film formation during the reactive spin coating proceeds in a very similar way independent of the chosen spin speed. In contrast, crystallite growth rates scatter much more when films are processed using the conventional time-based spin coating method.

As expected, the initially observed distinct interference pattern of the precursor solution layer in the absorption spectra mostly vanishes as soon as the AS is dispensed, and an absorption edge becomes visible at ~1.7 eV (Fig. 4d and e). This absorption edge is blue-shifted compared to $MAPbI_3$ bulk values of ~1.6 eV,[18] due to confinement of the forming perovskite crystallites. Interestingly though, at a closer look, we can still observe an interference pattern modulated on top of the signal of the growing perovskite layer for all films processed *via* reactive spin coating and for most films (2000, 1750, and 1500 rpm) processed *via* time-based spin coating. For the reactive spin-coated film (Fig. 4d), the interference pattern behaves similarly to the interference pattern of the precursor solution layer, *i.e.* its modulation frequency decreases with spin coating time. The origin of this additional interference effect is most probably the formation of an AS layer. The AS induces perovskite crystallization and consequently, a perovskite capping layer forms on top of the precursor solution layer. Therefore, excess AS cannot penetrate this capping layer and remains as AS layer on top, causing the observed spectral modulation *e.g.* between 1.11 und 1.80 s in Fig. 4d (also see Fig. 4f for illustration). Subsequent spinning off and evaporation of the AS layer then leads to the observed decrease in modulation frequency with spin coating time.

The absence of this second interference pattern for the 1250 rpm time-based spin coating suggests that no 'new' two-layer system (AS on top of perovskite capping layer) is formed, *i.e.* the addition of AS was not sufficient to drive the precursor solution into a thermodynamically state allowing for perovskite crystallization.

Furthermore, the significantly more pronounced scattering offset in the absorption spectra in Fig. 4e compared to Fig. 4d, suggests a more inhomogeneous perovskite growth and morphology of the final film processed at 1250 rpm in the time-based approach.

3.2 Comparison of the final film properties

The observations and indications obtained from the data during film formation are confirmed by the analysis of the final films after annealing. As expected from the evolution of crystallite size, the films prepared with reactive processing show an almost identical film structure in cross-section

View Article Online
Journal of Materials Chemistry C Paper

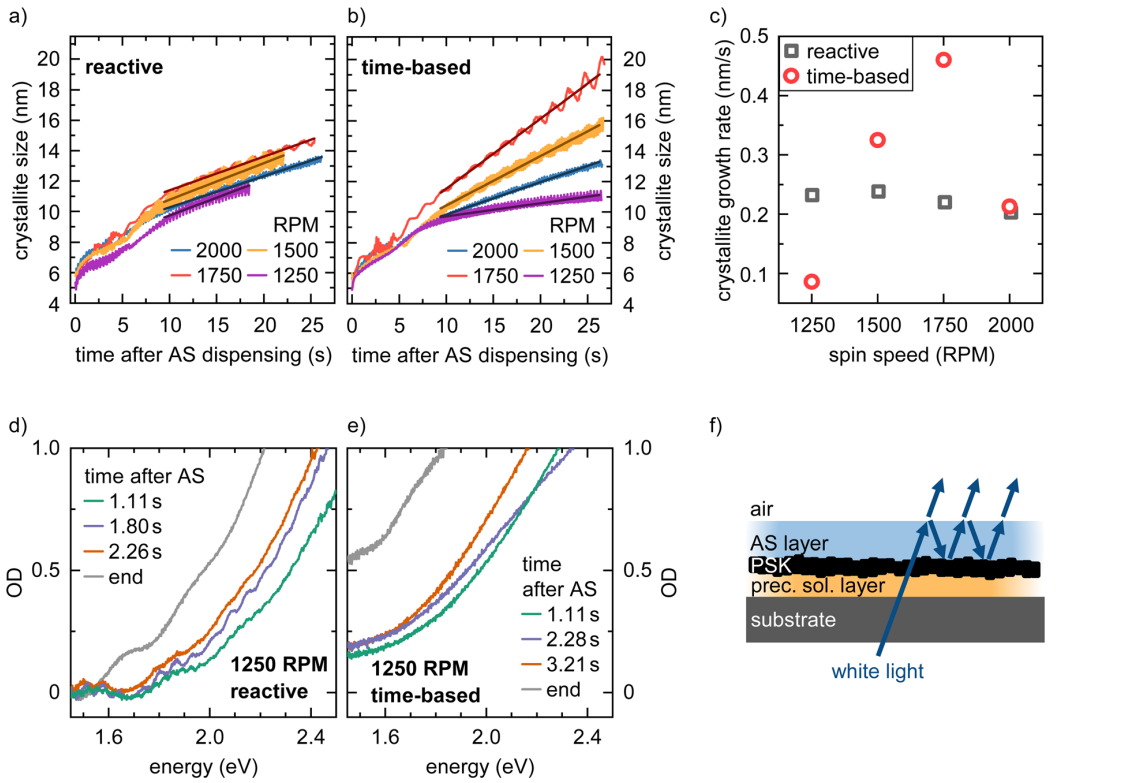

Fig. 4 Time evolution of the crystallite size for $MAPbI_3$ films processed *via* reactive (a) and time-based (b) spin coating for different rpms, extracted from the PL peak position considering quantum confinement. The time axis was shifted that $t = 0$ corresponds to the time of AS dispensing. (c) Calculated crystallite growth rates for different spin speeds and processing methods, extracted by linear fitting of the evolution of crystallite size over time in (a) and (b). OD spectra at different times during the processing of $MAPbI_3$ films *via* reactive (d) and time-based (e) spin coating at 1250 rpm. In (d) for 1.11 s and 1.80 s a modulation of the perovskite absorption spectrum is visible. (f) Schematics of the origin of the observed second spectral modulation due to thin film interference after dispensing the AS.

(Fig. 5a) and top view (Fig. S4, ESI†). The film thickness for reactive spin coating is virtually identical for all spin speeds. In contrast, time-based processed films show significant variation. Here, the film thickness is larger the smaller the spin speed. In addition, the existing voids become larger with decreasing spin speed. This confirms the observation during film formation that perovskite first forms on the upper surface of the solution film and then crystallizes downwards towards the substrate. We conjecture that with slower spin speeds and the time-based method, more and more solvent is trapped below the perovskite surface layer, which fully evaporates during the annealing step that follows the spin-coating. The absorption spectra of the reactive spin-coated and the time-based spin-coated series after annealing further substantiate this conclusion: While all films prepared *via* the reactive spin coating approach show a very similar absorption spectrum, a variation of scattering offset is seen in the films processed *via* the time-based method (Fig. S5, ESI†).

Both XRD (Fig. 5c and Fig. S6, ESI†) and top view SEM images (Fig. S4, ESI†), as well as steady-state PL spectra (Fig. S5, ESI†) and time-resolved PL (TRPL) curves (Fig. 5d), do not show significant differences between the films prepared by the different methods. This proves that on the length and time scales sampled by PL and XRD, the grain size and the intrinsic properties of the perovskite do not change due to our reactive approach. Additionally, there is no evidence of residual PbI_2 present in XRD pattern for all reactive spin-coated films, indicating that the reactive spin coating method robustly yields phase-pure films with uniform film thickness and quality independent of spin speed, whereas small signals of unreacted PbI_2 are visible in the XRD pattern in the case of time-based spin coating at spin speeds of 1500 rpm and 1250 rpm. Therefore, we conclude that the reactive approach does not affect the intrinsic morphological properties such as grain size and shape, but our approach preserves these properties independently of the spin speed throughout the perovskite layer.

In addition to the model system $MAPbI_3$, we also investigated if and how the reactive processing approach can be transferred to more complex mixed compositions, such as $(MA_{0.17}FA_{0.83})Pb(I_{0.83}Br_{0.17})_3$. The corresponding *in situ* data and detailed discussions of the measurements can be found in Section 3 in the ESI.† In brief, this mixed system indeed behaves similar to the model system $MAPbI_3$ so far discussed and the final films obtained are comparable to the $MAPbI_3$ layers. In particular, the

View Article Online
Paper Journal of Materials Chemistry C

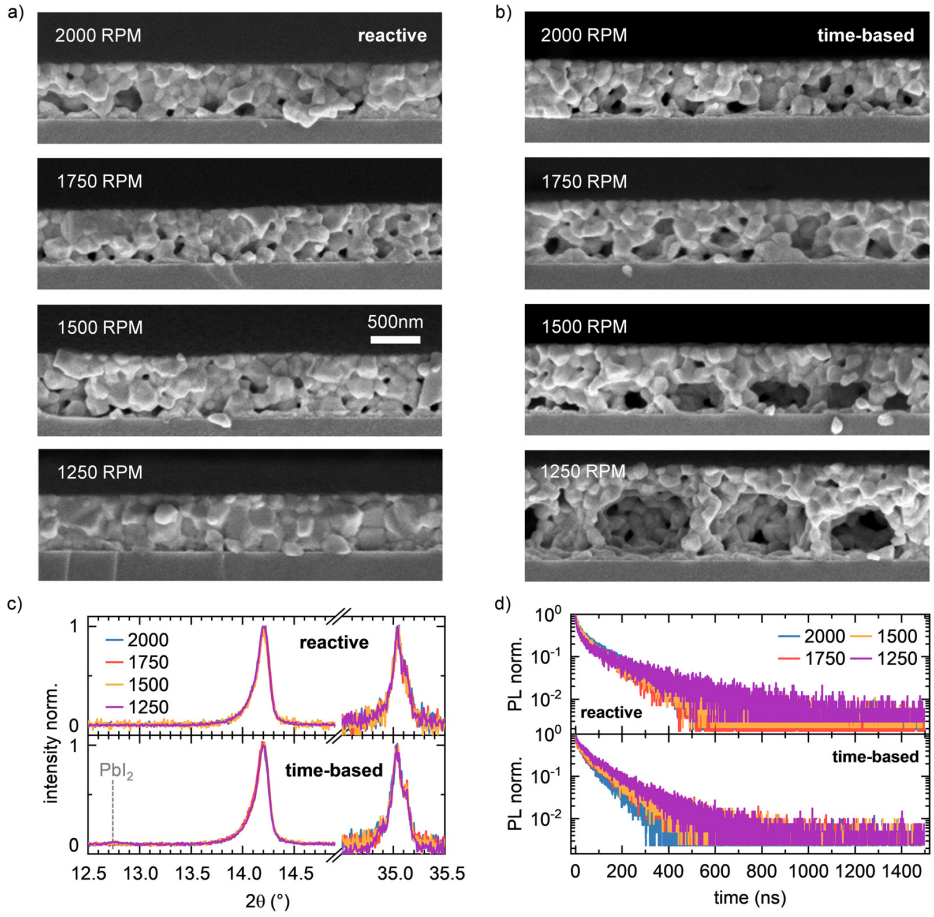

Fig. 5 (a) SEM cross-section images of the $MAPbI_3$ films fabricated *via* reactive spin coating approach at different spin speeds. (b) SEM cross-section images of the $MAPbI_3$ films fabricated *via* time-based spin coating approach at different spin speeds. (c) XRD peaks of the $MAPbI_3$ films fabricated *via* reactive (top) or time-based (bottom) spin coating approach at different spin speeds. (d) normalized TRPL curves of the $MAPbI_3$ films fabricated *via* reactive (top) or time-based (bottom) spin coating approach at different spin speeds.

SEM cross section images (see Fig. 6 and Fig. S10, ESI†) show that also for the mixed $(MA_{0.17}FA_{0.83})Pb(I_{0.83}Br_{0.17})_3$ composition, the resulting perovskite layer morphology remains independent of the spin speed for the reactive approach. In contrast, in the time-based approach the perovskite layers exhibit increasingly bigger voids with decreasing spin speed. These findings indicate that the reactive spin coating approach is not only limited to a ternary halide perovskite composition such as $MAPbI_3$, but also transfers to more complex, mixed compositions such as $(MA_{0.17}FA_{0.83})Pb(I_{0.83}Br_{0.17})_3$.

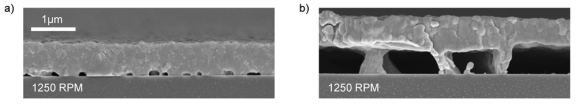

Fig. 6 (a) SEM cross-section images of the $(MA_{0.17}FA_{0.83})Pb(I_{0.83}Br_{0.17})_3$ films fabricated *via* reactive spin coating approach at 1250 rpm. (b) SEM cross-section images of the $(MA_{0.17}FA_{0.83})Pb(I_{0.83}Br_{0.17})_3$ films fabricated *via* time-based spin coating approach at 1250 rpm.

4. Conclusion

In summary, the reactive spin coating approach presented here allows to automatically dispense the AS when a certain parameter value, such as precursor solution layer thickness, has been reached, based on the live feedback from the real-time analysis of the optical spectra during spin coating. As a result, films with the same quality (crystallite size, microstructure, and film thickness) could be produced, down to spin speeds as low as 1250 rpm without any additional optimization steps for the model system $MAPbI_3$ as well as for the mixed $(MA_{0.17}FA_{0.83})Pb(I_{0.83}Br_{0.17})_3$ composition.

To substantiate the advantages of our newly developed method, we compared our new approach with a conventional time-based method, in which the AS is dispensed after a fixed time, leading to a clear variation in the crystallization behavior and differences in the final film properties depending on the spin speed. We emphasize that the reactive spin coating technique is not limited to the precursor solution layer

View Article Online
Journal of Materials Chemistry C Paper

thickness as a parameter of interest, but it can also be easily adapted to other parameters accessible by optical spectroscopy, such as the various PbI_x-related precursor absorption peaks that change during spin-coating.

Additionally, our approach enables fundamental film formation studies that rely on the variation of system- and process-internal parameters during film formation (*e.g.* influence of the properties of PbI_x species upon AS addition on the perovskite crystallization process), without the need to rely on variation of system- and/or process-external parameters (*e.g.* variation of moment of AS dripping, or (external) variation of precursor concentration). This likely will allow a more direct and simplified understanding of the complicated relationship between solution properties and final film properties of halide perovskites.

Thus, our reactive spin coating approach will open up future possibilities to simplify the transfer of recipes from one laboratory to the next by removing the influence of external effects, such as atmosphere or the human factor, on the layer formation as the processing is only based on system-internal parameters. Eventually, our approach also represents a valuable contribution for an in general improved process control in the solution processing of halide perovskite thin films, making it relevant for their successful upscaling and commercialization in optoelectronic devices in the future.

Experimental details

Precursor solution

All materials were used as received. Lead(II) iodide (PbI_2, 98%), methylammonium iodide (MAI, 99%), formamidinium iodide (FAI, 99%), lead bromide (PbBr, 99%) and methylammonium bromide (MABr, 99%) were purchased from TCI. For $MAPbI_3$ solutions, PbI_2 and MAI were weighed in a stoichiometry of 1 : 1 and dissolved in DMF (Acros) to obtain stock solution with a concentration of 1.2 M. For the $(MA_{0.13}FA_{0.83})Pb(I_{0.83}Br_{0.17})_3$ solutions, PbI_2, FAI, PbBr and MABr were weighed accordingly to obtain a stoichiometry of $(MA_{0.17}FA_{0.83})Pb(I_{0.83}Br_{0.17})_3$ and the precursor were dissolved in DMF to obtain a concentration of 1.2 M.

Thin film fabrication

The precursor solutions were spin coated on glass substrates at various spin speeds as detailed in the main text. After the spin coating step, the films were annealed on a hot plate at 100 °C for 10 min.

In situ setup

All optical *in situ* data were recorded with a home-built setup. In brief, photoluminescence and absorption were recorded alternating frame-by-frame at a frame rate of 15 Hz. To ensure reproducibility we recorded at least two coatings for each sample, which turned out to be quasi-identical. Further details are given in the ESI.†

XRD

The powder XRD pattern was recorded on a Bragg–Brentano-type diffractometer (Empyrean, Malvern Panalytical BV, Netherlands) equipped with a PIXcel-1D detector using Cu-Kα radiation (λ = 1.5419 Å)

REM

The film morphology was characterized by SEM using a Zeiss Leo 1530 instrument FE-SEM with Schottky-field-emission cathode, In-lens detector, and SE2 detector. The accelerating voltage was 3 kV. Prior to measurement, the samples were sputtered with 2 nm platinum.

TRPL

For time-resolved photoluminescence curves, time-correlated single-photon counting (TCSPC) measurements were performed with a PicoQuant MT200 confocal fluorescence microscope in combination with a PMA Hybrid PMT 40 photomultiplier tube (PicoQuant) and a TimeHarp 260 Pico TCSPC board (PicoQuant). The samples were excited with a 560 nm diode Laser (PicoQuant LDH-D-TA-560) with a frequency of 2.0 MHz and a pulse width of 68 ps. The laser beam was focused on the sample with an Olympus Objective with 4× magnification, and the emission was filtered with a 561 nm long-pass filter before detection. The excitation fluence was set to 300 nJ cm^{-2}.

Conflicts of interest

There are no conflicts to declare.

Acknowledgements

The authors acknowledge financial support from the German National Science Foundation DFG *via* the projects PA 3373/3-1, MO 1060/32-1, PA 3373/6-1, KO 3973/3-1, GR 5505/3-1 and the IRTG 2818 OPTEXC. We also thank Martina Heider and the KeyLabs "Electron and Optical Microscopy" and "Device Engineering" of the Bavarian Polymer Institute (BPI) for assistance with SEM images and access to the MT200 system. Further, we want to thank Christopher Greve for assistance with XRD measurements and Philipp Ramming for assistance with the TRPL measurements.

References

1 NREL, Best Research-Cell Efficiency Chart, **https://www.nrel.gov/pv/cell-efficiency.html**, accessed February 15, 2024.
2 Q. Cao, Y. Li, H. Zhang, J. Yang, J. Han, T. Xu, S. Wang, Z. Wang, B. Gao, J. Zhao, X. Li, X. Ma, S. M. Zakeeruddin, W. E. I. Sha, X. Li and M. Grätzel, *Sci. Adv.*, 2021, 7, eabg0633.
3 Y. Zhao, T. Heumueller, J. Zhang, J. Luo, O. Kasian, S. Langner, C. Kupfer, B. Liu, Y. Zhong, J. Elia, A. Osvet, J. Wu, C. Liu, Z. Wan, C. Jia, N. Li, J. Hauch and C. J. Brabec, *Nat. Energy*, 2022, 7, 144–152.

4 M. Saliba, J.-P. Correa-Baena, C. M. Wolff, M. Stolterfoht, N. Phung, S. Albrecht, D. Neher and A. Abate, *Chem. Mater.*, 2018, **30**, 4193–4201.
5 S. Biberger, K. Schötz, P. Ramming, N. Leupold, R. Moos, A. Köhler, H. Grüninger and F. Panzer, *J. Mater. Chem. A*, 2022, **10**, 18038–18049.
6 K. P. Goetz and Y. Vaynzof, *ACS Energy Lett.*, 2022, **7**, 1750–1757.
7 Y. Zou, Y. Li, X. Pang, Y. Song, W. Xu and B. Sun, *J. Phys. Chem. Lett.*, 2023, **14**, 5025–5032.
8 O. Shargaieva, H. Näsström, J. A. Smith, D. Többens, R. Munir and E. Unger, *Mater. Adv.*, 2020, **1**, 3314–3321.
9 A. D. Taylor, Q. Sun, K. P. Goetz, Q. An, T. Schramm, Y. Hofstetter, M. Litterst, F. Paulus and Y. Vaynzof, *Nat. Commun.*, 2021, **12**, 1878.
10 K. Wang, M.-C. Tang, H. X. Dang, R. Munir, D. Barrit, M. De Bastiani, E. Aydin, D.-M. Smilgies, S. De Wolf and A. Amassian, *Adv. Mater.*, 2019, **31**, 1808357.
11 Q. An, L. Vieler, K. P. Goetz, O. Telschow, Y. J. Hofstetter, R. Buschbeck, A. D. Taylor and Y. Vaynzof, *Adv. Energy Sustainability Res.*, 2021, **2**, 2100061.
12 T.-B. Song, Z. Yuan, F. Babbe, D. P. Nenon, E. Aydin, S. De Wolf and C. M. Sutter-Fella, *ACS Appl. Energy Mater.*, 2020, **3**, 2386–2393.
13 A. M. Valencia, O. Shargaieva, R. Schier, E. Unger and C. Cocchi, *J. Phys. Chem. Lett.*, 2021, **12**, 2299–2305.
14 D. E. Bornside, C. W. Macosko and L. E. Scriven, *J. Electrochem. Soc.*, 1991, **138**, 317.
15 J. Danglad-Flores, S. Eickelmann and H. Riegler, *Eng. Rep.*, 2021, **3**, e12390.
16 M. Buchhorn, S. Wedler and F. Panzer, *J. Phys. Chem. A*, 2018, **122**, 9115–9122.
17 H.-S. Yun, H. W. Kwon, M. J. Paik, S. Hong, J. Kim, E. Noh, J. Park, Y. Lee and S. I. Seok, *Nat. Energy*, 2022, **7**, 828–834.
18 M. Chauhan, Y. Zhong, K. Schötz, B. Tripathi, A. Köhler, S. Huettner and F. Panzer, *J. Mater. Chem. A*, 2020, **8**, 5086–5094.
19 L. Polavarapu, B. Nickel, J. Feldmann and A. S. Urban, *Adv. Energy Mater.*, 2017, **7**, 1700267.
20 K. Schötz, C. Greve, A. Langen, H. Gorter, I. Dogan, Y. Galagan, A. J. J. M. van Breemen, G. H. Gelinck, E. M. Herzig and F. Panzer, *Adv. Opt. Mater.*, 2021, **9**, 2101161.
21 J. C. Manifacier, J. Gasiot and J. P. Fillard, *J. Phys. E: Sci. Instrum.*, 1976, **9**, 1002–1004.
22 J. A. Sichert, Y. Tong, N. Mutz, M. Vollmer, S. Fischer, K. Z. Milowska, R. García Cortadella, B. Nickel, C. Cardenas-Daw, J. K. Stolarczyk, A. S. Urban and J. Feldmann, *Nano Lett.*, 2015, **15**, 6521–6527.
23 Y. Kayanuma, *Phys. Rev. B: Condens. Matter Mater. Phys.*, 1988, **38**, 9797–9805.

Supplementary Information

Reactive spin coating based on real-time In-Situ feedback for improved control of perovskite thin film fabrication

Simon Biberger[1], Maximilian Spies[1], Konstantin Schötz[1], Frank-Julian Kahle[1], Nico Leupold[2], Ralf Moos[2], Helen Grüninger[3], Anna Köhler[1], Fabian Panzer[1#]

[1]Soft Matter Optoelectronics (EP II), University of Bayreuth, Bayreuth 95440, Germany

[2]Department of Functional Materials, University of Bayreuth, Bayreuth 95440, Germany

[3]Northern Bavarian NMR Centre (NBNC) and Inorganic Chemistry, University of Bayreuth, Bayreuth 95440, Germany

Corresponding Author:

[#]E-Mail: fabian.panzer@uni-bayreuth.de

Section 1: In-Situ Spin coater Setup and fitting details

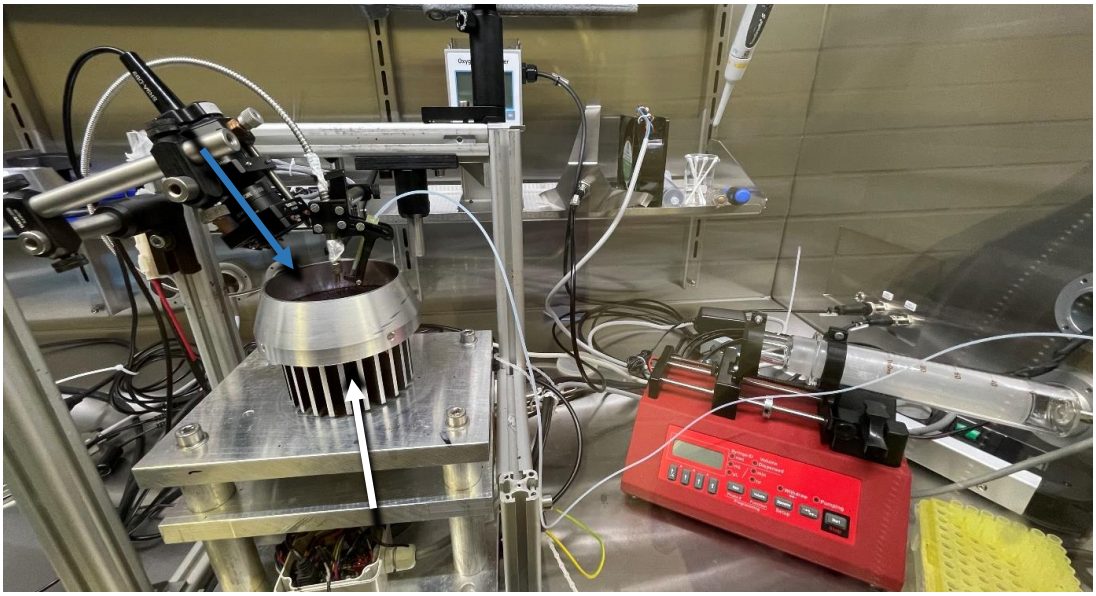

Figure S1: Photographs of the optical in situ spin coater setup used for the reactive spin coating approach, together with the connected syringe pump used for the antisolvent dispensing.

The setup for measuring the in situ optical data during spin-coating is shown in figure S1. It consists of a custom-built spin-coater with a hole in the middle. Underneath the spin-coater a white-light LED is placed. Its light shines through the hole in the middle of the spin coater and serves as a white light source for transmission measurements. A laser diode (405 nm) in combination with focusing optics and a diaphragm are mounted above the spin-coater for exciting the sample for PL measurements. The circular area probed by our optical measurements during the spin coating has a diameter of 5 mm in the center of the substrate. White-light and excitation laser are turned on and off alternatingly, so that either transmission or PL is probed. Transmitted light and PL are collected with one optical fiber, which is coupled to the detection system. The detection system consists of a CCD camera, coupled to a spectrograph, and a home-built detection setup, which is described in detail in Supporting Reference 1.[1] In brief, the detection setup switches the optical path between transmission and PL

measurements, so that for PL measurements, the laser wavelength is blocked by a suitable filter. In contrast, for transmission measurements, the transmitted light is coupled into the spectrograph without additional filtering. The detection setup further synchronizes the CCD camera with the white-light LED, the laser and the optical path switching. Using this setup, we can record PL and transmission during spin-coating quasi-simultaneously (i.e., alternating frame by frame) with a rate of 15 Hz. From the transmission measurements, the optical density (OD) is calculated based on a reference measurement prior to spin-coating. The antisolvent is automatically dispensed via a syringe pump (Model 540060, TSE Systems) through a connected capillary and pipette tip.

Derivation of eq. (2)

Given the following relation:

$$d = \frac{\lambda_1 \lambda_2}{2(\lambda_1 n_2 - \lambda_2 n_1)} \tag{S1}$$

where d is the thickness of the film, λ_1 and λ_2 are the wavelengths of two consecutive extrema in the OD. n_1 and n_2 are the refractive indices of the sample at the respective wavelengths. Assuming that n is constant in the investigated spectral range and is given by the refractive index of dimethylformamide (n_{DMF}) yields:

$$d = \frac{\lambda_1 \lambda_2}{2(\lambda_1 - \lambda_2) n_{DMF}} \tag{S2}$$

The frequency ω of the observed sine wave in units of energy is given by

$$\omega = \frac{2\pi}{E_2 - E_1} \tag{S3}$$

where E_1 and E_2 are the energetic positions of two consecutive extrema in the OD. Using the Planck constant h and speed of light c, one is able to rewrite the energy in terms of wavelength:

$$\omega = \frac{2\pi}{\frac{hc}{\lambda_2} - \frac{hc}{\lambda_1}} = \frac{2\pi}{hc} \frac{\lambda_1 \lambda_2}{\frac{\lambda_1 \lambda_2}{\lambda_2} - \frac{\lambda_1 \lambda_2}{\lambda_1}} = \frac{2\pi}{hc} \frac{\lambda_1 \lambda_2}{\lambda_1 - \lambda_2} \tag{S4}$$

Inserting eq. (S4) into eq. (S2) yields:

$$d = \frac{hc\omega}{4\pi\, n_{DMF}} \tag{S5}$$

Section 2: $MAPbI_3$

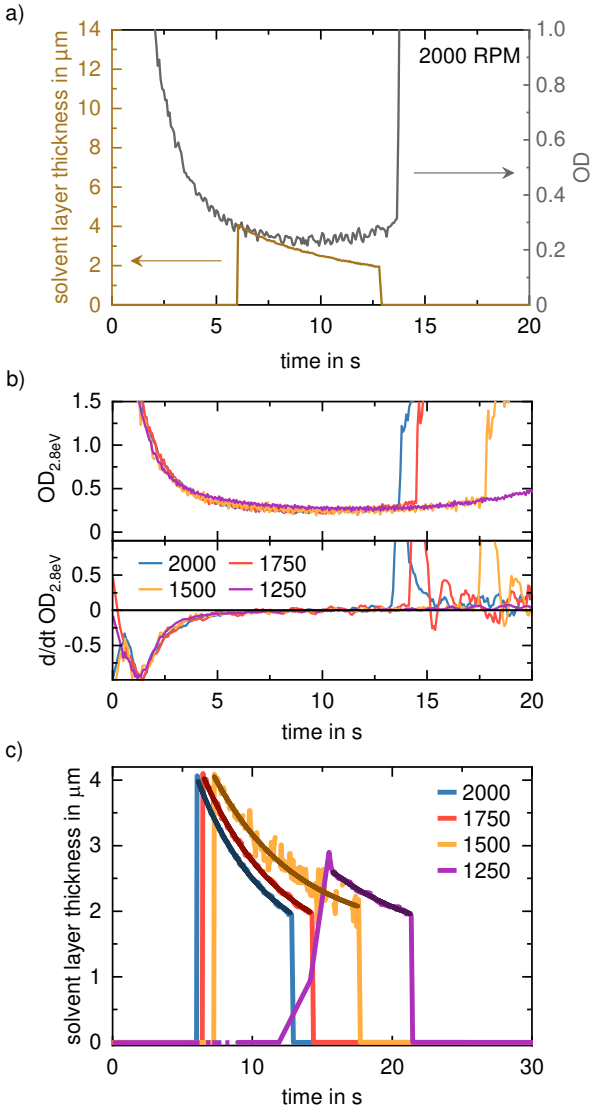

Figure S2: a) Evolution of the solvent layer thickness (ocher), together with the evolution of the OD at 2.8 eV (grey) for the film spin coated at 2000 RPM. b) Evolution of the OD at 2.8 eV for all four spin speeds (top) and the respective first time-derivatives (bottom) c) Evolution of the solvent layer thickness for all four spin speeds.

At the beginning of the observable interference pattern, both the solution layer thickness and the OD at 2.8 eV follow the same qualitative decrease. While the solution layer thickness continuously keeps decreasing, the OD at 2.8 eV stays constant after

5 s (see d/dt $OD_{2.8\ eV}$ in Fig. S2b). The fast decrease of the OD at the start indicates a throw-off of precursor solution. Afterwards the OD stays constant and only the solvent layer thickness decreases. This suggests a mere evaporation of the solvent. Since the exact description of the thinning of film during spin coating is complex,[2] we determined a rate constant as a measure for the thinning process of the solvent films due to evaporation for the different spin speeds by fitting the evolution of the solvent layer thickness with a mono-exponential decay. The resulting rate constants for all spin speed are summarized in table S1.

Table S1: Evaporation rate constants extracted from mono-exponential fitting of the evolution of the solvent layer thickness for all spin speeds.

Spin speed in RPM	2000	1750	1500	1250
rate constant in 1/s	0.205 ± 0.003	0.176 ± 0.003	0.169 ± 0.014	0.147 ± 0.011

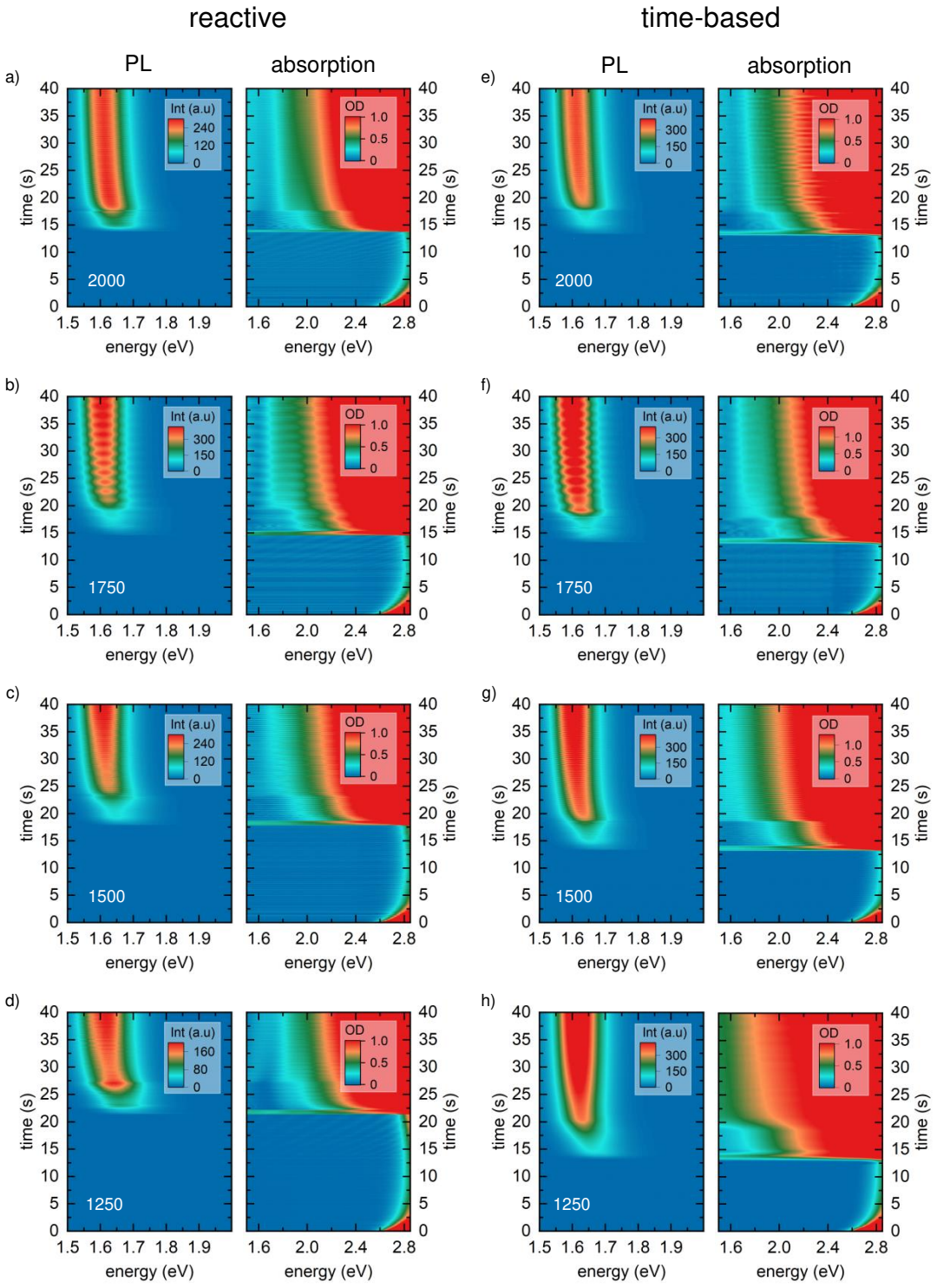

Figure S3: Heat maps of photoluminescence (PL), and absorption (OD) measurements of $MAPbI_3$ solutions during spin coating via the reactive spin coating approach (a-d) and for the time-based approach (e-h) for the different spin speeds (RPM in white numbers).

PL Peak Extraction and Crystallite size calculation

For fitting the PL spectra, we use an empirical line shape in the form of an asymmetric hyperbolic secant, that is

$$I(E) = I_0 \frac{2}{e^{\frac{E-E_0}{\sigma_1}} + e^{\frac{E-E_0}{\sigma_2}}} \quad \text{(S6)}$$

and extract the energy value of the maximum of this function for all recorded spectra over time.

This extracted peak position of the perovskite PL spectrum is considerably higher than typical bulk PL peak energies of 1.6 eV[3], which suggests the presence of a quantum confinement effect similar to a particle in a box approach. Considering this effect, the crystallite size *d* can be extracted from the energetic position of the PL peak via

$$E_{PL} = E_g + \frac{b}{d^2}, \quad \text{(S7)}$$

where we set the $MAPbI_3$ bulk band gap value E_g = 1.59 eV,[4–6] and the constant b = 3 eV nm^2,[7,8] based on literature values.

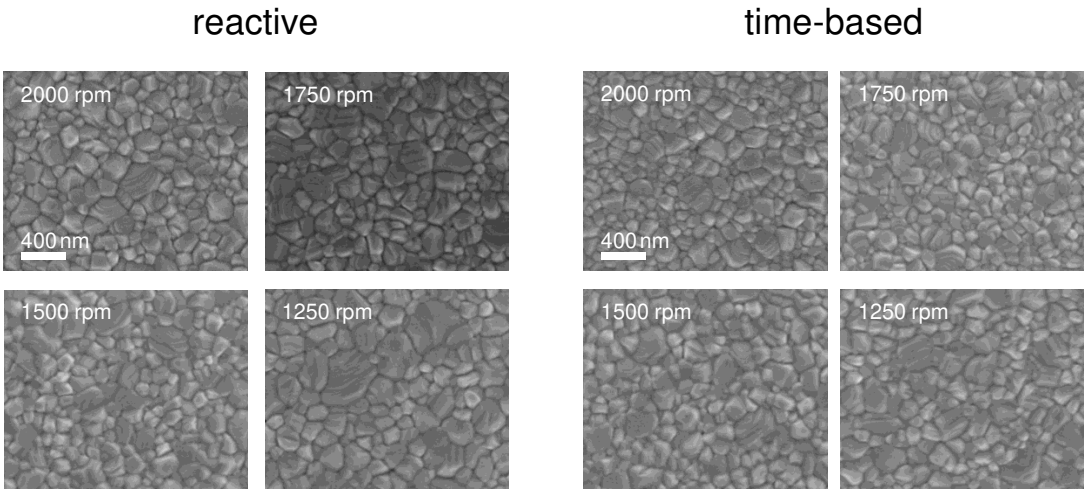

Figure S4: SEM top view images of the $MAPbI_3$ films fabricated via reactive (left) or time-based (right) spin coating approach at different spin speeds.

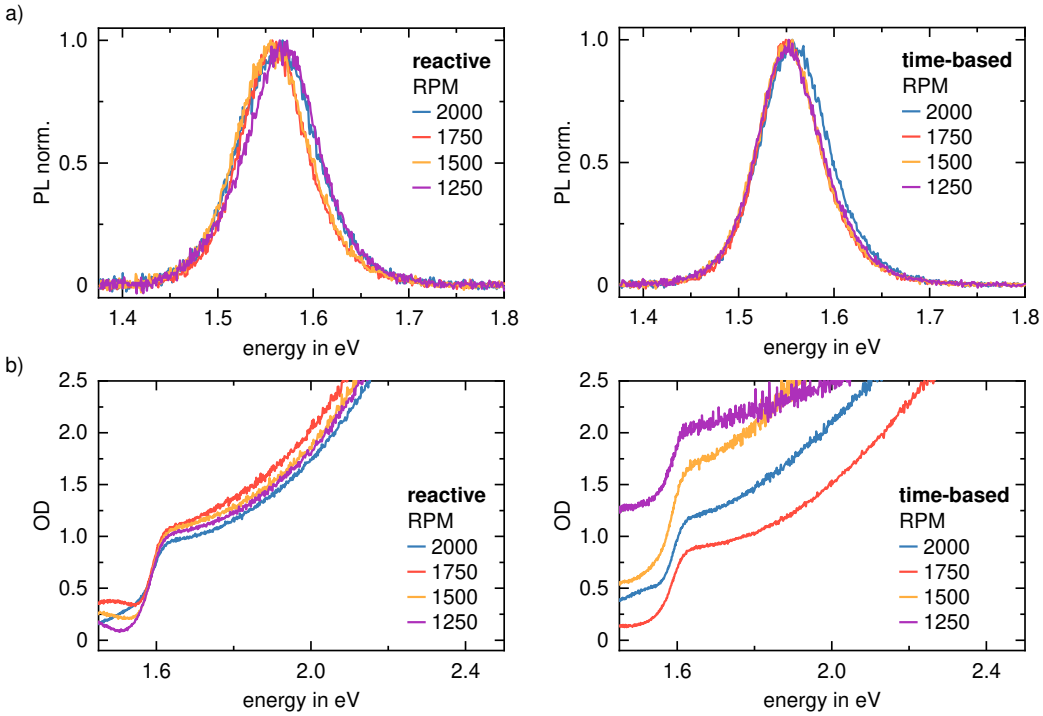

Figure S5: a) PL of $MAPbI_3$ films processed via reactive spin coating method (left) or via time-based spin coating (right) after annealing. The data is normalized to the maximum. b) OD spectra of $MAPbI_3$ films processed via reactive spin coating method (left) or via time-based spin coating (right) after annealing.

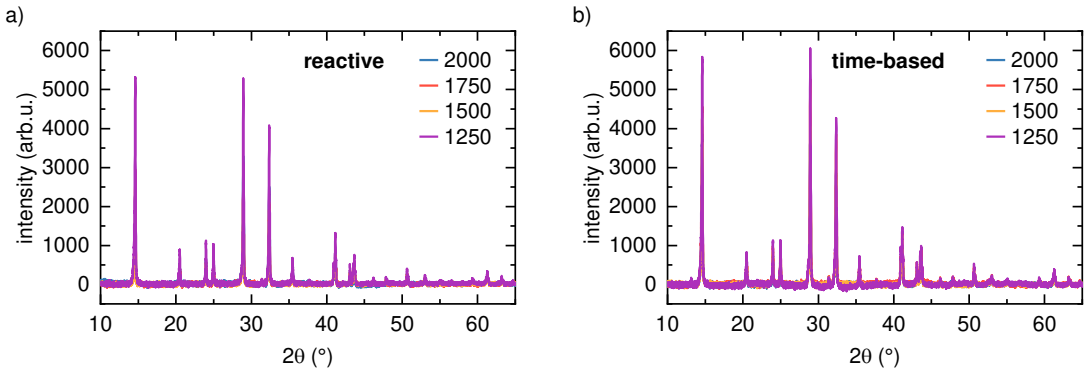

Figure S6: XRD patterns of the $MAPbI_3$ films fabricated via reactive (a) or time-based (b) spin coating approach at different spin speeds.

Section 3: $(MA_{0.13}FA_{0.83})Pb(I_{0.83}Br_{0.17})_3$

To investigate whether the reactive approach is also applicable to more complex mixed systems we also processed $(MA_{0.13}FA_{0.83})Pb(I_{0.83}Br_{0.17})_3$ (1.2M in DMF) via the reactive and time-based approach. We kept the value of the parameter of interest at 2000 nm and the antisolvent (AS) was dispensed once this value was reached for this solvent layer thickness. Analogously to the $MAPbI_3$ experiments, we also performed a set of coatings via the time-based approach where the AS was dispensed at a pre-set time. In the case of $(MA_{0.13}FA_{0.83})Pb(I_{0.83}Br_{0.17})_3$, this time was set to 11 s after spin coating start motivated by the fact that for a spin speed of 2000 RPM a solvent layer thickness of 2000 nm was reached after a spin coating time of 11 s.

Results and Discussion:

The heat maps for the different spin speeds and spin coating approaches are displayed in Figure S7. The behavior of the film formation is very similar to the discussed behavior for $MAPbI_3$ in the main text. As soon as the AS is dispensed the crystallization is induced and perovskite signatures (absorption edge and PL signal) are observed in the respective channels. Similar to the $MAPbI_3$ set, we tracked the PL peak position to extract the crystallite size as a function of time and to calculate the crystallite growth rate. By closer inspection of the PL data however, we noticed that our model to extract the crystallite size that assumes one species contributing to the PL signal is not fully applicable to the mixed composition. As it can be seen in Fig. S8 there are at least two different emitting species (possibly iodine and bromine rich phases) present in the forming layer. The relative contribution of the signature at higher energies decreases with spin coating time. This can either be due to an improved halide mixing or a more efficient energy transfer from the high energy species to species at lower energies from which the emission then occurs.[9] Therefore, we only extracted the energetic position of the PL signal maximum (see Fig. S9) for all spin speeds and the two processing approaches. However, to understand the film formation processes in detail, more investigations are needed, which will be focus of a follow-up investigation.

The final film properties (SEM images in Fig. 10 and optical properties in Fig. 11) of the processed films after annealing suggest a similar conclusion to the one that could be drawn for the $MAPbI_3$ experiments. The SEM images show that with decreasing

spin speed larger voids occur for the time-based approach. In contrast, for the reactive process, a similar perovskite layer is obtained independent of the spin speed. The optical characterizations reveal that – analogously to the $MAPbI_3$ results – the surface sensitive PL is identical for all films, proving that also in the case of $(MA_{0.13}FA_{0.83})Pb(I_{0.83}Br_{0.17})_3$ an identical top layer is formed for all films. In the OD spectra, agreeing with the $MAPbI_3$ findings, we observe a slight increase in scattering for the films processed via the time-based approach at lower spin speeds, which fits to the observed voids in the perovskite layer.

In conclusion, the results of the mixed composition $(MA_{0.13}FA_{0.83})Pb(I_{0.83}Br_{0.17})_3$ show good agreement with those of the $MAPbI_3$ experiments, discussed in the main text, demonstrating that the reactive spin coating approach is applicable for different perovskite compositions.

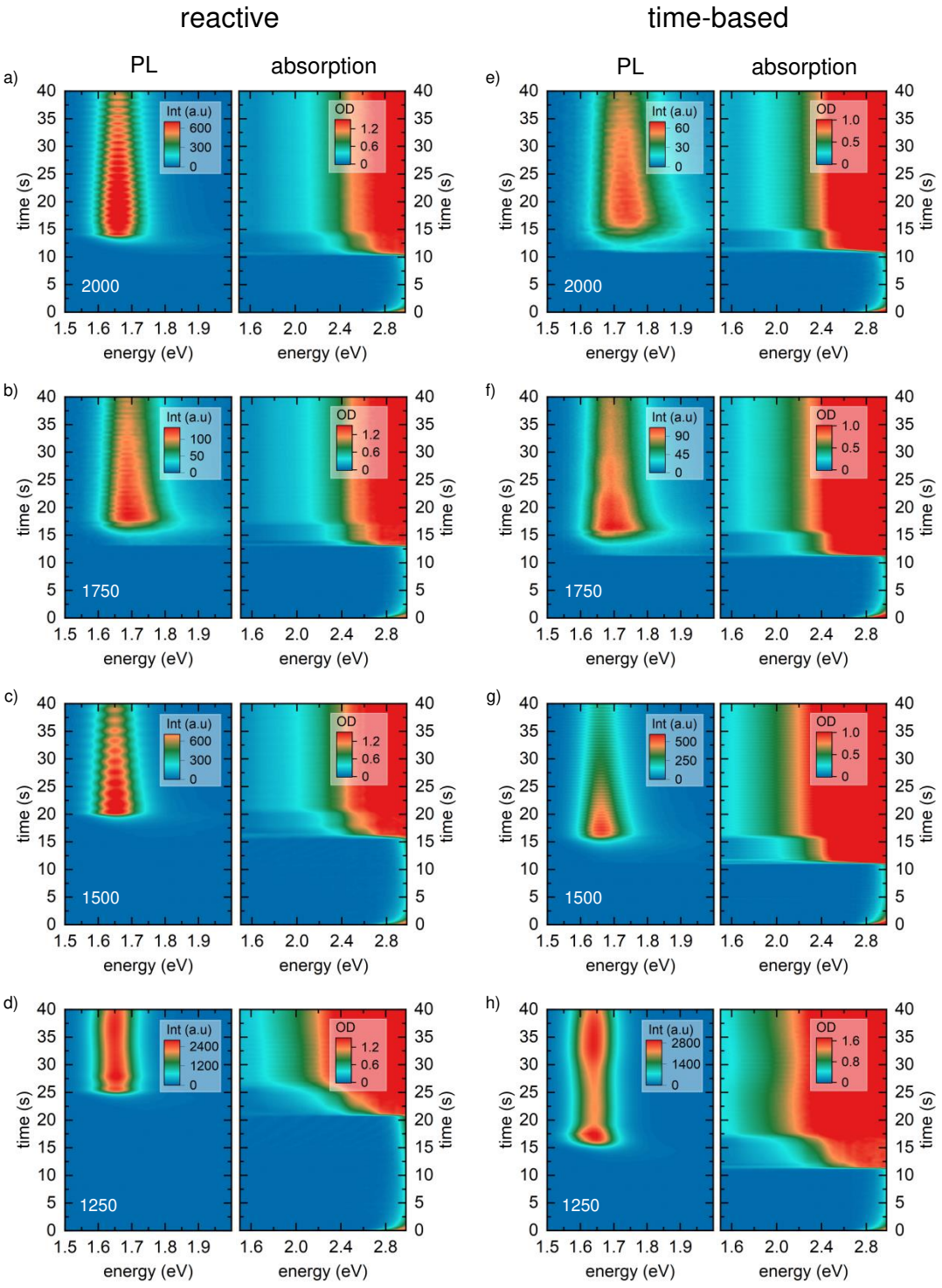

Figure S7: Heat maps of photoluminescence (PL), and absorption (OD) measurements of $(MA_{0.13}FA_{0.83})Pb(I_{0.83}Br_{0.17})_3$ solutions during spin coating via the reactive spin coating approach (a-d) and for the time-based approach (e-h) for the different spin speeds (RPM in white numbers).

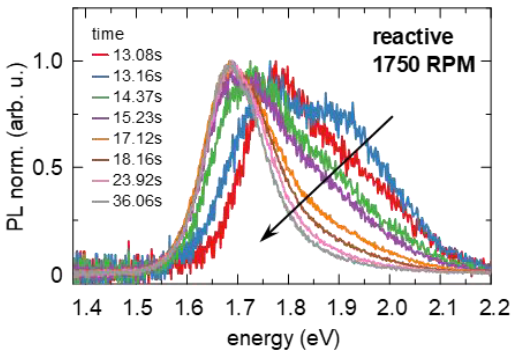

Figure S8: normalized PL spectra at different spin coating times for a $(MA_{0.13}FA_{0.83})Pb(I_{0.83}Br_{0.17})_3$ film processed at 1750 RPM. The arrow indicates decrease of an additional PL feature at higher energies with increasing spin coating time.

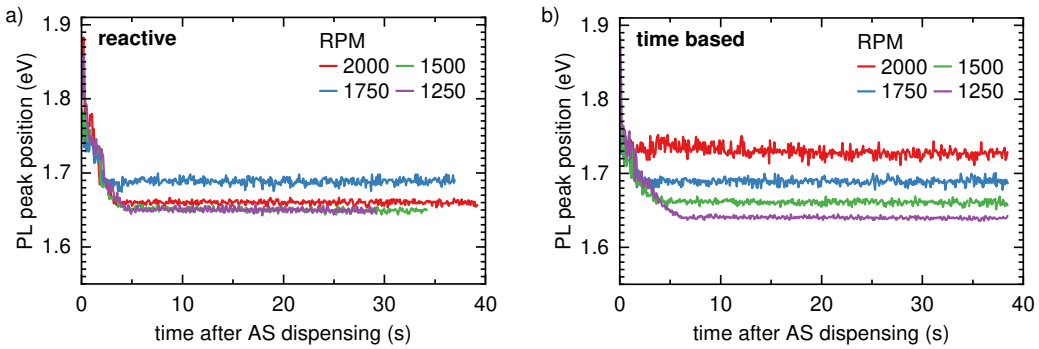

Figure S9: Time evolution of the energetic position of the maximum of the PL peak for $(MA_{0.13}FA_{0.83})Pb(I_{0.83}Br_{0.17})_3$ films processed via reactive (a) and time-based (b) spin coating for different RPMs.

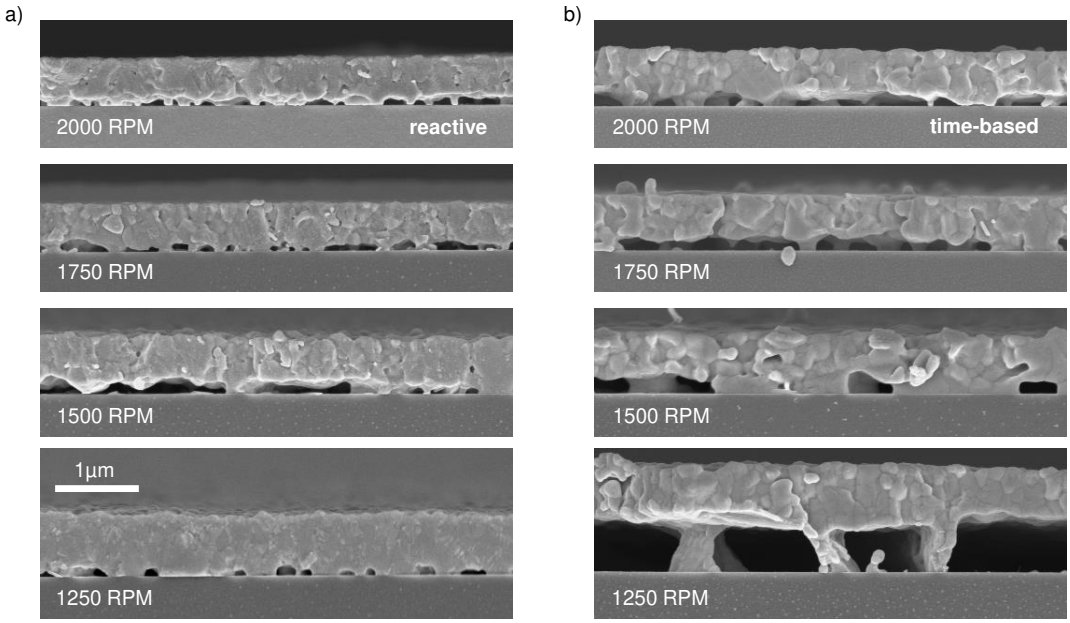

Figure S10: a) SEM cross-section images of the $(MA_{0.13}FA_{0.83})Pb(I_{0.83}Br_{0.17})_3$ films fabricated via reactive spin coating approach at different spin speeds. b) SEM cross-section images of the $(MA_{0.13}FA_{0.83})Pb(I_{0.83}Br_{0.17})_3$ films fabricated via time-based spin coating approach at different spin speeds.

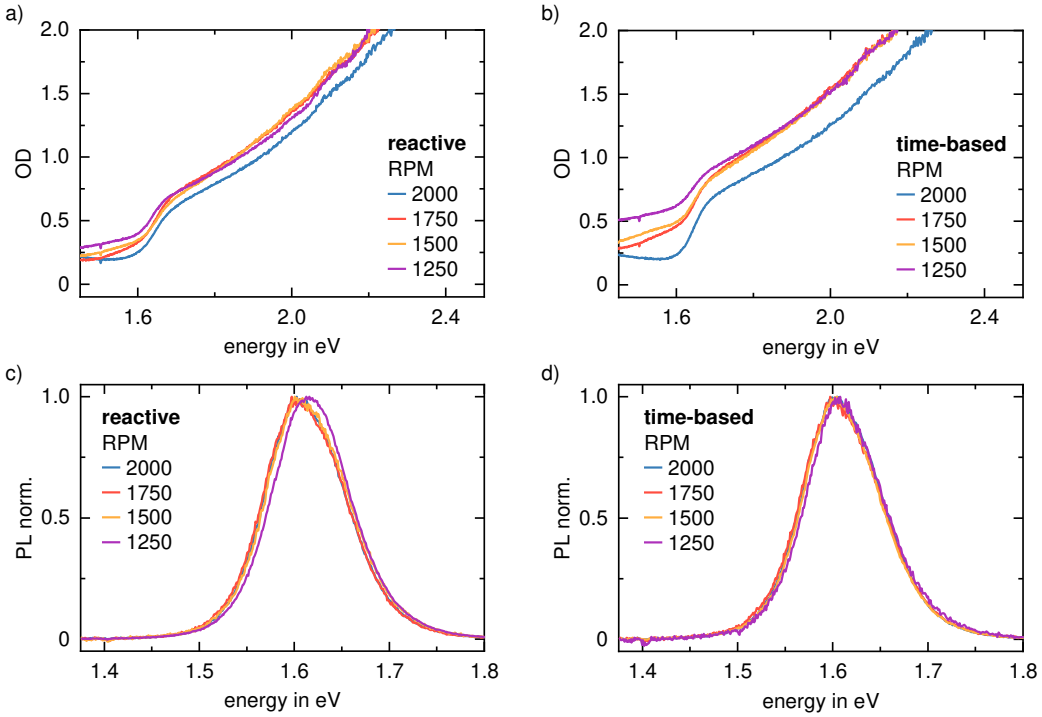

Figure S11: a) PL of $(MA_{0.13}FA_{0.83})Pb(I_{0.83}Br_{0.17})_3$ films processed via reactive spin coating method (left) or via time-based spin coating (right) after annealing. The data is normalized to the maximum. b) OD spectra of MAFA films processed via reactive spin coating method (left) or via time-based spin coating (right) after annealing.

Supporting References:

1) M. Buchhorn, S. Wedler and F. Panzer, *J. Phys. Chem. A*, 2018, **122**, 9115–9122.
2) S. Karpitschka, C. M. Weber and H. Riegler, *Chem. Eng. Sci.*, 2015, **129**, 243–248.
3) M. Chauhan, Y. Zhong, K. Schötz, B. Tripathi, A. Köhler, S. Huettner and F. Panzer, *J. Mater. Chem. A*, 2020, **8**, 5086–5094.
4) S. D. Stranks, P. K. Nayak, W. Zhang, T. Stergiopoulos and H. J. Snaith, *Angew. Chem. Int. Ed.*, 2015, **54**, 3240–3248.
5) T. Meier, T. P. Gujar, A. Schönleber, S. Olthof, K. Meerholz, S. van Smaalen, F. Panzer, M. Thelakkat and A. Köhler, *J. Mater. Chem. C*, 2018, **6**, 7512–7519.
6) Y. Kayanuma, *Phys. Rev. B*, 1988, **38**, 9797–9805.
7) K. P. Goetz, A. D. Taylor, F. Paulus and Y. Vaynzof, *Adv. Funct. Mater.*, 2020, **30**, 1910004.
8) A. Buin, R. Comin, A. H. Ip and E. H. Sargent, *J. Phys. Chem. C*, 2015, **119**, 13965–13971.
9) C. Greve, P. Ramming, M. Griesbach, N. Leupold, R. Moos, A. Köhler, E. M. Herzig, F. Panzer and H. Grüninger, *ACS Energy Lett.*, 2023, **8**, 5041–5049.

11 First of Their Kind: Solar Cells with a Dry-Processed Perovskite Absorber Layer via Powder Aerosol Deposition and Hot-Pressing

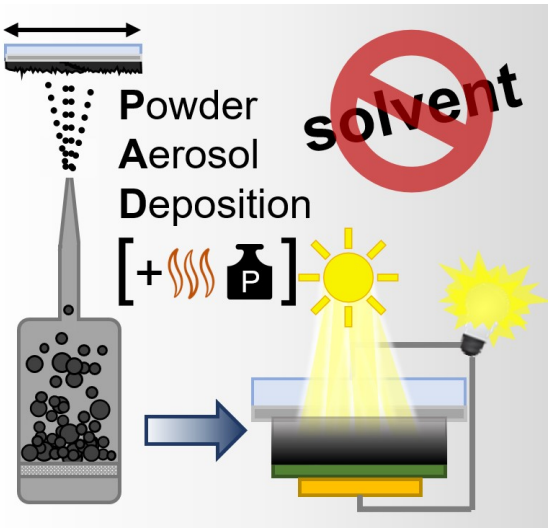

Simon Biberger*, Nico Leupold*, Christina Witt*, Christopher Greve, Paul Markus, Philipp Ramming, Daniel Lukas, Konstantin Schötz, Frank-Julian Kahle, Chenhui Zhu, Georg Papastavrou, Anna Köhler, Eva M Herzig, Ralf Moos, Fabian Panzer
*contributed equally

Published in
Solar RRL, **2023**, 2300261

RESEARCH ARTICLE

Solar RRL

www.solar-rrl.com

First of Their Kind: Solar Cells with a Dry-Processed Perovskite Absorber Layer via Powder Aerosol Deposition and Hot-Pressing

*Simon Biberger, Nico Leupold, Christina Witt, Christopher Greve, Paul Markus, Philipp Ramming, Daniel Lukas, Konstantin Schötz, Frank-Julian Kahle, Chenhui Zhu, Georg Papastavrou, Anna Köhler, Eva M. Herzig, Ralf Moos, and Fabian Panzer**

Preparing halide perovskite films by solvent-free, powder-based processing approaches currently attracts more and more attention. However, working solar cells employing dry, powder-based halide perovskite thin films, have not been demonstrated so far. Herein, perovskite solar cells are presented where the absorber layer is prepared by transferring readily synthesized perovskite powders into a compact thin film using a fully dry-powder-processing concept. Compact thin films are deposited via an optimized powder aerosol deposition (PAD) process. Pressing at 120 °C further improves the morphology and the optoelectronic film properties. Integrating the perovskite films in a solar cell configuration results in fully working devices, with champion power conversion efficiencies of >6%. While the (optoelectronic) properties of the PAD-processed films are found to be comparable with their solution-processed counterparts, investigations of the solar cell stack suggest deterioration of the electron-transport layer properties due to the PAD process, and the presence of hydrates at the perovskite surface to be important factors that contribute to the limited solar cell efficiency. Herein, perspectives to overcome the identified limitations are outlined, emphasizing the high potential and realizability of efficient perovskite solar cells based on dry-powder-processing approaches in the future.

1. Introduction

Within the last decade, the rise of metal-halide perovskites (MHP) as light absorber in solar cells has been remarkable. Power conversion efficiencies (PCEs) of up to 25.7%[1,2] and increasing device stabilities of up to several thousand hours[3,4] currently push perovskite solar cells on the verge to commercialization.

For high PCEs however, high-quality MHP films are required. Most of such high-quality perovskite films are currently prepared either by solution-based processing or evaporation methods.[2,4–6] Despite their widespread application in perovskite film fabrication, these approaches are still facing limitations.

One inherent limitation of solution-based and evaporation methods is the intrinsic coupling between perovskite synthesis and film formation, rendering the morphology and final optoelectronic functionality of perovskite films to be extremely sensitive to the precise processing conditions.[7–10] Moreover, a second drawback of solution-based processing is the need for toxic solvents such as dimethylfluorene (DMF)[11,12] to prepare the precursor

S. Biberger, C. Witt, P. Ramming, K. Schötz, F.-J. Kahle, A. Köhler, F. Panzer
Soft Matter Optoelectronics (EP II)
University of Bayreuth
95440 Bayreuth, Germany
E-mail: fabian.panzer@uni-bayreuth.de

The ORCID identification number(s) for the author(s) of this article can be found under https://doi.org/10.1002/solr.202300261.

DOI: 10.1002/solr.202300261

N. Leupold, D. Lukas, R. Moos
Department of Functional Materials
University of Bayreuth
95440 Bayreuth, Germany

C. Greve, E. M. Herzig
Dynamics and Structure Formation - Herzig Group
University of Bayreuth
95440 Bayreuth, Germany

P. Markus, G. Papastavrou
Physical Chemistry II
University of Bayreuth
95440 Bayreuth, Germany

C. Zhu
Advanced Light Source
Lawrence Berkeley National Lab
Berkeley, CA 94720, USA

ADVANCED SCIENCE NEWS
www.advancedsciencenews.com

Solar RRL
www.solar-rrl.com

stock solutions. Replacing these toxic solvents was already subject of several studies with the aim to find greener alternatives for perovskite stock solutions.[13–16]

An attractive film-processing approach, which does not rely on solvents and that decouples the perovskite synthesis and film formation, is the dry processing of already synthesized MHP powders via powder aerosol deposition (PAD).[17–19] Here, an aerosol is generated from powder and accelerated onto a substrate, where the powder particles break up and form a dense film. PAD is well established for a variety of different ceramic materials, like technical ceramics,[20–23] and ceramics for sensing and energy applications.[24] First commercial applications of PAD are already tested.[25]

Using a basic PAD setup, we showed in a previous work that thin films of MHPs such as the model perovskite methylammonium lead iodide ($MAPbI_3$) can be produced via PAD.[26] Yet, clear improvements in film morphology (compactness, surface roughness) were still required to realize film properties suitable for applications in optoelectronic thin film devices, such as perovskite solar cells.

In the past, it was demonstrated that the compactness and surface roughness of MHP can be improved by pressure treatment.[27–30] In addition, it became clear that performing the pressure treatment under elevated temperature not only further improved the surface roughness and the compactness, but even led to enlarged grain sizes, which is known to be beneficial regarding the MHP's optoelectronic functionality.[31–34]

Here, we present sophisticated technical developments in the PAD process that enable the deposition of thin (≈1 µm), yet dense $MAPbI_3$ films. In addition, we successfully employ pressure treatment of the optimized PAD films to further improve morphology and optoelectronic properties.

With these improvements, we demonstrate the first realization of pressed and unpressed PAD-processed $MAPbI_3$ thin films in a solar cell configuration, resulting in fully working devices with PCEs of >6%. We highlight in detail the challenges that remain and discuss approaches to tackle the current limitations to manufacture highly efficient solar cells in the future based on the here presented novel perovskite-processing method.

2. Process Development toward Dry-Processed Perovskite Absorber Layers Suitable for the Use in PSCs

2.1. PSC Fabrication Concept

The fabrication process of our perovskite solar cells with a completely dry, powder-based perovskite-processing approach is presented in **Figure 1**. First, we synthesize $MAPbI_3$ powder mechanochemically via ball milling (details in previous work[35,36]), and use this powder in a dry PAD process.

A PAD system consists of three main components: 1) a vacuum pump for generating a rough vacuum with an absolute pressure in the range of 1 mbar, 2) a deposition chamber in which the substrate is mounted on a movable substrate holder, and 3) an aerosol generating unit (Figure S1, Supporting Information). In the latter, a powder aerosol is generated from the dry mechanochemically synthesized powder by passing a carrier gas such as N_2, O_2, or He, for example, through a powder bed located on a porous tray in a glass flask.

The powder aerosol is transported from the aerosol generating unit to the evacuated deposition chamber due to the pressure difference between both components. In the deposition chamber, the powder aerosol is further accelerated through a nozzle to velocities between 100 and 600 $m\,s^{-1}$ and directed onto a glass substrate coated with indium tin oxide (ITO) as transparent electrode and SnO_2 as electron-transport layer (ETL).

Upon impact on the substrate, the powder particles in the aerosol deform, break up, and adhere to the substrate. Subsequently impacting particles increase the film thickness, further fragment previously deposited particles and densify the film. This mechanism is called room-temperature impact consolidation (RTIC).[37] The $MAPbI_3$ films, deposited via the PAD approach (further referred to as pristine films), are dense, fully covering the substrate (Figure S11, Supporting Information). To reduce the surface roughness and further improve the film quality of the pristine $MAPbI_3$ PAD films, we applied hot-pressing as an optional posttreatment step before spin-coating 2,2′,7,7′-Tetrakis[*N*,*N*-di(4-methoxyphenyl)amino]-9,9′-spirobifluorene (spiro-MeOTAD) as hole-transport layer (HTL) onto the $MAPbI_3$ film and thermally evaporating gold as top electrode to complete the solar cells.

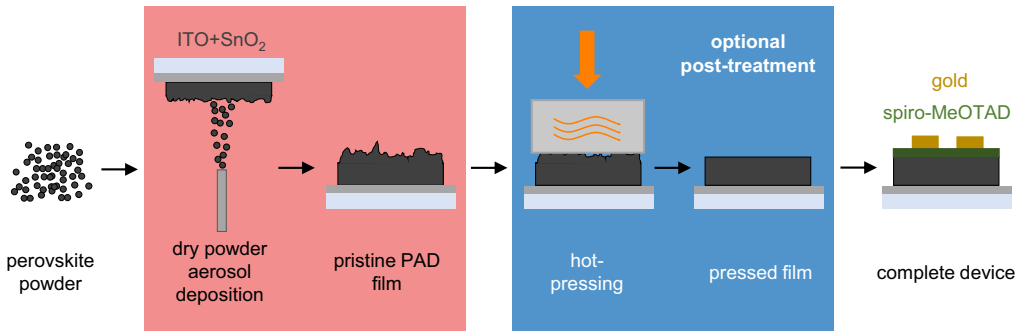

Figure 1. Fabrication concept for a solar cell with a perovskite absorber layer processed via the powder aerosol deposition (PAD) method and optional subsequent hot-pressing.

ADVANCED SCIENCE NEWS
www.advancedsciencenews.com

Solar RRL
www.solar-rrl.com

In the following, we first describe the key improvements in the PAD process that allow for successful fabrication of compact perovskite films with thicknesses in the range of ≈1 µm (Section 2.2.). Then, we outline relevant aspects in the hot-pressing step of the PAD perovskite films (Section 2.3) and discuss the properties of the fully dry-processed powder-based perovskite solar cells in Section 3.

2.2. Key Improvements in the PAD Process

In general, the powder particle size and the presence of agglomerates consisting of those powder particles are decisive for the film formation during PAD. Desired particle sizes are typically in the range between 200 nm to 5 µm.[38] Due to their low mass, smaller particles exhibit low kinetic energy and inertia so that they either do not reach the substrate or bounce off the substrate upon impact. In contrast, too high kinetic energy of larger particles can result in abrasion of the substrate, similar to sandblasting.[38]

The presence of large agglomerates in the PAD process is also detrimental to the film properties, as a large fraction of their kinetic energy is used to break up the initially large agglomerates into smaller agglomerates and individual powder particles when impacting the substrate. Thus, less energy is available for deforming and fracturing the individual particles as necessary for densification of the film via RTIC.[38] As a result, porous films with voids (pinholes through the whole film thickness) and bad contact to the substrate (Figure S2, Supporting Information) are deposited. Thus, the aerosol generation, that is, especially the reduction of the number of agglomerates within the powder aerosol, is a key to allow for PAD-deposited $MAPbI_3$ thin films suitable for solar cells.

Our mechanochemically synthesized powder used for PAD is phase pure und consists of 30–50 µm large agglomerates of powder particles in the 1 µm range (Figure S3 and S4, Supporting Information). While the powder particle size is well suitable for PAD, size and number of agglomerates impacting on the substrate have to be reduced to obtain high-quality PAD films. To fragment the agglomerates before they reach the substrate, we implemented an ejector unit after the aerosol flask. The ejector consists of 1) a horizontal tube, whose cross section narrows at a throat and expands afterward and 2) a second tube, that enters the first tube perpendicular in the expansion zone (**Figure 2**a).

The ejector unit serves two beneficial purposes. First, strong shear forces are present when $\dot{V}_{acc}$(gas flow for acceleration of aerosol) and $\dot{V}_{flask}$ (gas flow of carrier gas for aerosol generation in the flask) are merging perpendicular to each other after the throat in the ejector unit. In addition, agglomerates accelerate upon entering the gas flow $\dot{V}_{total}$ (Figure 2a). Both effects contribute to break up agglomerates within the aerosol.[39] The second advantage of the ejector is the possibility to independently control $\dot{V}_{flask}$ and $\dot{V}_{acc}$. This allows to apply a low $\dot{V}_{flask}$, and thus to reduce the overall $MAPbI_3$ aerosol concentration significantly. Consequently, while more passes, that is, a higher number of movements of the substrate over the nozzle, are necessary to realize a certain film thickness, fluctuations in the aerosol concentration are much better compensated, compared to a PAD setup without ejector unit. This eventually allows for producing PAD films with more homogeneous film coverage. In passing, we note that replacing the ejector with a simple tee to reduce the complexity of the setup does not result in satisfying film quality (Figure S5, Supporting Information).

Figure 2b, top panel, shows a scanning electron microscope (SEM) image of a $MAPbI_3$ PAD film deposited using the ejector. The film is compact with only small pores and has an overall good contact to the bottom layer. Yet, even with the ejector, the $MAPbI_3$ PAD films still exhibit voids (Figure 2b top). In addition, the film area deposited from the middle of the 10 mm slit nozzle is thicker compared to the area from the edges of the nozzle. This inhomogeneity in film thickness indicates that agglomerates are still present in the aerosol, most likely in the center of the aerosol jet hitting the substrate. An explanation of this observation is that agglomerates do not follow the gas flow due to their large inertia when the circular cross section of the tube leading the gas flow to the nozzle changes from a diameter of 4 mm to a slit orifice of 10 mm × 0.5 mm of the nozzle.

To finally remove these persisting agglomerates from the aerosol, we employed an inertial separator unit, consisting of a tee and a tube between the ejector and slit nozzle (Figure 2a). In the inertial separator, the aerosol jet coming from the ejector is deflected by 90° and directed to the slit nozzle. Consequently,

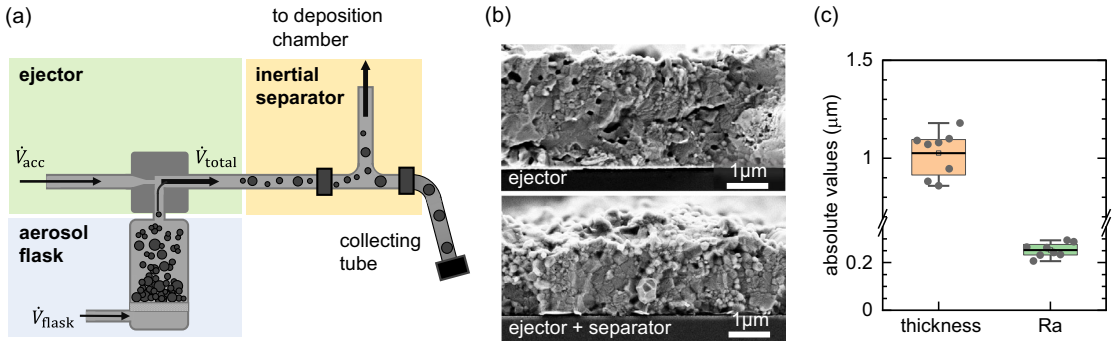

Figure 2. a) Concept of the improved aerosol generation employing an ejector unit and inertial separator. b) Scanning electron microscope (SEM) cross-section images of PAD films deposited with ejector (top) and with ejector and inertial separator (bottom). c) Resulting thickness and surface roughness Ra of the optimized pristine PAD films deposited with ejector and inertial separator.

ADVANCED SCIENCE NEWS
www.advancedsciencenews.com

Solar RRL
www.solar-rrl.com

only smaller agglomerates and particles in the aerosol jet can follow the gas flow to the nozzle, while larger agglomerates end up in the collecting tube due to their larger inertia.

In passing, we mention that in addition to these technical improvements addressing the agglomerates issue, we also integrated a smaller flask with a diameter of 3 cm in the aerosol generation unit allowing to use low powder quantities (<1 g) to further reduce the aerosol concentration and increase the general process control.

By these setup improvements, we obtain dense and void-free $MAPbI_3$ films (Figure 2b bottom) with mean thickness of (1.0 ± 0.1) µm and reasonable arithmetic mean roughness Ra of (0.25 ± 0.03) µm (Figure 2c, for details about chosen PAD process parameters, see Section S1, Supporting Information). Thus, the modified aerosol generation with ejector and inertial separator allows to deposit 1 µm thick $MAPbI_3$ films from highly agglomerated powders with, considering the field of PAD, high reproducibility.

2.3. Posttreatment via Hot-Pressing

Pressing at elevated temperature has emerged as powerful technique to improve $MAPbI_3$ film properties, that is, film morphology, optoelectronic properties, as well as related solar cell efficiencies.[31–34,40–42] In particular, a higher pressure–temperature combination is known to result in stronger improvements of $MAPbI_3$ film morphology and optoelectronic properties.[27,28,31–33,40,41,43] To further improve the perovskite film quality of the pristine PAD films, we therefore applied an additional hot-pressing posttreatment step.

First, we explored the possibility to employ press die materials commonly used for pressing MHP films. While silicon wafers and PTFE sheets were often used in the past,[31,33,34,40–45] their form stability is limited to pressures below 15 MPa in single action pressing.[31,34,40,41,44] To achieve clear improvements upon pressure treatment of our PAD films, we aimed for a pressure of 25 MPa, rendering silicon wafers and PTFE sheets unsuited for our approach. Polyimide foil exhibits high form stability under mechanical and thermal stress,[46] and was already used as press die material for the fabrication of MHP films with promising optoelectronic properties in the past.[47,48] We examined polyimide foil as press die material in our press setup but observed that after pressing the polyimide foil exhibited significant wear and the PAD film tended to stick to the polyimide foil (for detailed discussion, see Figure S6, Supporting Information).

Due to these issues, we explored the possibility to use glass blocks (thickness: 8 mm, roughness: 2 nm) as press die material, covered with a silanization coating (trichloro(octadecyl)silane in toluene from liquid phase) to prevent the glass blocks from sticking to the perovskite film. Using the silanized glass blocks, our PAD films can be pressed reliably and without breakage of glass substrates and glass blocks employing up to 25 MPa at 120 °C for 5 min. For our experiments, we thus choose this set of process parameters, as it is known that increased temperature and pressure are beneficial for improving the morphology and optoelectronic properties when pressing halide perovskite films[27,28,31–33,40,41,43] (also see Figure S7, Supporting Information, and previous work[28] for details on press setup and protocol).

Applying this pressing procedure to the pristine PAD films, which appear matt black before pressing, we obtain shiny gray films after the pressing step (**Figure 3**b left). This change in optical appearance already indicates a reduction in surface roughness, which is further evidenced from the comparison of top-view SEM images of a pressed film and a pristine film (Figure 3b right). We quantified the mean Ra value of the pressed films to be 18 nm, compared to 250 nm of the pristine films, confirming a reduction in surface roughness by >92% upon pressing (Figure 3c). Additionally, pressing the PAD films with 25 MPa at 120 °C reduced the film thickness by about 37% (Figure 3c), indicating an increased compaction of the pressed $MAPbI_3$ films. More details on the changes of morphology and optoelectronic properties of pristine and pressed $MAPbI_3$ films are discussed in Section 4.2.

In summary, by employing the previously described key developments in the PAD process, in combination with an optional hot-pressing step of the pristine PAD perovskite films, we demonstrated the successful production of phase pure and dense polycrystalline $MAPbI_3$ thin films that meet the film requirements for the use in functional perovskite solar cells.

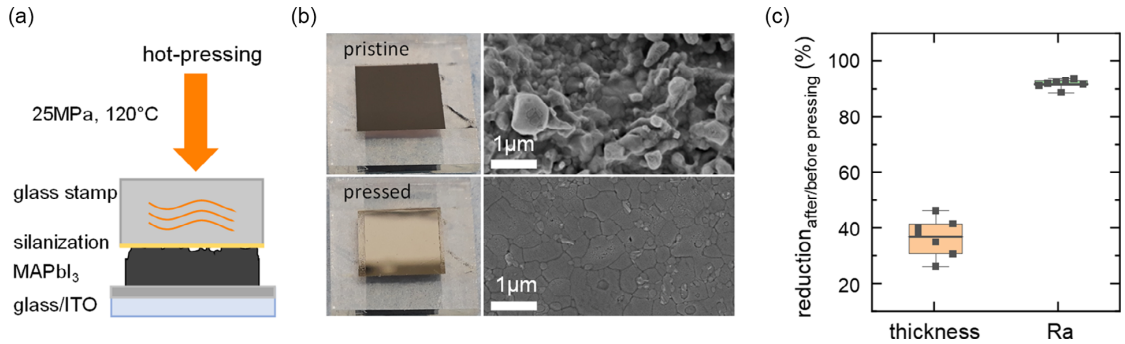

Figure 3. a) Sketch of hot-pressing a PAD film. b) Photographs (left) and top-view SEM images (right) of pristine (top) and pressed (bottom) $MAPbI_3$ PAD films. c) Reduction of thickness and surface roughness (Ra) of PAD films due to pressing (see Figure S8, Supporting Information, for absolute values).

ADVANCED SCIENCE NEWS
www.advancedsciencenews.com

Solar RRL
www.solar-rrl.com

3. Solar Cells

Based on the described process improvements and following the concept in Figure 1, we manufactured two types of complete solar cell stacks. One type uses a pristine PAD film as the absorber layer (hereafter referred to as "pristine" devices), while for the other type, we posttreated the PAD absorber layer via hot-pressing (referred to as "pressed" devices).

Figure 4a shows cross-section SEM images of the resulting n–i–p solar cell stacks with pristine (left) and pressed (right) $MAPbI_3$ film. To allow for a systematic comparison of the morphology before and after pressing, we choose devices with similar thickness. From Figure 4a, the glass substrate covered with ITO electrode (grey), the SnO_2 ETL (purple), the perovskite film (brown), the spiro-MeOTAD HTL (green), and the gold top electrode can be distinguished.

Exemplary current density–voltage (J–V) curves for each solar cell type are plotted in Figure 4b. Both, the pristine and the pressed devices exhibit a diode-like dark current characteristic (rectangles). Under AM1.5G illumination, the J–V curves measured in reverse direction (colored circles) exhibit photovoltaic behavior for both the pristine and the pressed devices. Considering the J–V curves measured in forward direction (grey circles), both types of devices show a pronounced hysteresis.

The solar cell metrics determined from the reverse measurement direction for 12 devices each are shown in Figure 3c for the pristine (red) and pressed (blue) absorber layer. These metrics were measured after storing the devices in dry ambient conditions in the lab for 9 weeks, where the metrics were stable and even slightly improved compared to the metrics measured 24 h after the fabrication (see Figure S9, Table S1 and S2, Supporting Information, for comparison between metrics determined 24 h and 9 weeks after fabrication including forward direction, for the operational stability, see Figure S10, Supporting Information). The mean open-circuit voltage (V_{OC}) for the pristine absorber layer is (0.90 ± 0.11) V, while the pressed devices exhibit an increased mean V_{OC} of (0.95 ± 0.04) V. The mean short-circuit current density (J_{sc}) also increases upon pressing from (7.2 ± 3.1) mA cm^{-2} for the pristine devices to (7.6 ± 2.7) mA cm^{-2} for the pressed devices. Similarly, the fill factor (FF) yields mean values of (52 ± 9)% and (56 ± 6)% for the pristine and pressed absorber layers, respectively. Overall, the resulting average PCE for the pristine absorber layer of (3.5 ± 1.8)% improves to a PCE of (4.1 ± 1.8)% for the pressed absorber layer, where the champion devices of

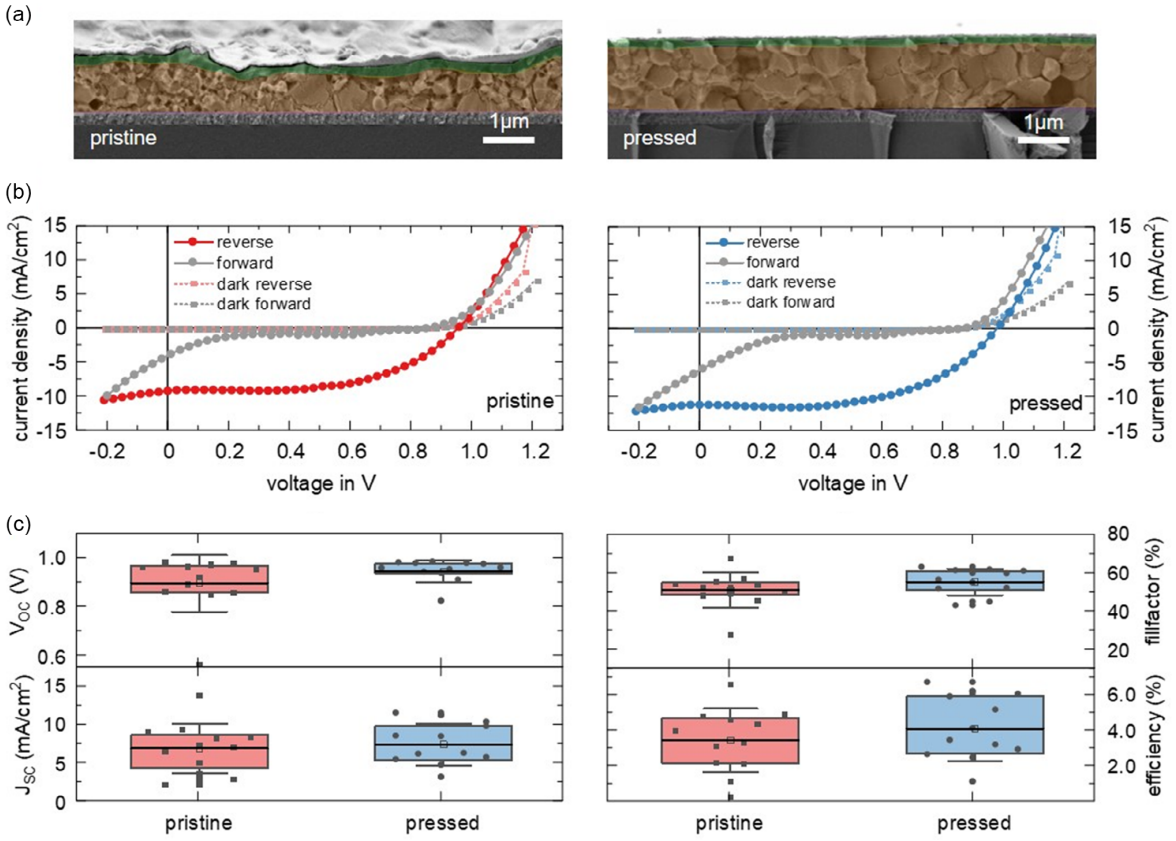

Figure 4. a) SEM cross-section images and b) current density–voltage (J–V) curves of a $MAPbI_3$ solar cell with a pristine (left) and with a pressed (right) PAD-processed absorber layer. c) Batch statistics (reverse direction) of solar cells fabricated with a pristine (red) and with a pressed (blue) absorber layer.

ADVANCED SCIENCE NEWS
www.advancedsciencenews.com

Solar RRL
www.solar-rrl.com

Table 1. Summary of solar cell metrics (mean values; individual champion values in brackets) for $MAPbI_3$ solar cells with pristine and with pressed PAD-processed absorber layer as extracted from reverse direction.

Type	V_{oc} [V]	J_{sc} [mA cm^{-2}]	FF [%]	PCE [%]
Pristine	0.90 ± 0.11 (0.96)	7.2 ± 3.1 (13.9)	52 ± 9 (49.5)	3.5 ± 1.8 (6.6)
Pressed	0.95 ± 0.04 (0.98)	7.6 ± 2.7 (11.2)	56 ± 6 (56.5)	4.1 ± 1.8 (6.2)

both types show an efficiency of >6% (see **Table 1** for a summary of the device metrics extracted from the reverse direction). Evidently, the additional pressing as posttreatment step results in a clearly increased number of devices with an efficiency of more than 6%.

Comparing these results with $MAPbI_3$ n–i–p solar cells that are solution-processed under ambient conditions with typical PCE values in the range of ≈15%,[49–53] it becomes clear that the V_{OC} values are in good agreement with literature values (0.85–1.10 V). While the FF values are at the lower end of the reported range (55%–75%), the obtained J_{sc} values are clearly below the literature values of around 21 mA cm^{-2}. Thus, the low J_{sc} values of our PAD-processed perovskite solar cells are the main limiting factor for the clearly lower PCE compared to corresponding solution-processed PSCs.

To better understand the origins of the losses and limitations in our PSCs with dry-processed $MAPbI_3$ film, in the following, we systematically investigate the device stack layer by layer, also deriving perspectives for strategies to optimize the PCE.

4. Detailed Evaluation of the Solar Cell Stack

4.1. SnO_2 Layer

First, we investigate the SnO_2 layer, acting as the ETL. To ensure proper electrical contact between the ETL and the $MAPbI_3$ film, sufficient physical contact and adhesion between both are mandatory. The physical contact is confirmed in the cross-section SEM image in **Figure 5**a. By scotch tape tests, we observe that the pristine $MAPbI_3$ film remains on the ETL after repeated applying and peeling off of a stripe of tape (Figure S11, Supporting Information), confirming good mechanical adhesion between ETL and perovskite film. On the peeled-off tape, only a marginal amount of $MAPbI_3$ powder is visible (Figure S11, Supporting Information), which stems from loose and uncompressed powder particles remaining on top of the film after PAD.

The ETL layer is subject to high mechanical and thermal stress during $MAPbI_3$ film deposition via PAD and pressing at elevated temperatures. During the deposition of the $MAPbI_3$ film via PAD, the accelerated perovskite powder particles impact on the ETL and potentially affect its electrical and optical properties. Similarly, the combination of pressure and temperature during hot-pressing may also alter the ETL properties.

To identify such potential changes in ETL properties, we carried out morphology characterizations and conductive atomic force microscopy (cAFM) for four different samples: 1) a native SnO_2 layer serving as reference, 2) a SnO_2 layer after removing a solution-processed $MAPbI_3$ film, 3) a SnO_2 layer after removing a pristine $MAPbI_3$ PAD film, and 4) a SnO_2 layer after removing a

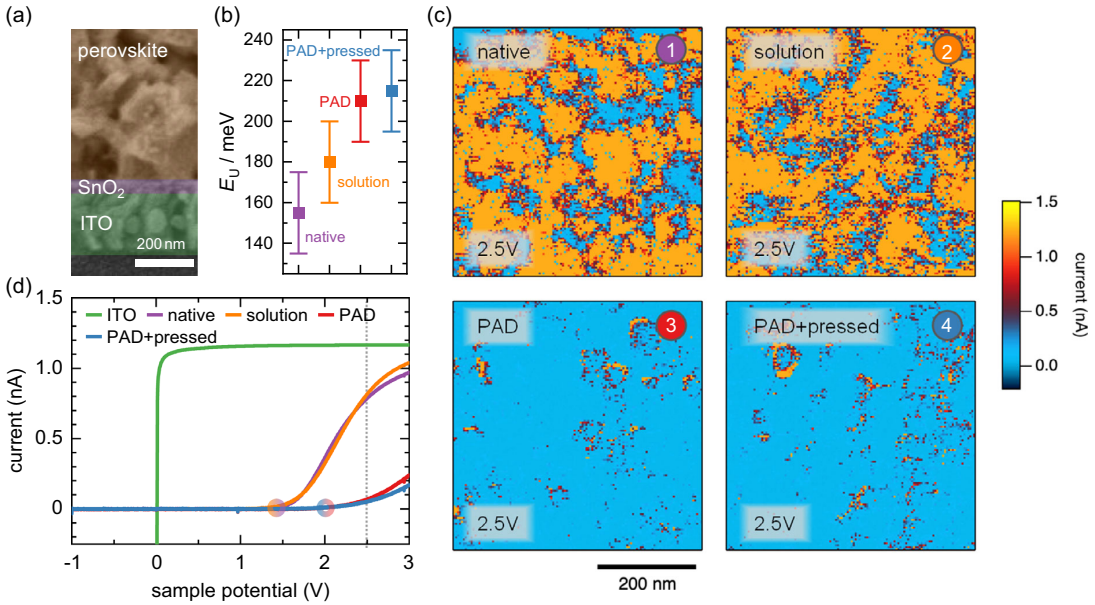

Figure 5. a) Cross-section SEM image of $MAPbI_3$ PAD film on indium tin oxide (ITO)/SnO_2. b) Urbach energy E_U of 1) a native SnO_2 layer serving as reference, 2) SnO_2 layer after removing a solution-processed $MAPbI_3$ film, 3) SnO_2 layer after removing a pristine $MAPbI_3$ PAD film, and 4) SnO_2 layer after removing a pressed $MAPbI_3$ PAD film. c) Conductive atomic force microscopy (cAFM) measurements at 2.5 V for the samples in (b). d) Current–voltage (I–V) characteristics for the samples in (c), averaged over the whole investigated area. For comparison, the I–V curve of an ITO layer is also shown.

ADVANCED SCIENCE NEWS
www.advancedsciencenews.com

Solar RRL
www.solar-rrl.com

pressed $MAPbI_3$ PAD film. The $MAPbI_3$ films were removed by dissolving them in dimethyl sulfoxide (DMSO).

First, we address possible changes in morphology and layer properties, where a reduction of the SnO_2 layer thickness or a fractioning of the grains within the layer might occur due to the PAD process. Here, height profiles of the four SnO_2 samples suggest that the SnO_2 layer thickness does not reduce due to the PAD process (see Figure S12, Supporting Information). Furthermore, no morphological changes between samples (1) and (4) are observed in atomic force microscopy (AFM) images (Figure S13, Supporting Information), suggesting that no lateral fractioning of the SnO_2 grains in the layer occurs.

In contrast to the morphology, the electrical properties of the ETL clearly change after the PAD deposition and pressing, as evident from cAFM measurements. At an applied potential of 2.5 V, the cAFM images (Figure 5c) show a decreased current for samples (3) and (4), compared to samples (1) and (2). This decreased current at 2.5 V is also reflected in corresponding *I–V* curves between −1 and 3 V (Figure 5d), where the current is averaged over the whole sampled areas in Figure 5c. Here, for samples (1) and (2), the onset potential is 1.4 V, compared to ≈2.0 V for samples (3) and (4), where also the steepness of the current rise appears lower compared to the corresponding steepness of samples (1) + (2). The latter observation suggests a lower electric conductivity in the ETLs that exhibited a prior PAD $MAPbI_3$ processing.

To better understand the origin of the decreased electrical conductivity of the PAD-treated SnO_2 layers, we conducted optical absorption measurements of all four SnO_2 samples in an integrating sphere, with a focus on investigating their Urbach absorption edge (Figure S14, Supporting Information). From the latter, we extract the so-called Urbach energy, a measure for the degree of energetic disorder within the investigated material.[54,55] Our analysis suggests that samples (3) + (4) exhibit E_U values in the range of ≈210 meV, compared to E_U values in the range of 160–180 meV for samples (1) + (2) (Figure 5b), indicating that indeed the PAD processing increases the energetic disorder and thus also the defect density of the SnO_2 ETL layer.

Here, increased disorder and defect density could result from the harsh impact of the $MAPbI_3$ powder particles and agglomerates on the SnO_2, where high mechanical stress might foster the formation of defects. Another aspect that could explain the increased disorder values for samples (3) + (4) is the incorporation of $MAPbI_3$ constituents into the SnO_2 layer. To investigate the latter aspect in more detail, we performed X-ray photoelectron spectroscopy (XPS) survey scans of all four samples, showing that lead species (signals at 138/143 and 414/436 eV) are present in samples (2)–(4) even after thorough removal of $MAPbI_3$ with DMSO (Figure S15, Supporting Information).[56,57] Here the Pb-concentration in samples (3) + (4) is ≈3–4 at%, twice as high as in sample (2). Interestingly, in all four samples we do not detect any iodine signals (619/631 eV).[56] This emphasizes that no iodoplumbate residuals are present on the SnO_2 layer, but rather metallic lead remains in the SnO_2 layer.

The incorporation of various materials such as Sb, Cr, or Nb_2O_5 into SnO_2 is known to lead to increased E_U (i.e., energetic disorder), and to a shift of the onset potential toward higher values,[58–60] fully in line with the findings from Figure 5. Thus, we conclude that the incorporation of Pb into the SnO_2 layers that exhibited a PAD-process contributes to the observed reduced conductivity and increased onset potential.

It is also clear that the increase in disorder is at first closely linked to the PAD process method. However, this issue could be addressed in the future, e.g., with the help of defect-chemical approaches, where, for example, Ru- or Sb-doped SnO_2 could be used to compensate for the presence of the Pb-induced defects.[61,62]

To counteract a possible mechanically induced increase in disorder, the use of SnO_2 layers with a more robust morphology and potentially higher mechanical hardness appears promising. For example, it was shown that SnO_2 layers prepared by an e-beam process show remarkably compact morphologies and that sputtered SnO_2 layers, in contrast to other preparation methods, show higher hardness values of up to 14 GPa.[63] Furthermore, it could be demonstrated that SnON coatings resulting from the incorporation of nitrogen into SnO_2 can exhibit hardness values of up to 23 GPa while maintaining excellent electrical properties.[64]

These examples underline that, by choosing a suitable preparation method and introducing additional constituents, it appears possible to produce mechanically more robust and defect-chemically optimized SnO_2 layers that still feature desired electrical properties even after the harsh mechanical treatment during perovskite powder deposition by PAD.

4.2. Dry-Processed $MAPbI_3$ Absorber Layer

Next, we investigate the film properties of our pristine and pressed $MAPbI_3$ thin films.

We first addressed whether our anti-sticking silanization coating (molecular formula: $C_{18}H_{37}Cl_3Si$) is transferred to our $MAPbI_3$ films upon pressing. **Figure 6**a shows an XPS spectrum of a pressed perovskite film, where only peaks corresponding to $MAPbI_3$ constituents and in particular no signatures of Si are visible.[56,65,66] Thus, we conclude that no significant amount of silane is transferred to the perovskite film during our pressing process.

Concerning the morphology of both types of $MAPbI_3$ films, deposited with our modified PAD setup, corresponding cross-section SEM images show that the pristine film is dense and void free, with a surface roughness in the range of $Ra \approx 200$ nm (Figure 4a left). The films exhibit a thickness of about 1 µm. While the perovskite film thickness of highly efficient solar cells often is below 1 µm, it was shown that a PCE of 20% can be achieved using $MAPbI_3$ films with thickness of about 1 µm, if the grain size is large thus the number of grain boundaries in vertical direction is low.[67] Cross-sectional SEM images of the pressed film demonstrate that hot-pressing increases the grain size, narrows grain boundaries, reduces surface roughness, and diminishes the number of pores (Figure 4a, right), indicating morphology improvements toward better PCE. These morphology improvements are fully consistent with the insights gained in Section 2.2 and 2.3., and can be associated to stem from a sintering effect occurring during hot-pressing.[27,68] From XPS measurements in a previous work, it is known that hot-pressing induces small amount of PbI_2 at the $MAPbI_3$ film surface.[28] However, in Figure S18, Supporting Information, the XRD

ADVANCED SCIENCE NEWS
www.advancedsciencenews.com

Solar RRL
www.solar-rrl.com

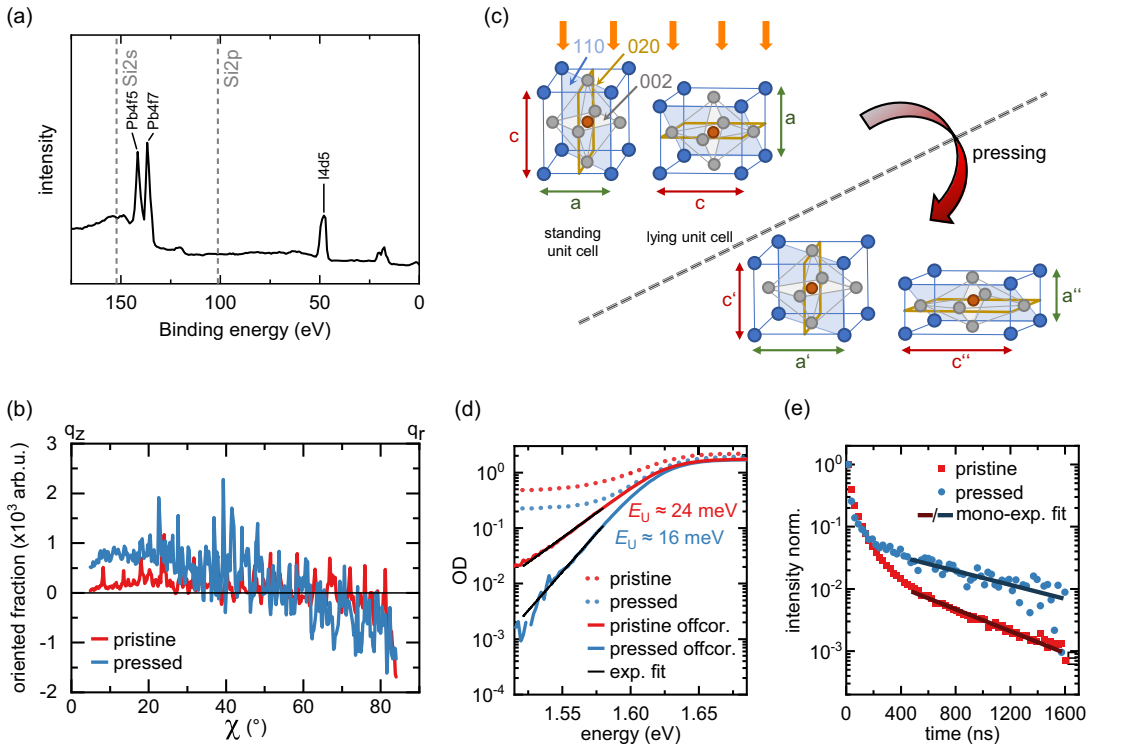

Figure 6. a) XPS spectrum of a $MAPbI_3$ PAD film after pressing. b) Oriented fraction of the (110) and (002) double peak as a function of χ for a pristine (red) and pressed (blue) $MAPbI_3$ film determined by grazing incidence wide-angle X-ray scattering (GIWAXS). c) Sketch of unit cell deformation due to hot-pressing as indicated by GIWAXS. d) Absorption spectra of a pristine and pressed $MAPbI_3$ film on glass as measured (dotted) and offset corrected (line). The Urbach energy E_U is extracted from an exponential fit for each sample. e) Time-resolved photoluminescence of a pristine and pressed $MAPbI_3$ film on glass, together with a mono-exponential fit.

spectra show only a negligible amount of PbI_2 for the pressed film, that is, all $MAPbI_3$ films are considered to be essentially phase pure.

To characterize the crystallographic orientation of the pristine and pressed $MAPbI_3$ films, we performed grazing incidence wide-angle X-ray scattering (GIWAXS). The corresponding 2D GIWAXS patterns of a pristine and a pressed $MAPbI_3$ film (Figure S16, Supporting Information) were examined using a χ analysis, that is, a reciprocal space analysis as a function of direction, on the (110) & (002) double peak (Figure 6b). Therefore, a semicircular cut over the full peak width of the (110) & (002) double peak was extracted (details in Figure S16, Supporting Information). Hereby, 90° corresponds to the direction along q_r (in-plane of the sample) and 0° corresponds to the direction along q_z (out-of-plane of the sample). The intensity distribution along the χ arc of the pristine film (red line in Figure 6b) shows a random (isotropic) orientation of the crystallites. In contrast, the intensity along χ deviates from the isotropic distribution for the pressed film (blue line in Figure 6b), indicating a preferred orientation particularly in q_z-direction (planes parallel to sample surface) due to hot-pressing.

A single pixel analysis within the χ arc (details in Figure S16 and S17, Supporting Information) indicates an overall increased number of large crystallites in the pressed film, consistent with XRD patterns measured in Bragg–Brentano geometry of pristine and pressed PAD-processed $MAPbI_3$ films (Figure S18, Supporting Information). Here, a smaller reflex width is found for a pressed film compared to a pristine film, again suggesting larger crystallite sizes in the pressed film. Moreover, the XRD patterns provide information about the crystallographic orientation in out-of-plane direction, where a random orientation is found in pristine films, changing to a (110) & (020)-preferred orientation upon pressing.

To further understand the impact of hot-pressing on the lattice parameters, we examine deformations of the unit cell by analyzing the GIWAXS data along different directions. The (110) and the (002) plane show the strongest changes as a function of direction. Depending on whether the interplanar distance d is examined parallel to the substrate (Figure S19 left, Supporting Information) or perpendicular to the substrate (Figure S19 right, Supporting Information), the separation increases or decreases upon hot-pressing. The shift of the (002) lattice spacing to smaller values along q_z in combination with the shift of the (110) spacing to larger values along q_r indicates the compression of the standing unit cell along the c-axis and its elongation along the a-axis (Figure 6c). Analogously, the change of the (002)

ADVANCED SCIENCE NEWS
www.advancedsciencenews.com

Solar RRL
www.solar-rrl.com

spacing to larger values along q_r, in combination with the shift of the (110) spacing to smaller values along q_z, indicates the compression of lying unit cells along the *a*-axis and their elongation along the *c*-axis (sketch in Figure 6c). Thus, the unit cells are flattened by pressing.

Overall, the analysis of the GIWAXS and XRD measurements suggest a compression of standing and lying $MAPbI_3$ unit cells, as well as an increase in (110)- and (020)-preferred orientation parallel to the substrate by hot-pressing. Such an increase in preferred orientation is known to correlate with improved excited-state properties.[28]

Thus, in the following, we analyze how the identified morphology differences between the pristine and pressed $MAPbI_3$ films are reflected in their optoelectronic properties. Figure 6d shows the optical absorption spectra of a pristine (red dotted line) and pressed (blue dotted line) $MAPbI_3$ film on glass with the typical absorption edge around 1.59 eV.[69,70] The absorption intensity for photon energies below the absorption edge is due to optical scattering, which we find to be strongly reduced for the pressed film compared to the pristine film. This indicates a more uniform morphology of the pressed film, in line with the previously identified higher compaction after hot-pressing. The Urbach energy, E_U, extracted from exponential fits to the offset corrected spectra, clearly reduces from (24.3 ± 0.2)meV for the pristine film to (15.5 ± 0.2)meV for the pressed film (see also Figure S20, Supporting Information), where the latter E_U value is in line with typical Urbach energies of solution-processed $MAPbI_3$ films.[55,71,72] The reduction of the Urbach energy upon pressing suggests less energetic disorder and a reduction in associated defect density in the pressed film.[73–75]

To examine differences in defect density between the PAD-processed films in more detail, we measured time-resolved photoluminescence (TRPL) decay curves after laser excitation (Figure 6e). Here, we considered pristine (red squares) and pressed (blue dots) $MAPbI_3$ films deposited on glass to exclude any impact of charge recombination processes at the perovskite/ETL interface. Compared to the pristine film, the pressed film shows a slower decrease of the TRPL intensity at times longer than 200 ns. By fitting the tail of the TRPL curves after 400 ns with a mono-exponential function (lines in Figure 6e), we extracted the defect-associated nonradiative decay rates k_1 according to

$$\mathrm{PL}(t) \propto A_1 \times \exp(-2 \times k_1 \times t) \quad (1)$$

By doing so, we find k_1 values of $(10.1 \pm 0.3) \times 10^5$ and $(6.5 \pm 0.6) \times 10^5\ s^{-1}$ for the pristine and the pressed film, respectively. Thus, our films exhibit k_1 values similar to typical values of solution-processed $MAPbI_3$ films.[76,77] The decrease in defect-associated decay rate upon pressing transfers to an increase in charge-carrier lifetime from (493 ± 15) ns for the pristine film to (768 ± 66) ns for the pressed film, indicating less defects being present in pressed films.

Overall, our characterizations of the pristine and pressed PAD-processed $MAPbI_3$ films prove that they exhibit suitable morphology and optoelectronic properties for solar cell application, in particular when the films are posttreated by pressing.

4.3. Perovskite-Transport Layer Interfaces

Having verified the satisfactory optoelectronic and morphological properties of the PAD-processed $MAPbI_3$ films, we finally evaluate the interface between the perovskite film and both charge-transport layers (ETL and HTL).

By light-intensity-dependent *J–V* measurements and corresponding analysis of the solar cell metrics, Glowienka et al. in detail investigated the electrical functionality of the perovskite/ETL and perovskite/HTL interfaces. Together with drift-diffusion modeling, they succeeded in pinpointing the dominating performance limiting effects in their perovskite solar cells.[78]

Following this approach, we measured the *J–V* curves for the pristine (red triangles) and pressed (blue dots) PAD-processed $MAPbI_3$ solar cells. We then compared the light dependency of the measured solar cell metrics with the expectations from Glowienka et al. for an ideal (i.e., without any recombination processes) and a more realistic (i.e., including perovskite bulk and interface recombination) perovskite solar cell. **Figure 7**a shows the experimentally determined light-intensity-dependent FF and V_{oc} of our devices, while in Figure 7b, the corresponding expectations from Glowienka et al. are shown.

For our devices with pristine and pressed absorber layer, the FF increases in the light intensity range from 10^{-3} to 10^{-1} sun. In contrast to the devices with pressed $MAPbI_3$ film where the FF monotonously increases, the FF of the devices with pristine $MAPbI_3$ film decreases again for light intensities above 10^{-1} sun. Overall, the pristine devices exhibit lower FF values over the whole measurement range. For an ideal device, the FF is expected to be independent of the light intensity, while including interface recombination, the FF is expected to exhibit a maximum. Furthermore, the presence of perovskite bulk recombination lowers the FF.[78] Comparing our experimental results with the theoretical expectations, it thus becomes clear that the light dependence of the FF in our case fits best to the theoretical expectations including interface recombination. Therefore, we conclude that in our PAD-processed solar cells interface recombination processes are present, limiting the overall device efficiency. Furthermore, the decrease of the FF for pristine devices above 10^{-1} sun indicates an increased interface recombination compared to pressed devices.[78] Furthermore, the overall lower FF values of the pristine devices compared to the pressed devices suggest more nonradiative recombination in the perovskite bulk of the pristine absorber layers, consistent with the higher nonradiative recombination rate k_1 found in the transient PL measurements (Figure 6e).

The V_{oc} for ideal device is expected to show a linear dependence on the light intensity in a semilogarithmic plot and a deviation at high intensities when interface recombination is present. For our pristine devices, we observe this deviation from the linear dependence for light intensities above 10^{-1} sun, further supporting that more pronounced interface recombination is present in the pristine devices than in the pressed devices.

To identify if monomolecular (trap-assisted, nonradiative) or bimolecular (band to band, radiative) recombination predominantly takes place at the interfaces, we determined the ideality factor n and the inverse Langevin recombination factor α from

ADVANCED SCIENCE NEWS
www.advancedsciencenews.com

Solar RRL
www.solar-rrl.com

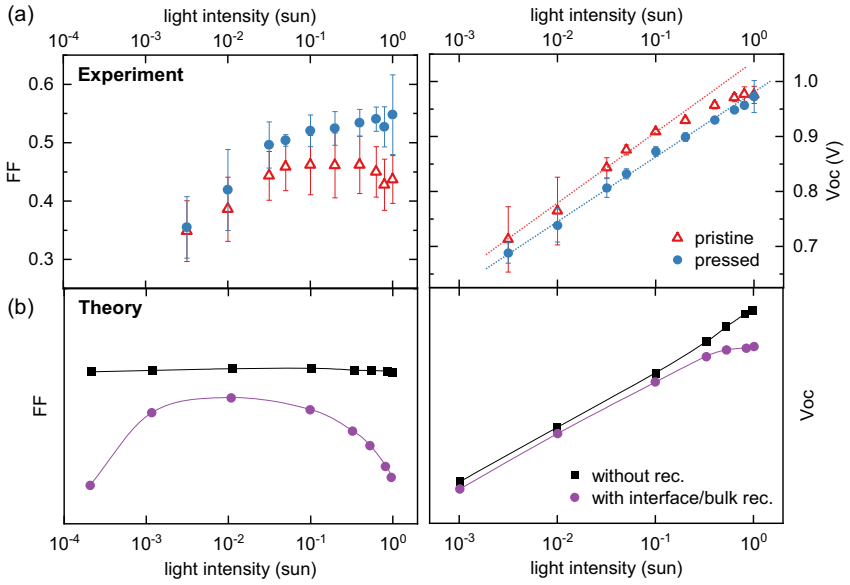

Figure 7. a) Measured light-intensity dependence of the fill factor (FF) (left) and the open-circuit voltage (V_{oc}) (right) for pristine (red triangles) and pressed (blue dots) $MAPbI_3$ absorber layers. b) Theoretical expectations for FF (left) and the V_{oc} (right) of ideal devices without any recombination (black squares) and of devices with recombination (purple circles), after Glowienka et al.[78] The lines in (a,b) serve as guide for the eye.

the V_{oc} versus J_{sc} plot and the J_{sc} versus light intensity plot, respectively (Figure S21, Supporting Information). In general, the ideality factor n ranges between values of 1 and 2, where a value of 1 is expected for ideal solar cells in which only bulk recombination occurs.[79] Deviations from 1 indicate energy misalignment and trap-assisted recombination at the interfaces.[80,81] We find values of $n \approx 2$ for all measured cells, which suggests trap-assisted monomolecular recombination as the dominant recombination mechanism at the interfaces in our case.

Theoretically expected values for α range from 0.5 to 1, with a value of 0.5 indicating pure bimolecular recombination and values close to 1 suggesting monomolecular recombination as the dominant recombination process. Thus, the extracted α values of $\approx$0.9 for our solar cells further support trap-assisted recombination being the dominant recombination mechanism at the interface.[82,83] This is consistent with the observed hysteresis in the J–V curves (Figure 4b) indicating an accumulation of ions at the interface, screening the internal electric field and promoting recombination there.[84]

Summing up the light-intensity-dependent investigations of the PAD-processed solar cells, we conclude that recombination losses at the interfaces between perovskite and charge-carrier extraction layers are present in our devices, likely contributing to their limited PCE. On the basis of our analyses, it is not possible to distinguish which interface (i.e., whether the perovskite/ETL or the perovskite/HTL interface) is predominantly responsible for the recombination losses. However, due to the alteration of the SnO_2 layer upon perovskite deposition via PAD discussed in Section 4.1, it is conceivable that the identified interface recombination losses mainly originate from the ETL/perovskite interface.

However, another aspect that might contribute to significant interface recombination and thus limit current values in our devices is the presence of hydrates at the transport layer/perovskite interface. The processing of the ETL and the perovskite, including pressing, was carried out under ambient conditions (relative humidity: 40%–50%), that is, within a humidity range, where the formation of monohydrates at the perovskite surface is known to happen.[85] And indeed the formation of hydrates on the perovskite film in our case can already be conjectured from the grey tarnishing perovskite surface after PAD processing (Figure 3b). It was shown that hydrates are mainly formed at the surface and the grain boundaries of the perovskite, where they act as defects within the perovskite film and the interface.[85,86] Thus, the presence of hydrates lead to additional pathways for charge recombination, reducing charge extraction from the perovskite to the transport layer. This is in line with the generally low current density of our PAD-processed devices.[87,88] Furthermore, the presence of hydrates also reduces the barrier for ion migration,[89] facilitating hysteresis in J–V curves of corresponding PSCs,[90] which is also fully consistent with our results in Section 3. Thus, we presume that the presence of hydrates also contributes considerably to the limited performance and pronounced hysteresis of the PAD-processed solar cells.

5. Conclusion and Perspective

We have successfully manufactured the first solar cells containing a completely dry-processed powder-based $MAPbI_3$ absorber layer. These absorber layers were deposited via PAD, where necessary key modifications such as the use of an ejector and an

ADVANCED SCIENCE NEWS
www.advancedsciencenews.com

Solar RRL
www.solar-rrl.com

inertial separator unit were introduced into our setup, resulting in dense and void-free $MAPbI_3$ films with thicknesses of ≈1 μm.

The solar cells are fully working with champion device efficiencies >6% in backward direction. Here, the V_{oc} (0.95 V) values, and to some extent also the FF values (56%) match literature values of cells processed from solution under ambient conditions. However, in addition to a pronounced hysteresis between the *J–V* sweep directions, especially the low J_{sc} values (7.6 mA cm^{-2}) limit the overall efficiency of our powder-processed devices.

We systematically analyzed our solar cell stacks and found that the pristine $MAPbI_3$ films show well-suited morphology and optoelectronic properties for solar cell application. The film properties further improve by posttreatment via (hot-)pressing, leading to increased grain size, crystallinity, crystallographic orientation, compaction, reduced surface roughness, and energetic disorder, as well as a longer charge-carrier lifetime, making the optoelectronic functionality of the optimized PAD-processed $MAPbI_3$ films to be on par with their typical solution-processed counterparts.

While the harsh mechanical impact of the $MAPbI_3$ powder particles in the course of the PAD process appears to not alter the SnO_2 layer thickness and its morphology, cAFM characterizations show a clearly reduced electrical functionality, that is, an increase of the onset potential for electrical conduction and a decreased overall conductivity. Here, absorption measurements indicate that the PAD processing increases the disorder of the SnO_2 layer. This increase could be associated to an increase in defect density within the SnO_2 due to the high mechanical impact, and/or the incorporation of metallic Pb into the SnO_2 (as suggested by XPS investigations).

Furthermore, analyzing light-intensity-dependent *J–V* measurements, we find that recombination at the interfaces between the perovskite and charge-transport layers also contributes to the limited performance of the PAD-processed solar cells.

Here, it appears plausible that the formation of hydrates at the perovskite surfaces, which lowers the barrier for ion migration associated to a more pronounced hysteresis, is a major contributing aspect, since the perovskite processing and posttreatment of our films happen under ambient conditions.

In summary, our work successfully demonstrates that it is possible to produce PSCs with completely dry-processed absorber layer based on perovskite powders. As we could pinpoint the main performance-limiting aspects to be associated with the presence of hydrates at the perovskite surface and the deterioration of the electrical properties of the SnO_2 layer due to the PAD process, optimized preparation methods and defect engineering of the SnO_2 layer, as well as moving all processing steps into a dry atmosphere and using passivated powders, represent important optimization strategies to reduce hysteresis and to improve overall device performance. Based on the various approaches already presented in the literature, we are thus confident that the current hurdles to optimize the efficiency of PAD-processed perovskite solar cells will be successfully overcome in the future.

6. Experimental Section

Powder Synthesis: For the mechanochemical synthesis of $MAPbI_3$, 1.9 g of the methylammonium iodide (MAI) reactant powder and 5.509 g of PbI_2 (99%, Acros Organics) were added to 80 mL ZrO_2 milling jars under ambient conditions. Then, 8 mL cyclohexane as a milling agent and 25 ZrO_2 milling balls with a diameter of 10 mm were added to the milling jar. A Fritsch "Pulverisette 5" planetary ball mill with 400 rpm was used for synthesis. After 5 min of milling, a pause of 20 min was implemented to prevent excessive heating of the milling jar. The process was repeated until a total milling time of 50 min was achieved. Afterward, the cyclohexane was evaporated in air and the obtained black $MAPbI_3$ powder was sieved using a mesh size of 63 μm.

Solar Cell Fabrication: Substrate Preparation and ETL: Substrates were cleaned in an ultrasonic bath with soap water (Hellmanex), deionized water, acetone, and isopropanol and treated with UV–ozone. SnO_2 nanoparticles (Alfa Aesar 15% in H_2O) were spin-coated onto the clean substrate at 3000 rpm for 30 s and the substrates were annealed at 180 °C for 30 min and again UV–ozone treated prior to perovskite deposition.

Solar Cell Fabrication: Perovskite Film Deposition: $MAPbI_3$ films were produced via PAD method using a custom-made apparatus. Prior to deposition, the mechanochemically synthesized $MAPbI_3$ powder was dried for at least 1 h at 120 °C. For each film, 1 g of the dried powder was filled into the aerosol generation unit. Using helium as a processing gas, 0.25 L min^{-1} were passed through the unit to generate the aerosol while the ejector was fed with 20 L min^{-1} to enhance acceleration of the aerosol through the converging slit nozzle with orifice size of 10 × 0.5 mm. The substrate to nozzle distance was set to 3 mm. The substrate was moved past the nozzle 30 times at a velocity of 1 mm s^{-1}. During deposition, a pressure of 122 mbar resulted in the aerosol generation unit and 6 mbar in the deposition chamber (for details about chosen PAD process parameters, as well as a discussion about lead safety considerations for the PAD, see Section S1, Supporting Information). The $MAPbI_3$ films for untreated devices were blown off with nitrogen before the HTL layer was applied to remove the loose $MAPbI_3$ particles on the surface.

Solar Cell Fabrication: HTL and Back Contact: Spiro-MeOTAD (Sigma Aldrich) solutions (72.5 mg mL^{-1} in chlorobenzene (CB), 17.5 mL Li-TFSI [520 mg mL^{-1} in acetonitrile], 42.5mL tBP) were spin-coated at 3000 rpm for 30 s onto the perovskite film. Finally, 100 nm gold was thermally evaporated onto the substrates as back contact which results in active area of 12.5 mm^2 for each solar cell.

Solar Cell Fabrication: Pressing: Pristine $MAPbI_3$ PAD films were hot-pressed with a homebuilt manual press (details on press setup in previous work).[28] The films were pressed with 25 MPa at 120 °C for 5 min (at target levels). For optimum pressing results, loose powder particles and agglomerates on the pristine PAD films were removed by means of a nitrogen gun before the pressing process. The glass blocks used as press die were treated with an anti-sticking coating (trichloro(octadecyl)silane in toluene from liquid phase) to prevent the pressed film from sticking.

Solar Cell Characterization: The *J–V* curves were obtained using an ORIEL Sol2A (Newport) solar simulator with a calibrated AM 1.5 G spectrum in combination with a Keithley 2400 sourcemeter and an aperture mask of 10 mm^2. The scan rate for all measurements was set to 150 mV s^{-1}. For the light-intensity-dependent measurements different neutral density filters were placed above the devices to reduce the light intensity.

Absorption: Absorption spectra were recorded using a Cary 5000 (Varian) equipped with an integrating sphere in reflection mode.

TRPL: For TRPL curves, time-correlated single-photon counting (TCSPC) measurements were performed with a PicoQuant MT200 confocal fluorescence microscope in combination with a PMA Hybrid PMT 40 photomultiplier tube (PicoQuant) and a TimeHarp 260 Pico TCSPC board (PicoQuant). The samples were excited with a 560 nm diode Laser (PicoQuant LDH-D-TA-560) with a frequency of 2.0 MHz and a pulse width of 68 ps. The laser beam was focused on the sample with an Olympus Objective with 4× magnification and the emission was filtered with a 561 nm long-pass filter before detection. The excitation fluence was set to 300 nJ cm^{-2}.

AFM: AFM was performed using a dimension ICON-GB system, equipped with a Nanoscope V controller (Bruker Corp., USA). The AFM unit was located in a glove box under argon atmosphere (water < 5 ppm; oxygen < 0.1 ppm). Multidimensional IV-Spectroscopy images were

ADVANCED SCIENCE NEWS
www.advancedsciencenews.com

Solar RRL
www.solar-rrl.com

obtained using the DataCube-TUNA mode of the measurement system in combination with the PF-TUNA application module. We used a conductive NSC14/Cr-Au Probe from MikroMasch for nanoscale electrical characterization (calibrated spring constant via Sader: 6.9 N m^{-1}). The applied loading force for *I–V* measurements was 100 nN and the sample bias voltage was swept from −1 to 3 V. The maximum current was limited to ±1.3 nA. Data processing and visualization of multidimensional AFM data was performed using Igor Pro (Wavemetrics Inc., USA). Additional AFM topography images (Supporting Information) were recorded under ambient conditions in TappingMode, using an AC160TS-R3 probe (Olympus Corp., Japan) with a nominal resonance frequency of 300 kHz.

GIWAXS: GIWAXS experiments were conducted at the beamline 7.3.3 at the Advanced Light Source at Lawrence Berkeley National Lab (Berkeley, USA).[91] The samples were illuminated with 10 keV radiation ($\lambda = 1.24$ Å) at an incident angle (α_i) of 0.25° at room temperature. The beam size was 300 µm (height) × 700 µm (width). The scattering signal was captured on a Pilatus 2M (172 µm pixel size, file format EDF, 1475 × 1679 pixels) located 274 mm from the sample. Acquisition times were 10 s for each frame. After correction for Ewald-sphere curvature with Xi-CAM,[92] the 2D data was reduced to 1D horizontal and vertical cuts using customized Python scripts. The software DPDAK (v1.4.1)[93] was used for Chi-integration. To track scattering peak parameters, the 1D intensity profiles were fitted with Gaussians and a local background using a Trust-Region-Reflective Least Squares algorithm.

X-Ray Diffraction: A Bruker "D8 Discover A25" with Cu-$K_{\alpha 1}$ radiation ($\lambda = 0.15406$ nm) and Ge-$K_{\alpha 1}$ monochromator in reflection mode was used to acquire XRD patterns with a 2θ step size of 0.008° in the 2θ range from 10° to 45° under ambient conditions. The X-ray source was operated with 40 kV and 40 mA.

Film Thickness and Surface Roughness: The film thickness and surface roughness *Ra* of the (pressed) PAD films were measured using either an LSM 900 M (Carl Zeiss AG) laser scanning microscope with a 405 nm laser or using a profilometer (Dektak 150, Veeco).

SEM: The film morphology was characterized by SEM using a Zeiss Leo 1530 instrument FE-SEM with Schottky-field-emission cathode, In-lens detector, and SE2 detector. The accelerating voltage was 3 kV. Prior to measurement, the samples were sputtered with 2 nm platinum.

XPS: XPS measurements were carried out with a Versa Probe III photoelectron spectrometer (PHI). The excitation was provided by an Al K α source ($h\nu = 1486.6$ eV) at a pass energy of 224 eV to achieve high sensitivity. The X-ray beam had a diameter of 100 µm and a power of 25 W. Ion (Ar^+) and electron neutralization was applied to the sample to avoid charging-induced energy shifts.

Supporting Information

Supporting Information is available from the Wiley Online Library or from the author.

Acknowledgements

S.B., N.L., and C.W. contributed equally to this work. The authors acknowledge financial support from the German National Science Foundation DFG via the projects PA 3373/3-1, MO 1060/32-1, PA 3373/6-1 and KO 3973/3-1. C.G. and E.M.H. are grateful for support by the Bavarian State Ministry of Science, Research, and Arts through the grant "Solar Technologies go Hybrid (SolTech)". Portions of this research were carried out at beamline 7.3.3 of the Advanced Light Source, which is supported by the Director of the Office of Science, Office of Basic Energy Sciences, of the U.S. Department of Energy under Contract No. DE-AC02-05CH11231. The authors also thank the Department of Metal and Alloys (Prof. Uwe Glatzel) for the possibility to conduct XRD measurements, and Martina Heider and the KeyLabs "Electron and Optical Microscopy" and "Device Engineering" of the Bavarian Polymer Institute (BPI) for assistance with SEM images and access to the MT200 system and to the Versa Probe III XPS system. The authors further thank Irene Bauer for MAI synthesis, Monika Daubinger for the powder preparation, and Angelika Mergner for preparation of SEM images. The authors further thank Paul Pistor, Wolfgang Tress, and Philip Schulz for fruitful discussions.

Open Access funding enabled and organized by Projekt DEAL.

Conflict of Interest

The authors declare no conflict of interest.

Data Availability Statement

The data that support the findings of this study are available from the corresponding author upon reasonable request.

Keywords

halide perovskites, optoelectronics, room-temperature impact consolidation, thermal imprint, vacuum kinetic spraying

Received: April 6, 2023
Revised: June 8, 2023
Published online:

[1] NREL, Best Research-Cell Efficiency Chart **2023**, https://www.nrel.gov/pv/cell-efficiency.html (accessed: April 2023).
[2] J. Jeong, M. Kim, J. Seo, H. Lu, P. Ahlawat, A. Mishra, Y. Yang, M. A. Hope, F. T. Eickemeyer, M. Kim, Y. J. Yoon, I. W. Choi, B. P. Darwich, S. J. Choi, Y. Jo, J. H. Lee, B. Walker, S. M. Zakeeruddin, L. Emsley, U. Rothlisberger, A. Hagfeldt, D. S. Kim, M. Grätzel, J. Y. Kim, *Nature* **2021**, *592*, 381.
[3] Q. Cao, Y. Li, H. Zhang, J. Yang, J. Han, T. Xu, S. Wang, Z. Wang, B. Gao, J. Zhao, X. Li, X. Ma, S. M. Zakeeruddin, W. E. I. Sha, X. Li, M. Grätzel, *Sci. Adv.* **2021**, *7*, eabg0633.
[4] Y. Zhao, T. Heumueller, J. Zhang, J. Luo, O. Kasian, S. Langner, C. Kupfer, B. Liu, Y. Zhong, J. Elia, A. Osvet, J. Wu, C. Liu, Z. Wan, C. Jia, N. Li, J. Hauch, C. J. Brabec, *Nat. Energy* **2022**, *7*, 144.
[5] H. Li, J. Zhou, L. Tan, M. Li, C. Jiang, S. Wang, X. Zhao, Y. Liu, Y. Zhang, Y. Ye, W. Tress, C. Yi, *Sci. Adv.* **2022**, *8*, eabo7422.
[6] J. Li, H. Wang, X. Y. Chin, H. A. Dewi, K. Vergeer, T. W. Goh, J. W. M. Lim, J. H. Lew, K. P. Loh, C. Soci, T. C. Sum, H. J. Bolink, N. Mathews, S. Mhaisalkar, A. Bruno, *Joule* **2020**, *4*, 1035.
[7] S. Biberger, K. Schötz, P. Ramming, N. Leupold, R. Moos, A. Köhler, H. Grüninger, F. Panzer, *J. Mater. Chem. A* **2022**, *10*, 18038.
[8] K. Schötz, C. Greve, A. Langen, H. Gorter, I. Dogan, Y. Galagan, A. J. J. M. van Breemen, G. H. Gelinck, E. M. Herzig, F. Panzer, *Adv. Opt. Mater.* **2021**, *9*, 2101161.
[9] O. Telschow, M. Albaladejo-Siguan, L. Merten, A. D. Taylor, K. P. Goetz, T. Schramm, O. V. Konovalov, M. Jankowski, A. Hinderhofer, F. Paulus, F. Schreiber, Y. Vaynzof, *J. Mater. Chem. A* **2022**, *10*, 19743.
[10] K. P. Goetz, Y. Vaynzof, *ACS Energy Lett.* **2022**, *7*, 1750.
[11] W. Massmann, *Occup. Environ. Med.* **1956**, *13*, 51.
[12] G. L. Kennedy, *Drug Chem. Toxicol.* **1986**, *9*, 147.
[13] D. Liu, C. J. Traverse, P. Chen, M. Elinski, C. Yang, L. Wang, M. Young, R. R. Lunt, *Adv. Sci.* **2018**, *5*, 1700484.
[14] X. Cao, G. Zhang, Y. Cai, L. Jiang, X. He, Q. Zeng, J. Wei, Y. Jia, G. Xing, W. Huang, *Sol. RRL* **2020**, *4*, 2000008.
[15] S. Öz, J. Burschka, E. Jung, R. Bhattacharjee, T. Fischer, A. Mettenbörger, H. Wang, S. Mathur, *Nano Energy* **2018**, *51*, 632.

ADVANCED SCIENCE NEWS
www.advancedsciencenews.com

Solar RRL
www.solar-rrl.com

[16] H.-S. Kim, Y.-J. An, J. I. Kwak, H. J. Kim, H. S. Jung, N.-G. Park, *ACS Energy Lett.* **2022**, *7*, 1154.
[17] A. These, N. H. Khansur, O. Almora, L. Luer, G. J. Matt, U. Eckstein, A. Barabash, A. Osvet, K. G. Webber, C. J. Brabec, *Adv. Electron. Mater.* **2021**, *7*, 2001165.
[18] M.-Y. Cho, S. Kim, I.-S. Kim, E.-S. Kim, Z.-J. Wang, N.-Y. Kim, S.-W. Kim, J.-M. Oh, *Adv. Funct. Mater.* **2020**, *30*, 1907449.
[19] N. Leupold, A. L. Seibel, R. Moos, F. Panzer, *Eur. J. Inorg. Chem.* **2021**, *2021*, 2882.
[20] K. Naoe, M. Nishiki, A. Yumoto, *J. Therm. Spray Technol.* **2013**, *22*, 1267.
[21] H. S. Ryu, T. S. Lim, J. Ryu, S.-H. Hong, *J. Electrochem. Soc.* **2012**, *160*, C42.
[22] J.-Y. Park, K.-A. Lee, S.-H. Kim, G.-S. Ham, *Arch. Metall. Mater.* **2017**, *62*, 2017.
[23] J.-H. Park, D.-S. Park, B.-D. Hahn, J.-J. Choi, J. Ryu, S.-Y. Choi, J. Kim, W.-H. Yoon, C. Park, *Ceram. Int.* **2016**, *42*, 3584.
[24] M. Schubert, D. Hanft, T. Nazarenus, J. Exner, M. Schubert, P. Nieke, P. Glosse, N. Leupold, J. Kita, R. Moos, *Funct. Mater. Lett.* **2019**, *12*, 1930005.
[25] J. Akedo, *J. Ceram. Soc. Jpn.* **2020**, *128*, 101.
[26] F. Panzer, D. Hanft, T. P. Gujar, F.-J. Kahle, M. Thelakkat, A. Köhler, R. Moos, *Materials* **2016**, *9*, 277.
[27] C. Witt, A. Schmid, N. Leupold, M. Schultz, J. Höcker, A. Baumann, R. Moos, F. Panzer, *ACS Appl. Electron. Mater.* **2020**, *2*, 2619.
[28] C. Witt, K. Schötz, M. Kuhn, N. Leupold, S. Biberger, P. Ramming, F.-J. Kahle, A. Köhler, R. Moos, E. M. Herzig, F. Panzer, *J. Phys. Chem. C* **2023**, *127*, 10563.
[29] P. Ramming, N. Leupold, K. Schötz, A. Köhler, R. Moos, H. Grüninger, F. Panzer, *J. Mater. Chem. C* **2021**, *9*, 11827.
[30] S. Shrestha, R. Fischer, G. J. Matt, P. Feldner, T. Michel, A. Osvet, I. Levchuk, B. Merle, S. Golkar, H. Chen, S. F. Tedde, O. Schmidt, R. Hock, M. Rührig, M. Göken, W. Heiss, G. Anton, C. J. Brabec, *Nat. Photonics* **2017**, *11*, 436.
[31] W. A. Dunlap-Shohl, T. Li, D. B. Mitzi, *ACS Appl. Energy Mater.* **2019**, *2*, 5083.
[32] W. Kim, M. S. Jung, S. Lee, Y. J. Choi, J. K. Kim, S. U. Chai, W. Kim, D.-G. Choi, H. Ahn, J. H. Cho, D. Choi, H. Shin, D. Kim, J. H. Park, *Adv. Energy Mater.* **2018**, *8*, 1702369.
[33] A. Mayer, M. Buchmüller, S. Wang, C. Steinberg, M. Papenheim, H.-C. Scheer, N. Pourdavoud, T. Haeger, T. Riedl, *J. Vac. Sci. Technol. B* **2017**, *35*, 06G803.
[34] J. Xiao, Y. Yang, X. Xu, J. Shi, L. Zhu, S. Lv, H. Wu, Y. Luo, D. Li, Q. Meng, *J. Mater. Chem. A* **2015**, *3*, 5289.
[35] N. Leupold, K. Schötz, S. Cacovich, I. Bauer, M. Schultz, M. Daubinger, L. Kaiser, A. Rebai, J. Rousset, A. Köhler, P. Schulz, R. Moos, F. Panzer, *ACS Appl. Mater. Interfaces* **2019**, *11*, 30259.
[36] N. Leupold, P. Ramming, I. Bauer, C. Witt, J. Jungklaus, R. Moos, H. Grüninger, F. Panzer, *Eur. J. Inorg. Chem.* **2023**, *26*.
[37] J. Akedo, *J. Therm. Spray Technol.* **2008**, *17*, 181.
[38] D. Hanft, J. Exner, M. Schubert, T. Stöcker, P. Fuierer, R. Moos, *J. Ceram. Sci. Tech.* **2015**, *6*, 147.
[39] F. S. Kong, Y. Z. Jin, H. D. Kim, *Shock Waves* **2016**, *26*, 771.
[40] B. A. Nejand, S. Gharibzadeh, V. Ahmadi, H. R. Shahverdi, *Sci. Rep.* **2016**, *6*, 33649.
[41] L. Huang, Z. Xing, X. Tang, D. Li, X. Meng, X. Hu, T. Hu, Y. Chen, *J. Mater. Chem. A* **2021**, *9*, 16178.
[42] Y. Yu, M. Shang, T. Wang, Q. Zhou, Y. Hao, Z. Pang, D. Cui, G. Lian, X. Zhang, S. Han, *J. Mater. Chem. C* **2021**, *9*, 15056.
[43] A. Mayer, N. Pourdavoud, Z. Doukkali, K. Brinkmann, J. Rond, J. Staabs, A.-C. Swertz, F. van gen Hassend, P. Görrn, T. Riedl, H.-C. Scheer, *Appl. Phys. A* **2021**, *127*, 237.
[44] J. Moon, S. Kwon, M. Alahbakhshi, Y. Lee, K. Cho, A. Zakhidov, M. J. Kim, Q. Gu, *ACS Appl. Mater. Interfaces* **2021**, *13*, 5368.
[45] T. Zhang, L. Zhang, G. Zhu, D. Cui, Q. Wang, G. Lian, Z. Zheng, H. Yu, *Adv. Mater. Interfaces* **2022**, *9*, 2200447.
[46] C. Qu, J. Hu, X. Liu, Z. Li, Y. Ding, *Materials* **2017**, *10*, 1329.
[47] T. Li, A. M. Zeidell, G. Findik, W. A. Dunlap-Shohl, J. Euvrard, K. Gundogdu, O. D. Jurchescu, D. B. Mitzi, *Chem. Mater.* **2019**, *31*, 4267.
[48] H. Chen, F. Ye, W. Tang, J. He, M. Yin, Y. Wang, F. Xie, E. Bi, X. Yang, M. Grätzel, L. Han, *Nature* **2017**, *550*, 92.
[49] G. Jang, H.-C. Kwon, S. Ma, S.-C. Yun, H. Yang, J. Moon, *Adv. Energy Mater.* **2019**, *9*, 1901719.
[50] R. Herckens, W. T. M. V. Gompel, W. Song, M. C. Gélvez-Rueda, A. Maufort, B. Ruttens, J. D'Haen, F. C. Grozema, T. Aernouts, L. Lutsen, D. Vanderzande, *J. Mater. Chem. A* **2018**, *6*, 22899.
[51] J. Su, H. Cai, X. Ye, X. Zhou, J. Yang, D. Wang, J. Ni, J. Li, J. Zhang, *ACS Appl. Mater. Interfaces* **2019**, *11*, 10689.
[52] C. Du, S. Wang, X. Miao, W. Sun, Y. Zhu, C. Wang, R. Ma, *Beilstein J. Nanotechnol.* **2019**, *10*, 2374.
[53] Z. Guo, L. Gao, Z. Xu, S. Teo, C. Zhang, Y. Kamata, S. Hayase, T. Ma, *Small* **2018**, *14*, 1802738.
[54] G. D. Cody, T. Tiedje, B. Abeles, B. Brooks, Y. Goldstein, *Phys. Rev. Lett.* **1981**, *47*, 1480.
[55] M. Ledinsky, T. Schönfeldová, J. Holovský, E. Aydin, Z. Hájková, L. Landová, N. Neyková, A. Fejfar, S. De Wolf, *J. Phys. Chem. Lett.* **2019**, *10*, 1368.
[56] J. Rodriguez-Pereira, J. Tirado, A. F. Gualdrón-Reyes, F. Jaramillo, R. Ospina, *Surf. Sci. Spectra* **2020**, *27*, 024003.
[57] M. J. Bozack, K. W. Bryant, *Surf. Sci. Spectra* **1992**, *1*, 324.
[58] S. B. O. dos Santos,M. H. Boratto, R. A. Ramos, L. V. A. Scalvi, *Mater. Chem. Phys.* **2022**, *278*, 125571.
[59] S. Tominc, A. Rečnik, Z. Samardžija, G. Dražić, M. Podlogar, S. Bernik, N. Daneu, *Ceram. Int.* **2018**, *44*, 1603.
[60] H. Zhao, W. Liang, F. Wang, Y. Zhou, Q. Xie, *Results Phys.* **2020**, *18*, 103314.
[61] Y. Bai, Y. Fang, Y. Deng, Q. Wang, J. Zhao, X. Zheng, Y. Zhang, J. Huang, *ChemSusChem* **2016**, *9*, 2686.
[62] S. Akin, *ACS Appl. Mater. Interfaces* **2019**, *11*, 39998.
[63] J. Chen, S. J. Bull, *J. Phys. Appl. Phys.* **2008**, *41*, 074009.
[64] H. J. Gwon, N.-R. Kang, Y. Lee, S. O. Won, H. J. Chang, J.-W. Choi, C.-Y. Kang, S. K. Kim, B. Kwon, S. Nahm, J.-Y. Kim, J.-S. Kim, S.-H. Baek, *Chem. Mater.* **2016**, *28*, 7051.
[65] G. M. Ingo, N. Zacchetti, D. della Sala, C. Coluzza, *J. Vac. Sci. Technol. Vac. Surf. Films* **1989**, *7*, 3048.
[66] A. Mesarwi, A. Ignatiev, *Surf. Sci.* **1991**, *244*, 15.
[67] Z. Liu, L. Qiu, E. J. Juarez-Perez, Z. Hawash, T. Kim, Y. Jiang, Z. Wu, S. R. Raga, L. K. Ono, S. (Frank) Liu, Y. Qi, *Nat. Commun.* **2018**, *9*, 3880.
[68] S. Deumel, A. van Breemen, G. Gelinck, B. Peeters, J. Maas, R. Verbeek, S. Shanmugam, H. Akkerman, E. Meulenkamp, J. E. Huerdler, M. Acharya, M. García-Batlle, O. Almora, A. Guerrero, G. Garcia-Belmonte, W. Heiss, O. Schmidt, S. F. Tedde, *Nat. Electron.* **2021**, *4*, 681.
[69] F. Panzer, C. Li, T. Meier, A. Köhler, S. Huettner, *Adv. Energy Mater.* **2017**, *7*, 1700286.
[70] K. P. Goetz, A. D. Taylor, F. Paulus, Y. Vaynzof, *Adv. Funct. Mater.* **2020**, *30*, 1910004.
[71] E. Ugur, M. Ledinský, T. G. Allen, J. Holovský, A. Vlk, S. De Wolf, *J. Phys. Chem. Lett.* **2022**, *13*, 7702.
[72] S. Zeiske, O. J. Sandberg, N. Zarrabi, C. M. Wolff, M. Raoufi, F. Peña-Camargo, E. Gutierrez-Partida, P. Meredith, M. Stolterfoht, A. Armin, *J. Phys. Chem. Lett.* **2022**, *13*, 7280.

ADVANCED SCIENCE NEWS
www.advancedsciencenews.com

Solar RRL
www.solar-rrl.com

[73] A. Rajagopal, P.-W. Liang, C.-C. Chueh, Z. Yang, A. K.-Y. Jen, *ACS Energy Lett.* **2017**, *2*, 2531.
[74] H. Mehdizadeh-Rad, J. Singh, *ChemPhysChem* **2019**, *20*, 2712.
[75] K. Frohna, M. Anaya, S. Macpherson, J. Sung, T. A. S. Doherty, Y.-H. Chiang, A. J. Winchester, K. W. P. Orr, J. E. Parker, P. D. Quinn, K. M. Dani, A. Rao, S. D. Stranks, *Nat. Nanotechnol.* **2022**, *17*, 190.
[76] D. W. de Quilettes, S. M. Vorpahl, S. D. Stranks, H. Nagaoka, G. E. Eperon, M. E. Ziffer, H. J. Snaith, D. S. Ginger, *Science* **2015**, *348*, 683.
[77] H. Zhou, Q. Chen, G. Li, S. Luo, T. Song, H.-S. Duan, Z. Hong, J. You, Y. Liu, Y. Yang, *Science* **2014**, *345*, 542.
[78] D. Glowienka, Y. Galagan, *Adv. Mater.* **2022**, *34*, 2105920.
[79] P. Caprioglio, C. M. Wolff, O. J. Sandberg, A. Armin, B. Rech, S. Albrecht, D. Neher, M. Stolterfoht, *Adv. Energy Mater.* **2020**, *10*, 2000502.
[80] Z. Sun, G. Sitbon, T. Pons, A. A. Bakulin, Z. Chen, *Sci. Rep.* **2015**, *5*, 10626.
[81] K. W. Kemp, A. J. Labelle, S. M. Thon, A. H. Ip, I. J. Kramer, S. Hoogland, E. H. Sargent, *Adv. Energy Mater.* **2013**, *3*, 917.
[82] F. Gao, Z. Li, J. Wang, A. Rao, I. A. Howard, A. Abrusci, S. Massip, C. R. McNeill, N. C. Greenham, *ACS Nano* **2014**, *8*, 3213.
[83] I. Riedel, J. Parisi, V. Dyakonov, L. Lutsen, D. Vanderzande, J. C. Hummelen, *Adv. Funct. Mater.* **2004**, *14*, 38.
[84] C. Li, S. Tscheuschner, F. Paulus, P. E. Hopkinson, J. Kießling, A. Köhler, Y. Vaynzof, S. Huettner, *Adv. Mater.* **2016**, *28*, 2446.
[85] A. M. A. Leguy, Y. Hu, M. Campoy-Quiles, M. I. Alonso, O. J. Weber, P. Azarhoosh, M. van Schilfgaarde, M. T. Weller, T. Bein, J. Nelson, P. Docampo, P. R. F. Barnes, *Chem. Mater.* **2015**, *27*, 3397.
[86] J. Huang, S. Tan, P. D. Lund, H. Zhou, *Energy Environ. Sci.* **2017**, *10*, 2284.
[87] S. Y. Kwon, B. Kang, J. H. Won, C. Y. Lee, K. Hwang, H. H. Kim, D. Park, W. K. Choi, I. S. Kim, G. Y. Kim, Y. H. Jang, P. Lee, S. H. Im, T. Kim, *Adv. Mater. Interfaces* **2023**, *10*, 2202249.
[88] I. Mesquita, L. Andrade, A. Mendes, *Sol. Energy* **2020**, *199*, 474.
[89] U.-G. Jong, C.-J. Yu, G.-C. Ri, A. P. McMahon, N. M. Harrison, P. R. F. Barnes, A. Walsh, *J. Mater. Chem. A* **2018**, *6*, 1067.
[90] J. A. Christians, P. A. Miranda Herrera, P. V. Kamat, *J. Am. Chem. Soc.* **2015**, *137*, 1530.
[91] A. Hexemer, W. Bras, J. Glossinger, E. Schaible, E. Gann, R. Kirian, A. MacDowell, M. Church, B. Rude, H. Padmore, *J. Phys. Conf. Ser.* **2010**, *247*, 012007.
[92] R. J. Pandolfi, D. B. Allan, E. Arenholz, L. Barroso-Luque, S. I. Campbell, T. A. Caswell, A. Blair, F. De Carlo, S. Fackler, A. P. Fournier, G. Freychet, M. Fukuto, D. Gürsoy, Z. Jiang, H. Krishnan, D. Kumar, R. J. Kline, R. Li, C. Liman, S. Marchesini, A. Mehta, A. T. N'Diaye, D. Y. Parkinson, H. Parks, L. A. Pellouchoud, T. Perciano, F. Ren, S. Sahoo, J. Strzalka, D. Sunday, et al., *J. Synchrotron Radiat.* **2018**, *25*, 1261.
[93] G. Benecke, W. Wagermaier, C. Li, M. Schwartzkopf, G. Flucke, R. Hoerth, I. Zizak, M. Burghammer, E. Metwalli, P. Müller-Buschbaum, M. Trebbin, S. Förster, O. Paris, S. V. Roth, P. Fratzl, *J. Appl. Crystallogr.* **2014**, *47*, 1797.

Supplementary Information

First of their kind: Solar cells with a dry-processed perovskite absorber layer via powder aerosol deposition and hot-pressing

Simon Biberger*[*,1]*, **Nico Leupold****[*,2]*, **Christina Witt****[*,1]*, Christopher Greve[3], Paul Markus[4], Philipp Ramming[1], Daniel Lukas[2], Konstantin Schötz[1], Frank-Julian Kahle[1], Chenhui Zhu[5], Georg Papastavrou[4], Anna Köhler[1], Eva M. Herzig[3], Ralf Moos[2], Fabian Panzer[1#]*

[*] Contributed equally

[1]Soft Matter Optoelectronics (EP II), University of Bayreuth, Bayreuth 95440, Germany

[2]Department of Functional Materials, University of Bayreuth, Bayreuth 95440, Germany

[3]Dynamics and Structure Formation - Herzig Group, University of Bayreuth, Bayreuth 95440, Germany

[4]Physical Chemistry II, University of Bayreuth, Bayreuth 95440, Germany

[5]Advanced Light Source, Lawrence Berkeley National Lab, 1 Cyclotron Rd, Berkeley, CA, 94720, USA

Corresponding Author:

[#]E-Mail: fabian.panzer@uni-bayreuth.de

1 PAD setup

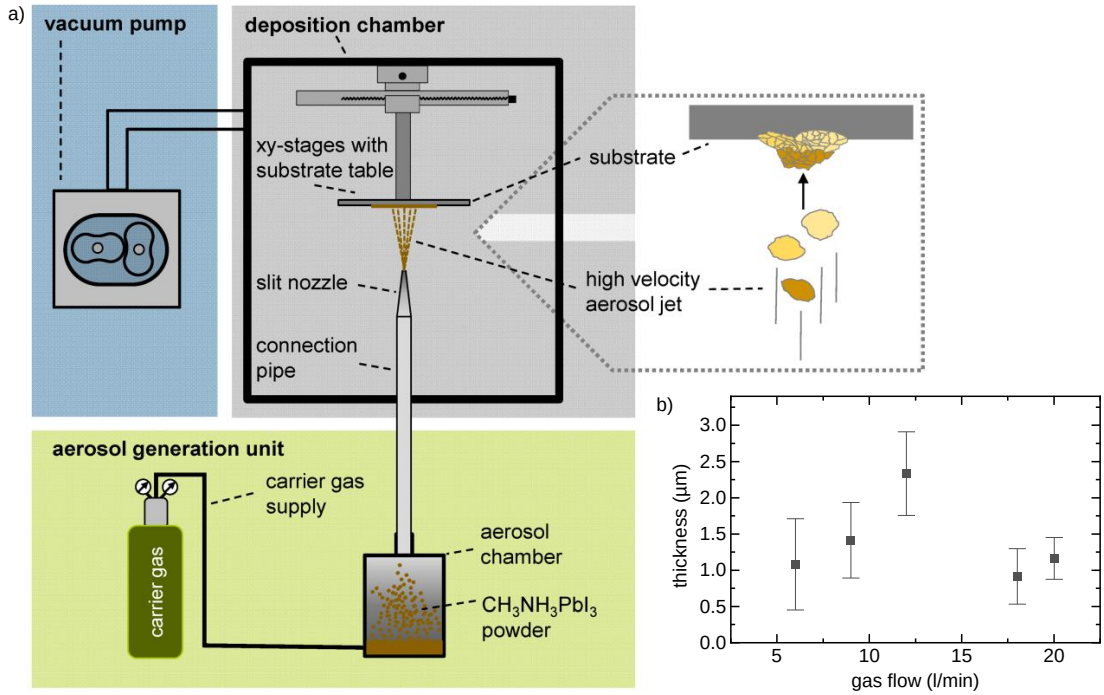

Figure S1: a) Schematic of a setup for powder aerosol deposition (PAD) showing its main components. The zoomed in area illustrates the film formation. Adapted under the terms of the CC-BY 4.0 license.[1] Copyright 2016, the authors. Published by MDPI AG. b) Thickness of $MAPbI_3$ films deposited via PAD using different gas flow.

Derivation of suitable PAD processing parameters

Suitable PAD processing parameters were derived for the deposition of $MAPbI_3$ thin films with appropriate thickness, morphology and homogeneity.

For the aerosol generation, a low gas flow of 0.25 l/min was used to get a low aerosol concentration, which is beneficial for a more homogeneous film coverage.

The gas flow that feeds the ejector to accelerate the aerosol in combination with the reduction of the cross-section at the ejector and the slit nozzle define the resulting carrier gas velocity. We tested different gas flow rates between 6 l/min and 20 l/min and evaluated the resulting film thickness at three different spots across a film. The resulting mean film thicknesses with standard deviation (represented by the error bars) are shown in Figure S1b. Here, a higher gas flow tends to lead to a more homogenous

thickness within a film. Consequently, we chose the maximum gas flow of 20 l/min limited by our setup and the geometry of the ejector.

The vacuum level in the deposition chamber of 6 mbar results from the gas flow, the ejector geometry, the nozzle geometry and the performance of the vacuum pump and is in a typical range for PAD.[2]

Regarding the substrate to nozzle distance, we chose a value of 3 mm, that has been proven well suited for deposition in the past in our lab and allows a homogeneous layer thickness across the nozzle width.[2] Moreover, the substrate to nozzle distance seems to have a rather small influence in the chosen range.[3]

Safety aspects of the lead containing PAD process:

Lead-based powder aerosol is a potential safety issue. Nevertheless, no powder aerosol can escape during the coating process, because everything is tightly sealed due to the required vacuum. In addition, a filter is installed before the vacuum pump to remove residual powder in the gas flow. After the deposition is finished and thus after aerosol generation is stopped, the vacuum is maintained for a short time to allow residual powder particles to settle. The machine operator gets in contact with lead-containing powder sticking on the wall of the deposition chamber only when the sample is removed from the coating chamber. For this step, personal protective equipment consisting of safety goggles, gloves, lab coat and particulate respirators is worn. In addition, the PAD machine is located in a fume hood to capture any perovskite particles that may be released into the air. No lead can be found by regular lead tests in the area surrounding the fume hood with the PAD machine. For use in industrial processes, it would be reasonable to use appropriate large-scale extraction systems and a robot to feed the deposition chamber or to employ a continuous process.

2 $MAPbI_3$ films without optimization of the aerosol generation

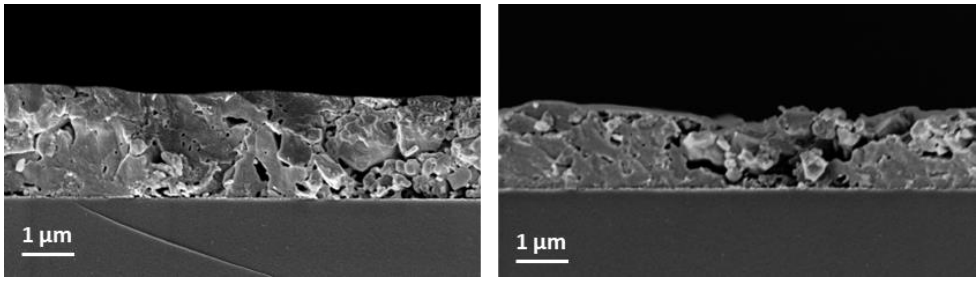

Figure S2: SEM images of rapidly grown $MAPbI_3$ films deposited using highly agglomerated mechanochemically synthesized $MAPbI_3$ powders for the PAD process without improvements in the aerosol generation. In the left image, large particles that have not been sufficiently crushed and deformed during deposition are clearly visible, while in the middle of the right image a loosely bound agglomerate can be seen. The films were wiped with a cloth, thus the rather smooth surface.

3 Morphology of mechanochemically synthesized $MAPbI_3$ powder

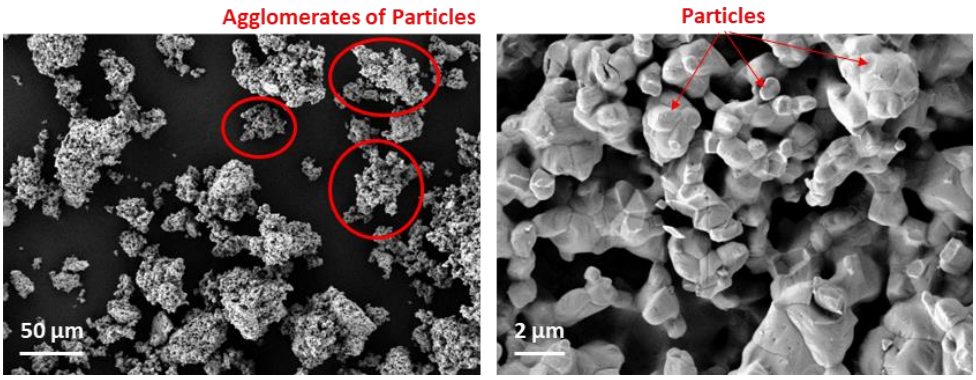

Figure S3: SEM images of mechanochemically synthesized $MAPbI_3$ powder used for PAD.

4 Phase purity of mechanochemically synthesized $MAPbI_3$ powder

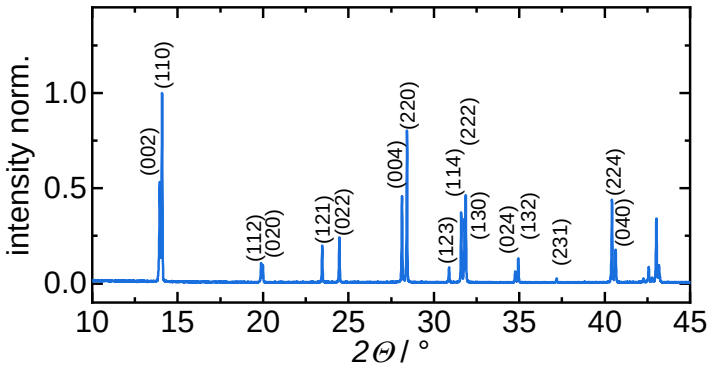

Figure S4: X-ray diffractogram of mechanochemically synthesized $MAPbI_3$ powder. All reflexes can be indexed to $MAPbI_3$ showing the phase purity of the powder[4].

5 Deposition of $MAPbI_3$ films with simple tee instead of the ejector

We also checked if the ejector can be replaced by a simple tee to simplify the setup. However, the resulting deposited films using the tee show large pores, voids (pinholes through the whole film) and particles that have not been crushed, as expected when too much kinetic energy is used to break up larger agglomerates instead of particles (Figure S5). Also, the film deposited with tee is quite thin as the larger agglomerates probably do not bond to the substrate during the first passes.

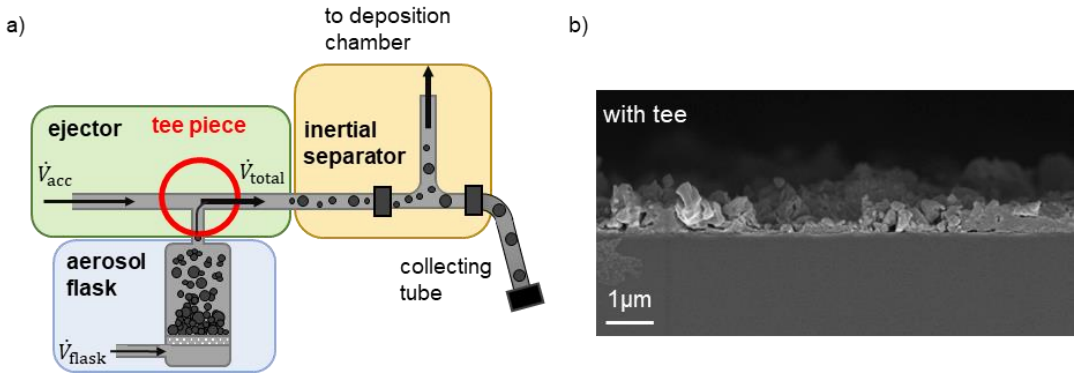

Figure S5: a) Concept of the aerosol generation employing a tee piece as the ejector unit. b) SEM image of a $MAPbI_3$ film deposited with a simple tee instead of the ejector.

6 Detailed discussion of the pressing process

When hot-pressing MHP thin films, silicon wafers are often used as press die because of their low surface roughness and the applicability of a hydrophobic coating.[5–12] This coating is necessary to prevent the perovskite film from sticking to the press die. [5,7–9,12] However, in single-action pressing, as performed in this work by means of a manual press, the use of silicon wafers as press die is limited to pressures below 10 MPa,[8,12] as otherwise the wafers may break. Alternatively, PTFE sheets are used as press die material owing to their anti-sticking behavior. However, due to the low form stability of PTFE, pressure is often kept far below 15 MPa.[13–15] In contrast, polyimide foil is characterized by high form stability under mechanical and thermal stress and also exhibits anti-sticking behavior due to its low surface roughness.[16] Using polyimide foil as press die material, MHP films with promising optoelectronic properties have been fabricated.[17,18] Thus, we tried pressing our pristine PAD films with polyimide foil

as press die material at a pressure of 25 MPa and a temperature of 120 °C. Unfortunately, the used polyimide foil (thickness: 125 µm, roughness: 43 nm) wears off during hot pressing (see Figure S6 top), which might be caused by the rough surface of the pristine PAD films. In addition, the polyimide foil is not reliably anti-sticking (see Figure S6 top), indicating that a lower surface roughness of the foil would be required. Due to these issues, we went over to glass blocks (thickness: 8 mm, roughness: 2 nm) as press die material, whose thickness is decisive for the fracture resistance under pressing. Despite the low surface roughness of the glass blocks, an anti-sticking coating (Trichloro(octadecyl)silane in toluene from liquid phase) is necessary (see Figure S6 bottom). Using the silanized glass blocks as press die in our manual press, our $MAPbI_3$ thin films can be reliably pressed with 25 MPa at 120 °C for 5 min (Figure 3a and previous work[19] for details on press setup, entire time profiles of pressure and temperature in Figure S7).

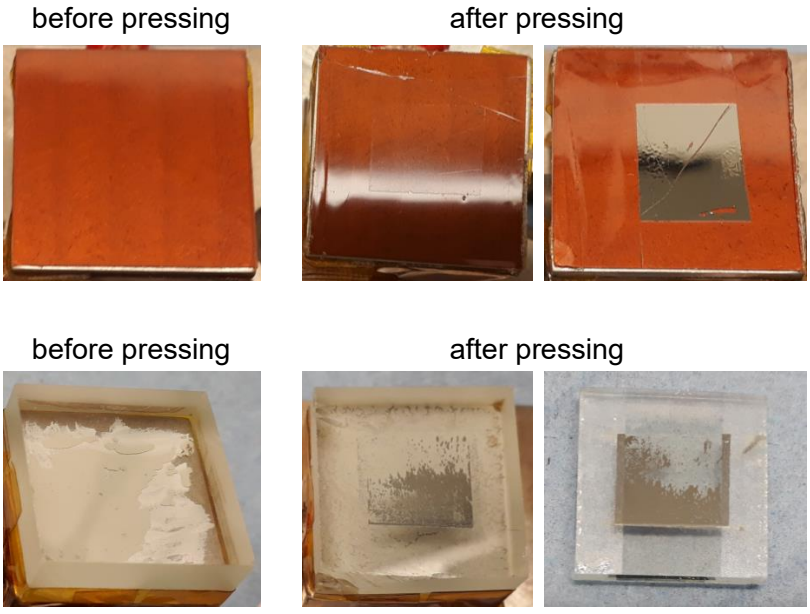

Figure S6: Top: Polyimide foil before (left) and after pressing (right): As a result of the increased pressure and temperature during the pressing process, the foil wears off and the pressed $MAPbI_3$ film may stick to the foil. Bottom: Glass die without silanization coating before (left) and after (middle) hot-pressing a $MAPbI_3$ PAD film (right). Parts of the $MAPbI_3$ PAD film have detached from the substrate and stick on the glass die.

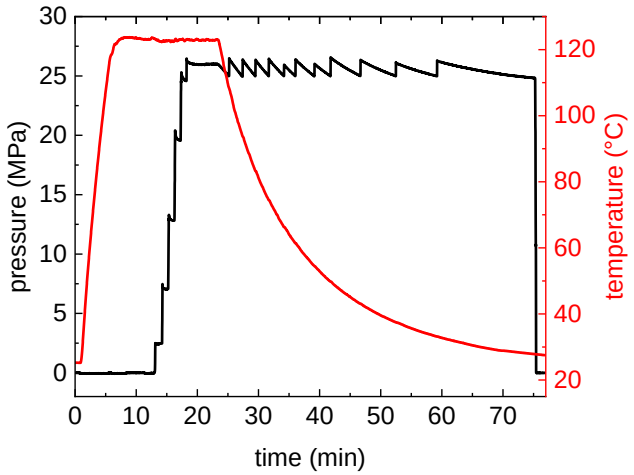

Figure S7: Time evolution of the applied pressure and temperature when pressing a $MAPbI_3$ PAD film 5 minutes at a target level of 25 MPa and 120 °C (pressure was manually readjusted to maintain the target pressure level).

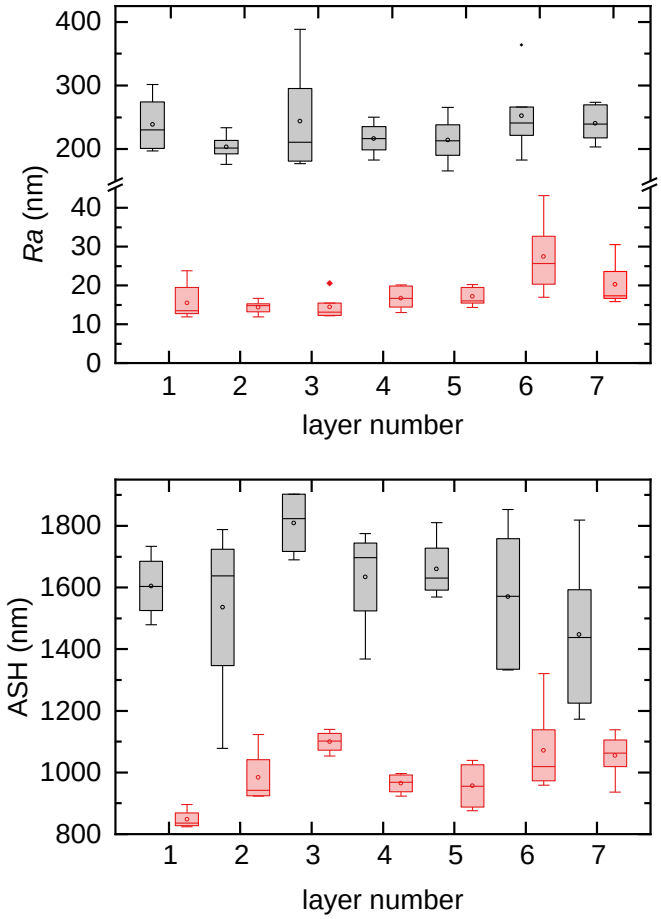

Figure S8: Surface roughness (top) and average surface height specifying film thickness (bottom) of 7 $MAPbI_3$ absorber layers before (grey, “pristine film”) and after hot-pressing (red, “pressed film”) determined using a profilometer.

7 Solar cell characteristics

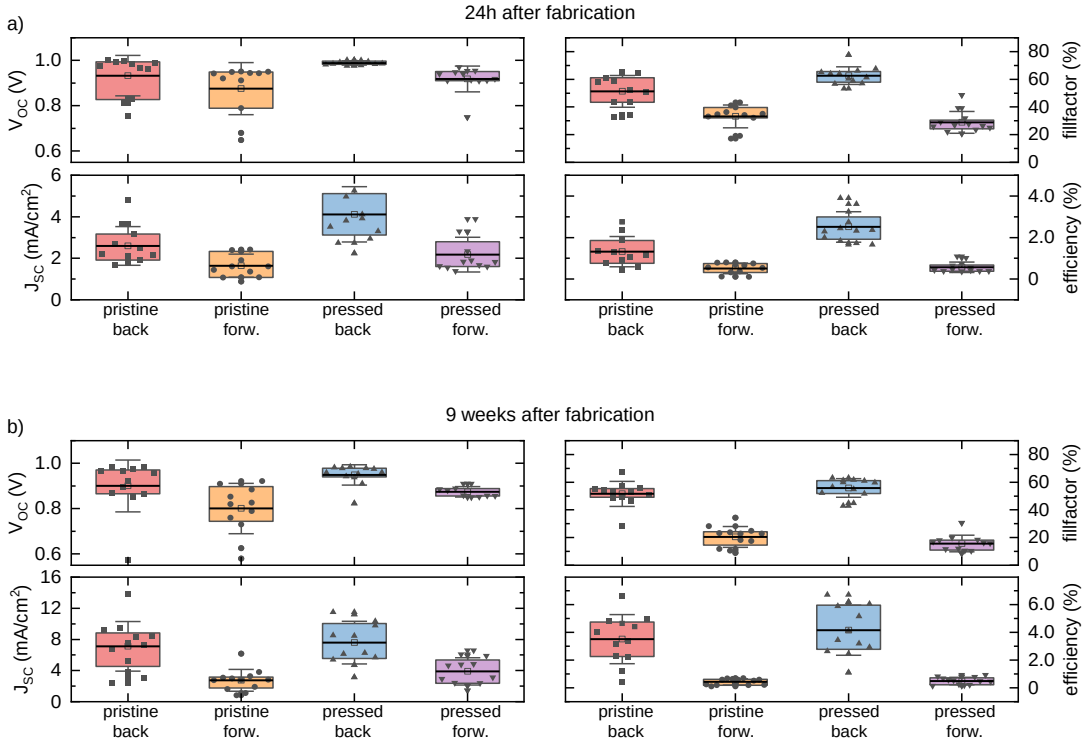

Figure S9: Batch statistics (back and forward direction) of solar cells with pristine absorber layer (red, orange) and with pressed absorber layer (blue, purple) obtained a) 24h after fabrication and b) 9 weeks after fabrication.

Table S1: Summary of solar cell metrics (mean values) for $MAPbI_3$ solar cells with pristine and with pressed PAD processed absorber layer measured 24h after fabrication, values for forward direction in brackets.

type	V_{oc} in V	J_{sc} in mA/cm²	FF in %	PCE in %
pristine	0.93 ± 0.09	2.6 ± 0.9	52 ± 12	1.3 ± 0.8
	(0.87 ± 0.12)	(1.6 ± 0.6)	(33 ± 8)	(0.5 ± 0.3)
pressed	0.99 ± 0.01	4.1 ± 1.4	63 ± 6	2.5 ± 0.7
	(0.92 ± 0.06)	(2.2 ± 0.8)	(29 ± 8)	(0.6 ± 0.2)

Table S2: Summary of solar cell metrics (mean values) for $MAPbI_3$ solar cells with pristine and with pressed PAD processed absorber layer measured 9 weeks after fabrication, values for forward direction in brackets.

type	V_{oc} in V	J_{sc} in mA/cm^2	FF in %	PCE in %
pristine	0.90 ± 0.11	7.2 ± 3.1	52 ± 9	3.5 ± 1.8
	(0.80± 0.11)	(2.8 ± 1.4)	(21 ± 7)	(0.4 ± 0.3)
pressed	0.95 ± 0.04	7.6 ± 2.7	56 ± 6	4.1 ± 1.8
	(0.87 ± 0.03)	(3.9 ± 1.8)	(16 ± 6)	(0.5 ± 0.3)

Operational Stability

In order to assess the operational stability, we recorded consecutive J-V measurements and plotted the extracted solar cell parameters as a function of number of measurements (Duration per scan: 30 seconds). From this tracking of solar cell parameters, it becomes clear that Voc and FF of the pressed device appears nearly constant, while the Jsc of devices 1 and 2 slightly decrease with the number of consecutive J-V scans. In contrast, for the three devices with pristine absorber layer shown here, the J-V characteristic exhibit different behavior as a function of number of consecutive J-V scans, which we speculate to be attributed to the differences in perovskite layer morphology, compactness and surface roughness.

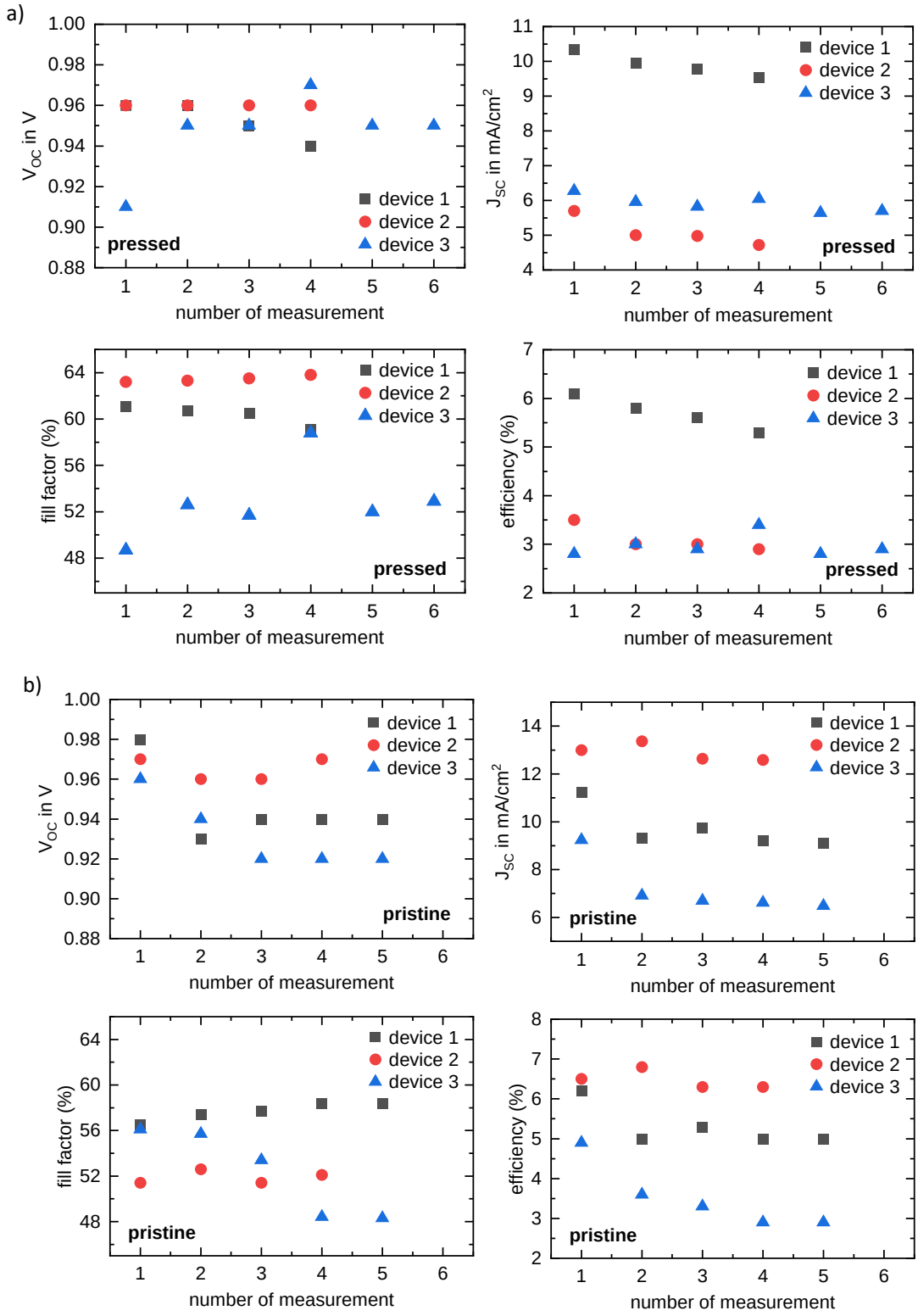

Figure S10: Solar metrics of three devices each for pressed (a) and pristine (b) $MAPbI_3$ absorber layers as function of number of measurements of consecutive J-V sweeps.

8 Prove of perovskite adhesion via scotch tape test

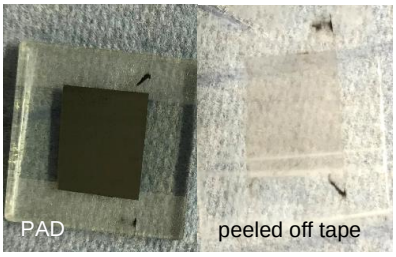

Figure S11: Photograph of the PAD film (left) after applying and removing a stripe of scotch tape on the pristine PAD film. On the peeled off tape (right), only a negligible amount of $MAPbI_3$ powder is visible which originates from loose and uncompressed powder particles remaining on top of the film after PAD.

9 Details on the SnO_2 layer

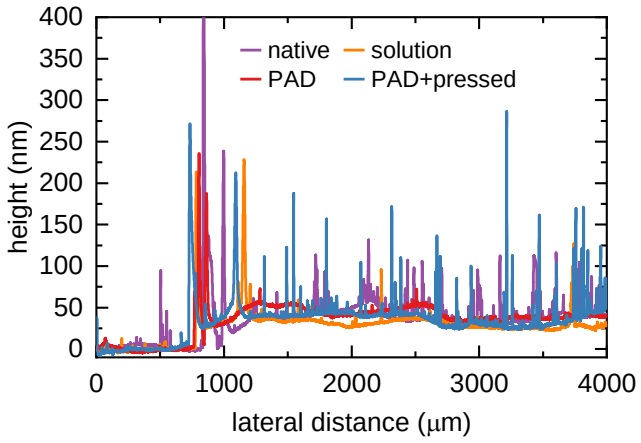

Figure S12: Height profiles of 1) a native SnO_2 layer serving as reference, 2) SnO_2 layer after removing a solution-processed $MAPbI_3$ film, 3) SnO_2 layer after removing a pristine $MAPbI_3$ PAD film, and 4) SnO_2 layer after removing a pressed $MAPbI_3$ PAD film.

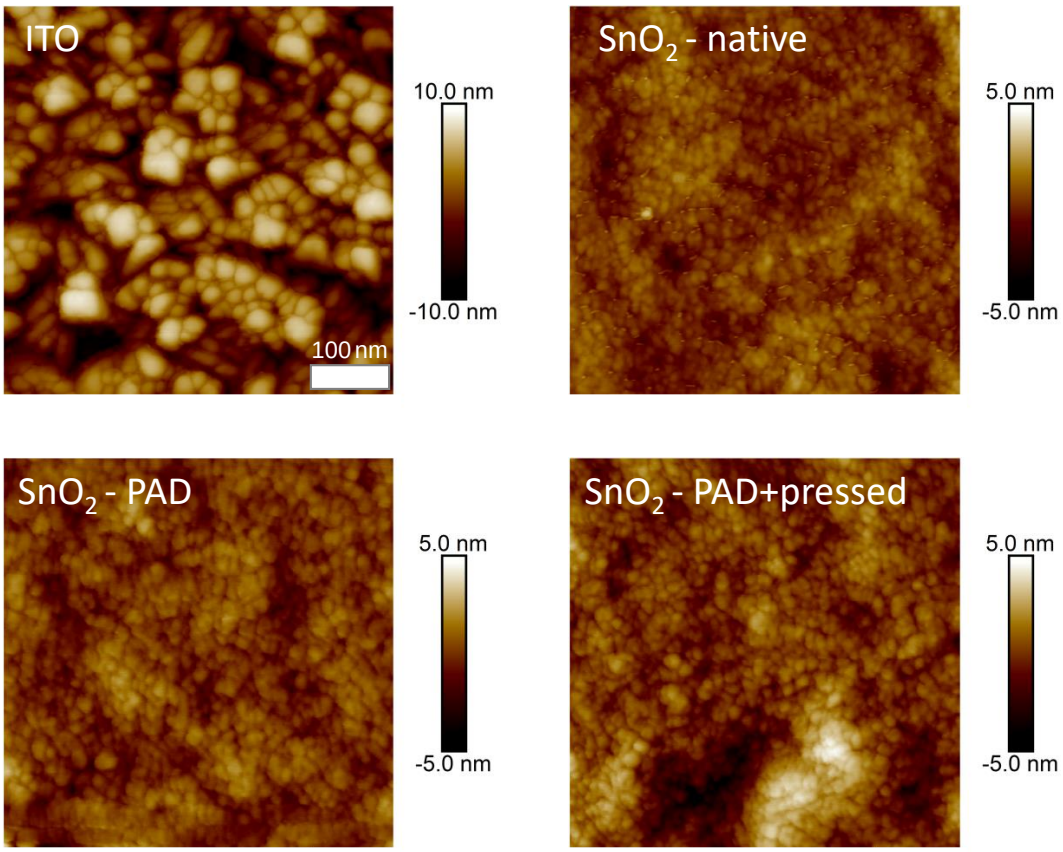

Figure S13: AFM topography images of a native SnO_2 layer and SnO_2 layers after applying a $MAPbI_3$ film via PAD (and pressing) and removing the $MAPbI_3$ film. The ITO topography is also shown for reference.

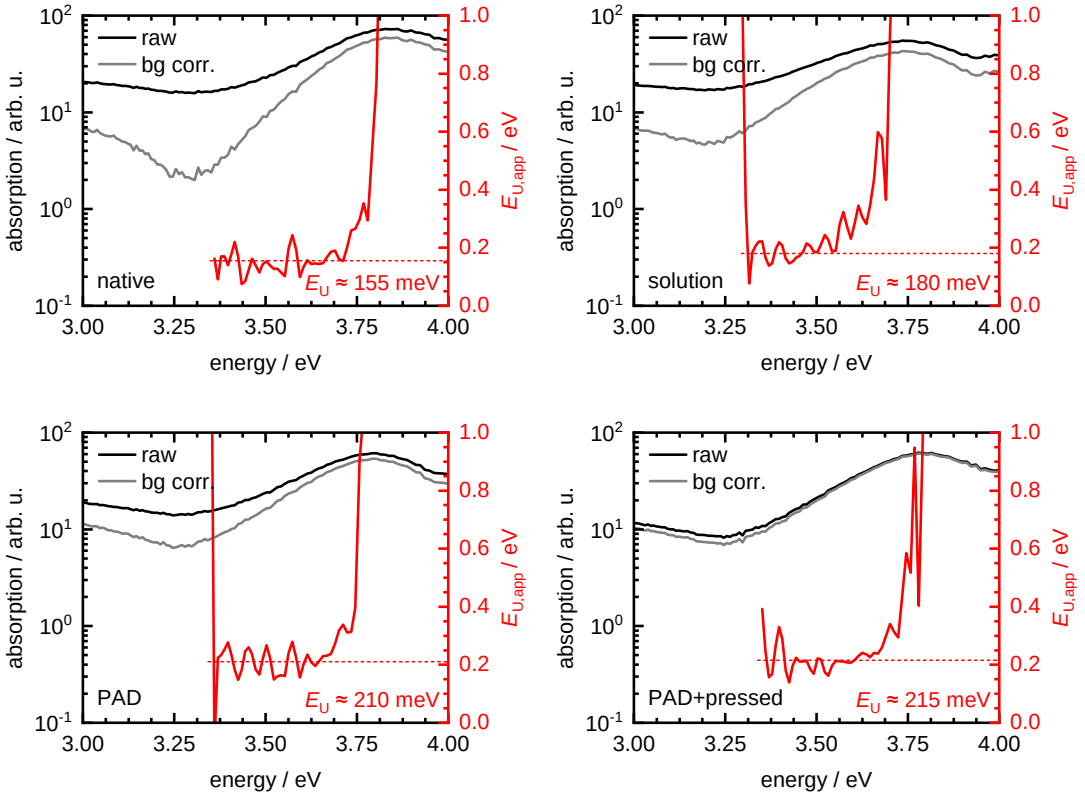

SnO_2	native	solution	PAD	PAD+pressed
E_U / meV	155 ± 20	180 ± 20	210 ± 20	215 ± 20

Figure S14: Extraction of Urbach energy E_U via calculated apparent Urbach energy $E_{U,app}$ (red) from measured (black) / background corrected (grey) absorption spectra of 1) a native SnO_2 layer serving as reference, 2) SnO_2 layer after removing a solution processed $MAPbI_3$ film, 3) SnO_2 layer after removing a pristine $MAPbI_3$ PAD film, and 4) SnO_2 layer after removing a pressed $MAPbI_3$ PAD film. The E_U values extracted from the horizontal part of $E_{U,app}$ (red dashed line) are summarized in the table below the graphs.

The Urbach energies E_U of the four different presented types of SnO_2 layers were extracted via calculating the apparent Urbach energy $E_{U,app}$ according to $E_{U,app} = \left(\frac{d}{dE}[\ln(\alpha - D)]\right)^{-1}$ from the absorption spectra (α) with subtracted scattering offset D.This analysis method has been introduced recently in the field of halide perovskite by Ugur et al. and Zeiske et al.[20,21] The horizontal part of the apparent Urbach energy $E_{U,app}$ represents the exponential part in the absorption spectra and thus yields the Urbach energy value E_U. Large error bars were estimated for the extracted Urbach

energy values E_U, because of the limited quality of the absorption spectra due to the small SnO_2 layer thickness (40-50 nm). This is also the reason why we used the novel more sophisticated analysis method of the Urbach energy via $E_{U,app}$ for the SnO_2 layer instead of fitting the absorption spectra directly with an exponential function as done for the $MAPbI_3$ absorber layer in Figure 6. The extracted higher Urbach energies for PAD treated SnO_2 layers suggest that the PAD-processing increases the energetic disorder in the SnO_2 layer.

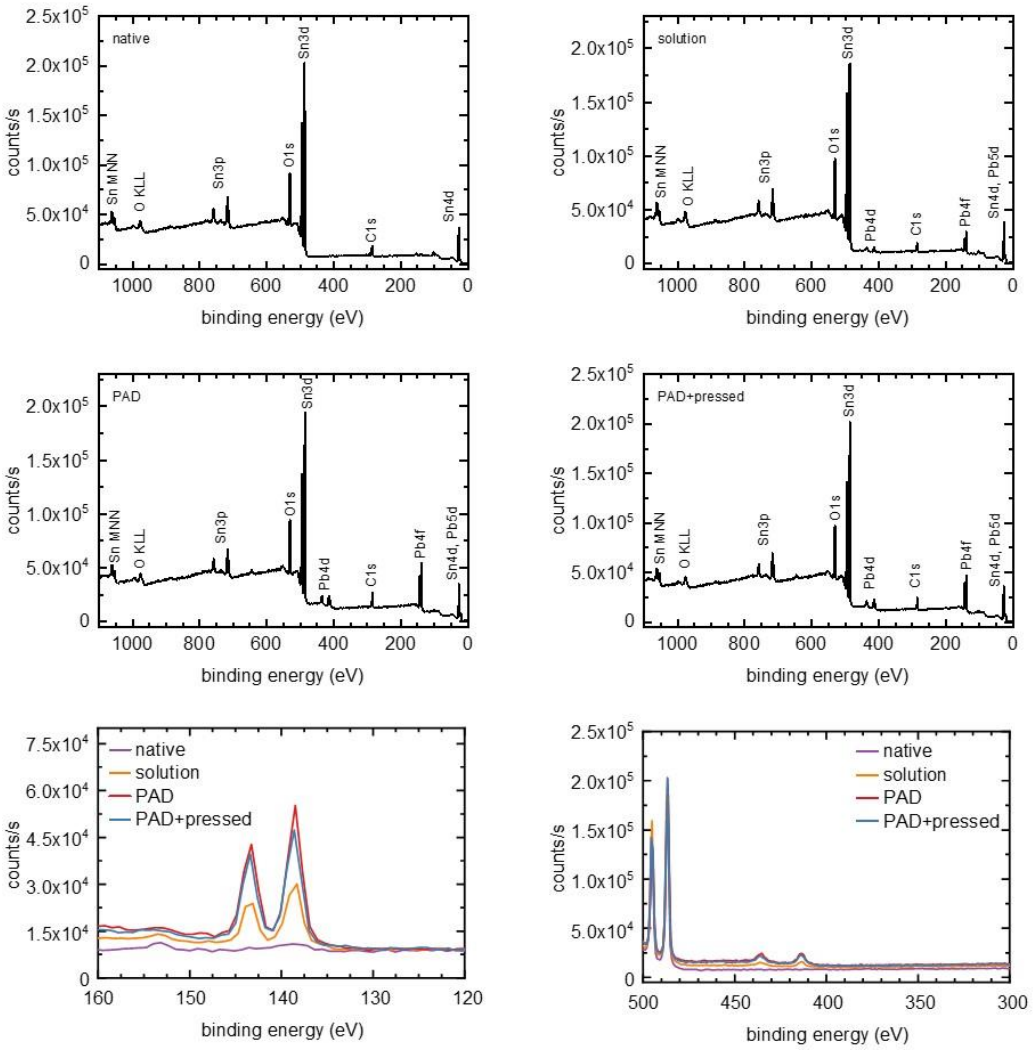

Figure S15: XPS spectra of 1) a native SnO_2 layer serving as reference, 2) SnO_2 layer after removing a solution-processed $MAPbI_3$ film, 3) SnO_2 layer after removing a pristine $MAPbI_3$ PAD film, and 4) SnO_2 layer after removing a pressed $MAPbI_3$ PAD film.

10 Further details on the perovskite layer

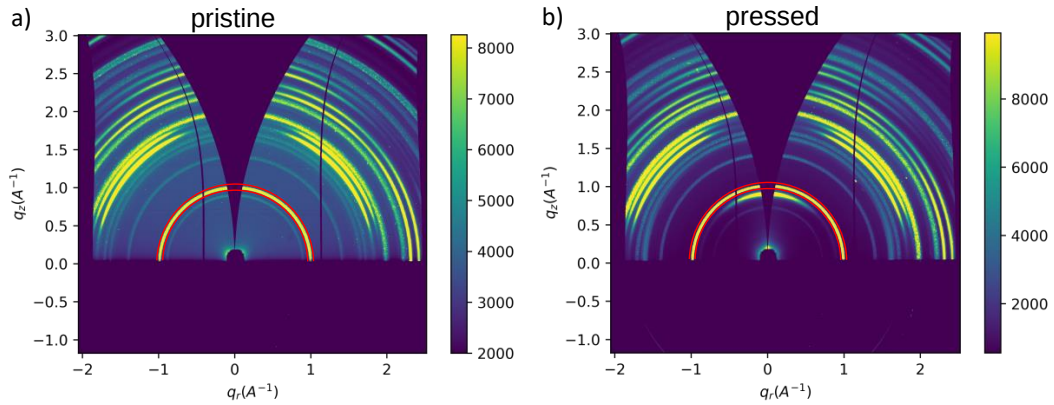

Figure S16: Ewald-curvature corrected 2D GIWAXS data of a) pristine and b) pressed $MAPbI_3$ thin films. The red lines mark the (110) & (002) double peak, which was examined for the χ analysis in the main text.

χ analysis and single pixel intensity variations

To distinguish changes in orientation for the pristine and pressed $MAPbI_3$ films the samples were examined with a χ analysis. Therefore, a line cut over the full peak width of the (110) & (002) double peak marked (red) in Figure S16 was extracted. Hereby 90° corresponds to the direction along q_r (in-plane of the sample) and 0° to the direction along q_z (out-of-plane of the sample). The upper limit of χ is given by the missing gap due to the curvature of the Ewald-sphere, while the lower limit is given by the position of the Yoneda streak at q_z = 0.083 $Å^{-1}$.[22] The Yoneda region needs to be discarded to ignore its intensity enhancement. Also, the data below the Yoneda region will be discarded because it emerges from below the horizon and is therefore attenuated. The resulting intensity plot versus angle χ was then corrected for the sample isotropy by subtracting the isotropic contribution. The resulting plot showing the oriented fraction is displayed in Figure 6b (main text).

The intensity within the (110) & (002) double peak marked in Figure S16 was further analyzed by extracting single pixel counting statistics to determine how the pressing changes the number of large crystallites within the film. The results are shown in Figure S17. One can see in subfigure b) that the median of the pixel intensity distribution of the hot-pressed $MAPbI_3$ film is at 2.5k counts/pixel, while the median of the distribution

in subfigure a) is at 4.7k counts/pixel. This is related to the overall higher background level of counts for the pristine sample, which is also visible in Figure S16. Further, the overall mean of the ratio of counts/pixel is higher (8.4k counts/pixel) for the hot-pressed sample, resulting in a local maximum visible at 20k counts/pixel. Similar behaviour is observed for the pristine sample, but the overall mean is lower (7.2k counts/pixel) with the local maximum shifting to lower values (15k counts/pixel). The higher mean and the higher single pixel counts of the local maximum around 20k of the pressed sample indicates an increased number of large crystallites within the hot-pressed sample.

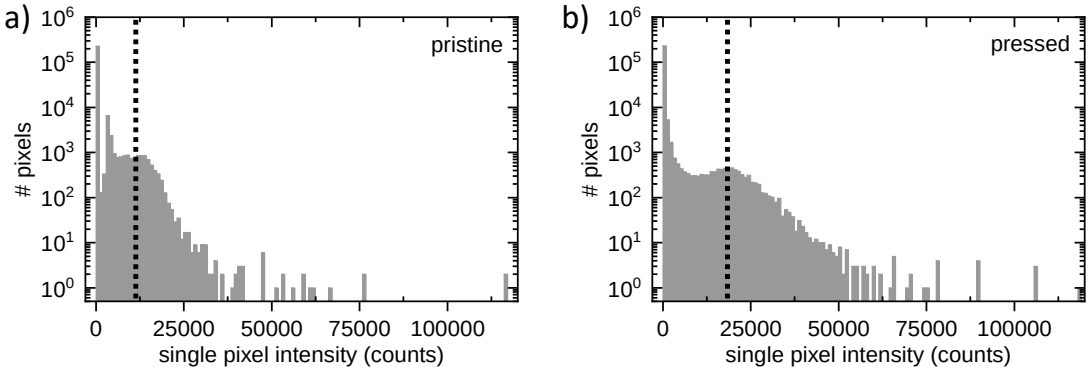

Figure S17: Histograms of single pixel counting statistics of the pixels within the marked area of the (110) & (002) double peak in Figure S15 for a a) pristine and b) pressed $MAPbI_3$ film.

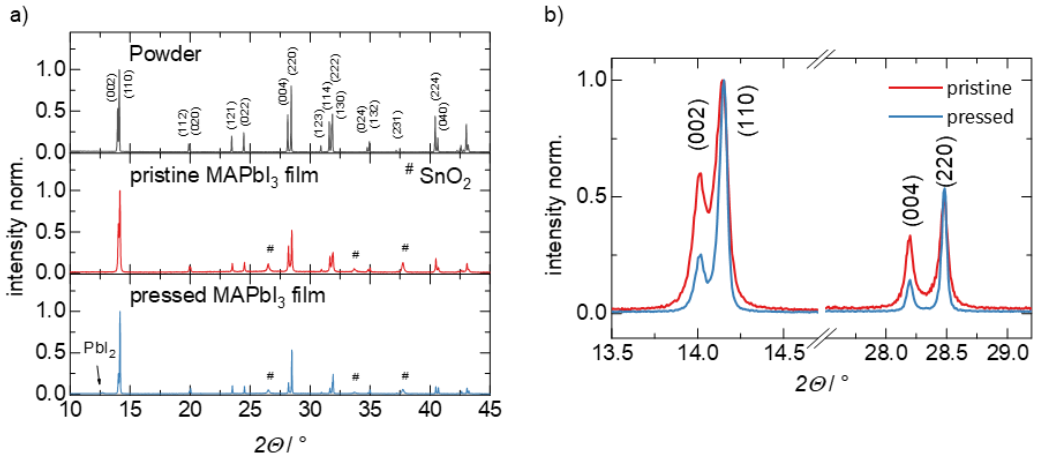

Figure S18: (a) X-ray diffractograms of mechanochemically synthesized $MAPbI_3$ powder, pristine $MAPbI_3$ PAD film, and pressed $MAPbI_3$ PAD film. All reflexes can be indexed to $MAPbI_3$ showing the phase purity of the powder and the pristine film.[4] In the pressed film only a negligible amount of PbI_2 is found. (b) Zoomed in version of the X-ray diffractograms from (a) for the pristine and pressed film showing the decrease in FWHM and the introduction of preferred orientation upon pressing.

Detailed q_r and q_z analysis

To examine the compression of unit cells upon pressure treatment, the (110) and (002) signal was examined in two perpendicular directions. Peak positions were separated by fitting two gaussian peaks and a local background in q_r and q_z direction. The obtained lattice spacings d are plotted in Fig S19 on the left for q_r and on the right for q_z.

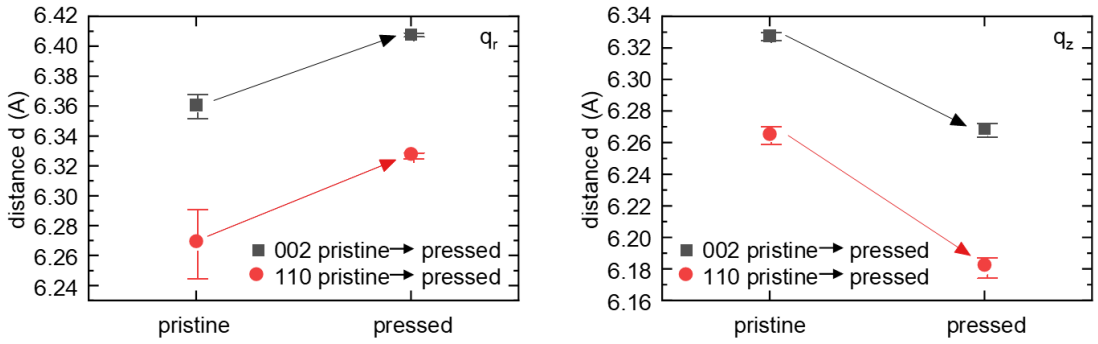

Figure S19: Lattice distances extracted from the (110) & (002) double peak along q_r (left) and q_z (right) for pristine and pressed $MAPbI_3$ thin films. The arrows indicate the change in lattice spacings with pressing.

11 Urbach Analysis

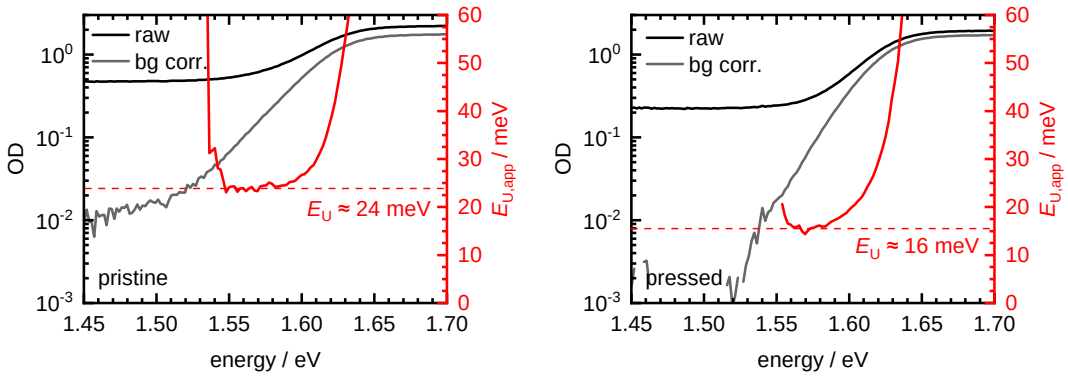

Figure S20: Extraction of Urbach energy E_U via calculated apparent Urbach energy $E_{U,app}$ (red) from measured (black) / background corrected (grey) absorption spectra of pristine (left) and pressed (right) $MAPbI_3$ PAD films. The E_U values are extracted from the horizontal part of $E_{U,app}$ (red dashed line).

The extraction of the Urbach energy in Figure 6 in the main text by exponential fits to the absorption spectra is commonly used. Recently, a novel sophisticated analysis method of the Urbach energy via $E_{U,app}$ has been introduced in the field of perovskites (see also Figure S14).[20,21] We additionally applied this novel method which yields Urbach energy values of approx. 24 meV and 16 meV for pristine and pressed $MAPbI_3$ PAD films, respectively (Figure S20). These values are similar to the values obtained by the method shown in Figure 6.

12 Ideality factors and α values

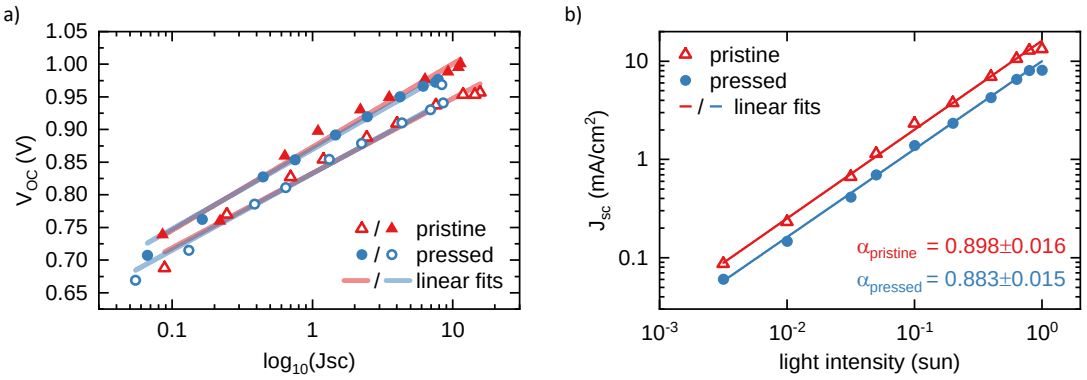

Figure S21: a) V_{OC} as a function of the J_{SC}, obtained from the light intensity-dependent J-V-curves. From the slope of the linear fitting the values of the ideality factors *n* (see main) are extracted. b) Light intensity-dependence of the J_{SC} for pristine and pressed $MAPbI_3$ PAD films. *α* values are extracted from the slope of the linear fitting.

Supporting References

[1] F. Panzer, D. Hanft, T. P. Gujar, F.-J. Kahle, M. Thelakkat, A. Köhler, R. Moos, *Materials* **2016**, *9*, 277.

[2] D. Hanft, J. Exner, M. Schubert, T. Stöcker, P. Fuierer, R. Moos, *J Ceram Sci Tech* **2015**, *6*, 147.

[3] A. Zabihi Yeganeh, M. Jadidi, C. Moreau, A. Dolatabadi, *Surf. Coat. Technol.* **2019**, *370*, 269.

[4] T. Baikie, Y. Fang, J. M. Kadro, M. Schreyer, F. Wei, S. G. Mhaisalkar, M. Graetzel, T. J. White, *J. Mater. Chem. A* **2013**, *1*, 5628.

[5] A. Mayer, M. Buchmüller, S. Wang, C. Steinberg, M. Papenheim, H.-C. Scheer, N. Pourdavoud, T. Haeger, T. Riedl, *J. Vac. Sci. Technol. B* **2017**, *35*, 06G803.

[6] T. Zhang, L. Zhang, G. Zhu, D. Cui, Q. Wang, G. Lian, Z. Zheng, H. Yu, *Adv. Mater. Interfaces* **2022**, *9*, 2200447.

[7] Y. Yu, M. Shang, T. Wang, Q. Zhou, Y. Hao, Z. Pang, D. Cui, G. Lian, X. Zhang, S. Han, *J. Mater. Chem. C* **2021**, *9*, 15056.

[8] L. Huang, Z. Xing, X. Tang, D. Li, X. Meng, X. Hu, T. Hu, Y. Chen, *J. Mater. Chem. A* **2021**, *9*, 16178.

[9] A. Mayer, N. Pourdavoud, Z. Doukkali, K. Brinkmann, J. Rond, J. Staabs, A.-C. Swertz, F. van gen Hassend, P. Görrn, T. Riedl, H.-C. Scheer, *Appl. Phys. A* **2021**, *127*, 237.

[10] N. Pourdavoud, A. Mayer, M. Buchmüller, K. Brinkmann, T. Häger, T. Hu, R. Heiderhoff, I. Shutsko, P. Görrn, Y. Chen, H.-C. Scheer, T. Riedl, *Adv. Mater. Technol.* **2018**, *3*, 1700253.

[11] N. Dong, X. Fu, G. Lian, S. Lv, Q. Wang, D. Cui, C.-P. Wong, *ACS Appl. Mater. Interfaces* **2018**, *10*, 8393.

[12] J. Moon, S. Kwon, M. Alahbakhshi, Y. Lee, K. Cho, A. Zakhidov, M. J. Kim, Q. Gu, *ACS Appl. Mater. Interfaces* **2021**, *13*, 5368.

[13] B. A. Nejand, S. Gharibzadeh, V. Ahmadi, H. R. Shahverdi, *Sci. Rep.* **2016**, *6*, 33649.

[14] W. A. Dunlap-Shohl, T. Li, D. B. Mitzi, *ACS Appl. Energy Mater.* **2019**, *2*, 5083.

[15] J. Xiao, Y. Yang, X. Xu, J. Shi, L. Zhu, S. Lv, H. Wu, Y. Luo, D. Li, Q. Meng, *J. Mater. Chem. A* **2015**, *3*, 5289.

[16] C. Qu, J. Hu, X. Liu, Z. Li, Y. Ding, *Materials* **2017**, *10*, 1329.

[17] T. Li, A. M. Zeidell, G. Findik, W. A. Dunlap-Shohl, J. Euvrard, K. Gundogdu, O. D. Jurchescu, D. B. Mitzi, *Chem. Mater.* **2019**, *31*, 4267.

[18] H. Chen, F. Ye, W. Tang, J. He, M. Yin, Y. Wang, F. Xie, E. Bi, X. Yang, M. Grätzel, L. Han, *Nature* **2017**, *550*, 92.

[19] C. Witt, K. Schötz, M. Kuhn, N. Leupold, S. Biberger, P. Ramming, F.-J. Kahle, A. Köhler, R. Moos, E. M. Herzig, F. Panzer, *J. Phys. Chem. C* **2023**, *under revision*.

[20] S. Zeiske, O. J. Sandberg, N. Zarrabi, C. M. Wolff, M. Raoufi, F. Peña-Camargo, E. Gutierrez-Partida, P. Meredith, M. Stolterfoht, A. Armin, *J. Phys. Chem. Lett.* **2022**, *13*, 7280.

[21] E. Ugur, M. Ledinský, T. G. Allen, J. Holovský, A. Vlk, S. De Wolf, *J. Phys. Chem. Lett.* **2022**, *13*, 7702.

[22] Y. Yoneda, *Phys. Rev.* **1963**, *131*, 2010.

12 Orientation and Grain Size in $MAPbI_3$ Thin Films: Influence on Phase Transition, Disorder, and Defects

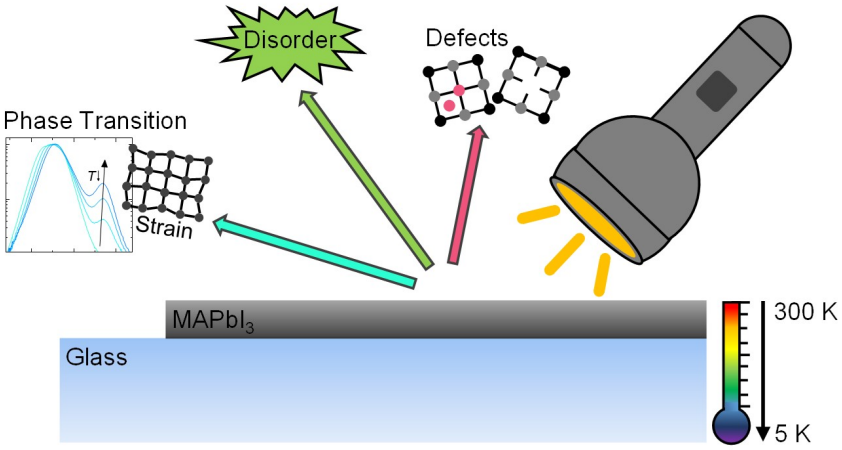

Christina Witt, Konstantin Schötz, Meike Kuhn, Nico Leupold, **Simon Biberger**, Philipp Ramming, Frank-Julian Kahle, Anna Köhler, Ralf Moos, Eva M Herzig, Fabian Panzer

Published in
The Journal of Physical Chemistry C, **2023**, 127, 22, 10563–10573

THE JOURNAL OF PHYSICAL CHEMISTRY C
A JOURNAL OF THE AMERICAN CHEMICAL SOCIETY

pubs.acs.org/JPCC Article

Orientation and Grain Size in $MAPbI_3$ Thin Films: Influence on Phase Transition, Disorder, and Defects

Christina Witt, Konstantin Schötz, Meike Kuhn, Nico Leupold, Simon Biberger, Philipp Ramming, Frank-Julian Kahle, Anna Köhler, Ralf Moos, Eva M. Herzig, and Fabian Panzer*

Cite This: *J. Phys. Chem. C* 2023, 127, 10563−10573 Read Online

ACCESS | Metrics & More | Article Recommendations | Supporting Information

ABSTRACT: In recent years, record efficiencies of halide perovskite-based devices have been achieved by processing high-quality thin films, where small morphology differences seem to be relevant for optimized optoelectronic functionality. However, a detailed understanding on how small morphological changes in perovskite films affect their structural and optoelectronic properties is still missing. Here, we investigate the influence of small morphology differences (i.e., increased grain size and crystallographic orientation), which are induced by hot-pressing methylammonium lead iodide ($MAPbI_3$) thin films, on the structural properties, phase transition behavior, energetic disorder, and defects. To this end, detailed temperature-dependent photoluminescence (PL) and absorption analyses from 300 K down to 5 K are performed. The morphology differences, confirmed by scanning electron microscopy and X-ray diffractometry analyses, result in an increased phase transition temperature for hot-pressed (HP) films, which we attribute to less strain. Moreover, fluence-dependent and transient PL measurements reveal a lower defect density in HP films. Here, besides grain size, also the degree of orientation appears to enhance the charge carrier lifetimes. The identified interdependence of strain and defect properties with film morphology suggests small differences in the perovskite's energetic disorder. Our work thus emphasizes the importance that even small structural differences in halide perovskites have on their optoelectronic functionality, spurring their further optimization.

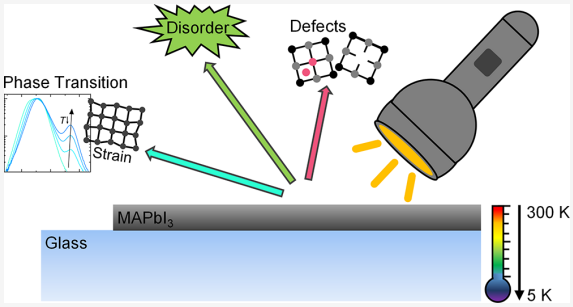

1. INTRODUCTION

Even though being relatively straightforward and inexpensive to produce, halide perovskites still exhibit remarkable semiconducting properties. Accordingly, they are currently considered one of the most promising candidates for the next generation of a variety of optoelectronic devices.[1,2] In contrast to conventional inorganic semiconductors, halide perovskites are exceptionally robust against the presence of defects as corresponding defect energy levels are typically located close to or in their conduction and valence bands, respectively.[3−5] That is why even with polycrystalline perovskite layers, remarkably high device efficiencies are achievable.[6−8]

However, to produce perovskite-based optoelectronic devices with record efficiencies, it is necessary to use perovskite films with optimized morphology. For example, large grain sizes and uniform crystallographic orientation are aimed for in the case of perovskite solar cells.[9−13] Various research reports indicate that even small improvements in the morphology of perovskites are important for further optimizing their optoelectronic functionality.[9,12−14]

Nevertheless, while various studies investigated the influence of distinct morphology changes on the resulting device properties in the past,[9−15] only little is known about how small morphology changes of perovskite thin films affect structural and optoelectronic properties, especially with respect to changes in strain and correlated energetic disorder as well as defect properties.[16−23]

Using films of the model halide perovskite methylammonium lead iodide ($MAPbI_3$), we investigate in detail how a small increase in grain size and orientation induced by hot-pressing of polycrystalline thin films affects crystallographic phase transitions, energetic disorder, and the properties of the excited states. On the one hand, detailed analyses of temperature-dependent absorption and photoluminescence (PL) measurements allow us to identify differences in the critical transition temperature between tetragonal and orthorhombic crystal structures, indicating differences in strain, depending on the film morphology. On the other hand, our

Received: December 22, 2022
Revised: May 12, 2023
Published: May 30, 2023

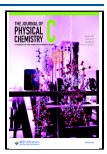

https://doi.org/10.1021/acs.jpcc.2c08968
J. Phys. Chem. C 2023, 127, 10563−10573

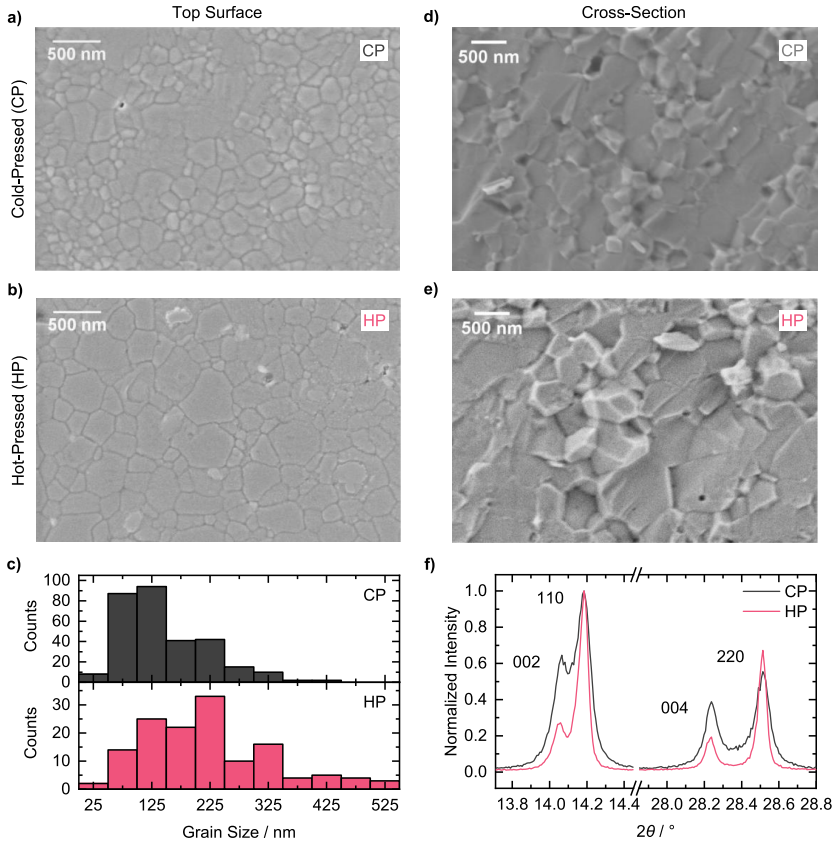

Figure 1. Morphology of CP (gray) and HP(red) $MAPbI_3$ thin films: (a,b) top-view SEM images and (c) corresponding grain size distributions. (d,e) Cross-sectional SEM images. (f) XRD patterns with 002, 110 and 004, 220 reflex pairs, normalized to the 110 reflex intensity.

analyses enable us to extract the Urbach energy—a measure for the energetic disorder in the semiconductor—from PL data, where within our error margins, no differences between the samples are observed. However, a clear impact of morphology changes induced by hot-pressing on the lifetimes of the photoexcited carriers is observed, which is investigated by means of transient PL measurements. Furthermore, a correlation between the lifetimes and changes in the preferred crystallographic orientation is observed.

2. EXPERIMENTAL SECTION

2.1. Film Preparation. $MAPbI_3$ powder was synthesized via mechanochemical synthesis using a Fritsch "Pulverisette 5/4" planetary ball mill with 400 rpm. Therefore, 1.900 g of MAI powder and 5.509 g of PbI_2 powder were put in a 80 mL ZrO_2 milling jar together with 25 ZrO_2 milling balls (diameter 10 mm) and 5 mL of cyclohexane as the milling agent. Milling was done for 5 min followed by a break of 20 min (to avoid too much heating due to rotation and friction) and both were repeated until a total milling time of 25 to 35 min was reached.

$MAPbI_3$ thin films with an area of about 1.0 cm × 1.4 cm were deposited onto 2 cm × 2 cm glass substrates (substrate thickness 3 mm) via the powder aerosol deposition method (PADM) using the mechanochemically synthesized $MAPbI_3$ powder and a custom-made apparatus for PAD. Then, these $MAPbI_3$ thin films were (hot-)pressed with a pressure of 25 MPa using a homebuilt mechanical press (for details, see Section S1).

2.2. Film Characterization. For morphology characterization of the $MAPbI_3$ thin films, SEM images were taken with a Zeiss Leo 1530 scanning electron microscope (with a Schottky-field-emission cathode, SE2 detector, and Inlens detector) using an accelerating voltage of 3.0 kV. Therefore, the thin films were fixed on a sample holder with conductive adhesion graphite pads (Plano) and sputtered with a 1.5 nm thin platinum layer. For details on grain size analysis from SEM images, see Section S1.

Structural characterization of the thin films was conducted by reflection mode XRD using a Bruker "D8 Discover A25" with Cu $K\alpha_I$ radiation (λ = 0.15406 nm). The $K\alpha_{II}$ rays were removed with a Ge $K\alpha_1$ monochromator. The instrument was operated with 40 kV and 40 mA. Diffractograms were recorded with a 2θ step size of 0.008° in the 2θ range from 10 to 45° under ambient conditions. Details on XPS measurements are given in Section S1.

The surface roughness *Ra* and the average surface height of the thin films were determined using a profilometer (Dektak 150, Veeco).

2.3. PL and Absorption Measurements. The temperature- and fluence-dependent steady-state PL and absorption spectra were measured using a homebuilt setup: the $MAPbI_3$ thin films were placed in an electrically heatable continuous flow cryostat (Oxford Instruments, Optistat CF) with an

https://doi.org/10.1021/acs.jpcc.2c08968
J. Phys. Chem. C 2023, 127, 10563−10573

automated temperature controller (Oxford Instruments ITC503S), and the temperature was regulated between 300 and 5 K. A tungsten lamp was used as a white-light source for the absorption measurements. To obtain the optical density (OD), the transmission through the sample and a reference beam that did not pass through the sample were recorded. A 630 nm long-pass filter was placed in the optical detection path to remove the 2nd diffraction order of the spectrograph. For measuring PL spectra, a 337 nm nitrogen laser (LTB MNL 100) was used for excitation. In the optical detection path, a 400 nm long-pass filter was used to remove scattered excitation light. The PL of $MAPbI_3$ thin films when measuring PL spectra and the transmission and reference beams when measuring absorption spectra were focused into a spectrograph (Andor Shamrock SR303i), respectively, and recorded with a Si-CCD camera (Andor iDus DU420a-OE). All spectra were corrected for transmission and detection efficiency of the setup.

For the extraction of charge carrier lifetimes, time-resolved PL (TRPL) curves of the $MAPbI_3$ thin films were measured at room temperature using time-correlated single-photon counting (TCSPC) in a PicoQuant MT200 confocal fluorescence microscope. A 561 nm diode laser (PicoQuant LDH-D-TA-560) with a frequency of 1.0 MHz and a pulse width of 68 ps was used for excitation, and the excitation fluence was set to 300 nJ/cm^2. An Olympus objective (4× magnification, numerical aperture of 0.1) was used to focus the laser beam on the thin film surface with a spot diameter of about 6 μm in the focal plane. In the optical detection path, a 561 nm long-pass filter was installed in order to remove scattered excitation light. A PMA Hybrid PMT 40 photomultiplier tube (PicoQuant) was used to detect the remaining emission from the $MAPbI_3$ thin films. This emission signal was processed by a TimeHarp 260 Pico TCSPC board (PicoQuant).

3. RESULTS AND DISCUSSION

3.1. Preparation of Films with Different Morphologies. For investigating the influence of orientation and grain size on the phase transition behavior, energetic disorder, as well as defect properties, we first manufactured $MAPbI_3$ thin films with different morphologies. To do so, we used a dry powder-based two-step processing method comprising (i) film formation by spraying mechanochemically synthesized $MAPbI_3$ powder onto a glass substrate via the PADM and (ii) post-treatment by applying a pressure of 25 MPa for about 50 min to the perovskite films (for details, see Section S1). We chose this approach as producing $MAPbI_3$ films by PADM results in polycrystalline film morphologies,[2,24,25] while pressing polycrystalline halide perovskite films increases the degree of orientation and grain size, especially when the pressing process proceeds at an elevated temperature.[14,26] Therefore, we pressed PADM-processed thin films at room temperature (referred to as cold pressed, CP) and at an elevated temperature of about 100 °C (referred to as hot pressed, HP), producing films with well defined, yet different morphologies.

Following this processing approach, compact films with thicknesses of around ∼4 μm were obtained (see Figure S3a for the cross-sectional SEM image). Top-view SEM images in Figure 1a,b show an average grain size of (150 ± 75) nm for the CP film and (220 ± 110) nm for the HP film (see Figure 1c and Section S1 for details of grain size analysis). Furthermore, less and narrower grain boundaries can be observed for the HP in contrast to the CP film (Figure 1a,b). Increased grain size and narrower grain boundaries in the HP film at the surface as well as throughout the layer thickness are also obvious in the corresponding cross-sectional SEM images (Figure 1d,e). Moreover, the HP film exhibits a reduced surface roughness of Ra_{HP} = 34 nm compared to the CP film with Ra_{CP} = 61 nm. The observed film morphology improvements are in line with previous literature reports about thermal pressure treatment of $MAPbI_3$ thin films.[26−29]

To investigate whether the increase in grain size is also accompanied by an increase in $MAPbI_3$ crystallite size, we measured XRD patterns of the HP and CP films. Figure 1f shows corresponding normalized XRD patterns in the 2θ range between 13.7 and 28.8°, which contain the reflex pairs 002, 110 and 004, 220 of $MAPbI_3$ in its tetragonal crystal structure.[30] From Figure 1f, it becomes clear that the HP film (red line) exhibits narrower reflexes compared to the CP film (gray line), indicating a larger crystallite size and/or reduced microstrain in the HP sample. Examining the reflex width by applying the Rietveld refinement method to the measured XRD patterns (Figure S3c), we extract crystallite size information from the width contribution changing with $1/\cos(\theta)$ and information on the microstrain in the sample from the width contribution changing with $\tan(\theta)$ (Section S1). We find crystallite sizes of ∼(130 ± 25) and ∼(350 ± 150) nm for the CP and the HP films, respectively. Within the respective error ranges, these crystallite sizes are similar to the corresponding average grain sizes extracted from the SEM images, suggesting that the grains observed in Figure 1a,b for both films are essentially single crystalline. Applying the Rietveld refinement method, we also find that the extracted microstrain in the HP film (0.028% ± 0.015%) tends to be lower than the corresponding microstrain in the CP film (0.047% ± 0.015%). This reduction is in line with the work of Osherov et al., who suggested that the fraction of the strained perovskite material is higher for smaller grains than for larger grains as strain is predominantly present in the grain boundaries.[31]

In addition to differences in the width of the reflexes in the measured XRD patterns, we find their relative intensities to differ as well (Figure 1f). The 110/002 peak intensity ratio for the HP film (∼3.68) is clearly higher than for the CP film (∼1.55). This behavior also applies to the ratios of corresponding higher order reflexes, such as the 220/004 ratio (see Figure S3c for XRD patterns between 10 and 45°). Exploiting the geometric relationship between the individual scattering planes over the full measured 2θ range, the observed changes in the peak intensity ratio can be well modeled by changes in the preferred orientation. Thus, the peak intensity ratio indicates that hot-pressing compared to cold-pressing induces an increased orientation of the (110) plane parallel to the substrate, i.e., the [110] direction is parallel to the direction where the pressure is applied. This is in line with the observations from our previous work[32] and with the results of Moon et al., where increased crystallite size and preferential crystal plane orientation parallel to the substrate are found for increased temperature during pressing of halide perovskite thin films.[14] In passing, we mention that we observe small amounts of PbI_2 in both samples, reflected by low-intensity reflexes at 12.7°, which are slightly higher in HP than in CP samples (Figure S3c). The increased PbI_2 content after hot-pressing is also reflected in the reduction of the I/Pb ratio from 3.08

https://doi.org/10.1021/acs.jpcc.2c08968
J. Phys. Chem. C 2023, 127, 10563−10573

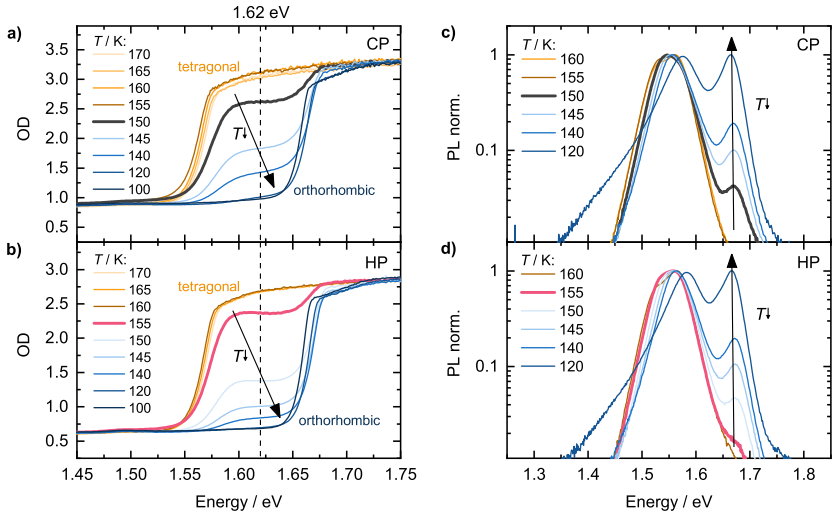

Figure 2. Absorption and PL spectra of $MAPbI_3$ thin films in the phase transition region between 170 and 100 K: optical density of (a) a CP film and (b) an HP film. Normalized PL of (c) a CP film and (d) an HP film. Arrows indicate the phase transition from the tetragonal to orthorhombic phase upon cooling. Gray and red lines represent the first sign of phase transition for CP and HP films, respectively.

(before pressing) to 2.76 after hot-pressing, extracted from XPS spectra (see Figure S4 and Section S1 for details).

Overall, by employing increased temperature during the pressing of the $MAPbI_3$ films, we were able to increase the grain size and induce higher preferred orientation in the film.

3.2. Structural Properties. To investigate how the changes in orientation and grain size of the $MAPbI_3$ films impact their defect properties, degree of energetic disorder, and their behavior when undergoing structural changes, such as crystallographic phase transitions, we measured temperature-dependent steady-state PL and absorption spectra from 300 K down to 5 K of the CP and HP samples.

When cooling and reheating a $MAPbI_3$ thin film across the phase transition between the tetragonal and orthorhombic phases, as it is done in this work, morphological changes are known to occur upon the second passing of the phase transition, i.e., during reheating.[31] To ensure that the small morphology differences induced by hot-pressing are not obscured by additional unintended morphology changes in our case, we first focus on the cooling stage (Sections 3.2.1 and 3.2.2) before also addressing the samples after reheating, shown in Section 3.2.3.

3.2.1. Phase Transition. In the following, we first focus on the phase transition behavior. Between ∼330 and ∼163 K, $MAPbI_3$ exhibits a tetragonal phase, while at temperatures below ∼160 K, it adopts an orthorhombic crystal structure.[33−35]

Figure 2 shows absorption and PL spectra of the CP and HP films between 170 and 100 K, i.e., in the temperature range of the phase transition. When transitioning between tetragonal and orthorhombic phases, it is known that the electronic structure and thus the optical properties of $MAPbI_3$ change substantially.[34,36] In the absorption spectra (Figure 2a,b) at 170 K, an absorption edge is present for both samples at about 1.56 eV, which is associated with the tetragonal phase.[37−39] Upon cooling below 160 K, the absorption reduces in the energy range up to 1.65 eV and vanishes below 120 K. In this temperature range, an absorption edge at about 1.65 eV becomes visible, which is associated to absorption of the orthorhombic phase.[37−39] In general, the temperature-dependent changes of the spectra of CP and HP appear similar. Nevertheless, the first indicator for the phase transition upon cooling is the initial decrease of absorption intensity of the tetragonal phase, occurring at 150 K for the CP sample (gray line in Figure 2a), but it is already occurring at 155 K for the HP sample (red line in Figure 2b). In passing, we mention that the absorption spectra saturate above an OD value of about 2.7 due to limited setup sensitivity.

Similar to the observations in absorption, the PL spectra measured in the phase transition region also exhibit distinct changes. Figure 2c,d shows the corresponding PL spectra between 160 and 120 K of both $MAPbI_3$ samples CP and HP normalized to the PL peak at ∼1.56 eV, which is associated with PL from the tetragonal phase (see Figure S5a,b for unnormalized PL spectra).[36,40,41] Upon cooling, a second PL peak at ∼1.67 eV arises, which corresponds to PL from the orthorhombic phase.[36,40,41] Similar to the absorption, the PL of the orthorhombic phase appears at 150 K for CP (see the gray line in Figure 2c), but it emerges already at 155 K for HP (see the red line in Figure 2d).

For a quantitative analysis of these differences in the phase transition dynamics between the two sample types, we determined the critical phase transition temperature from the absorption spectra in Figure 2a,b following an approach from earlier works.[42,43] To this end, for CP and HP samples, we considered the temperature dependence of the OD at 1.62 eV (Figure 3a), i.e., an energy where only the tetragonal phase absorbs. Then, we calculated the derivative of the temperature-dependent OD resulting in a peak in the temperature range of the phase transition (Figure 3b). The latter was fitted using a Gaussian function, where we associate the peak position with the critical phase transition temperature T_c and the full width at half-maximum (fwhm) with the temperature range over which the phase transition proceeds. We find T_c to be higher for HP ($T_{c,HP}$ = 151.9 K ± 0.3 K) compared to CP ($T_{c,CP}$ = 147.5 K ± 0.4 K). Both values are in agreement with reported phase transition temperatures of polycrystalline $MAPbI_3$ thin films, which cover a range from about 145 to 160

https://doi.org/10.1021/acs.jpcc.2c08968
J. Phys. Chem. C 2023, 127, 10563−10573

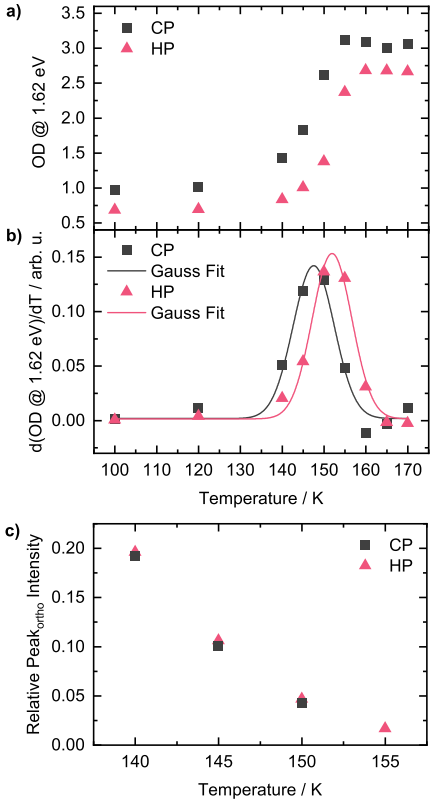

Figure 3. Phase transition analyses for CP (gray) and HP (red) $MAPbI_3$ thin films: (a) optical density@1.62 eV for temperatures between 170 and 100 K extracted from absorption spectra in Figure 2a,b. (b) Derivative of (a) resulting in a peak shape, where the peak position is associated with the critical phase transition temperature. (c) Intensity of the PL peak attributed to the orthorhombic phase relative to the intensity of the PL peak attributed to the tetragonal phase for temperatures between 155 and 140 K.

K.[31,37,39,40,43−45] The extracted fwhms of the transition are similar within the error range for the CP and HP films with $fwhm_{CP} = (11.6 \pm 1.2)$ K and $fwhm_{HP} = (11.1 \pm 0.8)$ K. These fwhm values are in line with the corresponding value of a solution-processed $MAPbI_3$ thin film found in a previous work.[43]

As a next step, we analyzed in more detail how the differences in phase transition are reflected in the PL properties of the two samples. We considered the intensity of the PL of the orthorhombic phase between 155 and 140 K relative to the one of the tetragonal phase (Figure 3c). With decreasing temperature, the relative intensity of the orthorhombic peak increases similarly for both HP and CP, with slightly higher relative intensity values for HP (see also comparison of PL spectra in Figure S5c).

Overall, a retention in the onset of the phase transition to lower temperatures is identified for the CP sample compared to the HP sample.

In the past, the phase transition temperature in $MAPbI_3$ was found to alter depending on the morphology of the investigated sample. For example, decreased phase transition temperatures were observed for $MAPbI_3$ films with smaller grains.[23,44] For nanoparticles and nanocrystals, even a fully suppressed phase transition was reported.[44] Such changes in phase transition behavior were associated with the degree of strain in the perovskite, which is supposed to increase for smaller grain sizes due to a higher fraction of grain boundaries.[19,23,31]

This conclusion is in good agreement with our identified lower phase transition temperature for the CP film, which exhibits a smaller grain size and a higher microstrain compared to that of the HP film (see Section 3.1). The increased PbI_2 content in HP (Figures S3 and S4) is not expected to induce a significant amount of additional distortion related strain[46] compared to strain located at the grain boundaries and thus should not affect the phase transition temperature significantly (see also Section S1). Overall, we suggest that the observed decrease in critical phase transition temperature of the CP sample compared to the HP sample in Figure 3 is associated with an increased amount of strain in the CP sample.

3.2.2. Energetic Disorder. As the degree of strain is known to be correlated with the degree of energetic disorder in halide perovskites,[18,47,48] we next focus on investigating the latter for our samples.

Energetic disorder in semiconductors impacts their optical properties. For example, often, an exponentially decreasing absorption tail below the band gap is observed, which is referred to as Urbach tail absorption.[49,50] The slope of this Urbach tail is determined by the so-called Urbach energy E_U, which in turn is influenced by static and dynamic disorder.[49,50]

E_U, and thus the degree of energetic disorder, is also reflected in the shape of the corresponding PL. Based on the reciprocity theorem, the (intrinsic) PL is proportional to

$$\mathrm{PL} \propto \alpha(E)\cdot E^2 \cdot \exp\left(-\frac{E}{k_B T}\right) \tag{1}$$

where E is the photon energy, α is the absorption coefficient, k_B is the Boltzmann constant, and T is the absolute temperature of the sample.[36,50,51] Equation 1 is valid for any two-state system that can be described by a spatially independent quasi-Fermi level splitting, which is a good approximation for lead halide perovskite thin films in the tetragonal phase.[52,53] Considering Urbach tail absorption and a constant absorption above the band gap, the shape of the absorption spectrum of $MAPbI_3$ can be satisfyingly approximated in the spectral range where PL occurs as

$$\alpha(E) \propto \frac{1}{\exp\left(-\frac{E-E_0}{E_U}\right)+1} \tag{2}$$

with E_0 being a fitting constant with a value near the band gap energy.[36] Inserting eq 2 into eq 1, it follows that the high energy edge of the PL (i.e., $E \gg E_0$) is essentially determined by $\exp(-E/k_BT)$, while the low energy edge (i.e., $E \ll E_0$) is proportional to $\exp\left(\frac{E-E_0}{E_U} - \frac{E}{k_BT}\right)$. Analysis approaches based on eq 1 have been used successfully in the past, e.g., by Fassl et al., to extract the Urbach energy from the PL spectra of $MAPbI_3$.[54]

For extracting the Urbach energy from our PL data, we focus on the PL of the tetragonal phase between 300 and 160 K as at lower temperatures, additional PL contributions (such as defect-associated PL, see, e.g., Figure S5) complicate or even inhibit the reliable extraction of the Urbach energy from the PL spectra. Figure 4a shows the PL spectra of the CP film

https://doi.org/10.1021/acs.jpcc.2c08968
J. Phys. Chem. C 2023, 127, 10563−10573

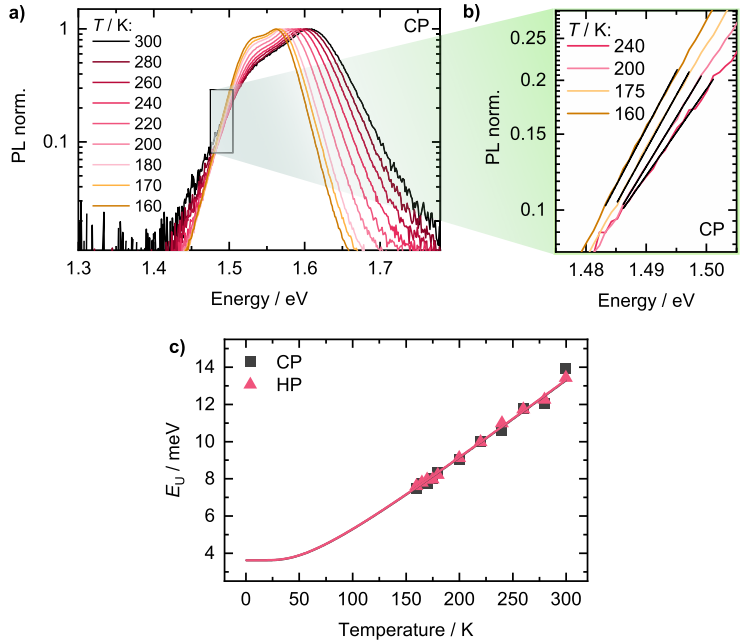

Figure 4. Energetic disorder analysis for pressed $MAPbI_3$ thin films by extracting the Urbach energy from PL spectra: (a) normalized PL spectra of a CP film in the tetragonal phase between 300 and 160 K and (b) corresponding exemplary fits of the low energy edge based on eq 1. (c) Extracted Urbach energies from fits as shown in (b) for a CP film (gray squares) and an HP film (red triangles). The lines represent fits according to eq 3 to extract the static disorder.

between 300 and 160 K (corresponding PL spectra of HP in Figure S6a). At 300 K, the spectrum consists of one main peak at 1.61 eV and a shoulder at about 1.53 eV, with the latter being associated with a self-absorption effect. The main PL peak originates from PL that comes directly from (near) the surface of the sample, whereas the feature at lower energies is caused by PL that is internally reflected and filtered by the absorption of the sample (see Figure S6b,c).[43,54,55] Upon cooling, the PL spectrum shifts to lower energies and becomes narrower.[44,45]

To extract the Urbach energies from the PL spectra, we fitted the low energy edge of the PL based on eq 1 according to $\mathrm{PL}(E \ll E_0) = C \cdot \exp\left(\frac{E - E_0}{E_U} - \frac{E}{k_B T}\right)$, where C is a fitting parameter accounting for the PL intensity (exemplary fits in Figure 4b). Figure 4c shows the extracted E_U values between 300 and 160 K for both samples CP and HP. Upon cooling, E_U decreases similarly for both samples from about 14 meV at 300 K to 7.5 meV at 160 K. The extracted Urbach energies are in very good agreement with results from our previous work about $MAPbI_3$ single crystals[36] and the work of Ledinsky et al. about $MAPbI_3$ thin films.[50]

As mentioned above, the Urbach energy is determined by static disorder E_U^{stat} and dynamic disorder E_U^{dyn}, and its temperature-dependence can be described by[50,56]

$$E_U(T) = E_U^{stat} + E_U^{dyn} = E_U^{stat} + 2 \cdot E_U^{stat} \left[\exp\left(\frac{\Theta}{T}\right) - 1\right]^{-1} \quad (3)$$

Here, E_U^{stat} is assumed to be temperature-independent. The temperature-dependence of E_U^{dyn} is described in terms of the interaction of charge carriers with phonons in the coupled Einstein oscillator model with the Einstein temperature Θ.[49,50,56] We fitted the extracted Urbach energies in Figure 4c using eq 3 (solid lines in Figure 4c). Assuming that the energies of the phonons interacting with charge carriers are essentially identical for both samples, we fixed Θ = 167 K (corresponding to a phonon energy of 14.4 meV) based on the work of Xia et al.[57] With this, we obtained $E_{U,CP}^{stat}$ = (3.61 ± 0.03) meV for CP and $E_{U,HP}^{stat}$ = (3.61 ± 0.01) meV for HP. These static disorder values are in very good agreement with reported values for $MAPbI_3$ single crystals[36] as well as $MAPbI_3$ thin films, and they are remarkably low compared to classical inorganic crystalline semiconductors (e.g., GaAs and c-Si).[50]

The identical values for the static disorder of both CP and HP are somewhat surprising as differences in phase transition behavior associated with different amounts of strain in the samples were identified in Section 3.2.1, and strain in turn is expected to affect the energetic disorder.[18,47] One reason for the identical E_U^{stat} values observed in our analysis for both CP and HP might be that PL tends to track more sites with lower energetic disorder since charge carriers relax to beneficial sites with lower energy before recombining radiatively.[58,59] Additionally, lower nonradiative decay rates are typically present at sites with lower energetic disorder.[16,20,60] Therefore, sites with lower energetic disorder may contribute overproportionally to the PL spectra and obscure the signatures of sites with higher energetic disorder. Another reason might be that PL, which mainly probes the top side of the films,[48] is not bulk-sensitive enough to detect strain-associated energetic disorder from the perovskite–substrate interface.[21,61−63] A systematic investigation differentiating the above-mentioned aspects by elaborating and applying more sophisticated Urbach analysis methods is beyond the scope of this work, but it will be addressed in a future study.

https://doi.org/10.1021/acs.jpcc.2c08968
J. Phys. Chem. C 2023, 127, 10563−10573

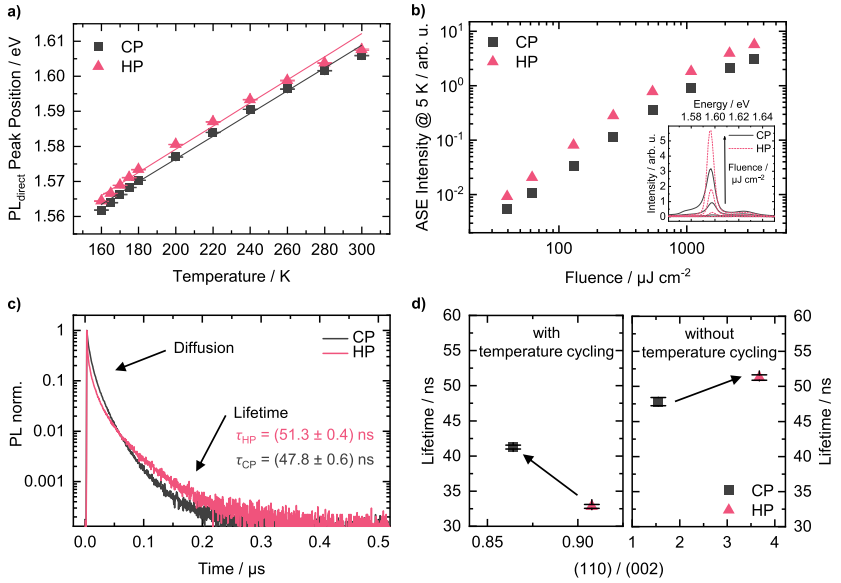

Figure 5. Excited state properties of CP (gray) and HP (red) $MAPbI_3$ thin films: (a) PL peak position between 300 and 160 K with linear fits. (b) Fluence-dependent ASE peak intensity@5 K and inset with corresponding exemplary PL spectra. (c) TRPL curves measured at room temperature with extracted lifetimes from the mono-exponential tail. (d) Left panel: lifetimes dependent on 002-preferred orientation after temperature cycling, i.e., cooling the sample to 5 K for the temperature-dependent measurements and heating it back to room temperature. Right panel: lifetimes dependent on the 110-preferred orientation without temperature cycling measured at room temperature.

3.2.3. Excited State Properties—Defects. Increased strain in halide perovskite films is correlated with increased energetic disorder,[18] and increased energetic disorder in turn is related to more defect states.[16,20,22] Moreover, increased strain in halide perovskites is known to be directly correlated with increased non-radiative losses and defect states.[17,19,21,23] Therefore, in the following, we investigate whether the larger strain in CP identified in Sections 3.1 and 3.2.1 is reflected in the excited state properties and thus in the defect densities. To this end, we performed further PL analyses.

Figure 5a shows the peak positions of the direct PL signature as a function of temperature between 300 and 160 K for both, CP and HP (see Section S2 for details). Solid lines represent linear fits to the data, with the corresponding slopes s serving as a measure of the known PL red shift with decreasing temperature (see also Figures 4a and S6a).[39,44,45] The extracted shifts of s_{CP} = (0.32 ± 0.01) meV K^{-1} for CP (R^2 ≈ 0.99) and s_{HP} = (0.33 ± 0.01) meV K^{-1} for HP (R^2 ≈ 0.99) are identical within the uncertainty of the fit. This suggests that the additional tensile strain induced by the substrate upon cooling[19,43,62,63] is similar in CP and HP, which is reasonable considering the identical substrate materials and the similar layer thickness for both samples (for details, see Section S2). The overall peak position of HP, however, is shifted by approximately 2 meV to higher energies compared to the values of CP. We associate this PL peak shift between both samples with different impacts of self-absorption on the direct PL caused by a lower defect density near the film surface in HP compared to CP: with lower defect density near the surface, more direct PL is emitted closer to the surface. Thereby, the influence of self-absorption on the direct PL is reduced, enabling more high-energy photons to contribute to the measured PL spectra. This, in turn, results in less peak shift to lower energies compared to the intrinsic PL spectrum.[43,64]

To verify the conclusion about differences in defect densities between CP and HP, we measured fluence-dependent PL spectra between about 40 μJ cm^{-2} and 3400 μJ cm^{-2} at 5 K, which are shown in the inset of Figure 5b and in detail in Figure S7. With increasing fluence, a sharp peak arises at 1.597 eV in the PL spectra, which is attributed to amplified spontaneous emission (ASE).[65,66] In Figure 5b, the fluence-dependent intensity of the ASE peak is shown for both CP and HP. The ASE intensity of HP is higher by about 70−150%, indicating higher crystallinity as well as longer charge carrier lifetimes in HP.[67,68] This is in line with the lower defect density in HP concluded from the analyses of Figure 5a.

To extract the charge carrier lifetimes for CP and HP, we measured TRPL of both samples at room temperature. The results are shown in Figure 5c. Up to 0.05 μs, the PL intensity of HP decreases faster than for CP, but it shows a slower decay at longer times. The faster initial decrease of the PL intensity of HP can be explained by stronger diffusion of charge carriers,[69] which is consistent with a higher crystallinity of HP compared to the CP film.[70] Furthermore, the slower decay of the PL intensity at longer times for HP indicates longer charge carrier lifetimes in HP. We extracted charge carrier lifetimes by applying mono-exponential fits to the tail of the PL curves at times higher than ~0.1 μs (see Figure S8a). As expected from the higher crystallinity and the slower decay at longer times of HP, the charge carrier lifetime τ_{HP} = (51.3 ± 0.4) ns of HP is higher than the extracted charge carrier lifetime τ_{CP} = (47.8 ± 0.6) ns of CP, again indicating less defects being present in HP than in CP.[59,71]

Since CP and HP show different degrees of preferred orientation (see Figure 1f), we aim to correlate the charge carrier lifetime with the degree of preferred orientation in our samples (Figure 5d). From Figure 5d right panel, it appears that the charge carrier lifetime increases with increasing

https://doi.org/10.1021/acs.jpcc.2c08968
J. Phys. Chem. C 2023, 127, 10563−10573

orientation of the (110) plane parallel to the substrate, i.e., from CP to HP. We note that this increase might be promoted by the larger grain sizes in HP. Remarkably, after a temperature cycle (i.e., cooling the sample to 5 K for the temperature-dependent measurements and heating it back to room temperature), the preferred orientation parallel to the substrate changed for both samples toward a 002-preferred orientation, where the CP sample shows a more pronounced 002 orientation than HP (Figure S8c,d). Here again, the charge carrier lifetime increases with increasing orientation, this time from HP to CP (see Figure 5d left panel) though CP consists of smaller grains than HP.

The crystallographic reorientation upon temperature cycling through a phase transition accompanied by a fusion of grain domains (Figure S9a) observed in our case has also been observed by Kavadiya et al. for the transition between tetragonal and cubic phases[72] as well as by Osherov et al. for the transition between tetragonal and orthorhombic phases.[31] By temperature-dependent XRD measurements, Osherov et al. found these morphological changes in $MAPbI_3$ thin films not to occur in the course of the initial phase transition during cooling but after the subsequent phase transition upon reheating the films.[31] We speculate that the overall decreased charge carrier lifetimes of the films after temperature cycling (Figure 5d) result from a detrimental effect of the morphological changes in the course of temperature cycling.

However, stronger crystallographic orientation—preferred either in the (110) or in (002) plane—in general seems to result in an increased excited state lifetime (Figure 5d). This might be related to the quality of the grain boundaries, which is expected to improve for a more aligned orientation of adjacent grains.[46] This observation is an interesting qualitative insight, possibly highlighting the importance of the degree of crystallographic orientation for the optimization of the perovskite's optoelectronic properties. In this regard, a detailed study about the correlation between crystallographic orientation and excited state properties would be interesting in the future, including consideration of aspects such as in-plane orientation or the role of a certain amount of PbI_2 present in the films due to processing and degradation.

4. CONCLUSIONS

In summary, we investigate the influence of small morphology differences in $MAPbI_3$ thin films on phase transition, energetic disorder, and defects by detailed PL and absorption analyses. To this end, $MAPbI_3$ thin films are manufactured via a two-step processing method comprising $MAPbI_3$ film deposition via PADM and pressing as post-treatment. By higher pressing temperature, we induce small increases in grain size and preferred orientation in the thin films.

The larger grains and increased orientation of the (110) plane parallel to the substrate go along with a higher phase transition temperature concluded from temperature-dependent PL and absorption analyses, which we attribute to less strain in HP samples. Although strain is known to correlate with energetic disorder, our Urbach analyses from temperature-dependent PL spectra do not show differences in static disorder between CP and HP films. However, differences in the excited state properties are observed. Here, a lower defect density in films with increased grain size and a higher degree of 110-preferred orientation is found from fluence-dependent and transient PL measurements. The observed interdependency of strain and defect density with grain size and orientation suggests that small differences in energetic disorder are indeed present. More sophisticated analysis methods of the optical spectra as they are currently developing[73,74] yield high potential to fully resolve these small differences in the future. Increased 110- or 002-preferred orientation is observed to result in longer charge carrier lifetimes. This emphasizes that besides the commonly considered grain size, the degree of orientation also seems to play an important role regarding the optoelectronic properties of halide perovskite thin films.

Thus, with the insights gained in this work, it will be possible to better understand and advance the functionality of halide perovskite-based optoelectronic devices such as solar cells in the future.

■ ASSOCIATED CONTENT

Supporting Information

The Supporting Information is available free of charge at https://pubs.acs.org/doi/10.1021/acs.jpcc.2c08968.

Details on film preparation via dry powder-based two-step processing method (PADM + pressing) and additional film morphology analyses including SEM images, XRD patterns, and XPS spectra; additional (temperature- or fluence-dependent) PL spectra, discussion of temperature-dependent PL peak shift, and sketch about direct and filtered PL; fits of TRPL curves for extraction of lifetimes; and XRD patterns, sketch of $MAPbI_3$ unit-cells, SEM and microscopy images for $MAPbI_3$ thin films without, with, and during temperature cycling together with a discussion of structural changes like reorientation in the course of temperature cycling (PDF)

■ AUTHOR INFORMATION

Corresponding Author

Fabian Panzer − *Soft Matter Optoelectronics, University of Bayreuth, Bayreuth 95440, Germany;* orcid.org/0000-0002-2191-9011; Email: fabian.panzer@uni-bayreuth.de

Authors

Christina Witt − *Soft Matter Optoelectronics, University of Bayreuth, Bayreuth 95440, Germany*

Konstantin Schötz − *Soft Matter Optoelectronics, University of Bayreuth, Bayreuth 95440, Germany*

Meike Kuhn − *Dynamics and Structure Formation—Herzig Group, University of Bayreuth, Bayreuth 95440, Germany*

Nico Leupold − *Department of Functional Materials, University of Bayreuth, Bayreuth 95440, Germany*

Simon Biberger − *Soft Matter Optoelectronics, University of Bayreuth, Bayreuth 95440, Germany*

Philipp Ramming − *Soft Matter Optoelectronics, University of Bayreuth, Bayreuth 95440, Germany*

Frank-Julian Kahle − *Soft Matter Optoelectronics, University of Bayreuth, Bayreuth 95440, Germany;* orcid.org/0000-0003-3416-0072

Anna Köhler − *Soft Matter Optoelectronics, University of Bayreuth, Bayreuth 95440, Germany;* orcid.org/0000-0001-5029-4420

Ralf Moos − *Department of Functional Materials, University of Bayreuth, Bayreuth 95440, Germany*

Eva M. Herzig − *Dynamics and Structure Formation—Herzig Group, University of Bayreuth, Bayreuth 95440, Germany;* orcid.org/0000-0002-0151-5562

https://doi.org/10.1021/acs.jpcc.2c08968
J. Phys. Chem. C 2023, 127, 10563−10573

Complete contact information is available at:
https://pubs.acs.org/10.1021/acs.jpcc.2c08968

Notes

The authors declare no competing financial interest.

■ ACKNOWLEDGMENTS

The authors acknowledge financial support from the German National Science Foundation DFG via the projects PA 3373/3-1, MO 1060/32-1, PA 3373/6-1, and KO 3973/3-1. M.K. and E.M.H. gratefully acknowledge funding by the Bavarian State Ministry of Science and the Arts—Collaborative Research Network "Solar Technologies Go Hybrid". The authors further thank Irene Bauer for MAI synthesis, Monika Daubinger for the powder preparation, Daniel Lukas for spraying PADM films, the Department of Metal and Alloys (Prof. Uwe Glatzel) of the University of Bayreuth for the possibility to conduct XRD measurements and the KeyLabs "Electron and Optical Microscopy" and "Device Engineering" of the Bavarian Polymer Institute (BPI) for access to the SEM, the MT200 confocal fluorescence microscope, and the Versa Probe III XPS system.

■ REFERENCES

(1) Teixeira, C. O.; Castro, D.; Andrade, L.; Mendes, A. Selection of the Ultimate Perovskite Solar Cell Materials and Fabrication Processes towards its Industrialization: A Review. *Energy Sci. Eng.* **2022**, *10*, 1478−1525.
(2) Leupold, N.; Panzer, F. Recent Advances and Perspectives on Powder-Based Halide Perovskite Film Processing. *Adv. Funct. Mater.* **2021**, *31*, 2007350.
(3) Buin, A.; Pietsch, P.; Xu, J.; Voznyy, O.; Ip, A. H.; Comin, R.; Sargent, E. H. Materials Processing Routes to Trap-Free Halide Perovskites. *Nano Lett.* **2014**, *14*, 6281−6286.
(4) Jena, A. K.; Kulkarni, A.; Miyasaka, T. Halide Perovskite Photovoltaics: Background, Status, and Future Prospects. *Chem. Rev.* **2019**, *119*, 3036−3103.
(5) Maiti, A.; Chatterjee, S.; Peedikakkandy, L.; Pal, A. J. Defects and Their Passivation in Hybrid Halide Perovskites toward Solar Cell Applications. *Sol. RRL* **2020**, *4*, 2000505.
(6) Jeong, M.; Choi, I. W.; Go, E. M.; Cho, Y.; Kim, M.; Lee, B.; Jeong, S.; Jo, Y.; Choi, H. W.; Lee, J.; et al. Stable Perovskite Solar Cells with Efficiency Exceeding 24.8% and 0.3-V Voltage Loss. *Science* **2020**, *369*, 1615−1620.
(7) Min, H.; Lee, D. Y.; Kim, J.; Kim, G.; Lee, K. S.; Kim, J.; Paik, M. J.; Kim, Y. K.; Kim, K. S.; Kim, M. G.; et al. Perovskite Solar Cells with Atomically Coherent Interlayers on SnO_2 Electrodes. *Nature* **2021**, *598*, 444−450.
(8) NREL. Best Research-Cell Efficiency Chart. https://www.nrel.gov/pv/cell-efficiency.html (accessed Nov 16, 2022).
(9) Kim, M.; Kim, G.-H.; Lee, T. K.; Choi, I. W.; Choi, H. W.; Jo, Y.; Yoon, Y. J.; Kim, J. W.; Lee, J.; Huh, D.; et al. Methylammonium Chloride Induces Intermediate Phase Stabilization for Efficient Perovskite Solar Cells. *Joule* **2019**, *3*, 2179−2192.
(10) Li, Y.; Ji, L.; Liu, R.; Zhang, C.; Mak, C. H.; Zou, X.; Shen, H.-H.; Leu, S.-Y.; Hsu, H.-Y. A Review on Morphology Engineering for Highly Efficient and Stable Hybrid Perovskite Solar Cells. *J. Mater. Chem. A* **2018**, *6*, 12842−12875.
(11) Salim, T.; Sun, S.; Abe, Y.; Krishna, A.; Grimsdale, A. C.; Lam, Y. M. Perovskite-Based Solar Cells: Impact of Morphology and Device Architecture on Device Performance. *J. Mater. Chem. A* **2015**, *3*, 8943−8969.
(12) Wieghold, S.; Correa-Baena, J.-P.; Nienhaus, L.; Sun, S.; Shulenberger, K. E.; Liu, Z.; Tresback, J. S.; Shin, S. S.; Bawendi, M. G.; Buonassisi, T. Precursor Concentration Affects Grain Size, Crystal Orientation, and Local Performance in Mixed-Ion Lead Perovskite Solar Cells. *ACS Appl. Energy Mater.* **2018**, *1*, 6801−6808.
(13) Wu, J.; Zhang, W.; Wang, Q.; Liu, S.; Du, J.; Mei, A.; Rong, Y.; Hu, Y.; Han, H. A Favored Crystal Orientation for Efficient Printable Mesoscopic Perovskite Solar Cells. *J. Mater. Chem. A* **2020**, *8*, 11148−11154.
(14) Moon, J.; Kwon, S.; Alahbakhshi, M.; Lee, Y.; Cho, K.; Zakhidov, A.; Kim, M. J.; Gu, Q. Surface Energy-Driven Preferential Grain Growth of Metal Halide Perovskites: Effects of Nanoimprint Lithography Beyond Direct Patterning. *ACS Appl. Mater. Interfaces* **2021**, *13*, 5368−5378.
(15) Liu, H.; Lee, J.; Kang, J. Characteristics of a Hybrid Detector Combined with a Perovskite Active Layer for Indirect X-ray Detection. *Sensors* **2020**, *20*, 6872.
(16) Frohna, K.; Anaya, M.; Macpherson, S.; Sung, J.; Doherty, T. A. S.; Chiang, Y.-H.; Winchester, A. J.; Orr, K. W. P.; Parker, J. E.; Quinn, P. D.; et al. Nanoscale Chemical Heterogeneity Dominates the Optoelectronic Response of Alloyed Perovskite Solar Cells. *Nat. Nanotechnol.* **2022**, *17*, 190−196.
(17) Jones, T. W.; Osherov, A.; Alsari, M.; Sponseller, M.; Duck, B. C.; Jung, Y.-K.; Settens, C.; Niroui, F.; Brenes, R.; Stan, C. V.; et al. Lattice Strain Causes Non-radiative Losses in Halide Perovskites. *Energy Environ. Sci.* **2019**, *12*, 596−606.
(18) Kim, G.; Min, H.; Lee, K. S.; Lee, D. Y.; Yoon, S. M.; Seok, S. I. Impact of strain relaxation on performance of α-formamidinium lead iodide perovskite solar cells. *Science* **2020**, *370*, 108−112.
(19) Liu, D.; Luo, D.; Iqbal, A. N.; Orr, K. W. P.; Doherty, T. A. S.; Lu, Z.-H.; Stranks, S. D.; Zhang, W. Strain Analysis and Engineering in Halide Perovskite Photovoltaics. *Nat. Mater.* **2021**, *20*, 1337−1346.
(20) Mehdizadeh-Rad, H.; Singh, J. Influence of Urbach Energy, Temperature, and Longitudinal Position in the Active Layer on Carrier Diffusion Length in Perovskite Solar Cells. *ChemPhysChem* **2019**, *20*, 2712−2717.
(21) Moloney, E. G.; Yeddu, V.; Saidaminov, M. I. Strain Engineering in Halide Perovskites. *ACS Mater. Lett.* **2020**, *2*, 1495−1508.
(22) Rajagopal, A.; Liang, P.-W.; Chueh, C.-C.; Yang, Z.; Jen, A. K. Y. Defect Passivation via a Graded Fullerene Heterojunction in Low-Bandgap Pb−Sn Binary Perovskite Photovoltaics. *ACS Energy Lett.* **2017**, *2*, 2531−2539.
(23) Stavrakas, C.; Zelewski, S. J.; Frohna, K.; Booker, E. P.; Galkowski, K.; Ji, K.; Ruggeri, E.; Mackowski, S.; Kudrawiec, R.; Plochocka, P.; et al. Influence of Grain Size on Phase Transitions in Halide Perovskite Films. *Adv. Energy Mater.* **2019**, *9*, 1901883.
(24) Leupold, N.; Seibel, A. L.; Moos, R.; Panzer, F. Electrical Conductivity of Halide Perovskites Follows Expectations from Classical Defect Chemistry. *Eur. J. Inorg. Chem.* **2021**, *2021*, 2882−2889.
(25) Panzer, F.; Hanft, D.; Gujar, T. P.; Kahle, F.-J.; Thelakkat, M.; Köhler, A.; Moos, R. Compact Layers of Hybrid Halide Perovskites Fabricated via the Aerosol Deposition Process—Uncoupling Material Synthesis and Layer Formation. *Materials* **2016**, *9*, 277.
(26) Kim, W.; Jung, M. S.; Lee, S.; Choi, Y. J.; Kim, J. K.; Chai, S. U.; Kim, W.; Choi, D.-G.; Ahn, H.; Cho, J. H.; et al. Oriented Grains with Preferred Low-Angle Grain Boundaries in Halide Perovskite Films by Pressure-Induced Crystallization. *Adv. Energy Mater.* **2018**, *8*, 1702369.
(27) Dunlap-Shohl, W. A.; Li, T.; Mitzi, D. B. Interfacial Effects during Rapid Lamination within $MAPbI_3$ Thin Films and Solar Cells. *ACS Appl. Energy Mater.* **2019**, *2*, 5083−5093.
(28) Mayer, A.; Buchmüller, M.; Wang, S.; Steinberg, C.; Papenheim, M.; Scheer, H.-C.; Pourdavoud, N.; Haeger, T.; Riedl, T. Thermal Nanoimprint to Improve the Morphology of $MAPbX_3$ (MA = methylammonium, X = I or Br). *J. Vac. Sci. Technol., B* **2017**, *35*, 06G803.
(29) Xiao, J.; Yang, Y.; Xu, X.; Shi, J.; Zhu, L.; Lv, S.; Wu, H.; Luo, Y.; Li, D.; Meng, Q. Pressure-Assisted $CH_3NH_3PbI_3$ Morphology Reconstruction to Improve the High Performance of Perovskite Solar Cells. *J. Mater. Chem. A* **2015**, *3*, 5289−5293.

(30) Baikie, T.; Fang, Y.; Kadro, J. M.; Schreyer, M.; Wei, F.; Mhaisalkar, S. G.; Graetzel, M.; White, T. J. Synthesis and Crystal Chemistry of the Hybrid Perovskite $(CH_3NH_3)PbI_3$ for Solid-State Sensitised Solar Cell Applications. *J. Mater. Chem. A* **2013**, *1*, 5628−5641.
(31) Osherov, A.; Hutter, E. M.; Galkowski, K.; Brenes, R.; Maude, D. K.; Nicholas, R. J.; Plochocka, P.; Bulović, V.; Savenije, T. J.; Stranks, S. D. The Impact of Phase Retention on the Structural and Optoelectronic Properties of Metal Halide Perovskites. *Adv. Mater.* **2016**, *28*, 10757−10763.
(32) Witt, C.; Schmid, A.; Leupold, N.; Schultz, M.; Höcker, J.; Baumann, A.; Moos, R.; Panzer, F. Impact of Pressure and Temperature on the Compaction Dynamics and Layer Properties of Powder-Pressed Methylammonium Lead Halide Thick Films. *ACS Appl. Electron. Mater.* **2020**, *2*, 2619−2628.
(33) Guo, X.; McCleese, C.; Kolodziej, C.; Samia, A. C. S.; Zhao, Y.; Burda, C. Identification and Characterization of the Intermediate Phase in Hybrid Organic−Inorganic $MAPbI_3$ Perovskite. *Dalton Trans.* **2016**, *45*, 3806−3813.
(34) Kong, W.; Ye, Z.; Qi, Z.; Zhang, B.; Wang, M.; Rahimi-Iman, A.; Wu, H. Characterization of an Abnormal Photoluminescence Behavior Upon Crystal-Phase Transition of Perovskite $CH_3NH_3PbI_3$. *Phys. Chem. Chem. Phys.* **2015**, *17*, 16405−16411.
(35) Onoda-Yamamuro, N.; Matsuo, T.; Suga, H. Calorimetric and IR Spectroscopic Studies of Phase Transitions in Methylammonium Trihalogenoplumbates (II). *J. Phys. Chem. Solids* **1990**, *51*, 1383−1395.
(36) Schötz, K.; Askar, A. M.; Köhler, A.; Shankar, K.; Panzer, F. Investigating the Tetragonal-to-Orthorhombic Phase Transition of Methylammonium Lead Iodide Single Crystals by Detailed Photoluminescence Analysis. *Adv. Opt. Mater.* **2020**, *8*, 2000455.
(37) Findik, G.; Biliroglu, M.; Seyitliyev, D.; Mendes, J.; Barrette, A.; Ardekani, H.; Lei, L.; Dong, Q.; So, F.; Gundogdu, K. High-temperature Superfluorescence in Methylammonium Lead Iodide. *Nat. Photonics* **2021**, *15*, 676−680.
(38) Panzer, F.; Li, C.; Meier, T.; Köhler, A.; Huettner, S. Impact of Structural Dynamics on the Optical Properties of Methylammonium Lead Iodide Perovskites. *Adv. Energy Mater.* **2017**, *7*, 1700286.
(39) Singh, S.; Li, C.; Panzer, F.; Narasimhan, K. L.; Graeser, A.; Gujar, T. P.; Köhler, A.; Thelakkat, M.; Huettner, S.; Kabra, D. Effect of Thermal and Structural Disorder on the Electronic Structure of Hybrid Perovskite Semiconductor $CH_3NH_3PbI_3$. *J. Phys. Chem. Lett.* **2016**, *7*, 3014−3021.
(40) Panzer, F.; Baderschneider, S.; Gujar, T. P.; Unger, T.; Bagnich, S.; Jakoby, M.; Bässler, H.; Hüttner, S.; Köhler, J.; Moos, R.; et al. Reversible Laser-Induced Amplified Spontaneous Emission from Coexisting Tetragonal and Orthorhombic Phases in Hybrid Lead Halide Perovskites. *Adv. Opt. Mater.* **2016**, *4*, 917−928.
(41) Wu, K.; Bera, A.; Ma, C.; Du, Y.; Yang, Y.; Li, L.; Wu, T. Temperature-Dependent Excitonic Photoluminescence of Hybrid Organometal Halide Perovskite Films. *Phys. Chem. Chem. Phys.* **2014**, *16*, 22476−22481.
(42) Meier, T.; Gujar, T. P.; Schönleber, A.; Olthof, S.; Meerholz, K.; van Smaalen, S.; Panzer, F.; Thelakkat, M.; Köhler, A. Impact of Excess PbI_2 on the Structure and the Temperature Dependent Optical Properties of Methylammonium Lead Iodide Perovskites. *J. Mater. Chem. C* **2018**, *6*, 7512−7519.
(43) Schötz, K.; Askar, A. M.; Peng, W.; Seeberger, D.; Gujar, T. P.; Thelakkat, M.; Köhler, A.; Huettner, S.; Bakr, O. M.; Shankar, K.; et al. Double Peak Emission in Lead Halide Perovskites by Self-Absorption. *J. Mater. Chem. C* **2020**, *8*, 2289−2300.
(44) Lee, K. J.; Turedi, B.; Giugni, A.; Lintangpradipto, M. N.; Zhumekenov, A. A.; Alsalloum, A. Y.; Min, J.-H.; Dursun, I.; Naphade, R.; Mitra, S.; et al. Domain-Size-Dependent Residual Stress Governs the Phase-Transition and Photoluminescence Behavior of Methylammonium Lead Iodide. *Adv. Funct. Mater.* **2021**, *31*, 2008088.
(45) Wright, A. D.; Verdi, C.; Milot, R. L.; Eperon, G. E.; Pérez-Osorio, M. A.; Snaith, H. J.; Giustino, F.; Johnston, M. B.; Herz, L. M. Electron−Phonon Coupling in Hybrid Lead Halide Perovskites. *Nat. Commun.* **2016**, *7*, 11755.
(46) Rothmann, M. U.; Kim, J. S.; Borchert, J.; Lohmann, K. B.; O'Leary, C. M.; Sheader, A. A.; Clark, L.; Snaith, H. J.; Johnston, M. B.; Nellist, P. D.; et al. Atomic-Scale Microstructure of Metal Halide Perovskite. *Science* **2020**, *370*, No. eabb5940.
(47) Qiao, L.; Fang, W.-H.; Long, R.; Prezhdo, O. V. Elimination of Charge Recombination Centers in Metal Halide Perovskites by Strain. *J. Am. Chem. Soc.* **2021**, *143*, 9982−9990.
(48) Regalado-Pérez, E.; Díaz-Cruz, E. B.; Landa-Bautista, J.; Mathews, N. R.; Mathew, X. Impact of Vertical Inhomogeneity on the Charge Extraction in Perovskite Solar Cells: A Study by Depth-Dependent Photoluminescence. *ACS Appl. Mater. Interfaces* **2021**, *13*, 11833−11844.
(49) Cody, G. D.; Tiedje, T.; Abeles, B.; Moustakas, T. D.; Brooks, B.; Goldstein, Y. Disorder and the Optical-Absorption Edge of Hydrogenated Amorphous Silicon. *Phys. Rev. Lett.* **1981**, *47*, 1480−1483.
(50) Ledinsky, M.; Schönfeldová, T.; Holovský, J.; Aydin, E.; Hájková, Z.; Landová, L.; Neyková, N.; Fejfar, A.; De Wolf, S. Temperature Dependence of the Urbach Energy in Lead Iodide Perovskites. *J. Phys. Chem. Lett.* **2019**, *10*, 1368−1373.
(51) Staub, F.; Hempel, H.; Hebig, J.-C.; Mock, J.; Paetzold, U. W.; Rau, U.; Unold, T.; Kirchartz, T. Beyond Bulk Lifetimes: Insights into Lead Halide Perovskite Films from Time-Resolved Photoluminescence. *Phys. Rev. Appl.* **2016**, *6*, 044017.
(52) Kirchartz, T.; Márquez, J. A.; Stolterfoht, M.; Unold, T. Photoluminescence-Based Characterization of Halide Perovskites for Photovoltaics. *Adv. Energy Mater.* **2020**, *10*, 1904134.
(53) Rey, G.; Spindler, C.; Babbe, F.; Rachad, W.; Siebentritt, S.; Nuys, M.; Carius, R.; Li, S.; Platzer-Björkman, C. Absorption Coefficient of a Semiconductor Thin Film from Photoluminescence. *Phys. Rev. Appl.* **2018**, *9*, 064008.
(54) Fassl, P.; Lami, V.; Berger, F. J.; Falk, L. M.; Zaumseil, J.; Richards, B. S.; Howard, I. A.; Vaynzof, Y.; Paetzold, U. W. Revealing the Internal Luminescence Quantum Efficiency of Perovskite Films via Accurate Quantification of Photon Recycling. *Matter* **2021**, *4*, 1391−1412.
(55) Patel, J. B.; Wright, A. D.; Lohmann, K. B.; Peng, K.; Xia, C. Q.; Ball, J. M.; Noel, N. K.; Crothers, T. W.; Wong-Leung, J.; Snaith, H. J.; et al. Light Absorption and Recycling in Hybrid Metal Halide Perovskite Photovoltaic Devices. *Adv. Energy Mater.* **2020**, *10*, 1903653.
(56) Ayik, C.; Studenyak, I.; Kranjec, M.; Kurik, M. Urbach Rule in Solid State Physics. *Int. J. Opt. Appl.* **2014**, *4*, 76−83.
(57) Xia, C. Q.; Peng, J.; Poncé, S.; Patel, J. B.; Wright, A. D.; Crothers, T. W.; Uller Rothmann, M.; Borchert, J.; Milot, R. L.; Kraus, H.; et al. Limits to Electrical Mobility in Lead-Halide Perovskite Semiconductors. *J. Phys. Chem. Lett.* **2021**, *12*, 3607−3617.
(58) Bhuyan, S.; Mondal, R.; Pal, B.; Bansal, B. Distinguishing Quantum Dot-like Localized States from Quantum Well-like Extended States Across the Exciton Emission Line in a Quantum Well. *J. Phys.: Condens. Matter* **2018**, *30*, 105402.
(59) Herz, L. M. Charge-Carrier Dynamics in Organic-Inorganic Metal Halide Perovskites. *Annu. Rev. Phys. Chem.* **2016**, *67*, 65−89.
(60) Mrkyvkova, N.; Held, V.; Nádaždy, P.; Subair, R.; Majkova, E.; Jergel, M.; Vlk, A.; Ledinsky, M.; Kotlár, M.; Tian, J.; et al. Combined in Situ Photoluminescence and X-ray Scattering Reveals Defect Formation in Lead-Halide Perovskite Films. *J. Phys. Chem. Lett.* **2021**, *12*, 10156−10162.
(61) Haeger, T.; Heiderhoff, R.; Riedl, T. Thermal Properties of Metal-Halide Perovskites. *J. Mater. Chem. C* **2020**, *8*, 14289−14311.
(62) Meng, W.; Zhang, K.; Osvet, A.; Zhang, J.; Gruber, W.; Forberich, K.; Meyer, B.; Heiss, W.; Unruh, T.; Li, N.; et al. Revealing the Strain-associated Physical Mechanisms Impacting the Performance and Stability of Perovskite Solar Cells. *Joule* **2022**, *6*, 458−475.
(63) Zhao, J.; Deng, Y.; Wei, H.; Zheng, X.; Yu, Z.; Shao, Y.; Shield, J. E.; Huang, J. Strained Hybrid Perovskite Thin Films and their

https://doi.org/10.1021/acs.jpcc.2c08968
J. Phys. Chem. C 2023, 127, 10563−10573

Impact on the Intrinsic Stability of Perovskite Solar Cells. *Sci. Adv.* **2017**, *3*, No. eaao5616.
(64) van der Pol, T. P. A.; Datta, K.; Wienk, M. M.; Janssen, R. A. J. The Intrinsic Photoluminescence Spectrum of Perovskite Films. *Adv. Opt. Mater.* **2022**, *10*, 2102557.
(65) Qaid, S. M. H.; Khan, M. N.; Alqasem, A.; Hezam, M.; Aldwayyan, A. Restraining Effect of Film Thickness on the Behaviour of Amplified Spontaneous Emission from Methylammonium Lead Iodide Perovskite. *IET Optoelectron.* **2019**, *13*, 2−6.
(66) Qin, L.; Lv, L.; Li, C.; Zhu, L.; Cui, Q.; Hu, Y.; Lou, Z.; Teng, F.; Hou, Y. Temperature Dependent Amplified Spontaneous Emission of Vacuum Annealed Perovskite Films. *RSC Adv.* **2017**, *7*, 15911−15916.
(67) Li, Y.; Allegro, I.; Kaiser, M.; Malla, A. J.; Richards, B. S.; Lemmer, U.; Paetzold, U. W.; Howard, I. A. Exciton Versus Free Carrier Emission: Implications for Photoluminescence Efficiency and Amplified Spontaneous Emission Thresholds in Quasi-2D and 3D Perovskites. *Mater. Today* **2021**, *49*, 35−47.
(68) Pourdavoud, N.; Haeger, T.; Mayer, A.; Cegielski, P. J.; Giesecke, A. L.; Heiderhoff, R.; Olthof, S.; Zaefferer, S.; Shutsko, I.; Henkel, A.; et al. Room-Temperature Stimulated Emission and Lasing in Recrystallized Cesium Lead Bromide Perovskite Thin Films. *Adv. Mater.* **2019**, *31*, 1903717.
(69) Witt, C.; Leupold, N.; Ramming, P.; Schötz, K.; Moos, R.; Panzer, F. How the Microstructure of $MAPbI_3$ Powder Impacts Pressure-Induced Compaction and Optoelectronic Thick-Film Properties. *J. Phys. Chem. C* **2022**, *126*, 15424−15435.
(70) Adhyaksa, G. W. P.; Veldhuizen, L. W.; Kuang, Y.; Brittman, S.; Schropp, R. E. I.; Garnett, E. C. Carrier Diffusion Lengths in Hybrid Perovskites: Processing, Composition, Aging, and Surface Passivation Effects. *Chem. Mater.* **2016**, *28*, 5259−5263.
(71) Crothers, T. W.; Milot, R. L.; Patel, J. B.; Parrott, E. S.; Schlipf, J.; Müller-Buschbaum, P.; Johnston, M. B.; Herz, L. M. Photon Reabsorption Masks Intrinsic Bimolecular Charge-Carrier Recombination in $CH_3NH_3PbI_3$ Perovskite. *Nano Lett.* **2017**, *17*, 5782−5789.
(72) Kavadiya, S.; Strzalka, J.; Niedzwiedzki, D. M.; Biswas, P. Crystal Reorientation in Methylammonium Lead Iodide Perovskite Thin Film with Thermal Annealing. *J. Mater. Chem. A* **2019**, *7*, 12790−12799.
(73) Ugur, E.; Ledinský, M.; Allen, T. G.; Holovský, J.; Vlk, A.; De Wolf, S. Life on the Urbach Edge. *J. Phys. Chem. Lett.* **2022**, *13*, 7702−7711.
(74) Zeiske, S.; Sandberg, O. J.; Zarrabi, N.; Wolff, C. M.; Raoufi, M.; Peña-Camargo, F.; Gutierrez-Partida, E.; Meredith, P.; Stolterfoht, M.; Armin, A. Static Disorder in Lead Halide Perovskites. *J. Phys. Chem. Lett.* **2022**, *13*, 7280−7285.

https://doi.org/10.1021/acs.jpcc.2c08968
J. Phys. Chem. C 2023, 127, 10563−10573

Supporting Information to

Orientation and Grain Size in $MAPbI_3$ Thin Films: Influence on Phase Transition, Disorder and Defects

Christina Witt[1], Konstantin Schötz[1], Meike Kuhn[2], Nico Leupold[3], Simon Biberger[1], Philipp Ramming[1], Frank-Julian Kahle[1], Anna Köhler[1], Ralf Moos[3], Eva M. Herzig[2], Fabian Panzer[1*]

[1] Soft Matter Optoelectronics, University of Bayreuth, Bayreuth 95440, Germany

[2] Dynamics and Structure Formation - Herzig Group, University of Bayreuth, Bayreuth 95440, Germany

[3] Department of Functional Materials, University of Bayreuth, Bayreuth 95440, Germany

Corresponding Author:

[*]E-Mail: fabian.panzer@uni-bayreuth.de

Keywords: halide perovskites, hot-pressing, thin films, solar cells, temperature-dependent PL and absorption measurements, dry-processed, structural and optoelectronic properties

1. Film Preparation

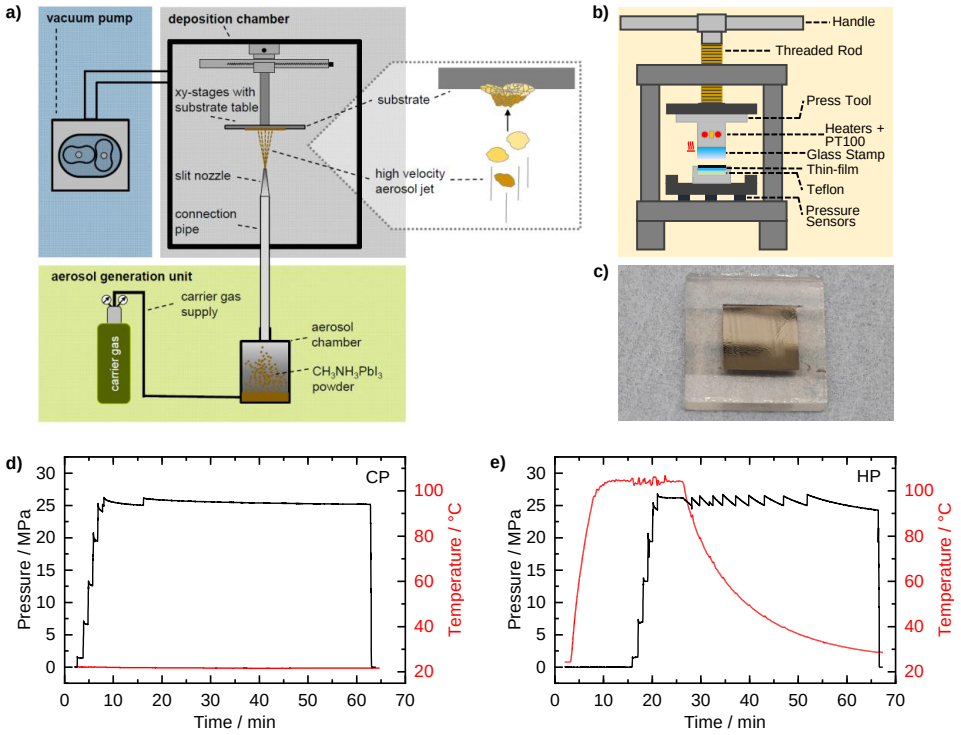

Figure S1: Dry powder-based two-step processing method for $MAPbI_3$ thin films: (a) Film formation via powder aerosol deposition method by using $MAPbI_3$ powder. Adapted under the terms of the CC-BY license.[1] Copyright 2016, the authors. Published by MDPI AG. (b) Post-treatment by (hot-) pressing the thin films with a home-built manual press. (c) Image of an as prepared $MAPbI_3$ thin film (hot-pressed) on a glass substrate. Temporal evolution of pressure and temperature of (d) a cold-pressed (CP) and (e) a hot-pressed (HP) film.

For the film formation we used the so-called powder aerosol deposition method (PADM) illustrated in Figure S1a. In this method, a dry powder aerosol is formed from mechanochemically synthesized $MAPbI_3$ powder in the aerosol generation unit using a carrier gas (for details regarding the powder synthesis see Experimental Section and Leupold N. et al. *ACS Applied Materials & Interfaces* **2019**, 11, 30259-30268[2]). Then the powder aerosol is transferred to the evacuated deposition chamber, where it is further accelerated by a nozzle and directed onto a glass substrate (3 mm thickness). When the powder particles impact the substrate, they break up, bond, and form a dense layer at room temperature. For more details

on PADM we refer to reviews by Hanft et al.,[3] Schubert et al.,[4] and Akedo.[5-6] For our work, before deposition, the powder was dried at 120 °C for 1h. For deposition a total flow rate of 22.5 l/min helium, 0.5 to 1 g of powder, a scan rate of 1 mm/s, at least 24 scans and a substrate-to-nozzle distance of 3 mm were used.

Pressing served as post-treatment for the deposited $MAPbI_3$ films. For this purpose, a manual press was used (sketch in Figure S1b), where pressure can be applied by turning down the installed press stamp. The glass stamp, attached to the metal stamp via heat-conducting paste, was silanized to prevent sticking of the $MAPbI_3$ layer. The substrate with the $MAPbI_3$ film was placed in a press mold. A Teflon plate was placed under the substrate to compensate for possible height differences and thus ensure uniform pressure distribution on the film. The pressure was monitored via the pressure sensors below the press mold. For hot-pressing, the press stamp was heated with two heating cartridges and the temperature was controlled with a PT100 sensor. The temperature could be recorded via the used temperature controller. Figure S1d,e show the time profile of pressure and temperature for a $MAPbI_3$ thin film pressed at room temperature (CP) and a $MAPbI_3$ thin film pressed at elevated temperature (about 100 °C, HP).

Grain sizes were determined for two CP/HP sample pairs from top-view SEM images (Figure 1a,b and Figure S2) using the software imageJ. The grain boundaries were traced with imageJ and the area of all grains completely shown in the image was determined (exemplary selection of grains for a HP film in Figure S3b). An equivalent diameter of a circle was calculated from the area of each grain and referred to as grain size. From all considered grains of a sample, the mean diameter and standard deviation were calculated. The resulting average grain sizes for the sample pair A of (150 ± 75) nm for the CP film and (220 ± 110) nm for the HP film are in good agreement with those of the sample pair B with (130 ± 85) nm for the CP film and (250 ± 150) nm for the HP film (Figure S2).

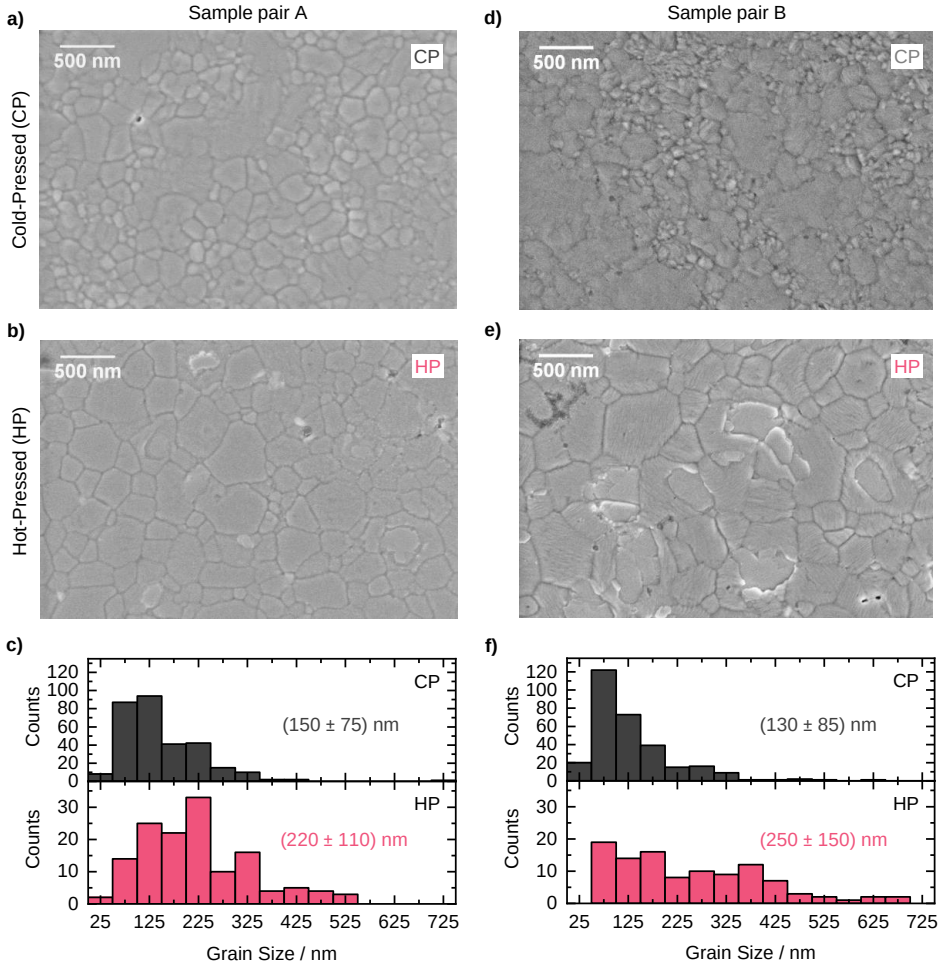

Figure S2: Grain sizes of cold-pressed (CP, grey) and hot-pressed (HP, red) $MAPbI_3$ thin films: (a, b) Top-view SEM images and (c) corresponding grain size distributions for the CP/HP sample pair shown in the main text. (d, e) Top-view SEM images and (f) corresponding grain size distributions for an additional CP/HP sample pair.

The XRD patterns over the entire recorded angular range from 10° to 45° (Figure S3c) are consistent with expectation for $MAPbI_3$ and show that, apart from a small PbI_2 reflex at 12.7°, the films are phase pure.[2] The fits from Rietveld Refinement were applied in the angular range from 19° to 45°, as below 15° the measured intensity may be slightly changed due to X-ray radiation blocked by the sample holder.

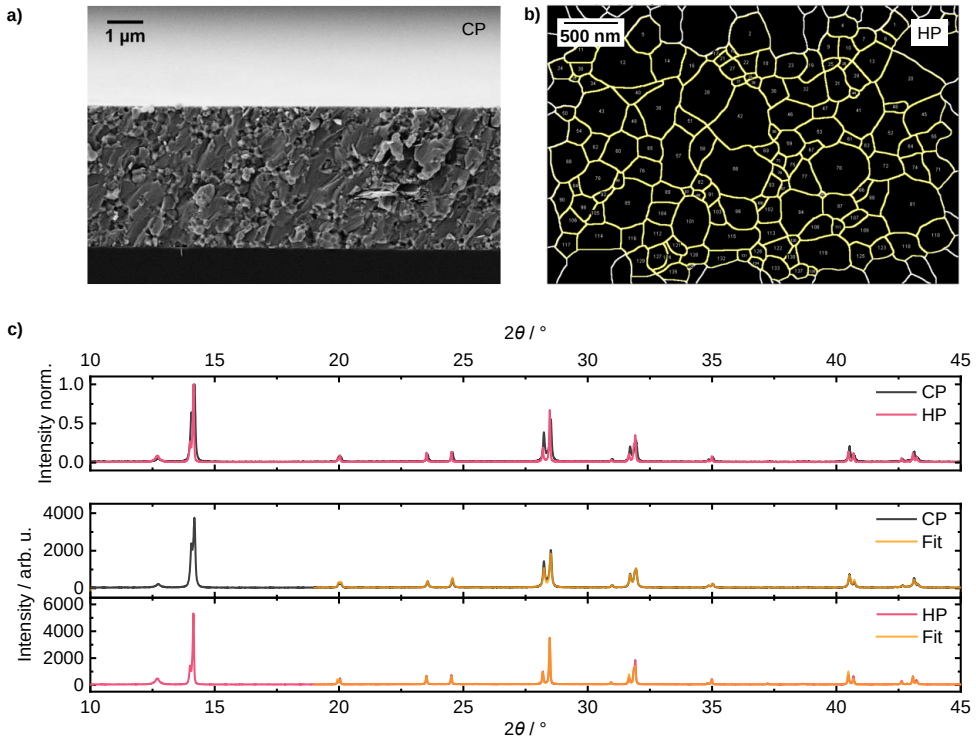

Figure S3: Morphology investigations of pressed $MAPbI_3$ thin films: (a) Cross-section SEM image of a CP film. (b) Grain size analysis via imageJ software from the top-view SEM image of an HP film shown in Figure 1b in the main text. (c) Normalized measured XRD patterns of a CP film (grey line) and an HP film (red line) in the entire measured angular range from 10° to 45° (top panel) and applied fits to the measured XRD patterns (orange lines) from Rietveld refinement in the angular range from 19° to 45° (bottom panel).

To investigate the influence of hot-pressing on the stoichiometry of our $MAPbI_3$ films, we measured XPS spectra (Figure S4) of a $MAPbI_3$ film before pressing (pristine, grey) and after hot-pressing (HP, red).

The XPS spectra give compositional information of the film surface and were measured with a PHI 5000 Versa Probe III Scanning XPS Microscope (ULVAC-PHI). An area of 300 µm x 300 µm in the center of the film was scanned by a microfocused Al Kα X-Ray beam (E = 1486.6 eV, 25 W, 100 µm) and the analyzer. The take-off angle of the photoelectrons was set to 45° and a dual-beam charge neutralizer was utilized for charge compensation.

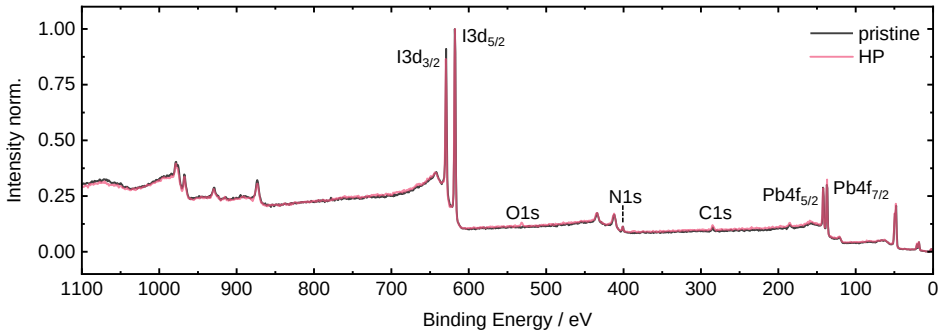

Figure S4: Normalized XPS spectra of a $MAPbI_3$ film before (pristine, grey) and after hot-pressing (HP, red).

The relevant peaks for the stoichiometry analysis of our $MAPbI_3$ ($CH_3NH_3PbI_3$) film corresponding to I3d, N1s, C1s and Pb4f are labeled in Figure S4 (H1s cannot be detected).[7] Overall, the spectra of the pristine and hot-pressed film appear similar at first. However, after hot-pressing an additional small peak corresponding to O1s at about 530 eV appears, as the hot-pressing is performed at ambient conditions. Furthermore, the peak intensities corresponding to I3d and Pb4f indicate a lower I:Pb ratio after hot-pressing. To quantify this, we determined the atomic concentrations from detail scans of the labeled peaks after background correction by evaluating the area under the peaks (for which the peaks were fitted). The atomic concentrations for I and Pb and the resulting I:Pb ratio for the pristine and hot-pressed film are summarized in Table S1. The I:Pb ratio of 3.08 for the pristine film is close to the expected value of 3. After hot-pressing the I:Pb ratio is reduced to a value of 2.76, which indicates more PbI_2 being present at the film surface of HP. This is in line with the increased amount of PbI_2 in the HP sample observed in XRD patterns.

$MAPbI_3$ film	I / %	Pb / %	I:Pb
pristine	47.38	15.37	3.08
HP	40.63	14.72	2.76

Table S1: Atomic concentrations of I and Pb and resulting I:Pb ratio extracted from the XPS spectra of a $MAPbI_3$ film measured before pressing (pristine) and after hot-pressing (HP).

As discussed in Section 3.2.1 in the main text, a decreased phase transition temperature is associated with an increased amount of strain located at the grain boundaries. As an increased amount of PbI_2 indicates imperfections / iodide vacancies in the film, it may be conceivable that PbI_2 leads to additional distortion related strain which further lowers the phase transition temperature.

In a previous work about solution processed $MAPbI_3$ thin films, an increased PbI_2 content was found to correlate with decreased grain size and lower phase transition temperature,[8] indicating that strain at the grain boundaries and/or PbI_2 induced distortion related strain are responsible for lower phase transition temperatures. In the current work, however, an increased PbI_2 content in the HP film goes along with a higher grain size and increased phase transition temperature, emphasizing strain at the grain boundaries to be the main aspect to impact the phase transition temperature. In contrast, PbI_2 induced distortion related strain seems not to have a significant effect on the phase transition temperature. The work of Rothmann et al. supports the minor relevance of PbI_2 induced distortion related strain, as atomic-resolution LAADF micrographs of $FAPbI_3$ show distortion-free transitions between $FAPbI_3$ and PbI_2.[9] Therefore, we conclude that strain at grain boundaries and thus the grain size is mainly affecting the phase transition temperature, whereas PbI_2 induced strain is negligible and thus not relevant regarding the phase transition.

2. PL Spectra

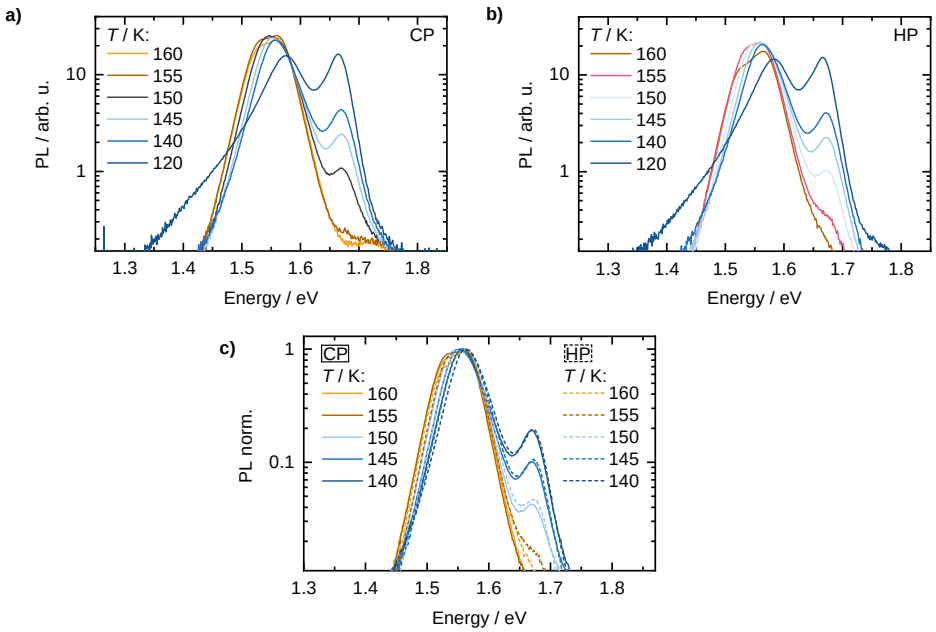

Figure S5: PL spectra of $MAPbI_3$ thin films in the phase transition region between 160 K and 120 K: PL spectra of (a) a CP film and (b) an HP film. (c) Normalized PL spectra of a CP film (solid lines) and an HP film (dashed lines).

The PL spectra between 300 K and 160 K (Figure S6a, Figure 4a in the main text) show a red-shift with decreasing temperature, in line with literature.[10-11] PL_{direct} peak positions were determined from the center of Gauss fits to the PL_{direct} peaks in the PL spectra. The red-shift was evaluated by the slope of linear fits to the temperature-dependent direct PL peak positions (see Figure 5a in the main text). The red-shift is identical within the uncertainty of the linear fits for both CP and HP with a value of about 0.32 meV K^{-1}. This value is in good agreement with reported values for halide perovskites.[12-13] In the past, it was found that in-plane tensile strain is induced by the substrate upon cooling due to its lower thermal expansion coefficient compared to the perovskite layer.[14-15] This substrate induced tensile strain hinders the perovskite lattice constant to decrease during cooling, resulting in a decreased temperature-dependent PL peak shift.[12-14] Since our PL shifts for CP and HP are identical, we conclude that the substrate induced tensile strain is similar in both samples,

which is reasonable with regard to the same substrate materials and the similar film thickness of both samples.

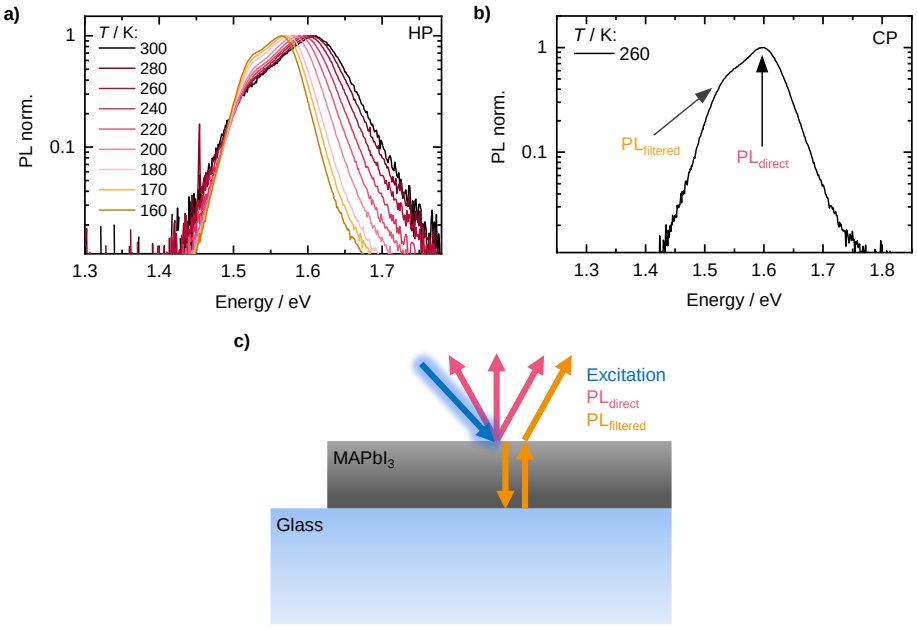

Figure S6: PL in $MAPbI_3$ thin films: (a) Normalized PL spectra of an HP film in the tetragonal phase between 300 K and 160 K. (b) Normalized PL spectrum of a CP film at 260 K with arrows indicating the direct PL peak and the shoulder due to filtered PL. (c) Illustration of emitted PL after excitation of a $MAPbI_3$ thin film on a glass substrate: After excitation (blue arrow) direct PL (red arrows) is emitted from (near) the surface. In addition, filtered PL (orange arrows) is emitted, which is PL travelling through the film, getting internally reflected and overall filtered by the absorption of the sample.

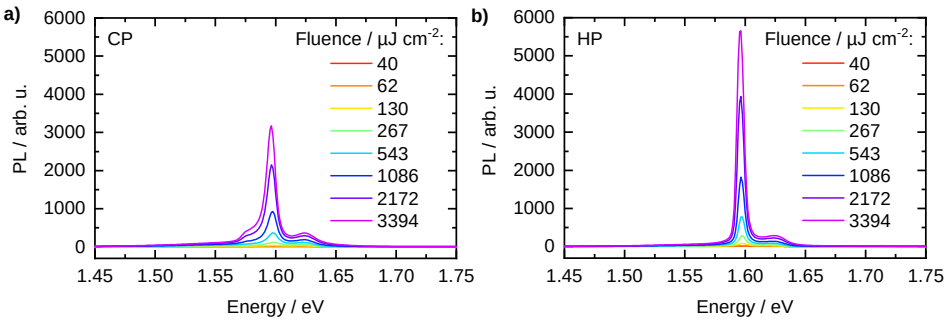

Figure S7: Fluence-dependent PL spectra of (a) a CP and (b) an HP $MAPbI_3$ thin film measured at 5 K.

3. PL Lifetime and Orientation

After temperature cycling (cooling from 300 K to 5 K and reheating to 300 K), our $MAPbI_3$ thin films exhibit morphological changes reflected in reorientation from the 110- to the 002-preferred orientation (see Figure S8b,c,d) and in the formation of strongly fused grain domains

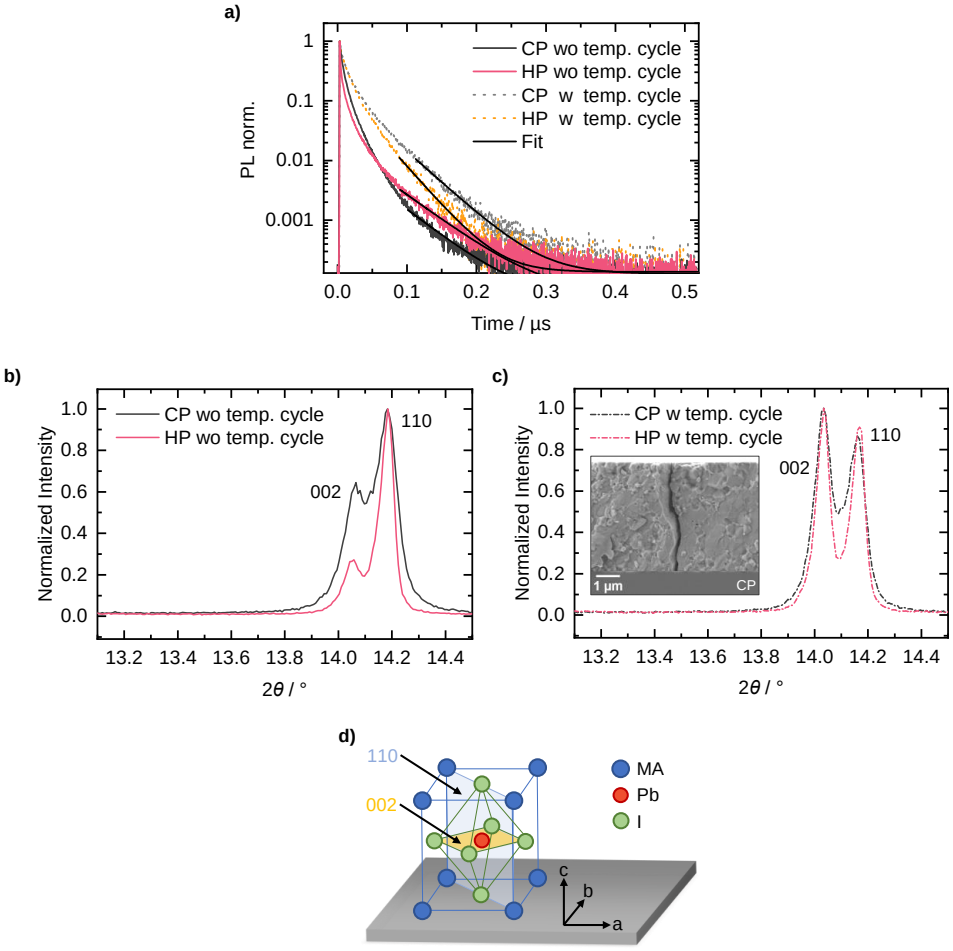

Figure S8: (a) TRPL curves of CP and HP $MAPbI_3$ thin films without (grey and red solid lines) and with (grey and orange dashed lines) temperature cycling. To extract charge carrier lifetimes, mono-exponential fits were applied to the tail of the PL curves (black solid lines). XRD pattern of the 002, 110 reflex pair for a CP (grey) and an HP (red) $MAPbI_3$ thin film (b) without and (c) with temperature cycling. The inset in (c) shows a cross-section SEM image of a CP film with a crack throughout the

film thickness after temperature cycling. (d) Sketch of $MAPbI_3$ unit cell with 110 (blue) and 002 (yellow) planes indicated.

(separated by cracks, see inset in Figure S8c and Figure S9a). Crystallographic reorientation in $MAPbI_3$ thin films due to temperature cycling through phase transitions as well as associated fusion of grains and grain domains have already been observed earlier.[16-17] Osherov et al. have investigated the morphological changes due to temperature cycling across the transition between tetragonal and orthorhombic phase using temperature-dependent XRD measurements. They observed that reorientation does not yet occur when $MAPbI_3$ thin films are cooled below the phase transition temperature but when they are reheated and pass the phase transition again. Since reorientation has been observed only in $MAPbI_3$ thin films and not in $MAPbI_3$ powder samples, Osherov et al. suggest that the morphological changes result from the (hindering or promoting) influence of the substrate in the alignment of crystallographic domains.[17] During temperature cycling, such an influence of the substrate can possibly result from the thermal coefficient mismatch between the glass substrate and the perovskite layer.[14] We suppose that similar to the morphological changes observed by Osherov et al., morphological changes were induced in our $MAPbI_3$ thin films by temperature cycling between 300 K and 5 K. In parallel to the observations of Osherov et al. we assume that the morphological changes occur when the phase transition is crossed during reheating.[17] Therefore, all optical measurements in this work, which were already recorded in the first part of the temperature cycle during cooling, are considered as unaffected by the discussed morphological changes, i.e., reorientation and fusion of grain domains with associated formation of cracks. Microscope images of an HP film during a temperature cycle between 300 K and 80 K (see Figure S9b,c and end of this Section), which show no formation of cracks, support our assumption that our optical measurements taken during initial cooling are unaffected by morphological changes. In addition, morphological changes in our $MAPbI_3$ thin films seem to occur only when the temperature is cycled significantly below the phase transition, e.g., down to 5 K (Figure S9a).

The microscope images of an HP film (pressing temperature about 120 °C) during a temperature cycle between 300 K and 80 K (Figure S9b,c) were taken with a digital microscope (Keyence VHX 970F with VH-Z250L objective). The microscope images were taken through the window of a LINKAM stage (THMS600 heating and freezing stage system, Serial No. DV1558-

0009 THMS600E-4), in which the $MAPbI_3$ thin film was placed for temperature cycling. A nitrogen atmosphere was created in the LINKAM stage before the start of the temperature cycle to prevent moisture from condensing on the film during cooling. Cooling of the sample in the LINKAM stage was performed by a nitrogen flow from a liquid nitrogen tank through the sample holder in the LINKAM stage using a LNP95 cooling pump. Warm recycled nitrogen gas was blown across the window of the LINKAM stage to avoid condensation. In addition to cooling with nitrogen flow, a heating unit integrated in the LINKAM stage was also provided for temperature control. The temperature was controlled and recorded via a controller with the LINK software.

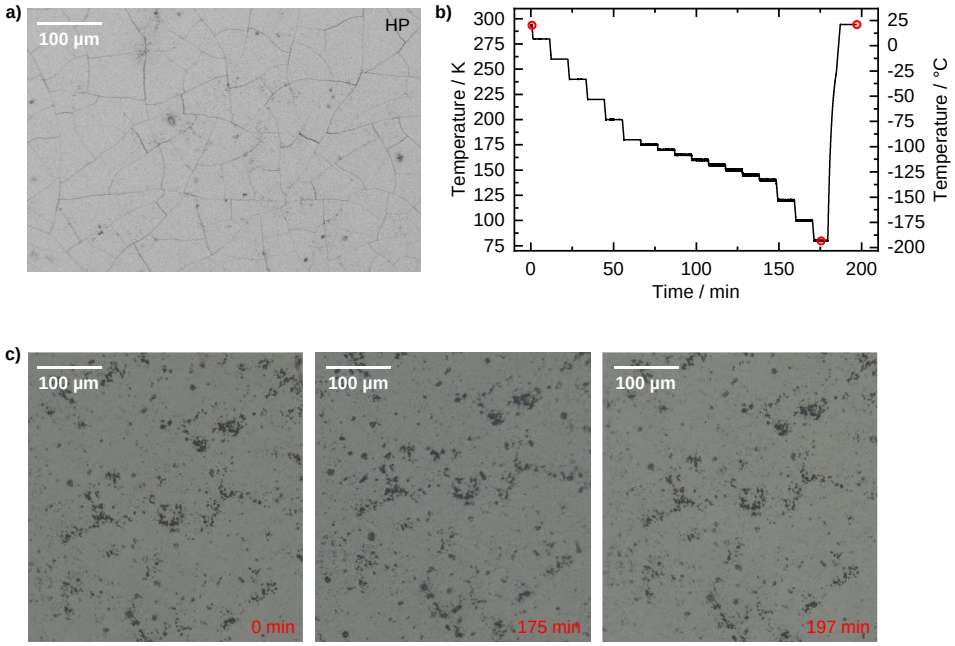

Figure S9: (a) Top-view SEM image of an HP $MAPbI_3$ thin film after temperature cycling between 300 K and 5 K. (b) Temperature as a function of time during a temperature cycle between 300 K and 80 K and (c) top-view microscope images of an HP $MAPbI_3$ thin film during the temperature cycling shown in (b) at different times as indicated (also see red open circles in b). The microscope images show no cracks even when crossing the phase transition.

References

1. Panzer, F.; Hanft, D.; Gujar, T. P.; Kahle, F.-J.; Thelakkat, M.; Köhler, A.; Moos, R. Compact Layers of Hybrid Halide Perovskites Fabricated via the Aerosol Deposition Process—Uncoupling Material Synthesis and Layer Formation. *Materials* **2016,** *9*, 277.
2. Leupold, N.; Schötz, K.; Cacovich, S.; Bauer, I.; Schultz, M.; Daubinger, M.; Kaiser, L.; Rebai, A.; Rousset, J.; Köhler, A., et al. High Versatility and Stability of Mechanochemically Synthesized Halide Perovskite Powders for Optoelectronic Devices. *ACS Appl. Mater. Interfaces* **2019,** *11*, 30259-30268.
3. Hanft, D.; Exner, J.; Schubert, M.; Stöcker, T.; Fuierer, P.; Moos, R. An Overview of the Aerosol Deposition Method: Process Fundamentals and New Trends in Materials Applications. *J. Ceram. Sci. Technol.* **2015,** *6*, 147-182.
4. Schubert, M.; Hanft, D.; Nazarenus, T.; Exner, J.; Schubert, M.; Nieke, P.; Glosse, P.; Leupold, N.; Kita, J.; Moos, R. Powder Aerosol Deposition Method — Novel Applications in the Field of Sensing and Energy Technology. *Funct. Mater. Lett.* **2019,** *12*, 1930005.
5. Akedo, J. Room Temperature Impact Consolidation (RTIC) of Fine Ceramic Powder by Aerosol Deposition Method and Applications to Microdevices. *J. Therm. Spray Technol.* **2008,** *17*, 181-198.
6. Akedo, J. Room Temperature Impact Consolidation and Application to Ceramic Coatings: Aerosol Deposition Method. *J. Ceram. Soc. Jpn.* **2020,** *128*, 101-116.
7. Dunlap-Shohl, W. A.; Li, T.; Mitzi, D. B. Interfacial Effects during Rapid Lamination within $MAPbI_3$ Thin Films and Solar Cells. *ACS Appl. Energy Mater.* **2019,** *2*, 5083-5093.
8. Meier, T.; Gujar, T. P.; Schönleber, A.; Olthof, S.; Meerholz, K.; van Smaalen, S.; Panzer, F.; Thelakkat, M.; Köhler, A. Impact of Excess PbI_2 on the Structure and the Temperature Dependent Optical Properties of Methylammonium Lead Iodide Perovskites. *J. Mater. Chem. C* **2018,** *6*, 7512-7519.
9. Rothmann, M. U.; Kim, J. S.; Borchert, J.; Lohmann, K. B.; O'Leary, C. M.; Sheader, A. A.; Clark, L.; Snaith, H. J.; Johnston, M. B.; Nellist, P. D., et al. Atomic-Scale Microstructure of Metal Halide Perovskite. *Science* **2020,** *370*, eabb5940.
10. Lee, K. J.; Turedi, B.; Giugni, A.; Lintangpradipto, M. N.; Zhumekenov, A. A.; Alsalloum, A. Y.; Min, J.-H.; Dursun, I.; Naphade, R.; Mitra, S., et al. Domain-Size-Dependent Residual Stress Governs the Phase-Transition and Photoluminescence Behavior of Methylammonium Lead Iodide. *Adv. Funct. Mater.* **2021,** *31*, 2008088.
11. Wright, A. D.; Verdi, C.; Milot, R. L.; Eperon, G. E.; Pérez-Osorio, M. A.; Snaith, H. J.; Giustino, F.; Johnston, M. B.; Herz, L. M. Electron–Phonon Coupling in Hybrid Lead Halide Perovskites. *Nat. Commun.* **2016,** *7*, 11755.
12. Meng, W.; Zhang, K.; Osvet, A.; Zhang, J.; Gruber, W.; Forberich, K.; Meyer, B.; Heiss, W.; Unruh, T.; Li, N., et al. Revealing the Strain-associated Physical Mechanisms Impacting the Performance and Stability of Perovskite Solar Cells. *Joule* **2022,** *6*, 458-475.
13. Schötz, K.; Askar, A. M.; Peng, W.; Seeberger, D.; Gujar, T. P.; Thelakkat, M.; Köhler, A.; Huettner, S.; Bakr, O. M.; Shankar, K., et al. Double Peak Emission in Lead Halide Perovskites by Self-Absorption. *J. Mater. Chem. C* **2020,** *8*, 2289-2300.
14. Liu, D.; Luo, D.; Iqbal, A. N.; Orr, K. W. P.; Doherty, T. A. S.; Lu, Z.-H.; Stranks, S. D.; Zhang, W. Strain Analysis and Engineering in Halide Perovskite Photovoltaics. *Nat. Mater.* **2021,** *20*, 1337-1346.
15. Zhao, J.; Deng, Y.; Wei, H.; Zheng, X.; Yu, Z.; Shao, Y.; Shield, J. E.; Huang, J. Strained Hybrid Perovskite Thin Films and their Impact on the Intrinsic Stability of Perovskite Solar Cells. *Sci. Adv.* **2017,** *3*, eaao5616.
16. Kavadiya, S.; Strzalka, J.; Niedzwiedzki, Dariusz M.; Biswas, P. Crystal Reorientation in Methylammonium Lead Iodide Perovskite Thin Film with Thermal Annealing. *J. Mater. Chem. A* **2019,** *7*, 12790-12799.
17. Osherov, A.; Hutter, E. M.; Galkowski, K.; Brenes, R.; Maude, D. K.; Nicholas, R. J.; Plochocka, P.; Bulović, V.; Savenije, T. J.; Stranks, S. D. The Impact of Phase Retention on the Structural and Optoelectronic Properties of Metal Halide Perovskites. *Adv. Mater.* **2016,** *28*, 10757-10763.

13 Structural Diversity in Layered Hybrid Perovskites, A_2PbBr_4 or $AA'PbBr_4$, Templated by Small Disc-Shaped Amines

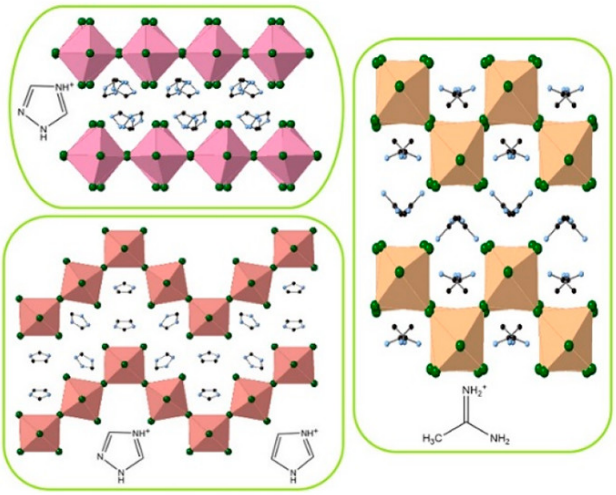

Yuan-Yuan Guo, Lin-Jie Yang, **Simon Biberger**, Jason A. McNulty, Konstantin Schötz, Fabian Panzer, Philip Lightfoot

Published in
Inorganic Chemistry, **2020**, 59, 17, 12858-12866

Inorganic Chemistry

pubs.acs.org/IC Article

Structural Diversity in Layered Hybrid Perovskites, A_2PbBr_4 or $AA'PbBr_4$, Templated by Small Disc-Shaped Amines

Yuan-Yuan Guo, Lin-Jie Yang, Simon Biberger, Jason A. McNulty, Teng Li, Konstantin Schötz, Fabian Panzer, and Philip Lightfoot*

Cite This: *Inorg. Chem.* 2020, 59, 12858−12866 Read Online

ACCESS | Metrics & More | Article Recommendations | Supporting Information

ABSTRACT: We present three new hybrid layered lead(II) bromide perovskites of generic composition A_2PbBr_4 or $AA'PbBr_4$ that exhibit three distinct structure types. $[TzH]_2PbBr_4$ ($[TzH^+]$ = 1,2,4-triazolium) adopts a (001)-oriented layer structure and $[AaH]_2PbBr_4$, ($[AaH^+]$ = acetamidinium) adopts a (110)-oriented type, whereas $[ImH][TzH]PbBr_4$, ($[ImH^+]$ = imidazolium) adopts a rare (110)-oriented structure with enhanced corrugation (i.e., 3 × 3 type). The crystal structures of each are discussed in terms of the differing nature of the templating molecular species. Photoluminescent spectra for each are reported and the behaviors discussed in relation to the different structure of each composition.

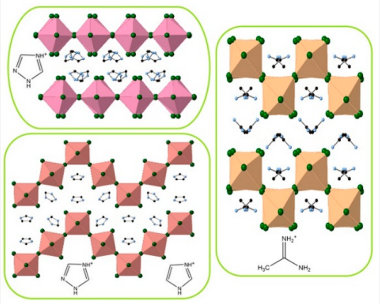

INTRODUCTION

The promising photophysical properties and enormous chemical and structural diversity shown by lead(II) halide perovskites (LHPs) has led to a considerable amount of exploratory synthetic work in this field.[1,2] Among these, lower-dimensional layered perovskites can be imagined as structural derivatives of the ABX_3 composition aristotype cubic perovskite structure, formed by slicing along specific crystallographic directions, and inserting additional moieties between these layers. Thus, the (001)-oriented perovskites can be regarded as derived from "slicing" along the (001) planes of the parent perovskite structure as shown in Figure 1a, resulting in trans ligands of the octahedral framework being terminal. The (001)-oriented layered perovskites are evidently particularly tolerant not only to inorganic but also organic interlayer components, producing a great diversity of compositional and structural variants. A related series of layered structure types, the (110)-oriented layered perovskites, can be regarded as derived from the parent ABX_3 perovskite by slicing along (110) planes, resulting in cis ligands of the octahedral framework being terminal. Depending on the degree of corrugation that occurs within the layers, these structures can be described as 2 × 2, 3 × 3, etc., as shown in Figure 1b.[3]

A further degree of variability, common to each of these generic families, is that it is feasible to incorporate either one or two distinct cations in the interlayer region, leading to generic compositions ABX_4 or $AA'BX_4$ (in the case of a single octahedral layer). Manipulations at the A and A′ sites can obviously lead to consequent modifications to the arrangement of the perovskite-like layers themselves, thus helping to tailor the resultant physical properties. In the case of the (001)-oriented layers and in the field of purely inorganic perovskites, the two generic families are the well-known Dion−Jacobson (DJ)[4] and Ruddlesden−Popper (RP)[5] series, having stoichiometries ABX_4 and $AA'BX_4$, respectively, for examples with

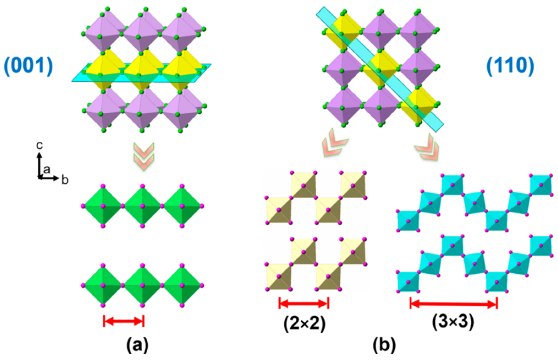

Figure 1. Schematic dimensional reduction of parent cubic perovskite to (a) (001)-oriented and (b) (110)-oriented layered perovskites.

Received: June 30, 2020
Published: August 11, 2020

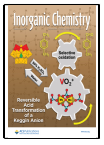

https://dx.doi.org/10.1021/acs.inorgchem.0c01807
Inorg. Chem. 2020, 59, 12858−12866

single octahedral layers. The corresponding inorganic-only (110)-oriented phases are much less common.[6] Indeed, the same can be said of the corresponding LHPs, where there are now countless examples of the (001)-type,[2] but still only a handful of the various (110)-types.[2,7−9] In the case of LHPs, the ABX_4 variant must contain a single divalent organo-cation, whereas the $AA'BX_4$ analogue will contain two (same or distinct) monovalent organic cations.[7]

In our previous work,[7] we reported two examples of the latter series, i.e., the 2 × 2 (110)-oriented structure type. We specifically chose two similarly sized, disc-shaped monoprotonated amines, in order to explore structure-directing effects, based on both size and H-bonding preferences, to produce $[ImH][GuH]PbBr_4$ ("$IGPbBr_4$") and $[TzH][GuH]PbBr_4$ ("$TGPbBr_4$"); $[ImH^+]$ = imidazolium, $[TzH^+]$ = 1,2,4-triazolium, $[GuH^+]$ = guanidinium). In the present work, we present another three new $AA'BX_4$ type LHPs: $[TzH]_2PbBr_4$ ("T_2PbBr_4"), $[AaH]_2PbBr_4$ ("A_2PbBr_4"; $[AaH^+]$ = acetamidinium), and $[ImH][TzH]PbBr_4$ ("$ITPbBr_4$"). Interestingly, they adopt three different structure types, *viz.* (001) for T_2PbBr_4, 2 × 2 (110) for A_2PbBr_4, and 3 × 3 (110) for $ITPbBr_4$. The crystal structures are discussed in detail in order to inform future considerations of the "designability" of these various structure types.

EXPERIMENTAL SECTION

Synthesis. 1,2,4-Triazole ($C_2H_3N_3$, 99%), acetamidine hydrochloride, ($C_2H_6N_2$·HCl, 97%), imidazole ($C_3H_4N_2$, 99%), lead(II) bromide ($PbBr_2$, ≥ 98%), and hydrobromic acid (HBr, 48%, w/w aqueous solution) were purchased from Alfa Aesar. Diethyl ether ($(C_2H_5)_2O$, 99.5%) was purchased from Sigma-Aldrich. All chemicals were directly used without further purification.

The title compounds, T_2PbBr_4, A_2PbBr_4, and $ITPbBr_4$, were crystallized by a slow evaporation method.

T_2PbBr_4 ($C_4H_8N_6PbBr_4$), 1,2,4-triazole (276 mg, 4 mmol), and $PbBr_2$ (734 mg, 2 mmol) were dissolved in conc. HBr (3 mL) with moderate heating. By cooling for a few hours, bright yellow, plate-shaped crystals were obtained. These crystals were filtered and washed with diethyl ether (yield 48% based on $PbBr_2$). Elemental anal. Calcd. (%) for T_2PbBr_4: C, 7.20; H, 1.21; N, 12.60. Found: C, 7.37; H, 1.15; N, 12.53.

A_2PbBr_4 ($C_4H_{14}N_4PbBr_4$), acetamidine hydrochloride (1890 mg, 20 mmol), and $PbBr_2$ (734 mg, 2 mmol) were dissolved in conc. HBr (6 mL) with moderate heating. By cooling for a few hours, colorless, plate-shaped crystals were obtained. These crystals were filtered and washed with diethyl ether (yield 41% based on $PbBr_2$). Elemental anal. Calcd (%) for A_2PbBr_4: C, 7.45; H, 2.19; N, 8.69. Found: C, 7.53; H, 2.11; N, 8.73.

$ITPbBr_4$ ($C_5H_9N_5PbBr_4$), imidazole (136 mg, 2 mmol), 1,2,4-triazole (138 mg, 2 mmol), and $PbBr_2$ (734 mg, 2 mmol) were dissolved in conc. HBr (4 mL) with moderate heating. By cooling for a few hours, pale yellow, needle-shaped crystals were obtained. These crystals were filtered and washed with diethyl ether (yield 40% based on $PbBr_2$). Elemental anal. Calcd (%) for $ITPbBr_4$: C, 9.02; H, 1.36; N, 10.52. Found: C, 8.94; H, 1.22; N, 10.54.

Characterization. Single-crystal X-ray diffraction data were collected at 173 and 298 K on a Rigaku SCX Mini diffractometer using Mo−K_α radiation. Data were collected using *CrystalClear* (Rigaku) software.[10] Structures were solved by direct methods using *SHELXT*,[11] and full-matrix least-squares refinements on F^2 were carried out using *SHELXL-2018/3*[11] incorporated in the WinGX program.[12] Absorption corrections were performed empirically from equivalent reflections on the basis of multiscans by using *CrystalClear*.[10] Non-H atoms were refined anisotropically and hydrogen atoms were treated as riding atoms. Powder X-ray diffraction data were collected on a PANalytical EMPYREAN diffractometer using Cu $K_{\alpha1}$ (λ = 1.5406 Å) radiation in the range of 3−70° to confirm the purity of each sample. Ambient temperature solid UV−vis absorbance spectra of powder T_2PbBr_4, A_2PbBr_4, and $ITPbBr_4$ were collected on a JASCO-V550 ultraviolet−visible spectrophotometer with a wavelength range of 200−900 nm. Temperature-dependent, steady-state PL measurements were carried out on powdered pellet samples of T_2PbBr_4, $ITPbBr_4$, and A_2PbBr_4 using a home-built setup that is described in more detail elsewhere.[13] In brief, the pellets were placed in a continuous flow cryostat (Oxford Instruments, Optistat CF) connected to a temperature controller (Oxford Instruments ITC503S) and the sample was excited with a pulsed 337 nm nitrogen laser (LTB MNL 100). The PL-signal was detected by a spectrograph (Andor Shamrock SR3030i) coupled to a CCD-camera (Andor iDus420a-OE). For PLQY measurements, we used the method described by de Mello et al.[14] The samples were excited using a 375 nm diode laser by PicoQuant and the spectra were recorded with a CCD-camera (Andor DU420A-OE).

RESULTS AND DISCUSSION

Crystal Structures. The single-crystal X-ray structures suggest no phase transitions in the regime 173 < T < 298 K, so the crystallographic details will be discussed based on the structures at 298 K. Details of the structures at 173 K are provided in the Supporting Information. Crystallographic parameters for all three structures at 298 K are given in Table 1.

Table 1. Crystal and Structure Refinement Data at 298 K

	T_2PbBr_4	A_2PbBr_4	$ITPbBr_4$
formula	$C_4H_8N_6PbBr_4$	$C_4H_{14}N_4PbBr_4$	$C_5H_9N_5PbBr_4$
form wt	666.99	645.02	666.00
color/habit	yellow/block	colorless/block	pale yellow prism
cryst size (mm^3)	0.23 × 0.17 × 0.09	0.22 × 0.18 × 0.13	0.21 × 0.12 × 0.11
cryst syst	monoclinic	monoclinic	orthorhombic
space group	$C2/c$	$P2_1/c$	$Pbcm$
a (Å)	11.9243(9)	12.6949(9)	6.0154(5)
b (Å)	11.9327(9)	9.2998(7)	25.873(2)
c (Å)	19.3394(15)	12.2739(7)	18.9242(17
α (deg)	90	90	90
β (deg)	95.212(6)	90.996(6)	90
γ (deg)	90	90	90
V ($Å^3$)	2740.4(4)	1448.84(18)	2945.3(4)
Z	8	4	8
ρ_{calcd} (g/cm^3)	3.233	2.957	3.004
μ (mm^{-1})	23.958	22.648	22.289
$F(000)$	2368	1152	2368
no. of reflns collected	11310	14371	23202
independent reflns	2394 [R(int) = 0.0545]	3294 [R(int) = 0.0478]	2664 [R(int) = 0.0834]
goodness of fit	0.939	0.939	0.94
final R indices ($I > 2\sigma(I)$)	R_1 = 0.0245 wR_2 = 0.0538	R_1 = 0.0233 wR_2 = 0.0459	R_1 = 0.0259 wR_2 = 0.0537
largest diff. peak/hole (e $Å^{-3}$)	1.504/−1.513	0.956/−1.224	1.028/−1.656

T_2PbBr_4. T_2PbBr_4 crystallizes in a (001)-oriented structure type (Figure 2). Although octahedral tilting occurs within each $[PbBr_4]_\infty$ layer, adjacent octahedral layers occur in an almost "eclipsed" conformation relative to each other, which resembles the DJ rather than the RP family, despite the A_2BX_4 stoichiometry. We note that there is currently controversy regarding the naming of families of layered hybrid

https://dx.doi.org/10.1021/acs.inorgchem.0c01807
Inorg. Chem. 2020, 59, 12858−12866

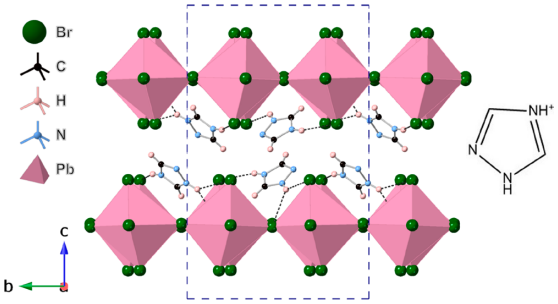

Figure 2. Crystal structure of T_2PbBr_4.

perovskites in relation to structural and compositional features,[15] though in terms of describing and comparing structural distortions within the inorganic layers in these materials, such comparisons can be helpful. Although the original naming of the RP and DJ phases referred to compositional differences, $A_2'A_{n-1}B_nO_{3n+1}$ and $A'A_{n-1}B_nO_{3n+1}$, respectively, a more useful distinction in the context of LHPs regards the nature and degree of "staggering" of adjacent perovskite-like octahedral layers. Here, we choose to describe the present structure as related to the DJ family, despite the compositional resemblance to the RP family, as the octahedral layers are almost eclipsed.

The unit cell of T_2PbBr_4 has a $2a_p \times 2a_p \times 2c_p$ supercell relative to the parent DJ structure ($TlAlF_4$), which is caused by a combination of octahedral tilting/distortion together with ordering of $[TzH^+]$ cations over two distinct sites and the cooperative minor staggering of adjacent octahedral layers. Figure 2 shows the packing arrangement, together with the H-bonding of the $[TzH^+]$ moieties to the inorganic layers. The driving force for this expanded supercell may be broken down into the effects of octahedral tilting together with the effects of the arrangement of the organic species. In the notation used by Li et al.,[16] the tilt system of T_2PbBr_4 is an unusual one: a^-b^0c, signifying rotation of octahedra around the *c*-axis and out-of-phase tilting of adjacent octahedra along only one of the in-plane axes. These tilt modes acting alone would lead to a supercell $2a_p \times 2a_p \times c_p$ in space group $C2/m$, with perfectly eclipsed octahedral layers: it can be seen that the additional *c*-axis doubling is due to the slight staggering of the adjacent layers, in an antiferrodistortive style along the *b*-axis, presumably caused by accommodation of the interlayer species. Tremblay et al.[17] have discussed the nature and variable extent of staggering of octahedral layers (i.e., the transition from "DJ-like" to "RP-like"), which serves as a useful parameter for comparison of structures of this type. We can find no previous example of a similar $2a_p \times 2a_p \times 2c_p$ supercell for a LHP of $APbX_4$, A_2PbX_4, or $AA'PbX_4$ composition. The near-eclipsing of adjacent $[PbBr_4]_\infty$ layers leads to noticeably short interlayer Br---Br nonbonded contacts of 4.096(1) Å. We can also find no previous examples of such a short interlayer contacts in a single-layer LHP, although Ke et al.[18] suggest I---I distances of around 4.2 Å in some iodide members of this family.

The different distortion modes, i.e., the distinct octahedral tilting schemes and the presence or absence of staggering of adjacent layers, which occur in T_2PbBr_4 and related materials, are most easily identified using the online software ISODISTORT,[19] which uses a normal-mode analysis: further details for T_2PbBr_4 are given in the Supporting Information. A similar analysis of all previously reported $APbX_4$ or A_2PbX_4 LHPs may be enlightening for the understanding of structure-directing effects of other amines, but this is beyond the scope of the present work.

Selected geometrical parameters and octahedral distortion parameters are given in Table 2. It can be seen that the two nitrogen atoms in the 1-position of the triazolium participate in two H-bonds each to Br; in contrast, the two in the 4-position only donate a single H-bond to Br. There are no H-bonds between triazolium moieties (Table S2).

A_2PbBr_4. A_2PbBr_4 crystallizes in a "corrugated 2 × 2 layer" (110)-oriented structure type (Figure 3). The unit cell and space group, $P2_1/c$, are consistent with a slight distortion of the framework (i.e., octahedral tilts and distortions) of the type seen in the first reported all-inorganic example of this structure type, $NdBaInO_4$.[20] The aristotype phase of the $AA'BX_4$ (110)-type (i.e., no octahedral tilting) has space group *Cmcm*, typified by $NdBaScO_4$.[6] This higher symmetry structure has not yet been seen among the known LHPs. The specific type of distortion (i.e., unit-cell metrics and space group) seen here for A_2PbBr_4 has previously been observed in [(aminoethyl)-isothiourea]$PbBr_4$[21] but this is the first example of a LHP with this structure type of the formula $AA'BX_4$.

As is the case in T_2PbBr_4, there is only one crystallographically unique Pb site but two distinct $[AaH^+]$ sites. The intralayer acetamidinium forms H-bonds only to the nearby

Table 2. Selected Geometrical and Octahedral Distortion Parameters at 298 K

	T_2PbBr_4	A_2PbBr_4	$ITPbBr_4$	
	Pb1	Pb1	Pb1	Pb2
Pb−Br (Å)	2.9841(6)	2.8901(5)	3.0023(7)	2.9082(6)
	2.9924(3)	2.9141(5)	3.0024(7)	2.9082(6)
	3.0041(8)	2.9297(5)	3.0024(9)	3.0027(9)
	3.0055(7)	3.1395(5)	3.0130(9)	3.0127(9)
	3.0157(3)	3.2112(5)	3.0152(6)	3.1597(6)
	3.0282(7)	3.3221(5)	3.0152(6)	3.1598(6)
Pb−Br−Pb (deg)	162.92(4)	162.35(2)	171.41(2)	
	165.82(3)	166.45(2)	179.53(4)	
	169.54(4)		180	
Br−Pb−Br range (deg)	81.921(15)-97.984(15)	80.551(16)-99.560(16)	85.616(13)-94.384(13)	85.233(11)-94.767(11)
Δd ($\times 10^{-4}$)	0.23	29.16	0.04	11.70
σ^2	33.56	26.12	7.01	26.58

https://dx.doi.org/10.1021/acs.inorgchem.0c01807
Inorg. Chem. 2020, 59, 12858−12866

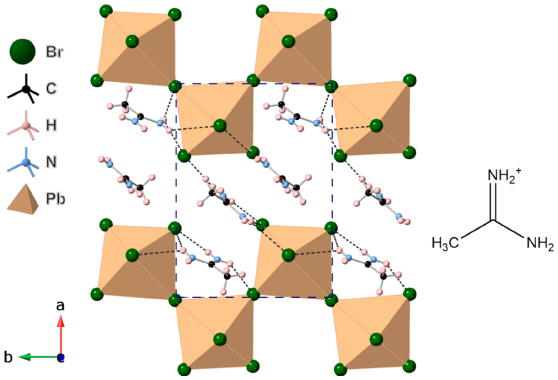

Figure 3. Crystal structure of A_2PbBr_4.

$[PbBr_4]_\infty$ layer, whereas the interlayer $[AaH^+]$ forms H-bonds to adjacent inorganic layers via N1 and N2. Among the relatively small number of reported 2 × 2 (110)-oriented layered hybrid perovskites, we have found only six that have a stoichiometry $AA'BX_4$ rather than ABX_4.[7,8,22,23] Four of these contain guanidinium $[GuH^+]$: $[GuH]_2PbI_4$, $[GuH]_2SnI_4$, [ImH][GuH]$PbBr_4$, and [TzH][GuH]$PbBr_4$. The latter two examples are interesting, as they show that $[GuH^+]$ is capable of occupying either the intralayer or interlayer site, depending on competition between $[GuH^+]$ and the second organic moiety. The occupation of both sites simultaneously by $[GuH^+]$ has recently been reported in a related 3 × 1 (110)-oriented perovskite, $[GuH]_{1.5}[4Me\text{-}ImH]_{0.5}SnI_4$.[24] In [TzH]-[GuH]$PbBr_4$, it is perhaps surprising that $[TzH^+]$ occupies the intralayer site. This was discussed by Guo et al.:[7] the ionic sizes of $[GuH^+]$ and $[TzH^+]$ are approximately the same, and it was reasoned that intermolecular $[GuH^+]$---$[TzH^+]$ hydrogen bonds may play a significant role in stabilizing the cation ordering in that case. Because $[AaH^+]$ is anticipated to be approximately the same size as $[GuH^+]$, it may be no surprise that A_2PbBr_4 adopts the (110)-oriented structure rather than any (001)-oriented option. The H-bonding options are, of course, more restricted for $[AaH^+]$ versus $[GuH^+]$. Nevertheless, Figure 3 and Table S4 show that there is interlayer H-bonding present here via the interlayer $[AaH^+]$.

Selected geometrical parameters for A_2PbBr_4 are given in Table 2. Although there are currently only a small number of (110)-oriented LHPs, these display quite a diversity of specific structural distortions (i.e., unit cell metrics and space groups derived from the aristotype phase). We therefore offer no universal trends regarding the nature of these distortions versus compositional features, in terms of interlayer interactions and other longer-range structural features. Moreover, there appears little systematic behavior regarding the local structural features within this family, such as the level of individual PbX_6 octahedral distortions and interoctahedral angles. Among the known (110)-oriented structure layered hybrid perovskites of $AA'BX_4$ stoichiometry, A_2PbBr_4 is seen to exhibit the largest octahedral distortions and among the largest interoctahedral distortions (i.e. B–X–B bond angles, Table 3). This is seen, for example, in comparing to the two previous A_2BX_4 compositions, $[GuH]_2PbI_4$ and $[GuH]_2SnI_4$, in their monoclinic polymorphs, which exist close to room temperature: these compounds show the largest interoctahedral distortions of this family. Surprisingly, and for reasons we cannot explain,

Table 3. Octahedral and Interoctahedral Distortions of Known (110)-Oriented Layered Hybrid Perovskites

	Δd ($\times 10^{-4}$)	σ^2	B–X–B (deg)
A_2PbBr_4	29.16	26.12	162.35(2)
			166.45(2)
[ImH][GuH]$PbBr_4$[7]	8.91	7.71	178.10(7)
			180
[TzH][GuH]$PbBr_4$[7]	7.59	22.06	171.51(3)
			180
[FA][HEA]$PbBr_4$[8]	5.70	11.59	173.13(6)
	13.66	14.46	177.96(4)
$[GuH]_2PbI_4$[22]	7.78	12.65	154.27(2)
			157.35(2)
	11.16	8.41	158.42(2)
			176.06(2)
$[GuH]_2SnI_4$[22]	20.06	6.78	157.08(2)
			159.63(2)
	23.47	6.14	161.48(2)
			177.10(2)
[IFA][MA]SnI_4[23]	2.02	7.77	173.30(10)
			180
[3APr]$PbCl_4$[26]	12.32	34.50	169.70
			170.50
[3APr]$PbBr_4$[26]	9.81	21.07	171.31
			173.24
[3APr]PbI_4[26]	11.92	22.04	169.58
			178.18

perhaps the closest compositional analogue to A_2PbBr_4, $[GuH]_2PbBr_4$ does not adopt a (110)-oriented structure, instead preferring an unusual chainlike structure.[25] The series of $[3APr]PbX_4$ structures,[26] for X = Cl, Br, I, are also compared in Table 3. This also suggests little direct correlation of distortion parameters versus the nature of X, based on the existing small data set.

ITPbBr$_4$. $ITPbBr_4$ adopts an unusual variant of the (110)-oriented structure, which has also been described as a "corrugated 3 × 3 layer" structure. This structure type contains rows of alternating cis- and trans-shared octahedra linked into (110) sheets (Figure 4). There are only four previously

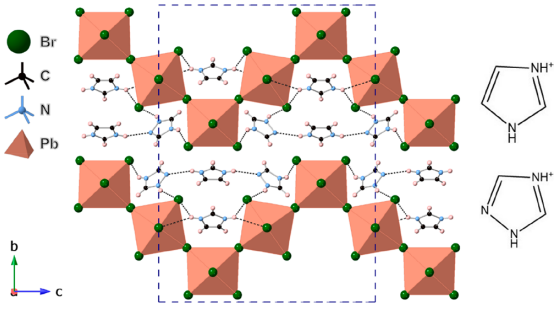

Figure 4. Crystal structure of $ITPbBr_4$.

reported examples of this structure type: [α-DMEN]$PbBr_4$ ($[DMEN]^{2+}$ = 2-(dimethylamino)ethylammonium),[3] [ImEA]-PbI_4 ($[ImEA]^{2+}$ = imidazoliumethylammonium),[27] and [4NPEA]PbX_4 (X = Br or I; 4NPEA = 4-nitrophenylethylammonium).[28] $ITPbBr_4$ is therefore the first example of a bromide of this structure type incorporating two distinct

https://dx.doi.org/10.1021/acs.inorgchem.0c01807
Inorg. Chem. 2020, 59, 12858–12866

molecular species. The two distinct types of PbX_6 octahedra (i.e., cis and trans ligands being terminal, respectively) in each case show very different degrees of distortion, with the trans site being much more regular (Table 2).

The unit-cell metrics of this type of structure, in its simplest form, are characterized by two axial lengths determined by the geometry of the linked PbX_6 octahedra and one dictated by the packing of the adjacent layers, and the nature of the interlayer moieties. Thus, an axial length of around 19 Å along the corrugation direction of the $[PbX_4]_\infty$ sheet (*c*-axis in $ITPbBr_4$, Figure 4) arises from the lateral edge-to-edge width of four linked octahedra. A length of about 6 Å derives from the Pb−Br−Pb distance between two vertex-linked octahedra perpendicular to this (*a*-axis in $ITPbBr_4$), and a variable interlayer distance is dictated by the nature and packing of the organic moieties ($b \approx 26$ Å in $ITPbBr_4$). By comparing the metrics of the known examples of this structure type (Table S9), it can be seen that $ITPbBr_4$ has one the "simplest" variants of this basic unit cell, exhibiting the simple 6 Å metric perpendicular to the corrugation direction, whereas each of the other examples has a doubled axis, because of octahedral tilting. Interestingly, only one example ($[ImEA]PbI_4$) has a structure where the interlayer unit-cell axis represents the distance between adjacent $[PbX_4]_\infty$ sheets: each of the others has a doubled axis here, apparently due to alternating orientations of the interlayer moieties.

There are no direct interlayer links via H-bonding in $ITPbBr_4$, although there are $[ImH^+]$---$[TzH^+]$ H-bonds between the moieties that both interact with the same $[PbBr_4]_\infty$ sheet. Because our previous study[7] suggested that $[ImH^+]$ and $[TzH^+]$ are approximately the same size, it seems that these H-bonding preferences may play a subtle role in dictating the observed cation ordering (i.e., ordering of $[ImH^+]$ into the intralayer sites in this structure) although this suggestion can only be speculative. Indeed, the features that favor the adoption of the 3 × 3 layer structure itself, rather than some of the possible competing polymorphs, are not clear from the limited amount of data available at this stage. It is likely that the energy landscapes discriminating different polymorphs in some of these systems are rather "flat", for example, $[DMEN]PbBr_4$ crystallizes in two distinct polymorphs, the thermodynamically stable α-phase, having the 3 × 3 layer structure and the β-phase, the kinetic product, having a (001) layer structure.[3]

Photophysical Properties. *UV−Vis.* All three absorption spectra (Figure 5) revealed features similar to previously reported 2D layered LHPs, viz., two separated absorption peaks.[7,29−31] That is, T_2PbBr_4 has two absorption peaks at 3.05 eV (407 nm) and 2.85 eV (435 nm), $ITPbBr_4$ has peaks at 3.27 eV (379 nm) and 3.02 eV (411 nm), and A_2PbBr_4 has peaks at 3.56 eV (348 nm) and 3.29 eV (377 nm).

From these spectra, it also becomes clear that the energetic spacing between the two peaks increases from 0.20 and 0.25 eV to 0.27 eV for T_2PbBr_4 and $ITPbBr_4$ to A_2PbBr_4, respectively. The peaks at lower energies can be attributed to exciton absorption in each system,[32,33] which precludes extracting the fundamental band gap with the help of a Tauc plot.[34] We thus estimate the optical gap from the absorption onset (dashed lines in Figure 5a), which increases from 2.68 eV (463 nm) and 2.82 eV (440 nm) to 3.03 eV (409 nm) when going from T_2PbBr_4 and $ITPbBr_4$ to A_2PbBr_4, respectively. The increasing optical gap and the increasing energetic spacing between the two absorption peaks is in

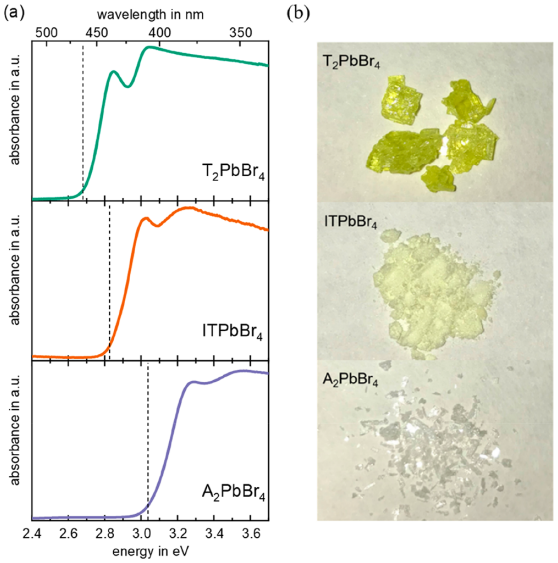

Figure 5. (a) UV−vis absorption spectra of T_2PbBr_4, $ITPbBr_4$, and A_2PbBr_4 and at room temperature; the dashed lines indicate the energy of the absorption onset. (b) Crystals of T_2PbBr_4, $ITPbBr_4$ and A_2PbBr_4.

agreement with the idea of a greater electronic confinement,[35,36] with the spread of the electron wave function being inhibited where the connectivity between neighboring octahedra change between cis and trans conformation ($ITPbBr_4$ < A_2PbBr_4).[37] Although the increase in optical gap essentially stems from the "particle in a box" solution to the Schrödinger equation,[38] the increased spacing between the absorption peaks reflects an increased exciton binding energy with greater confinement. Correspondingly, the colors of the three materials change from bright yellow (T_2PbBr_4) to pale yellow ($ITPbBr_4$) and then to white (A_2PbBr_4) (Figure 5b).

PL Spectra. Figure 6 shows the normalized PL spectra of all three compounds when they are excited at 3.67 eV (337 nm).

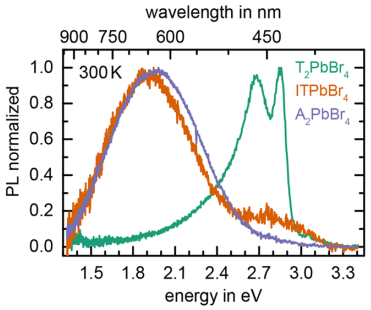

Figure 6. Normalized PL spectra (excited at 337 nm) for T_2PbBr_4, $ITPbBr_4$, and A_2PbBr_4 at room temperature.

The emission spectrum of T_2PbBr_4 shows two distinct sharp peaks at 2.68 eV (463 nm) and 2.85 eV (435 nm). The emission spectrum of A_2PbBr_4 shows a different behavior with a broad peak at ~1.97 eV (628 nm), corresponding to a large energetic spacing between the PL peak and the absorption

https://dx.doi.org/10.1021/acs.inorgchem.0c01807
Inorg. Chem. 2020, 59, 12858−12866

peak at 3.29 eV (377 nm). Furthermore, the full width at half-maximum (fwhm) of the broad PL peak is ~0.72 eV (240 nm). In contrast, two PL peaks are observed in the case of $ITPbBr_4$. The dominating broad signal at 1.92 eV (647 nm) has essentially the same shape as the PL of A_2PbBr_4, and the PL peak at 2.75 eV (451 nm) is in the energetic range similar to the emission of T_2PbBr_4. We measured the photoluminescence quantum efficiency PLQY at room temperature and found it to be below 1% for all three samples. Although these values are low compared to the highest reported PLQYs of low dimensional lead bromide perovskites,[29,39] several works also report comparably low PLQYs.[40,41]

To better understand the origin of the different emitting states, we performed temperature-dependent steady-state PL measurements from 300 to 120 K (20 K intervals) for all three compounds.

Figure 7 shows the temperature-dependent PL spectra for each perovskite system. For all materials, the overall PL

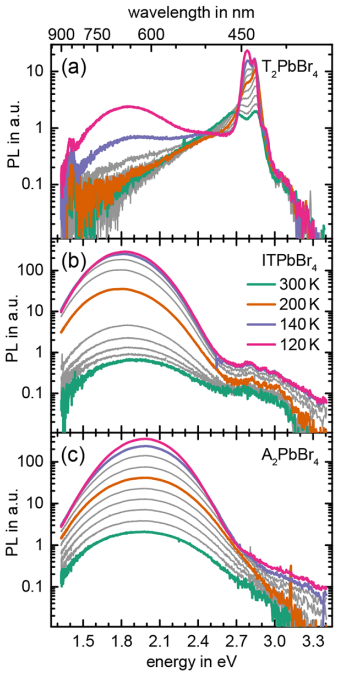

Figure 7. Temperature-dependent (300–120 K) steady-state PL spectra of (a) T_2PbBr_4, (b) $ITPbBr_4$, and (c) A_2PbBr_4.

intensity increases upon cooling to 120 K. For T_2PbBr_4, the peak at 2.68 eV (463 nm) at 300 K gradually shifts to higher energies upon cooling to 200 K (Figure 7a). From 200 K onward, it retains its position and raises in intensity, becoming the dominant PL feature at 120 K. Further, an additional low energy emission band (~1.87 eV, 663 nm) appears at temperatures below 160 K.

As mentioned above, $ITPbBr_4$ shows two emissive features, where the peak at higher energies (2.80 eV, 443 nm) exhibits a low relative intensity compared to the PL feature at lower energies at room temperature (Figure 7b). Upon cooling, the ratio between the PL peaks at high and low energy decreases. The emission band at lower energy (1.89 eV, 656 nm) remains the dominant PL feature in the entire investigated temperature range, where its fwhm narrows from 0.72 eV (258 nm) at 300 K to 0.46 eV (173 nm) at 120 K. Additionally, we observe that the high energy band becomes more structured at low temperatures, exhibiting several distinct PL features at similar peak positions compared to the high-energy PL features of T_2PbBr_4. PL of A_2PbBr_4 predominantly exhibits the low energy emission at ~1.97 eV in the investigated temperature range between 300 and 120 K (Figure 7c). Upon cooling, the fwhm of the PL peak continuously reduces from 0.72 eV (240 nm) at RT to 0.48 eV (154 nm) at 120 K, whereas its energetic position remains constant. Below 200 K, a weak PL at energies >2.8 eV (443 nm) appears. Compared to the PL band at ~1.97 eV, its intensity is lower by more than 3 orders of magnitude.

The results of the PL measurements suggest two different emitting species because the high energy signal in T_2PbBr_4 is rather narrow and structured, whereas the emission at lower energies is broad and significantly separated in energy from corresponding absorption onsets. The PL peak at 2.85 eV (435 nm) is nearly resonant with the exciton absorption shown in Figure 5, so that we associate this high energy PL band with exciton recombination.[42,43]

Broad emission features at low photon energies are often observed in 2D-perovskite systems,[44−47] and it was suggested that they stem from recombination via intrinsic (electron−phonon coupling) or extrinsic (electron−lattice defect) self-trapped excitons (STE).[40,48] This may also be a possible interpretation for the observed emission at lower energies of the materials investigated in our case. In contrast, we deem the occurrence of the low energy features due to a possible structural phase transition at low temperatures to be rather unlikely. In such a case, we would expect a decrease in the PL signals associated with the high-temperature phase, the abrupt appearance of low-temperature-phase PL features, also with a similar spectral width compared to the high-temperature-phase PL features.[49] Typically, this all would happen within a relatively small temperature range.[50]

The ratio between the high and low energy bands is temperature-dependent, i.e., reflecting some thermally activated detrapping process.[40,51] Nevertheless, overall, we observe a stronger dominance of the low energy band along the series from T_2PbBr_4 over $ITPbBr_4$ to A_2PbBr_4. This is in line with reports from literature showing that broad PL at low energies can be facilitated by an increase in distortions and corrugation.[44,45] Considering that the energy differences between high and low energy bands are fairly similar for all three systems, the lower intensity of the broad peak is likely to reflect a lower density of STE states in T_2PbBr_4 than in $ITPbBr_4$ and A_2PbBr_4. In the literature, a change in the PL intensity between high and low energy PL bands was associated with a change in the energy difference between the absorption onset and the energy of the STE emission.[26,52] It was suggested that a smaller energy difference is favorable for STE detrapping leading to an increased PL intensity of the high energy band. This at first sight is in line with our results; however, such a thermal detrapping process appears questionable to us, as the observed energy difference between low- and high-energy PL bands is large (~0.7 eV) compared to thermal energy. Furthermore, a recent study shows that the low energy PL band originates from in-gap states, rather than being due to STEs,[53] which emphasizes the general need for more detailed future studies.

https://dx.doi.org/10.1021/acs.inorgchem.0c01807
Inorg. Chem. 2020, 59, 12858−12866

CONCLUSIONS

We have prepared three new examples of hybrid lead bromide layered perovskites of different structural variations templated using small disc-shaped amines. The cationic ordering behavior of each composition have been discussed in terms of ionic size effects and hydrogen-bonding environments. In T_2PbBr_4, we introduce a previously unreported "DJ-like" (001)-oriented structure type with a $2a_p \times 2a_p \times 2c_p$ supercell arising from octahedral tilting and the arrangement of the $[TzH^+]$ moieties. The two (110)-oriented perovskites reported, A_2PbBr_4 and $ITPbBr_4$, represent two new examples of this rare structure-type featuring corrugation patterns of 2×2 and 3×3, respectively. The octahedral distortions present in A_2PbBr_4 are the largest reported for any material of the 2×2 type, however we are unable to identify any systematic behavior among known (110)-oriented structures to explain this. $ITPbBr_4$ is the first example of a bromide 3×3 type structure incorporating two distinct molecular species and represents the "simplest" variant of the basic unit cell among known materials of this structure type. All three materials exhibit peaks consistent with exciton absorption in UV−vis spectroscopy. Photoluminescence data indicate a distinct change in behavior with increasing structural corrugation. In T_2PbBr_4, there is a narrow and structured emission observed at higher energies attributed to exciton recombination, as well as a broad emission at lower energies corresponding to recombination via extrinsic or intrinsic STE. With the increasing structural distortions and corrugation in $ITPbBr_4$ and A_2PbBr_4, the broad emission feature dominates. The diverse structures and photoluminescent behavior exhibited in these materials obtained from similar disc-shaped amines highlights the need for greater exploration and study of hybrid layered perovskites toward potential functionalities.

ASSOCIATED CONTENT

Supporting Information

The Supporting Information is available free of charge at https://pubs.acs.org/doi/10.1021/acs.inorgchem.0c01807.

Crystallographic data at 173 K, hydrogen-bonding details, octahedral distortion parameters, brief review of (110)-oriented layered perovskite unit-cell details (PDF)

ISODISTORT mode amplitudes for T_2PbBr_4 (PDF)

Accession Codes

CCDC 1985833−1985838 contain the supplementary crystallographic data for this paper. These data can be obtained free of charge via www.ccdc.cam.ac.uk/data_request/cif, or by emailing data_request@ccdc.cam.ac.uk, or by contacting The Cambridge Crystallographic Data Centre, 12 Union Road, Cambridge CB2 1EZ, UK; fax: +44 1223 336033.

AUTHOR INFORMATION

Corresponding Author

Philip Lightfoot − *School of Chemistry and EaStChem, University of St. Andrews, St. Andrews KY16 9ST, United Kingdom;* orcid.org/0000-0001-7048-3982; Email: pl@st-andrews.ac.uk

Authors

Yuan-Yuan Guo − *School of Chemistry and EaStChem, University of St. Andrews, St. Andrews KY16 9ST, United Kingdom;* orcid.org/0000-0002-0618-1709

Lin-Jie Yang − *School of Chemistry and EaStChem, University of St. Andrews, St. Andrews KY16 9ST, United Kingdom*

Simon Biberger − *Soft Matter Optoelectronics, Department of Physics, University of Bayreuth, Bayreuth 95440, Germany*

Jason A. McNulty − *School of Chemistry and EaStChem, University of St. Andrews, St. Andrews KY16 9ST, United Kingdom;* orcid.org/0000-0003-4630-7086

Teng Li − *School of Chemistry and EaStChem, University of St. Andrews, St. Andrews KY16 9ST, United Kingdom*

Konstantin Schötz − *Soft Matter Optoelectronics, Department of Physics, University of Bayreuth, Bayreuth 95440, Germany*

Fabian Panzer − *Soft Matter Optoelectronics, Department of Physics, University of Bayreuth, Bayreuth 95440, Germany;* orcid.org/0000-0002-2191-9011

Complete contact information is available at: https://pubs.acs.org/10.1021/acs.inorgchem.0c01807

Notes

The authors declare no competing financial interest.

The research data pertaining to this paper are available at https://doi.org/10.17630/54781f80-3c71-48a2-aed7-45381cab7683.

ACKNOWLEDGMENTS

We thank Prof. E. Zysman-Colman and Prof. Anna Köhler for helpful suggestions throughout. Y.-Y.G. and T.L. acknowledge the University of St. Andrews and China Scholarship Council for funding of studentships (201603780005) and (201606280032), respectively. J.A.M. and P.L. acknowledge financial support from the Leverhulme trust (RPG-2018-065). S.B., K.S., and F.P. acknowledge financial support from the German National Science Foundation via the Projects 423895689, KO 3973/2-1 and PA 3373/3-1 and further acknowledge support by the Bavarian State Ministry of Science, Research, and the Arts for the Collaborative Research Network "Solar Technologies go Hybrid".

REFERENCES

(1) Saparov, B.; Mitzi, D. B. Organic-Inorganic Perovskites: Structural Versatility for Functional Materials Design. *Chem. Rev.* **2016**, *116* (7), 4558−4596.

(2) Smith, M. D.; Crace, E. J.; Jaffe, A.; Karunadasa, H. I. The Diversity of Layered Halide Perovskites. *Annu. Rev. Mater. Res.* **2018**, *48* (1), 111−136.

(3) Mao, L.; Wu, Y.; Stoumpos, C. C.; Wasielewski, M. R.; Kanatzidis, M. G. White-Light Emission and Structural Distortion in New Corrugated Two-Dimensional Lead Bromide Perovskites. *J. Am. Chem. Soc.* **2017**, *139* (14), 5210−5215.

(4) Benedek, N. A.; Rondinelli, J. M.; Djani, H.; Ghosez, P.; Lightfoot, P. Understanding Ferroelectricity in Layered Perovskites: New Ideas and Insights from Theory and Experiments. *Dalton Trans.* **2015**, *44* (23), 10543−10558.

(5) Balachandran, P. V.; Young, J.; Lookman, T.; Rondinelli, J. M. Learning from Data to Design Functional Materials without Inversion Symmetry. *Nat. Commun.* **2017**, *8*, 1−13.

(6) Cochrane, A. K.; Telfer, M.; Dixon, C. A. L.; Zhang, W.; Halasyamani, P. S.; Bousquet, E.; Lightfoot, P. $NdBaScO_4$: Aristotype of a New Family of Geometric Ferroelectrics? *Chem. Commun.* **2016**, *52* (73), 10980−10983.

(7) Guo, Y. Y.; McNulty, J. A.; Mica, N. A.; Samuel, I. D. W.; Slawin, A. M. Z.; Bühl, M.; Lightfoot, P. Structure-Directing Effects in (110)-Layered Hybrid Perovskites Containing Two Distinct Organic Moieties. *Chem. Commun.* **2019**, *55* (67), 9935−9938.

(8) Salah, M. B. H.; Mercier, N.; Allain, M.; Zouari, N.; Giovanella, U.; Botta, C. Mechanochromic and Electroluminescence Properties of

a Layered Hybrid Perovskite Belonging to the < 110> Series. *Eur. J. Inorg. Chem.* **2019**, *2019* (42), 4527−4531.
(9) Febriansyah, B.; Giovanni, D.; Ramesh, S.; Koh, T. M.; Li, Y.; Sum, T. C.; Mathews, N.; England, J. Inducing Formation of a Corrugated, White-Light Emitting 2D Lead-Bromide Perovskite via Subtle Changes in Templating Cation. *J. Mater. Chem. C* **2020**, *8* (110), 889−893.
(10) *CrystalClear*; Rigaku Corporation: Tokyo, 2014.
(11) Sheldrick, G. M. Crystal Structure Refinement with SHELXL. *Acta Crystallogr., Sect. C: Struct. Chem.* **2015**, *71*, 3−8.
(12) Farrugia, L. J. WinGX and ORTEP for Windows: An Update. *J. Appl. Crystallogr.* **2012**, *45* (4), 849−854.
(13) Schötz, K.; Askar, A. M.; Peng, W.; Seeberger, D.; Gujar, T. P.; Thelakkat, M.; Köhler, A.; Huettner, S.; Bakr, O. M.; Shankar, K.; et al. Double Peak Emission in Lead Halide Perovskites by Self-Absorption. *J. Mater. Chem. C* **2020**, *8* (7), 2289−2300.
(14) de Mello, J. C.; Wittmann, H. F.; Friend, R. H. An Improved Experimental Determination of External Photoluminescence Quantum Efficiency. *Adv. Mater.* **1997**, *9* (3), 230−232.
(15) Mercier, N. Hybrid Halide Perovskites: Discussions on Terminology and Materials. *Angew. Chem., Int. Ed.* **2019**, *58* (50), 17912−17917.
(16) Li, T.; Clulow, R.; Bradford, A. J.; Lee, S. L.; Slawin, A. M. Z.; Lightfoot, P. A Hybrid Fluoride Layered Perovskite, $(enH_2)MnF_4$. *Dalton Trans.* **2019**, *48* (15), 4784−4787.
(17) Tremblay, M.-H.; Bacsa, J.; Zhao, B.; Pulvirenti, F.; Barlow, S.; Marder, S. R. Structures of $(4\text{-Y-}C_6H_4CH_2NH_3)_2PbI_4$ {Y = H, F, Cl, Br, I}: Tuning of Hybrid Organic Inorganic Perovskite Structures from Ruddlesden−Popper to Dion−Jacobson Limits. *Chem. Mater.* **2019**, *31* (16), 6145−6153.
(18) Ke, W.; Mao, L.; Stoumpos, C. C.; Hoffman, J.; Spanopoulos, I.; Mohite, A. D.; Kanatzidis, M. G. Compositional and Solvent Engineering in Dion-Jacobson 2D Perovskites Boosts Solar Cell Efficiency and Stability. *Adv. Energy Mater.* **2019**, *9* (10), 1803384.
(19) Campbell, B. J.; Stokes, H. T.; Tanner, D. E.; Hatch, D. M. ISODISPLACE: A Web-Based Tool for Exploring Structural Distortions. *J. Appl. Crystallogr.* **2006**, *39* (4), 607−614.
(20) Fujii, K.; Esaki, Y.; Omoto, K.; Yashima, M.; Hoshikawa, A.; Ishigaki, T.; Hester, J. R. New Perovskite-Related Structure Family of Oxide-Ion Conducting Materials $NdBaInO_4$. *Chem. Mater.* **2014**, *26* (8), 2488−2491.
(21) Li, Y.; Zheng, G.; Lin, J. Synthesis, Structure, and Optical Properties of a Contorted ⟨110⟩-Oriented Layered Hybrid Perovskite: $C_3H_{11}SN_3PbBr_4$. *Eur. J. Inorg. Chem.* **2008**, *4* (10), 1689−1692.
(22) Daub, M.; Haber, C.; Hillebrecht, H. Synthesis, Crystal Structures, Optical Properties, and Phase Transitions of the Layered Guanidinium-Based Hybrid Perovskites $[C(NH_2)_3]_2MI_4$; M = Sn, Pb. *Eur. J. Inorg. Chem.* **2017**, *2017* (7), 1120−1126.
(23) Mitzi, D. B.; Wang, S.; Feild, C. A.; Chess, C. A.; Guloy, A. M. Conducting Layered Organic-Inorganic Halides Containing ⟨110⟩-Oriented Perovskite Sheets. *Science* **1995**, *267* (5203), 1473−1476.
(24) McNulty, J. A.; Lightfoot, P. Unprecedented Tin Iodide Perovskite-like Structures Featuring Ordering of Organic Moieties. *Chem. Commun.* **2020**, *56*, 4543−4546.
(25) Nazarenko, O.; Kotyrba, M. R.; Wörle, M.; Cuervo-Reyes, E.; Yakunin, S.; Kovalenko, M. V. Luminescent and Photoconductive Layered Lead Halide Perovskite Compounds Comprising Mixtures of Cesium and Guanidinium Cations. *Inorg. Chem.* **2017**, *56* (19), 11552−11564.
(26) Li, X.; Guo, P.; Kepenekian, M.; Hadar, I.; Katan, C.; Even, J.; Stoumpos, C. C.; Schaller, R. D.; Kanatzidis, M. G. Small Cyclic Diammonium Cation Templated (110)-Oriented 2D Halide (X = I, Br, Cl) Perovskites with White-Light Emission. *Chem. Mater.* **2019**, *31* (9), 3582−3590.
(27) Febriansyah, B.; Koh, T. M.; Lekina, Y.; Jamaludin, N. F.; Bruno, A.; Ganguly, R.; Shen, Z. X.; Mhaisalkar, S. G.; England, J. Improved Photovoltaic Efficiency and Amplified Photocurrent Generation in Mesoporous n = 1 Two-Dimensional Lead-Iodide Perovskite Solar Cells. *Chem. Mater.* **2019**, *31* (3), 890−898.
(28) Tremblay, M. H.; Thouin, F.; Leisen, J.; Bacsa, J.; Srimath Kandada, A. R.; Hoffman, J. M.; Kanatzidis, M. G.; Mohite, A. D.; Silva, C.; Barlow, S.; et al. $(4NPEA)_2PbI_4$ (4NPEA = 4-Nitrophenylethylammonium): Structural, NMR, and Optical Properties of a 3 × 3 Corrugated 2D Hybrid Perovskite. *J. Am. Chem. Soc.* **2019**, *141* (11), 4521−4525.
(29) Dohner, E. R.; Jaffe, A.; Bradshaw, L. R.; Karunadasa, H. I. Intrinsic White-Light Emission from Layered Hybrid Perovskites. *J. Am. Chem. Soc.* **2014**, *136* (38), 13154−13157.
(30) Gautier, R.; Massuyeau, F.; Galnon, G.; Paris, M. Lead Halide Post-Perovskite-Type Chains for High-Efficiency White-Light Emission. *Adv. Mater.* **2019**, *31* (14), 1807383.
(31) Nazarenko, O.; Kotyrba, M. R.; Yakunin, S.; Aebli, M.; Rainò, G.; Benin, B. M.; Wörle, M.; Kovalenko, M. V. Guanidinium-Formamidinium Lead Iodide: A Layered Perovskite-Related Compound with Red Luminescence at Room Temperature. *J. Am. Chem. Soc.* **2018**, *140* (11), 3850−3853.
(32) Stoumpos, C. C.; Soe, C. M. M.; Tsai, H.; Nie, W.; Blancon, J. C.; Cao, D. H.; Liu, F.; Traoré, B.; Katan, C.; Even, J.; et al. High Members of the 2D Ruddlesden-Popper Halide Perovskites: Synthesis, Optical Properties, and Solar Cells of $(CH_3(CH_2)_3NH_3)_2(CH_3NH_3)_4Pb_5I_{16}$. *Chem.* **2017**, *2* (3), 427−440.
(33) Cao, D. H.; Stoumpos, C. C.; Farha, O. K.; Hupp, J. T.; Kanatzidis, M. G. 2D Homologous Perovskites as Light-Absorbing Materials for Solar Cell Applications. *J. Am. Chem. Soc.* **2015**, *137* (24), 7843−7850.
(34) Green, M. A.; Jiang, Y.; Soufiani, A. M.; Ho-Baillie, A. Optical Properties of Photovoltaic Organic-Inorganic Lead Halide Perovskites. *J. Phys. Chem. Lett.* **2015**, *6* (23), 4774−4785.
(35) Dohner, E. R.; Hoke, E. T.; Karunadasa, H. I. Self-Assembly of Broadband White-Light Emitters. *J. Am. Chem. Soc.* **2014**, *136* (5), 1718−1721.
(36) Lermer, C.; Harm, S. P.; Birkhold, S. T.; Jaser, J. A.; Kutz, C. M.; Mayer, P.; Schmidt-Mende, L.; Lotsch, B. V. Benzimidazolium Lead Halide Perovskites: Effects of Anion Substitution and Dimensionality on the Bandgap. *Z. Anorg. Allg. Chem.* **2016**, *642* (23), 1369−1376.
(37) Tong, Y.; Bladt, E.; Aygüler, M. F.; Manzi, A.; Milowska, K. Z.; Hintermayr, V. A.; Docampo, P.; Bals, S.; Urban, A. S.; Polavarapu, L.; et al. Highly Luminescent Cesium Lead Halide Perovskite Nanocrystals with Tunable Composition and Thickness by Ultrasonication. *Angew. Chem., Int. Ed.* **2016**, *55* (44), 13887−13892.
(38) Parrott, E. S.; Patel, J. B.; Haghighirad, A. A.; Snaith, H. J.; Johnston, M. B.; Herz, L. M. Growth Modes and Quantum Confinement in Ultrathin Vapour-Deposited $MAPbI_3$ Films. *Nanoscale* **2019**, *11* (30), 14276−14284.
(39) Gong, X.; Voznyy, O.; Jain, A.; Liu, W.; Sabatini, R.; Piontkowski, Z.; Walters, G.; Bappi, G.; Nokhrin, S.; Bushuyev, O.; et al. Electron-Phonon Interaction in Efficient Perovskite Blue Emitters. *Nat. Mater.* **2018**, *17* (6), 550−556.
(40) Smith, M. D.; Karunadasa, H. I. White-Light Emission from Layered Halide Perovskites. *Acc. Chem. Res.* **2018**, *51* (3), 619−627.
(41) Shin, D. H.; Ko, J. S.; Kang, S. K.; Choi, S. H. Enhanced Flexibility and Stability in Perovskite Photodiode-Solar Cell Nanosystem Using MoS_2 Electron-Transport Layer. *ACS Appl. Mater. Interfaces* **2020**, *12* (4), 4586−4593.
(42) Kitazawa, N.; Aono, M.; Watanabe, Y. Temperature-Dependent Time-Resolved Photoluminescence of $(C_6H_5C_2H_4NH_3)_2PbX_4$ (X = Br and I). *Mater. Chem. Phys.* **2012**, *134* (2−3), 875−880.
(43) Kitazawa, N.; Ito, T.; Sakasegawa, D.; Watanabe, Y. Excitons in Self-Organized Layered Perovskite Films Prepared by the Two-Step Growth Process. *Thin Solid Films* **2006**, *500* (1−2), 133−137.
(44) Lin, H.; Zhou, C.; Tian, Y.; Siegrist, T.; Ma, B. Low-Dimensional Organometal Halide Perovskites. *ACS Energy Lett.* **2018**, *3* (1), 54−62.
(45) Cortecchia, D.; Yin, J.; Petrozza, A.; Soci, C. White Light Emission in Low-Dimensional Perovskites. *J. Mater. Chem. C* **2019**, *7* (17), 4956−4969.

https://dx.doi.org/10.1021/acs.inorgchem.0c01807
Inorg. Chem. 2020, 59, 12858−12866

(46) Mott, N. F.; Stoneham, A. M. The Lifetime of Electrons, Holes and Excitons before Self-Trapping. *J. Phys. C: Solid State Phys.* **1977**, *10* (17), 3391−3398.
(47) Yin, J.; Li, H.; Cortecchia, D.; Soci, C.; Brédas, J. L. Excitonic and Polaronic Properties of 2D Hybrid Organic-Inorganic Perovskites. *ACS Energy Lett.* **2017**, *2* (2), 417−423.
(48) Nagami, A.; Okamura, K.; Ishihara, T. Optical Properties of a Quantum Wire Crystal, C5H10NH2PbI3. *Phys. B* **1996**, *227* (1−4), 346−348.
(49) Schötz, K.; Askar, A. M.; Köhler, A.; Shankar, K.; Panzer, F. Investigating the Tetragonal-to-Orthorhombic Phase Transition of Methylammonium Lead Iodide Single Crystals by Detailed Photoluminescence Analysis. *Adv. Opt. Mater.* **2020**, 2000455.
(50) Panzer, F.; Li, C.; Meier, T.; Köhler, A.; Huettner, S. Impact of Structural Dynamics on the Optical Properties of Methylammonium Lead Iodide Perovskites. *Adv. Energy Mater.* **2017**, *7* (16), 1700286.
(51) Smith, M. D.; Jaffe, A.; Dohner, E. R.; Lindenberg, A. M.; Karunadasa, H. I. Structural Origins of Broadband Emission from Layered Pb-Br Hybrid Perovskites. *Chem. Sci.* **2017**, *8* (6), 4497−4504.
(52) Gautier, R.; Paris, M.; Massuyeau, F. Exciton Self-Trapping in Hybrid Lead Halides: Role of Halogen. *J. Am. Chem. Soc.* **2019**, *141* (32), 12619−12623.
(53) Kahmann, S.; Tekelenburg, E. K.; Duim, H.; Kamminga, M. E.; Loi, M. A. Extrinsic Nature of the Broad Photoluminescence in Lead Iodide-Based Ruddlesden−Popper Perovskites. *Nat. Commun.* **2020**, *11* (1), 1−8.

https://dx.doi.org/10.1021/acs.inorgchem.0c01807
Inorg. Chem. 2020, 59, 12858−12866

Structural diversity in layered hybrid perovskites, A_2PbBr_4 or $AA'PbBr_4$, templated by small disc-shaped amines

Yuan-Yuan Guo,[†] Lin-Jie Yang,[†] Simon Biberger,[§] Jason A. McNulty,[†] Teng Li,[†] Konstantin Schötz,[§] Fabian Panzer,[§] and Philip Lightfoot*,[†]

[†]School of Chemistry and EaStChem, University of St Andrews, St Andrews, KY16 9ST, United Kingdom

[§]Soft Matter Optoelectronics, Department of Physics, University of Bayreuth, 95440 Bayreuth, Germany

*e-mail: pl@st-andrews.ac.uk

Supplementary Information

Table S1: Crystal and structure refinement data of T_2PbBr_4, A_2PbBr_4 and $ITPbBr_4$ at 173 K

	T_2PbBr_4	A_2PbBr_4	$ITPbBr_4$
Formula	$C_4H_8N_6PbBr_4$	$C_4H_{14}N_4PbBr_4$	$C_5H_9N_5PbBr_4$
Formula weight	666.99	645.02	666.00
Colour/Habit	Yellow/Block	Colorless/Block	Colorless/Prism
Crystal size (mm^3)	0.23×0.17×0.09	0.22×0.18×0.13	0.21×0.12×0.11
Crystal system	Monoclinic	Monoclinic	Orthorhombic
Space group	*C*2/*c*	$P2_1/c$	*Pbcm*
***a* (Å)**	11.8775(9)	12.6112(9)	5.9958(4)
***b* (Å)**	11.8766(9)	9.2833(7)	25.7883(18)
***c* (Å)**	19.1913(14)	12.2101(9)	18.7851(13)
α (°)	90	90	90
β (°)	94.994(6)	90.972(5)	90
γ (°)	90	90	90
***V* ($Å^3$)**	2696.9(4)	1429.27(18)	2904.6(3)
Z	8	4	8
ρ_{calc} (g/cm^3)	3.285	2.997	3.046
μ (mm^{-1})	24.345	22.958	22.602
F(000)	2368	1152	2368
Reflns collected	11117	14279	22997
Independent reflns	2394 [R(int) =0.0438]	3258 [R(int) =0.0555]	2635 [R(int) =0.0419]
Goodness of Fit	0.939	0.936	1.222
Final *R* indices ($I > 2\sigma(I)$)	R_1 = 0.0245 wR_2 = 0.0476	R_1 = 0.0240 wR_2 = 0.0538	R_1 = 0.0228 wR_2 =0.0619
Largest diff. peak/hole (e $Å^{-3}$)	1.541/-1.166	1.407/-1.723	0.820/-2.029

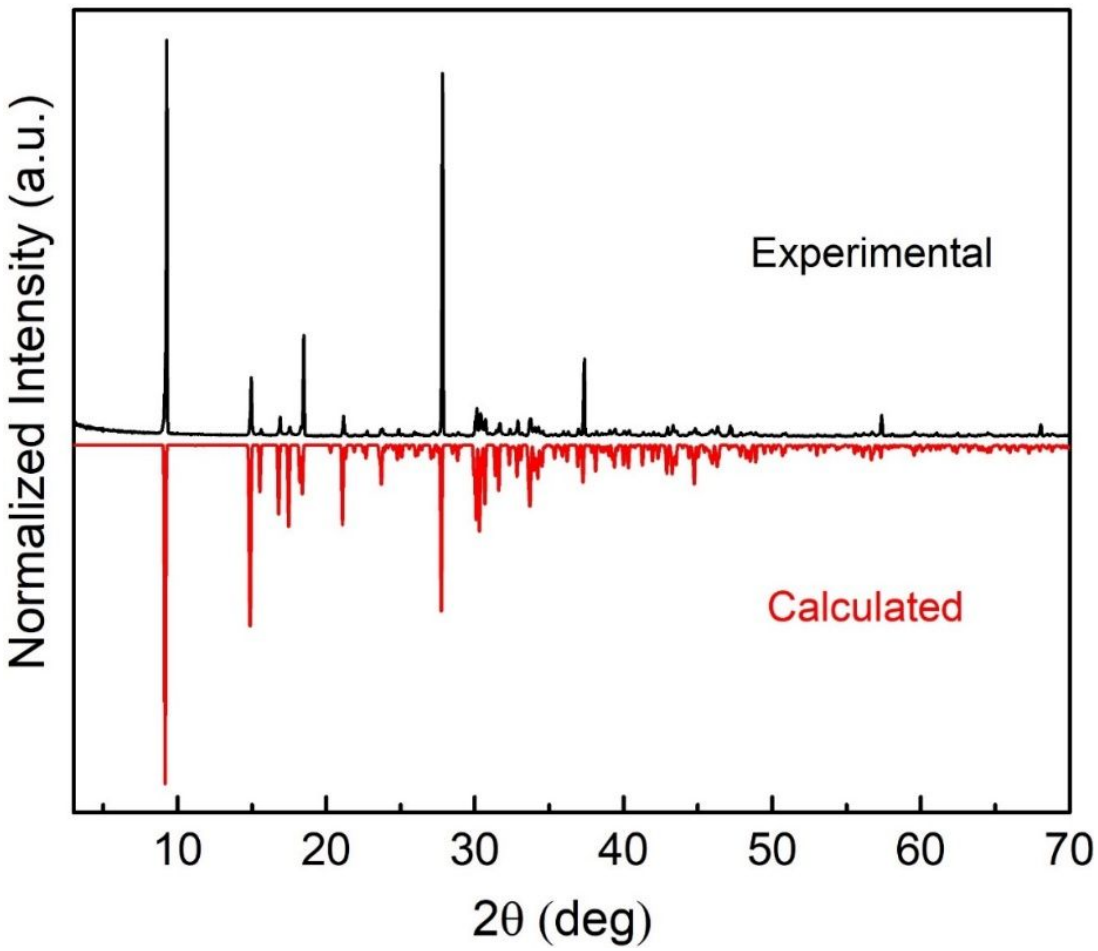

Figure S1: Raw and simulated powder X-ray diffraction data for T_2PbBr_4.

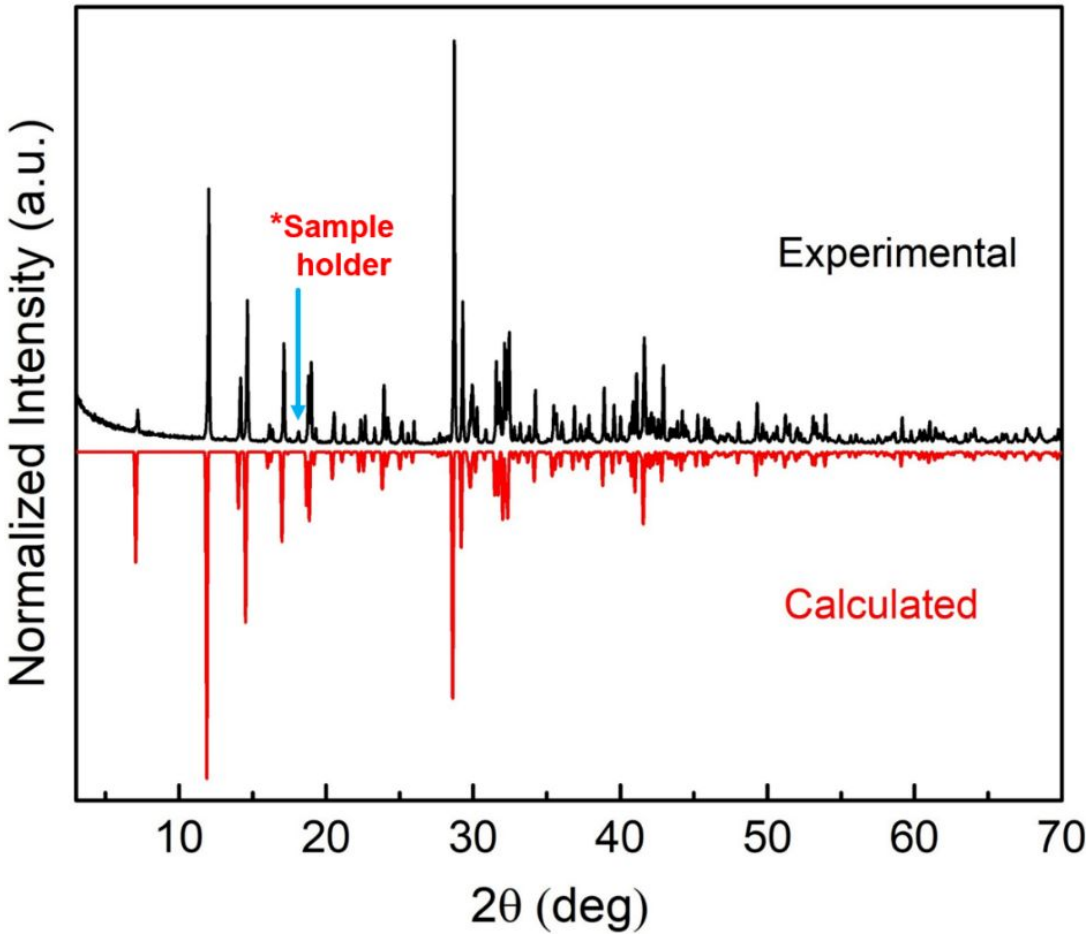

Figure S2: Raw and simulated powder X-ray diffraction data for A_2PbBr_4.

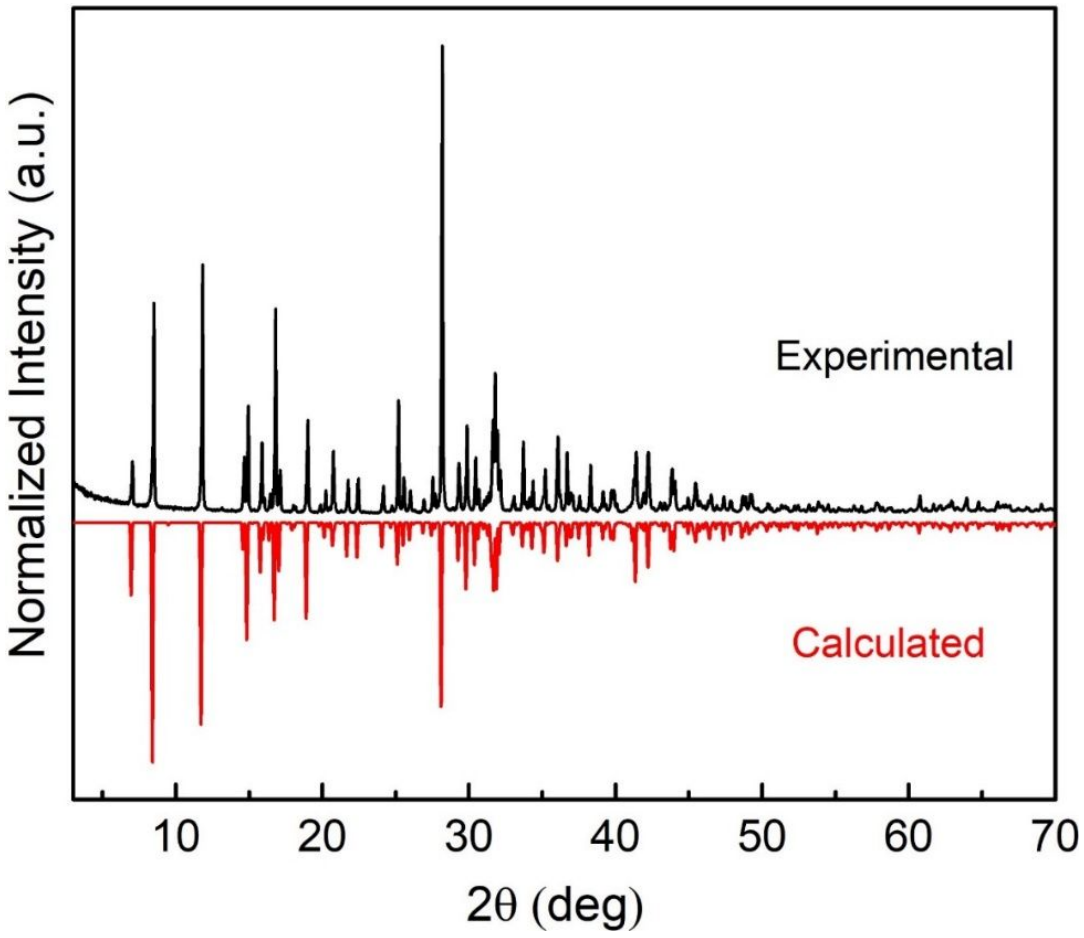

Figure S3: Raw and simulated powder X-ray diffraction data for $ITPbBr_4$.

Table S2: Hydrogen bond lengths (Å) and angles (°) for T_2PbBr_4 at 298 K.

D-H...A	d(D-H)	d(H...A)	d(D...A)	<(DHA)
N(2)-H(1)...Br(2)#5	0.86	2.76	3.435(6)	136
N(2)-H(1)...Br(4)#2	0.86	3.02	3.682(6)	135.7
N(3)-H(2)...Br(2)	0.86	2.53	3.326(5)	154.4
N(5)-H(5)...Br(1)#6	0.86	2.76	3.439(6)	137.5
N(5)-H(5)...Br(3)#7	0.86	2.94	3.593(6)	133.7
N(6)-H(6)...Br(1)#3	0.86	2.53	3.326(5)	154.1

Symmetry transformations used to generate equivalent atoms:

#1 -x+1/2,y-1/2,-z+3/2 #2 -x+1,y,-z+3/2 #3 -x+1/2,y+1/2,-z+3/2

#4 -x,y,-z+3/2 #5 x+1/2,y+1/2,z #6 -x+1,y+1,-z+3/2

#7 x,y+1,z

Table S3: Hydrogen bond lengths (Å) and angles (°) for T_2PbBr_4 at 173 K.

D-H...A	d(D-H)	d(H...A)	d(D...A)	<(DHA)
N(2)-H(1)...Br(2)#5	0.86	2.73	3.398(5)	135.8
N(2)-H(1)...Br(4)#2	0.86	2.97	3.636(5)	135.3
N(3)-H(2)...Br(2)	0.86	2.52	3.314(4)	153.6
N(5)-H(5)...Br(1)#6	0.86	2.71	3.398(5)	137.6
N(5)-H(5)...Br(3)#7	0.86	2.91	3.551(5)	132.6
N(6)-H(6)...Br(1)#3	0.86	2.52	3.310(4)	153.9

Symmetry transformations used to generate equivalent atoms:

#1 -x+1/2,y-1/2,-z+3/2 #2 -x+1,y,-z+3/2 #3 -x+1/2,y+1/2,-z+3/2

#4 -x,y,-z+3/2 #5 x+1/2,y+1/2,z #6 -x+1,y+1,-z+3/2

#7 x,y+1,z

Table S4: Hydrogen bond lengths (Å) and angles (°) for A_2PbBr_4 at 298 K.

D-H...A	d(D-H)	d(H...A)	d(D...A)	<(DHA)
N(1)-H(1)...Br(1)#3	0.86	2.83	3.604(4)	150.8
N(1)-H(1)...Br(4)#3	0.86	3.04	3.586(4)	123.7
N(1)-H(2)...Br(3)#4	0.86	2.58	3.435(4)	171.4
N(2)-H(3)...Br(1)#3	0.86	2.62	3.442(4)	160.6
N(2)-H(4)...Br(1)#5	0.86	2.65	3.504(4)	170.3
N(3)-H(8)...Br(3)	0.86	2.56	3.393(4)	162.4
N(3)-H(9)...Br(2)#3	0.86	2.64	3.402(4)	148
N(4)-H(10)...Br(3)	0.86	2.87	3.633(5)	148.3
N(4)-H(10)...Br(4)	0.86	3.04	3.588(5)	123.1
N(4)-H(11)...Br(1)#6	0.86	3.07	3.585(5)	120.9
N(4)-H(11)...Br(2)#6	0.86	2.89	3.656(5)	149

Symmetry transformations used to generate equivalent atoms:

#1 -x,y+1/2,-z+1/2 #2 -x,y-1/2,-z+1/2 #3 x,y+1,z

#4 x,-y+3/2,z+1/2 #5 -x+1,y+1/2,-z+1/2 #6 x,-y+1/2,z+1/2

Table S5: Hydrogen bond lengths (Å) and angles (°) for A_2PbBr_4 at 173 K.

D-H...A	d(D-H)	d(H...A)	d(D...A)	<(DHA)
N(1)-H(1)...Br(1)#3	0.86	2.82	3.590(4)	149.6
N(1)-H(1)...Br(4)#3	0.86	2.98	3.533(4)	124.1
N(1)-H(2)...Br(3)#4	0.86	2.56	3.416(4)	173.1
N(2)-H(3)...Br(1)#3	0.86	2.6	3.425(4)	160
N(2)-H(4)...Br(1)#5	0.86	2.63	3.483(4)	170.2
N(3)-H(8)...Br(3)	0.86	2.55	3.375(4)	161
N(3)-H(9)...Br(2)#3	0.86	2.62	3.389(4)	149
N(4)-H(10)...Br(3)	0.86	2.84	3.595(5)	148.3
N(4)-H(10)...Br(4)	0.86	3.06	3.583(4)	121.6
N(4)-H(11)...Br(1)#6	0.86	3.03	3.543(4)	120.4
N(4)-H(11)...Br(2)#6	0.86	2.86	3.625(5)	149

Symmetry transformations used to generate equivalent atoms:

#1 -x,y+1/2,-z+1/2 #2 -x,y-1/2,-z+1/2 #3 x,y+1,z

#4 x,-y+3/2,z+1/2 #5 -x+1,y+1/2,-z+1/2 #6 x,-y+1/2,z+1/2

Table S6: Hydrogen bond lengths (Å) and angles (°) for $ITPbBr_4$ at 298 K.

D-H...A	d(D-H)	d(H...A)	d(D...A)	<(DHA)
N(2)-H(1)...Br(3)	0.86	2.48	3.277(5)	154.5
N(3)-H(2)...Br(2)#6	0.86	2.56	3.309(5)	145.6
N(4)-H(5)...N(1)	0.86	2.36	3.085(9)	142.5
N(5A^a)-H(8A^a)...Br(3)	0.86	3.04	3.646(13)	129.3
N(5A^a)-H(8A^a)...Br(4)#2	0.86	3.08	3.791(11)	142.1
N(5B^b)-H(8B^b)...Br(4)#2	0.86	2.9	3.688(12)	152.7

Symmetry transformations used to generate equivalent atoms:

#1 x,-y+3/2,-z+1 #2 x-1,y,z #3 x,y,-z+1/2

#4 x,y,-z+3/2 #5 x+1,y,z #6 x-1,y,-z+1/2

Table S7: Hydrogen bond lengths (Å) and angles (°) for $ITPbBr_4$ at 173 K.

D-H...A	d(D-H)	d(H...A)	d(D...A)	<(DHA)
N(2)-H(1)...Br(3)	0.86	2.46	3.252(5)	152.7
N(3)-H(2)...Br(2)#6	0.86	2.54	3.290(4)	146.4
N(4)-H(5)...N(1)	0.86	2.31	3.019(7)	140.1
N(5A^a)-H(8A^a)...Br(3)	0.86	3	3.604(10)	129.4
N(5A^a)-H(8A^a)...Br(4)#2	0.86	3.06	3.762(9)	140.9
N(5B^b)-H(8B^b)...Br(4)#2	0.86	2.88	3.664(12)	153.1

Symmetry transformations used to generate equivalent atoms:

#1 x,-y+3/2,-z+1 #2 x-1,y,z #3 x,y,-z+1/2

#4 x,y,-z+3/2 #5 x+1,y,z #6 x-1,y,-z+1/2

The bond length distortion of the BX_6 octahedra in each composition was calculated using eq. 1,[1] where d is the average B-X bond distance and d_n are the six individual bond distances. The bond angle variance of each octahedron from the ideal 90° of an undistorted structure was calculated using eq. 2,[2] where θ_i is the individual X-B-X angle.

$$\Delta d = \left(\frac{1}{6}\right)\sum\left[\frac{d_n - d}{d}\right]^2 \quad \textbf{(1)}$$

$$\sigma^2 = \sum_{i=1}^{12} \frac{(\theta_i - 90)^2}{11} \quad (2)$$

Table S8: Octahedral distortion parameters of T_2PbBr_4, A_2PbBr_4, $ITPbBr_4$ and known (110)-oriented layered perovskites.

Composition[a]	**Temperature /K**	**Δd (×10⁻⁴)**	**σ²**
(100)-oriented:			
$[T]_2PbBr_4$[b]	298	0.23	33.56
$[T]_2PbBr_4$[b]	173	0.26	35.26
(110)-oriented 2×2:			
$[A]_2PbBr_4$[b]	298	29.16	26.12
$[A]_2PbBr_4$[b]	173	27.49	30.61
[TG]$PbBr_4$[3]	298	7.59	22.06
[TG]$PbBr_4$[3]	93	10.97	28.22
[IG]$PbBr_4$[3]	298	8.91	7.71
[IG]$PbBr_4$[3]	93	7.39	16.16
[NMEDA]$PbBr_4$[4]	373	8.20	24.51
[API]$PbBr_4$[5]	293	26.02	20.79
[2-(aminoethyl)isothiourea]$PbBr_4$[6]	293	9.67	38.91
[EDBE]$PbBr_4$[7]	100	24.00	23.93
[ImEA]$PbBr_4$[8]	100	22.93	53.66
[(FA)(HEA)]$PbBr_4$[9]	150	5.70	11.59
		13.66	14.46
[3APr]$PbBr_4$[10]	298	9.81	21.07
[3APr]PbI_4[10]	298	11.92	22.04
[EDBE]PbI_4[7]	100	18.97	14.36
$[G]_2PbI_4$[11]	100	7.78	12.65
		11.16	8.41
[3APr]$PbCl_4$[10]	298	12.32	34.50
$[pipzH_2]PbCl_4$[12]	293	2.12	32.23
$[G]_2SnI_4$[11]	273	20.06	6.78
		23.47	6.14
[(IFA)(MA)]SnI_4[13]	295	2.02	7.77
$[(G)_{1.5}(Me\text{-}I)_{0.5}]SnI_4$[14]	173	34.30	11.22
		45.71	15.35
(110)-oriented 3×3:			
[IT]$PbBr_4$[b]	298	0.04	7.01
		11.70	26.58
[IT]$PbBr_4$[b]	173	0.02	9.16
		8.30	28.52
[α-(DMEN)]$PbBr_4$[15]	293	3.92	8.87
		30.83	25.83
[ImEA]PbI_4[16]	100	1.29	7.08
		3.66	23.52
		21.37	39.16
$[4NPEA]_2PbBr_4$[17]	110	1.01	6.80
		1.31	15.10
		31.20	11.81
$[4NPEA]_2PbI_4$[17]	100	0.16	12.87
		1.17	6.76

			16.92	43.08

[a]Abbreviations used in the table correspond to the following organic molecules: [T] = 1,2,4-triazolium; [A] = acetamidinium; [G] = guanidinium; [I] = imidazolium; [NMEDA] = N'-methylethane-1,2-diammonium; [API] = N-(3-amino propyl)imidazolium; [EDBE] = 2,2'-(ethylenedioxy)bis(ethylammonium); [ImEA] = imidazolium ethylammonium; [FA] = formamidinium; [HEA] = hydroxyethylammonium; [3APr] = 3-aminopyrrolidinium; [$pipzH_2$] = piperazinium; [IFA] = iodoformamidinium; [MA] = methylammonium; [Me-I] = 4-methylimidazolium; [α-(DMEN)] = 2-(dimethylamino)ethylamine and [4NPEA] = 4-nitrophenylethylammonium.

[b]This work.

Table S9: Space group and unit cell metrics of known (110)-oriented layered perovskites where $a_p \sim 6$ Å (perpendicular to corrugation direction), $b \sim 9$ and 19 Å for 2 × 2 and 3 × 3 systems, respectively (along the corrugation direction) and c is the variable *inter*-layer distance dictated by the organic moieties. Compositions are grouped according to similar metrics.

Composition	**Space Group**	**metrics**	**metric *c* values (Å)**
<u>(110)-oriented 2×2:</u>			
[TG]$PbBr_4$ 298 K	$P2/c$	$a_p \times c \times b$	14.0000(9)
[TG]$PbBr_4$ 93 K	$P2_1/c$	$a_p \times c \times b$	26.969(9)
[API]$PbBr_4$	$P2_1/c$	$a_p \times c \times b$	27.6363(12)
[EDBE]$PbBr_4$	$P2_1/c$	$a_p \times c \times b$	28.7804(14)
[3APr]$PbBr_4$	$P2_1/c$	$a_p \times c \times b$	22.5450(1)
[EDBE]PbI_4	$P2_1/c$	$a_p \times c \times b$	29.461(2)
[3APr]$PbCl_4$	$P2_1/c$	$a_p \times c \times b$	21.757300(7)
[$pipzH_2$]$PbCl_4$	$P2_1/c$	$a_p \times c \times b$	22.612(26)
[IG]$PbBr_4$	P-1	$a_p \times b \times c$	12.8673(3)
[(IFA)(MA)]SnI_4	$P2_1/m$	$a_p \times b \times c$	14.787(2)
[NMEDA]$PbBr_4$	$P2_12_12_1$	$a_p \times b \times c$	23.7433(16)
[ImEA]$PbBr_4$	$P2_1/c$	$b \times 2a_p \times c$	23.518900(4)
[$(G)_{1.5}$(Me-$I)_{0.5}$]SnI_4	P-1	$b \times 2a_p \times c$	15.0588(11)
[3APr]PbI_4	$Pna2_1$	$b \times c \times a_p$	21.37600(3)
[(FA)(HEA)]$PbBr_4$	$P2/n$	$b \times c \times 2a_p$	13.1578(5)
$[G]_2PbI_4$	$P2_1/n$	$b \times c \times 2a_p$	26.8837(14)
$[G]_2SnI_4$	$P2_1/n$	$b \times c \times 2a_p$	26.954(2)
$[A]_2PbBr_4$[a]	$P2_1/c$	$c \times b \times 2a_p$	12.6949(9)
[2-(aminoethyl)isothiourea]$PbBr_4$	$P2_1/c$	$c \times b \times 2a_p$	13.2976(9)
<u>(110)-oriented 3×3:</u>			
[IT]$PbBr_4$[a]	$Pbcm$	$a_p \times c \times b$	25.873(2)
[α-(DMEN)]$PbBr_4$	$Pbca$	$b \times 2a_p \times c$	23.68000(5)
[ImEA]PbI_4	$P2_1/c$	$c \times b \times 2a_p$	12.494800(3)
$[4NPEA]_2PbBr_4$	$P2_1/c$	$c \times b \times 2a_p$	21.2912(5)
$[4NPEA]_2PbI_4$	$P2_1/c$	$c \times b \times 2a_p$	21.0976(4)

[a]This work.

Distortion mode analysis

The on-line crystallographic tool ISODISTORT provides a decomposition of a distorted crystal structure in terms of irreducible representation (*irrep*) analysis. In this case, ISODISTORT is used to compare the cif file for the refined crystal structure to that of an idealised 'parent' phase. For simplicity in comparing the 'BX_4' layer structure of the present compound T_2PbBr_4, without needing to consider the organic moieties, the cif for the parent phase has been adjusted from the aristotype inorganic n = 1 RP phase $TlAlF_4$ by removing Tl, renaming the Al and F positions to Pb and Br, respectively, and adjusting the unit cell parameters and z-coordinate of the Br2 atom, to produce Pb-Br bond lengths that are similar in dimensions to those expected. Since the ISODISTORT software uses normal mode analysis, none of these adjustments affect the key derived outputs, which are the symmetry-allowed distortion modes at the Brillouin zone boundary, and their magnitudes.

The primary modes evidenced act at the points M ($\boldsymbol{k}$ = ½, ½, 0) and Z ($\boldsymbol{k}$ = 0, 0, ½) of the parent *P*4/*mmm* Brillouin zone. The two *irrep*s describing octahedral tilting have the labels M_3^+ (concerted rotation of the octahedra around the *c*-axis of the resultant T_2PbBr_4 unit cell) and M_5^+ ('out-of-phase' tilting around the the *a*-axis of the T_2PbBr_4 unit cell). Acting alone, these modes produce only a 2 × 2 superlattice in the *ab* plane. This gives rise to the tilt system a^-b^0c, in Glazer-like notation. The other significant mode is labelled Z_5^-, and describes the lateral 'antiferrodistortive-like' displacement of adjacent $PbBr_4$ layers along the *b*-axis, leading to the further unit cell doubling along *c*.

Table S10: Distortion mode amplitudes for the inorganic portion of the structure in T_2PbBr_4, obtained from the ISODISTORT software suite[18]. The 'parent' phase is a simulated aristotype based on the Dion-Jacobson $TlAlF_4$ structure.[19] See attached file for full ISODISTORT output.

Mode	Amplitude (Å)		Origin	S, i	*k*-active
	298 K	173 K			
M_3^+	0.500	0.547	(0, 0, 0)	2, 2	(½, ½, 0)
M_5^+	0.550	0.551	(0, 0, 0)	2, 4	(½, ½, 0)
Z_5^-	1.030	0.997	(0, 0, ½)	2, 4	(0, 0, ½)

References

(1) Lufaso, M. W.; Woodward, P. M. Jahn-Teller Distortions, Cation Ordering and Octahedral Tilting in Perovskites. *Acta Crystallogr.* **2004**, *B60*, 10–20.

(2) Robinson, K.; Gibbs, G. V.; Ribbe, P. H. Quadratic Elongation: A Quantitative Measure of Distortion in Coordination Polyhedra. *Science* **1971**, *172* (3983), 567–570.

(3) Guo, Y.-Y.; McNulty, J. A.; Mica, N. A.; Samuel, I. D. W.; Slawin, A. M. Z.; Bühl, M.; Lightfoot, P. Structure-Directing Effects in (110)-Layered Hybrid Perovskites Containing Two Distinct Organic Moieties. *Chem. Commun.* **2019**, *55*, 9935–9938.

(4) Dohner, E. R.; Hoke, E. T.; Karunadasa, H. I. Self-Assembly of Broadband White-Light Emitters. *J. Am. Chem. Soc.* **2014**, *136* (5), 1718–1721.

(5) Li, Y. Y.; Lin, C. K.; Zheng, G. L.; Cheng, Z. Y.; You, H.; Wang, W. D.; Lin, J. Novel <110>-Oriented Organic-Inorganic Perovskite Compound Stabilized by N-(3-Aminopropyl)Imidazole with Improved Optical Properties. *Chem. Mater.* **2006**, *18*, 3463–3469.

(6) Li, Y.; Zheng, G.; Lin, J. Synthesis, Structure, and Optical Properties of a Contorted <110>-Oriented Layered Hybrid Perovskite: $C_3H_{11}SN_3PbBr_4$. *Eur. J. Inorg. Chem.* **2008**, *4*, 1689–1692.

(7) Dohner, E. R.; Jaffe, A.; Bradshaw, L. R.; Karunadasa, H. I. Intrinsic White-Light Emission from Layered Hybrid Perovskites. *J. Am. Chem. Soc.* **2014**, *136*, 13154–13157.

(8) Febriansyah, B.; Giovanni, D.; Ramesh, S.; Koh, T. M.; Li, Y.; Sum, T. C.; Mathews, N.; England, J. Inducing Formation of a Corrugated, White-Light Emitting 2D Lead-Bromide Perovskite via Subtle Changes in Templating Cation . *J. Mater. Chem. C* **2020**, 110, 889–893.

(9) Salah, M. B. H.; Mercier, N.; Allain, M.; Zouari, N.; Giovanella, U.; Botta, C. Mechanochromic and Electroluminescence Properties of a Layered Hybrid Perovskite Belonging to the <110> Series. *Eur. J. Inorg. Chem.* **2019**, *2019*, 4527–4531.

(10) Li, X.; Guo, P.; Kepenekian, M.; Hadar, I.; Katan, C.; Even, J.; Stoumpos, C. C.; Schaller, R. D.; Kanatzidis, M. G. Small Cyclic Diammonium Cation Templated (110)-Oriented 2D Halide (X = I, Br, Cl) Perovskites with White-Light Emission. *Chem. Mater.* **2019**, *31*, 3582–3590.

(11) Daub, M.; Haber, C.; Hillebrecht, H. Synthesis, Crystal Structures, Optical Properties, and Phase Transitions of the Layered Guanidinium-Based Hybrid Perovskites $[C(NH_2)_3]_2MI_4$; M = Sn, Pb. *Eur. J. Inorg. Chem.* **2017**, *2017*, 1120–1126.

(12) Bonamartini Corradi, A.; Ferrari, A. M.; Righi, L.; Sgarabotto, P. An Additional Structural and Electrical Study of Polymeric Haloplumbates(II) with Heterocyclic Diprotonated Amines. *Inorg. Chem.* **2001**, *40*, 218–223.

(13) Mitzi, D. B.; Wang, S.; Feild, C. A.; Chess, C. A.; Guloy, A. M. Conducting Layered Organic-Inorganic Halides Containing <110>-Oriented Perovskite Sheets. *Science* **1995**, *267*, 1473–1476.

(14) McNulty, J. A.; Lightfoot, P. Unprecedented Tin Iodide Perovskite-like Structures Featuring Ordering of Organic Moieties. *Chem. Commun.* **2020**, *56*, 4543–4546.

(15) Mao, L.; Wu, Y.; Stoumpos, C. C.; Wasielewski, M. R.; Kanatzidis, M. G. White-Light Emission and Structural Distortion in New Corrugated Two-Dimensional Lead Bromide Perovskites. *J. Am. Chem. Soc.* **2017**, *139*, 5210–5215.

(16) Febriansyah, B.; Koh, T. M.; Lekina, Y.; Jamaludin, N. F.; Bruno, A.; Ganguly, R.; Shen, Z. X.; Mhaisalkar, S. G.; England, J. Improved Photovoltaic Efficiency and Amplified Photocurrent Generation in Mesoporous n = 1 Two-Dimensional Lead-Iodide Perovskite Solar Cells. *Chem. Mater.* **2019**, *31*, 890–898.

(17) Tremblay, M. H.; Thouin, F.; Leisen, J.; Bacsa, J.; Srimath Kandada, A. R.; Hoffman, J. M.; Kanatzidis, M. G.; Mohite, A. D.; Silva, C.; Barlow, S.; et al. $(4NPEA)_2PbI_4$ (4NPEA = 4-Nitrophenylethylammonium): Structural, NMR, and Optical Properties of a 3 × 3 Corrugated 2D Hybrid Perovskite. *J. Am. Chem. Soc.* **2019**, *141*, 4521–4525.

(18) Campbell, B. J.; Stokes, H. T.; Tanner, D. E.; Hatch, D. M. ISODISPLACE: A Web-Based Tool for Exploring Structural Distortions. *J. Appl. Crystallogr.* **2006**, *39*, 607–614.

(19) Brosset, C. Herstellung Und Kristallbau Der Verbindungen $TlAlF_4$ Und Tl_3AlF_5. *Z. Anorg. Allg. Chem.* **1935**, *8*, 139–147.

14 Intricacies and Mechanism of p-Doping Spiro-MeOTAD Using $Cu(TFSI)_2$

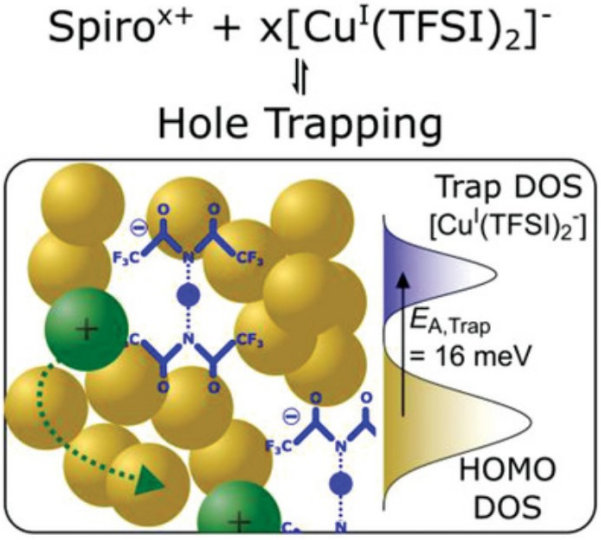

Adrian Hochgesang, **Simon Biberger**, Jeannine Grüne, John Mohanraj, Frank-Julian Kahle, Vladimir Dyakonov, Anna Köhler, Mukundan Thelakkat

Published in
Advanced Electronic Materials, **2022**, 8, 10, 2200113

RESEARCH ARTICLE

ADVANCED ELECTRONIC MATERIALS
www.advelectronicmat.de

Intricacies and Mechanism of p-Doping Spiro-MeOTAD Using $Cu(TFSI)_2$

*Adrian Hochgesang, Simon Biberger, Jeannine Grüne, John Mohanraj, Frank-Julian Kahle, Vladimir Dyakonov, Anna Köhler, and Mukundan Thelakkat**

Copper salts are a popular choice as *p*-dopants for organic semiconductors, particularly in $N^2,N^2,N^{2'},N^{2'},N^7,N^7,N^{7'},N^{7'}$-octakis(4-methoxyphenyl)-9,9′-spirobi[9H-fluoren]-2,2′,7,7′-tetramine (Spiro-MeOTAD) hole transport material for solar cells. While being exceptionally effective, no scientific consensus about their doping mechanism has been established so far. This study describes the thermodynamic equilibria of involved species in copper(II) bis(trifluoromethanesulfonyl)imide ($Cu(TFSI)_2$) doped, co-evaporated Spiro-MeOTAD. A temperature-independent formation of charge transfer states is found, followed by an endothermic release of free charge carriers. Impedance and electron paramagnetic resonance spectroscopy unravel low activation energies for hole release and hopping transport. As a result, (52.0 ± 6.4)% of the total $Cu(TFSI)_2$ molecules form free, dissociated holes at 10 mol% and room temperature. Cu^I species arising out of doping are stabilized by formation of a $[Cu^I(TFSI)_2]^-$ cuprate, inhibiting elemental copper formation. This Cu^I species presents a potent hole trap reducing their mobility, which can be averted by simple addition of a bathocuproine complexing agent. A nonlinear temperature-dependent conductivity and mobility that contradicts current charge transport models is observed. This is attributed to a combination of trap- and charge transfer state freeze-out. These insights may be adapted to other metal salts, providing guidelines for designing next-generation ultra-high efficiency dopants.

1. Introduction

Ever since the advent of organic solar cells and recent, but fast improvements in perovskite solar cells, a profound understanding of the fine interplay in these multilayer devices becomes a focus of research. With an ever-growing number of interfaces, extracting photogenerated charge carriers fast, efficient and selective is crucial for high-performance solar cells.[1] $N^2,N^2,N^{2'},N^{2'},N^7,N^7,N^{7'},N^{7'}$-octakis(4-methoxyphenyl)-9,9′-spirobi[9H-fluoren]-2,2′,7,7′-tetramine (Spiro-MeOTAD) has found widespread use as a hole transport material (HTM) in solar cell research, where it is commonly *p*-doped (i.e., oxidizing Spiro-MeOTAD) by air (O_2) with the help of LiTFSI additives to increase the free charge carrier density.[2,3] Li et al. first incorporated copper(I) thiocyanate and copper(I) iodide into Spiro-MeOTAD HTM and found distinct benefits such as improved power conversion efficiency and HTM conductivity over conventional dopants like $LiTFSI/O_2$ or the cobalt complex FK209.[4] This concept was refined by other groups designing stable copper(II) complexes with tunable valance band levels and solubilities by counter-ion choice.[5–7] We replaced the solution doping using copper salts by a solvent free and highly controlled co-evaporation route employing copper(II) bis(trifluoromethanesulfonyl)imide $Cu(TFSI)_2$ as a *p*-type dopant to yield conductive, uniform, and pinhole-free HTM layers. Our concept was previously successfully applied to conventional $MAPbI_3$ based 3D perovskite solar cells.[8] While practically proven to be useful in perovskite solar cells, the field still lacks a conclusive picture of the physical and chemical processes inside the Cu^{II} doped Spiro-MeOTAD bulk. Especially the role of dopant side

A. Hochgesang, J. Mohanraj, M. Thelakkat
Applied Functional Polymers
University of Bayreuth
95440 Bayreuth, Germany
E-mail: mukundan.thelakkat@uni-bayreuth.de

The ORCID identification number(s) for the author(s) of this article can be found under https://doi.org/10.1002/aelm.202200113.

DOI: 10.1002/aelm.202200113

S. Biberger, F.-J. Kahle, A. Köhler
Soft Matter Optoelectronics
Department of Physics
University of Bayreuth
95440 Bayreuth Germany

J. Grüne, V. Dyakonov
Experimental Physics VI
Faculty of Physics and Astronomy
University of Würzburg
97074 Würzburg, Germany

A. Köhler, M. Thelakkat
Bavarian Polymer Institute (BPI) and Bayreuth Institute of Macromolecular Research (BIMF)
University of Bayreuth
95440 Bayreuth, Germany

ADVANCED SCIENCE NEWS
www.advancedsciencenews.com

ADVANCED ELECTRONIC MATERIALS
www.advelectronicmat.de

products on charge transport is unclear, which turns out to be of quite complex nature. To close this gap, we herein report the occurring thermodynamic equilibria between redox states in co-evaporated, $Cu(TFSI)_2$ doped Spiro-MeOTAD necessary to draw a complete picture of the doping process and discuss the consequences thereof. First, the theoretically predicted and experimentally observed doping reaction of $Cu(TFSI)_2$ with Spiro-MeOTAD was investigated using ultraviolet photoelectron- and UV/vis/NIR absorption spectroscopy. Temperature controlled optical spectroscopy experiments are used to gain insight into the formation of charge transfer (CT) states as the product of the doping reaction. Via electron paramagnetic resonance spectroscopy (EPR), electrical conductivity and impedance spectroscopy, possible endothermic release of free charge carriers by dissociation of the CT state was monitored. We quantitatively pin-point the activation energies for CT dissociation $E_{A,CT}$ by temperature dependent studies.

A low $E_{A,CT}$ may result in high doping efficiencies even at increased dopant loadings, which will be experimentally verified in the course of this work. The mobility and thermodynamic equilibria of the bound and unbound charge carriers are investigated in detail by impedance- and EPR spectroscopy. Further, we determine the influence of the thermodynamic equilibria on the thermal activation energy for fundamental hopping processes $E_{A,Hop}$. Well-documented electronic properties of pristine Spiro-MeOTAD such as temperature-dependent mobility are thoroughly compared to that of $Cu(TFSI)_2$ doped samples. Distinct nonlinearities in conductivity, carrier concentration and mobility for $Cu(TFSU)_2$ doped Spiro-MeOTAD below 150 K are extensively studied. We try to shed light on the source of nonlinear behavior by investigating reversible CT- and trap state recombination with the help of $[Cu(MeCN)_4]BF_4$ as a model Cu^I source. Additional focus is set on the influence of dopant products on charge transport in the bulk.

2. Results and Discussion

2.1. Charge Transfer Formation

We investigate the doping mechanism of Cu-salts in Spiro-MeOTAD by first considering the process of charge transfer formation in thin films. In a typical *p*-doping experiment, the dopant is required to possess unoccupied energy levels deeper in energy than the highest occupied molecular orbital (HOMO) of the organic semiconductor (OSC).[9,10] If this condition is met, an exothermic electron transfer from OSC to dopant can be expected. By using UV photoelectron spectroscopy (UPS) we measured the ionization potential (IP), which is by Koopmans-theorem in first approximation identical to the HOMO, and workfunction of Spiro-MeOTAD (**Figure 1**a).[11] The electron

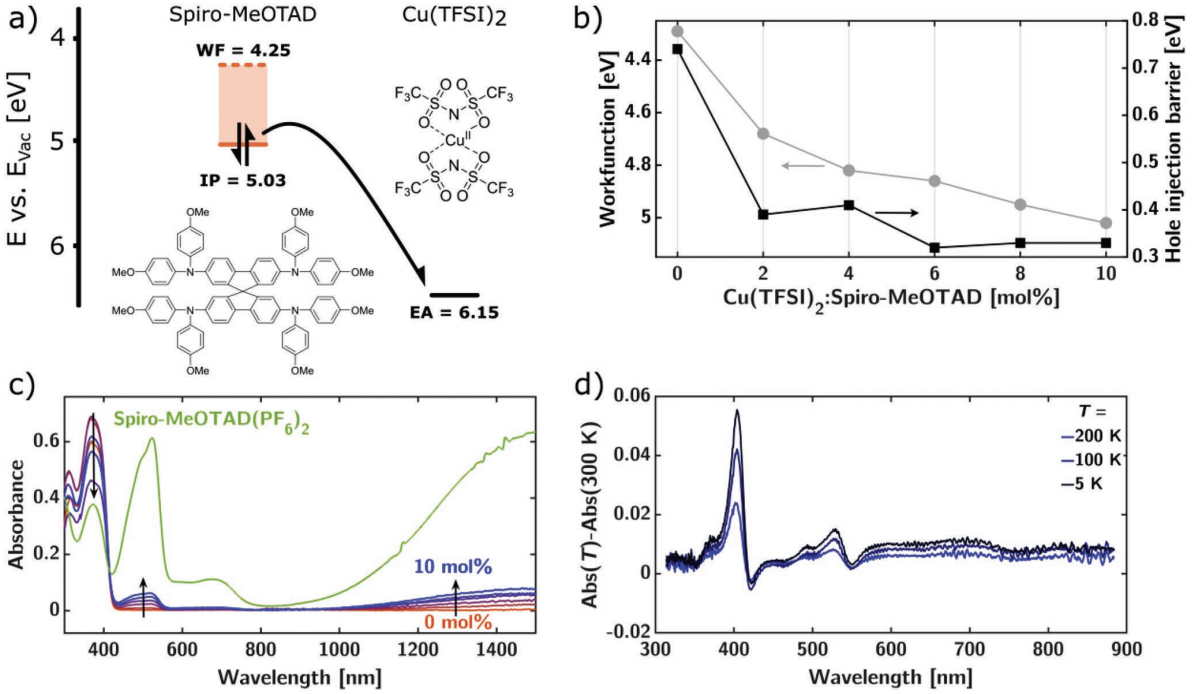

Figure 1. a) Energy level diagram of pristine Spiro-MeOTAD (orange) and $Cu(TFSI)_2$ (black) as determined by UPS (WF and IP of Spiro-MeOTAD) and CV (EA of $Cu(TFSI)_2$). b) Workfunction (left, grey circles) and hole-injection barrier HIB (right, black squares) of co-evaporated Spiro-MeOTAD films with increasing $Cu(TFSI)_2$ molar ratio. c) UV/vis/NIR absorption spectra of co-evaporated films with increasing molar ratios of $Cu(TFSI)_2$ highlighting the formation of spectral features identical to that of chemically synthesized, pure Spiro-MeOTAD$(PF_6)_2$ (green). d) Difference in optical absorption of 10 mol% $Cu(TFSI)_2$ doped Spiro-MeOTAD thin film UV/vis spectra obtained at 200 K (blue), 100 K (dark blue), and 5 K (black) to the spectrum obtained at 300 K (see Figure S3, Supporting Information).

ADVANCED SCIENCE NEWS
www.advancedsciencenews.com

ADVANCED ELECTRONIC MATERIALS
www.advelectronicmat.de

affinity EA with respect to vacuum level of $Cu(TFSI)_2$ was calculated from CV half-wave reduction potentials according to a known literature procedure (Figure S1, Supporting Information).[12] An electron affinity of EA = 6.15 eV of $Cu(TFSI)_2$ and IP = 5.03 eV of pristine Spiro-MeOTAD w.r.t. vacuum level were determined. Clearly, the EA of $Cu(TFSI)_2$ is positioned 1.12 eV deeper than the Spiro-MeOTAD HOMO, facilitating electron transfer. The removal of electrons from Spiro-MeOTAD upon doping is expected to result in a downshift of the workfunction toward the HOMO of the OSC. We monitored this electron transfer by UPS in a second experiment on co-evaporated Spiro-MeOTAD thin films with 0–10 mol% $Cu(TFSI)_2$ dopant ratio (Figure 1b). A continuous decrease of the workfunction from 4.25 eV down to 5.02 eV was recorded. This downshift was verified by a decreasing hole-injection barrier HIB (the difference between HOMO and workfunction) shown in Figure 1b. We noticed a slight variation in HOMO position during doping, which is responsible for the unexpectedly pronounced decrease of HIB between 2 and 4 mol% (See also summary of all UPS values collected in Table S1, Supporting Information). From Figure 1b, two distinct processes can be discerned: first, a strong initial HIB drop of ≈740 meV in the pristine state to 390 meV at 2 mol% $Cu(TFSI)_2$. This steep HIB gradient marks the region, where E_F moves through a lower density of states per energy interval compared to the deeper lying valence band. We assign these states lying higher in energy as trap states, that is, the generated holes are being consumed entirely in passivating these trap states above the valence band up to 2 mol% $Cu(TFSI)_2$.[13] We clearly differentiate those trap states from trap states originating from dopant products, which are characterized in Section 2.4. Despite the high purity of Spiro-MeOTAD used in this work of 99.9% (HPLC, see Supporting Information for manufacturer details), reducing impurities are common for organic semiconductors, shifting the Spiro-MeOTAD intrinsic carrier density from $\approx 9 \times 10^{14}$ cm^{-3} published by Abate et al. to 1.2×10^{17} cm^{-3} in this work (see Section 2.1).[14] However, we propose the influence of these intrinsic trap states on subsequent doping experiments to be low, being fully passivated after 2 mol% $Cu(TFSI)_2$ (Figure 1b). Further, the characteristic slope change of E_F (dopant concentration) has also been associated with the Fermi level crossing an mid-gap acceptor level, which originates from dopant:host interaction.[15] Second, for doping concentrations greater than 2 mol%, the Fermi level E_F (e.g., workfunction) is pinned at ≈330 meV above the Spiro-MeOTAD valence band. At this stage it can be assumed, that the dopant releases free holes, which moves E_F closer to the HOMO with a shallow slope.[16–18] Fortifying the designated role as a hole conductor, the workfunction of 5.02 eV at 10 mol% $Cu(TFSI)_2$ allows for a very efficient injection of holes in the co-evaporated Spiro-MeOTAD films using high workfunction electrodes such as Au. Due to the twisted nature of the spiro-core inducing steric hindrance and bulky (nonplanar) form of the Spiro-MeOTAD, we expect Spiro-MeOTAD and $Cu(TFSI)_2$ to react according to an integer charge transfer. This infers that no hybridization of frontier orbitals (HOMO or lowest unoccupied molecular orbital) takes place and the system can be treated like a conventional redox-couple forming CT states upon doping.[19] Optical UV/vis/NIR absorption spectroscopy was employed as a powerful tool to study the CT state evolution in 0–10 mol% $Cu(TFSI)_2$ doped Spiro-MeOTAD thin films (Figure 1c; Figure S2, Supporting Information). Simultaneous vacuum co-evaporation was used to deposit high-quality, pinhole-free thin films on glass, circumventing solvent influence and miscibility issues (see Supporting Information for experimental details).[8]

The ground-state absorption of Spiro-MeOTAD at 370 nm is continuously bleached upon adding $Cu(TFSI)_2$, with new peaks emerging at 517 nm, 687 nm, and 1445 nm (see Figure S2, Supporting Information, for difference spectrum). The broad NIR absorption at 1445 nm was assigned to intervalence charge-transfer (IV-CT) from a positively charged radical-cation triphenylamine to the linking biphenyl bridge.[20] In addition, a characteristic fingerprint for charged Spiro-MeOTAD species is the absorption at 517 nm (as well as 687 nm).[21] We conclude a steady formation of charged Spiro-MeOTAD species upon co-evaporation with $Cu(TFSI)_2$, complementing earlier studies by Mohanraj et al.[8] To study the thermodynamic nature of the CT state formation, we carried out temperature dependent absorption spectroscopy on co-evaporated films (Figure 1d, see Supporting Information, for spectra of all doping concentrations). No significant change in absorption intensity of the 517 nm band is observable. As a consequence, we conclude the formation of the CT states to be temperature independent, in line with experiments by Tietze et al. on doped small molecules.[22] Lastly, we want to shed light on the nature of the charged Spiro-MeOTAD species. Three stable oxidation states of Spiro-MeOTAD are known in literature, namely Spiro-MeOTAD^{1+}, Spiro-MeOTAD^{2+}, and Spiro-MeOTAD^{4+}.[23] UPS studies on Spiro-MeOTAD$(PF_6)_4$ revealed a HOMO energy of 5.25 eV, which is situated 0.90 eV above the EA of $Cu(TFSI)_2$. Consequently, all oxidation products of Spiro-MeOTAD are theoretically accessible by exothermic electron transfer to $Cu(TFSI)_2$, showcasing its capabilities as a powerful *p*-type dopant. For experimental identification of the formed oxidation state, we synthesized chemically pure Spiro-MeOTAD^{2+} by reacting Spiro-MeOTAD with two equivalents of the single-electron oxidant $NOPF_6$. Thin films of the obtained Spiro-MeOTAD$(PF_6)_2$ were characterized by UV/vis/NIR spectroscopy (Figure 1c, green curve). We noted very similar optical absorption features between pure Spiro-MeOTAD$(PF_6)_2$ and the $Cu(TFSI)_2$ doped Spiro-MeOTAD. However, we cannot reliably distinguish the two oxidation states Spiro-MeOTAD$^{1+/2+}$ due to i) both states being almost degenerate in energy, with a separation of less than 110 mV versus Ag/Ag^+ resp. Fc/Fc^+ and ii) a very similar optical absorption spectral profile.[21,24] A comparison with Spiro-MeOTAD$(PF_6)_4$ absorption spectrum reveals, that Spiro-MeOTAD$(PF_6)_4$ is characterized by a broad peak at 875 nm, which is absent in our experiments (Figure 1c).[23] Therefore, both Spiro-MeOTAD^{1+} and Spiro-MeOTAD^{2+} are presumed as the most probable products of Spiro-MeOTAD doped with ≤10 mol% Cu (TFSI).

After proving the temperature-independent formation of charged Spiro-MeOTAD$^{1+/2+}$ CT states upon doping by optical absorption spectroscopy and UPS, the next step is to investigate the dissociation of the CT state and generation of mobile charge carriers. However, the CT state, being a salt, can be subject to strong coulombic binding energies in the range of >100 meV.[22] Thus, a certain activation energy must be provided in order to separate CT states into free carriers. Only free charge carriers

ADVANCED SCIENCE NEWS
www.advancedsciencenews.com

ADVANCED ELECTRONIC MATERIALS
www.advelectronicmat.de

can contribute to the observed macroscopic conductivity in disordered organic semiconductors by thermally activated hopping processes. Our group has monitored and reported the change in electrical conductivity by measuring current-voltage scans of Spiro-MeOTAD:$Cu(TFSI)_2$ co-evaporated on top of interdigitated Au electrodes in a previous study.[8]

Upon co-evaporating $Cu(TFSI)_2$, a linear increase followed by conductivity saturation (at 6 mol% $Cu(TFSI)_2$) with an average value of $\approx 7 \times 10^{-4}$ S cm^{-1} was observed, in agreement with the constant HIB found in our UPS experiments above 6 mol% dopant. Elevated temperatures in the Spiro-MeOTAD effusion cell during evaporation do not significantly enhance the charge carrier density, as evidenced by the low conductivity (1×10^{-7} S cm^{-1}) of the evaporated pristine Spiro-MeOTAD sample. Increase in electrical conductivity values demonstrate the presence of mobile charge carriers in Spiro-MeOTAD:$Cu(TFSI)_2$ co-evaporated samples.

Here, we intend to quantify this observation by determining the amount of free charge carriers p in the doped bulk via solid state Mott-Schottky experiments. More precisely, this analysis yields the density of ionized acceptors (from dopants) N_A^- in the bulk, which is equal to the density of free holes p in the hole conductor, since charge neutrality must be obeyed. This is achieved by measuring the voltage dependent capacitance C(V) of a metal-insulator-semiconductor device stack such as FTO/Al_2O_3/Hexamethyldisilazane/$Cu(TFSI)_2$:Spiro-MeOTAD/Au using impedance spectroscopy. Since the spatial width of a depletion layer (which in turn dictates its electrical capacitance) is very sensitive to the number of free carriers present in the semiconductor, measuring the series capacitance can give information about N_A^-. Applying a negative bias voltage causes the formation of a charge carrier depletion zone at the insulator/p-type semiconductor interface, which changes the overall device capacitance. By evaluating the slope dC^{-2}/dV of the device capacitance versus applied potential, the number of free carriers N_A^- can be evaluated (**Figure 2**a, see Figure S4, Supporting Information, for exemplary fit). In agreement with a very strong decrease in HIB and increase in conductivity when adding 2 mol% $Cu(TFSI)_2$, the charge carrier density rises from 1.2×10^{17} cm^{-3} to 1.0×10^{19} cm^{-3} at 1.5 mol% dopant. Above 1.5 mol%, N_A^- is increasing in a linear fashion up to 3.2×10^{19} cm^{-3} at 10 mol% without showing saturation effects (Figure 2b). Having successfully quantified the density of free carriers, we focus on the density of bound CT states. Contrary to Mott–Schottky analysis, which is sensitive to only free charge carriers in the bulk, EPR detects all paramagnetic species within the sample volume. Specifically, EPR is used to determine the absolute sum of bound (in the form of a CT state) and free charge carriers. For measuring EPR, we co-evaporated $Cu(TFSI)_2$ and Spiro-MeOTAD onto poly(ethylene terephthalate) substrates of known area with a defined thickness, which were consequently sealed in quartz

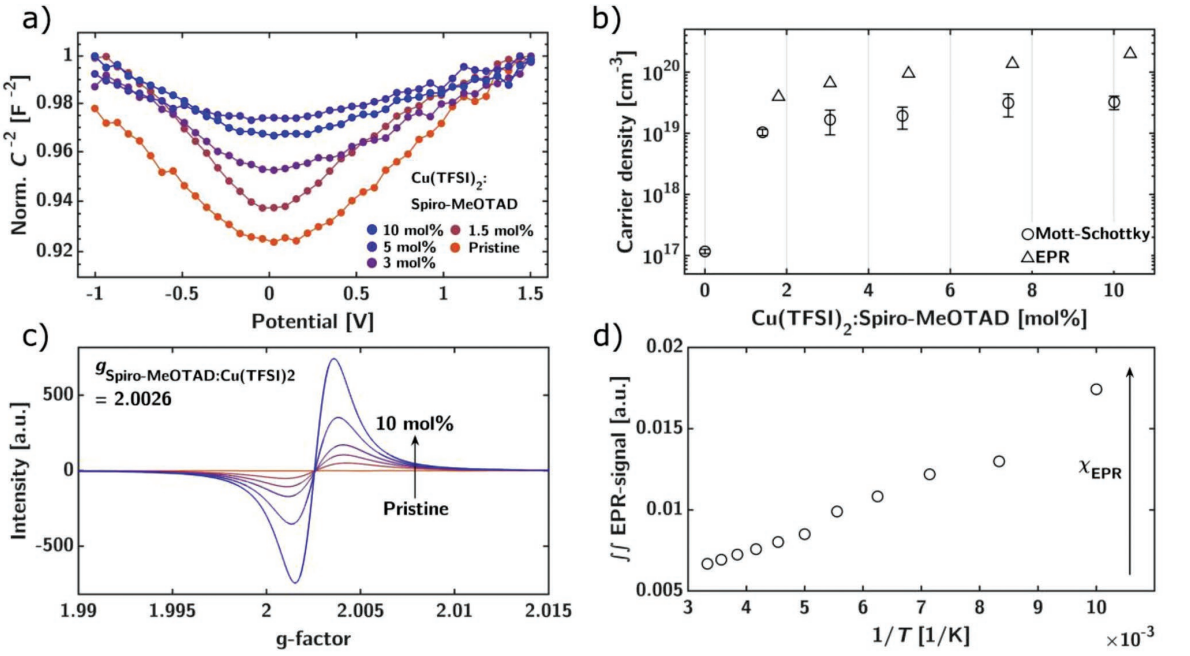

Figure 2. a) Exemplary, normalized C^{-2} versus applied potential plot of metal-insulator-semiconductor (MIS) devices fabricated with an FTO/Al_2O_3/Hexamethyldisilazane/$Cu(TFSI)_2$ doped Spiro-MeOTAD/Au structure. Negative potentials deplete the majority charge carriers (holes) from the interface, decreasing the capacitance. The positive slope in the positive potential range indicates low frequency inversion at the insulator/Spiro-MeOTAD interface. b) Charge carrier/spin densities obtained by Mott–Schottky (circles) and EPR (triangles) measurements. c) Doping concentration dependent EPR spectra of $Cu(TFSI)_2$ doped Spiro-MeOTAD thin films, co-evaporated on PET substrates. Modulation amplitude B_{mod} = 0.02 mT, microwave power P_{MW} = 0.8 mW. d) Double integral (proportional to spin susceptibility, i.e., spin density) of the EPR signal as a function of the inverse temperature proves localized spin species (Curie contribution). Doping concentration = 7.5 mol%.

ADVANCED SCIENCE NEWS
www.advancedsciencenews.com

ADVANCED ELECTRONIC MATERIALS
www.advelectronicmat.de

tubes under inert atmosphere. The EPR parameters are optimized for the highest signal of the 10 mol% doped film (B_{mod} = 0.02 mT, P_{MW} = 0.8 mW). As a fact, the presence of paramagnetic Cu^{II} ions is not affecting the results, as they cannot be resolved with the optimized parameters (Figure S5, Supporting Information). Cu^{I} cations are diamagnetic due to a $4s^0 3d^{10}$ electron configuration and therefore EPR inactive.[25] With increasing dopant concentration, the Lorentzian shaped EPR peak increases in area (Figure 2c). A *g*-value of 2.0026 was found, comparable to H-TFSI and Li-TFSI/O_2 doped Spiro-MeOTAD.[26–28] By convention, the EPR spectra (Figure 2c) are displayed as the first derivative of the original microwave absorption signal, thus double integration yields the absolute number of paramagnetic species N_{Spins}, normalized to unit volume and referenced to a sample with known spin concentration (Figure 2b). The quantity N_{Spins} includes all paramagnetic species per unit volume, whether bound to a counter ion (CT state) or free to move under the influence of an electric field (free holes *p*). N_{Spins} follows the same doping concentration dependent trend as N_A^-, yet we noticed a constant offset, which is equal to the states not detectable by Mott–Schottky measurements, the bound CT states. They contribute to about a factor of 4–6 in the range of 3–10 mol% doping ratio. It should be emphasized, that no information about the ratio between free and in CT states bound carriers can be deduced from the absolute number of spins N_{Spins}, owing to their high absolute error. Depending on the spin reference used, the absolute error is up to 1 order of magnitude, yet their relative values used in this work are exact. Hence, we used impedance spectroscopy to determine the ratio between bound and free charge carriers (see Section 2.3). Aiming to understand the evolution of ratio between N_A^- and N_{Spins} upon doping, we correlated both values with the UV/vis/NIR CT state absorbance integral from our previous experiment (Figure 1c). Both N_A^- and N_{Spins} were found to increase monotonic and linearly with the absorbance integral (Figure S6, Supporting Information). This indicates, that no additional EPR silent species or bipolaron species are formed at up to 10 mol% $Cu(TFSI)_2$. Notably, the electrical conductivity saturates despite a monotonical increase in N_A^- and N_{Spins}, which hints to effects of the doping on the carrier mobility μ and will be discussed in the next paragraph in detail.

Finally, for charge transport considerations later in this work, it is necessary to understand the degree of charge carrier localization in $Cu(TFSI)_2$ doped Spiro-MeOTAD. For this, we conducted temperature dependent EPR measurements on one typical sample (7.5 mol% $Cu(TFSI)_2$ doped Spiro-MeOTAD). The double integral of the EPR signal is proportional to the susceptibility *X* and was found to depend linearly on the inverse sample temperature $1/T$ in our experiment (Figure 2d).[29,30] It is well described by Curie contribution ($\approx N_{Spins}/T$), characteristic for localized spin species. The linear trend underlines the absence of additional paramagnetic species arising at different temperatures, which would induce a deviation from $1/T$ behavior, fitting to temperature-independent formation of CT states.[30] By correcting the internal spin reference density to the cavity temperature, we verified a temperature-independent spin density $N_{Spins}(T)$ for a 7.5 mol% $Cu(TFSI)_2$ doped sample (Figure S7, Supporting Information).

When extrapolating to the y-axis intercept, an offset remains in the magnitude of the determination inaccuracy. Nevertheless, Pauli contribution, that is, band like transport, is not typical for Spiro-MeOTAD even at high concentrations, as discussed below. Hence, free charge carriers are formed at room temperature in $Cu(TFSI)_2$ doped Spiro-MeOTAD, increasing the macroscopic bulk conductivity via hopping in mostly localized sites. To conclude, the ratio between free and in CT states bound charge carriers was determined and their changes upon varying the dopant concentration.

2.2. Charge Transport

As we quantified the nature and density of reaction products formed in $Cu(TFSI)_2$ doped Spiro-MeOTAD, we proceed further to complete the microscopic description of charge transport and thermally activated processes leading to free charge carriers. To select a proper model capable of describing the charge transport, we recorded the temperature dependent conductivity $\sigma(T)$ of co-evaporated $Cu(TFSI)_2$ doped Spiro-MeOTAD thin films from 400 K to 20 K in a He-cryostat (**Figure 3**a).

Focusing on the pristine sample, a distinct linear region was found between 400 K and 150 K. We observed a positive slope $d\sigma/dT$, clearly indicating a temperature activated hopping behavior. Commonly, the popular Mott law is employed to model $\sigma(T)$ in organic semiconductors.[31] As it assumes a constant density of states surrounding the Fermi energy, which can hardly be assumed, we refer to Efros-Shklovskii variable range hopping (ES-VRH) accounting for a Coulomb gap surrounding E_F.[32,33] As Spiro-MeOTAD is disordered in terms of the energetic landscape with localized, spatially randomly distributed states (amorphous nature), the ES-VRH model is sufficient to explain the pristine case.[33] In addition, this model accounts for a Coulomb interaction of localized states introduced by the dopant molecules and hopping distances exceeding the nearest neighbor distance at low temperatures.[34,35] ES-VRH predicts the dependence $\ln(\sigma/\sigma_0) \propto T^{-1/2}$ and the experimental data on pristine Spiro-MeOTAD is in accordance to this.[34,36] In $Cu(TFSI)_2$ doped Spiro-MeOTAD samples, we noticed a restriction of the linear $\sigma(T)$ region to smaller temperature ranges (Figure 3a). Additionally, in all doped samples, a distinct temperature independent behavior is found below 150 K. Li et al. pointed out, that a temperature independent charge carrier transport in organic semiconductors may be explained sufficiently within the VRH model framework. At high carrier densities and low temperatures, Li proposed that the energy required for a carrier hop is provided entirely by the electric field across the device. This implies, that no thermal activation is necessary and the transport can be described as field-assisted tunnelling in the low temperature regime.[37] We could qualitatively adapt Lis modified VRH model to $\sigma(T)$ of $Cu(TFSI)_2$ doped Spiro-MeOTAD using N_A^- from Mott–Schottky measurements (Figure 2b; Figure S13, Supporting Information). Applying Lis theory, one could assume the origin of $\sigma(T)$ nonlinearities in $Cu(TFSI)_2$ doped Spiro-MeOTAD to stem from field-assisted tunnelling. Yet, carefully analyzing Lis model suggests a similar trend for the temperature dependent mobility $\mu(T)$ if the Fermi level E_F

ADVANCED SCIENCE NEWS
www.advancedsciencenews.com

ADVANCED ELECTRONIC MATERIALS
www.advelectronicmat.de

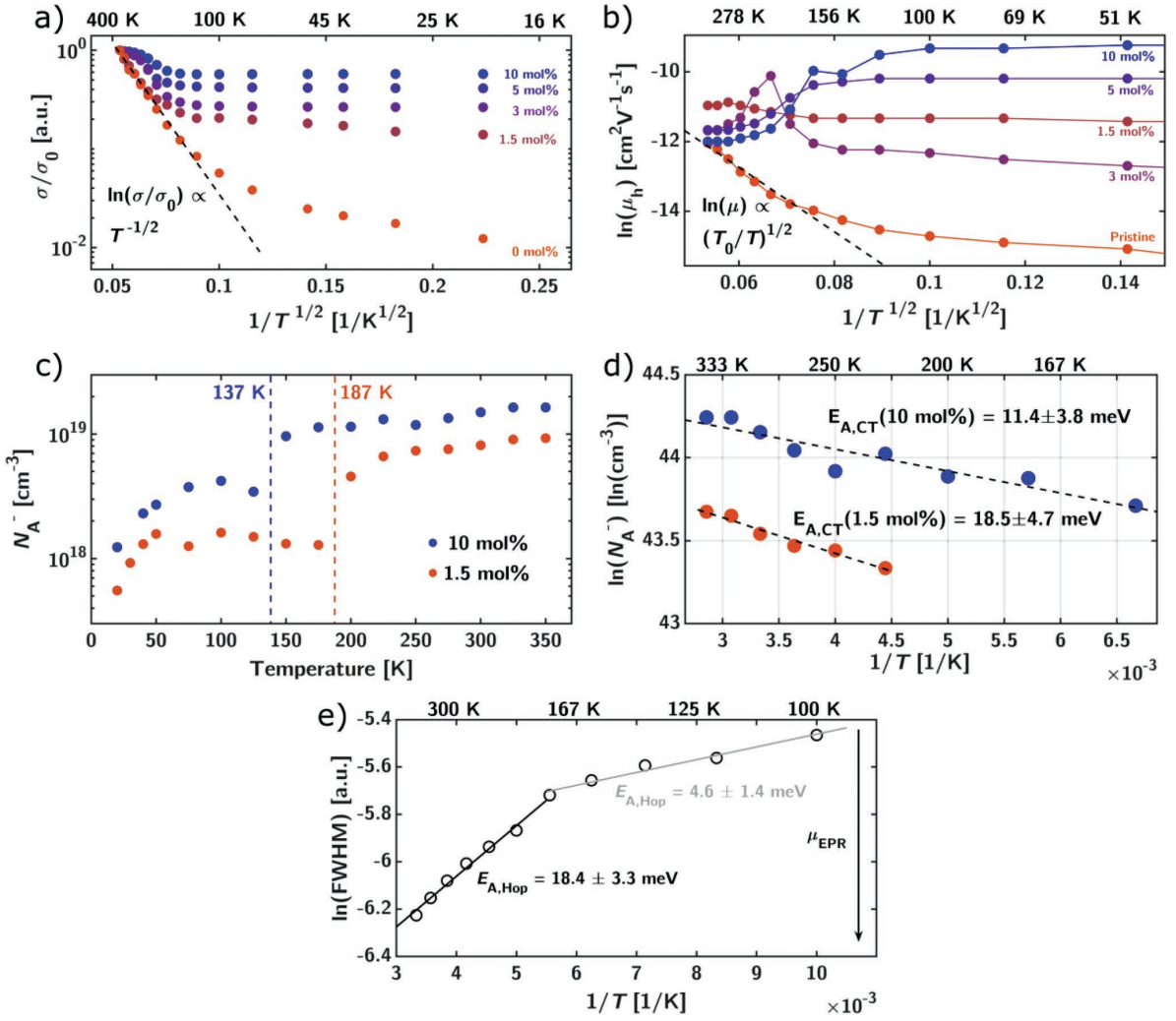

Figure 3. a) Temperature dependent, individually normalized conductivities σ measured on FTO/Cu(TFSI)$_2$:Spiro-MeOTAD/Au devices with different doping concentrations from 400 K to 20 K. b) Temperature dependent hole mobilities μ_h of Cu(TFSI)$_2$ doped Spiro-MeOTAD, determined from impedance measurements on FTO/Cu(TFSI)$_2$:Spiro-MeOTAD/Au devices using the negative differential susceptance $-\Delta B$. Black dashed fit line shows typical ES-VRH behavior $\ln(\mu_h) \propto (T_0/T)^{1/2}$ in the case of pristine Spiro-MeOTAD sample. All values were obtained at a constant electrical field $F = 100$ kV cm^{-1}. Full temperature scale measurements are shown in Figure S10, Supporting Information, detailed temperature dependent $-\Delta B$ versus frequency spectra in Figure S11, Supporting Information. c) Temperature dependent charge carrier densities $N_A^-(T)$ of 1.5 mol% and 10 mol% Cu(TFSI)$_2$ doped Spiro-MeOTAD, determined by Mott–Schottky measurements. A vertical dotted line demarcates the freeze-out points, for example, the thermal energy available below these marked values is not sufficient to dissociate the intimate CT pair. d) Arrhenius-type temperature dependency of $N_A^-(T)$ measured via Mott-Schottky experiments above the freeze-out point (150 K for 10 mol% Cu(TFSI)$_2$ (blue), resp. 200 K for 1.5 mol% (orange)) with fitted activation energies $E_{A,CT}$. e) Logarithmic EPR linewidth (FWHM) of a 7.5 mol% Cu(TFSI)$_2$ doped Spiro-MeOTAD thin film as a function of inverse temperature. An activation energy for hole transport $E_{A,Hop}$ = (18.4 ± 3.3) meV (black fit) for higher temperature and (4.6 ± 1.4) meV (grey fit) below 160 K can be determined. Full temperature dependent EPR spectra can be found in Figure S12, Supporting Information.

and N_A^- are considered constant;, i.e., a monotonic mobility decrease followed by a weakly temperature dependent region at lower temperatures. As a consequence, temperature dependent conductivity measurements are not sufficient to analyze the origin of nonlinear $\sigma(T)$, which shifts our focus toward temperature dependence of charge carrier mobility μ.

To probe the temperature dependent mobility of free charge carriers in Cu(TFSI)$_2$ doped Spiro-MeOTAD, we carried out impedance spectroscopy experiments on FTO/Cu(TFSI)$_2$:Spiro-MeOTAD/Au metal-semiconductor devices employing the negative differential susceptance method (see Supporting Information for details). Using a metal-semiconductor device structure, holes are injected at one electrode if a sufficient electrical field F across the device is applied. By measuring the capacitive response of the biased device at different frequencies, an average carrier transit time for a given organic layer

ADVANCED SCIENCE NEWS
www.advancedsciencenews.com

ADVANCED ELECTRONIC MATERIALS
www.advelectronicmat.de

thickness and electrical field can be deduced, even at moderate bulk conductivities of doped semiconductor samples (where most common methods fail). Indium-tin-oxide/Li(TFSI) doped Spiro-MeOTAD/Au devices have recently been used to study the Spiro-MeOTAD charge carrier mobility via negative differential susceptance by Li et al. Carrier densities of up to 2.8×10^{19} cm^{-3} were reported using Mott–Schottky measurements, proving the applicability of this method for highly doped Spiro-MeOTAD samples.[38] Again, pristine Spiro-MeOTAD follows a temperature activated behavior, characterized by an increase in carrier mobility upon heating the sample up to 400 K. Between 350 K and 175 K, $\ln(\mu)$ is proportional to the inverse sample temperature. Closer analysis yields a slope of 0.5, thus resembling ES-VRH dependency for the hole mobility with $\ln(\mu) \propto \left(\frac{T_0}{T}\right)^{1/2}$, where $T_0 = 8.5 \times 10^3$ K. (Figure 3b).[39] We like to point out, that for the temperature range between 350 K to 20 K, a poor fit was found for $\ln(\mu) \propto \left(\frac{1}{T}\right)^2$ predicted by models using a Gaussian density of states distribution, which are often employed in literature to describe the electrical behaviour of doped organic semiconductors (Figure S14, Supporting Information).[40] Röhr et al. obtained comparable $\mu(T)$ of undoped Spiro-MeOTAD in space charge limited current device data fitted by Mott–Gurney law, verifying the negative differential susceptance method used in this experiment.[41] Consequently, $\sigma(T)$ and $\mu(T)$ of pristine Spiro-MeOTAD is described sufficiently by the ES-VRH model. To our surprise, doped samples are clearly subject to a different nature of charge transport, even increasing in charge carrier mobility upon cooling the sample below a threshold point of ≈150 K, followed by a temperature independent region between 150 K and 20 K (Figure 3b). We further note, that the negative correlation $d\mu/dT < 0$ is exclusive to higher doping concentrations ≥5 mol%. At this point we want to highlight, that a negative temperature coefficient mobility is no unambiguous fingerprint of band-like transport typically found in metals. Exemplary, similar behavior was found in poly(2,5-bis(3-tetradecylthiophen-2-yl)thieno[3,2-b]thiophene) PBTTT field-effect transistors, explained by Luttinger liquid behavior.[42] Additionally, Spiro-MeOTAD, even at high doping ratios, cannot be described in terms of band transport due to the large amount of energetic disorder.[43] Thus, invoking VRH models, which expect a monotonic decrease in mobility and conductivity, are not able to explain the nonlinear charge transport in $Cu(TFSI)_2$ doped Spiro-MeOTAD samples.

Based on the relationship $\sigma = qN_A^-\mu$ with q being the elementary charge, we formulate the lack of thermal energy at low temperatures to dissociate the CT-state as a possible cause for the nonlinearities found in $Cu(TFSI)_2$ doped Spiro-MeOTAD. Intuitively, this so-called carrier freeze-out would be reflected in $N_A^-(T)$, necessitating a quantification. For this, we coupled the Mott-Schottky experimental setup as described in an earlier paragraph with a Helium cryostat. Figure 3c shows $N_A^-(T)$ measurements on 1.5 and 10 mol% $Cu(TFSI)_2$ doped Spiro-MeOTAD between 20 K and 350 K. Here we observe a sharp jump in carrier density at 137 K (for 10 mol% dopant) and 187 K (1.5 mol% dopant), which we denote as transition points. Above these transition points, N_A^- is proportional to the sample temperature. At lower temperatures, we noticed a decrease in free carrier concentration for both samples. Ultimately, N_A^- is not correlated to the sample temperature below these transition temperatures. We assign the distinct loss in free carrier concentration N_A^- at low temperatures to the recombination of free holes and counterion to re-form the bound CT state (freeze-out). Above the freeze-out, $N_A^-(T)$ can be well described by a Arrhenius type activation process, with the activation energy $E_{A,CT}$ corresponding to the CT state dissociation energy (Figure 3d).[22] $E_{A,CT}$ decreases from (18.5 ± 4.7) meV at 1.5 mol% $Cu(TFSI)_2$ to (11.4 ± 3.8) meV at 10 mol%, presumably due to increased energetic disorder, facilitating CT state dissociation.[22] These values are directly reflected in the freeze-out temperatures of 187 K and 137 K, which translate to thermal energy values of 16.1 meV (1.5 mol%) and 11.8 meV (10 mol%). $E_{A,CT}$ is in line with previously published results of disordered systems, ranging from 9 to 54 meV.[22] The measured freeze-out temperatures yield first evidence for our hypothesis, overlapping with the mid-point temperatures of nonlinear effects of $\sigma(T)$ and $\mu(T)$ (Figure 3a,b).

We aim to fortify our hypothesis by approaching the thermodynamics of carrier hopping. Our previous $\mu(T)$ measurements (Figure 3b) clearly show an increase in carrier mobility below the freeze-out. Therefore, we test the correlation between the average activation energy $E_{A,Hop}$ for carrier site transition (a "hop") and $N_A^-(T)$. The full width at half maximum (FWHM) of an EPR signal can be related to the average microscopic charge carrier mobility μ_{EPR} in doped organic systems.[30] In general, increasing microscopic mobility narrows the EPR linewidth due to averaging of hyperfine interactions (motional narrowing).[28,44] Subsequently, we determined $E_{A,Hop}$ by evaluating the FWHM of the EPR signal of a 7.5 mol% doped sample for different temperatures and applying Arrhenius fits (Figure 3e). With increasing temperature, the FWHM decreases continuously, indicating increasing mobility in doped samples. A distinct change in slope occurred for $FWHM_{EPR}(T)$ at ≈180 K, with a greater slope $d(\ln(FWHM_{EPR}))/d(1/T)$ above 180 K. The more decreasing EPR linewidth above 180 K is in contrast to impedance measurements (Figure 3b), where we observed a decrease in mobility upon increasing temperature between 150 K and 400 K for doped Spiro-MeOTAD. This can be explained by the fact that the linewidth of EPR is only affected by mobile polarons that arise after dissociation of CT states in this experiment (no active electron/hole injection via electrodes). In contrast, any trap states created simultaneously reduce the overall mobility of impedance spectroscopy by trapping the injected holes. We recorded an $E_{A,Hop}$ of (18.4 ± 3.3) meV above 180 K, with (4.6 ± 1.4) meV below for Arrhenius fits on $FWHM_{EPR}(T)$ (Figure 3e). The transition temperature of 180 K (≈16 meV thermal energy) fits to the CT state dissociation energies $E_{A,CT}$ = 11.4–18.5 meV for 1.5 and 10 mol% $Cu(TFSI)_2$ doped Spiro-MeOTAD (Figure 3c). From $FWHM_{EPR}(T)$ and $N_A^-(T)$ experiments we conclude, that the CT state freeze-out is directly influencing the carrier mobility and it is consequently responsible for the nonlinear conductivity of $Cu(TFSI)_2$ doped Spiro-MeOTAD. Both $E_{A,Hop}$ and $E_{A,CT}$ can be verified by linking them to the macroscopic observed thermal activation energy for conductivity $E_{A,\sigma}$. We analyzed $E_{A,\sigma}$ by Arrhenius fits on temperature dependent conductivity measurements of

ADVANCED SCIENCE NEWS
www.advancedsciencenews.com

ADVANCED ELECTRONIC MATERIALS
www.advelectronicmat.de

co-evaporated $Cu(TFSI)_2$ doped Spiro-MeOTAD films (Figure S15, Supporting Information). Privitera et al. pointed out, that $E_{A,\sigma}$ is the sum of both CT state binding energy $E_{A,CT}$ and hole transport activation energy $E_{A,Hop}$.[30] As displayed in Figure S16, Supporting Information, $E_{A,\sigma}$ values ranging from (39.0 ± 7.0) meV to (130.0 ± 15.9) meV were recorded for the $Cu(TFSI)_2$ doped Spiro-MeOTAD system, with most samples having values below 100 meV. $E_{A,\sigma}$ of F_4TCNQ doped Spiro-MeOTAD was reported as ca. 170 meV, generally the thermal activation energies for conductivity are broadly distributed for small molecule organic semiconductors, ranging roughly from 38 to 467 meV.[45,46] In comparison, $Cu(TFSI)_2$ doped Spiro-MeOTAD displays rather small $E_{A,\sigma}$ values. This result is remarkably well in line with an expected, approximated value of $E_{A,CT}$(10 mol%) + $E_{A,Hop}$(7.5 mol%) ≈ 30 meV. Higher measured $E_{A,\sigma}$ values are likely the result of additional factors such as electrostatic disorder of CT states (Figure S16, Supporting Information).[46] Summarizing, we were able to resolve all three major activation energy contributions to the doping process $E_{A,\sigma}$ (for conductivity), $E_{A,CT}$ (release of free charge carriers) and $E_{A,Hop}$ (hopping of free charge carriers). We conclude the nonlinear conductivity and mobility of $Cu(TFSI)_2$ doped Spiro-MeOTAD to be caused by reversible CT state freeze out.

2.3. Doping Efficiency

As discussed earlier, we found $E_{A,CT}$ of $Cu(TFSI)_2$ doped Spiro-MeOTAD to be low compared to other doped organic semiconductors, for example, in the case of *N,N,N′,N′*-tetrakis(4-methoxyphenyl)benzidine (4-MeO-TPD) doped with $C_{60}F_{36}$, ≈30 meV are required for CT state dissociation.[17] To test, if a low $E_{A,CT}$ facilitates carrier release in doped organic systems, we investigated the doping efficiency η_{Dop}. This figure of merit quantifies the ratio between free, dissociated charge carriers p and total density of dopant molecules in the system N_A as $\eta_{Dop} = p/N_A$. N_A^- was determined by Mott–Schottky experiments described in Section 2.1, where we assumed that the number of free holes p equals N_A^-. It is worth emphasizing, that the neutrality condition $p = N_A^-$ may not hold true for very high trap densities or a large number of free carriers bound in the CT state.[17,22] A detailed derivation of N_A can be found in the Supporting Information. Defining η_{Dop} via N_{Spins} and N_A^- was omitted due to the introduction of a large error source in absolute number of spins. As shown in **Figure 4**a, co-evaporated $Cu(TFSI)_2$ doped Spiro-MeOTAD retains a doping efficiency of up to (52.0 ± 6.4) % at 10 mol% dopant. Thus, in general η_{Dop} improves dramatically compared to other popular *p*-dopants, which drop below the 10.3% mark

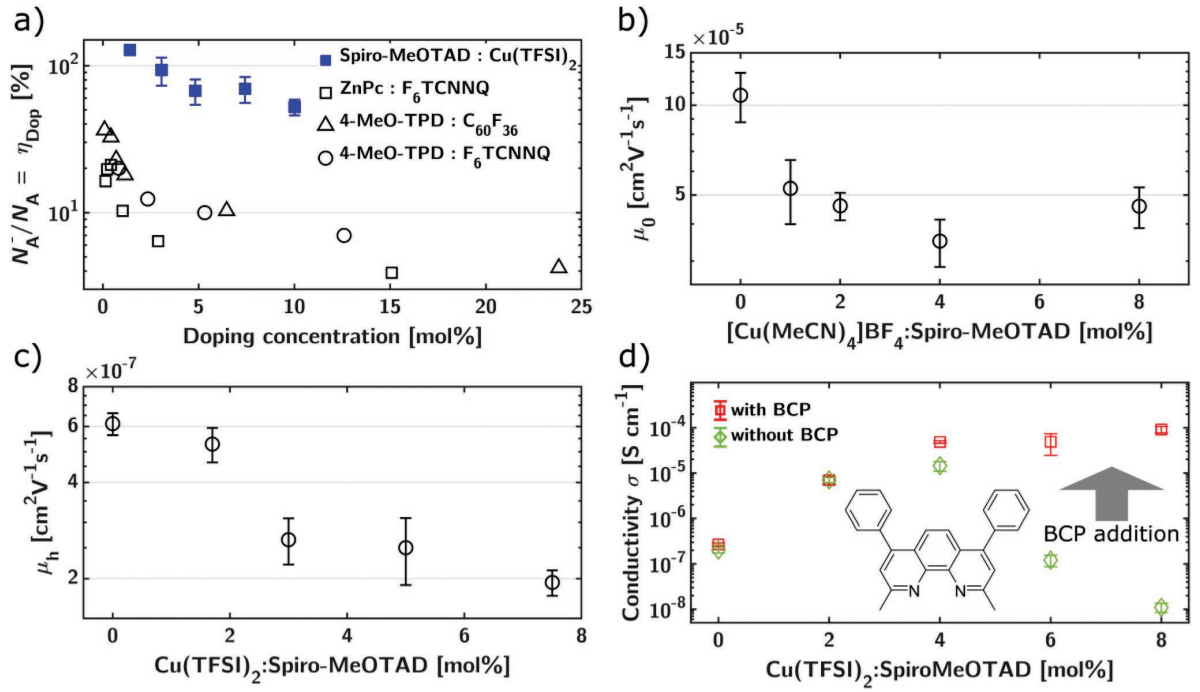

Figure 4. a) Doping efficiencies for different doping concentrations of $Cu(TFSI)_2$:Spiro-MeOTAD (blue squares). See Supporting Information for detailed information. Literature values for small molecule semiconductors: Zink-Phthalocyanine (abbr. ZnPc) doped with F_6TCNNQ (squares), 4-MeO-TPD doped with $C_{60}F_{36}$ (triangles) and F_6TCNNQ (circles).[17,22] b) Zero-field mobilities μ_0 of solution processed Spiro-MeOTAD thin films mixed with different molar amounts of $[Cu(MeCN)_4]BF_4$. c) Mobility μ of co-evaporated thin films of $Cu(TFSI)_2$ doped Spiro-MeOTAD using the CELIV method on FTO/Al_2O_3/$Cu(TFSI)_2$:Spiro-MeOTAD/Au devices. d) Thin film conductivities of solution processed, $Cu(TFSI)_2$ doped Spiro-MeOTAD without (green diamonds) and with bathocuproine (BCP, structure shown in graph) additive (red squares) at different dopant concentrations. BCP was added in equimolar amounts to $Cu(TFSI)_2$.

ADVANCED SCIENCE NEWS
www.advancedsciencenews.com

ADVANCED ELECTRONIC MATERIALS
www.advelectronicmat.de

at only 6.4 mol% in the case of the most efficient system in this series, $C_{60}F_{36}$ doped 4-MeO-TPD. Typically, η_{Dop} strongly decreases with increasing doping concentration, because charge carrier capture processes by dopant molecules become more likely.[17] In summary, the extraordinary low CT state binding energy $E_{A,CT}$ found in the Spiro-MeOTAD:$Cu(TFSI)_2$ system helps to greatly boost the doping efficiency compared to previously published *p*-dopants for organic systems.

2.4. Hole Trapping

In our previous studies, no elemental Cu^0 was found in XPS studies of $Cu(TFSI)_2$ doped, co-evaporated Spiro-MeOTAD samples.[8] In turn, the Cu^I state can be assumed as the final product of the doping reaction. Supplementary to the XPS studies, we tested if the doping reaction effectively stops at the Cu^I oxidation state. For this, a model Cu^I ion source, $[Cu^I(MeCN)_4]^+BF_4^-$ having the almost identical Cu^I/Cu^0 reduction potential compared to $Cu(TFSI)_2$ in acetonitrile solution was mixed with Spiro-MeOTAD to verify, if $[Cu^I(MeCN)_4]^+$can act as a dopant (Figure S1, Supporting Information).[47] Consequently, we prepared thin films from Spiro-MeOTAD mixed with increasing mole percent of $[Cu^I(MeCN)_4]BF_4$ in acetonitrile solution and conducted conductivity measurements (see Figure S17, Supporting Information, for details). Relative to pristine Spiro-MeOTAD, no increase in σ was found for up to 4 mol% $[Cu^I(MeCN)_4]BF_4$, the upper solubility limit of this complex in Spiro-MeOTAD. In line with XPS experiments, we conclude Cu^I to be the stable oxidation state formed after reacting $Cu(TFSI)_2$ and Spiro-MeOTAD.

Penultimately, we want to clarify the role of products of the doping reaction in the macroscopic charge transport of $Cu(TFSI)_2$ doped Spiro-MeOTAD. The two possible ions arising out of doping reaction are $TFSI^-$ and Cu^I. Any detrimental influence of the $TFSI^-$ anion on the charge transport was rejected for up to 10 mol% dopant concentration based on the fact that both LiTFSI(≈50 mol%)/O_2 or Spiro-MeOTAD$(TFSI)_2$ (17 mol% optimum) doped Spiro-MeOTAD and are known in literature to surpass the hole mobility of pristine Spiro-MeOTAD.[24,38] One may raise the question, if unbound Cu^{II} is responsible for trapping mobile holes. Careful analysis of temperature dependent absorption helps to answer this question: i) The first step of CT state formation is temperature independent as reported in literature and verified to be valid as shown in Figure 1d for our system (see also Figures S18, S7, Supporting Information); thus, no unreacted $Cu(TFSI)_2$ should remain up to 10 mol% doping concentration ii) hypothetical Cu^{III} as the product of hole capture by Cu^{II} is highly unstable without suitable, stabilizing ligands.[22,48] Based on these findings, we focus on Cu^I as the main trapping center for holes in this system. Using impedance spectroscopy, the effect of $[Cu^I(MeCN)_4]BF_4$ on the Spiro-MeOTAD hole mobility was probed. In impedance spectroscopy experiments, a continuous decrease of the zero-field mobility $\mu_{h,0}$ from the pristine $(1.1 \pm 0.2)\cdot10^{-4}$ cm^2 V^{-1} s^{-1} sample to $(4.6 \pm 0.7)\cdot10^{-5}$ cm^2 V^{-1} s^{-1} in 8 mol% $[Cu^I(MeCN)_4]BF_4$:Spiro-MeOTAD was observed (Figure 4b; Figure S19, Supporting Information). Complementary charge extraction by linearly increasing voltage CELIV measurements on $Cu(TFSI)_2$ doped Spiro-MeOTAD revealed an identical trend of continuous decrease of the hole mobility μ_h in co-evaporated samples; from $(6.1 \pm 0.5)\cdot10^{-7}$ cm^2 V^{-1} s^{-1} in the pristine sample to $(1.9 \pm 0.2)\cdot10^{-7}$ cm^2 V^{-1} s^{-1} at 7.5 mol% $Cu(TFSI)_2$ (Figure 4c; Figure S20, Supporting Information). As show in our previous work, co-evaporated samples of $Cu(TFSI)_2$ and Spiro-MeOTAD are uniform and pinhole-free, excluding morphological effects on carrier mobility in this experiment.[8] Yoo et al. studied evaporated triarylamine hole conductors, chemically and energetically very similar to Spiro-MeOTAD, doped with the transition metal oxide ReO_3 by impedance spectroscopy and found a profound loss in hole mobility. They attributed this effect to the ionized dopants acting as coulomb traps.[49] As a consequence, Cu^I is proposed to act as a hole trap by reversible oxidation to Cu^{II}, reducing the average mobility of holes μ_h in Spiro-MeOTAD. Further proof for Cu^I ions acting as hole traps is the distinct $[Cu^I(TFSI)_2]^-$ trap state freeze-out which recovers the mobility below ≈150 K for doping concentrations >3 mol% (Figure 3b). Temperature dependent linewidth in EPR experiments verifies this hypothesis, as it suspects a lower charge carrier motion frequency above 180 K ($E_{A,trap} \approx 16$ meV) with higher $E_{A,Hop}$, characteristic for an increased average residence time on a "free" Cu^I trap site (Figure 3e).[50]

Having identified Cu^I as a potent hole trap, we verified if it is possible to disrupt the accumulation of harmful $[Cu^I(TFSI)_2]^-$ species in doped Spiro-MeOTAD via selective ion complexation. 2,9-Dimethyl-4,7-diphenyl-1,10-phenanthroline (Bathocuproine, abbr. BCP) proves to be a suitable ligand to achieve the targeted selectivity, as it is known to form a stable tetrahedral bis-chelating complex with Cu^I.[51] Additionally, BCP stabilizes the copper(I) ion and inhibits further redox chemistry as it occurs in the hole trapping reaction.[52] We performed conductivity experiments on solution processed films, as co-evaporation does not allow sequential deposition without layered structure formation. First, $Cu(TFSI)_2$ was allowed to undergo a redox reaction with Spiro-MeOTAD in solution, then BCP was added in equimolar amounts to $Cu(TFSI)_2$ into the doped mixture solution to complex the resulting Cu^I ions. $Cu^I(BCP)_2$ complex formation was proven by UV/vis/NIR spectroscopy in solution and thin films (Figures S21, S22, Supporting Information). Afterward, the solution was spun-cast onto commercial interdigitated gold electrodes to determine the thin film conductivity σ. Following an initial strong increase, the conductivity saturates at high doping concentrations and even starts to decrease due to loss in doping efficiency and detrimental effects of by-products such as $[Cu^I(TFSI)_2]^-$ (Figure 4d). To our surprise, σ was amplified by a factor of $0.8\cdot10^4$ in the presence of BCP compared to the sample without BCP at 8 mol% $Cu(TFSI)_2$. However, we also observed a loss in solution-processed Spiro-MeOTAD film quality and disrupted morphology upon adding $Cu(TFSI)_2$ and $[Cu^I(MeCN)_4]BF_4$, similar to our previous work (Figures S23, S24, Supporting Information).[8] This effect was mitigated upon adding BCP. We argue, that morphology has minor influence on the bulk mobility, as both co-evaporated as well as solution-processed $Cu(TFSI)_2$:Spiro-MeOTAD display almost identical thin film conductivities.[8] Therefore, we conclude that any change in σ originates from Cu^I trap passivation. In essence, Cu^I species as the doping reaction side product was identified as a potent

ADVANCED SCIENCE NEWS
www.advancedsciencenews.com

ADVANCED ELECTRONIC MATERIALS
www.advelectronicmat.de

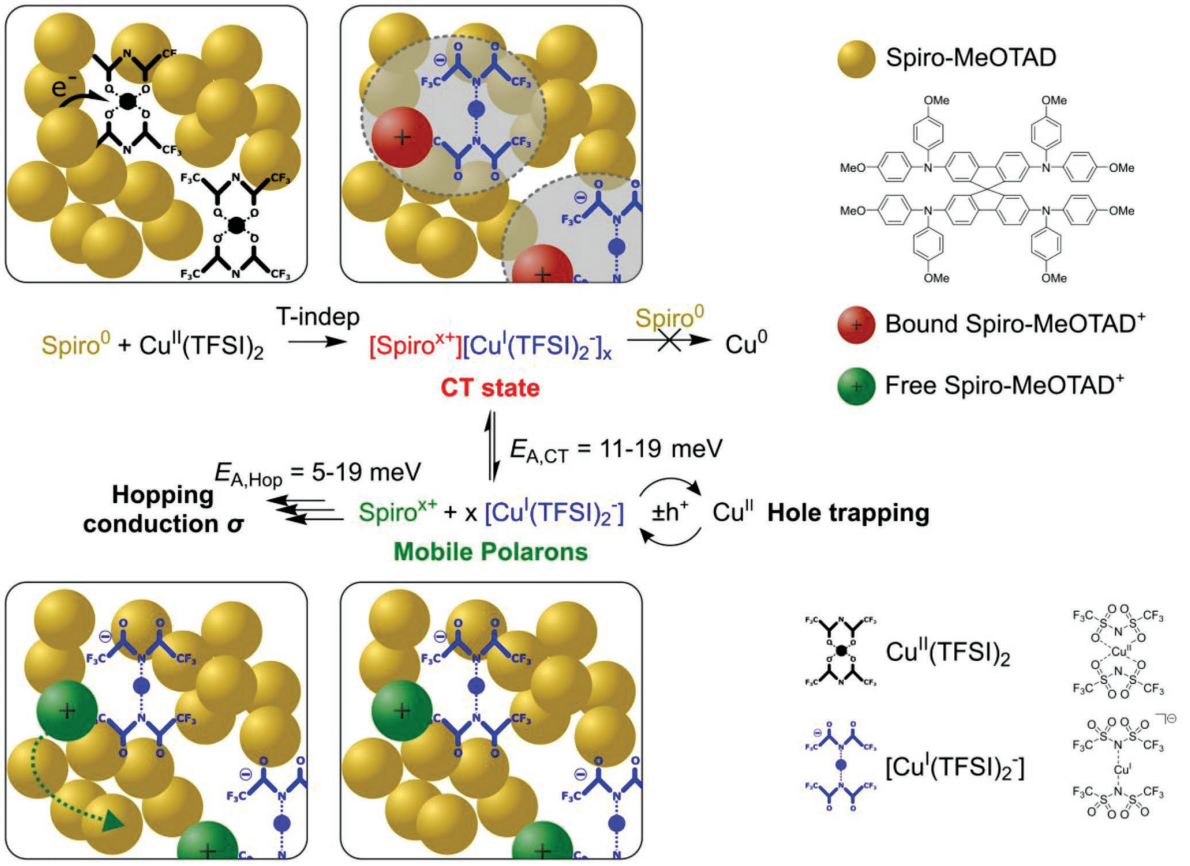

Scheme 1. Overview of the proposed individual reaction steps involving the small molecule hole-conductor Spiro-MeOTAD and *p*-dopant $Cu(TFSI)_2$. A temperature independent and irreversible redox reaction step first yields oxidized Spiro-MeOTAD$^+$ coulombically bound to the $[Cu^I(TFSI)_2]^-$ counter ion (Charge transfer state). $[Cu^I(TFSI)_2]^-$ is generated as a side product of $Cu(TFSI)_2$ reduction. Here, Cu(II) is depicted as black-, Cu(I) as blue spheres. $[Cu^I(TFSI)_2]^-$ traps free holes with an average trap depth of $E_{A,Trap}$ = 16 meV. Mobile Spiro-MeOTAD^{x+} charge carriers are thermally released from the CT state with an activation energy $E_{A,CT}$ in the order of 11–19 meV. Further, the free charge carrier transport responsible for the macroscopic observed conductivity in doped Spiro-MeOTAD is thermally activated with 5–19 meV.

hole trap, whose detrimental effects may be mitigated by selective complexation.

2.5. Absence of Elemental Cu

A final piece of the puzzle is the question concerning why no further reduction of the remaining Cu^I to Cu^0 occurs. This is surprising, as studies have proven the capability of a Cu^I iodide salt to successfully oxidize Spiro-MeOTAD with a reported copper iodide workfunction of ≈5.5 eV.[4,53,54] To answer this question, we refer back to cyclic voltammetry measurements on $Cu(TFSI)_2$ solutions in acetonitrile performed earlier (Figure S1, Supporting Information). Half-wave potentials of −0.439 V versus $Ag/AgNO_3$ for Cu^0/Cu^I and +1.51 V versus $Ag/AgNO_3$ of the Cu^I/Cu^{II} redox couple were recorded. These values translate to a deep lying $EA_{Cu(II)/Cu(I)}$ = 6.15 eV, whereas the electron affinity $EA_{Cu(I)/Cu(0)}$ for the reduction to elemental copper is positioned at 4.20 eV in the presence of TFSI- anions and in acetonitrile. As explained earlier, with respect to the HOMO of Spiro-MeOTAD at 5.03 eV, the high $EA_{Cu(II)/Cu(I)}$ of $Cu(TFSI)_2$ results in an exothermic single electron transfer between $Cu(TFSI)_2$ and Spiro-MeOTAD, explaining the experimentally observed high doping efficiency. However, we noticed a low electron affinity of 4.20 eV for the reduction of $[Cu^I(TFSI)_2]^-$ to elemental copper, compared to 5.5 eV for CuI. Because the low EA implies an endothermic electron transfer to the HOMO of Spiro-MeOTAD, the doping reaction stops at copper(I) with the formation of $[Cu^I(TFSI)_2]^-$.

We propose the $EA_{Cu(I)/Cu(0)}$ discrepancy between copper iodide and $[Cu^I(TFSI)_2]^-$ lies in the stabilization of the soft Lewis acid Cu^I by the adjacent ligands. Strikingly, Stricker et al. performed single crystal analysis on [1-ethyl-3-methylimidazolium]$^+$$[Cu^I(TFSI)_2]^-$, characterized by a d^{10} Cu^I ion coordinated linearly by the two $TFSI^-$ anions with an $N_{TFSI,1}$-Cu-$N_{TFSI,2}$ bond angle of 180.0 °. In this compound, $TFSI^-$ behaves as a monodentate N-donor (κN) ligand. The same cuprate(I) anion $[Cu^I(TFSI)_2]^-$ is very likely formed during our solvent and

ADVANCED SCIENCE NEWS
www.advancedsciencenews.com

ADVANCED ELECTRONIC MATERIALS
www.advelectronicmat.de

oxygen free doping environment and responsible for the high stability (low $EA_{Cu(I)/Cu(0)}$) via complexation and lower N_{TFSI}-Cu bond distance of ≈1.9 Å compared to I—Cu bond distance of 2.62 Å in γ-CuI.[55–57] To test the possibility for $[Cu^I(TFSI)_2]^-$ formation, we mixed equimolar amounts of Spiro-MeOTAD and $Cu(TFSI)_2$ in dichloromethane. A black, crystal-like salt was isolated by an anti-solvent approach (Figure S25, Supporting Information). A $[Spiro\text{-}MeOTAD]^+[Cu^I(TFSI)_2]^-$ composition was determined by elemental analysis (See Supporting Information). We conclude, that energetic mismatch between Cu^I and Spiro-MeOTAD prevents reduction of $Cu(TFSI)_2$ to elemental copper. In addition, $[Cu^I(TFSI)_2]^-$ anions are formed in $Cu(TFSI)_2$ doped Spiro-MeOTAD, further stabilizing the Cu^I state.

2.6. Doping Mechanism Overview

As a closing remark, we combined all our experimental findings to draw the complete doping mechanism between the *p*-dopant $Cu(TFSI)_2$ and Spiro-MeOTAD. We propose three consecutive steps in the doping reaction: i) formation of a coulombically bound CT state $[Spiro\text{-}MeOTAD]^{x+}[Cu^I(TFSI)_2^-]_x$, followed by ii) reversible, endothermic dissociation of the CT state into a free charge carrier and counterion and ultimately iii) transport of the free charge carriers with concurrent trapping involving the $[Cu^I(TFSI)_2]^-$ anions. This concept is in line with previously published results by Tietze et al. on the doping process of zinc phthalocyanine (ZnPc) and *N,N,N′,N′*-Tetrakis(4-methoxyphenyl)-benzidine (MeO-TPD) using the *p*-dopant 1,3,4,5,7,8-hexafluorotetracyanonaphthoquinodimethane F_6TCNNQ.[22] The proposed mechanism is shown in **Scheme 1**.

3. Conclusion

This report offers a comprehensive in-depth study of the doping process of Spiro-MeOTAD using Cu(II) salt, today one of the best hole collecting system in perovskite solar cells. The doping process itself is monitored by the observed shift of WF toward HOMO level and consequent decrease in HIB and the complex doping process is fully elucidated. Impedance and electron paramagnetic resonance spectroscopy clearly indicate low activation energies for hole release and hopping transport. Remarkably small activation barriers favor unprecedented doping efficiencies of up to 50% at 10 mol% doping using $Cu(TFSI)_2$. The reader is invited to recall Scheme 1, the central picture outlining all the important findings of this work regarding the mechanism. Prior to this study, many physical intricacies regarding $Cu(TFSI)_2$ as a *p*-dopant for Spiro-MeOTAD—and in general for molecular semiconductor systems—were poorly described in literature. We could verify the temperature-independent formation of charge transfer states, in line with general agreements on doped OSCs in literature. The CT states comprised of $Spiro\text{-}MeOTAD^{x+}$ and $[Cu^I(TFSI)_2]^-$ were observed to dissociate with an activation energy of (11.4 ± 3.8) meV above ≈150 K. Due to complexation of Cu^I in the cuprate complex $[Cu^I(TFSI)_2]^-$, no further reduction to Cu° can be observed. Thermal activation in the range of 5–19 meV leads to free hole hopping in the doped Spiro-MeOTAD bulk. The hole mobility was found to be greatly influenced by reversible CT state freeze-out, causing macroscopic nonlinear temperature dependent conductivities, which cannot be explained within the framework of charge transport models. Cu^I as the dopant product was identified as a potent hole trap limiting the electrical properties. An improved understanding of this co-evaporated system provides guidelines to passivate these species using bathocuproine, resulting in vastly improved electrical conductivity. These findings complement not only earlier studies on co-evaporated $Cu(TFSI)_2$:Spiro-MeOTAD as a hole transport layer in solar cells, but provide crucial insight into copper salts as *p*-dopants for organic semiconductors.

Supporting Information

Supporting Information is available from the Wiley Online Library or from the author.

Acknowledgements

The authors acknowledge financial support from DFG (SPP 2196) and Bavarian State Ministry of Science and Arts (Soltech). The XPS/UPS facility(PHI 5000 VersaProbe III system) at Keylab Device Engineering in Bavarian Polymer Institute, University of Bayreuth is acknowledged. The authors thank Anna-Maria Dietel from the University of Bayreuth for conducting elemental analysis. J.G. and V.D. acknowledge support from the DFG within the Research Training School "Molecular biradicals: Structure, properties and reactivity" (GRK2112).

Open access funding enabled and organized by Projekt DEAL.

Conflict of Interest

The authors declare no conflict of interest.

Data Availability Statement

The data that support the findings of this study are available from the corresponding author upon reasonable request.

Keywords

copper, doping, electron transfer, reaction mechanisms, semiconductors

Received: January 28, 2022
Revised: April 8, 2022
Published online:

[1] S. Yue, K. Liu, R. Xu, M. Li, M. Azam, K. Ren, J. Liu, Y. Sun, Z. Wang, D. Cao, X. Yan, S. Qu, Y. Lei, Z. Wang, *Energy Environ. Sci.* **2017**, *10*, 2570.
[2] H. J. Snaith, M. Grätzel, *Appl. Phys. Lett.* **2006**, *89*, 262114.
[3] T. Leijtens, J. Lim, J. Teuscher, T. Park, H. J. Snaith, *Adv. Mater.* **2013**, *25*, 3227.
[4] M. Li, Z.-K. Wang, Y.-G. Yang, Y. Hu, S.-L. Feng, J.-M. Wang, X.-Y. Gao, L.-S. Liao, *Adv. Energy Mater.* **2016**, *6*, 1601156.
[5] C. Chen, W. Zhang, J. Cong, M. Cheng, B. Zhang, H. Chen, P. Liu, R. Li, M. Safdari, L. Kloo, L. Sun, *ACS Energy Lett.* **2017**, *2*, 497.
[6] J. Zhang, Q. Daniel, T. Zhang, X. Wen, B. Xu, L. Sun, U. Bach, Y.-B. Cheng, *ACS Nano* **2018**, *12*, 10452.

ADVANCED SCIENCE NEWS
www.advancedsciencenews.com

ADVANCED ELECTRONIC MATERIALS
www.advelectronicmat.de

[7] L. Qiu, X. Zheng, J. Zhang, Y. Yang, W. Cao, Y. Dong, D. Xia, X. Zhou, R. Fan, *ACS Appl. Mater. Interfaces* **2020**, *12*, 546.
[8] J. Mohanraj, M. Stihl, E. Simon, O. von Sicard, G. Schmidt, M. Fleischer, C. Neuber, M. Thelakkat, *ACS Appl. Energy Mater.* **2019**, *2*, 3469.
[9] I. Salzmann, G. Heimel, M. Oehzelt, S. Winkler, N. Koch, *Acc. Chem. Res.* **2016**, *49*, 370.
[10] M. Goel, M. Siegert, G. Krauss, J. Mohanraj, A. Hochgesang, D. C. Heinrich, M. Fried, J. Pflaum, M. Thelakkat, *Adv. Mater.* **2020**, *32*, 2003596.
[11] T. Koopmans, *Physica* **1934**, *1*, 104.
[12] K. Gräf, M. A. Rahim, S. Das, M. Thelakkat, *Dyes Pigments* **2013**, *99*, 1101.
[13] S. Olthof, S. Mehraeen, S. K. Mohapatra, S. Barlow, V. Coropceanu, J. -L. Brédas, S. R. Marder, A. Kahn, *Phys. Rev. Lett.* **2012**, *109*, 176601.
[14] A. Abate, D. R. Staff, D. J. Hollman, H. J. Snaith, A. B. Walker, *Phys. Chem. Chem. Phys.* **2014**, *16*, 1132.
[15] M. L. Tietze, P. Pahner, K. Schmidt, K. Leo, B. Lüssem, *Adv. Funct. Mater.* **2015**, *25*, 2701.
[16] J.-P. Yang, W.-Q. Wang, F. Bussolotti, L.-W. Cheng, Y.-Q. Li, S. Kera, J.-X. Tang, X.-H. Zeng, N. Ueno, *Appl. Phys. Lett.* **2016**, *109*, 093302.
[17] M. L. Tietze, L. Burtone, M. Riede, B. Lüssem, K. Leo, *Phys. Rev. B* **2012**, *86*, 035320.
[18] S. Olthof, W. Tress, R. Meerheim, B. Lüssem, K. Leo, *J. Appl. Phys.* **2009**, *106*, 103711.
[19] H. Méndez, G. Heimel, A. Opitz, K. Sauer, P. Barkowski, M. Oehzelt, J. Soeda, T. Okamoto, J. Takeya, J.-B. Arlin, J.-Y. Balandier, Y. Geerts, N. Koch, I. Salzmann, *Angew. Chem.* **2013**, *125*, 7905.
[20] C. Lambert, G. Nöll, *J. Am. Chem. Soc.* **1999**, *121*, 8434.
[21] S. Fantacci, F. De Angelis, M. K. Nazeeruddin, M. Grätzel, *J. Phys. Chem. C* **2011**, *115*, 23126.
[22] M. L. Tietze, J. Benduhn, P. Pahner, B. Nell, M. Schwarze, H. Kleemann, M. Krammer, K. Zojer, K. Vandewal, K. Leo, *Nat. Commun.* **2018**, *9*, 1182.
[23] G. Krauss, A. Hochgesang, J. Mohanraj, M. Thelakkat, *Macromol. Rapid Commun.* **2021**, *42*, 2100443.
[24] W. Zhang, L. Wang, Y. Guo, B. Zhang, V. Leandri, B. Xu, Z. Li, J. M. Gardner, L. Sun, L. Kloo, *Chem. Commun.* **2020**, *56*, 1589.
[25] H. Oshio, T. Watanabe, A. Ohto, T. Ito, U. Nagashima, *Angew. Chem. Int. Ed. Engl.* **1994**, *33*, 670.
[26] A. Abate, D. J. Hollman, J. Teuscher, S. Pathak, R. Avolio, G. D'Errico, G. Vitiello, S. Fantacci, H. J. Snaith, *J. Am. Chem. Soc.* **2013**, *135*, 13538.
[27] M. Namatame, M. Yabusaki, T. Watanabe, Y. Ogomi, S. Hayase, K. Marumoto, *Appl. Phys. Lett.* **2017**, *110*, 123904.
[28] T. Watanabe, T. Yamanari, K. Marumoto, *Commun. Mater.* **2020**, *1*, 96.
[29] K. Kang, S. Watanabe, K. Broch, A. Sepe, A. Brown, I. Nasrallah, M. Nikolka, Z. Fei, M. Heeney, D. Matsumoto, K. Marumoto, H. Tanaka, S. Kuroda, H. Sirringhaus, *Nat. Mater.* **2016**, *15*, 896.
[30] A. Privitera, R. Warren, G. Londi, P. Kaienburg, J. Liu, A. Sperlich, A. E. Lauritzen, O. Thimm, A. Ardavan, D. Beljonne, M. Riede, *J. Mater. Chem. C* **2021**, *9*, 2944.
[31] N. F. Mott, *Philos. Mag.* **1969**, *19*, 835.
[32] B. I. Shklovskii, A. L. Efros, *Electronic Properties of Doped Semiconductors*, Springer Berlin Heidelberg, Berlin, Heidelberg **1984**.
[33] A. V. Nenashev, J. O. Oelerich, S. D. Baranovskii, *J. Phys. Condens. Matter* **2015**, *27*, 093201.
[34] R. Fujimoto, Y. Yamashita, S. Kumagai, J. Tsurumi, A. Hinderhofer, K. Broch, F. Schreiber, S. Watanabe, J. Takeya, *J. Mater. Chem. C* **2017**, *5*, 12023.
[35] R. Rosenbaum, *Phys. Rev. B* **1991**, *44*, 3599.
[36] A. L. Efros, B. I. Shklovskii, *J. Phys. C Solid State Phys.* **1975**, *8*, L49.
[37] L. Li, N. Lu, M. Liu, *J. Appl. Phys.* **2014**, *116*, 164504.
[38] B. Li, S. Zhang, F. Xia, Y. Huang, X. Ran, Y. Xia, Y. Chen, W. Huang, *J. Appl. Phys.* **2020**, *128*, 085501.
[39] M. Pei, J. Guo, B. Zhang, S. Jiang, Z. Hao, X. Xu, Y. Li, *Adv. Phys. X* **2020**, *5*, 1747945.
[40] A. Köhler, H. Bässler, *Electronic Processes in Organic Semiconductors: An Introduction*, Wiley-VCH, Weinheim **2015**.
[41] J. A. Röhr, X. Shi, S. A. Haque, T. Kirchartz, J. Nelson, *Phys. Rev. Appl.* **2018**, *9*, 044017.
[42] J. D. Yuen, R. Menon, N. E. Coates, E. B. Namdas, S. Cho, S. T. Hannahs, D. Moses, A. J. Heeger, *Nat. Mater.* **2009**, *8*, 572.
[43] D. Poplavskyy, J. Nelson, *J. Appl. Phys.* **2003**, *93*, 341.
[44] Y. Matsuo, D. Son, Y. Shimoi, K. Marumoto, *Chem. Phys. Lett.* **2014**, *607*, 29.
[45] K. A. Peterson, A. Patterson, A. Vega-Flick, B. Liao, M. L. Chabinyc, *Mater. Chem. Front.* **2020**, *4*, 3632.
[46] M. Schwarze, C. Gaul, R. Scholz, F. Bussolotti, A. Hofacker, K. S. Schellhammer, B. Nell, B. D. Naab, Z. Bao, D. Spoltore, K. Vandewal, J. Widmer, S. Kera, N. Ueno, F. Ortmann, K. Leo, *Nat. Mater.* **2019**, *18*, 242.
[47] A. Vaskevich, I. Rubinstein, *J. Electroanal. Chem.* **2000**, *491*, 87.
[48] A. M. Romine, N. Nebra, A. I. Konovalov, E. Martin, J. Benet-Buchholz, V. V. Grushin, *Angew. Chem., Int. Ed.* **2015**, *54*, 2745.
[49] S.-J. Yoo, J.-H. Lee, J.-M. Kim, J.-J. Kim, *Appl. Phys. Lett.* **2017**, *110*, 053303.
[50] H. Matsui, D. Kumaki, E. Takahashi, K. Takimiya, S. Tokito, T. Hasegawa, *Phys. Rev. B* **2012**, *85*, 035308.
[51] X. Ding, H. Xie, Y. J. Kang, *J. Nutr. Biochem.* **2011**, *22*, 301.
[52] R. P. Patel, D. Svistunenko, M. T. Wilson, V. M. Darley-Usmar, *Biochem. J.* **1997**, *322*, 425.
[53] P. Wang, J. Zhang, Z. Zeng, R. Chen, X. Huang, L. Wang, J. Xu, Z. Hu, Y. Zhu, *J. Mater. Chem. C* **2016**, *4*, 9003.
[54] S. Park, H. Lee, J. Lee, Y. Lee, Y. Yi, *Org. Electron.* **2014**, *15*, 3298.
[55] M. Stricker, B. Oelkers, C. P. Rosenau, J. Sundermeyer, *Chem. – Eur. J.* **2013**, *19*, 1042.
[56] N. Kuganathan, J. C. Green, *Chem. Commun.* **2008**, 2432.
[57] M. Kaiser, J. Göttlicher, T. Vitova, A. Hinz, *Chem. – Eur. J.* **2021**, *27*, 7998.

ADVANCED ELECTRONIC MATERIALS

Supporting Information

for *Adv. Electron. Mater.,* DOI: 10.1002/aelm.202200113

Intricacies and Mechanism of p-Doping Spiro-MeOTAD Using $Cu(TFSI)_2$

*Adrian Hochgesang, Simon Biberger, Jeannine Grüne, John Mohanraj, Frank-Julian Kahle, Vladimir Dyakonov, Anna Köhler, and Mukundan Thelakkat**

WILEY-VCH

Supporting Information

Intricacies and Mechanism of p-Doping Spiro-MeOTAD Using Cu(TFSI)$_2$

Hochgesang, Adrian; Biberger, Simon; Grüne, Jeannine; Mohanraj, John; Kahle, Frank-Julian; Dyakonov, Vladimir; Köhler, Anna; Thelakkat, Mukundan*

Table of Contents

Experimental Procedures

1. Materials and Equipment

Anhydrous solvents were purchased from Sigma Aldrich / Acros Organics in sealed bottles and were used as received. N2,N2,N2',N2',N7,N7,N7',N7'-octakis(4-methoxyphenyl)-9,9'-spirobi[fluorene]-2,2',7,7'-tetraamine Solarpur SHT-263 (abbreviated as "Spiro-MeOTAD") and copper(II)oxide were supplied by Sigma-Aldrich, Germany and used as received. Device grade, triple-sublimed copper(II)bis(trifluoromethanesulfonyl)imide (abbreviated as "$Cu(TFSI)_2$") for doping experiments was supplied by SIEMENS. 2,9-dimethyl-4,7-diphenyl-1,10-phenanthroline (abbreviated as "BCP") was obtained in > 98 % purity from Sigma-Aldrich, Germany and used as received. Tetrakis(acetonitrile)copper(I)tetrafluoroborate was obtained from Sigma-Aldrich, Germany and purified by recrystallisation from anhydrous acetonitrile under inert atmosphere immediately prior to experiments to obtain white, flaky crystals. Spiro-MeOTAD$(PF_6)_2$ was synthesized according to a previously published procedure[1]. Film thicknesses were measured using a Veeco Dektak 150 Profilometer. Optical images of thin films were taken using a Zeiss Axio Imager A1m microscope. Scanning electron microscopy was performed with a Phenom Pro SEM by Thermo Fisher Scientific on thin films coated onto oxide-free silicon substrates. A 4-segmented detector and accelerating voltage of 10 kV were used. Ultraviolet photoelectron spectroscopy was performed on a PHI 5000 VersaProbe III machine equipped with a helium discharge radiation source providing stable and continuous He I and II lines, under ultrahigh vacuum (10^{-10} mbar). Room temperature UV/Vis/NIR absorption measurements were carried out using a V-670 JASCO spectrometer. Impedance data on devices was measured using a Metrohm Autolab PGSTAT204 equipped with an FRA32M module. The NOVA 2.1.4 Software package provided by Metrohm, Germany and custom MATLAB code was used to process the impedance data. Co-evaporation of Spiro-MeOTAD and $Cu(TFSI)_2$ was performed on a Balzers PLS 500 E equipped with quartz crystal microbalances and switchable shadow masks, for further information, see previous publications[2]. All temperature dependent mobility, charge carrier density and conductivity measurements were performed under helium atmosphere using an Optistat CF2 He cryostat from Oxford Instruments, UK. Al_2O_3 thin films for Mott-Schottky and CELIV metal-insulator-semiconductor devices were prepared by atomic layer deposition from trimethylaluminium and H_2O in a VEECO Savannah Gen. 2 S300. EPR measurements were performed with an X-band spectrometer (Magnettech MS-

5000) equipped with a continuous-flow helium cryostat (Oxford ESR 900). Density measurements were carried out using a Mettler Toledo XP205 digital balance equipped with either a Millipore water or cyclohexane reference liquid bath. Solid samples for density determination were fabricated by pressing Spiro-MeOTAD and anhydrous $Cu(TFSI)_2$ into pellets of 1 cm diameter at 8 tons pressure for 15 min.

Synthesis of $N^2,N^2,N^{2'},N^{2'},N^7,N^7,N^{7'},N^{7'}$-octakis(4-methoxyphenyl)-9,9'-spirobi[fluorene]-2,2',7,7'-tetraamine^{I}, [Cu(I)(bis(trifluoromethanesulfonyl)imide$_2$] salt (1:1) (**1**)

A 100 mL flame-dried Schlenk flask was evacuated and consecutively flushed with Ar three times. The flask was charged with 119.6 mg ($9.76\cdot10^{-5}$ Mol) Spiro-MeOTAD and 60.9 mg ($9.76\cdot10^{-5}$ Mol) $Cu(TFSI)_2$ under inert atmosphere. 25 mL anhydrous dichloromethane were added, which immediately lead to the formation of a dark-purple color. A condenser was attached and the solution was stirred at 50 °C under reflux conditions for 2 h. The solvent was removed under vacuum and the as obtained powder was dried under high vacuum for 1 h at r.t. Single crystals were grown inside a glovebox by dissolving the compound in a minimal amount of anhydrous dichloromethane (ca. 1.5 mL) and placing the vial into another, bigger container. The outer container was filled with a small amount of anhydrous n-hexane and sealed hermetically to create a solvent saturated, inert atmosphere. After 24 h at r.t., black single crystals 1.5 mm in diameter were collected from the bottom of the inner vial. The crystals were carefully suspended in anhydrous n-hexane to clean the surfaces, ultrasonicated for 10 sec and placed on a polyester/cellulose fabric to dry under inert atmosphere yielding **1** (119.3 mg, 66 %). Elemental analysis calculated (m%) for $N^2,N^2,N^{2'},N^{2'},N^7,N^7,N^{7'},N^{7'}$-octakis(4-methoxyphenyl)-9,9'-spirobi[fluorene]-2,2',7,7'-tetraamine^{I}, [$Cu^{I}(TFSI)_2$] salt (1:1) (1849.27 g mol^{-1}): C 55.206, H 3.706, N 4.545, S 6.936; found: C 56.41, H 3.87, N 4.63, S 7.19.

Synthesis of copper(II) bis(trifluoromethanesulfonyl)imide for density determination (**2**)

A 500 mL flask was loaded with copper(II)oxide nanopowder (500 mg, 6.29 mmol), which was subsequently dispersed in 150 mL Millipore H_2O under strong stirring at r.t. Bis(trifluoromethane)sulfonimide (3.54 g, 12.6 mmol) was added in small portions. The dispersion was stirred at 80 °C for 4 h, until the black color completely disappears to form a light blue solution. Excess copper(II)oxide was removed by gravity filtration. The water was removed from the filtrate using a rotary evaporating, resulting in a blue, hydrated crystals. The hydrate was converted to the anhydrate by prolonged heating at 180 °C under high vacuum, yielding a white powder **2** (2.803 g, 71 %). The anhydrous copper(II)bis(trifluoromethanesulfonyl)imide was stored under Ar for further use.

2. General methods

All doping experiments and oxygen/water sensitive reactions were carried out in a nitrogen filled mBraun Labmaster 130 glovebox.

Ultraviolet Photoelectron Spectroscopy

UPS measurements were carried out on a PHI 5000 VersaProbe III system fitted with a He discharge light source providing stable and continuous He I and He II lines, under ultrahigh vacuum (ca. 10^{-9} mbar). Samples for UPS measurements were obtained by thermal co-evaporation of controlled amounts of $Cu(TFSI)_2$ and spiro-OMeTAD on clean ITO (15 Ω sq^{-1}), affording ca. 20 nm thick films (measured by using a dummy sample in a profilometer). The samples were transferred from the evaporation chamber to a N_2 filled glove box and further to the instrument in a nitrogen filled and sealed stainless steel transport vessel. Once the samples were loaded into the instrument main chamber, He I source (80 W) was used to induce photoelectrons and were collected at 90° take-off angle by using a multichannel semi-spherical analyzer. Both valence band maximum (VBM) and secondary electron cutoff (SECO) signals from the samples were measured by applying -5V between the analyzer and the substrate. Both VBM and SECO spectra were collected at least from 3 different areas in 2 different samples, and only the reproducible measurements were considered for further calculations and discussion. The VBM and SECO binding energy values necessary to determine ionization potential and workfunction, respectively, were obtained by linear extrapolation method. The Fermi level E_F of the samples (doped and pristine) were referenced to the Fermi level of sputter-cleaned Au foil. The energy resolution of the VBM and SECO is 0.15 eV, which was derived from the full-width half-maximum of the Au Fermi edge.

Table S1. . Ionisation energy IP, workfunction WF and hole-injection barrier of $Cu(TFSI)_2$ doped and pristine Spiro-MeOTAD HIB, determined by UPS experiments.

Sample	Ionisation Energy IP [eV]	Workfunction WF [eV]	Hole injection barrier HIB [eV]
Pristine Spiro-MeOTAD	5.03 ± 0.15	4.29 ± 0.15	0.74 ± 0.15
2 mol% $Cu(TFSI)_2$:Spiro-MeOTAD	5.07 ± 0.15	4.68 ± 0.15	0.39 ± 0.15
4 mol% $Cu(TFSI)_2$:Spiro-MeOTAD	5.23 ± 0.15	4.82 ± 0.15	0.41 ± 0.15
6 mol% $Cu(TFSI)_2$:Spiro-MeOTAD	5.17 ± 0.15	4.86 ± 0.15	0.31 ± 0.15
8 mol% $Cu(TFSI)_2$:Spiro-MeOTAD	5.28 ± 0.15	4.95 ± 0.15	0.33 ± 0.15
10 mol% $Cu(TFSI)_2$:Spiro-MeOTAD	5.35 ± 0.15	5.02 ± 0.15	0.33 ± 0.15

Temperature Dependent UV/Vis/NIR

For investigating possibly temperature-dependent absorption features of the doped Spiro-MeOTAD we used a home-built absorption setup. The films were transferred in a continuous flow cryostat by Oxford instruments under helium atmosphere and the temperature between 300K and 5K is controlled by an Oxford Instruments ITC 502. For each temperature step the temperature was held constant for 15 min before the measurement. The optical density is calculated by analysing the transmission spectra with a Shamrock SR-303i by Andor Technology equipped with CCD-camera (Andor iDus DU420-OE). For these experiments the (doped) Spiro-MeOTAD were evaporated on quartz glass.

Electrical conductivity

Electrical conductivities were measured using commercial Gen4 OFET substrates obtained from Fraunhofer IPMS, Germany. Every OFET substrate contains 30 nm thick interdigitated gold electrodes, patterned on thermally grown silicon oxide with a channel width of 2.5 µm, 5 µm, 10 µm and 25 µm and a channel length of 1 cm. The substrates were cleaned by sonication in isopropanol and acetone for 10 min each, followed by activation of the surface in an ozone plasma for 15 min at 50 °C. 100 nm thick $Cu(TFSI)_2$:Spiro-MeOTAD films were deposited by co-evaporation. I-V characteristics were measured using an Agilent Technologies B1500A Semiconductor Device Analyzer. The electrical conductivities were

extracted from the linear fit of the I-V curve in the Ohmic region according to Equation S1 below:

$$\sigma = \frac{a \cdot L}{W \cdot d} \quad \text{(S1)}$$

Where σ: electrical conductivity, a: slope of the linear fit, L: channel length, W: channel width, d: film thickness. The film thicknesses were measured after the conductivity measurements, using a profilometer. The film thicknesses were measured after the conductivity measurements, using a profilometer.

Solid State Mott Schottky Analysis

TEC-7 (XOP glass, 1" x 1" x 2.2 mm, 6 – 8 Ω sq^{-1}, ~500 nm FTO on glass) substrates were etched with dilute HCl/Zn-dust. After obtaining the etched electrode pattern, the substrates were brushed manually with sodium dodecyl sulfate and deionized water, followed by ultra-sonication in 2 vol% aqueous Hellmanex-III solution, water, acetone and isopropanol. The substrates were blown dry with nitrogen and pre-treated with O_3/UV for 15 min at 50 °C. 100 nm of Al_2O_3 were deposited on the FTO-electrodes using ALD (H_2O/$Al(CH_3)_3$, 15 ms pulse duration, 150 °C, 5 s purge time, 1111 cycles), while leaving areas insulator-free for contacting the device during measurements. The aluminium oxide layer was passivated by spin coating 100 nm of BCB (10 vol% Cyclotene 3022-35 in toluene, 70 µL, 50 sec, 3 krpm) on top and soft curing for 10 sec at 250 °C in air, followed by a hard bake at 250 °C for 1 h under Argon. 100 nm of $Cu(TFSI)_2$:Spiro-MeOTAD films were co-evaporated onto the substrates. Finally, Au electrodes were thermally evaporated using a shadow mask (d_{Au} = 70 nm). The impedance of the devices was measured with a two-electrode setup and varying electrical field (10 kHz to 10 Hz, 8 points per frequency decade, -1.5 to 1.5 V_{Bias} in 48 voltage steps, 7 mV_{RMS}) using a Metrohm Autolab PGSTAT204 equipped with an FRA32M module. The NOVA 2.1.4 Software package provided by Metrohm, Germany and custom MATLAB code was used to process the impedance data. The Au top electrode was connected to the counter and reference electrode, the FTO contact to the working and sense electrode of the potentiostat. Devices under test were shielded from ambient light, external electrical fields and kept under inert atmosphere. From the imaginary *Z*'' and real *Z*' impedance, the capacitance of the organic layer was extracted assuming an R_S(RC) equivalent circuit:

$$\hat{Z}(i\omega)_{R(RC)} = R_{Series} + \frac{1}{i\omega C_{Parallel} + \frac{1}{R_{Parallel}}} \quad \text{(S2)}$$

which can be solved for $C_{Parallel}$ to yield

$$C_{Parallel} = \frac{Im(Z)}{(-Im(Z)^2 + (Re(Z) - R_S)^2)\omega} \quad \text{(S3)}$$

The density of ionized acceptors N_A^- was the extracted by plotting C^{-2} vs the Boltzmann corrected applied bias voltage V_{Bias} and fitting (S5) to the linear depletion regime

$$C_{Parallel}^{-2} = \frac{2}{\varepsilon_{OSC}\varepsilon_0 A^2 q N_A^-}\left(V_{Bias} - \frac{k_B T}{q}\right) \quad \text{(S4)}$$

where ε_{OSC} and ε_0 are the dielectric constants of the organic semiconductor layer (Approximated with 3) and the vacuum permittivity, respectively. A^2 is the area of the organic layer in cm^2, q the elementary charge and k_B the Boltzmann constant in eV K^{-1}. A minimum of 4 working MIS devices were evaluated per dopant concentration. An exemplary fit of Equation S4 can be found in Figure S4.

Electron Paramagnetic Resonance Measurements

For EPR meaurements on co-evaporated samples, PET foil of 13 μm thickness was used as a substrate. The PET foil was cut into a 2 cm by 5 cm sheet of pre-cut 2 mm stripes and fixed onto a metal carrier plate for co-evaporation of 100 nm $Cu(TFSI)_2$:Spiro-MeOTAD, yielding a constant sample volume of $1 \cdot 10^4$ cm^3 for all doping concentrations. After deposition, the substrate was transferred to the glovebox and the 2 mm stripes were carefully placed into pre-dried (50 °C, 2 h, vacuum) quartz EPR tubes. The tubes were subsequently sealed using UHU Plus Endfest 300 2-component glue under nitrogen, which was degassed under vacuum after mixing to exclude enclosed oxygen and water. For each doping concentration, at least two individual tubes were prepared to exclude experimental errors. Shipping of the EPR tubes to cooperation facilities was conducted in a hermetically sealed, nitrogen filled metal tube closed with ISO-KF blind flanges on both ends. EPR measurements were carried out in an X-band spectrometer (Magnettech MS-5000) with a resonance frequency of 9.42 GHz and a quality factor of $Q \sim 2000 - 3000$. The experimental settings were optimized to a modulation frequency of B_{mod} = 0.02 mT and microwave power of P_{MW} = 0.8 W. For temperature-controlled measurements, a continuous-flow helium cryostat (Oxford ESR 900) was used. For quantitative EPR, the double integral (DI) of the measured signals were compared with a reference sample with known spin number (internal reference of the spectrometer). The spin number is then given by (s = ½): $N_{sample} = N_{ref} \times \frac{DI_{ref}}{DI_{sample}} \times \frac{Q_{sample}}{Q_{ref}}$ and subsequently scaled up to the entire sample size. When determining N_{sample}, a constant offset for each measurement occurs depending on the measurement of the reference sample.

Negative Differential Susceptance Mobility Measurement

TEC-7 (XOP glass, 1" x 1" x 2.2 mm, 6 – 8 Ω sq^{-1}, ~500 nm FTO on glass) substrates were etched with dilute HCl/Zn-dust. After obtaining the etched electrode pattern, the substrates were brushed manually with sodium dodecyl sulfate and deionized water, followed by ultra-sonication in 2 vol% aqueous Hellmanex-III solution, water, acetone and isopropanol. The substrates were blown dry with nitrogen and pre-treated with O_3/UV for 15 min at 50 °C. 100 nm of $Cu(TFSI)_2$:Spiro-MeOTAD films were co-evaporated onto the substrates. To avoid edge effects, a part of the conductive electrodes was masked with Kapton tape, which was removed after the OSC deposition. 100 nm of Au was thermally evaporated on top of the OSC layer using a shadow mask to complete the device stack. The impedance of the devices was

measured with a two-electrode setup and increasing electrical field (1 MHz to 100 Hz, 25 points per frequency decade, 0-2 V_{Bias} in 15 voltage steps, 10 mV_{RMS}) using a Metrohm Autolab PGSTAT204 equipped with an FRA32M module. The NOVA 2.1.4 Software package provided by Metrohm, Germany and custom MATLAB code was used to process the impedance data. The ITO back contact was connected to the working electrode (WE) and sense (S), while the Au top electrode was connected to the counter electrode (CE) and reference electrode (RE). Devices under test were shielded from ambient light and external electrical fields.

Based on frequency-dependent capacitance data of ITO/Spiro-MeOTAD:$Cu(TFSI)_2$/Au devices, a charge carrier mobility can be extracted based on unipolar space-charge limited current theory.[3] Extensive mathematical derivations can be found in the relevant literature.[4,5] Efficient electron/hole injection is required, as the transit-time effect responsible for the mobility determination using the negative differential susceptance method may only be observed, if the injection barrier is smaller than 0.4 eV.[6,7] As demonstrated for (doped) Spiro-MeOTAD, ITO forms ohmic contacts with low injection barriers suitable for this measurement.[8] First described by Martens et al, the mechanism for occurrence of a *negative* capacitive (= inductive) contribution in a biased, unipolar SCL diode can be formulated as: Injected charges move under the influence of an applied bias voltage, taking on a relaxed space-charge distribution. Upon applying an external AC stimulus (during impedance measurement, **Figure S8**), the AC current lags behind due to the finite transit time of the charge carriers across the film thickness, giving an inductive contribution in the measured admittance/impedance for a given frequency range.[9] The inductive contribution induces a characteristic negative capacitance region in a *C*(f) plot (**Figure S9**). This frequency dependent relaxation time can be measured and visualized using the negative differential susceptance method (**Figure S11**); ultimately yielding the charge carrier mobility from the transit time. Above the characteristic transit frequency f_{max} the space charge is not able to redistribute within the AC period, and the capacitance approaches the purely geometrical capacitance, treating the organic layer as a regular dielectric.[6] Experimentally, the capacitance of the organic layer was extracted assuming an R_S(RC) equivalent circuit from the imaginary *Z*'' and real *Z*' impedance (**Figure S8**):

$$\hat{Z}(i\omega)_{R(RC)} = R_{Series} + \frac{1}{i\omega C_{Parallel} + \frac{1}{R_{Parallel}}} \qquad \text{(S5)}$$

which can be solved for $C_{Parallel}$ to yield

$$C_{Parallel} = \frac{Im(Z)}{(-Im(Z)^2 + (Re(Z) - R_S)^2)\omega} \quad \text{(S6)}$$

For high parallel resistance, a total RC capacitance may also be calculated according to[10]

$$C_{Series} = \frac{-\sin(\theta)}{|Z|\omega} \quad \text{(S7)}$$

The geometric capacitance C_{Geo} of each device was determined in the high frequency region of the C(f)-plot (**Figure S9**). Together with the measured capacitance, the mobility was extracted from the negative differential susceptance $-\Delta B$ at different electrical fields. The negative differential susceptance $-\Delta B$ can be calculated from

$$-\Delta B = -\omega\big(C(\omega) - C_{geo}\big) \quad \text{(S8)}$$

$-\Delta B$(f) displays a global maximum $f_{\max}$ (**Figure S11**, marked red), which are used to calculate the transit time τ_{tr}

$$\tau_{tr} = 0.56 f_{max}^{-1} \quad \text{(S9)}$$

Local maxima above the transit frequency without physical meaning were discarded. The mobility can then be extracted as

$$\mu = \frac{d^2}{\tau_t V_{Bias}} \quad \text{(S10)}$$

with d being the thickness of the organic layer. The zero-field mobility μ_0 was calculated by extrapolating the obtained Poole-Frenkel type field dependency.

MIS-CELIV (Metal-Insulator-Semiconductor Charge Extraction by Linearly Increasing Voltage)

The MIS-CELIV technique was employed to extract the hole mobility at room temperature. For the MIS-architecture a 25nm thin insulating layer (Al2O3) was deposited on an FTO-

covered substrate via atomic layer deposition ($H_2O/Al(CH_3)_3$, 15 ms pulse duration, 150 °C, 5 s purge time, 278 cycles). These substrates were then transferred to a thermal evaporator where the (doped) Spiro-MeOTAD and the gold contacts were evaporated. By applying a triangular voltage ramp with a waveform generator (RIGOL DG4102) charges were firstly injected and accumulated at the semiconductor-insulating layer and then extracted again via the gold contact. The sample response was amplified by a DHPCA-100 (Femto) and recorded with a Tektronix TDS3000 oscilloscope. The obtained data was analyzed according to Sandberg et al[4]. The mobility was calculated by using the following Equation:

$$\mu = \frac{\pi^2 d_s^2 (1+f)}{8A * t^2} \left[1 + \frac{\pi^4 k_B T}{2eA * t}\right]^{-1} \quad \text{(S11)}$$

where d_s is the thickness of the Spiro-MeOTAD, f is the ratio between the between the geometric capacitance of the Spiro-MeOTAD and the insulator layer ($f = \frac{\epsilon_s d_i}{\epsilon_i d_s}$), A is the voltage ramp and t is the time in which the current signal rises from the plateau value j_0 to the $2 \cdot j_0$ value.

3. Supporting Measurement Data

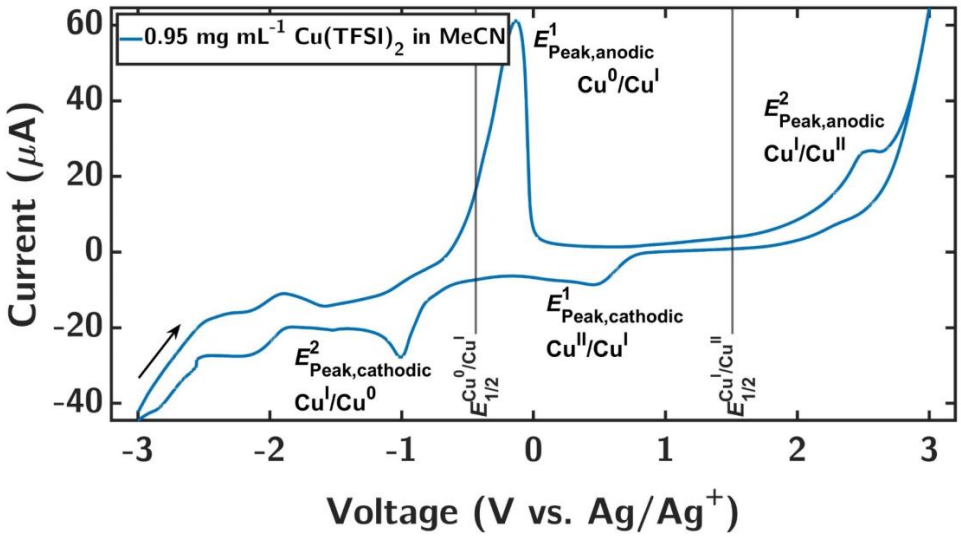

Figure S1. Cyclic voltammogram of $Cu(TFSI)_2$ in anhydrous MeCN (0.95 mg mL^{-1}) at 295 K, all voltages referenced to a $Ag/AgNO_3$ non-aqueous reference electrode. The working and counter electrode consists of two platinum disk electrodes with a diameter of 1 mm. $E^1_{Peak,anodic}$ = -131.8 mV; $E^2_{Peak,anodic}$ = +2.567 V; $E^1_{Peak,cathodic}$ = +452.2 mV; $E^2_{Peak,cathodic}$ = -1.008 V; $E^{Cu(0)/Cu(I)}_{1/2}$ = -438.5 mV; $E^{Cu(I)/Cu(II)}_{1/2}$ = +1.510V.

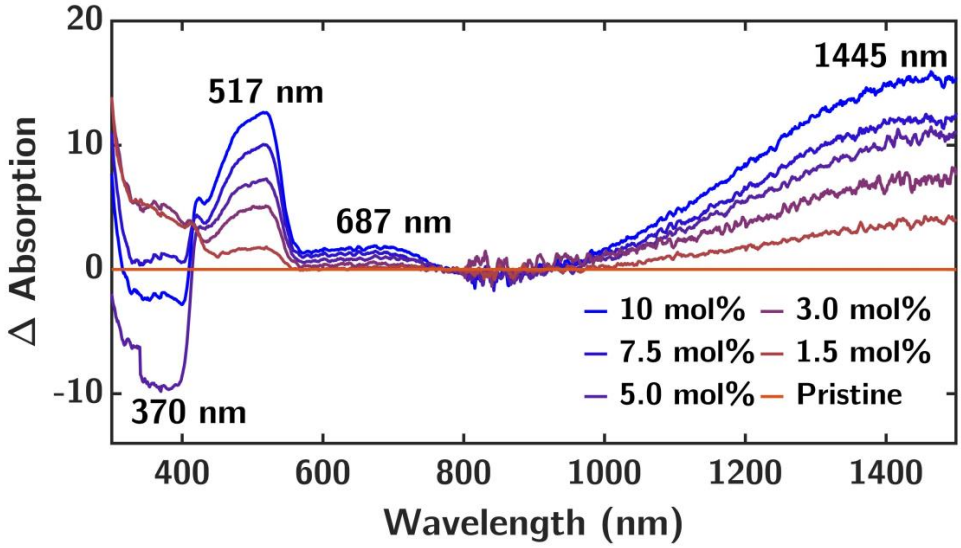

Figure S2. Differential plot of $Cu(TFSI)_2$ doped Spiro-MeOTAD UV/Vis/NIR absorbance compared to pristine Spiro-MeOTAD for different doping concentrations given in the legend (Figure 1c).

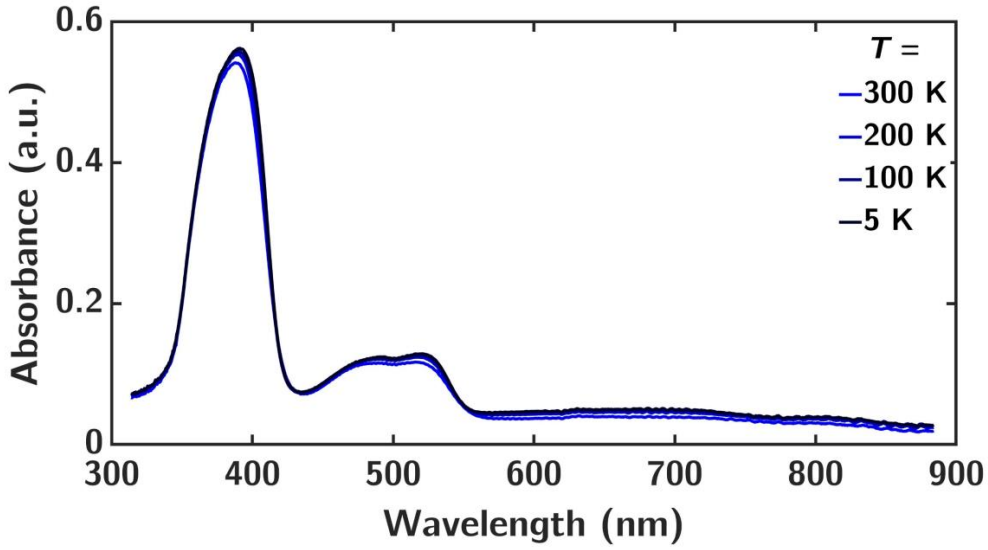

Figure S3. Temperature dependent UV/Vis/NIR absorption spectra of 10 mol% Cu(TFSI)2 doped Spiro-MeOTAD thin films under inert atmosphere at 300 K to 5 K.

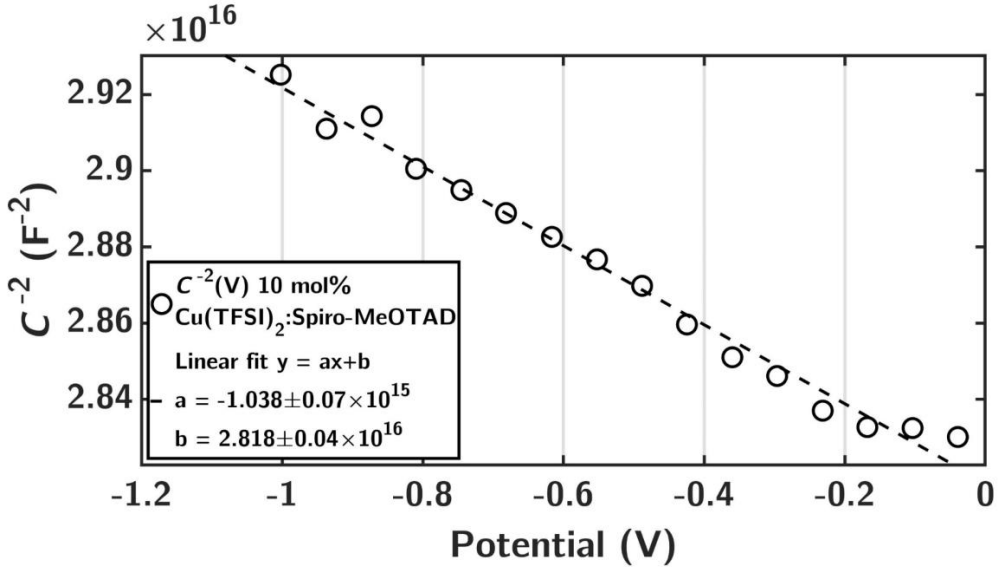

Figure S4. Exemplary fit of Equation S4 to the voltage dependent inverse squared capacitance of 10 mol% doped, co-evaporated films in a FTO/Al_2O_3/Hexamethyldisilazane/$Cu(TFSI)_2$ doped Spiro-MeOTAD/Au structure. The slope yields a charge carrier density N_A^- of (2.8 ± 0.2)·10^{19} cm^{-3} for ε_{OSC} = 3, A^2 = 0.04 cm^2 and T = 300 K in this sample.

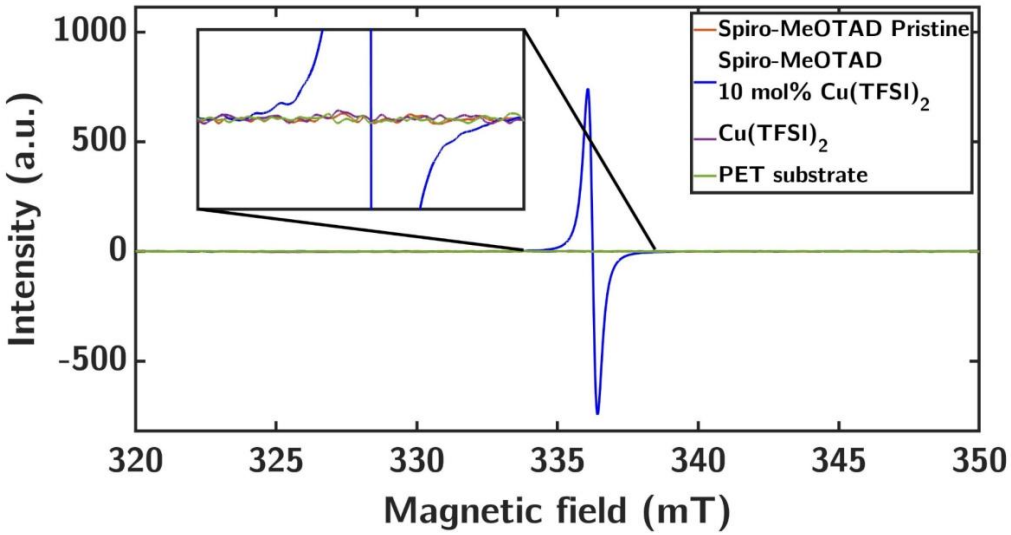

Figure S5. EPR spectra for different samples investigating Spiro-MeOTAD doped with Cu(TSFI)$_2$. Doping concentration of 10.4 mol% leads to a Lorentzian EPR signal while undoped Spiro-MeOTAD shows no intrinsic doping. The PET-substrate and Cu(TFSI)$_2$ have no measurable EPR signal. EPR parameters (modulation amplitude B_{mod} and microwave power P_{MW}) were optimized for highest signal of 10.4 mol%.

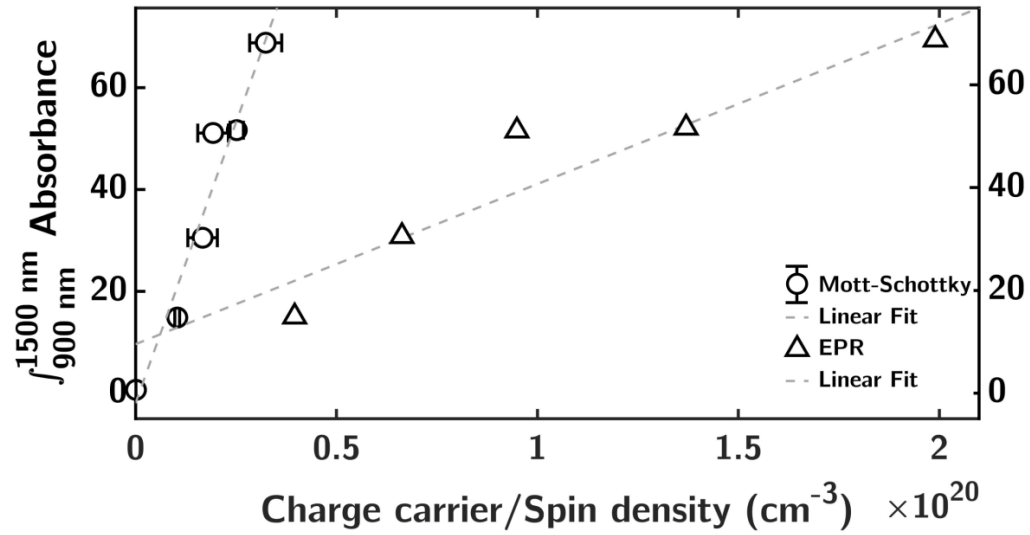

Figure S6. Linear correlation (grey dotted line) between charge carrier density N_A^- obtained from Mott-Schottky experiments (black circles), as well as spin density N_{Spins} obtained from EPR experiments (black triangles) and the integral of the polaron peak between 900 nm and 1500 nm for a series of doped films (See UV/Vis/NIR of doped, co-evaporated thin films in Figure 1c).

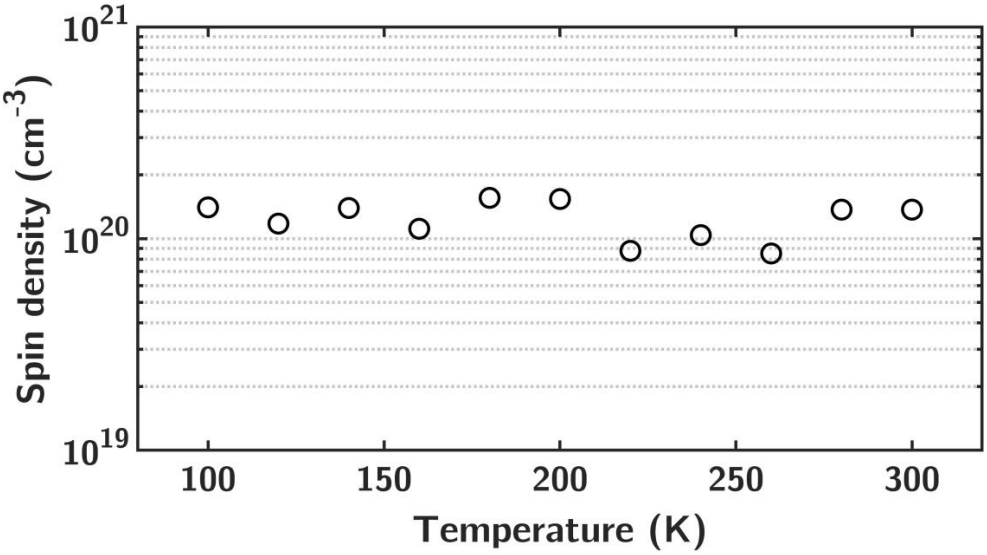

Figure S7. Spin density of 7.5 mol% $Cu(TFSI)_2$ doped Spiro-MeOTAD sample as a function of the temperature. Here, the spin density was referenced to the internal spin reference corrected for the cavity temperature. B_{mod} = 0.02 mT, microwave power P_{MW} = 0.8 mW.

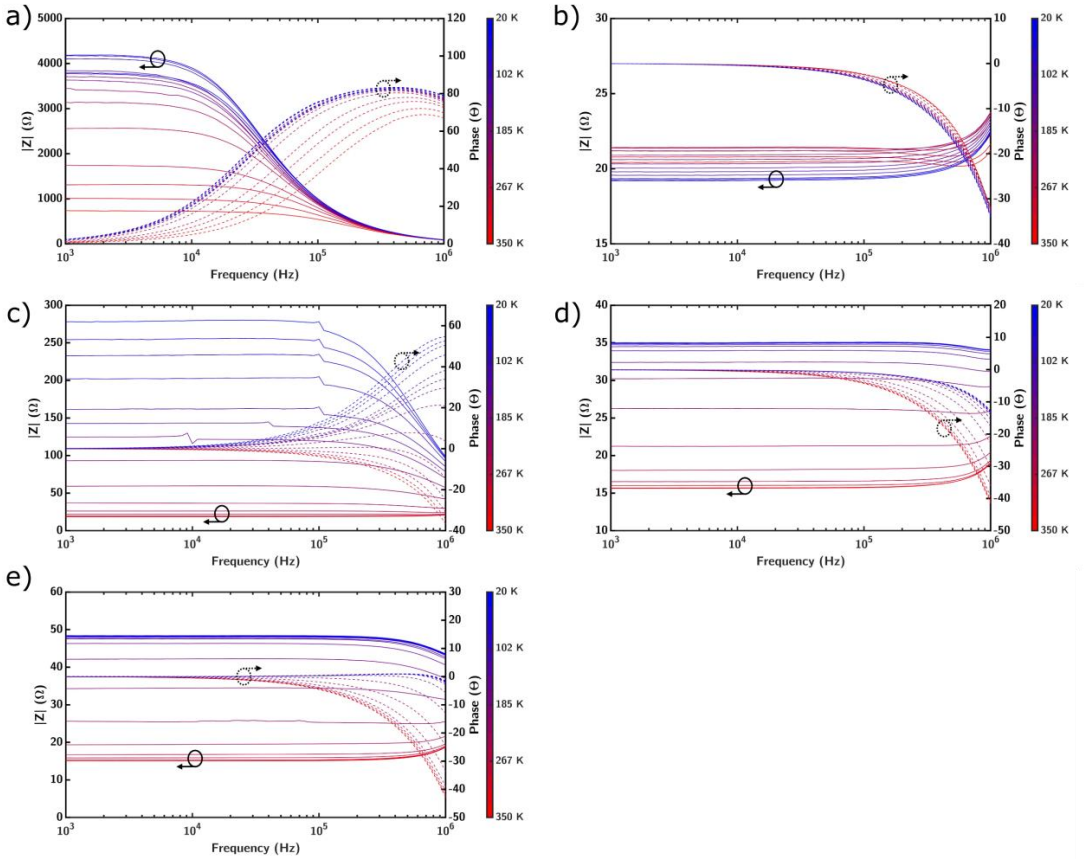

Figure S8. Temperature- (color bar) and frequency (x-axis) dependent impedance |Z| (left y-axis, solid lines) and phase angle (right y-axis, dashed lines) of $Cu(TFSI)_2$ doped Spiro-MeOTAD. Determined from impedance measurements on FTO/$Cu(TFSI)_2$:Spiro-MeOTAD/Au devices inside a He cryostat from 350 K to 20 K with a) 0 mol%, b) 1.5 mol%, c) 3 mol%, d) 5 mol% and e) 10 mol% $Cu(TFSI)_2$. The electrical field was kept constant at F = 100 kV cm^{-1}.

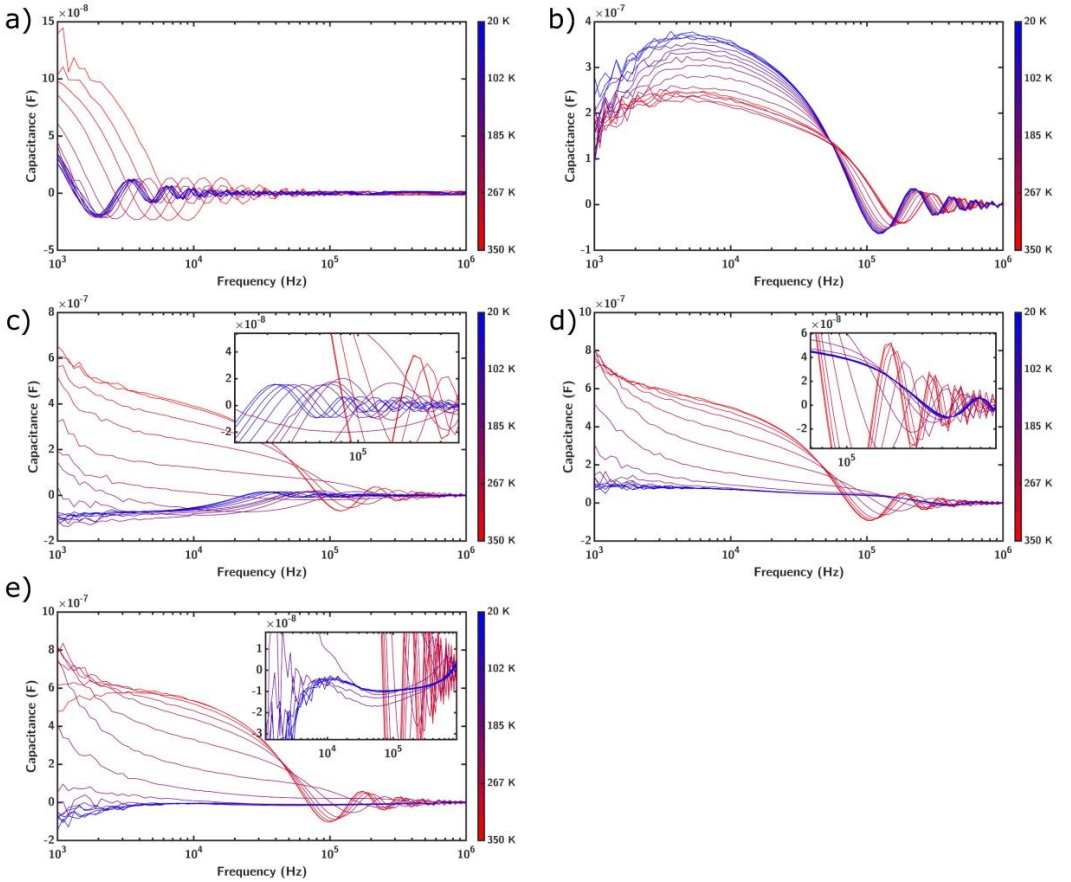

Figure S9. Temperature- (color bar) and frequency (x-axis) dependent capacitance *C* of Spiro-MeOTAD doped with a) 0 mol%, b) 1.5 mol%, d) 3 mol%, e) 5 mol% and f) 10 mol% $Cu(TFSI)_2$. *C* was calculated according to Equation S6 or Equation S7 from the impedance data shown in Figure S7. Determined from impedance measurements on FTO/$Cu(TFSI)_2$:Spiro-MeOTAD/Au devices inside a He cryostat from 350 K to 20 K. For 3 mol%, 5 mol% and 10 mol%, insets are given for better visualization of the low-temperature *C*(f) behaviour (axis units identical main plot). The electrical field was kept constant at $F = 100$ kV cm^{-1}.

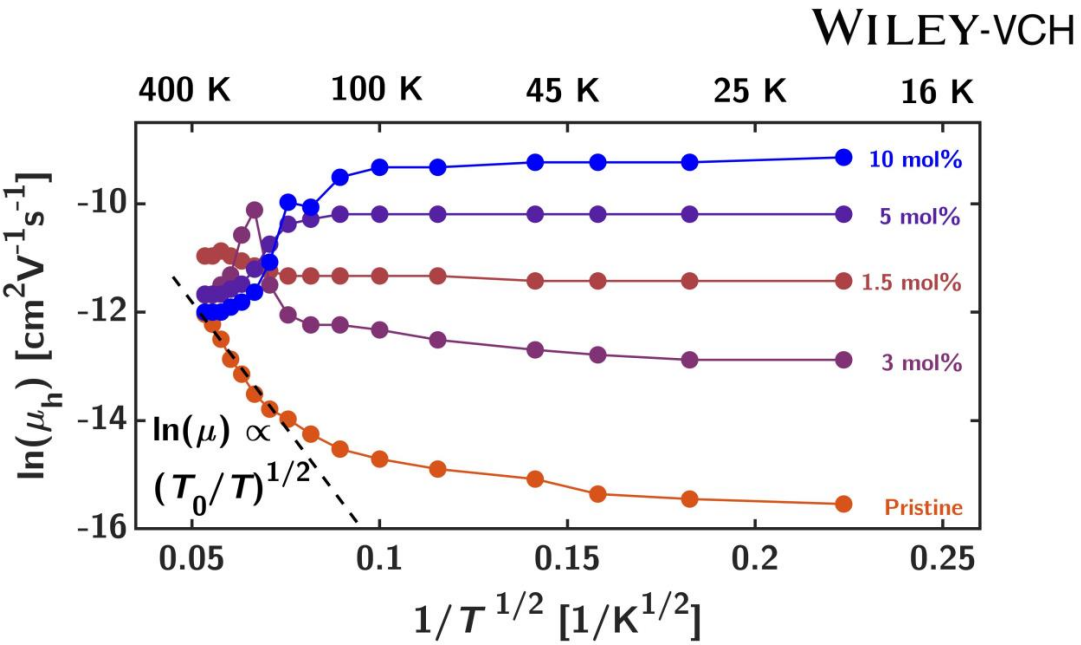

Figure S10. Temperature dependent hole mobilities μ_h of $Cu(TFSI)_2$ doped Spiro-MeOTAD, determined from impedance measurements on FTO/$Cu(TFSI)_2$:Spiro-MeOTAD/Au devices using the negative differential susceptance $-\Delta B$. Black dashed fit line shows typical ES-VRH behaviour $\ln(\mu_h) \propto (T_0/T)^{1/2}$ in the case of pristine Spiro-MeOTAD sample. All values were obtained at a constant electrical field F = 100 kV cm^{-1}.

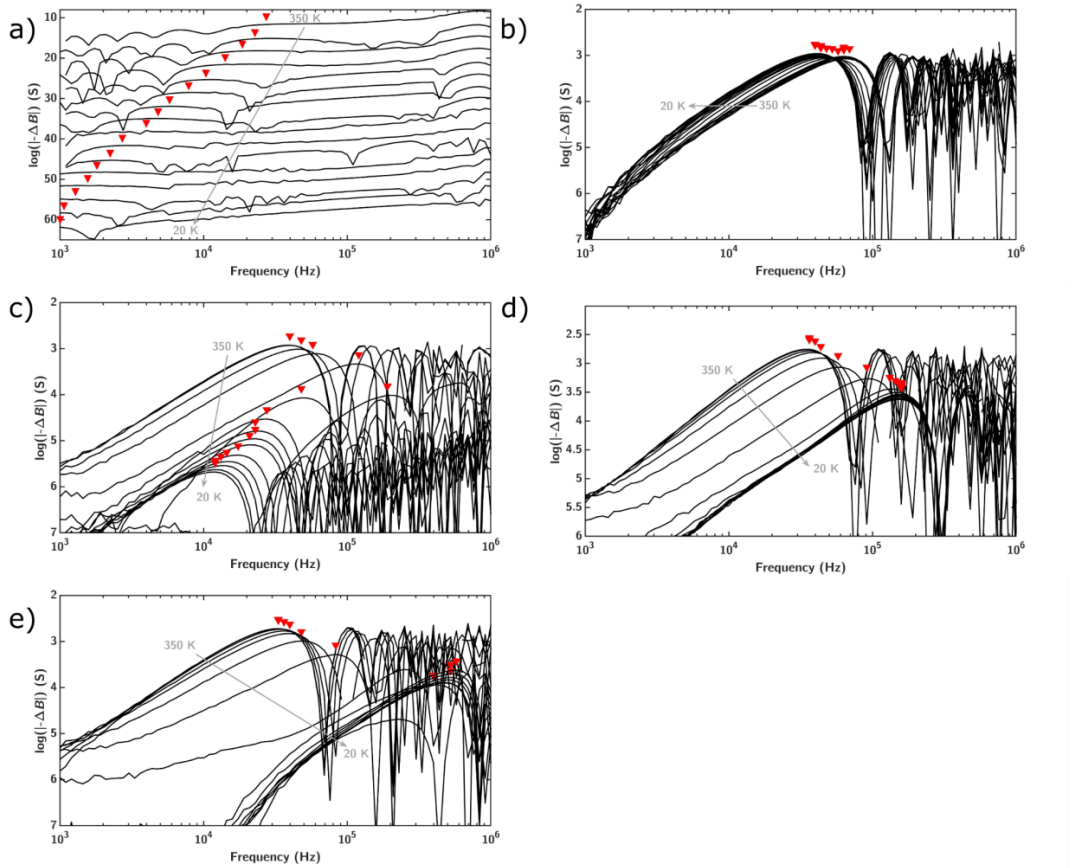

Figure S11. Temperature dependent logarithmic negative differential susceptance log(-Δ*B*) of $Cu(TFSI)_2$ doped Spiro-MeOTAD, determined from impedance measurements on FTO/$Cu(TFSI)_2$:Spiro-MeOTAD/Au devices inside a He cryostat from 350 K to 20 K. From the peak transition frequencies marked with red triangles, the temperature dependent hole mobility μ_h can be obtained, depicted in Figure 3b. Following $Cu(TFSI)_2$ concentrations were measured: a) 0 mol%, b) 1.5 mol%, c) 3 mol%, d) 5 mol%, e) 10 mol%. The electrical field was kept constant at F = 100 kV cm^{-1}.

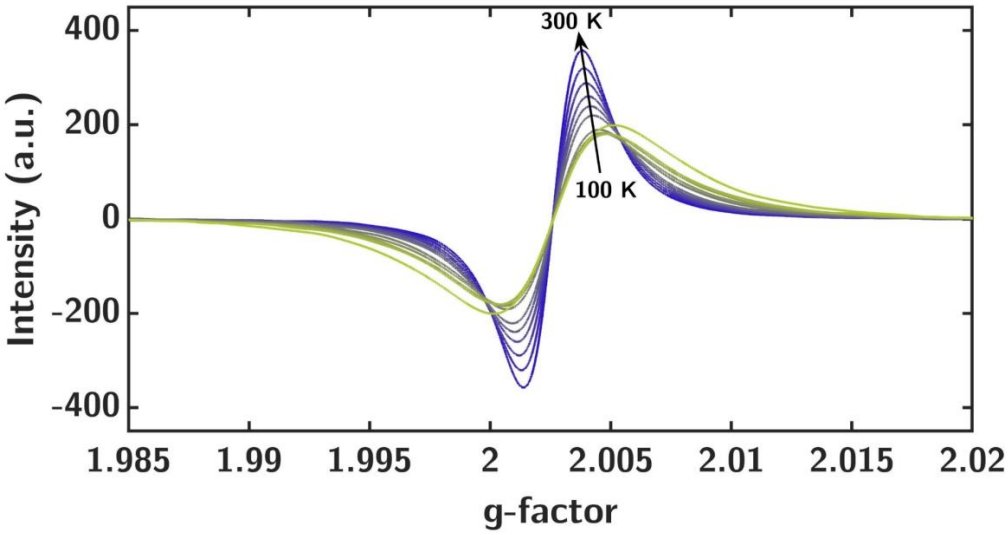

Figure S12. Temperature dependent EPR spectrum of Spiro-MeOTAD co-evaporated with 7.5 mol% $Cu(TFSI)_2$ going from 100 K (starting temperature) to 300 K.

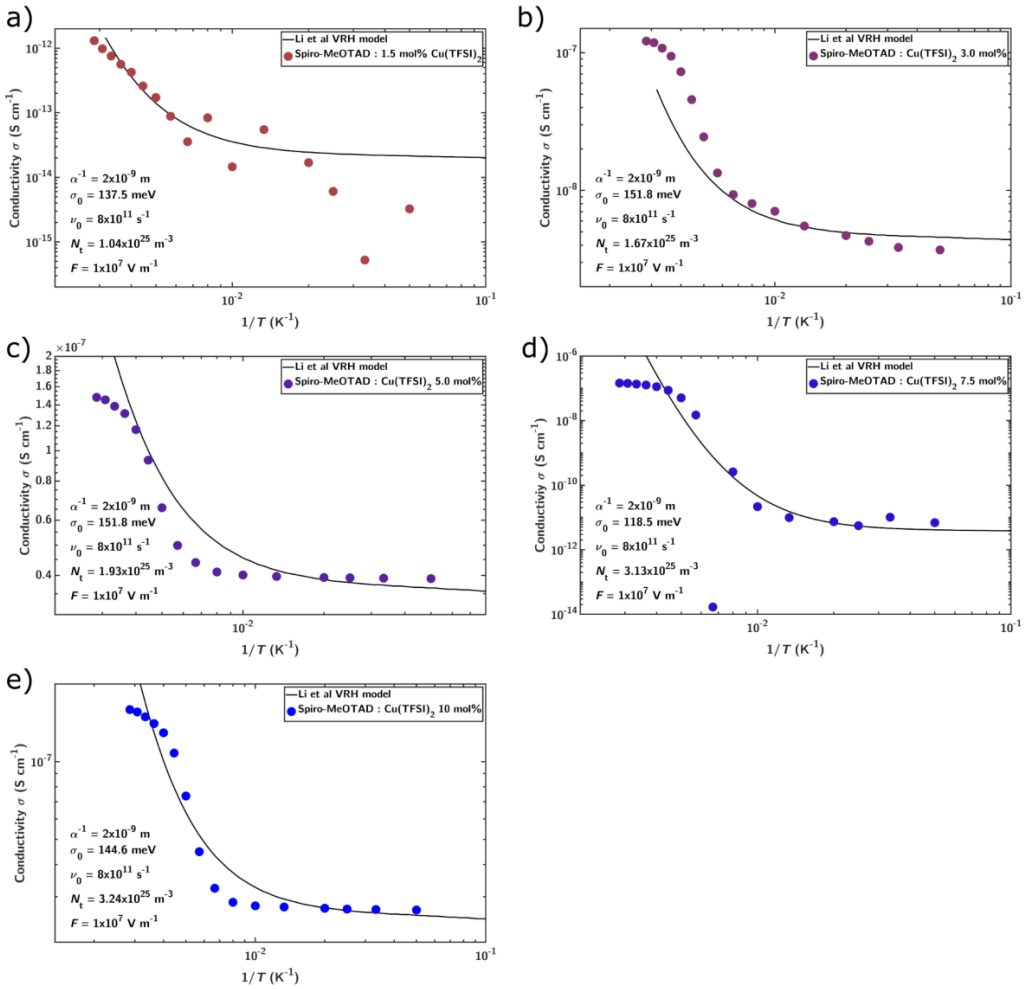

Figure S13. Temperature dependent conductivities (circles) of a) 1.5 mol%, b) 3.0 mol%, c) 5.0 mol%, d) 7.5 mol%, e) 10 mol% $Cu(TFSI)_2$ doped, co-evaporated FTO/Cu(TFSI)2:Spiro-MeOTAD/Au devices (data taken from Figure 3a). A variable range hopping model modified by Li et al. for high carrier densities and electrical fields was fitted (solid lines) with the parameters shown in each plot as a calculation input[5]. Here, α^{-1} is the inverse localized length, σ_0 the Gaussian DOS width, υ_0 the attempt-to-jump frequency, N_t the charge carrier density and F the electrical field (assuming 100 nm active layer thickness).

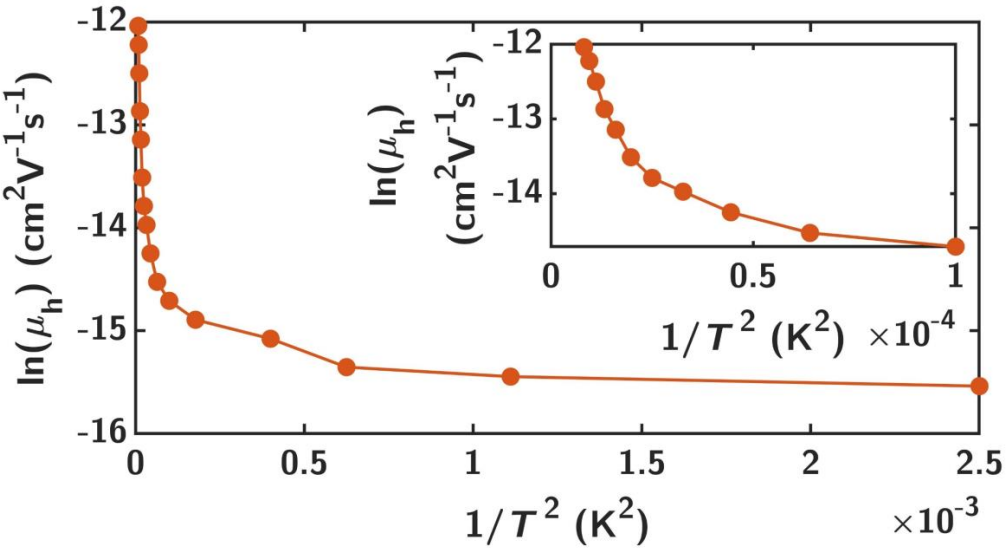

Figure S14. Logarithmic hole mobility μ_h of pristine evaporated Spiro-MeOTAD versus the inverse square root of the temperature (data taken from Figure 3b). The inset shops a detailed plot of μ_h between 350 K and 100 K.

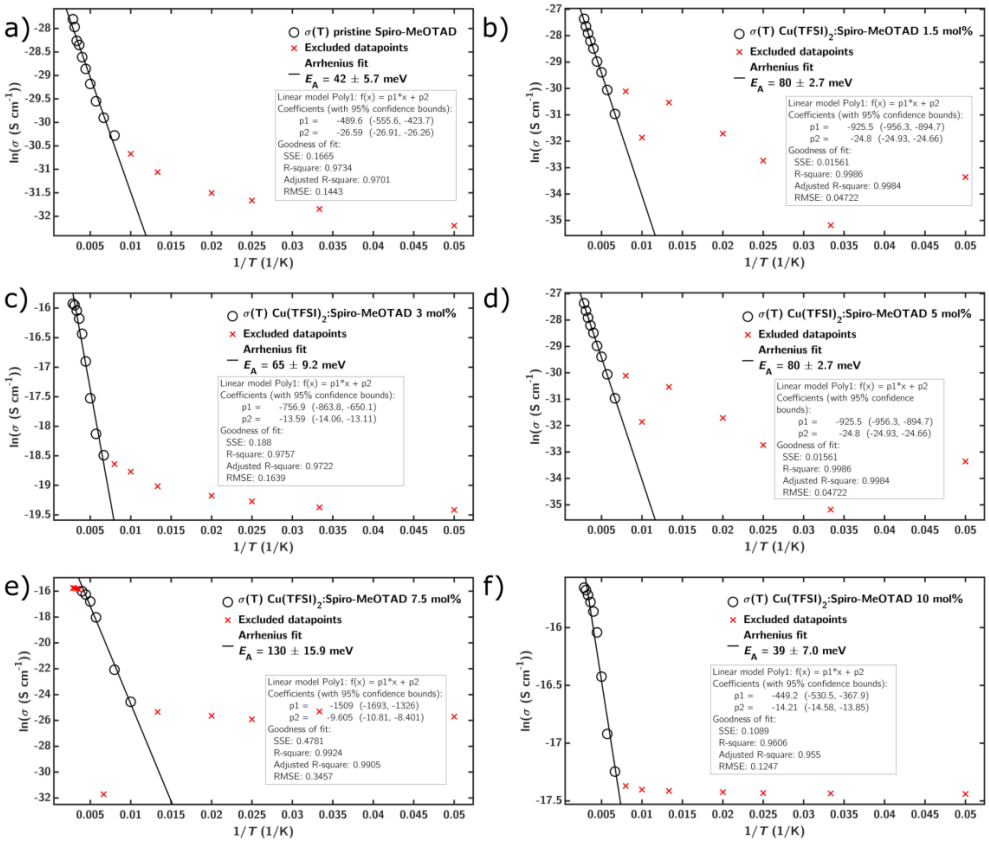

Figure S15. Temperature dependent conductivities (circles) of a) 0 mol% b) 1.5 mol%, c) 3.0 mol%, d) 5.0 mol%, e) 7.5 mol%, f) 10 mol% Cu(TFSI)$_2$ doped, co-evaporated FTO/Cu(TFSI)2:Spiro-MeOTAD/Au devices (100 nm active layer thickness; data taken from Figure 3a). Excluded datapoints below non-linearity shown in red crosses. Solid lines represent the linear Arrhenius fit to yield the thermal activation energy of conductivity $E_{A,\sigma}$ for the temperature range 400 K to 350 K summarized in Figure S16.

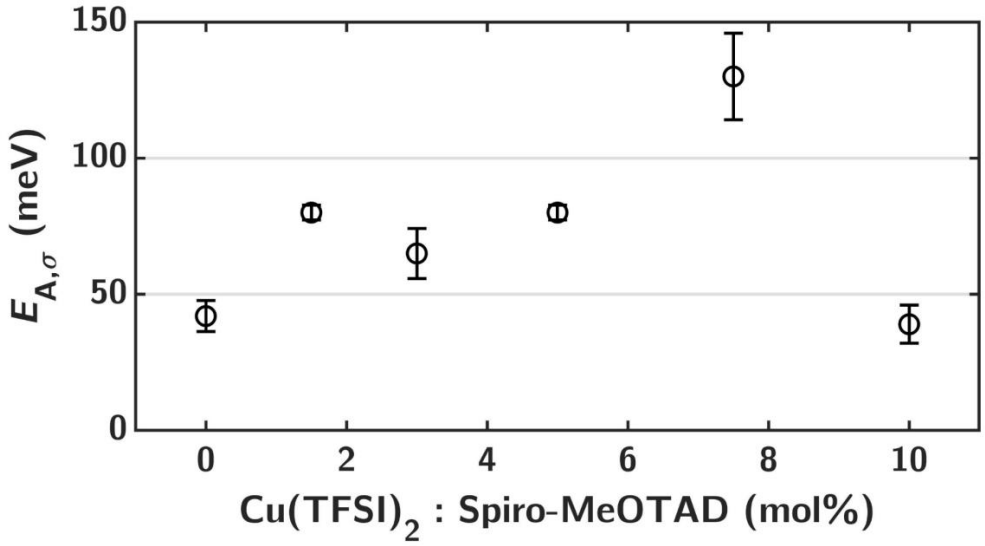

Figure S16. Thermal activation energy of conductivity $E_{A,\sigma}$ of 0 - 10 mol% $Cu(TFSI)_2$ doped, co-evaporated Spiro-MeOTAD thin films (100 nm).

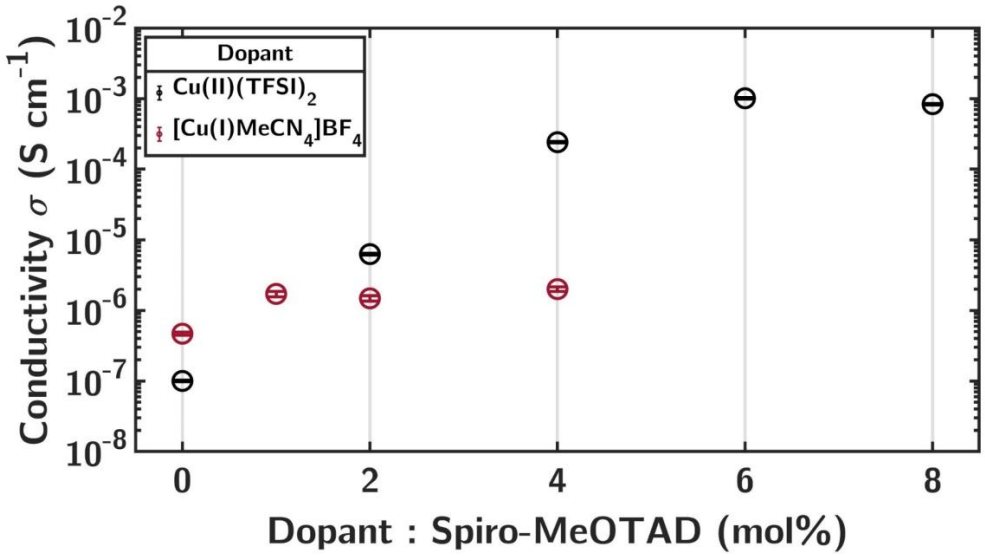

Figure S17. Thin film conductivities of $Cu(TFSI)_2$ doped, co-evaporated Spiro-MeOTAD (black circles) and a solution processed $[Cu(MeCN)_4]BF_4$:Spiro-MeOTAD mixture (red circles) at different doping/additive concentrations (black circles).

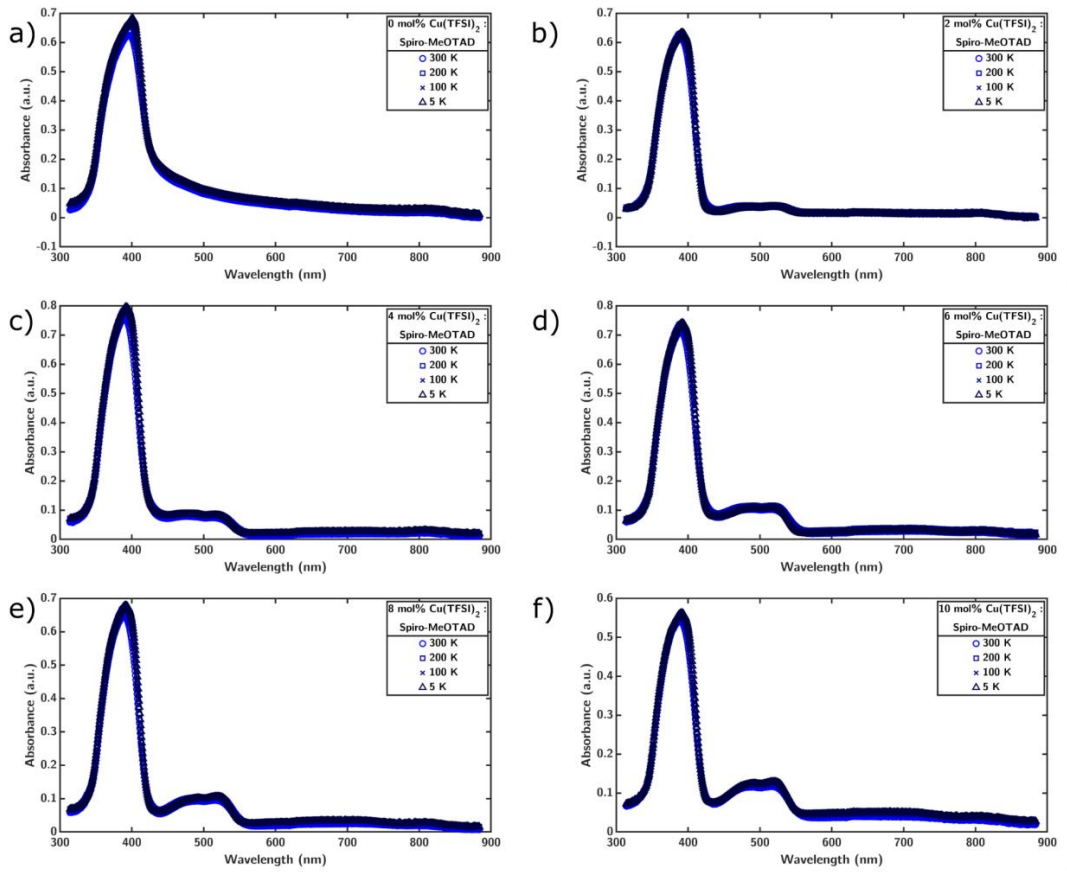

Figure S18. Temperature dependent thin film absorption measurements of co-evaporated Spiro-MeOTAD:$Cu(TFSI)_2$ samples at various doping ratios ranging from 0 mol% a) to 10 mol% f). Measured at 300 K (blue circles), 200 K (blue boxes), 100 K (black crosses) and 5 K (black triangles).

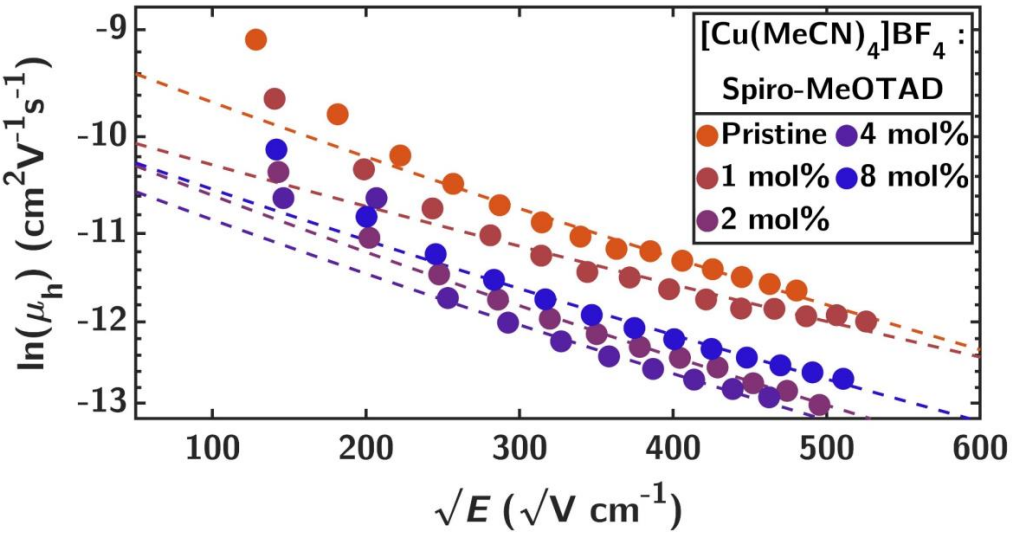

Figure S19. Field dependent mobility of solution processed Spiro-MeOTAD thin films mixed with different molar amounts of $[Cu(MeCN)_4]BF_4$. Linear fits yield the zero-field mobility μ_0 at the y-intercept. All μ_h values measured using the -Δ*B* method on FTO/$[Cu(MeCN)_4]BF_4$:Spiro-MeOTAD/Au devices.

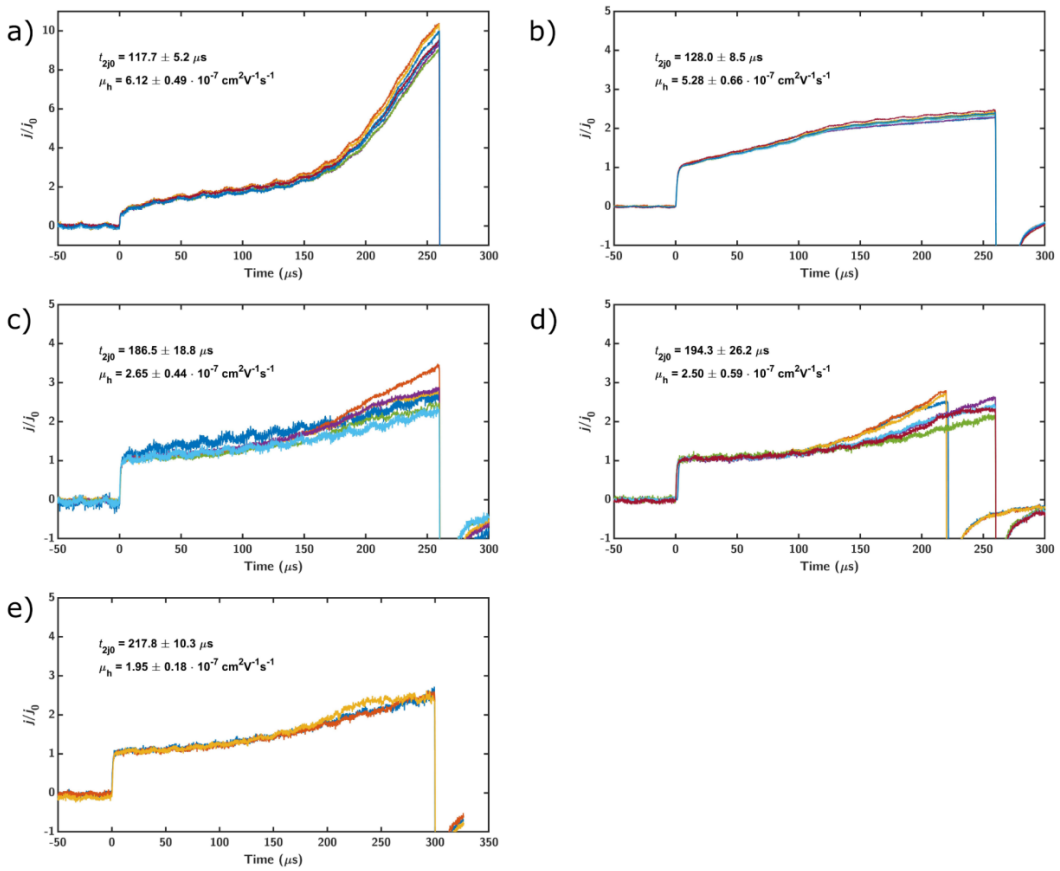

Figure S20. CELIV measurements on FTO/Al_2O_3 (25 nm) /Spiro-MeOTAD:$Cu(TFSI)_2$ (200 nm)/Au devices. An offset voltage of -3V was applied and the charges were extracted using a ramp of 0.05 V μs^{-1}. a) pristine Spiro-MeOTAD, b) 1.5mol% of $Cu(TFSI)_2$, c) 3.0 mol% of $Cu(TFSI)_2$, d) 5 mol% of $Cu(TFSI)_2$, e) 7.5mol% of $Cu(TFSI)_2$.

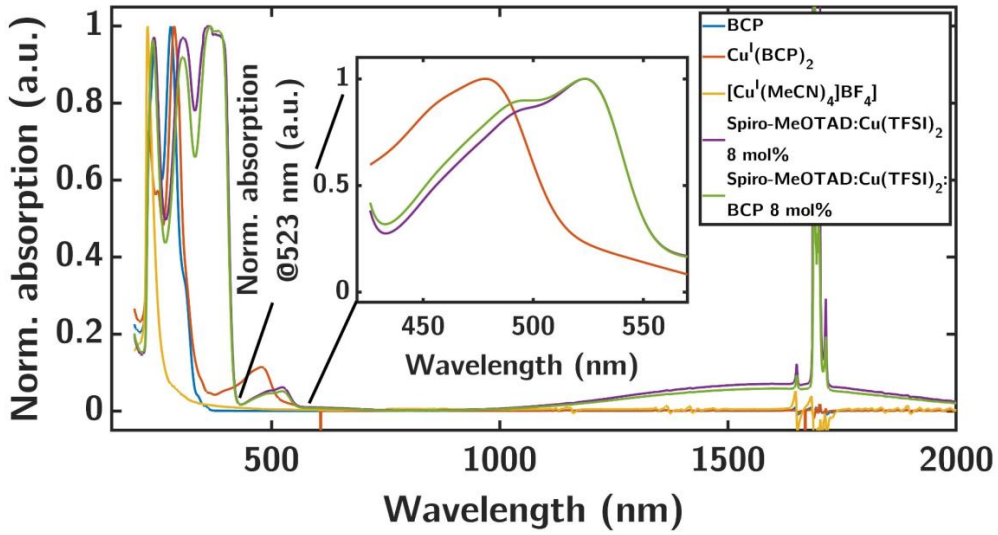

Figure S21. Normalized UV/Vis/NIR solution spectra of BCP (blue), $Cu^{I}(BCP)_2$ (red), $[Cu^{I}(MeCN)_4]BF_4$ (yellow), Spiro-MeOTAD:$Cu(TFSI)_2$ 8 mol% (purple) and Spiro-MeOTAD:$Cu(TFSI)_2$:BCP 8 mol% (green, 1:1 molar ratio $Cu(TFSI)_2$:BCP) in DCM (0.02 mg mL^{-1} of BCP, $Cu^{I}(BCP)_2$ and Spiro-MeOTAD). The inset shows the region of the oxidized Spiro-MeOTAD HOMO/HOMO-1/LUMO/LUMO-1 transition peak at 523 nm, normalized to this peak absorption. The formation of $Cu^{I}(BCP)_2$ complex (red) increases the absorption at 478 nm for the solution with BCP (green) compared to the solution without BCP (purple). All spectra measured under inert atmosphere and in anhydrous solvents.

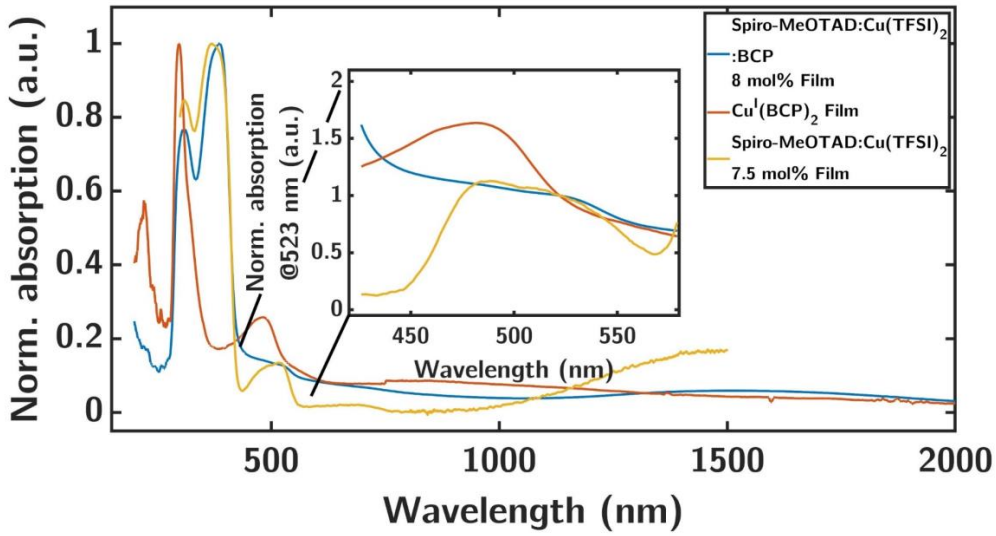

Figure S22. Normalized UV/Vis/NIR thin film spectra on quartz substrates of solution processed $Cu^{I}(BCP)_2$ (red), co-evaporated Spiro-MeOTAD:$Cu(TFSI)_2$ 7.5 mol% (yellow) and solution processed Spiro-MeOTAD:$Cu(TFSI)_2$:BCP 8 mol% (blue, 1:1 molar ratio $Cu(TFSI)_2$:BCP). The inset shows the region of the oxidized Spiro-MeOTAD HOMO/HOMO-1/LUMO/LUMO-1 transition peak at 523 nm, normalized to this peak absorption. The formation of $Cu^{I}(BCP)_2$ complex (red) increases the absorption below 478 nm for the film with BCP (blue) compared to the solution without BCP (yellow). All spectra measured under inert atmosphere.

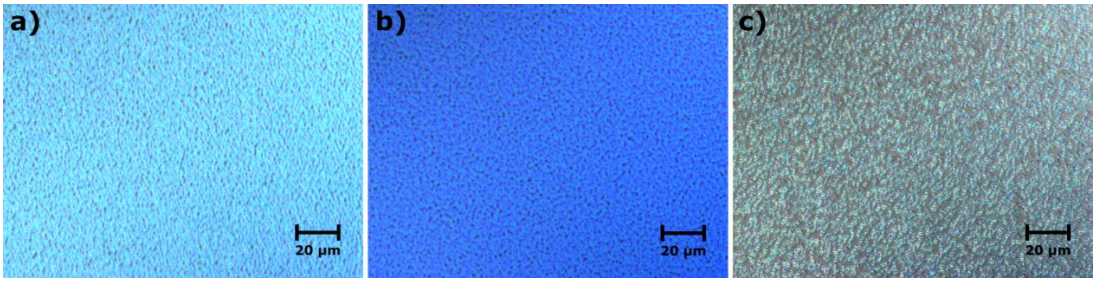

Figure S23. Unpolarized light microscopic images with a magnification of 50x showing the morphology of solution processed films of a) $Cu(TFSI)_2$(8 mol%):Spiro-MeOTAD, b) $Cu(TFSI)_2$(8 mol%):BCP(8 mol%):Spiro-MeOTAD, c) $[Cu(MeCN)_4]BF_4$(8 mol%):Spiro-MeOTAD. Scale bar: 20 µm.

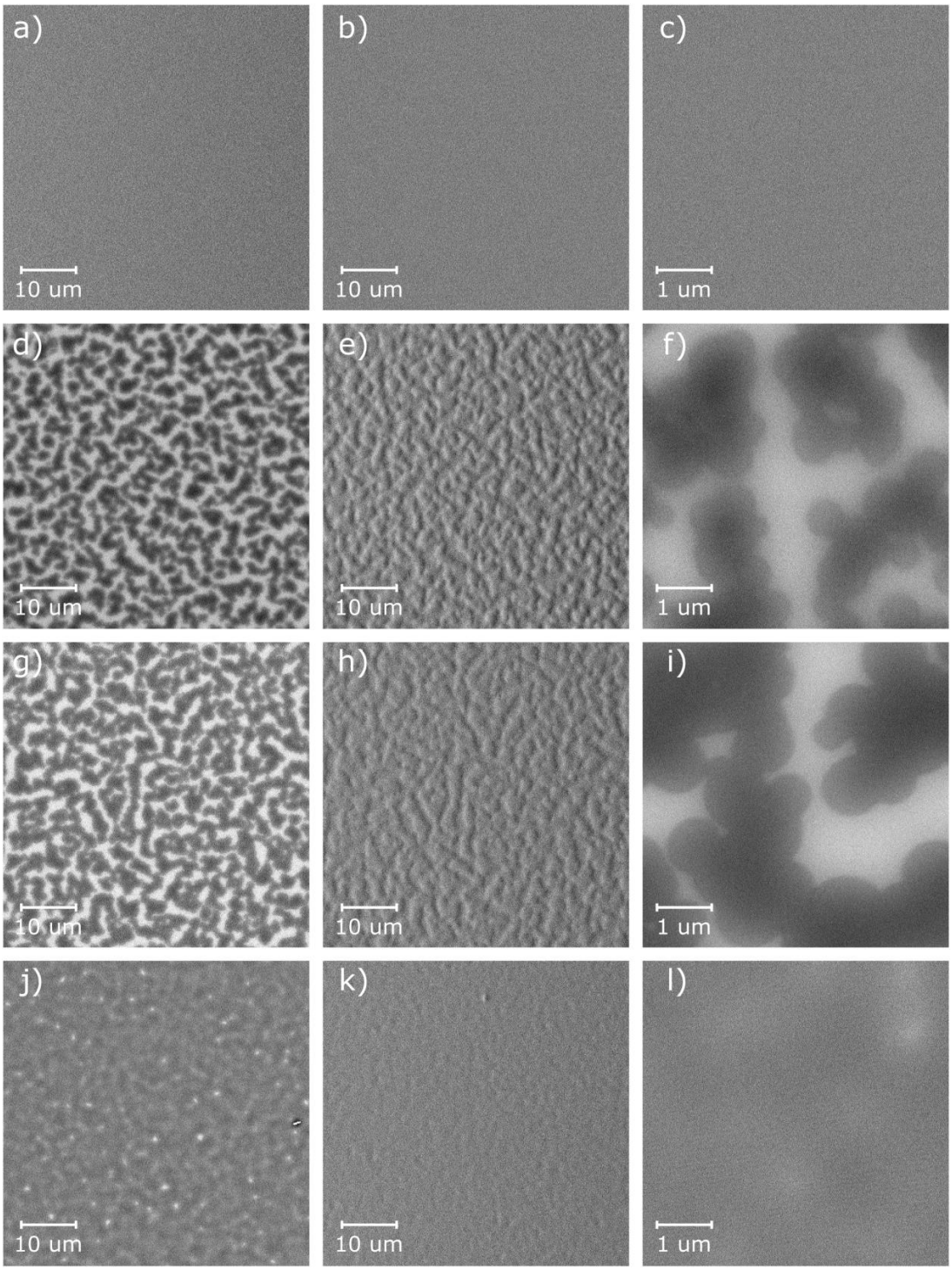

Figure S24. SEM micrographs of pristine Spiro-MeOTAD a)-c), $[Cu(MeCN)_4]BF_4$(8 mol%):Spiro-MeOTAD d)-f), $Cu(TFSI)_2$(8 mol%):Spiro-MeOTAD g)-i) and $Cu(TFSI)_2$(8 mol%):BCP(8 mol%):Spiro-MeOTAD j)-l) thin films (ca. 100 nm) on silicon substrates at two different magnifications. b), e), h) and k) were recorded using the topographic detector mode.

Figure S25. Microscopic images of $[Spiro\text{-}MeOTAD]^+[Cu^I(TFSI)_2]^-$ crystals before the hexane washing step. Lines in the background are 2 mm by 1 mm.

Doping Efficiency Calculation

The doping efficiency η_{Dop} was calculated from the amount of ionized Cu^{I} dopant molecules N_A^- obtained from Mott-Schottky measurements, and the total number of dopants N_A per unit volume. From the mole fraction of the dopant $x_{Cu(TFSI)2}$ and molar masses of Spiro-MeOTAD M_{Spiro} and $Cu(TFSI)_2$ $M_{\mathrm{Cu(TFSI)2}}$, the average molar mass $\bar{M}$ of the mixture at a given doping concentration can be determined:

$$x_{Cu(TFSI)2} = \frac{C_{Dop}}{100} \tag{S12}$$

$$\bar{M} = x_{Cu(TFSI)2} M_{Cu(TFSI)2} + \left(1 - x_{Cu(TFSI)2}\right) M_{Spiro} \tag{S13}$$

Which in turn gives the mass fraction $w_{\mathrm{Cu(TFSI)2}}$ of the dopant:

$$w_{Cu(TFSI)2} = x_{Cu(TFSI)2} \frac{M_{Cu(TFSI)2}}{\bar{M}} \tag{S14}$$

From $w_{\mathrm{Cu(TFSI)2}}$, the average density ρ_{mix} of the solid mixture is calculated. For Spiro-MeOTAD and $Cu(TFSI)_2$, densities of ρ_{Spiro} = (1.159 ± 0.003) g cm^{-3} and $\rho_{Cu(TFSI)2}$ = (2.925 ± 0.019) g cm^{-3} were determined experimentally.

$$\rho_{mix} = \frac{1}{\frac{w_{Cu(TFSI)2}}{\rho_{Cu(TFSI)2}} + \frac{1 - w_{Cu(TFSI)2}}{\rho_{Spiro}}} \tag{S15}$$

Using ρ_{mix}, $\bar{M}$ and the Avogadro constant N_{Avogadro}, the absolute number of molecules per unit volume N_0 (Dopant and Spiro-MeOTAD) for a given doping concentration can be found:

$$N_0 = \frac{N_{Avogadro} \rho_{mix}}{\bar{M}} \tag{S16}$$

For a certain doping concentration C_{Dop} and volume, the number of dopant molecules/acceptors N_{A} present is:

$$N_A = \frac{C_{Dop}}{100} N_0 \tag{S17}$$

Which can be used to determine the percentage of ionized acceptors η_{Dop} from the density of ionized acceptors N_{A}^- determined by Mott-Schottky experiments:

$$\eta_{Dop} = 100 \frac{N_A^-}{N_A} \tag{S18}$$

The error of η_{Dop} may be determined by propagation of uncertainty, considering the main error sources ρ_{Spiro}, $\rho_{Cu(TFSI)2}$ and N_{A}^- as not correlated.

4. References

[1] G. Krauss, A. Hochgesang, J. Mohanraj, M. Thelakkat, *Macromol. Rapid Commun.* **2021**, *42*, 2100443.

[2] J. Mohanraj, M. Stihl, E. Simon, S. von Sicard, G. Schmidt, M. Fleischer, C. Neuber, M. Thelakkat, *ACS Appl. Energy Mater.* **2019**, *2*, 3469-3478.

[3] S. Ishihara, T. Okachi, H. Naito, *Thin Solid Films* **2009**, *518*, 452-456.

[4] N. D. Nguyen, M. Schmeits, *Phys. Rev. B* **2007**, *75*, 075307.

[5] H. C. F. Martens, H. B. Brom, P. W. M. Blom, *Phys. Rev. B* **1999**, *60*, R8489.

[6] T. Okachi, T. Nagase, T. Kobayashi, H. Naito, *Thin Solid Films* **2008**, *517*, 1331.

[7] T. Okachi, T. Nagase, T. Kobayashi, H. Naito, *Jpn. J. Appl. Phys.* **2008**, *47*, 8965.

[8] B. Li, S. Zhang, F. Xia, Y. Huang, X. Ran, Y. Xia, Y. Chen, W. Huang, *J. Appl. Phys.* **2020**, *128*, 085501.

[9] H. C. F. Martens, W. F. Pasveer, H. B. Brom, J. N. Huiberts, P. W. M. Blom, *Phys. Rev. B* **2001**, *63*, 125328.

[10] E. J. Meijer, A. V. G. Mangnus, C. M. Hart, D. M. de Leeuw, T. M. Klapwijk, *Appl. Phys. Lett*. **2001**, *78*, 3902-3904.

[4] O. J. Sandberg, M. Nyman, S. Dahlström, S. Sandén, B. Törngren, J.-H. Smått, R. Österbacka, *Appl. Phys. Lett.* **2017**, *110*, 153504.

[5] L. Li, N. Lu, M. Liu, *J. Appl. Phys.* **2014**, *116*, 164504.

15 Conclusion and Outlook

This thesis and the conducted studies within it show how the optoelectronic properties of lead halide perovskite layers and charge extraction layers used in lead halide perovskite-based optoelectronic devices are affected by the processing and the resulting nanostructure of the corresponding layers. The projects focusing on perovskites (chapters 9-13) show how sensitive the properties of the obtained perovskite layers are correlated with the processing and the final nanostructure, independent of whether the films are wet-processed from solution or dry-processed from powders. In the last project (chapter 14), the mechanism for an alternative, stable and solvent-free doping approach of organic semiconductors, which are commonly used as charge transport layer in perovskite-based optoelectronic devices, was investigated.

In more detail, my first in-situ study in chapter 9 during spin coating revealed that mixing small amounts of additive, in this case a passivating agent, into the precursor solution changes the crystallization behavior of the forming perovskite film. This was observed for the simpler one-step spin coating method as well as for the state-of-the-art solvent engineering method. I found that the precusor states were evolving slightly differently depending on the amount of passivating agent in the precursor solution. In addition, the final structural as well as optoelectronic film properties were also affected as a consequence of the present passivating agent. These findings suggest that it could be necessary to revise established and optimized spin coating recipes when additives such as passivating agents or surfactants are added to the perovskite precursor solution.
The second study (chapter 10) I conducted using our in-situ spectroscopy setup was inspired by these findings. Since I understood that small changes in processing conditions, such as an additive or a variation of the atmosphere, can consequently influence the film formation and the resulting final film properties, the fundamental idea of my second project was to induce the perovskite crystallization based on real-time feedback from film properties obtained via optical spectroscopy. I could show that inducing the perovskite crystallization based on a system-internal parameter (e.g. the solvent layer thickness), rather than an external (e.g. time) parameter, results in a reproducible film quality independent of a variation of the processing environment.
These two studies show that the film formation and perovskite synthesis are inseparably linked and thus many parameters need to be considered when small changes in processing protocol are intentionally (e.g. composition) or unintentionally (e.g. atmospheric environment) varied. In addition, the presented works underpin that in-situ methods are an important tool to gain fundamental insights into the sensitive perovskite film formation processes and thus can help to reduce the trial and error optimization experiments. With this knowledge of the fundamental processes, in-situ methods could be implemented

into production lines for real-time quality control and, if necessary, to finetune the fabrication steps depending on the observed change in film properties.

A way to overcome the need for solvent and the sensitive interconnection between material synthesis and film formation altogether is the use of readily synthesized perovskite powders. The perovskite powders can be deposited as a thin film via powder aerosol deposition (PAD) as investigated in chapters 11 and 12. This way, the film formation is decoupled from the synthesis step. In the study presented in chapter 11, we could, for the first time, produce perovskite films via PAD and a subsequent hot-pressing step with a thickness suitable for solar cell application. I succeeded to build and characterize functioning solar cells with perovskite PAD absorber layers. Unfortunately, the device efficiencies lacked behind those of their solution-processed counterparts. However, via an in-depth study of the different layers of the solar cells stack, we could identify limitations of the current processing, such as the detrimental effect of the PAD process on the ETL properties, and discussed potential steps to overcome these limitations in the future. The (hot-)pressing step of the PAD perovskite films and how this pressure and temperature treatment affects the nanostructure and thus the optoelectronic properties was further investigated in the study in chapter 12. Similar to the solar cell study, it could be observed that pressing at elevated temperatures increases grain size and orientation, and also reduces the strain and defect density within the layer compared to pressure treatment at room temperature.
By simple pressing of perovskite powders, thick films, e.g. in form of pellets, can also be produced. In chapter 13 the influence of different spacer molecules on the crystal structure and thus the corresponding optical properties of low dimensional perovskite thick films was investigated. A variation of spacer molecule in between the perovskite sheets had a strong impact on the resulting crystal structure and consequently on the degree of corrugation of the perovskite sheets. I identified that depending on the degree of corrugation, a systematic change in the optical properties, such as absorption and emission, of the low dimensional perovskites can be observed. These findings provide important guidelines for the spacer molecule design and the resulting crystal structures in order to tailor the optoelectronic properties of novel low dimensional perovskites.
Overall, as the dry powder-based processing decouples material synthesis and film formation, this approach can be a viable and good alternative to the established wet-processing from solution, once the process (PAD and pressing) is optimized so that the performance of the resulting devices is on par with the solution processed ones'.

In the last work within this thesis, chapter 14, the doping mechanism of Spiro-MeOTAD, a commonly used charge transport material, with $Cu(TFSI)_2$ via co-evaporation was investigated. The evaporation approach provides an interesting opportunity to further reduce the need for solvents in the fabrication of solar cells. The additional advantages of this evaporation approach are that the film processing can be easily controlled, and the dopant within the resulting transport layer is homogeneously distributed and does not require air-oxidation compared to the typically used doping approach of solution-processed Spiro-MeOTAD layers. We could identify a three step doping mechanism where first temperature-independently a dopant-Spiro-MeOTAD complex is formed. Upon temperature activation, this charge transfer complex can consequently dissociate, and finally a transport of these free charges is enabled.

This doping process occurs with a remarkable doping efficiency of over 50%. In the larger picture, the investigated co-evaporation process can, especially in combination with the dry PAD process, thus further reduce the need for large quantities of solvents while the controllability of the HTL formation and its doping efficiency increased. In addition, understanding the doping mechanism and the key processes will help to foster the development of stable doping strategies for HTL, and thus more stable devices in the future.

In summary, the findings within this work on the impact of processing and nanostructure on solution- or dry-processed perovskite and hole transport layer will be beneficial for (1) the improvement for the established wet perovskite processing and (2) the development of novel dry perovskite processing and HTL doping approaches in order to further increase perovskite based optoelectronic device performance.

16 References

[1] A. Kojima, K. Teshima, Y. Shirai, and T. Miyasaka (2009). Organometal Halide Perovskites as Visible-Light Sensitizers for Photovoltaic Cells. *Journal of the American Chemical Society* **131** (17), 6050–6051. DOI: 10.1021/ja809598r.

[2] G. Grancini et al. (2017). One-Year stable perovskite solar cells by 2D/3D interface engineering. *Nature Communications* **8** (1), 15684. DOI: 10.1038/ncomms15684.

[3] H. Li et al. (2022). Sequential vacuum-evaporated perovskite solar cells with more than 24% efficiency. *Science Advances* **8** (28), eabo7422. DOI: 10.1126/sciadv.abo7422.

[4] D.-Y. Son et al. (2018). Universal Approach toward Hysteresis-Free Perovskite Solar Cell via Defect Engineering. *Journal of the American Chemical Society* **140** (4), 1358–1364. DOI: 10.1021/jacs.7b10430.

[5] H.-S. Kim et al. (2012). Lead Iodide Perovskite Sensitized All-Solid-State Submicron Thin Film Mesoscopic Solar Cell with Efficiency Exceeding 9%. *Scientific Reports* **2** (1), 591. DOI: 10.1038/srep00591.

[6] NREL. *Best Research-Cell Efficiency Chart*. (2023). URL: https://www.nrel.gov/pv/cell-efficiency.html (visited on 01/24/2024).

[7] H. Min et al. (2021). Perovskite solar cells with atomically coherent interlayers on SnO2 electrodes. *Nature* **598** (7881), 444–450. DOI: 10.1038/s41586-021-03964-8.

[8] M. Karlsson et al. (2021). Mixed halide perovskites for spectrally stable and high-efficiency blue light-emitting diodes. *Nature Communications* **12** (1), 361. DOI: 10.1038/s41467-020-20582-6.

[9] Z.-K. Tan et al. (2014). Bright light-emitting diodes based on organometal halide perovskite. *Nature Nanotechnology* **9** (9), 687–692. DOI: 10.1038/nnano.2014.149.

[10] D. Yang et al. (2022). Toward Stable and Efficient Perovskite Light-Emitting Diodes. *Advanced Functional Materials* **32** (9), 2109495. DOI: 10.1002/adfm.202109495.

[11] B. Zhao et al. (2018). High-efficiency perovskite–polymer bulk heterostructure light-emitting diodes. *Nature Photonics* **12** (12), 783–789. DOI: 10.1038/s41566-018-0283-4.

[12] L. N. Quan, F. P. García de Arquer, R. P. Sabatini, and E. H. Sargent (2018). Perovskites for Light Emission. *Advanced Materials* **30** (45), 1801996. DOI: 10.1002/adma.201801996.

[13] K. Lin et al. (2018). Perovskite light-emitting diodes with external quantum efficiency exceeding 20 per cent. *Nature* **562** (7726), 245–248. DOI: 10.1038/s41586-018-0575-3.

[14] M.-H. Park et al. (2019). Efficient Perovskite Light-Emitting Diodes Using Polycrystalline Core–Shell-Mimicked Nanograins. *Advanced Functional Materials* **29** (22), 1902017. DOI: 10.1002/adfm.201902017.

[15] W. Xu et al. (2019). Rational molecular passivation for high-performance perovskite light-emitting diodes. *Nature Photonics* **13** (6), 418–424. DOI: 10.1038/s41566-019-0390-x.

[16] Y. Zhou, J. Chen, O. M. Bakr, and O. F. Mohammed (2021). Metal Halide Perovskites for X-ray Imaging Scintillators and Detectors. *ACS Energy Letters* **6** (2), 739–768. DOI: 10.1021/acsenergylett.0c02430.

[17] M. Sytnyk, S. Deumel, S. F. Tedde, G. J. Matt, and W. Heiss (2019). A perspective on the bright future of metal halide perovskites for X-ray detection. *Applied Physics Letters* **115** (19), 190501. DOI: 10.1063/1.5125999.

[18] H. Wei and J. Huang (2019). Halide lead perovskites for ionizing radiation detection. *Nature Communications* **10** (1), 1066. DOI: 10.1038/s41467-019-08981-w.

[19] K. P. Goetz, A. D. Taylor, F. Paulus, and Y. Vaynzof (2020). Shining Light on the Photoluminescence Properties of Metal Halide Perovskites. *Advanced Functional Materials* **30** (23), 1910004. DOI: https://doi.org/10.1002/adfm.201910004.

[20] M. D. Smith, E. J. Crace, A. Jaffe, and H. I. Karunadasa (2018). The Diversity of Layered Halide Perovskites. *Annual Review of Materials Research* **48** (1), 111–136. DOI: 10.1146/annurev-matsci-070317-124406.

[21] M. Roy et al. (2021). Spontaneous Ion Migration via Mechanochemical Ultrasonication in Mixed Halide Perovskite Phase Formation: Experimental and Theoretical Insights. *The Journal of Physical Chemistry Letters* **12** (4), 1189–1194. DOI: 10.1021/acs.jpclett.0c03426.

[22] N. Meftahi et al. (2023). Machine Learning Enhanced High-Throughput Fabrication and Optimization of Quasi-2D Ruddlesden–Popper Perovskite Solar Cells. *Advanced Energy Materials* **13** (38), 2203859. DOI: 10.1002/aenm.202203859.

[23] Y.-M. Xie et al. (2022). Homogeneous Grain Boundary Passivation in Wide-Bandgap Perovskite Films Enables Fabrication of Monolithic Perovskite/Organic Tandem Solar Cells with over 21% Efficiency. *Advanced Functional Materials* **32** (19), 2112126. DOI: 10.1002/adfm.202112126.

[24] J. Han et al. (2021). Genetic Manipulation of M13 Bacteriophage for Enhancing the Efficiency of Virus-Inoculated Perovskite Solar Cells with a Certified Efficiency of 22.3%. *Advanced Energy Materials* **11** (38), 2101221. DOI: 10.1002/aenm.202101221.

[25] M. Wang et al. (2022). Synergetic Co-Modulation of Crystallization and Co-Passivation of Defects for FAPbI3 Perovskite Solar Cells. *Advanced Functional Materials* **32** (6), 2108567. DOI: 10.1002/adfm.202108567.

[26] T. Chiba et al. (2018). Anion-exchange red perovskite quantum dots with ammonium iodine salts for highly efficient light-emitting devices. *Nature Photonics* **12** (11), 681–687. DOI: 10.1038/s41566-018-0260-y.

[27] W. Bai et al. (2023). Perovskite Light-Emitting Diodes with an External Quantum Efficiency Exceeding 30%. *Advanced Materials* **35** (39), 2302283. DOI: 10.1002/adma.202302283.

[28] J. S. Kim et al. (2022). Ultra-bright, efficient and stable perovskite light-emitting diodes. *Nature* **611** (7937), 688–694. DOI: 10.1038/s41586-022-05304-w.

[29] K. P. Goetz and Y. Vaynzof (2022). The Challenge of Making the Same Device Twice in Perovskite Photovoltaics. *ACS Energy Letters* **7** (5), 1750–1757. DOI: 10.1021/acsenergylett.2c00463.

[30] Y. Zou et al. (2023). Unraveling Deposition Atmosphere Impact on Reproducibility of Perovskite Light-Emitting Diodes. *The Journal of Physical Chemistry Letters* **14** (21), 5025–5032. DOI: 10.1021/acs.jpclett.3c01067.

[31] O. Shargaieva et al. (2020). Hybrid perovskite crystallization from binary solvent mixtures: interplay of evaporation rate and binding strength of solvents. *Materials Advances* **1** (9), 3314–3321. DOI: 10.1039/D0MA00815J.

[32] A. D. Taylor et al. (2021). A general approach to high-efficiency perovskite solar cells by any antisolvent. *Nature Communications* **12** (1), 1878. DOI: 10.1038/s41467-021-22049-8.

[33] K. Wang et al. (2019). Kinetic Stabilization of the Sol–Gel State in Perovskites Enables Facile Processing of High-Efficiency Solar Cells. *Advanced Materials* **31** (32), 1808357. DOI: 10.1002/adma.201808357.

[34] Q. An et al. (2021). Effect of Antisolvent Application Rate on Film Formation and Photovoltaic Performance of Methylammonium-Free Perovskite Solar Cells. *Advanced Energy and Sustainability Research* **2** (11), 2100061. DOI: 10.1002/aesr.202100061.

[35] T.-B. Song et al. (2020). Dynamics of Antisolvent Processed Hybrid Metal Halide Perovskites Studied by In Situ Photoluminescence and Its Influence on Optoelectronic Properties. *ACS Applied Energy Materials* **3** (3), 2386–2393. DOI: 10.1021/acsaem.9b02052.

[36] R. Munir et al. (2017). Hybrid Perovskite Thin-Film Photovoltaics: In Situ Diagnostics and Importance of the Precursor Solvate Phases. *Advanced Materials* **29** (2), 1604113. DOI: 10.1002/adma.201604113.

[37] M. Qin, P. F. Chan, and X. Lu (2021). A Systematic Review of Metal Halide Perovskite Crystallization and Film Formation Mechanism Unveiled by In Situ GIWAXS. *Advanced Materials* **33** (51), 2105290. DOI: 10.1002/adma.202105290.

[38] S. Pratap et al. (2021). Out-of-equilibrium processes in crystallization of organic-inorganic perovskites during spin coating. *Nature Communications* **12** (1), 5624. DOI: 10.1038/s41467-021-25898-5.

[39] M.-C. Tang et al. (2021). Wide and Tunable Bandgap MAPbBr3-xClx Hybrid Perovskites with Enhanced Phase Stability: In Situ Investigation and Photovoltaic Devices. *Solar RRL* **5** (4), 2000718. DOI: 10.1002/solr.202000718.

[40] T. Kodalle et al. (2023). Revealing the Transient Formation Dynamics and Optoelectronic Properties of 2D Ruddlesden-Popper Phases on 3D Perovskites. *Advanced Energy Materials* **13** (33), 2201490. DOI: 10.1002/aenm.202201490.

[41] K. Schötz et al. (2021). Understanding Differences in the Crystallization Kinetics between One-Step Slot-Die Coating and Spin Coating of MAPbI3 Using Multimodal In Situ Optical Spectroscopy. *Advanced Optical Materials* **9** (21), 2101161. DOI: 10.1002/adom.202101161.

[42] M. Chauhan et al. (2020). Investigating two-step MAPbI 3 thin film formation during spin coating by simultaneous in situ absorption and photoluminescence spectroscopy. *Journal of Materials Chemistry A* **8** (10), 5086–5094. DOI: 10.1039/C9TA12409H.

[43] K. Schötz and F. Panzer (2021). Using In Situ Optical Spectroscopy to Elucidate Film Formation of Metal Halide Perovskites. *The Journal of Physical Chemistry A* **125** (11), 2209–2225. DOI: 10.1021/acs.jpca.0c10765.

[44] L. Bi et al. (2023). Deciphering the Roles of MA-Based Volatile Additives for alpha-FAPbI3 to Enable Efficient Inverted Perovskite Solar Cells. *Journal of the American Chemical Society*. DOI: 10.1021/jacs.2c13566.

[45] O. Shargaieva, H. Näsström, J. Li, D. M. Többens, and E. L. Unger (2021). Temperature-Dependent Crystallization Mechanisms of Methylammonium Lead Iodide Perovskite From Different Solvents. *Frontiers in Energy Research* **9**. DOI: 10.3389/fenrg.2021.749604.

[46] K. Suchan, J. Just, P. Becker, E. L. Unger, and T. Unold (2020). Optical in situ monitoring during the synthesis of halide perovskite solar cells reveals formation kinetics and evolution of optoelectronic properties. *Journal of Materials Chemistry A* **8** (20), 10439–10449. DOI: 10.1039/D0TA01237H.

[47] L. Zhang et al. (2021). High-performance quasi-2D perovskite light-emitting diodes: from materials to devices. *Light: Science & Applications* **10** (1), 61. DOI: 10.1038/s41377-021-00501-0.

[48] X. Jiang et al. (2023). Mixing Dion–Jacobson and Ruddlesden–Popper Structures in Quasi-2D Perovskite Films for Thermal- and Photo-Stable Stimulated Emission. *Advanced Optical Materials* **11** (21), 2300806. DOI: 10.1002/adom.202300806.

[49] B. Saparov and D. B. Mitzi (2016). Organic–Inorganic Perovskites: Structural Versatility for Functional Materials Design. *Chemical Reviews* **116** (7), 4558–4596. DOI: 10.1021/acs.chemrev.5b00715.

[50] L. Mao, Y. Wu, C. C. Stoumpos, M. R. Wasielewski, and M. G. Kanatzidis (2017). White-Light Emission and Structural Distortion in New Corrugated Two-Dimensional Lead Bromide Perovskites. *Journal of the American Chemical Society* **139** (14), 5210–5215. DOI: 10.1021/jacs.7b01312.

[51] P. Ramming et al. (2021). Suppressed ion migration in powder-based perovskite thick films using an ionic liquid. *Journal of Materials Chemistry C* **9** (35), 11827–11837. DOI: 10.1039/D1TC01554K.

[52] S. Tie et al. (2020). Robust Fabrication of Hybrid Lead-Free Perovskite Pellets for Stable X-ray Detectors with Low Detection Limit. *Advanced Materials* **32** (31), 2001981. DOI: 10.1002/adma.202001981.

[53] C. Witt et al. (2020). Impact of Pressure and Temperature on the Compaction Dynamics and Layer Properties of Powder-Pressed Methylammonium Lead Halide Thick Films. *ACS Applied Electronic Materials* **2** (8), 2619–2628. DOI: 10.1021/acsaelm.0c00493.

[54] S. Shrestha et al. (2017). High-performance direct conversion X-ray detectors based on sintered hybrid lead triiodide perovskite wafers. *Nature Photonics* **11** (7), 436–440. DOI: 10.1038/nphoton.2017.94.

[55] C. Witt et al. (2022). How the Microstructure of MAPbI3 Powder Impacts Pressure-Induced Compaction and Optoelectronic Thick-Film Properties. *The Journal of Physical Chemistry C* **126** (36), 15424–15435. DOI: 10.1021/acs.jpcc.2c03329.

[56] C. Zhou et al. (2024). Vacuum Processed Metal Halide Perovskite Light-Emitting Diodes. *Advanced Functional Materials* **34** (8), 2307682. DOI: 10.1002/adfm.202307682.

[57] Q. Guesnay et al. (2024). Pizza Oven Processing of Organohalide Perovskites (POPOP): A Simple, Versatile and Efficient Vapor Deposition Method. *Advanced Energy Materials* **14** (10), 2303423. DOI: 10.1002/aenm.202303423.

[58] T. Schramm et al. (2024). Electrical Doping of Metal Halide Perovskites by Co-evaporation and Application in PN Junctions. *Advanced Materials* **n/a**, 2314289. DOI: 10.1002/adma.202314289.

[59] F. Panzer et al. (2016). Compact Layers of Hybrid Halide Perovskites Fabricated via the Aerosol Deposition Process-Uncoupling Material Synthesis and Layer Formation. *Materials* **9** (4), 277. DOI: 10.3390/ma9040277.

[60] A. These et al. (2021). Characterization of Aerosol Deposited Cesium Lead Tribromide Perovskite Films on Interdigited ITO Electrodes. *Advanced Electronic Materials* **7** (3), 2001165. DOI: 10.1002/aelm.202001165.

[61] M.-Y. Cho et al. (2021). Unique Noncontact Monitoring of Human Respiration and Sweat Evaporation Using a CsPb2Br5-Based Sensor. *ACS Applied Materials & Interfaces* **13** (4), 5602–5613. DOI: 10.1021/acsami.0c21097.

[62] N. Leupold, A. L. Seibel, R. Moos, and F. Panzer (2021). Electrical Conductivity of Halide Perovskites Follows Expectations from Classical Defect Chemistry. *European Journal of Inorganic Chemistry* **2021** (28), 2882–2889. DOI: 10.1002/ejic.202100381.

[63] N. Leupold et al. (2019). High Versatility and Stability of Mechanochemically Synthesized Halide Perovskite Powders for Optoelectronic Devices. *ACS Applied Materials & Interfaces* **11** (33), 30259–30268. DOI: 10.1021/acsami.9b09160.

[64] W. Massmann (1956). Toxicological Investigations on Dimethylformamide. *Occupational and Environmental Medicine* **13** (1), 51–54. DOI: 10.1136/oem.13.1.51.

[65] G. L. Kennedy (1986). Acute and Subchronic Toxicity of Dimethylformam Ide and Dimethylacetamide Following Various Routes of Administration. *Drug and Chemical Toxicology* **9** (2), 147–170. DOI: 10.3109/01480548608998272.

[66] A. K. Jena, A. Kulkarni, and T. Miyasaka (2019). Halide Perovskite Photovoltaics: Background, Status, and Future Prospects. *Chemical Reviews* **119** (5), 3036–3103. DOI: 10.1021/acs.chemrev.8b00539.

[67] F. Yang et al. (2021). Upscaling Solution-Processed Perovskite Photovoltaics. *Advanced Energy Materials* **11** (42), 2101973. DOI: 10.1002/aenm.202101973.

[68] D. B. Ritzer et al. (2022). Upscaling of perovskite solar modules: The synergy of fully evaporated layer fabrication and all-laser-scribed interconnections. *Progress in Photovoltaics: Research and Applications* **30** (4), 360–373. DOI: 10.1002/pip.3489.

[69] J. Warby et al. (2022). Understanding Performance Limiting Interfacial Recombination in pin Perovskite Solar Cells. *Advanced Energy Materials* **12** (12), 2103567. DOI: 10.1002/aenm.202103567.

[70] L. Schmidt-Mende et al. (2021). Roadmap on organic–inorganic hybrid perovskite semiconductors and devices. *APL Materials* **9** (10), 109202. DOI: 10.1063/5.0047616.

[71] J.-E. Jeong, J. H. Park, C. H. Jang, M. H. Song, and H. Y. Woo (2020). Multifunctional Charge Transporting Materials for Perovskite Light-Emitting Diodes. *Advanced Materials* **32** (51), 2002176. DOI: 10.1002/adma.202002176.

[72] H. J. Snaith and M. Grätzel (2006). Enhanced charge mobility in a molecular hole transporter via addition of redox inactive ionic dopant: Implication to dye-sensitized solar cells. *Applied Physics Letters* **89** (26), 262114. DOI: 10.1063/1.2424552.

[73] T. Leijtens, J. Lim, J. Teuscher, T. Park, and H. J. Snaith (2013). Charge Density Dependent Mobility of Organic Hole-Transporters and Mesoporous TiO2 Determined by Transient Mobility Spectroscopy: Implications to Dye-Sensitized and Organic Solar Cells. *Advanced Materials* **25** (23), 3227–3233. DOI: 10.1002/adma.201300947.

[74] A. Abate et al. (2013). Lithium salts as "redox active" p-type dopants for organic semiconductors and their impact in solid-state dye-sensitized solar cells. *Physical Chemistry Chemical Physics* **15** (7), 2572–2579. DOI: 10.1039/C2CP44397J.

[75] P. Agarwala and D. Kabra (2017). A review on triphenylamine (TPA) based organic hole transport materials (HTMs) for dye sensitized solar cells (DSSCs) and perovskite solar cells (PSCs): evolution and molecular engineering. *Journal of Materials Chemistry A* **5** (4), 1348–1373. DOI: 10.1039/C6TA08449D.

[76] U. Bach et al. (1998). Solid-state dye-sensitized mesoporous TiO2 solar cells with high photon-to-electron conversion efficiencies. *Nature* **395** (6702), 583–585. DOI: 10.1038/26936.

[77] U. B. Cappel, T. Daeneke, and U. Bach (2012). Oxygen-Induced Doping of Spiro-MeOTAD in Solid-State Dye-Sensitized Solar Cells and Its Impact on Device Performance. *Nano Letters* **12** (9), 4925–4931. DOI: 10.1021/nl302509q.

[78] F. M. Rombach, S. A. Haque, and T. J. Macdonald (2021). Lessons learned from spiro-OMeTAD and PTAA in perovskite solar cells. *Energy & Environmental Science*. DOI: 10.1039/D1EE02095A.

[79] M. Xu et al. (2013). Improvement in Solid-State Dye Sensitized Solar Cells by p-Type Doping with Lewis Acid SnCl4. *The Journal of Physical Chemistry C* **117** (44), 22492–22496. DOI: 10.1021/jp406506d.

[80] B. Xu et al. (2014). AgTFSI as p-Type Dopant for Efficient and Stable Solid-State Dye-Sensitized and Perovskite Solar Cells. *ChemSusChem* **7** (12), 3252–3256. DOI: 10.1002/cssc.201402678.

[81] Y. Yao et al. (2022). Organic Hole-Transport Layers for Efficient, Stable, and Scalable Inverted Perovskite Solar Cells. *Advanced Materials* **34** (44), 2203794. DOI: 10.1002/adma.202203794.

[82] Q. Zhu et al. (2024). LiTFSI-Free Hole Transport Materials for Robust Perovskite Solar Cells and Modules with High Efficiencies. *ACS Applied Materials & Interfaces*. DOI: 10.1021/acsami.3c17468.

[83] G. Rose (1840). Ueber einige neue Mineralien des Urals. *Journal für Praktische Chemie* **19** (1), 459–468. DOI: 10.1002/prac.18400190179.

[84] L. M. Herz (2016). Charge-Carrier Dynamics in Organic-Inorganic Metal Halide Perovskites. *Annual Review of Physical Chemistry* **67** (1), 65–89. DOI: 10.1146/annurev-physchem-040215-112222.

[85] T. Miyasaka, ed. (2022). *Perovskite Photovoltaics and Optoelectronics*. Weinheim: Wiley VCH Verlag GmbH.

[86] V. M. Goldschmidt (1926). Die Gesetze der Krystallochemie. *Naturwissenschaften* **14** (21), 477–485. DOI: 10.1007/BF01507527.

[87] M. A. Peña and J. L. G. Fierro (2001). Chemical Structures and Performance of Perovskite Oxides. *Chemical Reviews* **101** (7), 1981–2018. DOI: 10.1021/cr980129f.

[88] A. M. Glazer (1972). The classification of tilted octahedra in perovskites. *Acta Crystallographica Section B: Structural Crystallography and Crystal Chemistry* **28** (11), 3384–3392. DOI: 10.1107/S0567740872007976.

[89] H. L. Wells (1893). Über die Cäsium- und Kalium-Bleihalogenide. *Zeitschrift für anorganische Chemie* **3** (1), 195–210. DOI: 10.1002/zaac.18930030124.

[90] D. Weber (1978). CH3NH3PbX3, ein Pb(II)-System mit kubischer Perowskitstruktur / CH3NH3PbX3, a Pb(II)-System with Cubic Perovskite Structure. *Zeitschrift für Naturforschung B* **33** (12), 1443–1445. DOI: 10.1515/znb-1978-1214.

[91] S. X. Tao, X. Cao, and P. A. Bobbert (2017). Accurate and efficient band gap predictions of metal halide perovskites using the DFT-1/2 method: GW accuracy with DFT expense. *Scientific Reports* **7** (1), 14386. DOI: 10.1038/s41598-017-14435-4.

[92] F. Brivio, A. B. Walker, and A. Walsh (2013). Structural and electronic properties of hybrid perovskites for high-efficiency thin-film photovoltaics from first-principles. *APL Materials* **1** (4), 042111. DOI: 10.1063/1.4824147.

[93] E. Mosconi, A. Amat, M. K. Nazeeruddin, M. Grätzel, and F. De Angelis (2013). First-Principles Modeling of Mixed Halide Organometal Perovskites for Photovoltaic Applications. *The Journal of Physical Chemistry C* **117** (27), 13902–13913. DOI: 10.1021/jp4048659.

[94] K. Tanaka et al. (2003). Comparative study on the excitons in lead-halide-based perovskite-type crystals CH3NH3PbBr3 CH3NH3PbI3. *Solid State Communications* **127** (9), 619–623. DOI: 10.1016/S0038-1098(03)00566-0.

[95] G. E. Eperon et al. (2014). Formamidinium lead trihalide: a broadly tunable perovskite for efficient planar heterojunction solar cells. *Energy & Environmental Science* **7** (3), 982–988. DOI: 10.1039/C3EE43822H.

[96] C. C. Stoumpos, C. D. Malliakas, and M. G. Kanatzidis (2013). Semiconducting Tin and Lead Iodide Perovskites with Organic Cations: Phase Transitions, High Mobilities, and Near-Infrared Photoluminescent Properties. *Inorganic Chemistry* **52** (15), 9019–9038. DOI: 10.1021/ic401215x.

[97] N. K. Noel et al. (2014). Lead-free organic–inorganic tin halide perovskites for photovoltaic applications. *Energy & Environmental Science* **7** (9), 3061–3068. DOI: 10.1039/C4EE01076K.

[98] F. Hao, C. C. Stoumpos, D. H. Cao, R. P. H. Chang, and M. G. Kanatzidis (2014). Lead-free solid-state organic–inorganic halide perovskite solar cells. *Nature Photonics* **8** (6), 489–494. DOI: 10.1038/nphoton.2014.82.

[99] C. Wehrenfennig, G. E. Eperon, M. B. Johnston, H. J. Snaith, and L. M. Herz (2014). High Charge Carrier Mobilities and Lifetimes in Organolead Trihalide Perovskites. *Advanced Materials* **26** (10), 1584–1589. DOI: 10.1002/adma.201305172.

[100] Y. Yamada, T. Nakamura, M. Endo, A. Wakamiya, and Y. Kanemitsu (2014). Photocarrier Recombination Dynamics in Perovskite CH3NH3PbI3 for Solar Cell Applications. *Journal of the American Chemical Society* **136** (33), 11610–11613. DOI: 10.1021/ja506624n.

[101] C. S. J. Ponseca et al. (2014). Organometal Halide Perovskite Solar Cell Materials Rationalized: Ultrafast Charge Generation, High and Microsecond-Long Balanced Mobilities, and Slow Recombination. *Journal of the American Chemical Society* **136** (14), 5189–5192. DOI: 10.1021/ja412583t.

[102] S. D. Stranks et al. (2013). Electron-Hole Diffusion Lengths Exceeding 1 Micrometer in an Organometal Trihalide Perovskite Absorber. *Science* **342** (6156), 341–344. DOI: 10.1126/science.1243982.

[103] Q. Lin, A. Armin, R. C. R. Nagiri, P. L. Burn, and P. Meredith (2015). Electro-optics of perovskite solar cells. *Nature Photonics* **9** (2), 106–112. DOI: 10.1038/nphoton.2014.284.

[104] M. Sendner et al. (2016). Optical phonons in methylammonium lead halide perovskites and implications for charge transport. *Materials Horizons* **3** (6), 613–620. DOI: 10.1039/C6MH00275G.

[105] S. D. Stranks and H. J. Snaith (2015). Metal-halide perovskites for photovoltaic and light-emitting devices. *Nature Nanotechnology* **10** (5), 391–402. DOI: 10.1038/nnano.2015.90.

[106] D. W. DE Quilettes et al. (2015). Impact of microstructure on local carrier lifetime in perovskite solar cells. *Science* **348** (6235), 683–686. DOI: 10.1126/science.aaa5333.

[107] K. Schötz, A. M. Askar, A. Köhler, K. Shankar, and F. Panzer (2020). Investigating the Tetragonal-to-Orthorhombic Phase Transition of Methylammonium Lead Iodide Single Crystals by Detailed Photoluminescence Analysis. *Advanced Optical Materials* **8** (17), 2000455. DOI: 10.1002/adom.202000455.

[108] T. Meier et al. (2018). Impact of excess PbI2 on the structure and the temperature dependent optical properties of methylammonium lead iodide perovskites. *Journal of Materials Chemistry C* **6** (28), 7512–7519. DOI: 10.1039/C8TC02237B.

[109] C. Quarti et al. (2016). Structural and optical properties of methylammonium lead iodide across the tetragonal to cubic phase transition: implications for perovskite solar cells. *Energy & Environmental Science* **9** (1), 155–163. DOI: 10.1039/C5EE02925B.

[110] Y. Kawamura, H. Mashiyama, and K. Hasebe (2002). Structural Study on Cubic–Tetragonal Transition of CH3NH3PbI3. *Journal of the Physical Society of Japan* **71** (7), 1694–1697. DOI: 10.1143/JPSJ.71.1694.

[111] A. Poglitsch and D. Weber (1987). Dynamic disorder in methylammoniumtrihalogenoplumbates (II) observed by millimeter-wave spectroscopy. *The Journal of Chemical Physics* **87** (11), 6373–6378. DOI: 10.1063/1.453467.

[112] F. Zhang et al. (2020). Advances in two-dimensional organic–inorganic hybrid perovskites. *Energy & Environmental Science* **13** (4), 1154–1186. DOI: 10.1039/C9EE03757H.

[113] C. Ortiz-Cervantes, P. Carmona-Monroy, and D. Solis-Ibarra (2019). Two-Dimensional Halide Perovskites in Solar Cells: 2D or not 2D? *ChemSusChem* **12** (8), 1560–1575. DOI: 10.1002/cssc.201802992.

[114] N. K. Tailor et al. (2021). Advances in Lead-Free Perovskite Single Crystals: Fundamentals and Applications. *ACS Materials Letters* **3** (7), 1025–1080. DOI: 10.1021/acsmaterialslett.1c00242.

[115] K. Dave, W.-T. Huang, and R.-S. Liu (2023). All Inorganic Lead-Free Zero-Dimensional Metal Halide Luminescent Materials and Applications. *Crystals* **13** (3), 499. DOI: 10.3390/cryst13030499.

[116] S. Sun et al. (2021). 0D Perovskites: Unique Properties, Synthesis, and Their Applications. *Advanced Science* **8** (24), 2102689. DOI: 10.1002/advs.202102689.

[117] L. Mao et al. (2018). Hybrid Dion–Jacobson 2D Lead Iodide Perovskites. *Journal of the American Chemical Society* **140** (10), 3775–3783. DOI: 10.1021/jacs.8b00542.

[118] D. B. Straus and C. R. Kagan (2018). Electrons, Excitons, and Phonons in Two-Dimensional Hybrid Perovskites: Connecting Structural, Optical, and Electronic Properties. *The Journal of Physical Chemistry Letters* **9** (6), 1434–1447. DOI: 10.1021/acs.jpclett.8b00201.

[119] Z. Guo, X. Wu, T. Zhu, X. Zhu, and L. Huang (2016). Electron–Phonon Scattering in Atomically Thin 2D Perovskites. *ACS Nano* **10** (11), 9992–9998. DOI: 10.1021/acsnano.6b04265.

[120] P. Gao, A. R. Bin Mohd Yusoff, and M. K. Nazeeruddin (2018). Dimensionality engineering of hybrid halide perovskite light absorbers. *Nature Communications* **9** (1), 5028. DOI: 10.1038/s41467-018-07382-9.

[121] C. M. M. Soe et al. (2019). Structural and thermodynamic limits of layer thickness in 2D halide perovskites. *Proceedings of the National Academy of Sciences* **116** (1), 58–66. DOI: 10.1073/pnas.1811006115.

[122] B. A. Connor, A. C. Su, A. H. Slavney, L. Leppert, and H. I. Karunadasa (2023). Understanding the evolution of double perovskite band structure upon dimensional reduction. *Chemical Science* **14** (42), 11858–11871. DOI: 10.1039/D3SC03105E.

[123] G. Wu et al. (2022). Surface Passivation Using 2D Perovskites toward Efficient and Stable Perovskite Solar Cells. *Advanced Materials* **34** (8), 2105635. DOI: 10.1002/adma.202105635.

[124] F. Wang et al. (2016). Phenylalkylamine Passivation of Organolead Halide Perovskites Enabling High-Efficiency and Air-Stable Photovoltaic Cells. *Advanced Materials* **28** (45), 9986–9992. DOI: 10.1002/adma.201603062.

[125] X. Xiao et al. (2018). Suppressed Ion Migration along the In-Plane Direction in Layered Perovskites. *ACS Energy Letters* **3** (3), 684–688. DOI: 10.1021/acsenergylett.8b00047.

[126] J. Jeong et al. (2021). Pseudo-halide anion engineering for alpha-FAPbI3 perovskite solar cells. *Nature* **592** (7854), 381–385. DOI: 10.1038/s41586-021-03406-5.

[127] S. Kahmann, E. K. Tekelenburg, H. Duim, M. E. Kamminga, and M. A. Loi (2020). Extrinsic nature of the broad photoluminescence in lead iodide-based Ruddlesden–Popper perovskites. *Nature Communications* **11** (1), 2344. DOI: 10.1038/s41467-020-15970-x.

[128] R. Gautier, M. Paris, and F. Massuyeau (2019). Exciton Self-Trapping in Hybrid Lead Halides: Role of Halogen. *Journal of the American Chemical Society* **141** (32), 12619–12623. DOI: 10.1021/jacs.9b04262.

[129] D. Cortecchia, J. Yin, A. Petrozza, and C. Soci (2019). White light emission in low-dimensional perovskites. *Journal of Materials Chemistry C* **7** (17), 4956–4969. DOI: 10.1039/C9TC01036J.

[130] M. D. Smith, A. Jaffe, E. R. Dohner, A. M. Lindenberg, and H. I. Karunadasa (2017). Structural origins of broadband emission from layered Pb–Br hybrid perovskites. *Chemical Science* **8** (6), 4497–4504. DOI: 10.1039/C7SC01590A.

[131] J. Yin, H. Li, D. Cortecchia, C. Soci, and J.-L. Brédas (2017). Excitonic and Polaronic Properties of 2D Hybrid Organic–Inorganic Perovskites. *ACS Energy Letters* **2** (2), 417–423. DOI: 10.1021/acsenergylett.6b00659.

[132] N. F. Mott and A. M. Stoneham (1977). The lifetime of electrons, holes and excitons before self-trapping. *Journal of Physics C: Solid State Physics* **10** (17), 3391. DOI: 10.1088/0022-3719/10/17/022.

[133] O. Telschow et al. (2022). Preserving the stoichiometry of triple-cation perovskites by carrier-gas-free antisolvent spraying. *Journal of Materials Chemistry A* **10** (37), 19743–19749. DOI: 10.1039/D1TA10566C.

[134] S.-G. Kim et al. (2021). How antisolvent miscibility affects perovskite film wrinkling and photovoltaic properties. *Nature Communications* **12** (1), 1554. DOI: 10.1038/s41467-021-21803-2.

[135] J. Li et al. (2020). Highly Efficient Thermally Co-evaporated Perovskite Solar Cells and Mini-modules. *Joule* **4** (5), 1035–1053. DOI: 10.1016/j.joule.2020.03.005.

[136] S. Biberger et al. (2022). How the ionic liquid BMIMBF4 influences the formation and optoelectronic properties of MAPbI3 thin films. *Journal of Materials Chemistry A* **10** (35), 18038–18049. DOI: 10.1039/D2TA04448J.

[137] R. Swartwout, M. T. Hoerantner, and V. Bulović (2019). Scalable Deposition Methods for Large-area Production of Perovskite Thin Films. *ENERGY & ENVIRONMENTAL MATERIALS* **2** (2), 119–145. DOI: 10.1002/eem2.12043.

[138] S. Biberger et al. (2023). First of Their Kind: Solar Cells with a Dry-Processed Perovskite Absorber Layer via Powder Aerosol Deposition and Hot-Pressing. *Solar RRL* **7** (16), 2300261. DOI: 10.1002/solr.202300261.

[139] L. Gao and Q. Yan (2020). Recent Advances in Lead Halide Perovskites for Radiation Detectors. *Solar RRL* **4** (2), 1900210. DOI: 10.1002/solr.201900210.

[140] X. Fang et al. (2017). Annealing-free perovskite films based on solvent engineering for efficient solar cells. *Journal of Materials Chemistry C* **5** (4), 842–847. DOI: 10.1039/C6TC04944C.

[141] C.-S. Du, I.-H. Ho, Y.-J. Huang, and R.-H. Lee (2022). Quaternary ammonium halide-containing cellulose derivatives for defect passivation in MAPbI3-based perovskite solar cells. *Sustainable Energy & Fuels* **6** (14), 3349–3362. DOI: 10.1039/D2SE00516F.

[142] S. Lee et al. (2020). In situ study of the film formation mechanism of organic–inorganic hybrid perovskite solar cells: controlling the solvate phase using an additive system. *Journal of Materials Chemistry A* **8** (16), 7695–7703. DOI: 10.1039/D0TA00048E.

[143] N. J. Jeon et al. (2014). Solvent engineering for high-performance inorganic–organic hybrid perovskite solar cells. *Nature Materials* **13** (9), 897–903. DOI: 10.1038/nmat4014.

[144] N. Leupold and F. Panzer (2021). Recent Advances and Perspectives on Powder-Based Halide Perovskite Film Processing. *Advanced Functional Materials* **31** (14), 2007350. DOI: 10.1002/adfm.202007350.

[145] B. A. Rosales, L. Wei, and J. Vela (2019). Synthesis and mixing of complex halide perovskites by solvent-free solid-state methods. *Journal of Solid State Chemistry* **271**, 206–215. DOI: 10.1016/j.jssc.2018.12.054.

[146] P. Pal, S. Saha, A. Banik, A. Sarkar, and K. Biswas (2018). All-Solid-State Mechanochemical Synthesis and Post-Synthetic Transformation of Inorganic Perovskite-type Halides. *Chemistry – A European Journal* **24** (8), 1811–1815. DOI: 10.1002/chem.201705682.

[147] F. Palazon et al. (2019). Mechanochemical synthesis of inorganic halide perovskites: evolution of phase-purity, morphology, and photoluminescence. *Journal of Materials Chemistry C* **7** (37), 11406–11410. DOI: 10.1039/C9TC03778K.

[148] M. C. Alvarez-Galván et al. (2019). Crystal Growth, Structural Phase Transitions, and Optical Gap Evolution of CH3NH3Pb(Br1–xClx)3 Perovskites. *Crystal Growth & Design* **19** (2), 918–924. DOI: 10.1021/acs.cgd.8b01463.

[149] F. Zhu et al. (2015). Shape Evolution and Single Particle Luminescence of Organometal Halide Perovskite Nanocrystals. *ACS Nano* **9** (3), 2948–2959. DOI: 10.1021/nn507020s.

[150] R. Singh, S. Sandhu, H. Yadav, and J.-J. Lee (2019). Stable Triple-Cation (Cs+–MA+–FA+) Perovskite Powder Formation under Ambient Conditions for Hysteresis-Free High-Efficiency Solar Cells. *ACS Applied Materials & Interfaces* **11** (33), 29941–29949. DOI: 10.1021/acsami.9b09121.

[151] B. A. Rosales et al. (2016). Persistent Dopants and Phase Segregation in Organolead Mixed-Halide Perovskites. *Chemistry of Materials* **28** (19), 6848–6859. DOI: 10.1021/acs.chemmater.6b01874.

[152] B. A. Rosales et al. (2017). Lead Halide Perovskites: Challenges and Opportunities in Advanced Synthesis and Spectroscopy. *ACS Energy Letters* **2** (4), 906–914. DOI: 10.1021/acsenergylett.6b00674.

[153] J. Akedo (2008). Room Temperature Impact Consolidation (RTIC) of Fine Ceramic Powder by Aerosol Deposition Method and Applications to Microdevices. *Journal of Thermal Spray Technology* **17** (2), 181–198. DOI: 10.1007/s11666-008-9163-7.

[154] C. Witt et al. (2023). Orientation and Grain Size in MAPbI3 Thin Films: Influence on Phase Transition, Disorder and Defects. *Journal of Physical Chemistry C* **127** (22), 10563–10573. DOI: doi.org/10.1021/acs.jpcc.2c08968.

[155] E. Gibson, ed. (2019). *Solar Energy Capture Materials*. The Royal Society of Chemistry. DOI: 10.1039/9781788013512.

[156] M. M. Lee, J. Teuscher, T. Miyasaka, T. N. Murakami, and H. J. Snaith (2012). Efficient Hybrid Solar Cells Based on Meso-Superstructured Organometal Halide Perovskites. *Science* **338** (6107), 643–647. DOI: 10.1126/science.1228604.

[157] J.-H. Im, C.-R. Lee, J.-W. Lee, S.-W. Park, and N.-G. Park (2011). 6.5% efficient perovskite quantum-dot-sensitized solar cell. *Nanoscale* **3** (10), 4088–4093. DOI: 10.1039/C1NR10867K.

[158] I. Chung, B. Lee, J. He, R. P. H. Chang, and M. G. Kanatzidis (2012). All-solid-state dye-sensitized solar cells with high efficiency. *Nature* **485** (7399), 486–489. DOI: 10.1038/nature11067.

[159] Y. Zhao and K. Zhu (2013). Charge Transport and Recombination in Perovskite (CH3NH3)PbI3 Sensitized TiO2 Solar Cells. *The Journal of Physical Chemistry Letters* **4** (17), 2880–2884. DOI: 10.1021/jz401527q.

[160] D. Liu and T. L. Kelly (2014). Perovskite solar cells with a planar heterojunction structure prepared using room-temperature solution processing techniques. *Nature Photonics* **8** (2), 133–138. DOI: 10.1038/nphoton.2013.342.

[161] M. Saliba et al. (2018). How to Make over 20% Efficient Perovskite Solar Cells in Regular (n–i–p) and Inverted (p–i–n) Architectures. *Chemistry of Materials* **30** (13), 4193–4201. DOI: 10.1021/acs.chemmater.8b00136.

[162] J. Carrillo et al. (2016). Ionic Reactivity at Contacts and Aging of Methylammonium Lead Triiodide Perovskite Solar Cells. *Advanced Energy Materials* **6** (9), 1502246. DOI: 10.1002/aenm.201502246.

[163] Y. Zhao et al. (2017). Mobile-Ion-Induced Degradation of Organic Hole-Selective Layers in Perovskite Solar Cells. *The Journal of Physical Chemistry C* **121** (27), 14517–14523. DOI: 10.1021/acs.jpcc.7b04684.

[164] Y. Meng et al. (2022). Energy Transfer Induced by TADF Polymer Enables the Recycling of Excitons in Perovskite Solar Cells. *Advanced Functional Materials* **n/a**, 2210600. DOI: 10.1002/adfm.202210600.

[165] Y. M. Ou et al. (2021). Rational design of D–π–D hole-transporting materials for efficient perovskite solar cells. *Materials Chemistry Frontiers* **5** (21), 7824–7832. DOI: 10.1039/D1QM01015H.

[166] N. Arora et al. (2017). Perovskite solar cells with CuSCN hole extraction layers yield stabilized efficiencies greater than 20%. *Science* **358** (6364), 768–771. DOI: 10.1126/science.aam5655.

[167] Y. Wei et al. (2023). Star-Shaped Organic Semiconductor with Extraordinary Thermomechanical Property and Solution Processability for Stable Perovskite Solar Cells. *Advanced Functional Materials* **33** (43), 2307501. DOI: 10.1002/adfm.202307501.

[168] G.-W. Kim et al. (2020). Hole Transport Materials in Conventional Structural (n–i–p) Perovskite Solar Cells: From Past to the Future. *Advanced Energy Materials* **10** (8), 1903403. DOI: 10.1002/aenm.201903403.

[169] W. Li, E. Martínez-Ferrero, and E. Palomares (2024). Self-assembled molecules as selective contacts for efficient and stable perovskite solar cells. *Materials Chemistry Frontiers* **8** (3), 681–699. DOI: 10.1039/D3QM01017A.

[170] J. Hu et al. (2023). Triiodide Attacks the Organic Cation in Hybrid Lead Halide Perovskites: Mechanism and Suppression. *Advanced Materials* **35** (40), 2303373. DOI: 10.1002/adma.202303373.

[171] W. Demtröder (2016). *Experimentalphysik 3 - Atome, Moleküle und Festkörper*. Springer-Verlag GmbH.

[172] A. Köhler and H. Bässler (2015). *Electronic Processes in Organic Semiconductors*. Weinheim: Wiley VCH Verlag GmbH.

[173] B. Chen, M. Yang, S. Priya, and K. Zhu (2016). Origin of J–V Hysteresis in Perovskite Solar Cells. *The Journal of Physical Chemistry Letters* **7** (5), 905–917. DOI: 10.1021/acs.jpclett.6b00215.

[174] W. Tress (2017). Metal Halide Perovskites as Mixed Electronic–Ionic Conductors: Challenges and Opportunities—From Hysteresis to Memristivity. *The Journal of Physical Chemistry Letters* **8** (13), 3106–3114. DOI: 10.1021/acs.jpclett.7b00975.

[175] H.-S. Kim and N.-G. Park (2014). Parameters Affecting I–V Hysteresis of CH3NH3PbI3 Perovskite Solar Cells: Effects of Perovskite Crystal Size and Mesoporous TiO2 Layer. *The Journal of Physical Chemistry Letters* **5** (17), 2927–2934. DOI: 10.1021/jz501392m.

[176] H. J. Snaith et al. (2014). Anomalous Hysteresis in Perovskite Solar Cells. *The Journal of Physical Chemistry Letters* **5** (9), 1511–1515. DOI: 10.1021/jz500113x.

[177] D.-H. Kang and N.-G. Park (2019). On the Current–Voltage Hysteresis in Perovskite Solar Cells: Dependence on Perovskite Composition and Methods to Remove Hysteresis. *Advanced Materials* **31** (34), 1805214. DOI: 10.1002/adma.201805214.

[178] E. L. Unger, A. Czudek, H.-S. Kim, and W. Tress (2020). Chapter 4 - Current-voltage analysis: lessons learned from hysteresis. In: *Characterization Techniques for Perovskite Solar Cell Materials*. Ed. by M. Pazoki, A. Hagfeldt, and T. Edvinsson. Micro and Nano Technologies. Elsevier, 81–108. DOI: 10.1016/B978-0-12-814727-6.00004-9.

[179] J.-W. Lee et al. (2017). The Interplay between Trap Density and Hysteresis in Planar Heterojunction Perovskite Solar Cells. *Nano Letters* **17** (7), 4270–4276. DOI: 10.1021/acs.nanolett.7b01211.

[180] D. W. Miller et al. (2016). Defect states in perovskite solar cells associated with hysteresis and performance. *Applied Physics Letters* **109** (15), 153902. DOI: 10.1063/1.4963760.

[181] H.-S. Kim et al. (2015). Control of I–V Hysteresis in CH3NH3PbI3 Perovskite Solar Cell. *The Journal of Physical Chemistry Letters* **6** (22), 4633–4639. DOI: 10.1021/acs.jpclett.5b02273.

[182] O. Almora et al. (2015). Capacitive Dark Currents, Hysteresis, and Electrode Polarization in Lead Halide Perovskite Solar Cells. *The Journal of Physical Chemistry Letters* **6** (9), 1645–1652. DOI: 10.1021/acs.jpclett.5b00480.

[183] J. Wei et al. (2014). Hysteresis Analysis Based on the Ferroelectric Effect in Hybrid Perovskite Solar Cells. *The Journal of Physical Chemistry Letters* **5** (21), 3937–3945. DOI: 10.1021/jz502111u.

[184] W. Ma et al. (2020). Reducing Anomalous Hysteresis in Perovskite Solar Cells by Suppressing the Interfacial Ferroelectric Order. *ACS Applied Materials & Interfaces* **12** (10), 12275–12284. DOI: 10.1021/acsami.9b20988.

[185] A. Dualeh et al. (2014). Impedance Spectroscopic Analysis of Lead Iodide Perovskite-Sensitized Solid-State Solar Cells. *ACS Nano* **8** (1), 362–373. DOI: 10.1021/nn404323g.

[186] C. Li et al. (2016). Iodine Migration and its Effect on Hysteresis in Perovskite Solar Cells. *Advanced Materials* **28** (12), 2446–2454. DOI: 10.1002/adma.201503832.

[187] W. Tress et al. (2015). Understanding the rate-dependent J–V hysteresis, slow time component, and aging in CH3NH3PbI3 perovskite solar cells: the role of a compensated electric field. *Energy & Environmental Science* **8** (3), 995–1004. DOI: 10.1039/C4EE03664F.

[188] G. Richardson et al. (2016). Can slow-moving ions explain hysteresis in the current–voltage curves of perovskite solar cells? *Energy & Environmental Science* **9** (4), 1476–1485. DOI: 10.1039/C5EE02740C.

[189] S. N. Habisreutinger, N. K. Noel, and H. J. Snaith (2018). Hysteresis Index: A Figure without Merit for Quantifying Hysteresis in Perovskite Solar Cells. *ACS Energy Letters* **3** (10), 2472–2476. DOI: 10.1021/acsenergylett.8b01627.

[190] E. H. Balaguera and J. Bisquert (2024). Accelerating the Assessment of Hysteresis in Perovskite Solar Cells. *ACS Energy Letters*, 478–486. DOI: 10.1021/acsenergylett.3c02779.

[191] S. Meloni et al. (2016). Ionic polarization-induced current–voltage hysteresis in CH3NH3PbX3 perovskite solar cells. *Nature Communications* **7** (1), 10334. DOI: 10.1038/ncomms10334.

[192] Y. Shao et al. (2016). Grain boundary dominated ion migration in polycrystalline organic–inorganic halide perovskite films. *Energy & Environmental Science* **9** (5), 1752–1759. DOI: 10.1039/C6EE00413J.

[193] P.-W. Liang et al. (2014). Additive Enhanced Crystallization of Solution-Processed Perovskite for Highly Efficient Planar-Heterojunction Solar Cells. *Advanced Materials* **26** (22), 3748–3754. DOI: 10.1002/adma.201400231.

[194] N. De Marco et al. (2016). Guanidinium: A Route to Enhanced Carrier Lifetime and Open-Circuit Voltage in Hybrid Perovskite Solar Cells. *Nano Letters* **16** (2), 1009–1016. DOI: 10.1021/acs.nanolett.5b04060.

[195] D.-H. Kang, C. Ma, and N.-G. Park (2022). Antiseptic Povidone–Iodine Heals the Grain Boundary of Perovskite Solar Cells. *ACS Applied Materials & Interfaces* **14** (7), 8984–8991. DOI: 10.1021/acsami.1c21479.

[196] W. Zhao et al. (2022). Symmetrical Acceptor–Donor–Acceptor Molecule as a Versatile Defect Passivation Agent toward Efficient FA0.85MA0.15PbI3 Perovskite Solar Cells. *Advanced Functional Materials* **32** (19), 2112032. DOI: 10.1002/adfm.202112032.

[197] F. Zhang et al. (2018). Suppressing defects through the synergistic effect of a Lewis base and a Lewis acid for highly efficient and stable perovskite solar cells. *Energy & Environmental Science* **11** (12), 3480–3490. DOI: 10.1039/C8EE02252F.

[198] S. Y. Park and K. Zhu (2022). Advances in SnO2 for Efficient and Stable n–i–p Perovskite Solar Cells. *Advanced Materials* **34** (27), 2110438. DOI: 10.1002/adma.202110438.

[199] J. Thiesbrummel et al. (2021). Universal Current Losses in Perovskite Solar Cells Due to Mobile Ions. *Advanced Energy Materials* **11** (34), 2101447. DOI: 10.1002/aenm.202101447.

[200] L. Zhang, X. Zhou, C. Liu, X. Wang, and B. Xu (2020). A Review on Solution-Processable Dopant-Free Small Molecules as Hole-Transporting Materials for Efficient Perovskite Solar Cells. *Small Methods* **4** (9), 2000254. DOI: https://doi.org/10.1002/smtd.202000254.

[201] V. Manjunath, S. Bimli, P. A. Shaikh, S. B. Ogale, and R. S. Devan (2022). Understanding the role of inorganic carrier transport layer materials and interfaces in emerging perovskite solar cells. *Journal of Materials Chemistry C* **10** (42), 15725–15780. DOI: 10.1039/D2TC02911A.

[202] M. Degani et al. (2021). 23.7% Efficient inverted perovskite solar cells by dual interfacial modification. *Science Advances* **7** (49), eabj7930. DOI: 10.1126/sciadv.abj7930.

[203] P. Xu et al. (2021). Simultaneous Passivation of the SnO2/Perovskite Interface and Perovskite Absorber Layer in Perovskite Solar Cells Using KF Surface Treatment. *ACS Applied Energy Materials* **4** (10), 10921–10930. DOI: 10.1021/acsaem.1c01893.

[204] Z. Cheng et al. (2021). Interfacial and Permeating Modification Effect of n-type Non-fullerene Acceptors toward High-Performance Perovskite Solar Cells. *ACS Applied Materials & Interfaces* **13** (34), 40778–40787. DOI: 10.1021/acsami.1c13447.

[205] T. Bu et al. (2018). Universal passivation strategy to slot-die printed SnO2 for hysteresis-free efficient flexible perovskite solar module. *Nature Communications* **9** (1), 4609. DOI: 10.1038/s41467-018-07099-9.

[206] R. Yin et al. (2021). Dual-Interface Modification with BMIMPF6 for High-Efficiency and Stable Carbon-Based CsPbI2Br Perovskite Solar Cells. *ACS Applied Energy Materials* **4** (9), 9294–9303. DOI: 10.1021/acsaem.1c01521.

[207] M. T. Hörantner et al. (2016). Shunt-Blocking Layers for Semitransparent Perovskite Solar Cells. *Advanced Materials Interfaces* **3** (10), 1500837. DOI: 10.1002/admi.201500837.

[208] Y. Galagan, E. W. C. Coenen, W. J. H. Verhees, and R. Andriessen (2016). Towards the scaling up of perovskite solar cells and modules. *Journal of Materials Chemistry A* **4** (15), 5700–5705. DOI: 10.1039/C6TA01134A.

[209] D. Prochowicz et al. (2020). Suppressing recombination in perovskite solar cells via surface engineering of TiO2 ETL. *Solar Energy* **197**, 50–57. DOI: 10.1016/j.solener.2019.12.070.

[210] D. Glowienka and Y. Galagan (2022). Light Intensity Analysis of Photovoltaic Parameters for Perovskite Solar Cells. *Advanced Materials* **34** (2), 2105920. DOI: 10.1002/adma.202105920.

[211] D. Głowienka et al. (2020). Role of surface recombination in perovskite solar cells at the interface of HTL/CH3NH3PbI3. *Nano Energy* **67**, 104186. DOI: 10.1016/j.nanoen.2019.104186.

[212] W. Tress et al. (2018). Interpretation and evolution of open-circuit voltage, recombination, ideality factor and subgap defect states during reversible light-soaking and irreversible degradation of perovskite solar cells. *Energy & Environmental Science* **11** (1), 151–165. DOI: 10.1039/C7EE02415K.

[213] P. Caprioglio et al. (2020). On the Origin of the Ideality Factor in Perovskite Solar Cells. *Advanced Energy Materials* **10** (27), 2000502. DOI: 10.1002/aenm.202000502.

[214] I. Riedel et al. (2004). Effect of Temperature and Illumination on the Electrical Characteristics of Polymer–Fullerene Bulk-Heterojunction Solar Cells. *Advanced Functional Materials* **14** (1), 38–44. DOI: 10.1002/adfm.200304399.

[215] F. Gao et al. (2014). Trap-Induced Losses in Hybrid Photovoltaics. *ACS Nano* **8** (4), 3213–3221. DOI: 10.1021/nn501185h.

[216] M. Stolterfoht et al. (2018). Visualization and suppression of interfacial recombination for high-efficiency large-area pin perovskite solar cells. *Nature Energy* **3** (10), 847–854. DOI: 10.1038/s41560-018-0219-8.

[217] M. Schwoerer and H. C. Wolf (2005). *Organische Molekulare Festkörper*. Weinheim: Wiley VCH Verlag GmbH.

[218] H. Bässler (1993). Charge Transport in Disordered Organic Photoconductors a Monte Carlo Simulation Study. *physica status solidi (b)* **175** (1), 15–56. DOI: 10.1002/pssb.2221750102.

[219] H. Bässler and A. Köhler (2012). Charge Transport in Organic Semiconductors. In: *Unimolecular and Supramolecular Electronics I: Chemistry and Physics Meet at Metal-Molecule Interfaces*. Ed. by R. M. Metzger. Topics in Current Chemistry. Berlin, Heidelberg: Springer, 1–65. DOI: 10.1007/128_2011_218.

[220] K. Walzer, B. Maennig, M. Pfeiffer, and K. Leo (2007). Highly Efficient Organic Devices Based on Electrically Doped Transport Layers. *Chemical Reviews* **107** (4), 1233–1271. DOI: 10.1021/cr050156n.

[221] H. Shirakawa, E. J. Louis, A. G. MacDiarmid, C. K. Chiang, and A. J. Heeger (1977). Synthesis of electrically conducting organic polymers: halogen derivatives of polyacetylene, (CH)x. *Journal of the Chemical Society, Chemical Communications* (16), 578–580. DOI: 10.1039/C39770000578.

[222] G. Parthasarathy, C. Shen, A. Kahn, and S. R. Forrest (2001). Lithium doping of semiconducting organic charge transport materials. *Journal of Applied Physics* **89** (9), 4986–4992. DOI: 10.1063/1.1359161.

[223] J. Blochwitz, M. Pfeiffer, T. Fritz, and K. Leo (1998). Low voltage organic light emitting diodes featuring doped phthalocyanine as hole transport material. *Applied Physics Letters* **73** (6), 729–731. DOI: 10.1063/1.121982.

[224] I. Salzmann, G. Heimel, M. Oehzelt, S. Winkler, and N. Koch (2016). Molecular Electrical Doping of Organic Semiconductors: Fundamental Mechanisms and Emerging Dopant Design Rules. *Accounts of Chemical Research* **49** (3), 370–378. DOI: 10.1021/acs.accounts.5b00438.

[225] B. Lüssem, M. Riede, and K. Leo (2013). Doping of organic semiconductors. *physica status solidi (a)* **210** (1), 9–43. DOI: 10.1002/pssa.201228310.

[226] H. Méndez et al. (2013). Doping of Organic Semiconductors: Impact of Dopant Strength and Electronic Coupling. *Angewandte Chemie International Edition* **52** (30), 7751–7755. DOI: 10.1002/anie.201302396.

[227] H. Méndez et al. (2015). Charge-transfer crystallites as molecular electrical dopants. *Nature Communications* **6** (1), 8560. DOI: 10.1038/ncomms9560.

[228] I. Salzmann and G. Heimel (2015). Toward a comprehensive understanding of molecular doping organic semiconductors (review). *Journal of Electron Spectroscopy and Related Phenomena*. Organic Electronics **204**, 208–222. DOI: 10.1016/j.elspec.2015.05.001.

[229] M. L. Tietze et al. (2018). Elementary steps in electrical doping of organic semiconductors. *Nature Communications* **9** (1), 1182. DOI: 10.1038/s41467-018-03302-z.

[230] I. Salzmann et al. (2012). Intermolecular Hybridization Governs Molecular Electrical Doping. *Physical Review Letters* **108** (3), 035502. DOI: 10.1103/PhysRevLett.108.035502.

[231] S. Wang et al. (2016). Role of 4-tert-Butylpyridine as a Hole Transport Layer Morphological Controller in Perovskite Solar Cells. *Nano Letters* **16** (9), 5594–5600. DOI: 10.1021/acs.nanolett.6b02158.

[232] J. H. Noh et al. (2013). Nanostructured TiO2/CH3NH3PbI3 heterojunction solar cells employing spiro-OMeTAD/Co-complex as hole-transporting material. *Journal of Materials Chemistry A* **1** (38), 11842–11847. DOI: 10.1039/C3TA12681A.

[233] J. Burschka, F. Kessler, M. K. Nazeeruddin, and M. Grätzel (2013). Co(III) Complexes as p-Dopants in Solid-State Dye-Sensitized Solar Cells. *Chemistry of Materials* **25** (15), 2986–2990. DOI: 10.1021/cm400796u.

[234] G. Ren et al. (2021). Strategies of modifying spiro-OMeTAD materials for perovskite solar cells: a review. *Journal of Materials Chemistry A* **9** (8), 4589–4625. DOI: 10.1039/D0TA11564A.

[235] S. Bai et al. (2019). Planar perovskite solar cells with long-term stability using ionic liquid additives. *Nature* **571** (7764), 245–250. DOI: 10.1038/s41586-019-1357-2.

17 Full list of Publications

1. **Atomic-level insight into the postsynthesis band gap engineering of a Lewis base polymer using Lewis acid tris (pentafluorophenyl) borane**
   Brett Yurash, Dirk Leifert, GN Manjunatha Reddy, David Xi Cao, Simon Biberger, Viktor V Brus, Martin Seifrid, Peter J Santiago, Anna Köhler, Bradley F Chmelka, Guillermo C Bazan, Thuc-Quyen Nguyen
   in *Chemistry of Materials*, **2019**, 9 31, 17, 6715-6725

2. **Structural Diversity in Layered Hybrid Perovskites, A_2PbBr_4 or $AA'PbBr_4$, Templated by Small Disc-Shaped Amines**
   Yuan-Yuan Guo, Lin-Jie Yang, Simon Biberger, Jason A McNulty, Teng Li, Konstantin Schötz, Fabian Panzer, Philip Lightfoot
   in *Inorganic Chemistry*, **2020**, 59, 17, 12858–12866

3. **Posttreatment of powder aerosol deposited oxide ceramic films by high power LED**
   Tobias Nazarenus, Kira Schlesier, Simon Biberger, Jörg Exner, Jaroslaw Kita, Anna Köhler, Ralf Moos
   in *International Journal of Applied Ceramic Technologies*, **2022**, 19, 1540–1553

4. **Intricacies and Mechanism of p-Doping Spiro-MeOTAD Using $Cu(TFSI)_2$**
   Adrian Hochgesang, Simon Biberger, Jeannine Grüne, John Mohanraj, Frank-Julian Kahle, Vladimir Dyakonov, Anna Köhler, Mukundan Thelakkat
   in *Advanced Electronic Materials*, **2022**, 8, 10, 2200113

5. **How the ionic liquid $BMIMBF_4$ influences the formation and optoelectronic properties of $MAPbI_3$ thin films**
   Simon Biberger, Konstantin Schötz, Philipp Ramming, Nico Leupold, Ralf Moos, Anna Köhler, Helen Grüninger, Fabian Panzer
   in *Journal of Materials Chemistry A*, **2022**, 10, 35, 18038-18049

6. **Orientation and Grain Size in $MAPbI_3$ Thin Films: Influence on Phase Transition, Disorder and Defects**
   Christina Witt, Konstantin Schötz, Meike Kuhn, Nico Leupold, Simon Biberger, Philipp Ramming, Anna Köhler, Ralf Moos, Eva M. Herzig, Fabian Panzer
   in *The Journal of Physical Chemistry C*, **2023**, 127, 22, 10563-10573

7. **First of their kind: Solar cells with a dry-processed perovskite absorber layer via powder aerosol deposition and hot-pressing**
   Simon Biberger*, Nico Leupold*, Christina Witt*, Christopher Greve, Paul Markus, Philipp Ramming, Daniel Lukas, Konstantin Schötz, Frank-Julian Kahle, Chenhui Zhu, Georg Papastavrou, Eva M. Herzig, Anna Köhler, Ralf Moos, Fabian Panzer (*Contributed equally)
   in *Solar RRL*, **2023**, 2300261

8. **Reactive Spin Coating based on Real-Time In-Situ Feedback for Improved Control of Perovskite Thin Film Fabrication**
   Simon Biberger, Maximilian Spies, Konstantin Schötz, Frank-Julian Kahle, Nico Leupold, Ralf Moos, Helen Grüninger, Anna Köhler, Fabian Panzer
   in *Journal of Materials Chemistry C*, **2024**, 12, 6415-6422

Danksagung

An dieser Stelle möchte ich mich bei allen bedanken, die mich während meiner Promotion und bei der Entstehung dieser Arbeit unterstützt haben.

Zu allererst möchte ich bei Prof. Dr. Anna Köhler für die Gelegenheit bedanken, diese Arbeit an ihrem Lehrstuhl durchzuführen und für die Betreuung meiner Arbeit. Vielen Dank auch dafür, dass du immer ein offenes Ohr für mich hattest und es mir immer ermöglichst hast, an diversen Konferenzen teilzunehmen und sogar ein paar Monate in Australien zu verbringen. Mir haben die vergangenen acht Jahre in deiner Arbeitsgruppe sehr viel Spaß gemacht.

Mindestens genauso viel Dank schulde ich Dr. habil. Fabian Panzer. Vielen Dank, dass du mich in die Perovskit-Gruppe aufgenommen hast und mich und meine Projekte, auch nach deiner offiziellen Zeit an der Uni, immer mit Begeisterung und vollem Einsatz betreut und begleitest hast. Ohne dich wäre diese Arbeit in der Form nicht möglich gewesen. Auch möchte mich bei dir bedanken, dass du mir die Möglichkeit für Forschungsaufenthalte in Frankreich und Südkorea gegeben hast. Ich bin froh ein Teil deiner Pero-Gruppe gewesen zu sein.

Auch bei Dr. Julian Kahle möchte ich mich bedanken. Du hast immer ein offenes Ohr und eine Idee, wenn Probleme im Laboralltag auftreten. Vielen Danke für deine Ratschläge und deine Hilfe über die Bachelor-, Master- und Promotionszeit hinweg.

Besonderer Dank geht ebenfalls an Dr. Konstantin Schötz. Deine Ideen, wertvollen Hinweise und die vielen Diskussionen, für die du dir immer Zeit genommen hast, haben sehr zum Gelingen der einzelnen Projekte beigetragen. Mit dir und dem Rest des Kompetenzzentrums für In-Situ Spektroskopie (Tobias Siegert und Maximilian Spies) gab es immer gute Stimmung im Büro.

Natürlich auch vielen Dank für die gute Atmosphäre und Stimmung an den Rest der Pero-Gruppe – Nico Leupold, Christina Witt, Philipp Ramming, Maximilian Schultz, Lorenz Kiel, Markus Griesbach – und den Organikern – Dani Kroh, Andrei Stankevich, Rishab Saxena, Stefan Wedler. Ohne euch und alle, die ich nicht genannt habe, hätte der Alltag im und außerhalb des Labors nur halb so viel Spaß gemacht.

Ebenfalls möchte ich mich bei Irene Bauer, Christina Gräbner und Frank Schirmer bedanken, bei Irene und Christina für ihre Hilfe bei allen chemischen Problemen und Fragen und bei Frank für seine Unterstützung bei allen technischen Problemen. Ohne euch würde unsere Arbeit nicht so reibungslos laufen!

Danke auch an Dani, Meike Kuhn, Andreas Erhardt und Eliza Rokhsat, die maßgeblich dazu beigetragen haben, dass meine Zeit in Australien ein Highlight meiner Promotion geworden ist.

Ein großer Dank geht an Dr. Joe Renner, Jana Kehrer, Simon Durst, Miriam Bloß, Annelie Müller, Andreas Schneider und Magdalena Haaf. Vielen Dank für die vielen schönen Abende und Wochenenden (mit vielleicht wieder zu viel Physik-Diskussionen :D), an denen ich wieder neue Energie für die manchmal frustrierenden Tage im Labor sammeln konnte.

Natürlich will ich meinen Eltern und meinem Bruder besonders danken für die bedingungslose Unterstützung während meines Studiums und der Promotion. Ich wusste und weiß es sehr zu schätzen, welche Möglichkeiten und Chancen ihr mir eröffnet habt.

Last, but not least, gilt mein größter Dank meiner Frau Anja für die uneingeschränkte Unterstützung in jeder Situation und dein Verständnis, wenn es wieder mal später wurde oder am Wochenende noch etwas erledigt werden musste. Danke auch dafür, dass du mir immer wieder klar gemacht hast, dass Experimente und deren Ergebnisse nicht das Wichtigste im Leben sind. Ich bin gespannt, was das Leben in Zukunft für uns bereithält. Love you!

Eidesstattliche Versicherung

Hiermit versichere ich an Eides statt, dass ich die vorliegende Arbeit selbstständig verfasst und keine anderen als die von mir angegebenen Quellen und Hilfsmittel verwendet habe.

Weiterhin erkläre ich, dass ich die Hilfe von gewerblichen Promotionsberatern bzw. –vermittlern oder ähnlichen Dienstleistern weder bisher in Anspruch genommen habe, noch künftig in Anspruch nehmen werde.

Zusätzlich erkläre ich hiermit, dass ich keinerlei frühere Promotionsversuche unternommen habe.

Bayreuth, den